

# MICROBEAM ANALYSIS

## 1979

Dale E. Newbury, *Editor*

Proceedings of the 14th Annual Conference  
of the  
Microbeam Analysis Society  
San Antonio, Texas, 12-17 August 1979



*San Francisco Press, Inc.*

547 Howard Street, San Francisco, California 94105

Dale E. Newbury, Ed., *Microbeam Analysis* — 1979  
Copyright © 1979 by San Francisco Press, Inc., 547 Howard St., San Francisco, CA 94105

*Printed in the U.S.A.*

*ISSN 0146-6725*



## Foreword

It has been my privilege to act as the technical program chairman for the 14th Annual Conference of the Microbeam Analysis Society (San Antonio, Texas, 13-17 August 1979), a joint meeting with the Electron Microscopy Society of America. I have been greatly aided in arranging the technical program by several of my colleagues who have undertaken the organization of sessions on specialized topics: Edgar Etz, National Bureau of Standards ("Raman Microanalysis"); Philip DeNee, Inhalation Toxicology Research Institute ("Back-scattered Electron Imaging in Scanning Electron Microscopy"); Ronald Warner, Harvard University ("Biological Microanalysis"); and Noel MacDonald, Physical Electronics Industries ("Surface Microanalysis"). In addition, I wish to acknowledge the special aid of the officers of the Microbeam Analysis Society: David Kyser, IBM (President); Robert Myklebust, National Bureau of Standards (Secretary); and Roger Bolon, General Electric Research and Development (Treasurer).

The publication of the Proceedings of the 14th Annual Conference of the Microbeam Analysis Society marks a major change in the format of the Society's annual publication. By agreement with the San Francisco Press, Inc., the MAS Proceedings will now be published as a bound, citable volume. Furthermore, San Francisco Press, Inc., will now act as the distributor for the MAS Proceedings, including past volumes, where available. MAS looks forward to a long and fruitful association with the San Francisco Press.

As evidenced by the fine papers submitted to this year's conference, the members of MAS continue to lead microanalysis efforts in many branches of science and technology. In addition, the interests of MAS are clearly broadening with the introduction of new techniques. The 1979 Conference contains sessions on analytical electron microscopy, which extends conventional electron probe microanalysis into much finer spatial resolution; and on laser Raman microanalysis, a molecular microanalysis technique that complements the elemental analysis derived from the techniques of x-ray, electron, and ion microanalysis. Interest still remains high in the continued development of quantitative electron-probe microanalysis and its extensions to specimens of special scientific and technological importance: particles, films, and rough samples. Finally, in these Proceedings a new feature is introduced that we hope will be continued in future volumes, a detailed bibliography on a specific subject of interest in microanalysis. Charles Fiori of the National Institutes of Health has prepared an exhaustive bibliography on energy-dispersive x-ray spectrometry to initiate this series.

For those who have the good fortune to attend the 14th Conference, the oral presentations of the papers and the subsequent discussions will be a rich source of information. For others who cannot attend, I hope the published Proceedings will aid them in obtaining a view of the current state of the art and science of microanalysis.

DALE E. NEWBURY  
Technical Program Chairman  
Microbeam Analysis Society

*National Bureau of Standards, 1979*

## Table of Contents\*

Foreword (Newbury), *iii*

Officers of the Microbeam Analysis Society (1979), *vii*

MAS sustaining members' information, *viii*

### 1. SCANNING ELECTRON MICROSCOPY (BACKSCATTERED ELECTRON IMAGING), 1

Backscattered electron imaging of biological specimens (Carter), 1

Visualization by backscattered electron imaging of the accessory (outer dense) fibers and mitochondria of sperm (Becker, Vogel), 3

Application of heavy-metal staining ( $\text{OsO}_4$ )/backscattered electron imaging technique to the study of organic aerosols (DeNee, Carpenter), 8

Application of SEM backscattered electron imaging to the study of the effects of fibrous glass and asbestos on lung tissue (DeNee, Rebar, DeNicola, Pickrell), 11

Backscattered electron imaging for automated particulate analysis (Lee, Kelly), 15

Type-2 magnetic contrast with normal electron incidence in the SEM (Wells, Savoy), 17

The preparation of ceramic surfaces for selected-area electron channeling (Davidson, Lankford), 22

Full surface examination of small spheres with a computer-controlled SEM (Ward, Willenborg, Montgomery), 27

### 2. MONTE CARLO TECHNIQUES IN ELECTRON MICROSCOPY AND MICROANALYSIS, 30

Application of Monte Carlo calculation technique to quantitative analysis by Auger electron spectroscopy (Shimizu, Ichimura, Aratama; invited paper), 30

Monte Carlo simulation of electron scattering at 1-10 keV and its application to thin-film analysis (Murata, Kotera, Nagami; invited paper), 35

Monte Carlo simulation applied to electron microprobe thickness measurement of lead-tin oxide films (Cvikevich, Pihl), 39

Electron microprobe analysis of antireflection coatings for silicon solar cells with Monte Carlo simulation (Armigliato, Desalvo, Rinaldi, Rosa, Ruffini), 43

Determination of thin-film composition or thickness from electron-probe data by Monte Carlo calculations (Miller, Koffman), 47

Monte Carlo calculations of absolute x-ray generation from solid targets (Newbury, Myklebust), 51

### 3. BIOLOGICAL MICROANALYSIS, 54

Electron probe analysis of muscle: A progress report (Somlyo, Shuman, Somlyo; invited paper), 54

Electron probe microanalysis of bulk frozen hydrated biological samples (Lechene; invited paper), 59

Secondary ion mass spectrometry: Applications to biological problems (Burns; invited paper), 61

Recent advances of laser microprobe mass analysis (LAMMA) as applied to biological and engineering specimens (Kaufmann, Heinen, Schürmann, Wechsung; invited paper), 63

Minimum detectable concentrations with the liquid-droplet technique (Quinton, Warner, Lechene), 73

Instrumental factors affecting the accuracy of microprobe quantitation of electrolyte concentrations in frozen sections (Tormey, Platz), 77

Ultrastructural analysis of biliary calculi (McConville), 80

Electron irradiation products from organic materials and implications for microanalysis of biological sections (Edie, Glick), 81

Microanalysis of elemental distributions in minerals and cells performed with a proton microprobe (Martin), 85

### 4. APPLICATIONS, 91

Automated WDS qualitative and quantitative microanalysis in geosciences (Giraud, Remond, Pajon, Henoc, Conty, Tong), 91

Automated electron microprobe identification of minerals in stream sediments for the National Uranium Resources Evaluation program (Mosley), 101

---

\*An Author Index appears on p. 382.

Interactions of simulated waste radionuclides and rocks (Hlava, Hinkebein), 103  
 Relative abundance of common elements in coal macerals (Raymond), 105  
 EPMA--SEM as tools in the investigation of hydrocracking processes (Packwood, Kriz, Patmore), 110  
 Microprobe examination of nitrogen and oxygen contamination in zirconium alloys (Bohning), 114

5. ANALYTICAL ELECTRON MICROSCOPY, 117  
 Multiple scattering of fast electrons in thin specimens (Rez), 117  
 Determination of Cliff-Lorimer k calibration factors for thin-foil x-ray microanalysis of Na, Mg, and Al in the STEM (Mehta, Goldstein, Williams, Romig), 119  
 Detectability limit and spatial resolution in STEM x-ray analysis: Application to Fe-Ni alloys (Romig, Goldstein), 124  
 A comparison of procedures for quantitative x-ray analysis in thin films (Sabatini, Pande), 129  
 Sulfur and phosphorus segregation in duplex stainless steel weld metal (Lyman), 135  
 The use of TEM and SEM for the detection of individual submicrometer-size sulfate and nitrate particles (Mamane, Pueschel), 139  
 Calculations of instrument response to plasmon excitations in EELS (Farrow, Joy, Maher), 141  
 Electron energy losses and associated secondary-electron emission of carbon, oxygen, and hydrogen on metals (Pellerin, Fontaine, Le Gressus, Duraud), 145

6. RAMAN MICROANALYSIS, 148  
 Raman microprobe characterization of South Pole aerosols (Cunningham, Etz, Zoller), 148  
 Developments and applications of the MOLE laser Raman microprobe (Dhamelincourt; invited paper), 155  
 Raman microanalysis of SiO source materials by means of MOLE (Adar, Mitchell, Ramsey), 165  
 Raman microprobe study of biological mineralization *in situ*: Enamel of the rat incisor (Casciani, Etz), 169  
 Investigations into the critical measurement aspects of Raman microprobe analysis (Etz, Blaha), 173  
 The development of instrumentation for microparticle analysis by Raman spectroscopy (Landon), 185  
 Inelastic light scattering from a distribution of microparticles (Benner, Dornhaus, Long, Chang), 191  
 Design considerations in a micro-Raman spectrometer (Hirschfeld), 196

7. QUANTITATIVE X-RAY MICROANALYSIS, 197  
 Prospects for improved correction procedures in EPMA (Love, Scott), 197  
 The effect of the critical excitation potential on the x-ray absorption in electron probe analysis (Heinrich, Myklebust), 201  
 Determination of x-ray WDS efficiency for absolute and relative intensity measurements (Bolon, McConnell, Gill), 204  
 Some investigations for the determination of the spatial distribution of the ionization density (Dudek), 211  
 EDS k-ratio determination using a minimum set of standards (Jackson, Strobe), 215  
 Statistical parameters useful for characterizing samples by electron microprobe (Fricke, Gray), 218  
 Microhomogeneity studies of NBS standards (Marinenko, Heinrich, Ruegg), 221  
 An empirical investigation into possible nonlinearities of the microprobe correction factors in the system MgO-CaO-Al<sub>2</sub>O<sub>3</sub>-SiO (Shaw, Albee), 227  
 The use and abuse of a quantitative analysis procedure for energy-dispersive x-ray microanalysis (Myklebust, Newbury), 231  
 Quantitative analysis by  $\phi(\rho z)$  curves (Brown, Robinson), 231  
 Quantitative carbon analysis from  $\phi(\rho z)$  curves (Brown, von Rosenstiel, Krisch), 241  
 Analysis of particles and rough samples of FRAME P, a ZAF method incorporating peak-to-background measurements (Small, Newbury, Myklebust), 243

A ZAF procedure for microprobe analysis based on measurement of peak-to-background ratios (Statham), 247

Rapid quantitative analysis of individual particles by energy-dispersive spectrometry (Aden, Buseck), 254

Quantitative analysis of multiphase samples (Russ), 259

Computer evaluation of photon, electron, and proton-induced x-ray spectra (Van Espen, Nullens, Maenhaut), 265

Modifications and extensions of NBS FRAME C (Russ), 268

EDATA2: A FORTRAN IV computer program for processing wavelength- and/or energy-dispersive electron microprobe analyses (Smith, Gold), 273

A user-oriented software system for electron microprobes (Chambers, Doyle), 279

New topics about an on-line correction procedure (Henoc, Conty, Tong), 281

Elemental distribution maps and line profiles in x-ray analysis (Skinner, Barbi), 285

New methods to obtain and present SEM x-ray line scans (Russ), 292

A new technique for beam current normalization in energy-dispersive analysis (McCarthy), 305

Applications of a digital scan generator to EDS analysis (McCarthy), 307

Backscatter electron detectors on energy-dispersive x-ray spectrometers (Hayashi, Bolon), 310

8. SURFACE MICROANALYSIS, 311

Auger electron spectroscopy (AES) for characterization of semiconductor manufacturing processes (Brandis, Wildman; invited paper), 311

Simultaneous multitechnique analysis; SEM, SAM, and EDX (Hovland, Gerlach; invited paper), 315

Applications of surface analytic techniques to materials science (Marcus; invited paper), 317

Accuracy of quantitative Auger analysis of Cr-Fe-Ni alloys (Bacon, Morris), 318

High-resolution scanning Auger electron microscope equipped with a field-emission gun (Todokoro, Sakitani, Fukuhara, Okajima), 319

Extending replicating methods to Auger spectroscopy by using conductive replicas (DeGroot, Scott), 321

Detection of monolayer quantities of carbon and oxygen on surfaces using energy-dispersive x-ray spectrometry (Musket, Strausser), 324

Reconstructing the outer few Ångströms of a surface by SIMS and ISS techniques (Sparrow), 325

Secondary-ion mass spectrometry using selected primary ions and variation of the partial pressure of selected gases in the specimen region (Guo, Wittry), 333

The influence of instrumental sensitivity variations on quantitative analysis by secondary-ion mass spectrometry (Newbury), 335

Ion probe analysis of natural olivine: Secondary ion intensity variation and systematics for a simple binary silicate (Steele, Hutcheon), 338

Adaption of the Deitz detector to an ARL ion microprobe mass analyzer (Wittry, Guo), 341

Use of the IMS 3F high mass resolving power (Gourgot, Lepareur, Conty), 343

Element distributions in geological materials by image processing of scanning ion microprobe data (Schilling), 345

Quantitative ion microprobe analysis of chlorine in selenium (LaForce, Short), 350

Quantitative analysis of Se alloy thin films by ion-microprobe mass analysis and transmission electron microscopy (LaForce, Johnson), 354

Energy-dispersive detectors: A bibliography (Fiori), 361

Author index, 382

## Officers of the Microbeam Analysis Society (1979)

President: David Kyser  
1258 Pampas Drive  
San Jose, CA 95120

President Elect: Oliver C. Wells  
1324 LeLand Drive  
Yorktown Heights, NY 10598

Past President: James D. Brown  
95 Cumberland Drive  
London, Ont., Canada N5X 1B7

Secretary: Robert L. Myklebust  
Chemistry 222/A121  
National Bureau of Standards  
Washington, DC 20234

Treasurer: Roger B. Bolon  
R.D. #2 Lake Road  
Ballston, NY 12019

### Members at Large

<p>Mary C. Finn Lincoln Laboratory 244 Wood Street Lexington, MA 02173</p>	<p>Noel C. MacDonald Physical Electronics Industries, Inc. 6509 Flying Cloud Drive Eden Prairie, MN 55343</p>	<p>Dale E. Newbury Chemistry 222/A121 National Bureau of Standards Washington, DC 20234</p>
--	---	---

### Honorary Members

<p>L. S. Birks Naval Research Laboratory Washington, DC 20390</p>	<p>L. L. Marton<sup>†</sup> Museum of History and Technology Smithsonian Institution Washington, DC 20560</p>	<p>I. B. Borovskii Institute of Solid State Physics Academy of Sciences Moscow, U.S.S.R.</p>
<p>Peter Duncumb Tube Investments Research Laboratories North Saffron Walden, Essex, England</p>	<p>Raymond Castaing University of Paris Faculté des Sciences Orsay, France</p>	<p>V. E. Cosslett The Cavendish Laboratory University of Cambridge Cambridge, England</p>
	<p>Gunji Shinoda Osaka University Osaka, Japan</p>	

---

<sup>†</sup>Deceased 1979.

## MAS Sustaining Members' Information

### AMR CORPORATION

160 Middlesex Turnpike  
Bedford, MA 01730

Contact: K. A. Lindberg, (616) 275-1400

Product Line: Manufacturer and distributor of scanning electron microscopes and a complete line of accessories.

#### Sales Offices:

Mid Atlantic--George Russell and Ken Benoit  
Mid Eastern--Parker Brinkman  
Southeast--Floyd Hunsaker

### APPLIED RESEARCH LABORATORIES

9545 Wentworth Street  
P. O. Box 129  
Sunland, CA 91040

Contact: Bryce I. Hanna, (213) 352-6011

Product Line: Electron microprobes, ion microprobes, optical emission spectrometers, x-ray fluorescence instrumentation.

#### Sales Offices:

239 Newburyport Turnpike, Topsfield, MA 01983, (617) 887-8995  
20200 W. Outer Drive, Dearborn, MI 48124, (313) 565-6633  
842 Hamilton Mall, Allentown, PA 18101, (215) 434-7441

### BABCOCK AND WILCOX RESEARCH CENTER

Alliance Research Center  
P. O. Box 835  
Alliance, OH 44601

Contact: Alex S. Miller, (216) 821-9110 Ext. 360

### CAMECA INSTRUMENTS, INC.

37 Brownhouse Road  
Stamford, CT 06902

Contact: Robert J. Hessler, (203) 348-5252

Product Line: Electron probe analyzers, scanning electron microscopes, combination SEM/EMP instruments and ion mass analyzers. The IMS-800, a new SIMS instrument, has the features of improved performance at a lower price. The new IMS is the only direct imaging instrument available. The CAMECA MBX is a flexible combination SEM/EMP with an extensive array of accessories.

#### Sales Office:

Robert D. Boies, P. O. Box 262, Reedley, CA 93654, (209) 266-6372  
Thomas Fisher, 37 Brownhouse Rd., Stamford, CT 06902, (203) 348-5252

## EDAX INTERNATIONAL, INC.

103 Schelter Rd.  
P. O. Box 135  
Prairie View, IL 60069

Contact: Luis F. Lopez, (312) 634-0600

Product Line: Manufactures energy-dispersive x-ray analysis systems for x-ray microanalysis in SEMs, TEMs, electron probes, as well as energy-dispersive x-ray fluorescence spectrometers. System configurations from basic qualitative to fully automated quantitative (with computer control and data processing) are available, including an automated WD/ED system with stage and spectrometer controls.

### Sales Offices:

V. Balmer, 637 Sunnyside Rd., Vermilion, OH 44089, (216) 967-4148  
Frank Mannino, 769 Shadow Lake Dr., Thousand Oaks, CA 91360, (805) 495-1632

## EG & G/ORTEC

100 Midland Road  
Oak Ridge, TN 37830

Contact: Michael J. Kirchoff, (615) 482-4411 Ext. 500

Product Line: Energy-dispersive systems for electron optical microscopes of all types. Wavelength dispersive system electronics. Backscattered electron detection systems.

### Sales Offices:

Val Johnson, P. O. Box 1678, Boulder, CO 80306, (303) 449-5933  
Gene Embry, P. O. Box 631, Cary, NC 27511, (919) 467-8028  
Charles Thomas, 24222 Via Luisa, Mission Viejo, CA 92675, (800) 251-9732  
Nick Alen, 5257 Arquilla Dr., Richton Park, IL 60471, (800) 251-9732  
Bob Bardorf, P. O. Box 3355, Oak Ridge, TN 37830, (615) 482-9072  
Tim Bates and Jacqueline Rams, Suite 311, 11800 Sunrise Valley Dr., Reston, VA, (800) 336-0122

## ETEC CORPORATION

3392 Investment Boulevard  
Hayward, CA 94545

Contact: Mrs. P. J. Breton, (415) 783-9210

Product Line: High-performance electron microprobes and scanning electron microscopes. Modular design allows alternative configurations to be offered with a wide range of retrofitable accessories. Instruments are available for manual operation, with automated control through dedicated minicomputers, with shielding for imaging and analysis of radioactive materials, and for laboratory and manufacturing electron beam lithography. Microbeam products include: Autoscan, Omniscan, Autoprobe, LEBES, Vistascan, Viewpoint, Biosea, and ADRES.

### Sales Offices:

Throughout the USA: Call toll-free (800) 227-1222 or (415) 783-9210

## GERHARD WITZSTROCK PUBLISHING HOUSE INC.

381 Park Avenue So.  
Suite 1123  
New York, NY 10016

Contact: Roger L. Manwaring, (212) 686-7280

Product Line: Publishes SCANNING: INTERNATIONAL JOURNAL OF SCANNING ELECTRON MICROSCOPY AND RELATED METHODS. SCANNING provides an international and interdisciplinary medium for the rapid exchange of information between all scientists interested in scanning



electron microscopy. It publishes original scholarly papers, which are of a practical nature, reporting new analytical, methodological, and specimen preparation aspects of scanning electron microscopy.

#### INTERNATIONAL SCIENTIFIC INSTRUMENTS, INC.

3255-6C Scott Blvd.  
Santa Clara, CA 95050

Contact: Robert Ruscica, (408) 249-9840

Product Line: Scanning electron microscopes with a full complement of accessories including WDX spectrometers. The ISI SEM line includes: Alpha-9, Super IIIA, ISI-40, ISI-60A, and ISI S-100A. A complete line of scanning electron microscopes suited for any application and budget.

#### Sales Offices:

Bill Maguire, 795 N. Mountain Rd., Newington, CT, (203) 246-5639  
Mike McCarthy, 415 W. Golf Rd., Suite 37, Arlington Heights, IL 60005, (312) 437-7790  
Bob Bromelow, Santa Clara  
Richard Lois, 6655 Hillcroft, Suite 100, Houston, TX, (713) 777-0321

#### JEOL U.S.A. INC.

477 Riverside Avenue  
Medford, MA 02155

Contact: Robert T. Santorelli, (617) 391-7240

Product Line: Manufacturer of scanning electron microscopes, transmission electron microscopes, scanning electron microprobes, and electron energy loss spectrometers.

#### Sales Offices:

R. Steiner, Chicago, (312) 825-7164  
Jack Francis, Cincinnati  
Jeff Wolfe, Pittsburgh  
James Sealey, Ridge Instruments, Tucker, GA 30084  
Jean-Pierre Slakmon, Sequelec Ltd., 5925 Monkland Avenue, Montreal, Quebec, Canada  
Thomas Gildea, Boston  
Ray Gundersdorff, Washington, D.C.  
Roland Marti, Los Angeles  
Thayer Brickman, San Francisco

#### KEVEX CORPORATION

1101 Chess Drive  
Foster City, CA 94404

Contact: Henry S. Culver, (415) 573-5866

Product Line: Analytical systems for x-ray energy spectrometry, wavelength-dispersive x-ray spectrometry and electron energy spectrometry. Kevex detector/cryostats and analytical spectrometer systems are compatible with all electron microprobe, scanning electron microscopes and transmission electron microscopes in current production. Systems are available for both qualitative and quantitative analysis.

#### Sales Offices:

Fred Luehrs, 9410 Island Road, North Ridgeville, OH 44039  
David Janson, Toktela, Inc., Box 41, Upperville, VA 22176  
John Scott, 16 Higate Rd., Chelmsford, MA 01824, (617) 256-4961  
APTEC Engineering, Ltd., 4251 Steeles Avenue West, Downsview, Ontario, Canada M3N 1V7, (416) 661-9722  
George Kladnik, Foster City



WALTER C. McCRONE ASSOCIATES, INC.

2820 South Michigan Avenue  
Chicago, IL 60616

Contact: Ian M. Stewart, (312) 842-7100

Product Line: Analytical services in disciplines such as pharmaceuticals, forensic sciences, contamination control, metallography, air and water pollution, painting and document authentication, and corrosion. Analytical tools available: electron and ion microprobes, TEM, SEM, EMMA, ESCA, XRD, XRF, GC-MS, IR-UV, and optical microscopy.

MICRON INC.

Lancaster Pike and Centre Road  
P. O. Box 3536  
Wilmington, DE 19807

Contact: James F. Ficca Jr., (302) 998-1184

Product Line: Scanning electron microscopy, electron spectroscopy, electron probe x-ray analysis, transmission electron microscopy, quantitative image analysis, x-ray diffraction, x-ray fluorescence, optical microscopy and metallography, micro hardness, optical emission spectroscopy, differential scanning calorimetry, ultra microtomy, sample preparation.

MICROSPEC CORPORATION

265-G Sobrante Way  
Sunnyvale, CA 94086

Contact: Richard C. Wolf or William D. Donnelly, (408) 733-3540

Product Line: WDX-210 wavelength-dispersive x-ray spectrometer systems. X-ray microanalysis systems for use as accessories on scanning electron microscopes and other electron beam instruments. Capable of quantitative x-ray analysis of all elements down to beryllium, atomic number 4. Unique design permits attachment to most SEM electron columns without interference to other detectors or operational modes.

3M COMPANY, ANALYTICAL SYSTEMS

Building 53-3  
3M Center  
St. Paul, MN 55101

Contact: Peggy Willingham

Product Line: Complete ion scattering spectrometer (ISS) and secondary ion mass spectrometer (SIMS). Systems with vacuum or as attachments to existing vacuum systems. Ion Gun Systems for surface analysis and sputtering.

Sales Offices:

Gerald H. Rosenthal, 15 Henderson Dr., P. O. Box 76, West Caldwell, NJ 07006,  
(201) 575-2123

Robert W. Geiger, P. O. Box 460, Noblesville, IN 46060

Paul B. Clark, 346 Drexel Avenue, Ventura, CA 93003, (213) 726-6417

THE PERKIN-ELMER CORPORATION

411 Clyde Avenue  
Mountain View, CA 94043

Contact: Ned Shikashio, (415) 961-0461

Product Line: Transmission and scanning electron microscopes and a complete line of accessories.

Sales Offices:

Ronald Lunn, One Cherlyn Drive, Northboro, MA 01532, (517) 756-5331  
Morton Harloe, 328 Eisenhower Lane, Lombard, IL 60148, (312) 495-9440  
Michael E. Mullen, 11110 Los Alamitos Boulevard, #202 Los Alamitos, CA (213) 596-2512  
R. E. McDuffie, 15825 Shady Grove Rd., #120, Rockville, MD 20850

PHILIPS ELECTRONIC INSTRUMENTS, INC.

85-91 McKee Drive  
Mahwah, NJ 07430

Contact: J. D. Rodgers, (201) 529-3800

Product Line: Electron optical instrumentation, electron energy analyzers, and x-ray analytical instrumentation.

Sales Offices:

Main Line Professional Building, Suite A 1104, Rt. 130, Cinna-minson, NJ, (609) 829-4454  
7525 Long Avenue, Skokie, IL 60076, (312) 676-1714  
11141 Georgia Avenue, Suite 210, Silver Spring, MD (301) 933-3002  
3000 Scott Boulevard, Suite 113, Santa Clara, CA 95050, (408) 247-5333  
3760 Cahuenga Boulevard W., Suite 101, North Hollywood, CA 91604, (213) 980-2884

PHYSICAL ELECTRONICS INDUSTRIES, INC.

6509 Flying Cloud Drive  
Eden Prairie, MN 55344

Contact: Robert C. Cargill, (612) 941-5540

Product Line: ESCA/Auger electron spectrometers, scanning auger microprobes, thin-film analyzers, secondary-ion mass spectrometers, specialized combination systems, and a broad range of components including electron energy analyzers, sputter-etching systems, specimen manipulators, x-ray generators, UV sources, and sample introduction stages. Also operates an analytical service laboratory for custom surface analysis.

Sales Offices:

G. N. Rosenthal, Pittsburg, (412) 963-6717  
Tom J. Baum, 324 N. Central Expy., Richardson, TX 75080, (214) 231-8661  
Rod Palmborg Assoc., P. O. Box 200, Mercer Island, WA 98040, (206) 232-3444  
S. W. Seamans, 655 Deep Valley Drive, Rolling Hills Estates, CA 90274, (213) 377-7750

PRINCETON GAMMA-TECH

Box 641  
Princeton, NJ 08540

Contact: Chellie Goldberg, (609) 924-7310

Product Line: X-ray energy-dispersive and x-ray fluorescence microanalysis systems. An application laboratory and extensive program library.

Sales Offices:

Bill Hendrixson, 405 Vernon Rd., Jenkintown, PA 19046, (215) 885-3077  
Tom Griffin, 701 Morewood Pkwy., Rocky River, OH 44116, (216) 331-0120  
Fred Feeley, Box 4319, Thousand Oaks, CA 91359, (213) 991-3898  
Joe Piersante, Route 2, Box 50-A16, Gainesville, GA 30501, (404) 887-9100  
Don Dunkin, Box 641, Princeton, NJ 08540, (609) 924-7310  
Denny Cannon, P. O. Box 36157, Denver, CO 80236, (303) 978-0786  
Dick Neiman, 21718 Rotherham, Spring, TX 77379, (713) 353-0078  
Ernie Frost, Box 5817, Stanford, CA 94305, (415) 941-3560

#### QBI INTERNATIONAL

2034 Golden Gate Avenue  
San Francisco, CA 94115

Contact: Quentin A. Brown, (415) 929-1622

Product Line: Signal processors for the scanning electron microscope and STEM. Video systems for the electron microprobe. X-ray systems for the electron microprobe. Crystals and detectors. Stage and goniometer drive systems. Computer control of the SEM or electron microprobe. Computerized data acquisition systems.

#### Sales Office:

Box 6A, Russell Road, Bloomington, IN 47401, (812) 336-6244

#### CHARLES M. TAYLOR CO.

P. O. Box 7087  
Stanford, CA 94305

Contact: Dr. Charles M. Taylor, (415) 497-3479 or (408) 245-4229

Product Line: Various types of multielement standards for microbeam analysis by SEM, microprobe, and ion probe using energy, wavelength, and mass spectrometers. The standards available exceed 135 different metals, alloys, or compounds. Bence-Albee standards are available. Also supply sample holders for ARL-EMX and ARL-EMX-SM stages, and many types of sample holders and polishing jigs for sample preparation. Offer analytical services to customers desiring electron beam microprobe analysis, MAC-5 instrument.

#### TRACOR NORTHERN

2551 West Beltline Highway  
Middleton, WI 53562

Contact: Tyler North, (608) 831-6511

Product Line: Wide range of data-processing instrumentation for qualitative and quantitative x-ray analysis. Products include data acquisition, reduction and automation instruments for electron microprobe, SEM, TEM, and STEM. Featuring simultaneous EDS/WDS acquisition/reduction; beam control allowing for digital mapping, line scans, and other digital image processing. Other products are used in nuclear, optical, signal averaging and medical applications.

#### Sales Offices:

1430 Danzig Plaza #110, Concord, CA 94520

Technical Instrument Co., Suite 333, 13612 Midway Road, Dallas, TX 75240

Scientific Systems Sales Corp., 6901 Jericho Tpk., Syosset, NY 11791, (516) 921-3737

Contemporary Science, Inc., P. O. Box 205, Mt Prospect, IL 60056, (312) 255-3793

Pulcir, Inc., P. O. Box 357, Oak Ridge, TN 37830, (615) 483-6358

Buhrke Company, 2180 Sand Hill Road, Suite 160, Menlo Park, CA 94025, (415) 854-5689

Tracor Europa, Schiphol Airport Amsterdam, Bldg. 106, P. O. Box 7553, Amsterdam, The Netherlands, (020) 41-1865

#### UNITED SCIENTIFIC CORPORATION ANALYTICAL INSTRUMENT DIVISION

1400 D Stierlin Road  
P. O. Box 1389  
Mountain View, CA 94042

Contact: William D. Stewart, (415) 969-9400

Product Line: Automated x-ray analysis systems, including x-ray tube and isotopes, Si(Li) x-ray detector, and computer-based x-ray analyzer; Si(Li) x-ray detection systems for

use on scanning electron microscopes, transmission electron microscopes and electron microprobes; Si(Li) x-ray detectors for basic research; and portable x-ray spectrometers.

Sales Offices:

The Buhrke Company, 2180 Sand Hill Road, Menlo Park, CA (415) 854-5689  
International Instrument Corp., 64 E. Main St., Marlton, NJ 08053 (609) 983-6550  
Instruments and Technology, 220 E. 14th St., Naperville, IL 60540, (312) 355-7748  
Overall Engineering Inc., 15755 Daleport Circle, Dallas, TX 75240 (214) 233-2311  
North Eastern Analytical Corp., 17 Sherman Rd., Millis, MA 02054, (617) 376-4132

VARIAN ASSOCIATES

Vacuum Division  
611 Hansen Way, MS G017  
Palo Alto, CA 94303

Contact: Douglas R. Hillier, (415) 493-4000 Ext. 2815

Product Line: Analytical surface analysis equipment including Auger spectrometers, low energy electron diffraction system, UHV vacuum systems and components. A new automated Auger microprobe features spatial resolution capability of 0.2 microns, permanent storage of direct energy data, digital processing of Auger data, and clean-pumping UHV equipment.

Sales Offices:

25 Route 22, Springfield, NJ 07081, (201) 376-6610  
Ste 306, 25000 Euclid Avenue, Euclid, OH 44117, (216) 261-2115  
4940 El Camino Real, Los Altos, CA 94022, (415) 968-4936

## Scanning Electron Microscopy (Backscattered Electron Imaging)

### BACKSCATTERED ELECTRON IMAGING OF BIOLOGICAL SPECIMENS

Harry W. Carter

Backscattered electron imaging (BSI) has the potential of making the scanning electron microscope (SEM) a definitive instrument for studying biologic samples. Secondary-electron images (SEI) have been shown to be unreliable as definitive data for classification of cells in suspension. The surfaces of cells are controlled more by the conditions of their environment than by their cell type. Internal structures, particularly the nucleus, are used to classify cells as well as to assess the general condition of the cell. Therefore, a proper evaluation of cells with the SEM requires either a correlative study with some form of transmission microscopy or the use of BSI of specimens stained selectively with materials of high atomic number.

Correlative studies are time consuming and not well suited for clinical situations, where time plays a role in the importance the information has on patient care. BSI may be done either simultaneously with SEI or sequentially, depending on the equipment being used. Either way the superior image registration makes time-consuming correlative studies with either transmission electron microscopy (TEM) or light microscopy (LM) unnecessary in most cases.

Stains that employ metals as contrasting agents in biologic material have been used in LM for almost a century. Heavy-metal staining has become universal in TEM methods including the identification of enzymatic and immunologic reactions.

The use of such well-established metal staining techniques for atomic number contrast in BEI is immediately apparent. In fact, silver has been already used to demonstrate nuclei, basement membranes, and reticulin by BEI in sections of embedded tissue.<sup>2-4</sup>

A modification of the Gomori methenamine silver stain has been recently prepared by Becker<sup>5</sup> which gives excellent detail by nuclei within cells. The same stain can be used to visualize the A band within heart muscle cells.<sup>6</sup> Enzymatic reactions have been used to demonstrate peroxidase<sup>7</sup> and cytochrome C oxidase<sup>8</sup> localization using the DAB osmium technique. Acid phosphatase reactive sites have been imaged with lead used as the capture agent.<sup>9</sup> In the acid phosphase preparations cell nuclei were stained secondarily by the silver stain cited above (Fig. 1).

Ligands may prove to be helpful in increasing the density of metal deposited, in situations involving low initial concentrations of stain, so as to improve the backscattered electron signal. In some staining applications several metals can be used, so that one has a choice of contrasting methods.<sup>10</sup>

The images generated by backscattered electrons are almost identical to black-and-white photomicrographs of LM if the polarity of the image is reversed (Fig. 2). The advantages BEI has over LM for viewing internal structures are an extended range of magnification and a greatly increased depth of focus. The main advantages BEI has over TEM is that the thickness of the specimen can be much greater, even bulk samples, and the whole specimen can be viewed without grid-bar interference.<sup>11</sup> Slotted grids could overcome the grid-bar problem; however, slotted grids have their own problems. In addition neither LM or TEM can give the topographic information generated by SE in the SEM. It is this combination of SEI and BEI that is of importance in a diagnostic sense. The combination has already been emphasized in the study of urothelium<sup>12</sup> and pulmonary diseases.<sup>13</sup> Other clinical applications will follow.

#### References

1. B. Wetzel, "Cell kinesics: An interpretative review of the significance of cell surface form," *IITRI/SEM*, 1976, 135.
2. J. L. Abraham and P. B. DeNee, "Scanning electron microscope histochemistry using backscatter electrons and metal stains," *Lancet* i: 1125, 1973.

Dr. Carter is at Saint Barnabus Medical Center in Livingston, NJ 07039,

3. P. B. DeNee, J. L. Abraham, and P. A. Willard, "Histochemical stains for the scanning electron microscope: Qualitative and semiquantitative aspects of specific silver stains," *IITRI/SEM*, 1974, 259.

4. J. L. Abraham and P. B. DeNee, "Biomedical applications of backscattered electron imaging: One year's experience with SEM histochemistry," *IITRI/SEM*, 1974, 251.

5. R. P. Becker, personal communication.

6. S. Philips, personal communication.

7. R. P. Becker and P. P. H. DeBruyn, "Backscattered electron imaging of endogenous and exogenous peroxidase activity in rat bone marrow," *IITRI/SEM*, 1976, 171.

8. R. P. Becker, personal communication.

9. H. W. Carter and M. Tannenbaum, unpublished observation.

10. G. Vogel, R. P. Becker, and H. Swift, "Backscattered electron imaging of nuclei in rat testis," *IITRI/SEM*, 1976, 409.

11. P. B. DeNee and R. G. Frederickson, "Comparison of scanning transmission and back-scattered electron imaging in the SEM, using heavy metal stained sections of biological tissue," *34th Ann. Proc. Electron Microscopy Soc. Am.* 1976, 322.

12. M. Tannenbaum, S. Tannenbaum, and H. W. Carter. "SEM and TEM ultrastructural characteristics of normal preneoplastic and neoplastic human transitional epithelium," *SEM Proc.*, 1978, II-949.

13. J. L. Abraham, "SEM as an aid in diagnosis: An overview," *IITRI/SEM*, 1977, 119.

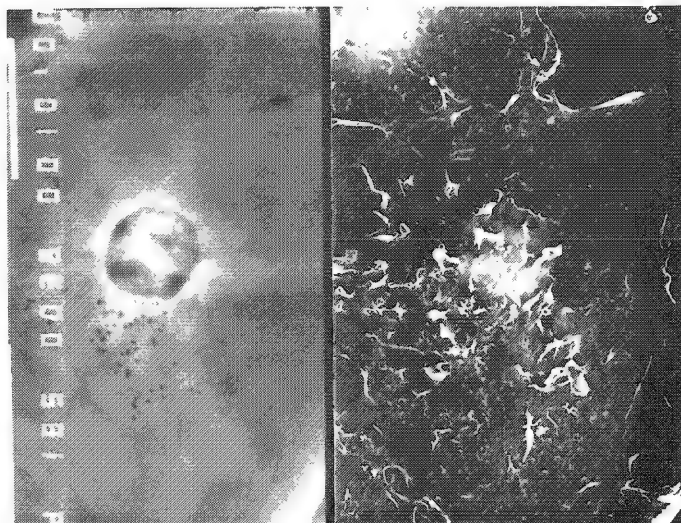


FIG. 1.--BEI (left) and SEI (right) of macrophage to demonstrate acid phosphatase (small black dots) with lead as capture agent, and nucleus with silver stain. Right side is SEI done simultaneously. Both pictures 1800 $\times$ .

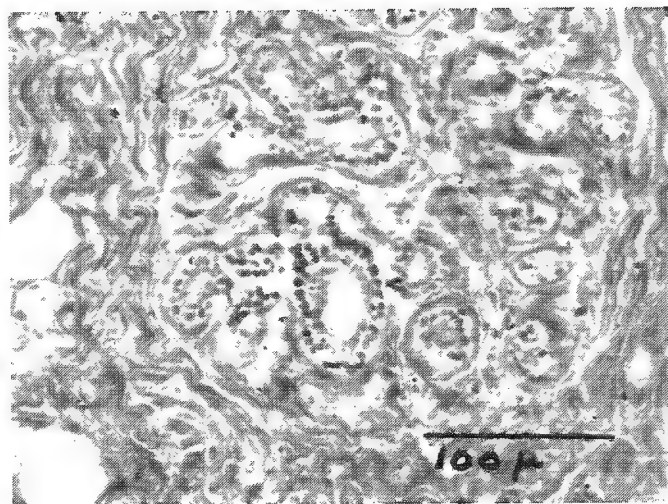
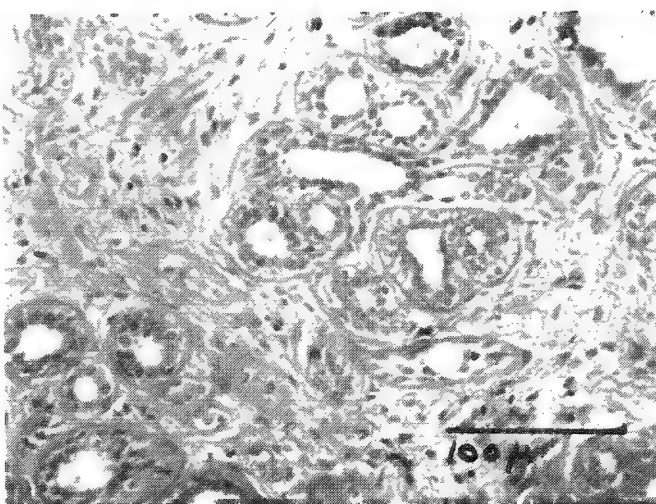


FIG. 2.--Light micrograph of breast tissue stained with hematoxylin and eosin (left), and BEI of breast tissue stained with silver (right), both at 200 $\times$ . Note similarities in images.

## VISUALIZATION BY BACKSCATTERED ELECTRON IMAGING OF THE ACCESSORY (OUTER DENSE) FIBERS AND MITOCHONDRIA OF SPERM

R. P. Becker and Garry Vogel

Visualization of subsurface structures in cells by backscattered electron imaging (BEI) in a scanning electron microscope (SEM) promises to be an important tool in biomedical investigation. If one is able selectively to stain internal structures such as cell nuclei or lysosomes with heavy metals,<sup>1-4</sup> one may be able to take advantage of the increased number of primary (beam) electrons that scatter back from such stained organelles and contrast them against surrounding unstained cell components. In this manner, subject to certain constraints on depth, one is able to visualize structures beneath intact cell surfaces, and to do so concurrently with the viewing of the surface, as performed by conventional secondary electron imaging (SEI). For a good general review and bibliography on the backscattered image in the SEM consult Wells.<sup>5</sup>

This paper describes BEI methods applicable to the study of sperm: the visualization of the accessory fibers of the flagellum and of the mitochondria of the middle piece sheath.

### *Materials and Methods*

*Staining of Accessory Fibers.* The testes and epididymis of adult Wistar rats were excised and dissociated in a pool of fixative consisting of 1.5% formaldehyde (prepared from paraformaldehyde) together with 2.5% glutaraldehyde in 0.08M sodium cacodylate buffer, pH 7.2. After further fixation for 2 hr in the same solution, testis tissue was washed free of fixative by immersion in the same buffer (several changes in 24 hr), further rinsed (3 changes in 15 min) with distilled water to remove buffer salts, and then immersed in 10 ml of Gomori's methenamine silver reagent<sup>6</sup> contained in a capped vial. The methenamine silver solution was prepared fresh by adding 5 ml of distilled water and 0.4 ml of a 5% sodium borate solution to 5 ml of methenamine silver stock (100 ml of 3% hexamethylene tetramine plus 5 ml of 5% silver nitrate). The capped vial was warmed to 50°C in a water bath and removed as soon as the solution became just perceptibly gray (typically 30 to 45 min). Thereafter the tissue was rinsed free of the staining solution by immersion in a large excess of distilled water, immersed in 5% sodium thiosulfate for 15 min, and further rinsed in distilled water prior to ethanolic dehydration and critical point drying from CO<sub>2</sub> with Freon TF as an intermediate fluid. Some testis tissue was cryofractured in absolute ethanol prior to drying.<sup>7</sup> Dry tissue was mounted on carbon slabs with a carbon containing adhesive (Tube Coat, G. C. Electronics, Rockford, Ill., Cat. No. 49-2) and coated with carbon by evaporation prior to viewing.

*Staining of Sheath Mitochondria.* The testes and epididymis of adult Wistar rats were excised, dissociated and immersed for 20 min in a 4°C pool of 4% formaldehyde (prepared from paraformaldehyde) in 0.05M sodium phosphate buffer, pH 7.4, to which 5% sucrose had been added. Following fixation a crude suspension of sperm was prepared by a gentle pelleting of the larger tissue and cell aggregates. Serial dilutions of the supernatant were then prepared by addition of 0.05M sodium phosphate buffer, pH 7.4, to which 5% sucrose had

---

R. P. Becker is at the Department of Anatomy in the University of Illinois Medical Center in Chicago, IL 60612; Garry Vogel is at the Department of Biology, University of Chicago, IL 60637. A portion of this study was conducted while Dr. Becker was at the University of Chicago's Department of Anatomy. The study was supported in part by USPHS grants CA05493 and HD-174, in part by NSF grant BNS-7728493, and in part by a grant from the Louis Block Fund, University of Chicago. The SEM employed in this study is located in the University of Chicago Users Microscope Laboratory, which is supported by a grant from the Biotechnology Resources Branch of the National Institutes of Health.



been added. A 5ml volume of each dilution was then passed through a 0.22 $\mu$ m pore size Millipore filter (Millipore Corp. GSWP01300) contained in a 13mm Swinnex holder (Millipore Corp. GX0001300). The filters plus collected sperm were removed from the holder, washed overnight in the same buffer plus sucrose, and incubated for 1 hr at 37°C in a medium modified from Seligman et al.<sup>8</sup> for the demonstration of cytochrome oxidase. The medium consisted of 5 mg of 3,3'-diaminobenzidine (Sigma Chemical Co., St. Louis) and 750 mg of sucrose in 9 ml of 0.05M sodium phosphate buffer, pH 7.4. Some control incubations were performed with the cytochrome oxidase inhibitor, potassium cyanide (6.5 mg, 0.01M), added to the incubation medium. Following incubation sperm were washed with several changes of the same sucrose buffer, followed by a rinse with distilled water, and then immersed in 0.5% OsO<sub>4</sub> for 10 min at 20°C. Excess OsO<sub>4</sub> was quickly washed from the filters with distilled water. The filters were dehydrated in graded ethanols and critical-point dried from CO<sub>2</sub> with Freon TF as an intermediate fluid. Dry filters were mounted and coated with carbon for viewing as detailed for the silver-stained testis tissue above.

The pelleted testis tissue was also incubated for the demonstration of cytochrome oxidase (as above), and subsequently osmicated and prepared for transmission electron microscopy (TEM).

*Scanning Electron Microscopy.* The heavy metal-stained preparations were viewed in secondary-electron (SE) and backscattered-electron (BE) imaging modes in a Hitachi HFS-2 SEM equipped with a scintillator-light guide-photomultiplier tube BE detector of original design (Fig. 1). This detector collects BE over a solid angle of about 2.5 steradians and

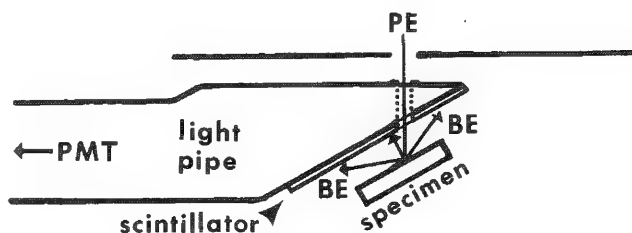


FIG. 1.--Diagrammatic representation of scintillator-light guide BE detector employed in this study. Primary (beam) electrons (PE) are focused onto specimen through hole in wedge-shaped end of light pipe. Backscattered primary electrons strike face of scintillator, a Ca F<sub>2</sub> (Eu) crystal, which converts electron signal to light signal. Light pipe, machined from optical-grade quartz, conveys light signal out of microscope to standard photomultiplier tube (PMT), which reconverts light signal to electron signal. All exposed surfaces of light pipe and scintillator are aluminized and grounded. Light pipe is maneuverable from outside the microscope by use of high-vacuum bellows, to allow detector to be properly positioned or retracted out of the way. Hitachi HFS-2 SEM preamplifier and analog circuitry process PMT signal for display.

offers an improved signal-to-noise ratio over that of the annular silicon diode detector previously employed in the HFS-2.<sup>9</sup> The microscope was operated at 25 kV with a beam current at the specimen of 2 to 5  $\times 10^{-11}$  A.

### Results and Discussion

For a major part of the length of the mammalian sperm tail, the axonemal "9+2" pairs of microtubules are surrounded by nine "outer dense" fibers, presumed to be somehow accessory in function to the axonemal microtubules. The Gomori methenamine silver (GMS) reagent, as used here, contrasts these fibers effectively for BEI (Figs. 2 and 3). Accessory fibers may be viewed within the tails and in profile at the fracture plane by BEI (Fig. 2b), and conveniently compared with a SE image of the same site (Fig. 2a). Since two detectors are employed, it is entirely possible to view and record both images simultaneously with one raster sweep of the beam. The resolution attained in the case at hand is improved over that available by light microscopy and sufficient to correlate with the familiar TEM appearance of the fibers (see, for example, Fawcett<sup>10</sup>).



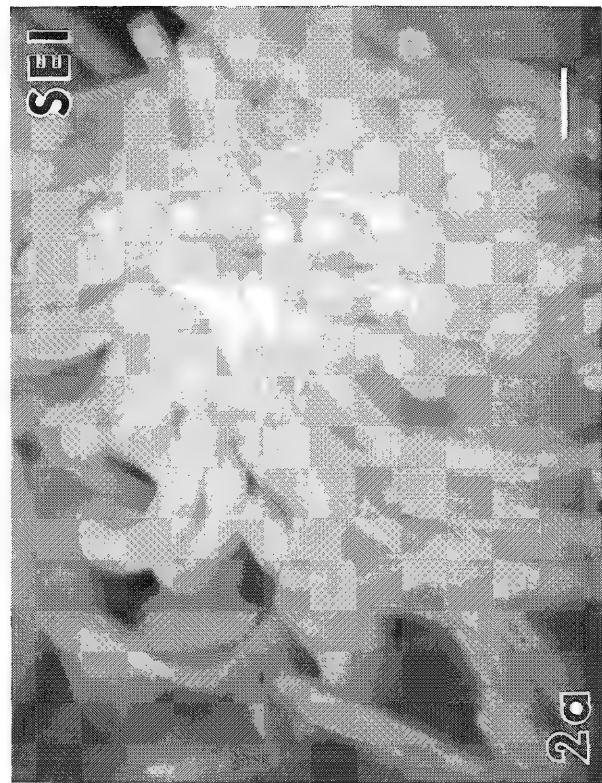


FIG. 2.--Correlative secondary-electron (a) and backscattered-electron (b) images of same site within testis seminiferous tubule. Ethanollic cryofracture was used to expose lumen of tubule and to section this bundle of sperm tails. In (b) accessory fibers of flagella are selectively highlighted by increased number of beam electrons scattered back from heavy-metal (silver,  $Z = 47$ ) stained fibers within tails, as compared to the few electrons that scatter back from unstained components of tails. Emerging BEs produce SEs, which results in faint visualization of accessory fibers in secondary image (a). Methenamine silver stain. Scale bar = 1  $\mu$ m.



FIG. 3.--Higher magnification BEI of several cryofractured sperm tails located adjacent to field seen in Fig. 2. One cross-fractured tail (arrowhead) shows characteristic cross-sectional profiles of the nine accessory fibers. Methenamine silver stain. Scale bar = 1  $\mu$ m.

The staining of the accessory fibers is apparently due to the reducing power of the sulfur-containing proteins in the fibers, since the fibers are known to be particularly rich in cystine<sup>11</sup> and thiol reduction followed by alkylation eliminates the staining.<sup>4</sup> If so, then the GMS protocol used here should also be effective in contrasting other structures rich in sulfur-containing amino acids, such as elastic fibers<sup>12</sup> or the insulin-rich  $\beta$  cells of the endocrine pancreas.

The "middle piece" of mammalian sperm is notable for the presence of a tight helical coil of mitochondria, arranged end to end, which ensheaths the axoneme and accessory fibers over this segment.<sup>10</sup> These mitochondria are presumed to generate the energy for sperm locomotion. Middle-piece mitochondria can be contrasted for BEI visualization by selective heavy metal staining of the reaction product of the mitochondrial enzyme, cytochrome oxidase, which is deposited in the mitochondrial intracrystal space and between the inner and outer mitochondrial membranes.<sup>8</sup> That is, by localizing a component restricted to mitochondria, and which delimits the margins of mitochondria, one may in turn localize mitochondria. Figure 4 shows in correlating SE and BE images of the same sperm, the tightly coiled mitochondria of the sperm middle piece. Sperm prepared similarly for TEM showed the selective localization of the DAB-osmium reaction product in the intracrystal space and between the inner and outer membranes of mitochondria (Fig. 5). Addition of cyanide to the incubation medium abolished both the localization of DAB-osmium reaction product in TEM sections and the BEI visualization of mitochondria in SEM preparations.

These results demonstrate the visualization of mitochondria within intact sperm prepared for SEM and the possibility for correlating mitochondrial disposition with the cell exterior. It is suggested that this approach may be applicable to investigations of other cell types and of particular value in studies dealing with the quantification of mitochondria in individual cells. These results further support the general feasibility of a SEM histochemistry based on a linking of established TEM methodology with BE imaging.

#### References

1. J. L. Abraham and P. B. De Nee, "Biomedical applications of backscattered electron imaging: One year's experience with SEM histochemistry," in O. Johari and I. Corvin, Eds., *Scanning Electron Microscopy/1974*, Chicago: IIT Research Institute, 1974, 252.
2. P. B. De Nee et al., "Histochemical stains for the scanning electron microscope: Qualitative and semiquantitative aspects of specific silver stains," *ibid.*, 259.
3. R. P. Becker and P. P. H. De Bruyn, "Backscattered electron imaging of endogenous and exogenous peroxidase activity in rat bone marrow," in O. Johari and R. P. Becker, Eds., *Scanning Electron Microscopy/1976/II*, Chicago: IIT Research Institute, 1976, 171.
4. G. Vogel et al., "Backscattered electron imaging of nuclei in rat testis," *ibid.*, 409.
5. O. C. Wells, "Backscattered electron image (BSI) in the scanning electron microscope (SEM)," in O. Johari, Ed., *Scanning Electron Microscopy/1977/I*, Chicago: IIT Research Institute, 1977, 747.
6. G. G. Gomori, "A new histochemical test for glycogen and mucin," *Am. J. Clin. Path.* 16: 177, 1946.
7. W. J. Humphreys et al., "Critical point drying of ethanol infiltrated cryofractured biological specimens for SEM," in O. Johari and I. Corvin, Eds., *Scanning Electron Microscopy/1974*, Chicago: IIT Research Institute, 1974, 275.
8. A. M. Seligman et al., "Nondroplet ultrastructural demonstration of cytochrome oxidase activity with a polymerizing osmiophilic reagent, diaminobenzidine (DAB)," *J. Cell Biol.* 38: 1, 1968.
9. P. S. D. Lin and R. P. Becker, "Detection of backscattered electrons with high resolution," in O. Johari and I. Corvin, Eds., *Scanning Electron Microscopy/1975*, Chicago: IIT Research Institute, 1975, 61.
10. D. W. Fawcett, "The mammalian sperm," *Devel. Biol.* 44: 394, 1975.
11. B. Baccetti et al., "Accessory fibers of the sperm tail: I. Structure and chemical composition of the bull 'coarse fibers,'" *J. Submicro. Cytol.* 5: 237, 1973.
12. R. Ross and P. Bornstein, "The elastic fiber: I. The Separation and partial characterization of its macromolecular components," *J. Cell Biol.* 40: 366, 1969.

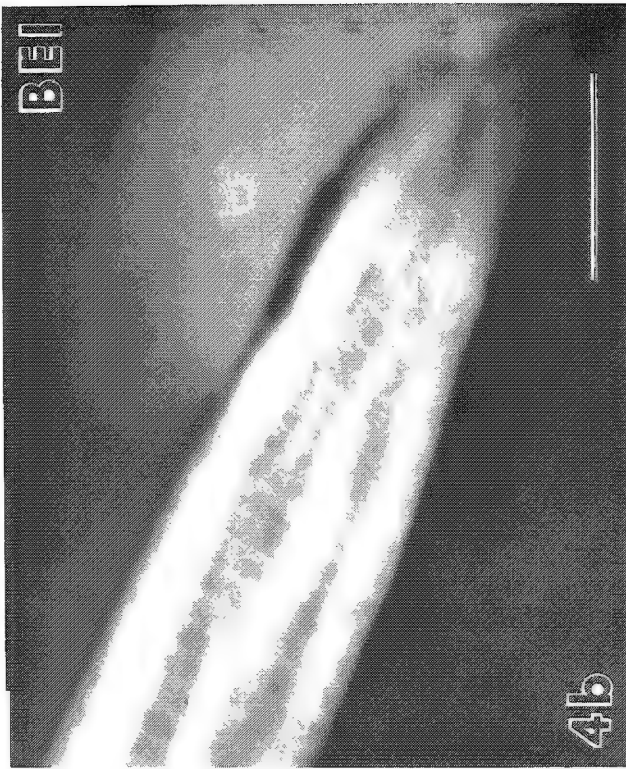
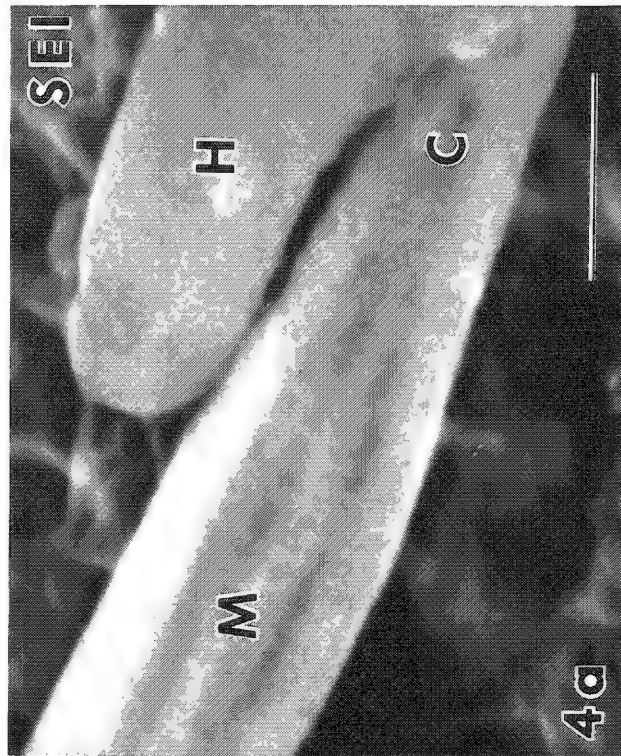


FIG. 4.--Correlating SE (a) and BE (b) images of rat sperm. Portion of middle piece (M), connecting piece (C), and head (H) are seen. In BE image (b), helical coil of mitochondria (individual mitochondria abutting end to end) within middle piece is viewed to good advantage, owing to increased number of beam electrons scattered back from heavy metal (osmium,  $Z = 76$ ) deposited selectively at sites of cytochrome oxidase activity. DAB-osmium histochemical stain for cytochrome oxidase/mitochondria. Scale bar = 1  $\mu\text{m}$ .

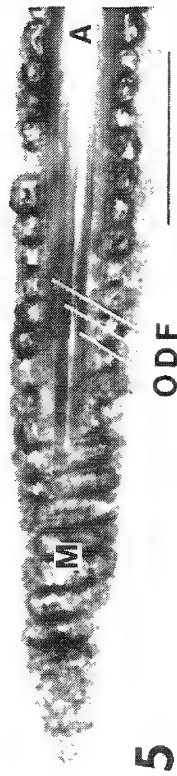


FIG. 5.--TEM image of paralongitudinal section through middle piece of sperm incubated for visualization of mitochondria by BEI as seen in Fig. 4. Osmium has been preferentially deposited at sites of cytochrome oxidase activity, rendering mitochondria (M) more electron opaque than axoneme (A). ODF = outer dense fibers. DAB-osmium histochemical stain for cytochrome oxidase (mitochondria). Scale bar = 1  $\mu\text{m}$ .

## APPLICATION OF HEAVY-METAL STAINING ( $\text{OsO}_4$ )/BACKSCATTERED ELECTRON IMAGING TECHNIQUE TO THE STUDY OF ORGANIC AEROSOLS

P. B. DeNee and R. L. Carpenter

The backscattered electron imaging (BSI) mode of the SEM has been used for several years to visualize inorganic particles in biological tissue and in aerosol samples.<sup>1,2</sup> This technique has not been used for organic particles of low atomic number (Z), since the backscattered-electron (BSE) yield is low and is thus frequently masked by electronic noise. This paper describes the application of a relatively new technique: heavy-metal staining (HMS) and backscattered-electron imaging<sup>3</sup> to visualize organic aerosol particles. The HMS/BSI technique has been used only recently outside the biological sciences.<sup>4</sup> The HMS/BSI technique has been applied to coal-gas aerosols in this work.

The coal-gas aerosol particles were collected on polished carbon stubs by means of a point-to-plane electrostatic precipitator. The samples were then stained with osmium tetroxide ( $\text{OsO}_4$ ) vapors by the method of Green, DeNee, and Frederickson.<sup>4</sup> All SEM micrographs were taken at 25keV accelerating voltage, 10nA beam current, and 45° tilt. All samples were uncoated.

These aerosols were chosen because they are quite difficult to study with either light microscopy (LM) or transmission electron microscopy (TEM). The particles are too small to be adequately resolved with LM. Although the TEM has adequate resolution, the particles have insufficient electron density to produce adequate contrast and may often evaporate owing to the intense electron beam.

The SEM has adequate resolution and a less intense electron beam, but it is frequently difficult to differentiate the organic particles from the SEM stub surface. For example, comparison of a clean stub surface (Fig. 1) with the surface of a stub bearing coal gas aerosol particles (Fig. 2 and 3) makes the presence of inorganic (fly ash) particles obvious; however, it is difficult, if not impossible, to distinguish between organic particles (tar droplets) and stub surface features. Comparison of Figs. 2 and 3 shows that different stub-surface morphology does not necessarily alleviate this problem.

The HMS/BSI technique solves this problem. When osmium tetroxide is used to stain the particles, the particles are then clearly differentiable by BSI (Fig. 4A). The surface of the carbon stubs has stained slightly but in a subtle, mottled pattern, which may be caused by the staining of the organic binder used to hold the carbon particles together. Energy-dispersive x-ray analysis was used to analyze several Os-stained particles and the surface of the stub where no particles were present. It was found that the particle contained about five times more Os than the carbon stub.

Heavy metal staining also enhances the secondary-electron image (SEI) of coal gas-aerosol particles (Fig. 4B). However, there are particle-like features (arrows, Fig. 4B) that do not stain by the HMS/BSI technique. They may be a different type of organic particles or may be part of the stub surface.

Heavy-metal staining and BSI show potential for the visualization of organic aerosols. The use of this technique and BSI/SEI prior to HMS allows one to differentiate between inorganic (fly ash) and organic (tar and oil) particles. Additional applications to the identification of various types of aerosols have been developed.



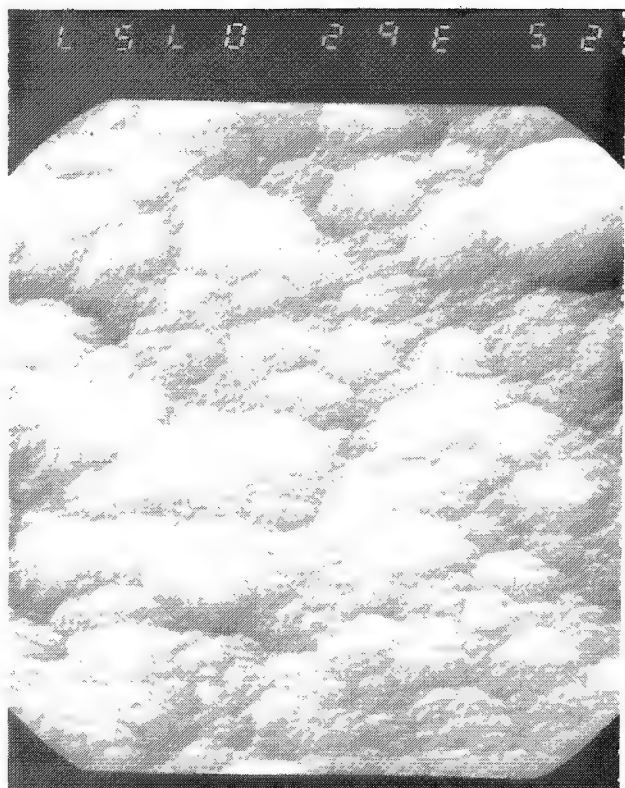


FIG. 1.--SEM of clean polished carbon stub, secondary-electron image (SEI).  $\text{---}$  3  $\mu\text{m}$ .

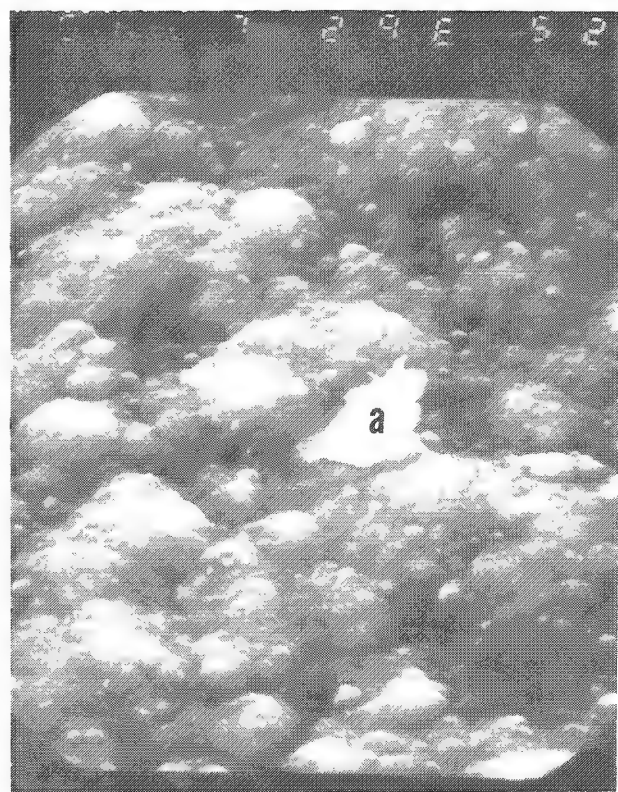


FIG. 2 (bottom left).--SEM of polished carbon stub with coal-gas aerosol particles. Note fly-ash particle (a) but difficulty in visualizing organic particles.  $\longleftrightarrow$  3  $\mu$ m.

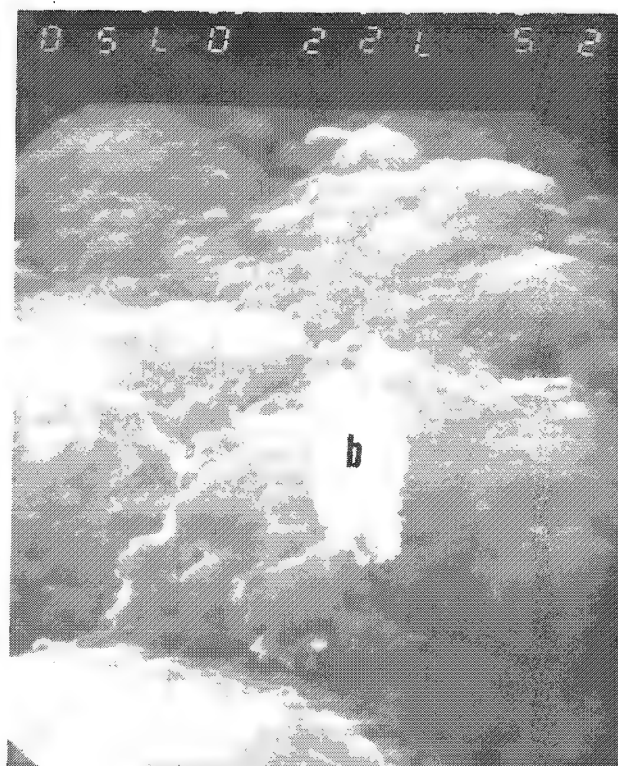



FIG. 3 (bottom right).--SEM of another polished carbon stub with coal-gas aerosol particles. Smoother stub than in Fig. 2. Note fly-ash particle (b) but difficulty in visualizing organic particles.  1.5  $\mu$ m.

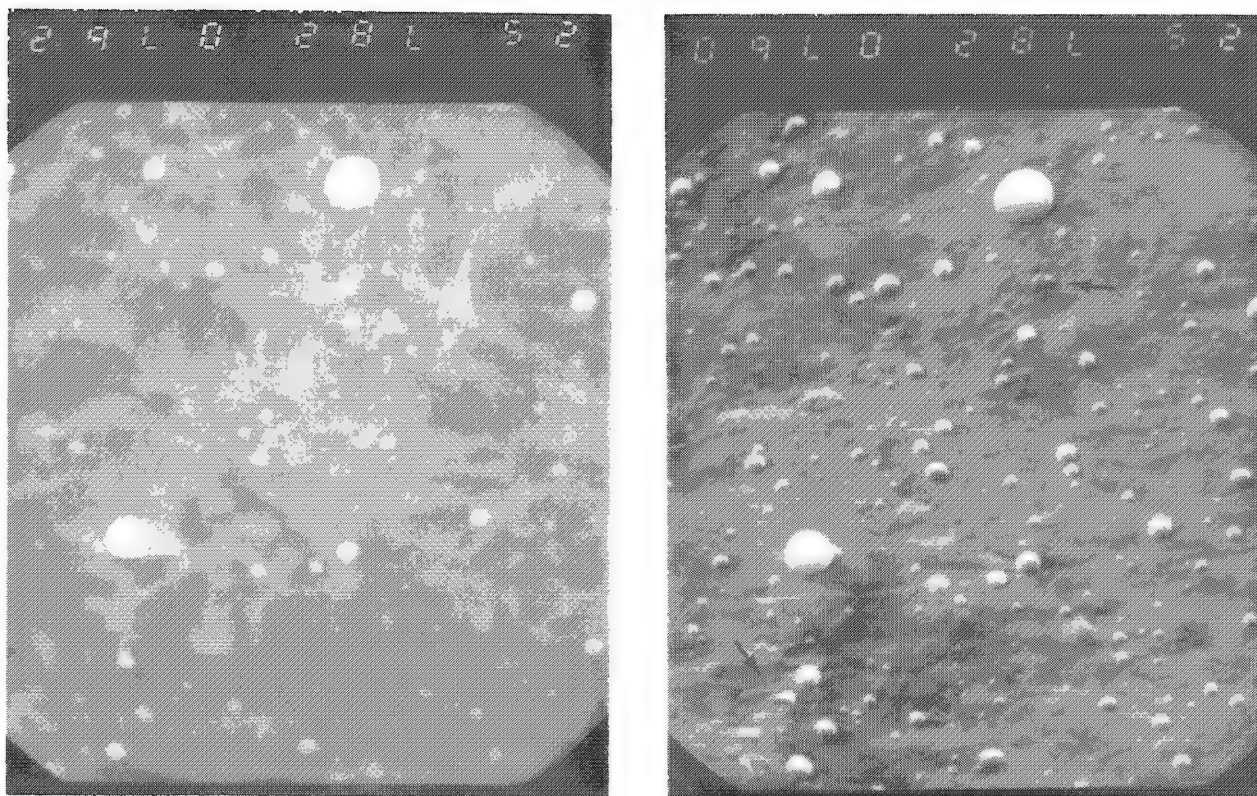


FIG. 4.--SEM of coal-gas aerosol particles on polished carbon stub. Particles have been stained with osmium tetroxide vapors. (A) backscattered electron image, (B) SEI.  $\text{—————}$  1.5  $\mu\text{m}$ .

#### References

1. P. B. DeNee, "The use of backscattered electron imaging (BSI) in the scanning electron microscope for the detection of microfibers in airborne dust samples and biological tissue," *Symposium on Electron Microscopy of Microfibers*, proceedings of an FDA Summer Symposium, Pennsylvania State University, 1976; Washington, D.C.: HEW Publ. (FDA) 77-1033, 1977, 68-72.
2. P. B. DeNee, "The detection of respirable dust by SEM backscattered electron imaging," in P. A. Russell and A. E. Hutchings, Eds., *Electron Microscopy and X-ray Applications to Environmental and Occupational Health Analysis*, Ann Arbor, Mich.: Ann Arbor Science Publishers, 1978, 237-245.
3. P. B. DeNee, R. G. Frederickson, and R. S. Pope, "Heavy metal staining of paraffin, epoxy and glycol methacrylate embedded biological tissue for scanning electron microscopy histology," *SEM II*, Chicago, Ill.: ITT Research Institute, 1977, 83-92.
4. D. A. Green, P. B. DeNee, and R. G. Frederickson, "Application of the heavy metal staining ( $\text{OsO}_4$ ) backscattered electron imaging technique to the detection and localization of organic (combustible) material in gas and oil shales," *SEMI*, SEM, Inc., AMF O'Hare, IL 60666, 1979, in press.

## APPLICATION OF SEM BACKSCATTERED ELECTRON IMAGING TO THE STUDY OF THE EFFECTS OF FIBROUS GLASS AND ASBESTOS ON LUNG TISSUE

P. B. DeNee, A. H. Rebar, D. B. DeNicola, and J. A. Pickrell

Many respirable-size glass fibers become airborne during the manufacture and installation of fibrous glass insulation<sup>1,2</sup> and thus can be inhaled. Inhaled fibers whose lengths are  $\geq 8 \mu\text{m}$ , and whose aerodynamic diameter is  $\leq 5 \mu\text{m}$ , may cause a tissue response in the lung.<sup>3-5</sup> No direct association of this tissue response with the presence of other than large glass fibers has been made by the light microscope (LM). That is because glass fibers are transparent and nonbirefringent, their index of refraction is close to that of most tissue-mounting media, and the smallest dimension of many of the fibers is below the resolution of the LM (about  $0.7 \mu\text{m}$ ).<sup>6,7</sup> The transmission electron microscope (TEM) can be used to resolve the fibers (resolution about 1 nm). However, its use is not feasible because it requires very thin sections (60-100 nm). Thin sectioning results in loss and damage of the fibers and requires very small sections, which makes it difficult to associate fibers and tissue responses.

It is possible to resolve the fibers with the Scanning Electron Microscope (SEM) in the Secondary Electron Imaging (SEI) mode, but it is difficult if not impossible to differentiate the fibers from the tissue. Backscattered Electron Imaging (BSI) with the SEM was previously introduced by DeNee to overcome this difficulty.<sup>6,7</sup> The backscattered electron yield from a material (backscattered electron image brightness) increases with increasing atomic number (Z) of the material; thus a glass fiber of  $Z \approx 10$  will appear brighter than biological tissue ( $Z \approx 5$ ) or a carbon stub ( $Z \approx 6$ ).

This paper demonstrates the application of scanning electron microscopy and backscattered electron imaging to the study of toxic effects of fibrous glass on lung tissue in conjunction with light microscopy. The examples are taken from a preliminary screening study made by means of intratracheal instillation of (a) one type of fibrous glass, (b) a positive control known to be fibrogenic and carcinogenic (crocidolite asbestos), and (c) a negative control (saline).

### *Experimental Method*

Male Syrian hamsters (Charles River [Lak: (SYR)]; 10-12 weeks of age) were utilized in the study. Each animal was anesthetized with 4% halothane in oxygen mixture delivered via a catheter inserted into the trachea following the technique of Mauderly.<sup>8</sup> Physiological saline solutions ( $37^\circ\text{C}$ ) were prepared both with and without fibers and a 0.5ml bolus was instilled into the trachea of each animal. Twenty animals were each administered a total of 2 mg of a bare (uncoated) fibrous glass in two biweekly doses. A second group of 20 animals was each administered a total of 6 mg of crocidolite asbestos in four weekly doses. Thirty control animals were each administered saline without fibers in either four weekly doses (five animals) or two biweekly doses (25 animals).

Five or six animals from each fiber exposure group and eight controls were sacrificed at 1 and 3.5 months after initial instillation. The animals were sacrificed by means of halothane anesthesia and cervical dislocation. The heart-lung block was removed *in toto* and the left diaphragmatic lobe was fixed by intratracheal perfusion with 10% buffered formalin. When fixation was complete (over 72 hr), the tissues were embedded in paraffin and  $5\mu\text{m}$ -thick serial sections cut. The sections were floated onto both glass light microscope slides and polished carbon stubs. The LM sections were stained with hematoxylin and eosin (H&E). The paraffin was removed from the SEM samples with xylene and either (a) air-

---

This research was performed at the Lovelace Inhalation Toxicology Research Institute, Box 5890, Albuquerque, NM 87115, under Department of Energy contract EY-76-C-04-1013, in facilities fully accredited by the American Association for the Accreditation of Laboratory Animal Care.

dried for quick results but with some sacrifice of good morphology, or (b) critical-point-dried with CO<sub>2</sub> to obtain good morphology. These sections were then given a light carbon coating (50-100 Å) and viewed in the SEM at 25kV accelerating voltage and 10nA beam current, by both secondary electron imaging (SEI) and backscattered electron imaging (BSI).

### *Results*

*LM Histopathology.* Lesions in the lungs of hamsters exposed to the bare glass fibers consisted of a granulomatous bronchopneumonia. Both large and small airways were involved (Fig. 1). Large bronchioles were filled with exudate consisting of an admixture of large foamy alveolar macrophages, necrotic debris, and fibers of varying lengths. Although the reaction in the large bronchioles was generally limited to the bronchiolar lumen, there was focal goblet cell metaplasia and focal hyperplasia of bronchiolar lining epithelium. Lung parenchyma surrounding large bronchioles was generally uninvolved. In contrast, the response involving the terminal bronchioles frequently extended into adjacent alveoli. Response in these areas consisted principally of accumulations of large foamy alveolar macrophages and occasional giant cells. Fibers were not readily identified. There was no significant morphologic difference in lungs of animals sacrificed at 1 or 3.5 months after exposure.

Lesions in lungs of hamsters exposed to asbestos were similar to those in the animals exposed to bare glass fiber, but the asbestos-induced lesions were more severe. Giant cells were a major component of the granulomatous inflammatory response (Fig. 2). Needle-like asbestos fibers of varying lengths were readily identified within giant cells. Bronchiolar cell metaplasia and hyperplasia were not a feature of the asbestos-induced lesions.

Lung tissues from all hamsters exposed to saline alone were histologically normal.

*SEM.* Scanning electron microscopic evaluation of tissues from the animals exposed to bare glass fiber supported those morphological alterations detected by light microscopy. Large bronchioles were often filled with macrophages, necrotic debris, and numerous fibers of varying lengths. Some fibers were observed penetrating bronchiolar lining epithelium (Fig. 3). The bare glass fibers were readily seen with the SEM/BSI (in contrast to LM observations). The number of fibers present in pulmonary tissues examined was markedly greater than the amount demonstrable with light microscopy.

The SEM examination of lung tissue from the animals exposed to crocidolite asbestos also yielded observations that correlated well with LM observations. Numerous large, fiber-filled cells (probably macrophages) within alveolar septae and alveolar spaces as well as possible giant cells filled with fibers were identified. Figure 4 is a BSI of one or more macrophages (possibly a giant cell) containing asbestos fibers. The fibers can easily be seen in the BSI.

No fibers were detected with SEM examination in the hamsters exposed to only saline.

### *Discussion*

The two primary instruments used in this study have been the light microscope and the scanning electron microscope. Each instrument plays an important role in this study. The function served by the light microscope is to identify the tissue components, both normal and abnormal. It is limited in resolution to about 0.7 µm, so that it can only resolve the larger fibers. In addition, certain fibers either have an index of refraction similar to that of the tissue-mounting media or are transparent and cannot be seen by LM. Polarized light microscopy can be used to "see" certain birefringent fibers (such as chrysotile) but not amorphous material like glass. Many more tissue sections can be scanned in a given time by LM than by SEM.

The SEM serves a complementary function. Its superior resolution and ability to utilize atomic-number contrast allows it to "see" glass and asbestos fibers in the lung tissue. One example is the multitude of small fibers in Fig. 4 as seen by BSI. In addition to "seeing" the fibers, one can analyze single fibers or clusters of fibers by x-ray analysis. Also, certain heavy metal stains can be used in conjunction with BSI in order to identify tissue components.

The tissue response to the two test fibers was similar but the asbestos-induced lesions were generally more severe, involving greater areas of lung parenchyma. In animals



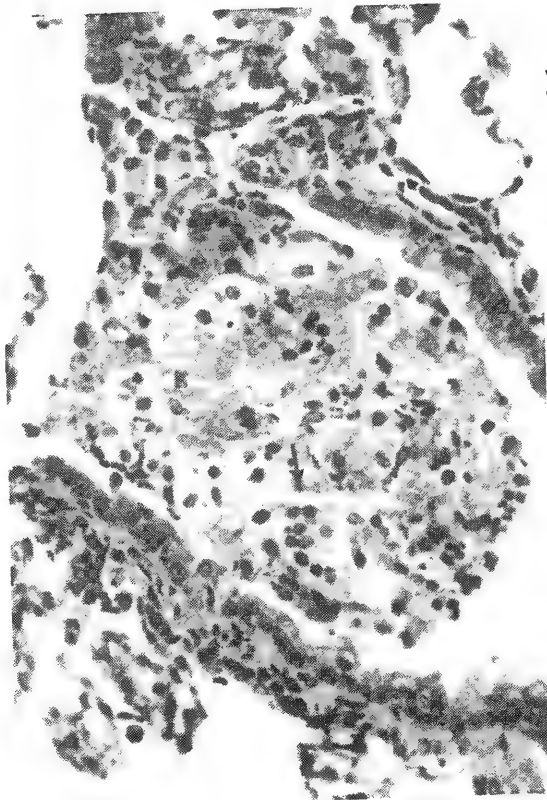


FIG. 1.--Terminal bronchiole of bare-glass-exposed hamster lung 28 days post exposure. Bronchiolar plug consists of large foamy macrophages, necrotic debris, and few fibers discernible only out of plane of focus. Cleft-like space (arrow) is large fiber trapped in plug. LM (H&E)  $\times$  25  $\mu$ m.

13



FIG. 3.--Serial section from same tissue as in Fig. 1. Several fibers are seen to be penetrating bronchiolar lining epithelium (arrows).  $\times$  10  $\mu$ m. SEM/BSI at 0°.

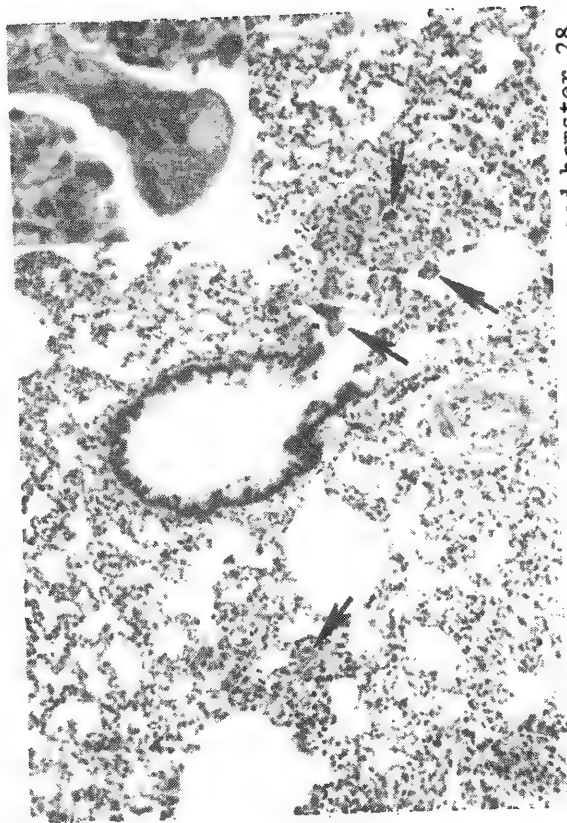


FIG. 2.--Lung from crocidolite-asbestos-exposed hamster 28 days post exposure: marked thickening of alveolar septae with proliferating macrophages and several giant cells (arrows). LM (H&E)  $\times$  60  $\mu$ m. Inset: High magnification of one giant cell filled with readily discernible asbestos fibers. LM (H&E)  $\times$  15  $\mu$ m.



FIG. 4.--Serial section from the same tissue as in Fig. 2. Numerous crocidolite asbestos fibers are readily discernible within a giant cell.  $\times$  5  $\mu$ m. SEM/BSI at 0°.

exposed to asbestos, macrophages and giant cells contained numerous fibers of varying sizes visible with light microscopy. Fibers were only rarely seen in the fibrous-glass-exposed lungs with LM.

These examples are part of a larger study now under way to compare the response of the lung to various types of fibrous glass and to asbestos. The same techniques will be applied to the lungs from other animals. The goal is to associate injury to the lung with location and physical characteristics (i.e., length, diameter, composition) of the fiber.

We have shown that SEM and LM complement one another for certain types of studies, such as the response of the lung to fibrous materials. When used together, they can aid in determining the local effect of the foreign body (i.e., to correlate the injury with the agent), something that cannot always be demonstrated by means of either instrument alone.

#### *Acknowledgments*

The authors are indebted to Mss. K. Sass, F. Straus, and D. Villa for their technical support, Drs. D. Brownstien, F. Hahn, and C. Hobbs for technical review of the manuscript, Mss. J. Miller and M. DeNee for preparation of the manuscript, and Ms. A. Ferris for editorial assistance.

#### *References*

1. D. P. Fowler, J. L. Balzer, and W. C. Cooper, "Exposure of insulation workers to airborne fibrous glass," *Amer. Ind. Hyg. Assn. J.* 32: 86-91, 1971.
2. M. Corn, Y. Hammad, D. Whittier, and N. Kotsko, "Employee exposure to airborne fiber and total particulate matter in two mineral wool facilities," *Env. Res.* 12: 59-74, 1976.
3. M. F. Stanton, M. Layard, A. Tegeris, E. Miller, M. May, and E. Kent, "Carcinogenicity of fibrous glass: Pleural response in the rat in relation to fiber dimension," *J. Natl. Cancer Inst.* 58: 587-603, 1977.
4. M. Kuschner and G. Wright, "The effects of intratracheal instillation of glass fiber of varying sizes in guinea pigs," in *Occupational Exposure to Fibrous Glass*, proceedings of a 1974 NIOSH symposium at College Park, 1974, Washington, D.C.: HEW Publ. (NIOSH) 76-131, 1976, 151-168.
5. P. Gross, "The effects of fibrous glass on the lungs of animals," in *Occupational Exposure to Fibrous Glass*, 1976, 169-178.
6. P. B. DeNee, "The use of backscattered electron imaging (BSI) in the scanning electron microscope for the detection of microfibers in airborne dust samples and biological tissue," *Symposium on Electron Microscopy of Microfibers*, proceedings of an FDA Summer Symposium, Pennsylvania State University, 1976, Washington, D.C.: HEW Publ. (FDA) 77-1033, 1977, 68-72.
7. P. B. DeNee, "The detection of respirable dust by SEM backscattered electron imaging," in P. A. Russell and A. E. Hutchings, Eds., *Electron Microscopy and X-ray Applications to Environmental and Occupational Health Analysis*, Ann Arbor, Mich.: Ann Arbor Science Publishers, 1978, 237-245.
8. J. L. Mauderly, "Bronchopulmonary lavage of small laboratory animals," *Lab. An. Sci.* 27: 255-261, 1977.

## BACK-SCATTERED ELECTRON IMAGING FOR AUTOMATED PARTICULATE ANALYSIS

R. J. Lee and J. F. Kelly

Characterization of the morphology and composition of individual particles collected in ambient air samples may permit the measurement of the impact of various sources on ambient air quality. This important problem has been the subject of many SEM studies, most of which have had only limited success because of an inability to produce statistically significant results.

Recently LeMont Scientific developed a system which offers computer-control of the electron beam.<sup>1</sup> Integrating this system with a Tracor Northern TN2000 software-based multichannel analyzer resulted in an Automatic Image Analysis (AIA) system capable of rapid, reproducible measurement of the size, shape, and composition of all detectable individual features in the SEM field of view.<sup>2,3</sup> Image contrast, noise level, and edge effects are all important factors in the detection process.

For AIA, the back-scattered electron (BSE), long the poor cousin of the secondary electron (SE), is indispensable. Efficient, fast-response BSE detectors now permit imaging and focusing at normal SEM scan rates. These detectors eliminate many of the objectionable aspects of BSE imaging and permit the use of BSE in automated studies. The harsh, high-contrast BSE image, lacking the esthetic qualities of the SE image, is well suited for AIA, where the optimum number of gray levels is two: black and white.

The particulates collected on an ambient air sample include a large range of atomic numbers. For example, carbon, flyash, and iron oxide particles are often present in one sample. The most convenient method would be to analyze the particles on the original filter used to collect the sample. This procedure precludes the use of the Hi Vol fiberglass filters, as they present topographic and compositional interferences. A suitable substrate for the majority of the particulates would be the polycarbonate membrane filters often used to collect ambient air samples. However, particles of low atomic number may present special problems.

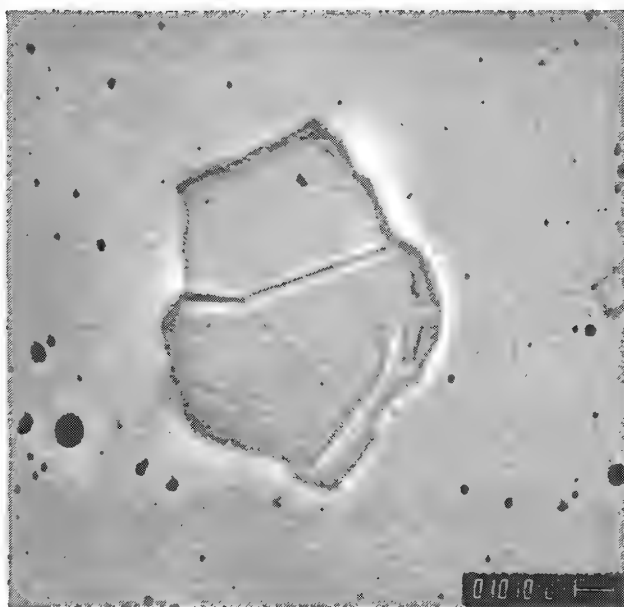
To illustrate, thin samples containing platy graphite particles and spherical hematite particles were prepared on several substrates. The BSE image of a graphite flake on a polycarbonate substrate is shown in Fig. 1a. Figure 1b shows the corresponding inverted BSE signal waveform for a single line scan across this particle. The signal peaks at the edges of the particle and drops in the center. The solid line in Fig. 1b is the threshold level used by LeMont to determine whether the beam is on or off a particle. The beam is assumed to be on a particle whenever the BSE signal is above the threshold level. As illustrated here, a slight variation in the threshold level would cause the particle to be detected as two particles or not detected at all.

Figure 2a shows the BSE image of a graphite and hematite sample. To prepare this sample, techniques developed for the analysis of asbestos in the electron microscope were used.<sup>4</sup> The polycarbonate filter was carbon coated and placed on a polished Be substrate, and the filter was dissolved, which left the carbon-entrained particulates on the substrate. In this case, both the graphite and hematite are readily detectable. As shown in Fig. 2b the threshold level could be changed significantly without a change in the apparent dimensions of the particle.

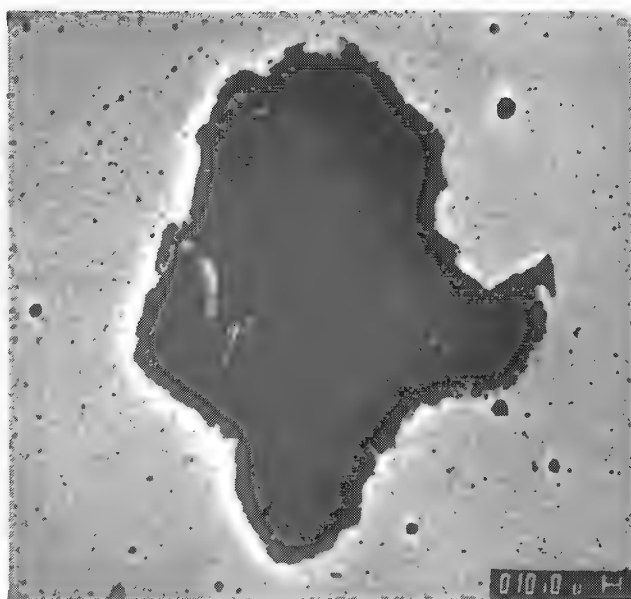
We propose to compare these and several other materials for use as substrates in particulate analysis, describing the advantages and limitations of each; to outline the instrumental parameters and detector criteria leading to optimum performance for image analysis; and to describe briefly the results of AIA studies on representative ambient air samples, to provide an indication of the utility of BSE imaging.

---

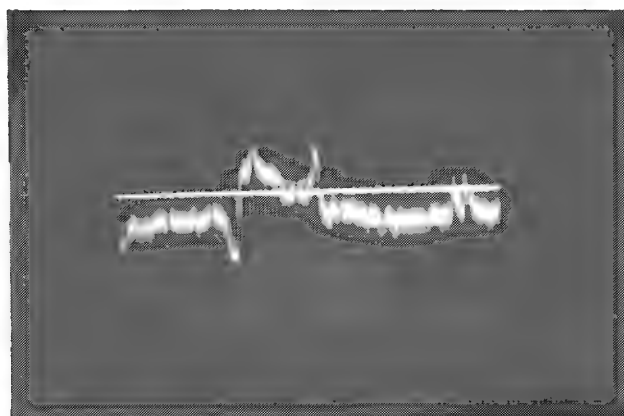
The authors are with U.S. Steel Research, Monroeville, PA 15146.



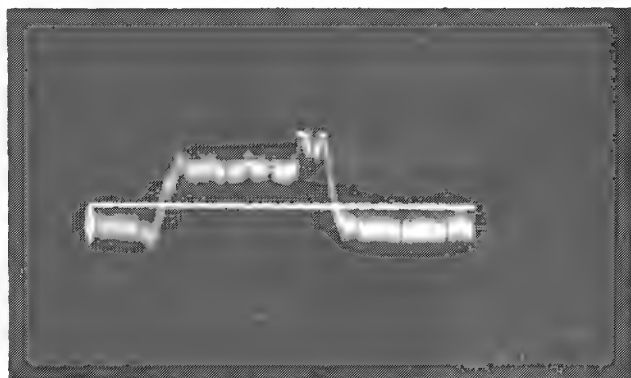
(a)



(a)



(b)



(b)

FIG. 1.--(a) BSE image of large graphite flake and spherical iron oxide particles on polycarbonate membrane substrate; (b) inverted BSE waveform for single line scan across graphite flake shown in (a).

FIG. 2.--(a) BSE image of large graphite flake and spherical iron oxide particles on Be substrate; (b) inverted BSE waveform for single line scan across graphite flake shown in (a).

#### References

1. J. Lebieczik, *Multiple Electron Detector Method for Quantitative Microtopographic Characterization in the SEM*, Doctoral Thesis, Pennsylvania State University, March 1975.
2. R. J. Lee, F. E. Huggins, and G. P. Huffman, "Correlated Mössbauer-SEM studies of Coal mineralogy," *SEM/1978*, vol. 1, 561.
3. R. J. Lee and R. M. Fisher, "Quantitative characterization of particulates by scanning and high voltage electron microscopy," *Proc. 13th MAS Conf.*, 1978, 63.
4. R. J. Lee, "Basic concepts of electron diffraction and asbestos identification using SAD. Part I: Current methods of asbestos identification using SAD," *SEM/1978*, vol. 1, 677.

## TYPE-2 MAGNETIC CONTRAST WITH NORMAL ELECTRON INCIDENCE IN THE SCANNING ELECTRON MICROSCOPE (SEM)

Oliver C. Wells and Richard J. Savoy

Type-2 magnetic contrast is obtained in the backscattered electron (BSE) image in the scanning electron microscope (SEM) because the incident electrons are deflected by the magnetic field inside the specimen during the backscattering process. Two sorts of this contrast have been reported: *Domain contrast*, in which the alternate domains appear bright and dark,<sup>1-6</sup> and *wall contrast*, in which domain contrast is zero, but bright or dark lines are seen along the domain walls.<sup>7,8</sup> A typical magnitude for domain contrast is 0.4% for a silicon-iron sample examined at oblique incidence at 30 kV.<sup>1</sup> These contrasts must be expanded by background-subtraction followed by amplification so as to be clearly seen in the micrograph. Competing contrasts caused by surface topography must be minimized by a suitable choice of incident angle and collector position.

*Topographic Contrast.* Fathers et al.<sup>1</sup> reported that, for a fixed collector position, the contrasts caused by surface topography can be minimized by tilting of the specimen at a critical angle. Fortunately, the magnetic contrast is still close to its maximum for collector positions that give rise to the smallest topographic contrasts.

It is a point of some interest to discover under what circumstances the topographic contrast can be eliminated by suitable positioning of the detector. The use of a solid-state BSE detector that can be moved around the specimen to vary the takeoff angle has been described previously.<sup>5,6</sup> Three positions A, B, and C for the detector are shown in Fig. 1; the corresponding images obtained from a copper electron microscope specimen grid are shown in Figs. 2(a), 2(b), and 2(c).

In Figs. 2(a) and 2(c) the detector is positioned with a low takeoff angle. The forward scattered image shown in Fig. 2(c) shows surface topography very clearly, whereas the backward scattered image shown in Fig. 2(a) is less clear. Contrasts caused by surface corrugations are of opposite signs in these two cases. For a critical takeoff angle shown in Fig. 2(b) the contrast caused by surface corrugations is almost entirely eliminated, but the contrast caused by small holes is still clearly visible. From these (and similar) micrographs it is concluded: first, that the use of a low takeoff angle in the forward direction gives the best image of shallow surface corrugations; and second, that these contrasts can be reversed by moving the detector across a point at which they are essentially zero, but for certain types of surface feature such as the small holes shown in Fig. 2(b) the contrasts do not reverse and so cannot be eliminated by this means.

*Magnetic Contrast.* Previously it has been stated that domain contrast is at a maximum when the incident electron beam makes an angle of  $55^\circ$  with the normal to the specimen surface, and that it is zero at normal electron incidence.<sup>1,2</sup> We have found that if the backscattered electron (BSE) signal is obtained by means of a detector that can be moved around the specimen, then domain contrast can also be obtained at normal electron incidence, and that it can be made to reverse if the detector is moved from one side of the beam to the other. Four images that were obtained from a Fe-3.22% Si sample are shown in Figs. 3(a) through 3(d); they correspond to the collector positions A, B, C, and D in Fig. 4. (These images were recorded with a 1 $\mu$ F condenser in series with the diode to facilitate contrast expansion.)

In Figs. 3(a) and 3(d) the detector was in the positions A and D of Fig. 4, with a low takeoff angle. Topographic contrasts predominate and, as expected, the apparent illumination of the sample is from the direction of the detector in each case. In Figs. 3(b) and 3(c) the effect of raising the detector until it almost cuts off the incident beam is shown.

---

The authors are with the IBM Thomas J. Watson Research Center, Box 218, Yorktown Heights, NY 10598.



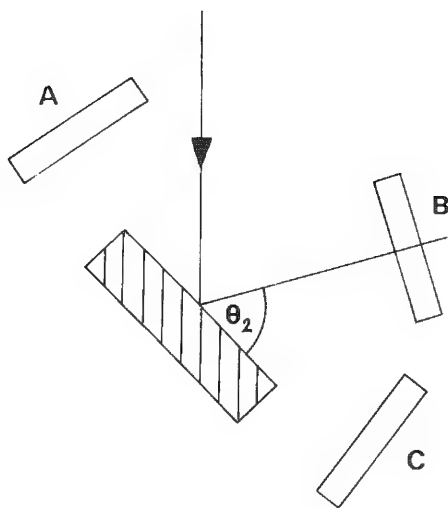


FIG. 1.--Positions for the BSE detector when sample is examined at oblique incidence.

Direction(s) of  
collector(s)

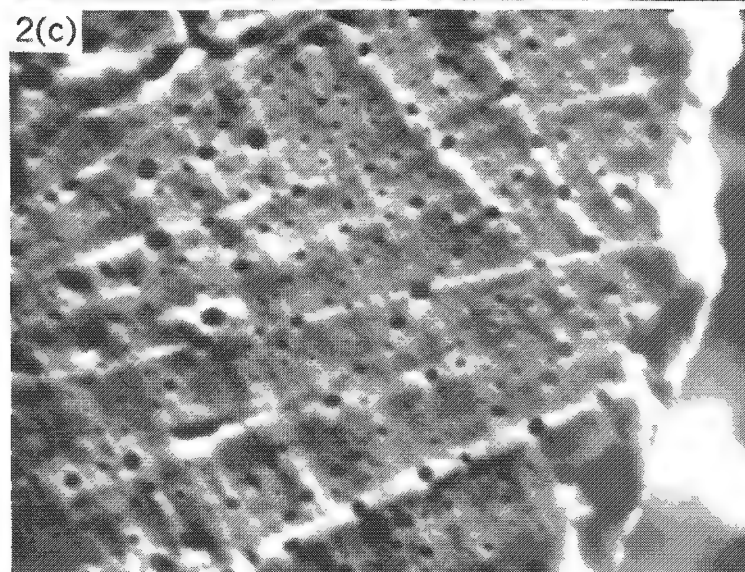
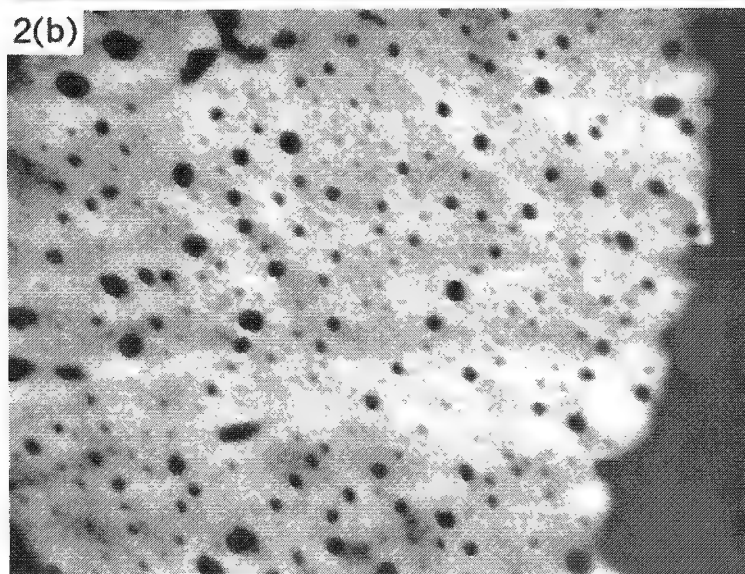
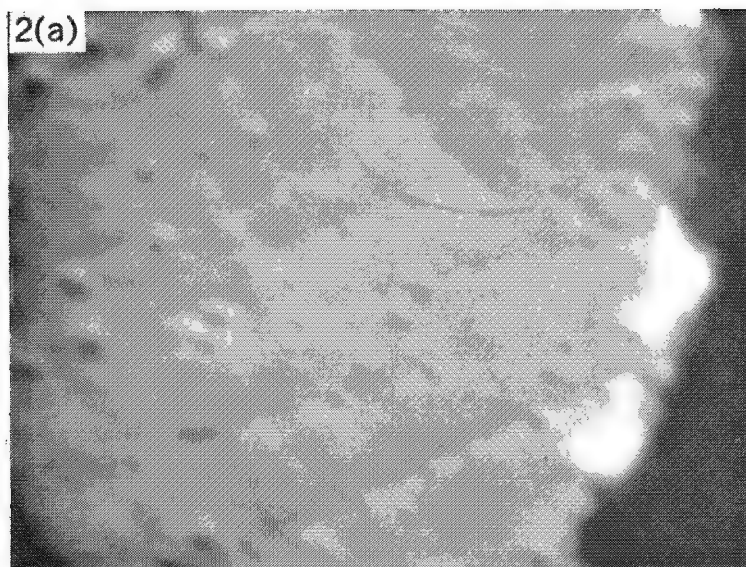


FIG. 2.--BSE images at 30 kV of copper electron microscope specimen grid in positions shown in Fig. 1. Angle of incidence,  $45^\circ$ . Field of view measures  $17\text{ }\mu\text{m}$  from left to right.

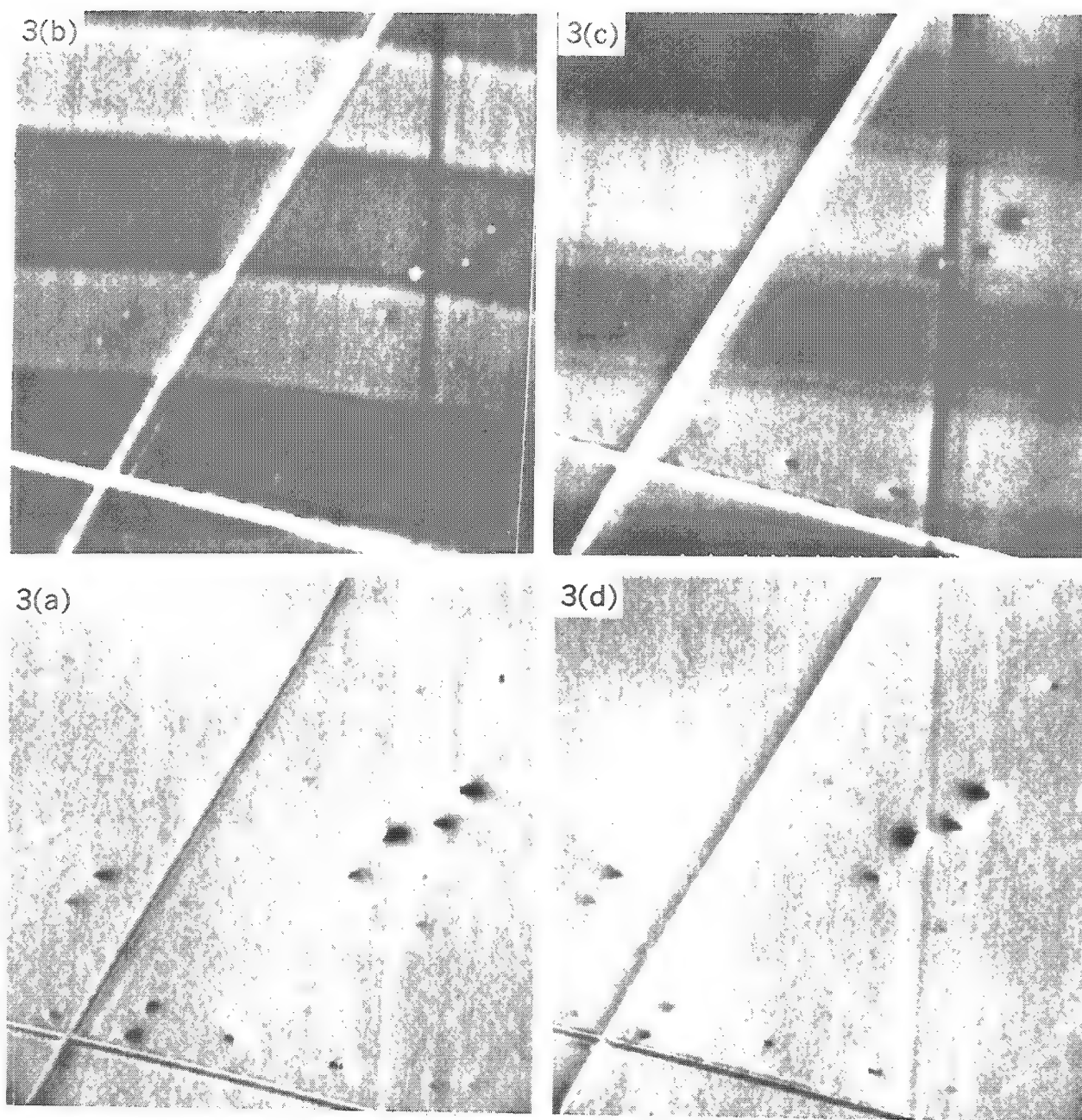


FIG. 3.--BSE images of Fe-3.22%Si sample at detector positions A, B, C, and D in Fig. 4 to show effect of collector position on topographic and magnetic contrasts. Field of view measures 75  $\mu\text{m}$  from left to right. [Normal incidence;  $\theta_2 =$  (a)  $22.5^\circ$ , (b)  $67.5^\circ$ , (c)  $112.5^\circ$ , and (d)  $157.5^\circ$ ; 40 kV;  $1.5 \times 10^{-7}$  A; 80sec scan.]

The topographic contrast has been reduced. The magnetic-domain contrast with normal electron incidence (and when operated with a single BSE detector in this way) amounts to 0.1% of the collected current at 30 kV, which is about four times smaller than can be obtained with an oblique angle of incidence.

The above experiments were continued by displaying either the sum or the difference signal from a pair of diodes in the positions B and C in Fig. 4.<sup>9</sup> The magnetic contrast that is visible in Figs. 3(b) and 3(c) consists of a superposition of domain contrast as defined above, together with wall contrast of a different sort, as can be seen by an examination of the difference image shown in Fig. 5(a) and the sum image shown in 5(b). In the difference image the domain contrast is enhanced, whereas in the sum image the domain contrast is zero but a modified form of wall contrast is seen. The wall contrast seen in Fig. 5(b) is smaller by a factor of 5 to 10 than the domain contrast seen in Fig. 5(a). If the specimen is tilted towards either detector then the sum image also shows domain contrast.

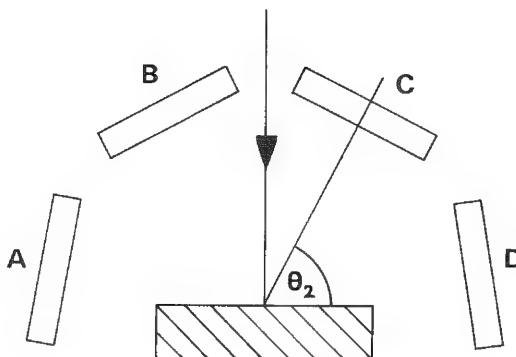


FIG. 4.--Positions for BSE detector when sample is examined at normal incidence.

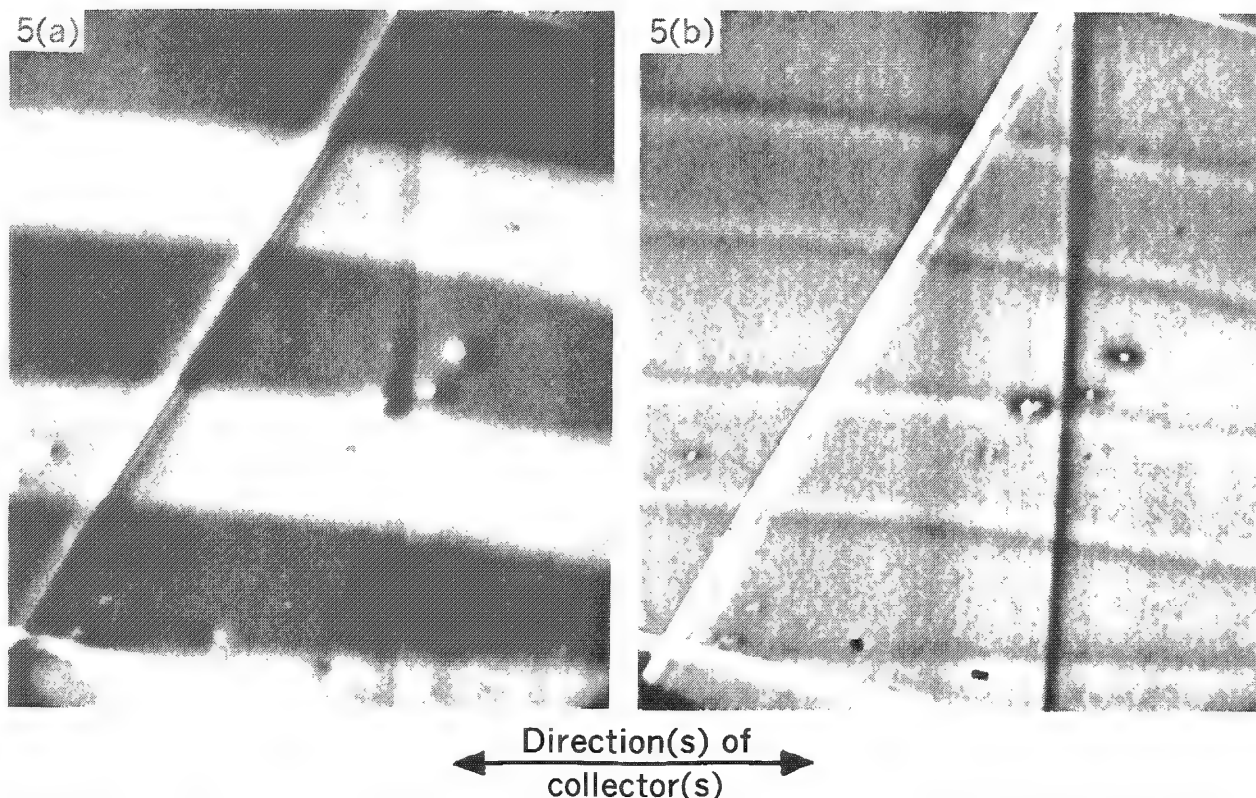


FIG. 5.--BSE images of Fe-3.22%Si sample obtained with pair of detectors in positions B and C in Fig. 4 to show (a) difference image showing domain contrast, (b) sum image showing wall contrast. (Same recording conditions as in Fig. 3.)



The wall contrast shown in Fig. 5(b) is different from that reported previously. In Ref. 7 and 8, the signal was obtained from a single BSE detector and the sample was rotated and/or tilted until the domain contrast was zero. The wall contrast then appeared as a narrow bright or dark band centered on the domain wall. In a typical case these bands would be alternately bright and dark at the successive domain walls across the specimen. In Fig. 5(b) the contrast appears as a double line, which is bright on one side of the domain wall and dark on the other.

The difference image has the advantage that the effects of beam instabilities caused by short-term variations in the brightness of the electron gun and by 60Hz modulation of the beam by external fields are minimized in comparison with the images obtained when the signals from either diode are displayed separately. To cancel the effects of beam instabilities from the sum image it will probably be necessary to obtain the current used for background-subtraction from the current that can be collected from the beam-limiting aperture in the SEM final lens. (Of course, whereas the effects of beam instabilities of these particular kinds can be largely eliminated by the difference technique, the random noise that arises from statistical variations in the number of signal-carrying quanta at the noise bottleneck of the system cannot be eliminated by these means.)

*Conclusion.* This work verifies the value of a movable BSE detector for studies of surface topography and magnetic contrast. The detailed effects of specimen tilt and collector position on domain contrast and wall contrast are now being investigated in more detail.

#### References

1. D. J. Fathers et al., "A new method of observing magnetic domains by scanning electron microscopy," *Phys. Stat. Sol.* (a) 20: 535, 1973 and 22: 609, 1974.
2. D. E. Newbury et al., "Monte Carlo calculations of magnetic contrast from cubic materials in the scanning electron microscope," *Appl. Phys. Lett.* 23: 488, 1973.
3. T. Ikuta and R. Shimizu, "Magnetic domain contrast from ferromagnetic materials in the scanning electron microscope," *Phys. Stat. Sol.* (a) 23: 605, 1974.
4. T. Yamamoto et al., "Magnetic domain contrast in backscattered electron images obtained with a scanning electron microscope," *Phil. Mag.* 34: 311, 1976.
5. O. C. Wells, "Effect of collector position on type-2 magnetic contrast in the SEM," *Scanning Electron Microscopy/1978/Vol. 1* 293, 1978.
6. M. Kikuchi and S. Takashima, "Multi-purpose backscattered electron detector," *Ninth Int. Cong. Electron Microsc.*, Toronto, 1: 82, 1978.
7. T. Yamamoto and K. Tsuno, "Unusual magnetic contrast of domain images obtained in the reflective mode of scanning electron microscopy," *Phil. Mag.* [8] 34: 479, 1976.
8. D. C. Joy et al., "Domain wall image contrast in the SEM," *Appl. Phys. Lett.* 28: 466, 1976.
9. S. Kimoto and H. Hashimoto, "Stereoscopic observation in scanning microscopy using multiple detectors," in T. D. McKinley et al., Eds., *The Electron Microprobe*, New York: Wiley, 1966, 480-489.

## THE PREPARATION OF CERAMIC SURFACES FOR SELECTED-AREA ELECTRON CHANNELING

D. L. Davidson and J. Lankford

The discovery of the phenomena of electron channeling was made by Donald Coates<sup>1</sup> while he observed a fractured specimen of GaAs ceramic in the scanning electron microscope (SEM). Until recently, studies of ceramics by the beam-rocking technique of selected area electron channeling have been confined almost solely to Si; in fact, the first channeling map ever published was for this material.<sup>2</sup> This paper reports on channeling work done on several other ceramics in which the technique of ion milling was used for surface preparation.

With ceramic materials, several problems in specimen preparation must be overcome that are not common to metals. As with metals, several ceramics are also conductors; both GaAs and Si fall into this category. Generally, a material need not be a particularly good conductor, because of the relatively low currents normally required for imaging by secondary electrons ( $10^{-11}$  A). However, the electron-specimen interaction which generates crystallographically related electron backscattering (channeling) results in a requirement for higher beam currents ( $10^{-8}$  A) than those required for topographic contrast. Thus, many ceramics cannot be used as specimens for electron channeling studies without steps being taken to overcome the charging problem created by their insulating properties. Two methods have been conceived for solving this problem: (1) coat the sample to be observed with a conductive material, or (2) increase the conductivity of the sample itself by implanting ions in it. The coating approach is by far the best, because it can be used on any material and is easier to implement than the second method. Carbon is the obvious coating material because of its electron transparency, but it must be deposited very carefully to insure a very thin coating. Since precise control of layer thickness is difficult, it may be necessary to try several times until the optimum coating thickness is obtained. A very thin layer must be used because electron channeling contrast is developed within only a few hundred atomic layers of the surface; thus, electron absorption by an amorphous layer at the surface must be avoided. The conductive coating method has been successfully used by Stanley and Ramaswamy for determining the orientation of  $\text{LiTaO}_3$  layers, of several orientations, used in optical waveguide devices.<sup>3</sup>

Another use for selected area electron channeling (besides crystallographic orientation) is to assess crystal damage within a small surface area (5-50  $\mu\text{m}$ ). This application of electron channeling has been extensively used in metals for the study of localized plasticity, particularly for wear<sup>4</sup> and fatigue crack propagation.<sup>5</sup> With the increasing need for using ceramics in structural applications, it is desirable to extend this technique to ceramics as well. Two demonstrations of the usefulness of this capability in ceramics have been accomplished. The first was a study of the plasticity associated with indentation and microfracture in  $\text{SiC}$ <sup>6</sup>; the other measured the depth of subsurface damage due to the polishing and grinding of  $\text{Al}_2\text{O}_3$ ,  $\text{SiC}$ , Si, and GaAs.<sup>7</sup>

The use of electron channeling on structural materials requires careful techniques of materials preparation, as often the surfaces have been heavily deformed during manufacturing operation. With metals, a deformed layer may be made increasingly thinner by grinding with smaller and smaller abrasives, with final surface preparation by electropolishing. For most metals, this procedure provides a surface free of preparation-induced deformation, and having a very thin, uniform oxide layer.

The chemical and electrolytic removal of material from ceramics is, conversely, an uncommon practice, and even when possible, it often requires high temperatures and strong

---

The authors are with Southwest Research Institute, P.O. Drawer 28510, San Antonio, Texas. The Office of Naval Research supported this work through contract N00014-75-C-0668.

oxidents. Thus, the chemical removal of plasticity from ceramic surfaces is virtually precluded as a viable technique of specimen preparation when localized plasticity is to be studied.

Ion milling, or sputter etching, which is the removal of material by ion bombardment, is a technique that has been developed for the thinning of both ceramic and metallic specimens for transmission electron microscopy.<sup>8</sup> The technique uses low-energy ions and low ion currents to prevent substantial damage to the specimen. Rates of material removal vary with material and the configuration of the ion milling fixture, but an often-quoted value<sup>8</sup> is 1-2  $\mu\text{m/hr}$  for a  $20^\circ$  angle of beam incidence at 6 keV, with an ion current density of 200  $\mu\text{A/cm}^2$ .

Ion-induced damage thus far has not been found to be a problem, although defect clusters have been seen by TEM.<sup>8</sup> Very little published information on radiation damage due to ion milling in the 1-6keV range is to be found, but several private communications<sup>9,10</sup> have indicated the following:

1. Ion damage is generally expected to be in the form of single vacancies or interstitial atoms, and to be limited to within 50 Å of the surface. Another possibility is that 10Å-dia. size clusters of defects are formed rather than single defects.

2. The heat generated by a 100keV TEM electron beam during extended observation may be sufficient to cause the clustering of smaller defects into the 100Å size that has been reported.<sup>8</sup>

From the evidence at hand, it appears that even though the exact nature of the defects is unknown, they are concentrated very near to the surface, within 50-100 Å. The depth within the material from which the information in an electron channeling pattern is generated is not well known. Theoretical assessment has indicated that for beam accelerating voltages of 20 to 30 keV, the information depth is approximately 500 Å.

Theoretical estimates also indicate that the total penetration depth for 30keV electrons in Al is about 3.5  $\mu\text{m}$  (35 000 Å), meaning that the channeling information could be coming from as deep as 10 000-15 000 Å. Although the question of the depth of information is not at present resolved, it does appear that the information depth is much greater than the depth of damage due to ion milling.

To prepare ceramic specimens for electron channeling studies of localized plasticity, the usual grinding and polishing operation, by means of ever smaller abrasive particles at normal loads and speeds may be used, as with metals, followed by ion milling, and if necessary, by coating. The amount of material to be removed to achieve a surface free of preparation-induced damage has only been partially determined.

The damage layer depths due to standardized grinding and polishing operations were, in fact, determined by selected area channeling.<sup>8</sup> Single crystals of SiC,  $\text{Al}_2\text{O}_3$ , Si, and GaAs were prepared by use of both a polishing and grinding procedure.

The grinding operation was done by gripping a cylinder of each material in a lathe chuck. A section 25  $\mu\text{m}$  deep was then removed from the exposed face of the specimen by one pass of an 800-grit, diamond-bonded cup wheel lubricated by a steady stream of water-soluble oil mixture. The 76mm-dia. wheel was turned at 3500 rpm at a feed rate of 25  $\mu\text{m/sec}$ .

The polishing procedure was as follows. Each specimen was abraded by 600-grit SiC in a water-lubricated automatic metallographic preparation apparatus at a load of 2.3 kg. Polishing was continued until an equilibrium condition of surface finish was achieved, as determined optically.

The specimens from both surface preparation procedures were then taper-sectioned by grinding at  $15^\circ$  to the specimen surface in a Buehler discplane machine with a 120-grit SiC wheel. The specimen was then polished with the same automatic metallographic apparatus described in the previous paragraph, with a load of 0.8 kg, using successively 240, 320, 400, and 600-grit SiC, then 6 $\mu\text{m}$  and 1 $\mu\text{m}$  diamond in a lubricant slurry. These surfaces were then ion milled under the conditions given in Table 1.

Although the removal rate from each material is likely to be different, no better estimate than that given in the Table can be made. The critical point is that the ion milling was sufficient to remove the damage induced by the taper section preparation technique. Selected area electron channeling patterns from these ion milled taper sections are shown in Figs. 1 and 2. Figure 1 shows patterns from deformed and undeformed

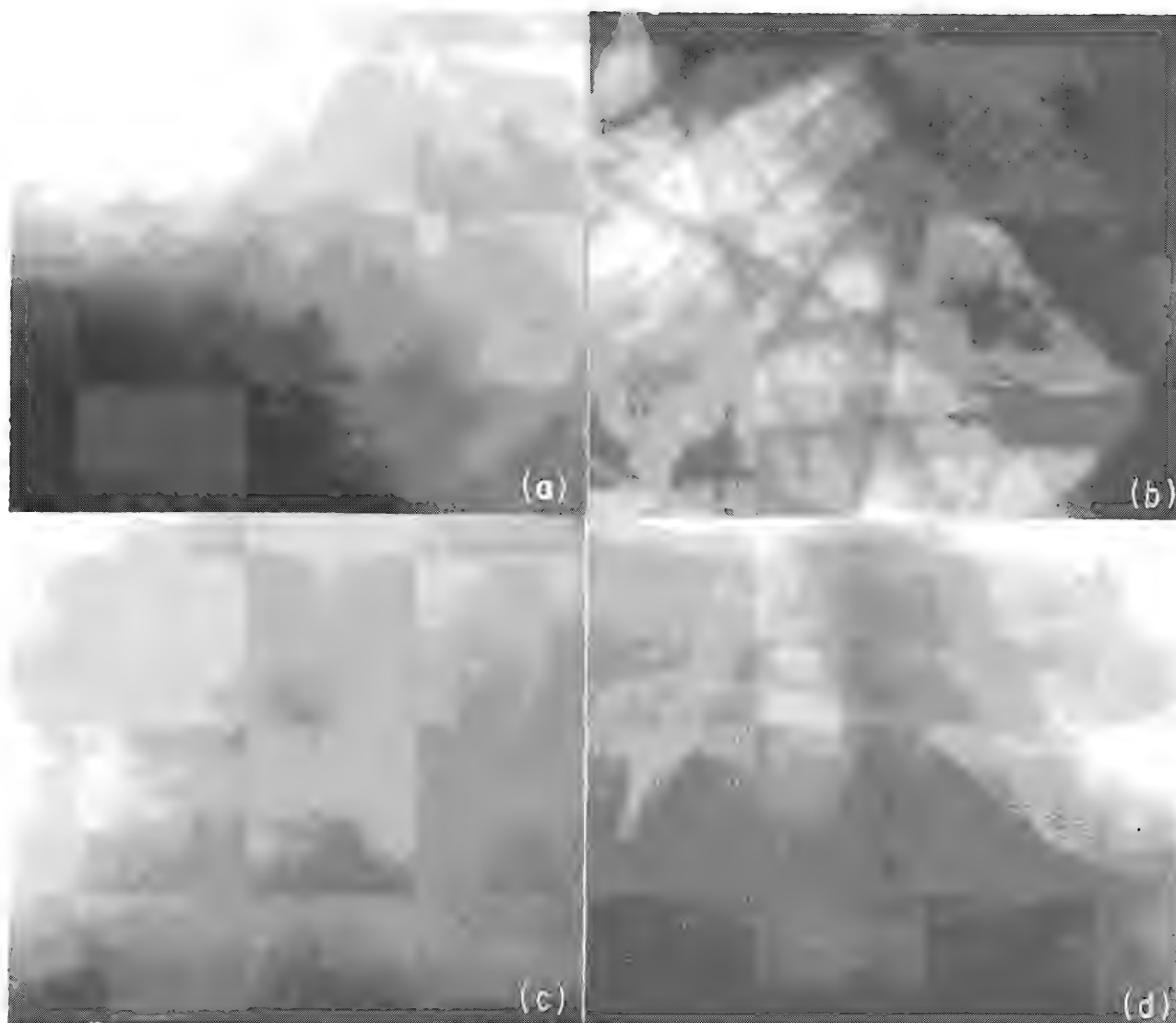


FIG. 1.--Comparison of channeling patterns made from surfaces prepared by ion milling. Surfaces were ground as described in text prior to taper sectioning. (a) Si within deformed region, (b) Si remote to deformation, (c)  $\text{Al}_2\text{O}_3$  within deformed region, (d)  $\text{Al}_2\text{O}_3$  remote to deformed region.

regions of ground Si and  $\text{Al}_2\text{O}_3$ . Figure 2 shows patterns from deformed and undeformed regions of polished SiC and GaAs. The electron-optical conditions used in all cases is shown in Table 2.

The damage layer depths determined for the grinding and polishing operations are summarized in Fig. 3, where it may be seen that the damage sustained by each material is related to its hardness, as determined by indentation. Thus, depending on the hardness of the material, it is necessary to remove different amounts of damage during specimen preparation.

#### *Summary and Conclusions*

1. Localized plasticity may be studied in ceramic materials by selected area electron channeling, provided careful specimen preparation procedures are followed.

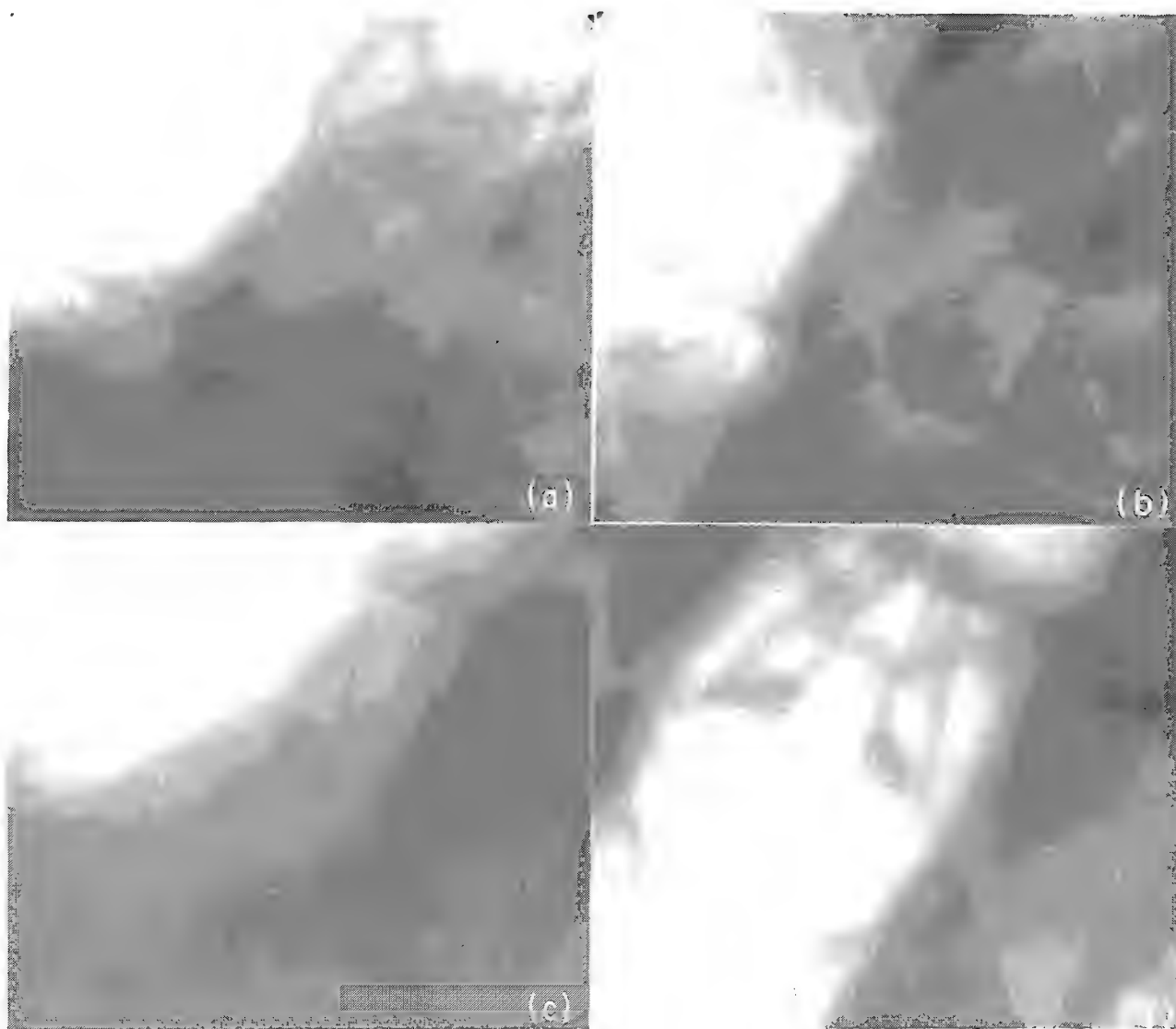


FIG. 2.-- Comparison of channeling patterns made from surfaces prepared by ion milling. Surfaces were polished as described in text prior to taper sectioning. (a) SiC within deformed zone, (b) SiC remote to deformation, (c) GaAs within deformed zone, (d) Ga As remote to deformation.

TABLE 1.--Ion milling conditions.

Ion-beam accelerating potential	5-7 keV
Ion beam current	500 $\mu\text{A}/\text{cm}^2$
Ion	Argon
Angle of incidence	15°
Time	10-12 hr
Estimated material removal	10-20 $\mu\text{m}$

TABLE 2.--SEM electron-optical parameters used for selected areas.

Beam energy	30 keV
Beam current	$3 \times 10^{-8}$ A (approximately)
Beam divergence	$4 \times 10^{-3}$
Rocking angle	7° (approximately)
Diameter of region channeled	10 $\mu\text{m}$ (approximately)

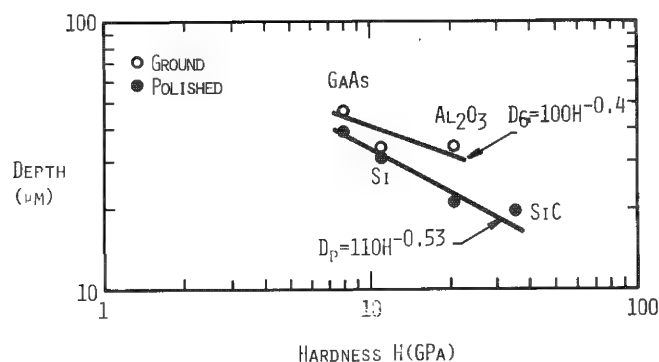


FIG. 3.--Depth of deformed material vs hardness.

2. Surface grinding and polishing operations typical of those used in ceramic material preparation procedures were found to produce damage to a depth related to the hardness of the material. The approximate expressions are  $D_G = 100H^{-0.40}$  and  $D_P = 110H^{-0.53}$ , where the hardness (H) is expressed in GPa and the damage depths for grinding ( $D_G$ ) and polishing ( $D_P$ ) are in  $\mu\text{m}$ .

3. Argon ion milling at 5-7 keV for 10 hr at  $500 \mu\text{A}/\text{cm}^2$  was found to remove the residual polishing damage incurred in specimen preparation, at least to a degree sufficient to give channeling patterns indicating no damage.

4. Carbon coating, if carefully applied, gives sufficient conductivity with minimal contrast attenuation; channeling patterns can be obtained from ceramics of extremely low conductivity.

#### References

1. D. G. Coates, "Kikuchi-like reflection patterns obtained with the scanning electron microscope," *Phil. Mag.* [8] 16: 1179, 1977.
2. D. G. Coates and Om Johari, Eds., "Pseudo-Kikuchi orientation analysis in the scanning electron microscope," in *Scanning Electron Microscopy/1969*, Chicago: IIT Research Institute, 1969, 27-40.
3. R. D. Standley and V. Ramaswamy, "Pseudo-Kikuchi maps of Nb-diffused  $\text{LiTaO}_3$  thin film optical waveguides," *J. Appl. Physics* 46: 4887, 1975.
4. A. W. Ruff, "Deformation studies at sliding wear tracks in iron," *Wear* 40: 59, 1976.
5. D. L. Davidson and J. Lankford, "Plastic strain distribution at the tips of propagating fatigue cracks," *J. Engineering Mater. and Technol.* (ASME), 98 (Ser. H): 24, 1976.
6. J. Lankford and D. L. Davidson, "Indention plasticity and microfracture in silicon carbide," *J. Mater. Sci.* 14 (in press).
7. J. Lankford and D. L. Davidson, "Characterization of surface damage in ceramics using selected area electron channeling," in B. Hockey, Ed., *The Science of Ceramic Machining and Surface Finishing II*, Washington, D.C.: National Bureau of Standards, Special Publication, 1979.
8. D. J. Barber, "Thin foils in non-metals made for electron microscopy by sputter-etching," *J. Mater. Sci.* 5: 1, 1970.
9. B. J. Hockey, National Bureau of Standards, private communication, February 1979.
10. T. E. Mitchell, Case-Western University, Cleveland, Ohio, private communication, February 1979.
11. C. J. Humphreys et al., "Theory and practice of revealing crystallographic defects with the SEM by means of diffraction contrast," *Scanning Electron Microscopy/1972*, Pt. 1., Chicago: IIT Research Institute, 1972, 205-214.



## FULL SURFACE EXAMINATION OF SMALL SPHERES WITH A COMPUTER-CONTROLLED SCANNING ELECTRON MICROSCOPE

C. M. Ward, D. L. Willenborg, and K. L. Montgomery

Targets for inertial-confinement laser-fusion experiments require 70-300 $\mu$ m diameter glass spheres that meet precise dimensional requirements, including surface finishes better than a few thousand Angstroms. Interferometry is effective in detecting defects down to a spatial width of a micron and is routinely used in target selection.<sup>1</sup> Submicron-wide defects are observed by means of scanning electron microscopy (SEM), where the high resolution and easy image interpretation is effective. The main disadvantage of SEM examination is that the sample must be permanently attached to a mount which prevents an acceptable sphere from being used as a target. A manual-rotation SEM stage demonstrated that it is possible to manipulate spheres and examine them through  $4\pi$  steradians.<sup>2</sup> Application of this stage to target selection showed that many apparently good spheres contained unacceptable submicron defects that were not discovered in other inspections. Consequently, a computer automated stage and SEM system for spheres has been developed (Fig. 1) that permits examination of candidate spheres prior to inclusion in targets.

The stage consists of two groups of slides, each with independent Y and Z stepper motor-driven motions (Fig. 2). On each slide group is mounted a glass capillary with a plane surface formed on the end in conductively coated silicone rubber. A sphere is lightly contained between the rubber tips such that when counter Y and Z motions are applied the sample rotates in place. By means of the resultant  $\theta_z$  and  $\theta_y$  motions, a sphere is scanned from pole to pole along lines of longitude. Under computer control microspheres are sequentially rotated and pictures are recorded at preset points. A simple inspection requires around 150 pictures at 1000 $\times$ ; careful evaluations may require more than 1000 pictures at magnifications up to 10 000 $\times$ . During the analysis, the sphere remains in focus and in the field of view.

Primary image recording is made on a raster-scanning video disk that is arranged to synchronize with the SEM. In normal operation an SEM picture is recorded on photographic sheet film. This process is unacceptable for automatic operation and insufficient to provide rapid feedback as to system operation. A video disk can store up to 300 images with almost instant retrieval and at an acceptable contrast range; however, standard units operate at TV sweep rate, which is too fast to yield adequate signal-to-noise ratio in SEM pictures. We employ a microprocessor-based system developed in conjunction with Information Processing Systems of Belmont, Calif., which has a full-line buffer on the input that permits 400-line by 500-point SEM recording at 30-250 sec per frame with TV playback. An improvement up to 70 times in signal-to-noise ratio is achieved. Synchronization of the disk to the SEM permits the computer to tell the disk to step and take a picture, with the disk in turn initiating the SEM scan. If the examination requires more than 300 pictures the system stops at track 299 and waits for the operator to record the stored images on videotape before continuing.

Operation of the SEM is basically unchanged for  $4\pi$  steradian examination except that since some scans of more than 1000 pictures are necessary, total continuous recording time may exceed 36 hr. This requirement means that the instrument must have sufficient stability to need no readjustment during this time. Achieving this goal has been a matter of electronics adjustment, attention to contamination control, and the use of a stable electron emitter. We use a Broers-style electron-bombardment-heated lanthanum hex-

---

This work was performed under the auspices of the U.S. Department of Energy (DOE) at Lawrence Livermore Laboratory under Contract W-7405-Eng-48. This report was prepared as an account of work sponsored by the U.S. Government. Neither the United States, nor DOE, nor any of their contractors, subcontractors, or their employees, makes any warranty, express or implied, for the accuracy, completeness, or usefulness of any information, apparatus, product, or process disclosed, or represents that its use would not infringe privately owned rights. Reference to a company or product name does not imply approval or recommendation of the product by the University of California or DOE to the exclusion of others that may be suitable.

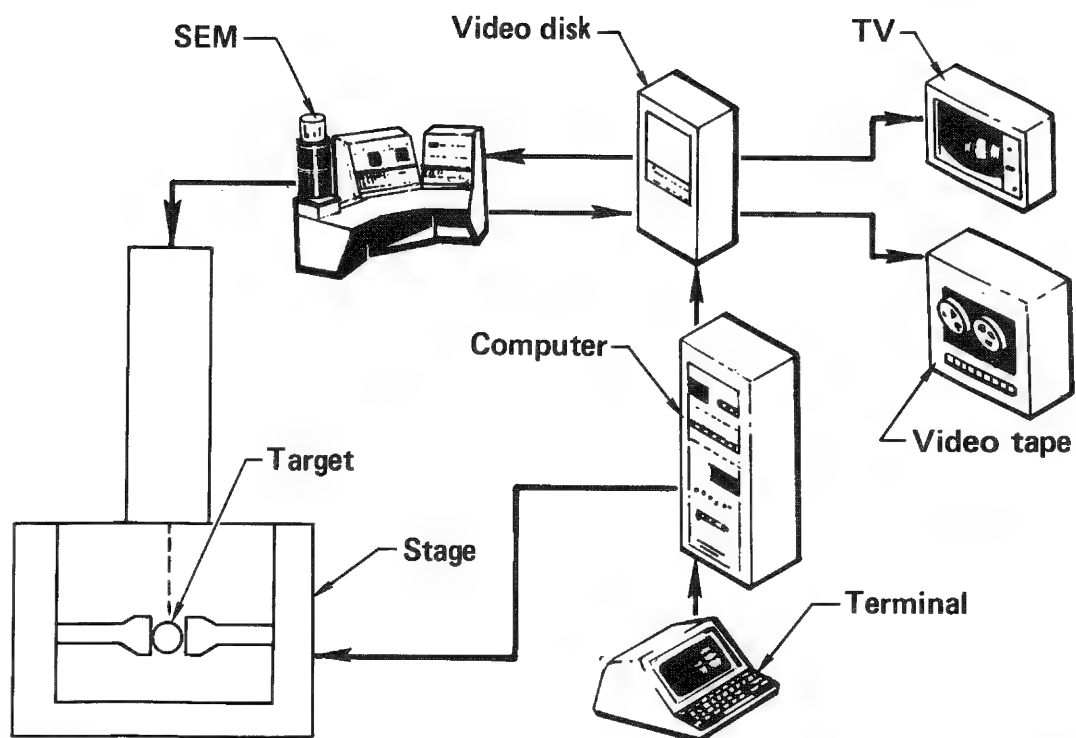


FIG. 1.--Full surface examination system layout.

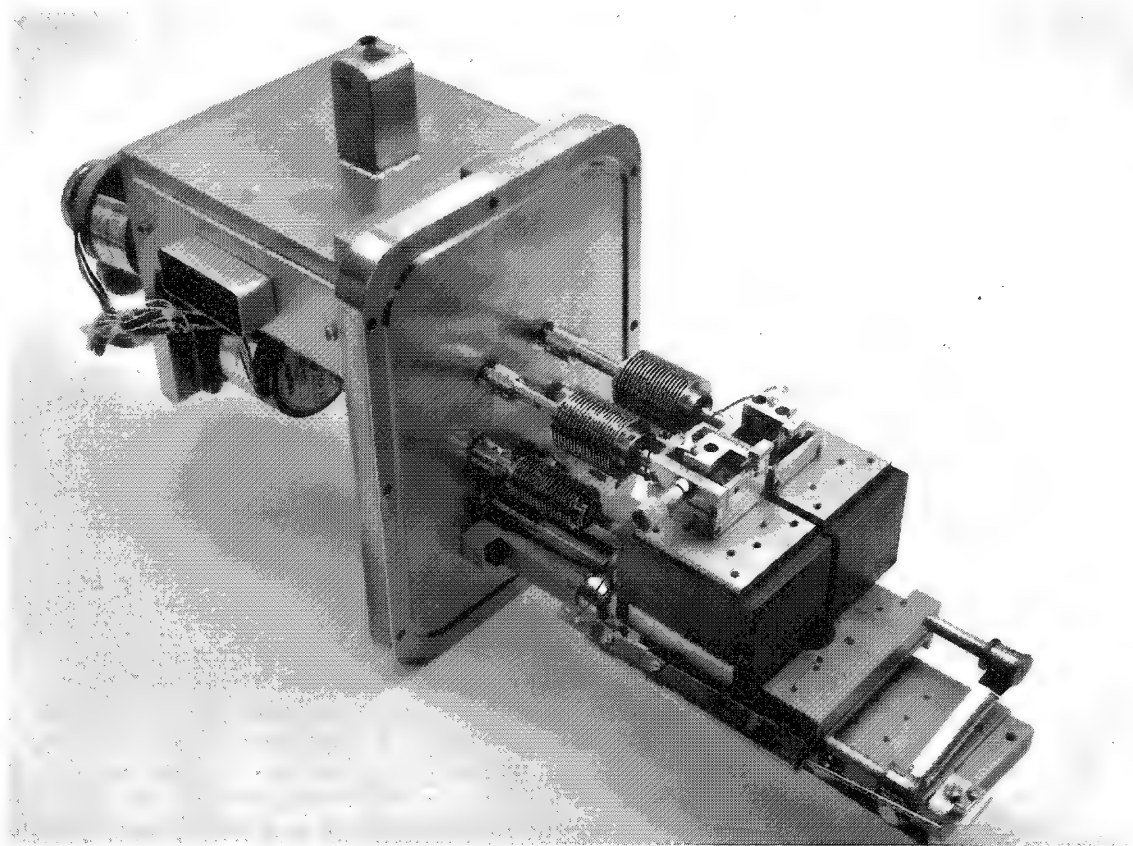


FIG. 2.--Stepper stage for sphere manipulation.

aboride ( $\text{LaB}_6$ ) emitter<sup>3</sup> that gives high brightness and stable emission for over 100 hr. Experience to date has indicated no problems with SEM stability through even the longest scans.

Figure 3 is a portion of an automated 3000 $\times$  scan on a 140 $\mu\text{m}$  glass sphere with a carbon coating of about 100 Å. Each image from upper left to lower right shows the surface of the sphere rotated by 24° along one longitudinal scan. Initial 4 $\pi$  scans were made by

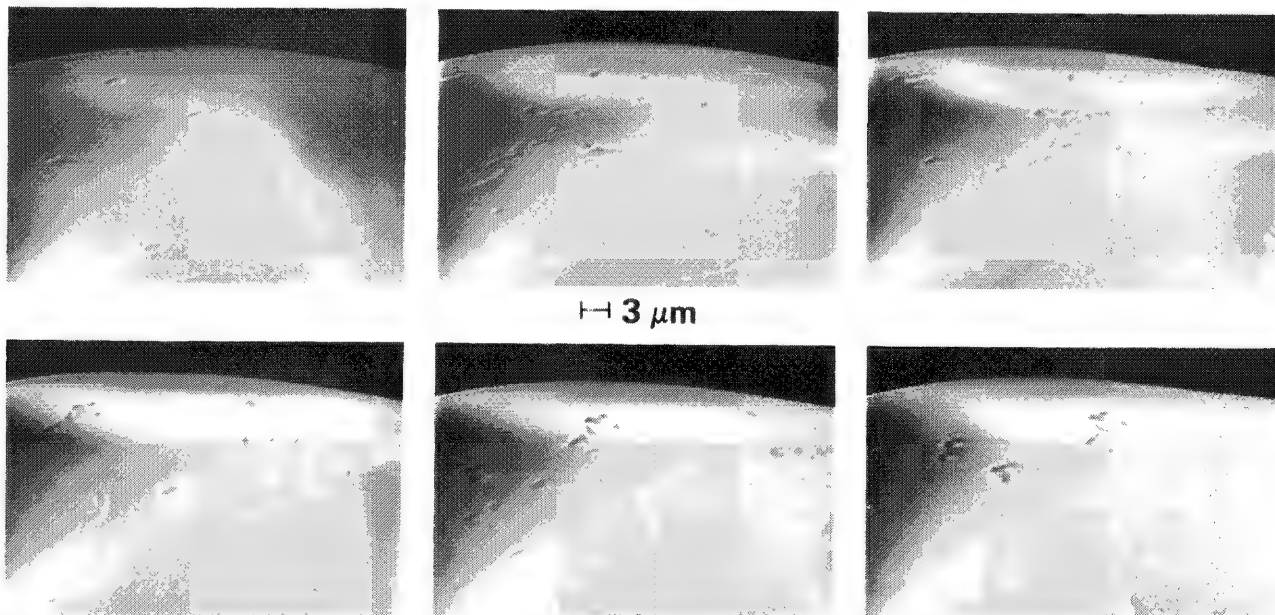


FIG. 3.--Computerized 4 $\pi$  steradian SEM scan of a carbon coated 140 $\mu\text{m}$  glass sphere at 3000 $\times$  magnification. Steps are 24° along a line of longitude starting from the upper left.

viewing normal to the surface. Although photo mosaics could be made by this procedure, they were difficult to use for height measurements. By recording the examination looking over the horizon one can detect significant items more easily and a scan can always be found with the object in profile for a height measurement. The larger defects in these pictures would be detected on an interferometer; however, many small defects at or below the resolution of the interferometer can also be seen. The broad light and dark areas on the images are due to charging effects from the thinly coated sphere. An analog homomorphic processor is used to suppress this artifact where objectionable levels are encountered. Software also allows a point on the sphere to be rotated to a position where a side-looking Si(Li) x-ray detector can be inserted in front of the secondary detector, so that analysis of defect compositions can be made.

This system is proving to be relatively simple to operate and quite versatile. Its primary application is currently in the understanding of submicron defects on target spheres, and insuring that spheres used in critical laser-fusion experiments meet all surface requirements.

#### References

1. B. W. Weinstein and C. D. Hendricks, "Interferometric measurement of laser fusion targets," *Applied Optics* 17: 3641, 1978.
2. C. M. Ward, C. D. Hendricks, and B. W. Weinstein, "A technique for full surface examination of small spheres in the scanning electron microscope," *Scanning Electron Microscopy* 1: 783-788, 1978.
3. A. N. Broers, "Recent advances in scanning electron microscopy with  $\text{LaB}_6$  cathodes," *Scanning Electron Microscopy* 1974, 12-18.

## Monte Carlo Techniques in Electron Microscopy and Microanalysis

### APPLICATION OF MONTE CARLO CALCULATION TECHNIQUE TO QUANTITATIVE ANALYSES BY AUGER ELECTRON SPECTROSCOPY

Ryuichi Shimizu, Shingo Ichimura, and Mikio Aratama

Recent advances in the instrumentation used in Auger electron spectroscopy (AES) have made selected area surface analysis with high lateral resolution (less than 1  $\mu\text{m}$ ) possible. This scanning Auger microprobe (SAM) allows us to perform AES studies with a primary electron beam of wider energy range than that for conventional AES, which is usually done with a primary beam of less than 5 keV. This development may lead to AES with high accuracy through improvement of the signal-to-noise ratio by appropriate choice of primary energy for operation.

The use of AES for accurate quantitative analyses, however, has been fairly limited, although basic approaches for quantitation have been extensively discussed<sup>1,2,3</sup> in analogy with quantitative analyses by electron probe microanalysis (EPMA).<sup>4</sup> One of main difficulties for the quantitative AES analyses is probably a lack of precise knowledge on the contribution of backscattered electrons to the generation of signals, which is familiar as atomic number effect in quantitative EPMA.<sup>4</sup>

Since the excitation energy of the signals (characteristic x rays) is usually in keV region, we need only take into account the scattering process of electrons with kinetic energy greater than a few keV. This fact has made theoretical treatment of the atomic number effect much easier. A Monte Carlo calculation, based on the Born approximation for elastic scattering and on Bethe's stopping power for the continuous slowing down approximation (CSDA), has been widely applied to quantitative analyses by EPMA with considerable success.<sup>5</sup>

In AES, however, the excitation energy of the Auger signal is usually below 2 keV. Hence, theoretical treatment of the atomic number effect is required to describe the scattering processes of a penetrating electron in the energy region from the primary energy to below 1 keV. Here one cannot very well use the Rutherford-type scattering formula, for instance, which has widely been used in quantitative EPMA for describing the elastic scattering of a penetrating electron in a specimen. Furthermore, the low energy for the Auger electron excitation leads to a situation in which secondary electrons of high energy can be a significant source of Auger signals.

In the previous paper<sup>6</sup> we proposed a Monte Carlo calculation incorporating both the elementary differential cross sections for inelastic scattering and those for elastic scattering numerically calculated by the partial wave expansion method (PWEM) as a more comprehensive theoretical approach for quantitative AES analyses. This Monte Carlo approach has described the edge effect appearing in a high resolution SAM with reasonable quantitative accuracy. This result is encouraging enough for us to attempt further extension of the Monte Carlo calculation approach for quantitative AES analyses.

This paper provides a basic study of the atomic number effect for quantitative AES analyses by Monte Carlo calculation technique. Since the direct simulation of each individual inelastic scattering process used in the previous papers<sup>6,7</sup> applies to only a few materials, we have attempted to incorporate a semi-empirical stopping power formula proposed by Krefting and Reimer<sup>8</sup> instead of the individual inelastic scattering. The result has described the dependence of Auger electron intensity on primary energy obtained with a commercial SAM, JEOL JAMP III, with considerable accuracy.

#### *Basic Model*

1. *Elastic Scattering.* It has already been pointed out by Krefting and Reimer<sup>8</sup> that

---

The authors are at Department of Applied Physics, Osaka University, Osaka, Japan. This work was partially supported by the aid of the Toyota Foundation.

the Rutherford scattering formula is a poor approximation in describing elastic scattering of even keV electrons in EPMA studies. Hence, a more accurate differential cross section for elastic scattering is highly desirable. A PWEM calculation for the energy region below 20 keV allows us to describe the scattering process of a penetrating electron for the present study of Auger electron excitation in a specimen.

From analytical expressions for the Thomas-Fermi-Dirac potential the differential cross sections were numerically calculated for various elements by PWEM after Bühring's "reduced atomic radius method" as described in detail elsewhere.<sup>9</sup> The results were compared with those published by Fink and Yates<sup>10</sup> and confirmed that the present calculation is in satisfactory agreement with them in the energy region from 100 to 1500 eV.

Figure 1 shows typical examples of differential cross sections for elastic scattering for Al, Cu, Ag, and Au, in which the ratio of the cross section obtained by PWEM to that of the screened Rutherford with the screening parameter of Nigam et al.<sup>11</sup> is plotted for each element so as to permit the determination of the discrepancy between the two cross sections after Krefting and Reimer.

2. *Inelastic Scattering.* Since Bethe's stopping-power equation based on CSDA provides the average rate of energy loss of a primary electron, one cannot take into account the secondary electrons associated with the energy-loss process, which are particularly important in determining the generation of Auger electrons of low excitation energy.

So far as exact knowledge of individual inelastic scattering exists, one can perform a direct simulation of the individual inelastic scattering to describe the energy-loss process incorporating the generation of secondary electrons. This treatment, however, can only be applied to a few materials (including aluminum) with considerable accuracy and confidence. Thus, we have attempted to adopt the Krefting and Reimer's semi-empirical approach in which they used Gryzinski's excitation function for inner shell; for the other excitations they used the difference between Bethe's stopping power and that due to the inner-shell (core) electron excitation:

$$\left. \frac{dE}{dx} \right|_{\text{valence}} = \left. \frac{dE}{dx} \right|_{\text{Bethe}} - \left. \frac{dE}{dx} \right|_{\text{core}}$$

This approach allows us to extend it to a compound specimen quite easily.

The direct-stimulation approach described in the previous paper and the present approach have provided the same results with respect to Auger electron generation for aluminum. Hence this result may support the present approach, and we have extended it to copper as mentioned below.

## Results

In order to examine usefulness of the present Monte Carlo calculation to the quantitative AES analyses we have carried out AES studies on dependence of Auger signals on primary-electron energy for aluminum and copper.

The measurement was done with a commercial type SAM, JEOL JAMP-3. The Auger signal intensity was measured by the peak-to-peak heights in the  $dN(E)/dE$  mode spectra with a modulation amplitude 5 eV<sub>p-p</sub>. Both the Auger signals of high and low energies were measured by a change in the primary electron energy from 3 to 15 keV at an angle of incidence of 45°. The primary-beam current intensity was kept constant at 0.2 µA throughout the measurement. The measurement proceeded by an increase in the primary energy from 3 to 15 keV, followed by a decrease from 15 to 3 keV and vice versa. The primary electron energy was measured by use of a calibration curve between the reference and output voltage, which was checked before and after the measurement. Another check of the primary electron energy was also made by measuring the elastic peak with a cylindrical mirror analyzer at low primary energies. Although the ambient pressure during this experiment was less than  $5 \times 10^{-9}$  Torr, the specimen, particularly aluminum, was sensitive to oxidation, which incurred large experimental errors. We therefore repeated the sputter-cleaning procedure before each measurement. Furthermore, to avoid electron-beam-enhanced absorption, the incident beam was scanned in the region of about 100 µm square during the measurement.

Both the theoretical and experimental results are plotted in Fig. 2 for Al-KLL and -LVV and Cu-LMM and -MVV Auger signals for Al and Cu samples, respectively. The results in the

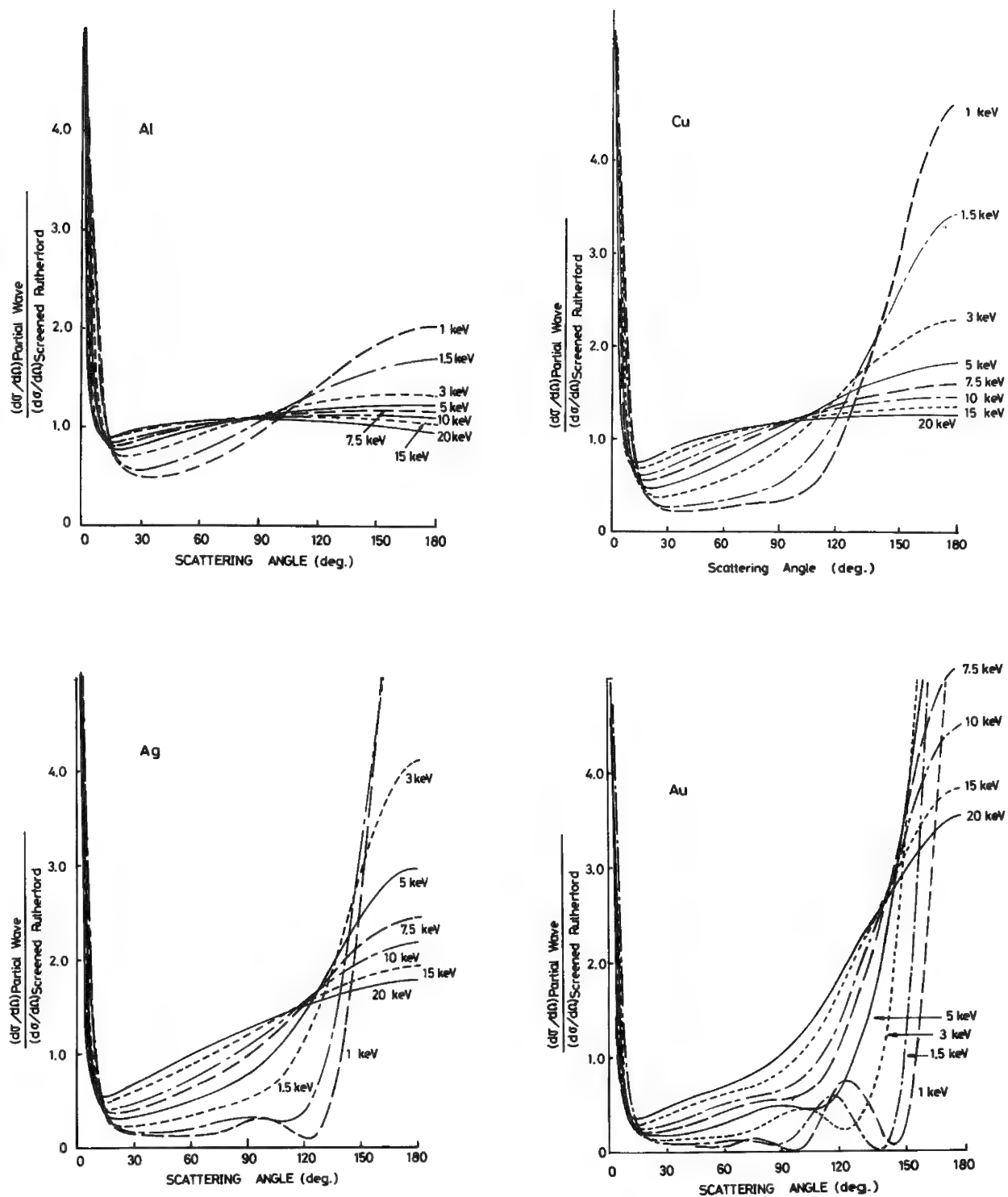


FIG. 1.--The ratio of cross section obtained by partial wave expansion method (PWEM) to screened Rutherford cross section as function of scattering angle  $\theta$  for Al, Cu, Ag, and Au.



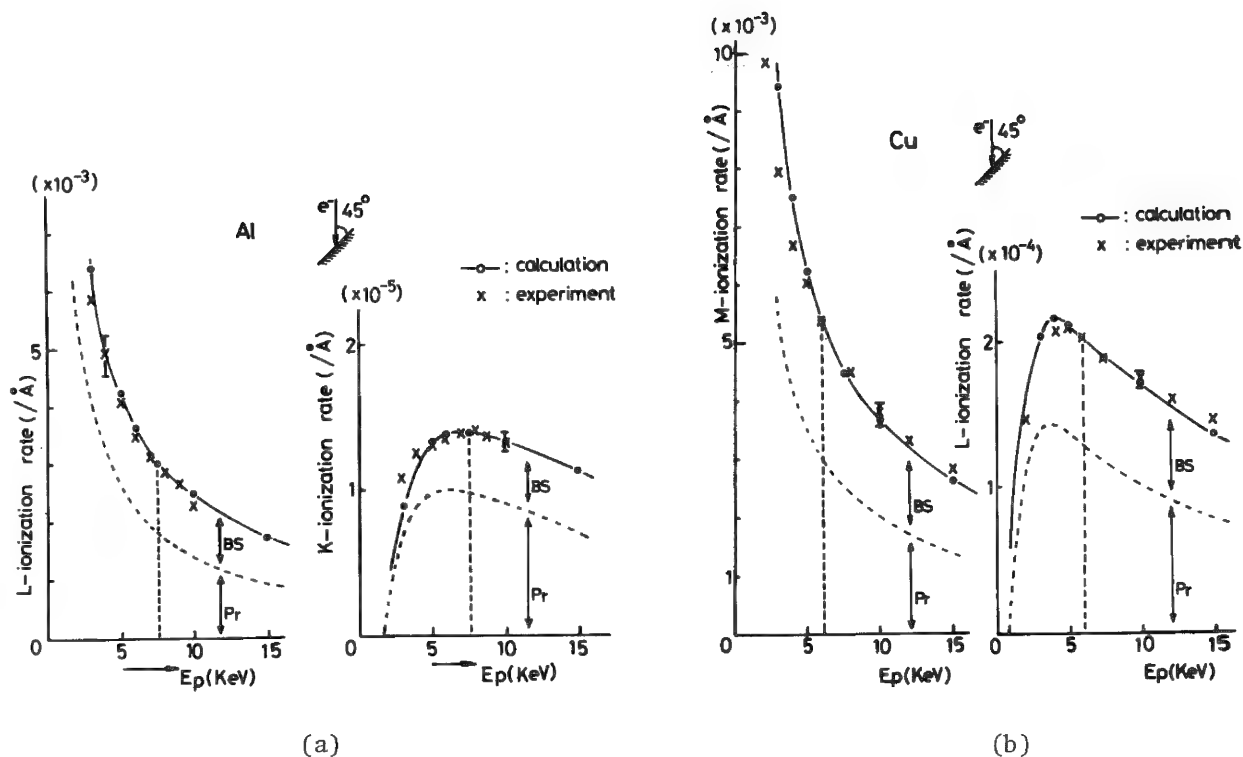


FIG. 2.--The dependence of Auger electron intensities on primary electron energy for (a) Al and (b) Cu at angle of incidence  $45^\circ$ : experiment (x) and calculation (o) solid line, total intensity of Auger electrons (calculated); dashed line, intensity of Auger electrons generated by primary electrons alone (calculated).

figure are normalized at 7.5 and 6.0 KeV for Al and Cu, respectively, for convenient comparison. The solid line represents total intensity of Auger electron signals; the broken line, the intensity of Auger signals generated by the primary electrons alone. The difference between the solid and broken lines therefore shows the contribution of backscattered electrons and the secondary electrons with high energy. Thus, extending the calculation to compound materials one can directly see the matrix effect due to the backscattered and secondary electrons, which is of utmost importance for quantitative analyses by AES as well as EPMA.

All the theoretical results were based on 5000 trajectories.

In conclusion, the present Monte Carlo calculation has described the dependence of Auger signals on primary electron energy for Al and Cu quite well. This result suggests that the model used in this calculation provides a practical way for extending Monte Carlo calculation technique to various compound materials widely used in practice in quantitative AES studies.

### References

1. C. C. Chang, "Analytical Auger electron spectroscopy," in P. F. Kane and G. B. Larrabee, Eds., *Characterization of Solid Surfaces*, New York: Plenum Press, 1974, 509.
2. P. W. Palmberg, "Quantitative analysis of solid surfaces by AES," *Analyt. Chem.* 45: 549A, 1973.
3. H. E. Bishop and J. C. Riviere, "Estimates of the efficiencies of production and detection of electron-excited Auger emission," *J. Appl. Phys.* 40: 1740, 1969.
4. See, for instance, K. F. J. Heinrich, Ed., *Quantitative Electron Probe Microanalysis*, Special Publication 298, Washington D.C.: National Bureau of Standards 1968.
5. For the references on applications of Monte Carlo calculations of the present to EPMA see, K. F. J. Heinrich, D. E. Newbury, and H. Yakowitz, Eds., *Use of Monte Carlo Calculations in Electron Probe Microanalysis and Scanning Electron Microscopy*, Special Publication 460, Washington, D.C.: National Bureau of Standards 1976.

6. R. Shimizu, M. Aratama, S. Ichimura, Y. Yamazaki, and T. Ikuta, "Application of Monte Carlo calculation," *Appl. Phys. Lett.* 31: 692, 1977.
7. R. Shimizu, T. E. Everhart, N. C. MacDonald and C. T. Hovland, "Edge effect in high resolution SAM," *Appl. Phys. Lett.* 33: 549, 1978.
8. E. R. Krefting and L. Reimer, "Monte-Carlo-Rechnung zur Electronendiffusion," in E. Preuss, Ed., *Quantitative Analysis with Electron Microprobe and Secondary Ion Mass Spectrometry*, Jürich: Zentralbibliothek der KFA, 1973, 114.
9. Y. Yamazaki, R. Shimizu and H. Hashimoto, "Calculation of electron spin polarization," *J. Phys. Soc. Japan* 41: 721, 1976.
10. M. Fink and A. C. Yates, "Tables of scattering amplitudes and spin polarizations," Technical Reports 88 (1970) and 160 (1974), Austin: University of Texas (Electronics Research Center).
11. B. P. Nigam, M. K. Sundersen, and Wu Ta-You, "Theory of multiple scattering," *Phys. Rev.* 115: 491, 1959.
12. M. Gryzinski, "Classical theory of atomic collisions," *Phys. Rev.* 126: 1453, 1965.

# MONTE CARLO SIMULATION OF ELECTRON SCATTERING AT 1-10 keV AND ITS APPLICATION TO THIN FILM ANALYSIS

Kenji Murata, Masatoshi Kotera, and Koichi Nagami

The two basic equations have been used in a previous Monte Carlo simulation of electron scattering,<sup>1</sup> the energy loss equation of Bethe and the screened Rutherford cross section as given in the following.

$$-\frac{dE}{dx} = \frac{2\pi e^4 n Z}{E} \ln \frac{1.166E}{J} \quad (1)$$

$$\frac{d\sigma}{d\Omega} = \frac{Z(Z+1)e^4}{4E^2(1 - \cos \theta + 2\beta)^2} \quad (2)$$

$$\beta = \frac{1}{4} \left( \mu \frac{\hbar \lambda_0}{p} \right)^2, \quad \lambda_0 = \frac{Z^{1/3}}{0.885 a_H}$$

where  $\mu$  is a constant determined empirically. In a previous model a value of  $\mu = 1.12$  is used. The simulation has been found to be in fairly good agreement with the experimental results for electrons with an energy above 10 keV. However, these equations have failed to give agreement with experiments at low energies even for a light element because of the Born approximation. The purpose of the present paper is to check the accuracy of the previous simulation at low energies in comparison with the experiment and to investigate a new expression for energy loss when an expression for the elastic scattering cross section is kept unchanged. A detailed description here will be made only for aluminum.

First, we checked the results from the old model. The electron range is a physical quantity that is well suited to be compared between experiment and theory. Experimental results of the extrapolated electron range were collected from various papers.<sup>2-7</sup> In Fig. 1 one example of the results is plotted as a function of energy. Although these results are obtained from various measurements such as backscattering, electron transmission, and luminescence or energy dissipation, the accuracy of the measurements is not sufficiently high to yield a difference among the ranges. The reason the values by Lane and Zaffarano are too low seems to be that these investigators used a plastic film to support a thin Al film. The previous Monte Carlo results are shown in Fig. 1 for comparison. To prevent a failure of Eq. (1) at very low energies, the following equation was utilized.<sup>8</sup>

$$-\frac{dE}{dx} = \frac{2\pi e^4 n Z}{1.26 (JE)^{1/2}} \quad (3)$$

where  $E \leq E_{inf} = 6.338J$  eV. The extrapolated range obtained by Gruen<sup>9</sup> or Everhart and Hoff<sup>10</sup> (hereafter called the Gruen range) from the distribution of energy dissipation comes near the theoretical range. Their results seem to give a good prediction of the energy down to 5 keV, as they pointed out. Although there is a fluctuation in experimental data, it is observed that the accuracy of the calculation becomes worse with a decrease in energy, as anticipated.

Next, we introduced the following energy loss expression by Kanaya and Okayama,<sup>11</sup> which was derived from the Lindhard theory for an ion beam:

---

The authors are with the Electronics Department of the College of Engineering at the University of Osaka Prefecture, Mozu-Umemachi, Sakai, Osaka, Japan.

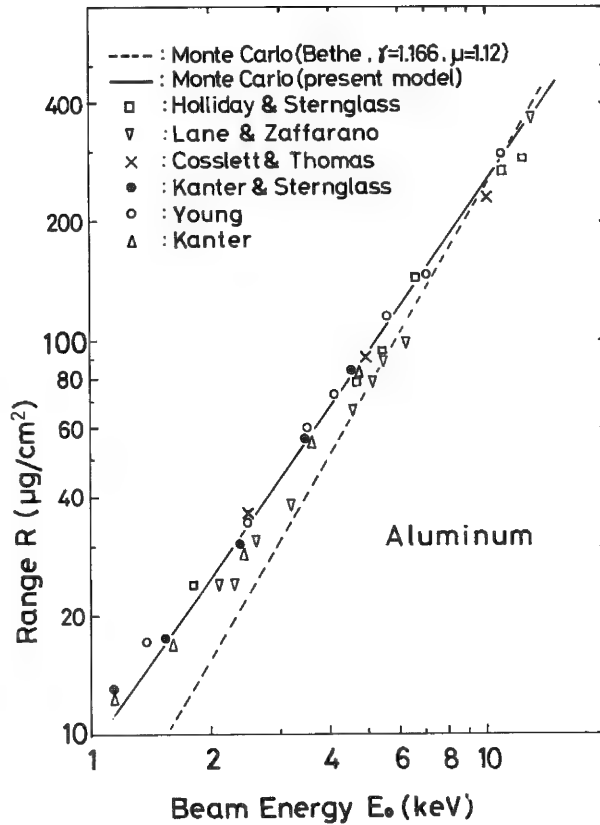


FIG. 1.--Extrapolated range as function of primary energy for aluminum. Results obtained from both new and old models are compared with experiments.

$$-\frac{dE}{dx} = \lambda_s \frac{\pi 2^{(2/s)-1} a^{2-(2/s)} e^{4/s} n Z}{1 - \frac{1}{s}} E^{1-(2/s)} \quad (4)$$

$$a = 0.885 a_H Z^{-1/3}$$

where the parameters  $s$  and  $\lambda_s$  are arbitrarily taken so that the calculated result fits the experiment. Any type of the ranges mentioned above (backscattering, electron transmission, and energy dissipation) can be derived from the Monte Carlo calculation. We found a difference of about 10% among the ranges; the Gruen range was the largest one. We tentatively adopted the Gruen range in comparison with the experimental results in Fig. 1. We found from several trials of the calculation based on a new model that the parameter  $s$  determines a gradient of the range-energy curve, and  $\lambda_s$  shifts the curve up and down. Making use of this insight we obtained  $s = 1.7$  and  $\lambda_s = 0.07$  for Al. The range-energy curve obtained with the above parameters is shown by a solid line in Fig. 1. The calculated result obey a power law of the form  $R = cE^n$  (where  $n = 1.46$ ,  $c = 8.67 \mu\text{g}/\text{cm}^2$  for Al, and  $E$  is in keV).

The backscattering coefficient is also an important physical quantity to be compared with the experiment to check a validity of the new model. Experimental data were taken from a recent paper by Darlington and Cosslett.<sup>12</sup> A variation of the backscattering coefficient  $\eta$  with electron energy is shown in Fig. 2.

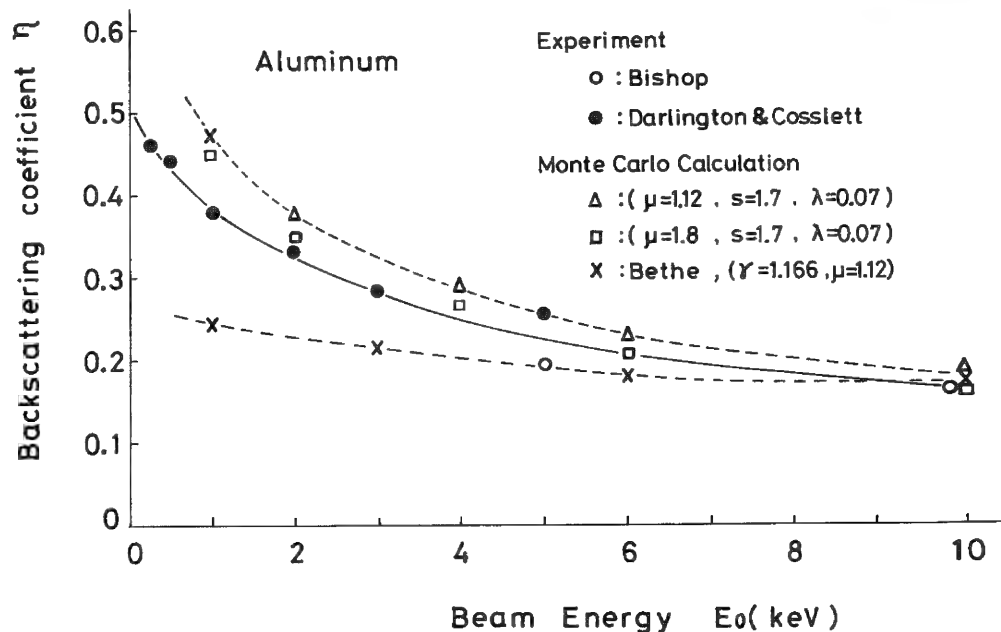


FIG. 2.--Variation of backscattering coefficient  $\eta$  with primary energy for aluminum.

The agreement between experiment and theory is relatively good, whereas the Monte Carlo results with the old model are too low.

The Monte Carlo simulation with the new model was applied to a prediction of the x-ray intensity distribution  $\phi(\rho z)$ . In Fig. 3 calculated results are compared with the experiments by Brown and Parobek,<sup>13</sup> who used a Si tracer in an Al target. The results are normalized so that the areas of the  $\phi(\rho z)$  curves are identical. Although there is a discrepancy in the peak position of the curve, we can see a good prediction of the maximum depth of x-ray production.

We also applied the new model to thin-film analysis by the electron-probe microanalyzer. The calculation procedure is the same as previously published,<sup>14</sup> except that we did not introduce the mean-free-path parameter  $\mu_s = (300 + Z)/300$  but took  $\mu_s = 1$ . The parameters  $s$  and  $\lambda_s$  for Al were extended to Si and O. In Fig. 4 the k-ratios are shown in a comparison between theory and experiment. The results with the old model are also shown in the figure. A clear improvement is observed in the k-ratio.

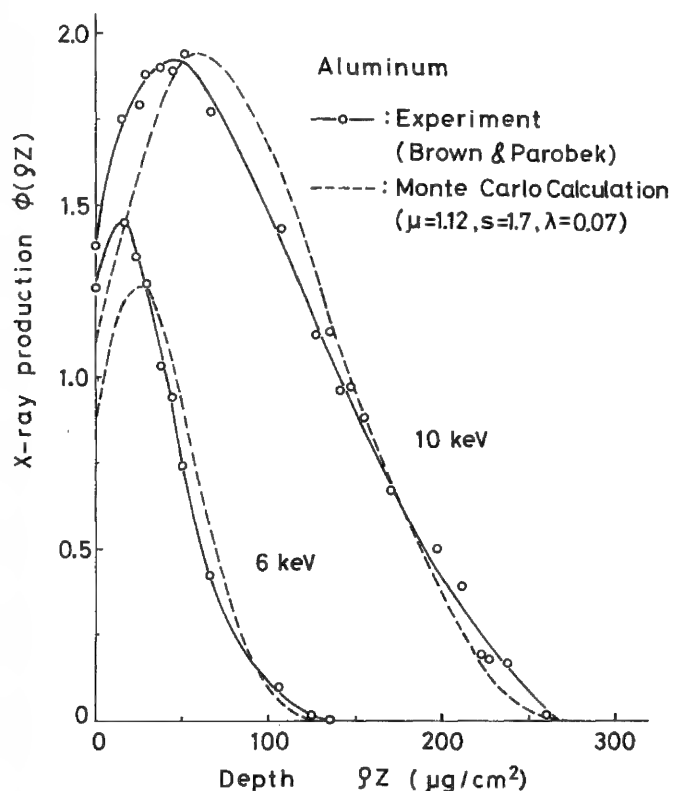


FIG. 3.--Theoretical and experimental depth distributions of x-ray production for aluminum at 6 and 10 keV.

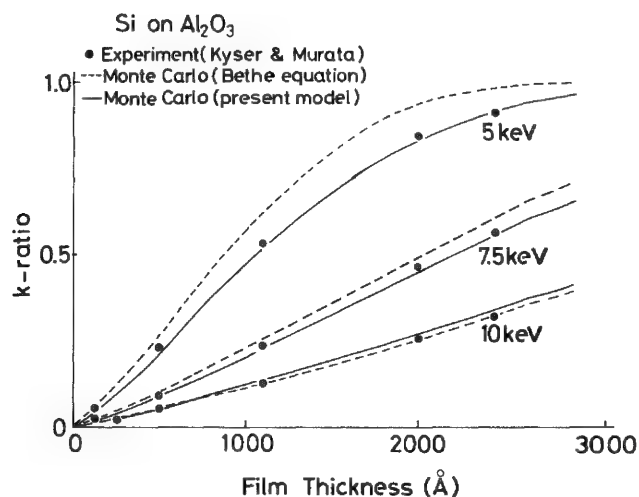


FIG. 4.--Comparison between Monte Carlo theory and experiment in k-ratio for Si film on  $\text{Al}_2\text{O}_3$ .

### Discussion

Although a similar variation is obtained in the curve of  $\eta$  vs  $E_0$ , there is a large error in the absolute value at the very-low-energy end. We can make the backscattering coefficient  $\eta$  small by increasing the energy loss rate, because the chance for an electron to escape from the sample decreases as the length the electron travels decreases. On the other hand, Eq. (4) was evaluated with parameters  $s$  and  $\lambda_s$  determined from a comparison with the experiment. A typical value of  $-dE/dx$  is  $0.76 \text{ eV/\AA}$  at 2 keV, which is very close to the value of  $0.8 \text{ eV/\AA}$  obtained experimentally by Fitting.<sup>15</sup> If we change the energy loss rate to  $0.8 \text{ eV/\AA}$  by making the parameter  $\lambda_s$  large, we can make the backscattering coefficient come close to the experimental value. However, the calculated electron range decreases owing to an increase in the energy loss rate.

The elastic scattering cross section is an important factor in the control of electron backscattering, especially at low energies. We have used the same expression as the previous one for the cross section (Eq. 2), and a value of  $\mu = 1.12$ , because the calculation of an electron scattering angle is simplified when this type of equation is used. Perhaps this expression is no longer valid at low energies. According to a proposal by Nigam et al.,<sup>16</sup> we tried another value,  $\mu = 1.8$ . The result for backscattering is shown in Fig. 2.

A better agreement with the experiment is obtained. The use of  $\mu = 1.8$  makes a value of the electron range increase by about 20% at 2 keV. Therefore the energy loss rate must be increased in order to fit the experimental values. This is in a right direction for a further decrease in the backscattering coefficient  $\eta$ . A value of  $\mu = 1.8$  might be a better estimate.

We have done a similar calculation for Au. The old model shows a larger discrepancy in the electron range for Au than for Al. From a comparison with experimental results of the electron range we obtained the parameters  $s$  and  $\lambda_s$  for Au, which are different from those for Al. However, there is a problem in that the calculated backscattering coefficient is very large and moreover seems to show a somewhat different variation with energy from the experiment. It is clear that a more accurate expression for the elastic scattering cross section must be adopted.

### References

1. For example, K. Murata, T. Matsukawa and R. Shimizu, "Monte Carlo calculations on electron scattering in a solid target," *Jap. J. Appl. Phys.* 10: 678, 1971.
2. H. Kanter and E. J. Sternglass, "Interpretation of range measurements for kilovolt electrons in solids," *J. Appl. Phys.* 126: 620, 1962.
3. J. R. Young, "Penetration of electrons and ions in aluminum," *J. Appl. Phys.* 27: 1, 1956.
4. H. Kanter, "Electron scattering by thin foils for energies below 10 keV," *Phys. Rev* 121: 461, 1961.
5. J. E. Holliday and E. J. Sternglass, "New method for range measurements of low-energy electrons in solids," *J. Appl. Phys.* 30: 1428, 1959.
6. R. O. Lane and D. J. Zaffarano, "Transmission of 0-40 keV electrons by thin films with application to beta-ray spectroscopy," *Phys. Rev.* 94: 960, 1954.
7. V. E. Cosslett and R. N. Thomas, "Multiple scattering of 5-30 keV electrons in evaporated metal films: II. Range-energy relations," *Brit. J. Appl. Phys.* 15: 1283, 1964.
8. T. S. Rao-Sahib and D. B. Wittry, "The x-ray continuum from thick targets," *Proc. 6th Intern. Conf. X-ray Optics and Microanalysis*, 1971, 131.
9. A. E. Gruen, "Photometric measurement of luminescence of energy absorption in the radiation field of electron sources: One dimensional case in air," *Z. Naturforschung* 12A: 89 1957.
10. T. E. Everhart and P. H. Hoff, "Determination of kilovolt electron energy dissipation vs penetration distance in solid materials," *J. Appl. Phys.* 42: 5837, 1971.
11. K. Kanaya and S. Okayama, "Penetration and energy loss theory of electrons in solid targets," *J. Physics* [D]5: 43, 1972.
12. E. H. Darlington and V. E. Cosslett, "Backscattering of 0.5-10 keV electrons from solid targets," *J. Physics* [D]5: 1969, 1972.
13. J. D. Brown and L. Parobek, "X-ray production as a function of depth for low electron energies," *X-ray spectroscopy* 5: 36, 1976.
14. D. F. Kyser and K. Murata, "Quantitative electron microprobe analysis of thin films on substrates," *IBM J. Res. and Develop.* 18: 352, 1974.
15. H. J. Fitting, "Transmission, energy dissipation, and SE excitation of fast electrons in thin solid films," *Phys. Stat. Sol.* [A]26: 525, 1974.
16. B. P. Nigam, M. K. Sundaresan, and Ta-You Wu, "Theory of multiple scattering: Second Born approximation and corrections to Moliere's work," *Phys. Rev.* 115: 491, 1959.



## MONTE CARLO SIMULATION APPLIED TO ELECTRON MICROPROBE THICKNESS MEASUREMENT OF LEAD-TIN OXIDE FILMS

Serge Cvikevich and Carl Pihl

The two main objectives of this paper are, first, to show the utility of Monte Carlo simulation as an aid in setting optimum electron microprobe operating conditions in advance of data collection; and second, to give an application in the analysis of a complex surface reaction system of lead-tin solders.

Monte Carlo computer simulation for the calculation of x-ray fluorescence intensity excited within a microvolume by a focused high-energy beam is well established and used in quantitative electron microprobe analysis.<sup>1</sup> A specific application to the simulation of thin films on substrates was developed by Kyser and Murata,<sup>2</sup> and the resulting model and programs are used in this work.

For reasons given in Ref. 2, quantitative analysis is best done at excitation potentials that result in penetration of a film and involve interactions in both the film and substrate. The simulation process is a backward running procedure in that a theoretical  $k$  ratio is calculated as a function of film composition and mass thickness ( $\rho t$ ) for a given excitation potential. Atomic number and absorption corrections are provided. In practice, an iterative process is required to produce a family of theoretical calibration curves that cover a range of composition and thickness. From these data, a unique combination of compositions and mass thickness exists for which the theoretical  $k$  ratios equal the measured experimental values. Recent work by Cvikevich and Pihl has shown this approach to be applicable to practical quantitative analysis of refractory thin films of Ta-W and Ti-W.<sup>3,4</sup>

The present work concerns the surface oxides formed during processing of lead-tin solders. Measurement and possible control of oxide mass thickness is the primary requirement. Previous study suggests that a complex system of oxide compositions exists. The scope of this study covers three lead oxides and two tin oxides, of known composition, as thin films on both lead and tin substrates.

Initially, the oxygen ( $O K\alpha$ ) intensity was chosen for simulation. This choice recognizes the experimental complication in measuring the lead or tin intensity where either element is present in both the film and substrate.

Figures 1 through 4 show the results of simulation of the above combinations, and form the basis for the following discussion. Figures 1 and 2 show, for the three lead oxides on both lead and tin substrates, the theoretical  $k$  ratio versus film thickness at two electron acceleration potentials, 5 and 10 kV, respectively. In addition, in each figure an expanded region is shown for the nearly linear portion observed. Figures 3 and 4 show results for the two tin oxides on both lead and tin substrates, again at 5 and 10 kV. The following important observations are possible.

1. The various oxide compositions produce well-separated  $O K\alpha$  intensity vs film thickness curves.
2. The substantial difference between the atomic numbers of the two substrates has a relatively small effect on  $O K\alpha$  intensity.
3. The film thickness equivalent to a semi-infinite solid is predicted. This thickness is a measure of effective beam penetration beyond which no additional information is obtained.
4. The film thickness over which a nearly linear  $O K\alpha$  intensity exists is predicted. This relationship is important in further experimental measurements.
5. The effect of electron acceleration potential can be observed, and set initially to a nearly optimum value.

---

The authors are at IBM Data Systems Division, East Fishkill Facility, Hopewell Junction, NY 12533.

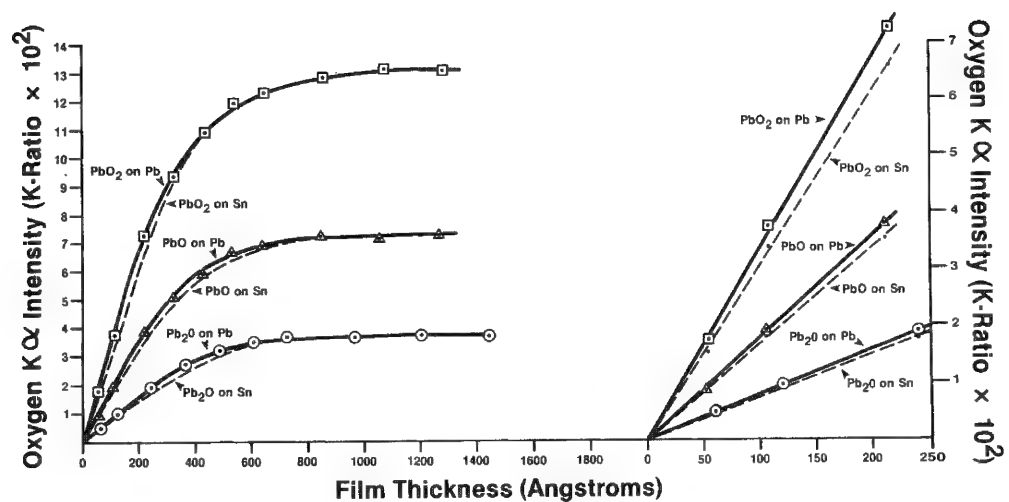


FIG. 1.--Oxygen K $\alpha$  intensity (k-ratio) vs film thickness for lead oxide films on lead and tin substrates. Electron acceleration potential, 5 kV.

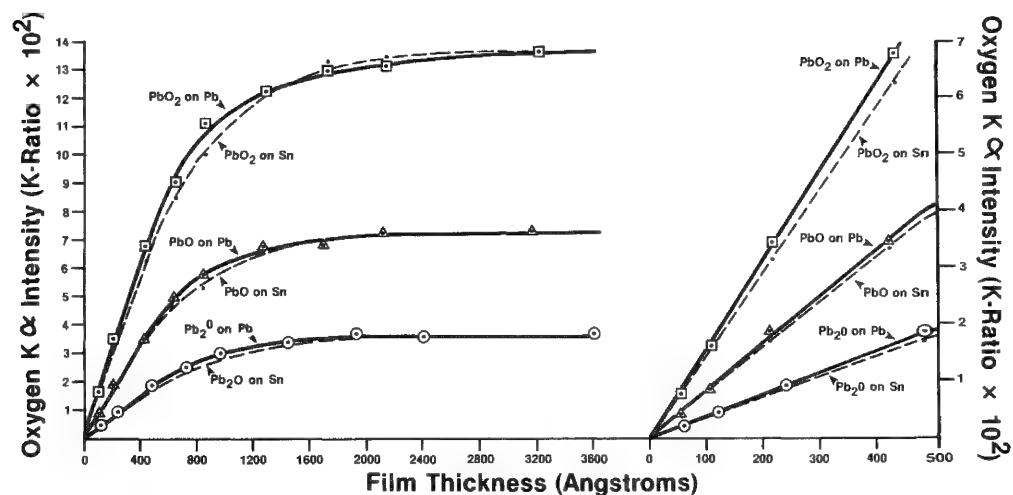


FIG. 2.--Oxygen K $\alpha$  intensity (k-ratio) vs film thickness for lead oxide films on lead and tin substrates. Electron acceleration potential, 10 kV.

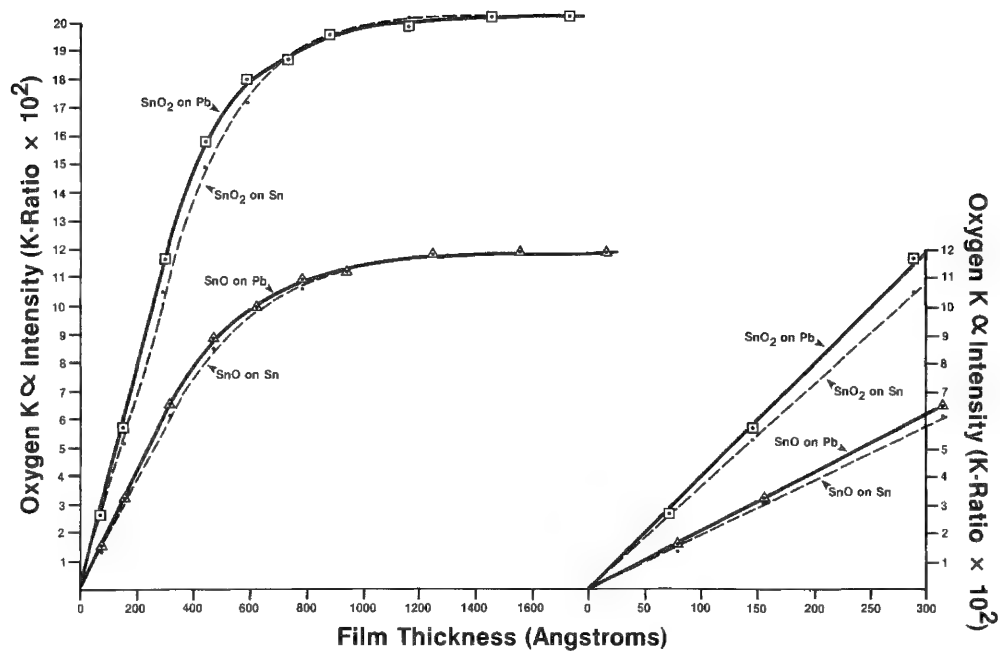


FIG. 3.--Oxygen K $\alpha$  intensity (k-ratio) vs film thickness for tin oxide films on lead and tin substrates. Electron acceleration potential, 5 kV.

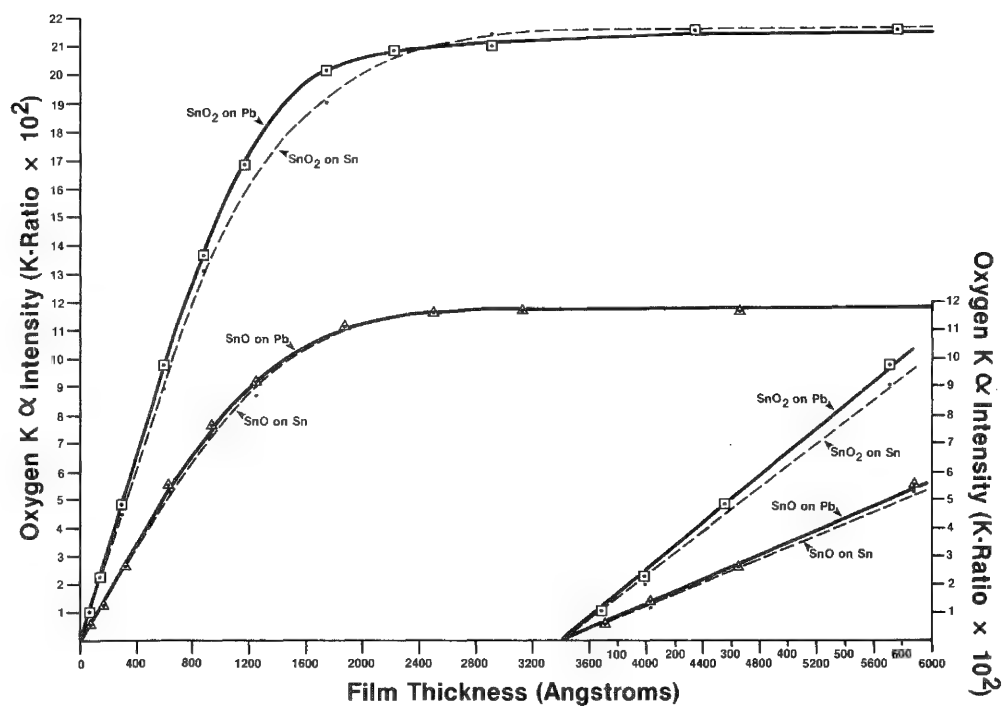


FIG. 4.--Oxygen K $\alpha$  intensity (k-ratio) vs film thickness for tin oxide films on lead and tin substrates. Electron acceleration potential, 10 kV.

In this work, the linear range of O K $\alpha$  vs film thickness is increased by a factor of two when the acceleration potential is increased from 5 to 10 kV. However, at the same time there is a decrease in the generated O K $\alpha$  intensity. Thus, from the experimental viewpoint, there is a trade-off between linear range and measurement sensitivity. An optimum acceleration potential is chosen to give maximum sensitivity consistent with the requirement for a linear range extending to the maximum expected oxide thickness.

Monte Carlo simulation answers numerous initial questions and saves a significant amount of valuable experimental effort to establish optimum conditions.

The lead-tin solder oxide system as produced is complex, and in fact contains a mixture of oxides depending on the processing conditions in use. Supplemental analysis techniques available for film composition determination include (1) x-ray diffraction, (2) Auger, and (3) ESCA. An independent determination of film composition permits direct calculation of mass thickness from electron microprobe measurements. Examples of experimental measurements on a series of oxides can be given.

### References

1. *Use of Monte Carlo Calculations in Electron Probe Microanalysis and Scanning Microscopy*, NBS Special Publication 460, 1976.
2. D. F. Kyser and K. Murata, "Quantitative electron microprobe analysis of thin films on substrates," *IBM J. Res. & Dev.* 18: 352-363, 1974.
3. Paper 116, *Proc. 12th MAS Conf.*, 1977.
4. Paper 25.8, *Fifth Annual Meeting of FACSS*, Boston, 1978.

## ELECTRON MICROPROBE ANALYSIS OF ANTIREFLECTION COATINGS FOR SILICON SOLAR CELLS WITH MONTE CARLO SIMULATION

A. Armigliato, A. Desalvo, R. Rinaldi, R. Rosa, and G. Ruffini

The antireflection coating (ARC) is one of the most important parts of a solar cell design.<sup>1</sup> Most semiconductors have a high refractive index and therefore a high reflectance, as given by the Fresnel relation at normal incidence (if absorption is neglected):

$$R = [(n_1 - n_2)/(n_1 + n_2)]^2 \quad (1)$$

where  $R$  is the reflectance at the interface between the two media of refractive indices  $n_1$  and  $n_2$ . If medium 1 is air,  $n_1 = 1$ .

The refractive index  $n_2$  varies throughout the sunlight spectrum and ranges in the case of silicon, from  $n_2 = 3.5$  at a wavelength  $\lambda = 1.1 \mu\text{m}$  to  $n_2 = 6.0$  at  $\lambda = 0.40 \mu\text{m}$ . From Eq. (1) it follows that  $R$  will vary from 31% at  $\lambda = 1.1 \mu\text{m}$  to 51% at  $\lambda = 0.40 \mu\text{m}$ . Thus, if no ARC is applied, the silicon would only transmit into the cell about 70% and 50% of the infrared and ultraviolet portions of the sunlight, respectively. If the reflectance could be reduced to zero, the percentage of transmittance would increase to 100%, with a significant gain in electrical output over the bare cell. This simple example illustrates the need for low cell reflectance, and then for an ARC.<sup>2</sup>

If an ARC is interposed between a medium of refractive index  $n_1$  and the silicon (index  $n_2$ ) to minimize  $R$ , its index  $n$  and its thickness  $t$  should satisfy the following equations:

$$n = \sqrt{n_1 n_2} \quad (2)$$

$$nt = \lambda/4 \quad (2')$$

At  $\lambda = 0.55 \mu\text{m}$  one obtains  $n \approx 2$  and  $t \approx 700 \text{ \AA}$  for uncovered solar cells; if a cover-slip is applied  $n_1 \approx 1.4$  and then  $n \approx 2.4$  and  $t \approx 600 \text{ \AA}$ .

Among the various materials used as ARCs in silicon solar cells technology, we have chosen  $\text{TiO}_x$  since it has both a suitable index and low absorption throughout the visible region.

This paper is part of research undertaken recently to determine the correlations between the optical, structural, and compositional properties of these  $\text{TiO}_x$ -based ARCs.<sup>3</sup> Films of  $\text{TiO}_x$  have been deposited onto silicon substrates by vacuum evaporation of TiO with an electron gun in an oxidizing environment (reactive evaporation). Coatings of various optical properties have been obtained by variations in the substrate temperature, the oxygen partial pressure, and the evaporation rate. The films have been analyzed with the ARL-SEM electron microprobe of the University of Modena. The accelerating voltage was 10 keV and the specimen current 250 nA; the crystals chosen were a PET and a RAP for the Ti  $K\alpha$  and the O  $K\alpha$  lines, respectively. The  $k$ -ratios were obtained by measurement of the x-ray intensities in the specimens and in standards of pure Ti and  $\text{SiO}_2$ .

The composition and the mass thickness of the ARCs analyzed were obtained by a Monte Carlo computer program, described in detail elsewhere.<sup>4</sup> Here we recall that the program, named CARLONE, is based on the single-scattering model developed by Murata et al.<sup>5</sup> and extended to compounds by Kyser and Murata.<sup>6</sup> With respect to the previous version,<sup>4</sup> CARLONE

---

Authors Armigliato, Rosa, Ruffini, and Desalvo are at LAMEL-CNR, via de Castagnoli 1, 40126 Bologna, and the last named is also at the Chemical Institute of the Faculty of Engineering of the University of Bologna; author Rinaldi is at the Institute of Mineralogy of the University of Modena. They are indebted to S. Guerri for the preparation of the films and to Drs. G. Celotti, G. Martinelli, and P. Ostojia for the optical measurements and many stimulating discussions.

was supplied with a numerical convergence method that leads to a unique solution for composition and mass thickness. In this manner the rather tedious graphical procedure by Kyser and Murata<sup>6</sup> is carried out in a straightforward way by the program, which leads to a reduction in errors. The mass absorption coefficients employed in the calculations were the ones listed by Veigele.<sup>7</sup>

The stoichiometry and the mass thickness of the films examined are reported in Table 1, together with the deposition parameters as well as the refractive index measured with an

TABLE 1.--Deposition parameters, refractive index, stoichiometry, and mass thickness of various  $\text{TiO}_x$  antireflection coatings.

Film	T (°C)	p (torr)	rate (Å/s)	n	x = O/Ti	$\rho t$ ( $\mu\text{g}/\text{cm}^2$ )
3D	60	$4 \times 10^{-4}$	1	2.13	1.83	24.00
4D	125	$3 \times 10^{-4}$	1	2.30	2.00	26.77
5C	125	$3 \times 10^{-4}$	1	2.37	2.04	22.01
2A	200	$1 \times 10^{-4}$	1	2.71	2.08	22.08
6A	125	$6 \times 10^{-4}$	1	2.23	2.17	20.99
6C	125	$6 \times 10^{-5}$	1	2.23	1.73	25.79
10A	125	$6 \times 10^{-4}$	0.12	2.27	2.13	21.82
10B	125	$6 \times 10^{-4}$	3.8	2.41	2.12	23.56

ellipsometer. The composition of the ARCs proved to be in a substantial agreement with the results obtained from backscattering and nuclear reactions experiments. From the data in Table 1 it can be inferred that no monotonic variation of the stoichiometry as a function of the refractive index is observed, as can be seen in Fig. 1; rather, the index reaches a maximum in correspondence of a composition close to the one of  $\text{TiO}_2$ .

On the other hand, TEM observations show that the films contain crystallites of various sizes dispersed in an amorphous matrix; the structural analysis of such crystallites indicates that they are a mixture of crystallographic phases of various titanium oxides. As an example, Fig. 2 shows (a) bright-field and (b) dark-field electron micrographs of the most crystalline ARC, the film labelled 2A in Table 1. The crystallite size appears to have a strong influence on the refractive index: in fact, the index of the film increases linearly with the logarithm of grain sizes (Fig. 3).

This work is in progress, and in the near future we propose to set up a computer program that will allow us to deduce from the ellipsometric measurements the absorption parameter  $k$  ( $\hat{n} = n - ik$ ) and hence the percentage of transmittance of the ARCs. This parameter will be correlated with the structure and the composition of the above reported films.

#### References

1. H. J. Hovel, *Solar cells*, New York: Academic Press, 1975, 203.
2. P. A. Iles, "Antireflection coatings for solar cells," *J. Vac. Sci. Technol.* 14: 1100, 1977.
3. A. Armigliato et al., "Optical, structural and compositional characterization of  $\text{TiO}_x$  antireflection coatings," *Proc. 1979 Photovoltaic Solar Energy Conference*, Berlin, 1979, to be published.
4. A. Armigliato et al., "Application of Monte Carlo technique to the electron probe microanalysis of ternary Si-B-O films on silicon," *J. Physics [D]*, 1979 (to be published).
5. K. Murata et al., "Monte Carlo calculations on electron scattering in a solid target," *Japan. J. Appl. Phys.* 10: 678, 1971; "Application of Monte Carlo calculations based



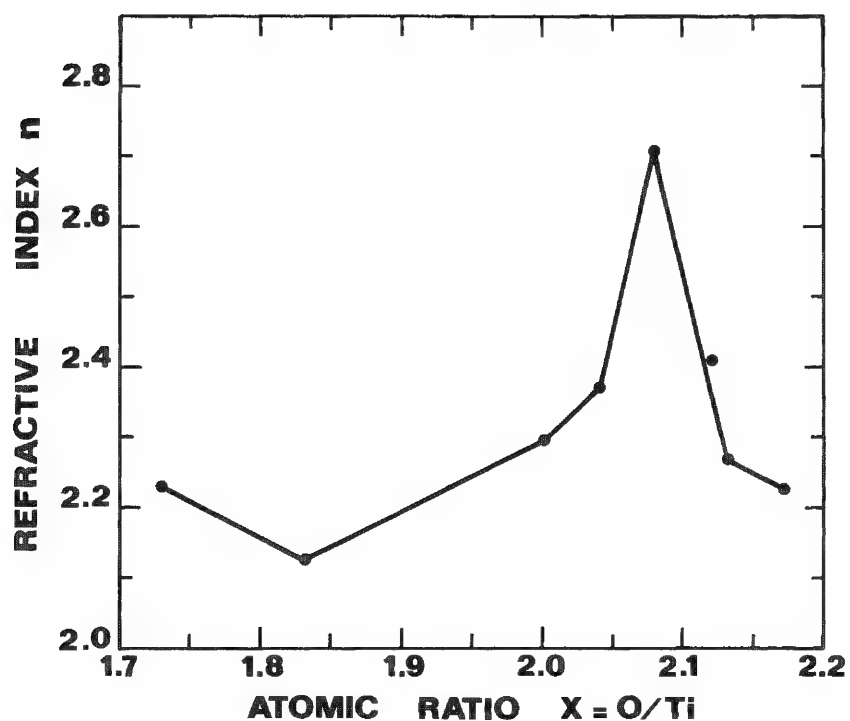


FIG. 1.--Variation of the refractive index  $n$  as function of stoichiometry of the ARCs listed in Table 1.

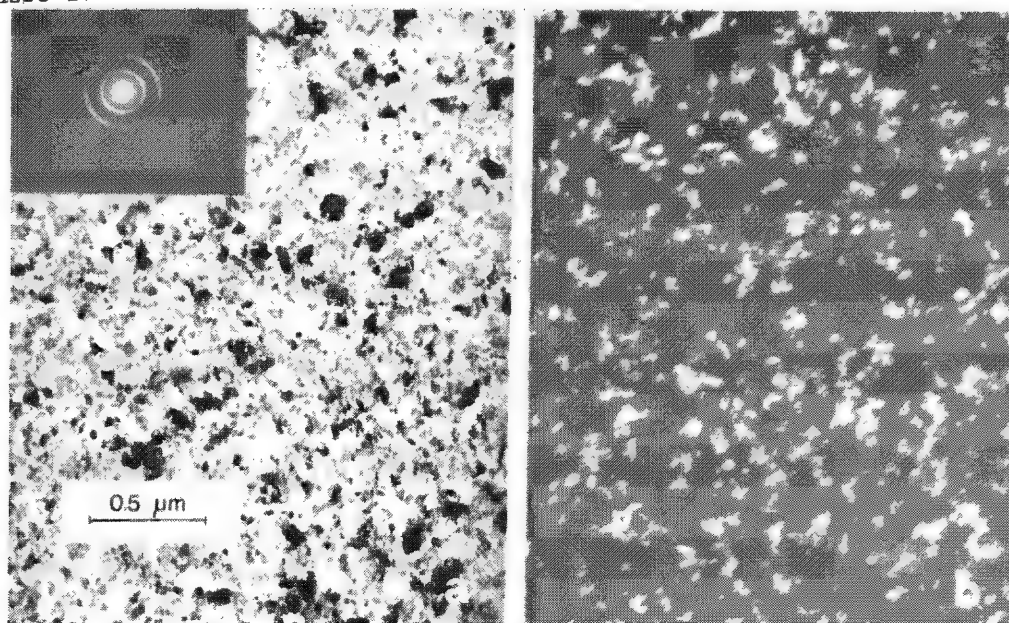


FIG. 2.--(a) TEM bright field micrograph of  $TiO_x$  film labeled 2A in Table 1; insert shows corresponding diffraction pattern, which includes rings from polycrystalline rutile. (b) Dark field image taken with first ring of diffraction pattern in (a).

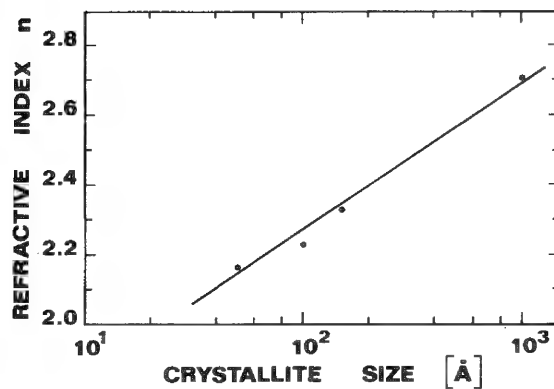


FIG. 3.--Variation of refractive index  $n$  with crystallite size of ARCs.

on the single scattering model to electron probe microanalysis," *Proc. 8th Intern. Conf. X-ray Optics and Microanalysis*, 1971, 105.

6. D. F. Kyser and K. Murata, "Quantitative electron microprobe analysis of thin films on substrates," *IBM J. Res. Develop.* 18: 352, 1974.

7. W. J. Veigele, "Photon cross sections from 0.1 keV to 1 MeV for elements  $Z = 1$  to  $Z = 94$ ," *Atomic Data* 5: 51, 1973.

## DETERMINATION OF THIN-FILM COMPOSITION OR THICKNESS FROM ELECTRON-PROBE DATA BY MONTE CARLO CALCULATIONS

N. C. Miller and D. M. Koffman

The composition and/or thickness of thin films on substrates has been determined by fitting of theoretical calibration curves obtained from Monte Carlo simulations to experimental electron-probe measurements of atomic x-ray intensity ratios  $k_i$ , by means of the model of Kyser and Murata.<sup>1</sup> Film thickness has been computed for elemental films of Pt and Al on silicon, and for PtSi on silicon. The program has also been extended to include the case of two films on a substrate, and the thicknesses of Pt films on Al films on silicon have been obtained via simulation. The composition and thickness of pseudoternary  $P_2O_5$ - $SiO_2$  films on germanium, silicon, and aluminum oxide substrates have been treated as well.

Our program, FILMS, handles up to five elements in each of two films and in the substrate. (This number can be easily expanded.) The trajectories of 1000 electrons are followed. In order to conserve computer time, a separate routine is used for the bulk standards. For each film composition, theoretical calibration curves of  $k_i$  vs film mass thickness  $\rho Z$  are obtained.

The Monte Carlo calibrations were simulated on an IBM 370/168 computer, and are straight lines in Figs. 1 through 7. Experimental  $k$  values were measured on a Phillips 4500 electron probe. Film thickness was measured by a multiple beam interferometer or a Dektak (for thicker films). Films were deposited simultaneously on separate substrates for electron probe and for thickness measurements.

A variety of deposition techniques was employed for coating the substrates. The Al films were electron-beam evaporated. The Pt films were rf sputtered simultaneously onto silicon and onto the Al films on silicon. The  $P_2O_5$ - $SiO_2$  films were fabricated by chemical vapor deposition onto Ge and Si simultaneously and onto  $Al_2O_3$  and Si simultaneously. The same deposition parameters were used in the two runs.

### Results

For the thickness of Pt films on silicon, good agreement is obtained between experiment and theory of both  $k_{Pt}$  and  $k_{Si}$  (Fig. 1). For the Al films on silicon, the experimental  $k_{Al}$  are somewhat lower than theory, whereas the  $k_{Si}$  are in good agreement with theory (Fig. 2). The discrepancy for aluminum cannot be explained by the absence of a secondary fluorescence correction.

For the PtSi film on silicon, the same  $\rho Z$  value is predicted from the theoretical curves by use of the experimental  $k_{Pt}$  or  $k_{Si}$  at three different accelerating voltages (Fig. 3). From  $k_{Pt}$ , the thickness is determined to be 247 Å; from  $k_{Si}$ , it is 283 Å. (The density is taken from a paper by Andrews).<sup>2</sup> This result is very insensitive to composition over the range 48-52%Pt; the 50%Pt-50%Si composition was used in the simulations.

For Pt films on Al films on silicon, the results for  $k_{Pt}$  vs  $\rho Z$  are in good agreement with theory (Fig. 4). When the substrate  $k_{Si}$  is plotted vs total mass thickness, holding  $(\rho Z)_{Al}$  fixed, good agreement is also obtained (Fig. 5). For Al, the experimental  $k_{Al}$  values are again lower than theory (Fig. 6), but the substrate  $k_{Si}$  vs total mass thickness, with  $(\rho Z)_{Pt}$  held fixed, are in good agreement with theory (Fig. 7).

For pseudoternary  $P_2O_5$ - $SiO_2$  films on Ge,  $Al_2O_3$ , and Si, theoretical calibration curves were simulated for a range of thicknesses and compositions (Figs. 8 and 9). The composition is determined by the convergence method used by Kyser and Murata.<sup>1</sup>  $SiO_2$ , GaP, and  $Al_2O_3$  compound standards are used. For the film deposited simultaneously onto Ge and onto Si, the compositions determined are given in Tables 1 and 2. For the second film deposited onto  $Al_2O_3$  and onto Si simultaneously, the composition of the film on  $Al_2O_3$  is identical to

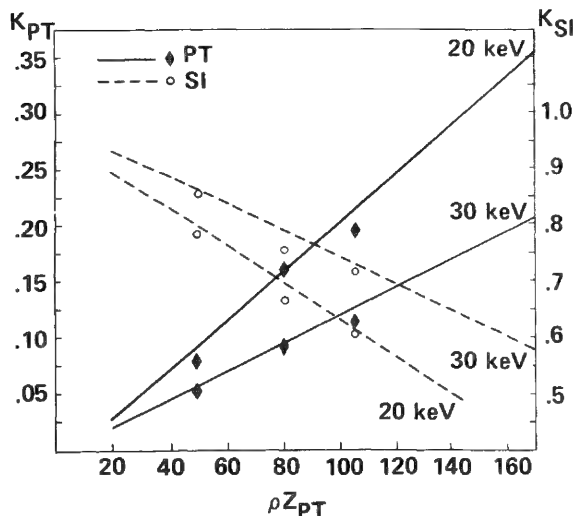


FIG. 1.--Pt and Si x-ray intensity ratios vs mass thickness, platinum films on silicon.

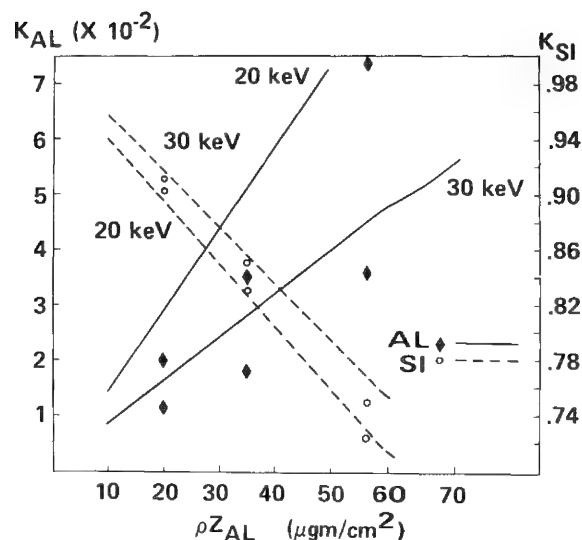


FIG. 2.--Al and Si x-ray intensity ratios vs mass thickness, aluminum films on silicon.

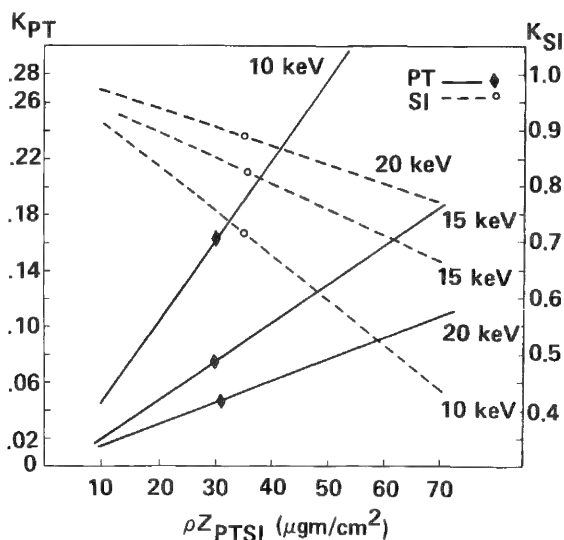


FIG. 3.--Pt and Si x-ray intensity ratios vs mass thickness, platinum silicide on silicon.

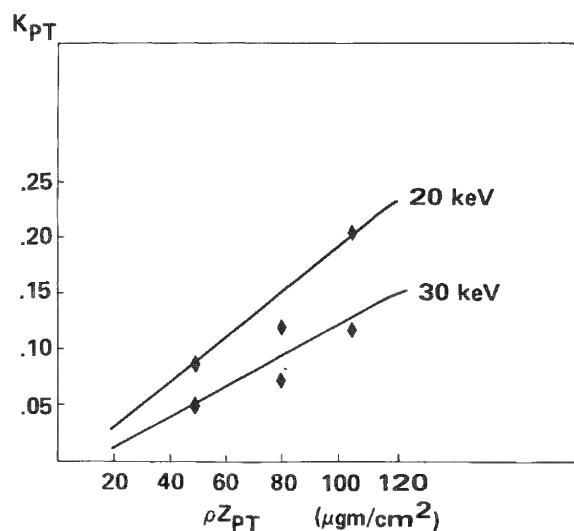


FIG. 4.--Pt x-ray intensity ratio vs Pt mass thickness, Pt on Al on Si.

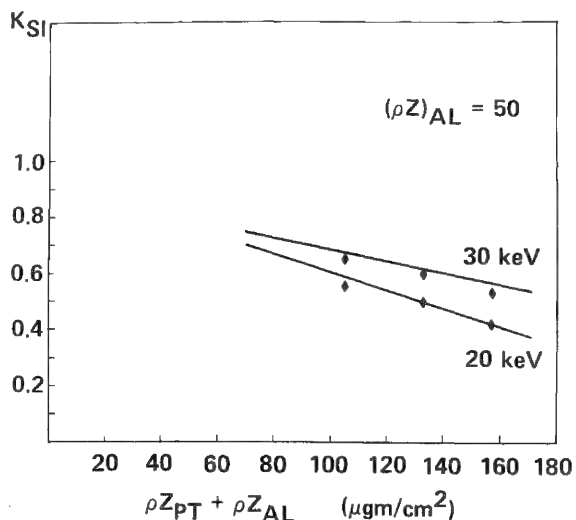


FIG. 5.--Si x-ray intensity ratio vs total film mass thickness, Pt on Al on Si.

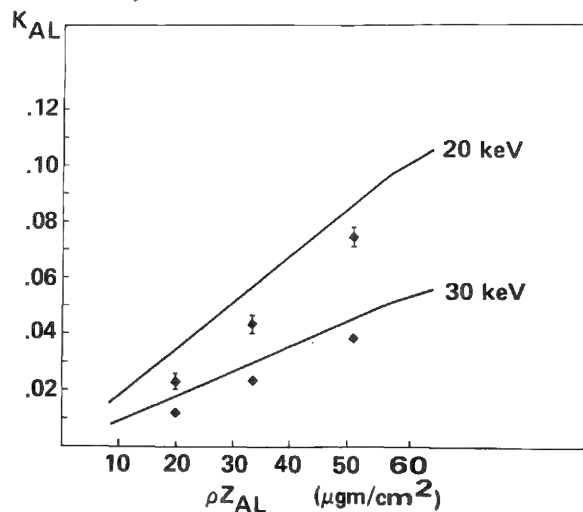


FIG. 6.--Al x-ray intensity ratio vs Al mass thickness, Pt on Al on Si.

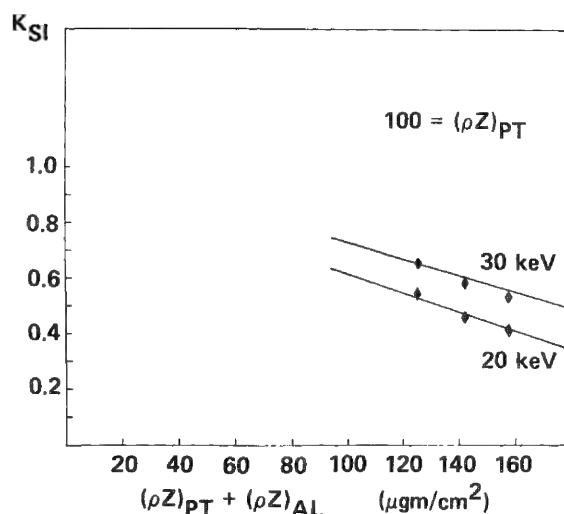


FIG. 7.--Si x-ray intensity ratio vs total film thickness, Pt on Al on Si.

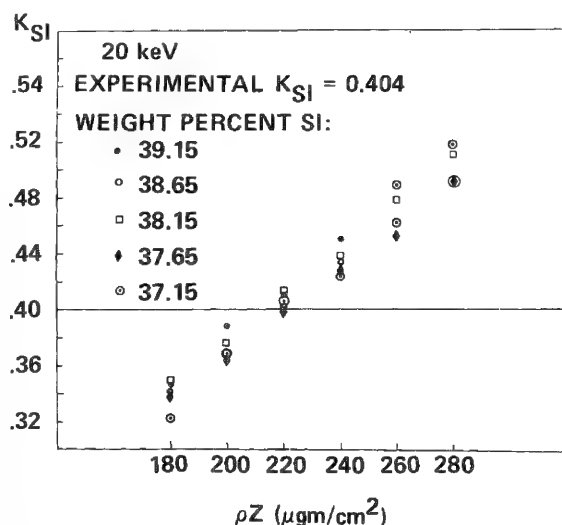


FIG. 8.--Theoretical Si x-ray intensity ratio vs mass thickness,  $P_2O_5$ - $SiO_2$  on Ge.

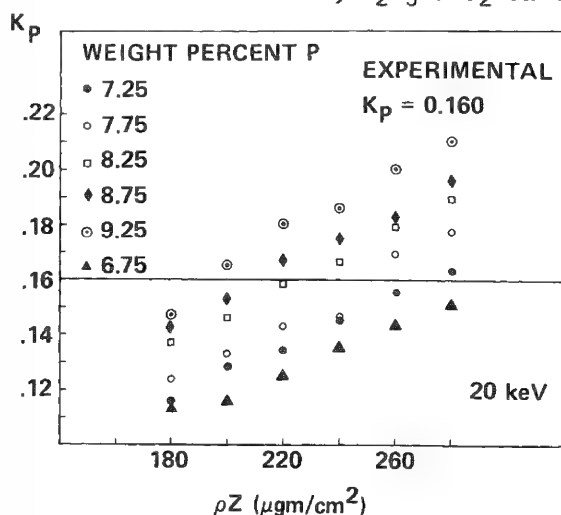


FIG. 9.--Theoretical P x-ray intensity ratio vs mass thickness,  $P_2O_5$ - $SiO_2$  on Ge.

that on Ge, whereas the composition on Si is identical to that of the first film on Si. The Si concentration predicted is larger in the films deposited on a silicon substrate. The predicted film compositions can be compared with experimental calibration curves determined by measurement of the P concentration with a dc plasma emission spectrometer. The latter method predicted 7-7.5 wt% P with an accuracy of approximately 0.5wt%. Agreement between the two methods is satisfactory.

TABLE 1.--Composition of  $P_2O_5$ - $SiO_2$  film on Ge;  $\rho Z$  is  $220 \mu g/cm^2$  at convergence. The measured thickness is  $1.00 \mu m$ .

	WEIGHT PERCENT	ATOMIC PERCENT
P	8.5	5.5
Si	37.9	27.1
O	53.6	67.4

TABLE 2.--Composition of  $P_2O_5$ - $SiO_2$  film on Si. Predicted  $\rho Z$  is  $270 \mu g/cm^2$ .

	WEIGHT PERCENT	ATOMIC PERCENT
P	6.1	4.0
Si	40.3	28.8
O	53.6	67.3

The film mass thickness at convergence ( $220 \mu g/cm^2$ ) is in good agreement with the measured film thickness,  $1.00 \mu m$ , which is  $230 \mu g/cm^3$  from the bulk density of  $SiO_2$ .

### Conclusions

The Monte Carlo model of Kyser and Murata is in good agreement with experiment for the thicknesses of Pt and Al films on silicon and for PtSi films on silicon. The model has been extended to two films on a substrate and, for predicting thickness, is in good agreement for Pt films on Al films on silicon. The Al experimental  $k_{Al}$  values are somewhat lower than the predicted values.

For all these films, the substrate  $k_{Si}$  value is in good agreement with theory, and can be used to measure film thickness.

The predicted compositions of pseudo-ternary  $P_2O_5$ - $SiO_2$  films of equivalent thickness and composition on germanium and on aluminum oxide substrates are in excellent agreement with each other, but are lower in silicon content than the composition predicted for the equivalent film on a silicon substrate. Predicted and measured  $P_2O_5$ - $SiO_2$  film thickness are in good agreement.

It appears that more accurate film compositions are predicted when the substrate

element is not an element in the film (silicon in this case). However, meaningful compositions can still be determined when the substrate element is a significant weight fraction of the film. Moreover, film thickness can be predicted even when the substrate element is a significant weight percent of the film.

#### *References*

1. D. F. Kyser and K. Murata, *IBM J. Res. Develop.* 18: 352, 1974.
2. J. M. Andrews, *J. Vac. Sci. Technol.* 11: 972, 1974.



## MONTE CARLO CALCULATIONS OF ABSOLUTE X-RAY GENERATION FROM SOLID TARGETS

D. E. Newbury and R. L. Myklebust

The development of the energy-dispersive x-ray spectrometer (EDS), which has a reasonably constant efficiency of x-ray detection, has led to an increased interest in quantitative analysis based on a "standardless" approach.<sup>1</sup> In such an analysis scheme, a calculation of the absolute intensity of characteristic x-ray production must be made with an appropriate cross section for inner-shell ionization. As an alternative, in some schemes a single pure element standard is measured, and the required intensities for other pure element standards are calculated relative to this measured standard, again by the use of a cross section for inner-shell ionization. Powell has recently reviewed the numerous formulas available for the calculation of inner-shell ionization.<sup>2</sup> Most of the available formulas are strictly valid for overvoltages greater than 4, where the overvoltage  $U = E/E_c$ , with  $E$  the electron energy and  $E_c$  the critical ionization energy. In electron probe microanalysis, however, the overvoltage is frequently less than 4, particularly for characteristic x rays in the range 5-10 keV. Moreover, the generation of x rays occurs from the initial value  $U_0$  down to  $U = 1$  for electrons that remain in a solid target. It is thus necessary to have a cross section that accurately describes inner-shell ionization at low overvoltages. From the available information in the literature, it is difficult to assess the accuracy of the cross sections in this region, primarily because of the paucity of experimental data.<sup>2</sup>

Recently, Lifshin et al. have reported new measurements of the absolute x-ray generation from solid targets under electron bombardment, as measured by energy-dispersive x-ray spectrometry.<sup>3</sup> In order to test the theoretical cross sections against the new data, we have carried out calculations of the absolute x-ray generation in solid targets by means of a Monte Carlo electron trajectory simulation, which incorporates several of the ionization cross sections. The Monte Carlo procedure is of the hybrid type; it uses single-event elastic scattering for the initial portion of the electron trajectory (from  $E_0$  to  $0.95 E_0$ ) and multiple scattering for the balance of the trajectory, to increase the calculational speed.<sup>4</sup> The Bethe continuous-energy-loss approximation is used for the simulation of inelastic scattering.<sup>5</sup> This Monte Carlo simulation has been extensively tested.<sup>5</sup> In particular, the simulation has been found to yield accurate values of the total electron backscattering coefficient that agree closely with experimental values. A realistic energy distribution of the backscattered electrons is also calculated. Finally, the depth distribution of the inner-shell ionization has been found to correspond well to experimental distributions.<sup>4</sup> The simulation should thus be capable of accurately correcting for the loss of ionization due to electron backscattering.

At the present time, four cross sections for inner-shell ionization have been examined:

(1) Bethe (Mott-Massey)<sup>2</sup>

$$Q = 6.51 \times 10^{-20} \frac{Z_K^b \log(cU_K)}{E_c^2 U_K} \quad (\text{cm}^2) \quad (1)$$

where  $Z_K$  is the number of electrons in the K shell,  $E_c$  is the critical ionization energy (keV),  $U$  is the overvoltage, and  $b$  and  $c$  are constants, with  $b = 0.35$  and  $c = 2.42$  for the K-shell.

---

The authors are with the Microanalysis Group, Center for Analytical Chemistry, National Bureau of Standards, Washington, DC 20234.

(2) Green and Cosslett<sup>2</sup>

$$Q = \frac{7.92 \times 10^{-20} \log U_K}{E_c^2 U_K} \text{ (cm}^2\text{)} \quad (2)$$

(3) Fabre<sup>2</sup>

$$Q = \frac{6.51 \times 10^{-20} Z_K \log U_K}{E_c^2 D_K (U_K + F_K)} \text{ (cm}^2\text{)} \quad (3)$$

where  $D_K = 1.18$  and  $F_K = 1.32$ .

(4) Worthington and Tomlin<sup>6</sup> (a modification suggested by Philibert and Tixier<sup>7</sup>)

$$Q = 6.51 \times 10^{-20} \frac{Z_K b_K \log U_K}{E_c^2 U_K} \text{ (cm}^2\text{)} \quad (4)$$

where  $b_K = 0.35$ .

The results calculated with the Monte Carlo simulation for three elements at several beam energies are listed in Table 1 together with the experimental results of Lifshin et al.<sup>3</sup> The results indicate that none of the cross sections tested is satisfactory for the range of atomic number and beam energy tested. The cross sections produce values of the absolute x-ray production which differ among themselves by a factor of as much as 3. For nickel and chromium, the Bethe (Mott-Massey) cross section produced results which are closest to the experimental measurements; whereas for silicon at low beam energies, the Fabre cross section gave the best agreement.

TABLE 1.--Comparison of calculated and experimental absolute x-ray yields (photons/electron-steradian).

Energy (keV)	Green - Cosslett*	Fabre*	Worthington-Tomlin*	Bethe - Mott - Massey*	Lifshin et al. (experimental)
Silicon					
5	7.69E-5	6.51E-5	4.44E-5	1.11E-4	6.57E-5
7.5	1.77E-4	1.68E-4	1.02E-4	2.06E-4	1.44E-4
10	2.92E-4	2.98E-4	1.70E-4	3.10E-4	2.36E-4
15	5.49E-4	5.98E-4	3.18E-4	5.31E-4	4.51E-4
20	8.28E-4	9.45E-4	4.82E-4	7.47E-4	6.96E-4
Chromium					
10	2.70E-5	1.97E-5	1.57E-5	6.29E-5	4.03E-5
15	9.71E-5	8.04E-5	5.58E-5	1.48E-4	1.38E-4
20	1.88E-4	1.69E-4	1.08E-4	2.40E-4	2.69E-4
25	2.94E-4	2.79E-4	1.69E-4	3.39E-4	4.29E-4
Nickel					
10	4.10E-6	2.58E-6	2.29E-6	2.20E-5	8.78E-6
15	4.00E-5	3.00E-5	2.30E-5	8.19E-5	6.72E-5
20	9.88E-5	8.02E-5	5.70E-5	1.55E-5	1.53E-5
25	1.68E-4	1.48E-4	9.70E-5	2.24E-4	2.59E-4

\*The precision of the Monte Carlo calculations is estimated to be  $\pm 3$  percent.

If we consider x-ray generation of one element relative to another (Table 2), the Bethe cross section produces values reasonably close to the experimental values at 20 keV, but all the cross sections differ significantly from the experimental values at 10 keV. The large deviations of the relative x-ray yields predicted by the cross sections traditionally used in microprobe analysis suggest that the development of a theoretical basis for "standardless" or "single-standard" analysis will require a more careful examination of the choice of the ionization cross section.

TABLE 2.--Comparison of calculated and experimental relative x-ray yields.

Energy (keV)	Green - Cosslett	Fabre	Worthington- Tomlin	Bethe - Mott - Massey	Lifshin et al. (experimental)
Chromium/Silicon					
10	0.0925	0.0661	0.0926	0.202	0.171
15	0.177	0.134	0.175	0.279	0.306
20	0.227	0.178	0.224	0.321	0.386
Nickel/Silicon					
10	0.0140	0.00866	0.0135	0.0708	0.0372
15	0.0729	0.0501	0.0724	0.154	0.149
20	0.119	0.0849	0.118	0.207	0.220
Nickel/Chromium					
10	0.152	0.131	0.146	0.349	0.218
15	0.412	0.373	0.413	0.553	0.487
20	0.525	0.474	0.528	0.645	0.569

Further calculations will be carried out with the cross section proposed by Gryzinski, which is also recommended by Powell for the low-overvoltage case.<sup>2</sup> The calculations will be extended to additional elements and beam energies. The absolute yield also depends on the exact choice of the stopping power and the fluorescence yield. These parameters will be tested in future work.

#### References

1. J. C. Russ, "A Fast, Self-Contained, No-Standards Quantitative Program for EDS", *Proc. 13th MAS Conf.*, 1978, 46A-F.
2. C. J. Powell, "Evaluation of formulas for inner-shell ionization cross sections," in K. F. J. Heinrich, D. E. Newbury, and H. Yakowitz, Eds., *Use of Monte Carlo Calculations in Electron Probe Microanalysis and Scanning Electron Microscopy*, Special Publication 460, Washington, D.C.: National Bureau of Standards, 1976, 97-104.
3. E. Lifshin, M. F. Ciccarelli, and R. B. Bolon, "New measurements of the voltage dependence of absolute x-ray yields using energy dispersive spectrometry," *Proc. 12th MASS Conf.*, Boston, 1977, 104A-C.
4. D. E. Newbury, R. L. Myklebust, and K. F. J. Heinrich, "A Monte Carlo procedure employing single and multiple scattering," *Proc. 12th MAS Conf.*, Boston, 1977, 27A-G.
5. R. L. Myklebust, D. E. Newbury, and H. Yakowitz, "NBS Monte Carlo electron trajectory calculation program," in Ref. 2 above, pp. 105-128.
6. C. R. Worthington and S. G. Tomlin, "The intensity of characteristic X-radiation," *Proc. Phys. Soc.* [A]69: 401-412, 1956.
7. J. Philibert and R. Tixier, "Some problems with quantitative electron probe microanalysis," in K. F. J. Heinrich, Ed., *Quantitative Electron Probe Microanalysis*, Washington, D.C.: National Bureau of Standards, Special Publication 298, 1968, 13-33.

## Biological Microanalysis

### ELECTRON PROBE ANALYSIS OF MUSCLE: A PROGRESS REPORT

A. P. Somlyo, Henry Shuman, and A. V. Somlyo

Muscle contraction is controlled by the level of cytoplasmic free Ca concentration that, in turn, is regulated by cell organelles and the surface membrane.<sup>1-6</sup> Therefore, the identification of intracellular calcium storage sites and of the mechanism(s) of calcium release and uptake are central to the problem of excitation-contraction coupling. Much evidence suggests that, in striated muscle,  $\text{Ca}^{++}$  is released from the terminal cisternae (TC) of the sarcoplasmic reticulum (SR) by some as yet undetermined trigger mechanism at the triadic junction between the T-tubules and the TC.<sup>7,8</sup> The ability of the sarcoplasmic reticulum of striated muscle to accumulate calcium against a large ( $\approx 10^4$ ) gradient has been demonstrated in isolated fractions (e.g., 1,3,9), radioautography<sup>10</sup> and electron-probe analysis of muscles loaded with oxalate.<sup>11</sup> However, because of their high permeability to monovalent ions,<sup>12,13</sup> isolated SR vesicle preparations do not provide information about the *in vivo* monovalent ion composition. Specifically, although it is known that macromolecular extracellular tracers, such as ferritin, do not penetrate the SR,<sup>14,15</sup> some ion flux studies have been interpreted to show high concentrations of extracellular ions (NaCl) in the SR.<sup>16,17</sup> It was of considerable interest to determine whether the *in situ* composition of the SR in striated muscle resembled that of the extracellular space, to quantitate the amount of calcium that is released during activation, and to determine the counter ions, if any, that may move into the SR during calcium release to maintain electron neutrality.

In *smooth muscle*, the role of the sarcoplasmic reticulum as a calcium storage site has also been established,<sup>18,19</sup> but the sparsity of SR in at least some smooth muscles<sup>20</sup> raised the possibility that mitochondria may also serve as calcium stores. This communication summarizes results obtained with electron-probe analysis of muscle dealing with some of the above questions, which are described in greater detail elsewhere.<sup>17,21-23</sup>

Muscle, in retrospect, was a fortunate choice for biological electron-probe analysis. Tension can be monitored in bundles (or single fibers) of striated muscles that are sufficiently small for rapid freezing and can be dissected without damage and associated ion movements. That is an important consideration, because diffusible elements can only be quantitated in rapidly frozen tissues, and even with the best available techniques only the superficial, approximately 5-20  $\mu\text{m}$  of tissue is frozen without electron-microscopically detectable ice crystal formation.<sup>24</sup> Furthermore, normal muscle contains no large aqueous domains, such as the lumen of epithelial organs, which require the use of frozen hydrated sections to prevent the collapse and loss of the solutes contained in the aqueous compartment,<sup>25,26</sup> so that quantitative electron probe analysis of dry cryosections of muscle is feasible. This is an advantageous approach, inasmuch as the considerable contrast gained in dehydrated (as compared to frozen hydrated) specimens<sup>25,27</sup> permits visualization of small organelles, such as the SR. In addition, the x-ray background that would originate from water is absent in dry specimens, which leads to improved sensitivity of analysis.

The preparation and freezing of tissues in supercooled liquid freon 22,<sup>17,24</sup> the freezing rates attainable,<sup>28</sup> and our methods and instrumentation for quantitative electron probe analysis have been described.<sup>29-32</sup> To minimize contamination and radiation damage, we find the use of a high-vacuum electron microscope and liquid-nitrogen-cooled stage important, and for some experiments, essential. Our current instrument is equipped with a field-emission source operated usually at 80 kV. We have used a variety of grid materials suited for specific applications including copper, titanium, nylon, stainless steel, and beryllium. The contribution of extraneous (largely generated by grid material) x-rays has been mini-

---

The authors are at the Pennsylvania Muscle Institute of the University of Pennsylvania, 51 North 39th Street, Philadelphia, PA 19104. The work was supported by NIH grants HL 1583 and GM 00092.

mized by spray apertures, and the continuum contributed by the grid is scaled to the characteristic (Cu or Ti, etc.) peak and subtracted.<sup>29</sup> This procedure, together with the choice of the continuum used for quantitative thin-section analysis (1.34-1.64 kV), sufficiently reduces the error due to extraneous contributions, to permit analysis well within the approximately 15% precision of the measurements. In a typical analysis of a 100nm-thick cryosection of muscle, the continuum counts (before subtraction) due to the copper grid in the 1.34-1.64 region are only approximately 6% of the continuum count due to the specimen. The interference by the Cu L with the Na peak does not preclude quantitative analysis of sodium in specimens on copper grids, since commercially available detectors combined with a multiple-least-squares fitting routine can readily resolve the two peaks separated by 100 eV,<sup>29</sup> and sodium values not significantly different from those obtained on copper grids have been obtained from cryosections on titanium grids.<sup>23</sup> Nevertheless, for analysis of relatively low concentrations of Na, avoidance of the Cu line is preferable, and we suggest that further improvement in quantitation could be gained by the use of beryllium grids if the specimen-generated continuum can be included as one of the parameters in the fit.<sup>30</sup> Manufacturers should also be urged to provide better beam collimation and shielding from radiation generated in the column.

With the instrumentation described and with a conventional source, analysis of the iron core of a single ferritin molecule was feasible,<sup>33</sup> and with a field-emission gun x-ray maps have been obtained from Hg-labelled tropomyosin paracrystals<sup>32</sup> showing the characteristic 40nm period.

In *striated muscle*, the major result of electron probe analysis was the demonstration that, both at rest and during a tetanic contraction, the NaCl content of the TC of the SR resembles that of the cytoplasm rather than that of the extracellular space.<sup>17,21,34</sup> Validation of the preparatory techniques used for this work included the demonstration of a sharp and quantitative boundary between the intracellular and extracellular domains<sup>17,24</sup> and excellent agreement between the results of quantitative electron-probe analysis and bulk chemical measurements of the most reliably measured intracellular ions (K and Mg) in both striated<sup>17</sup> and smooth muscle.<sup>23</sup> These findings indicate that significant translocations of diffusible elements do not occur, at least across membranous domains, during freezing or cryosectioning at -100 to -130°C and subsequent freeze-drying.

The high concentration of calcium (66-100mmol/kg dry weight) in the TC of the SR confirms their role as calcium sequestration sites.<sup>1-3</sup> Ongoing studies in our laboratory have shown that approximately 60% of this total calcium can be released during a tetanus,<sup>34</sup> without the uptake of an equivalent amount of Na, K, or Mg. The latter findings suggest that proton movements or a change in the net charges on calsequestrin<sup>3</sup> may maintain electro-neutrality in the TC during (massive) calcium release.

Granules containing high concentrations of Ca and P were observed in some of the longitudinal tubules of the SR in muscles treated with hypertonic solutions,<sup>17</sup> which suggests that some of the uncoupling of contraction by hypertonicity may be due to a translocation of calcium from the TC to the longitudinal tubules. In addition, however, hypertonic solutions also cause swelling of the T-tubules of striated muscle,<sup>17,35</sup> and we note that the spatial resolution attainable with stationary probes is sufficient (at least 50-100 nm) to resolve the different composition (high NaCl) of the lumen of the T-tubule vacuoles and the adjacent cytoplasm in both hypertonically treated and in fatigued muscles.<sup>17,22</sup> Furthermore, electron probe analysis of fatigued muscle also demonstrated that the Ca content of the TC is not reduced and that mitochondria contain normal (low) concentrations of Ca, which indicates that neither the absence of activator Ca from the TC nor mitochondrial uncoupling due to Ca loading of these organelles can be implicated in the mechanism of fatigue.

In smooth muscle, bulk chemical methods have shown an excess of cellular Cl over that predicted by a Donnan distribution.<sup>36-39</sup> Electron-probe analysis of dry cryosections of rabbit portal-anterior mesenteric vein (PAMV) smooth muscle verified the high cellular concentration of Cl, and also established that it is distributed throughout the cytoplasm and not sequestered in organelles such as the nucleus or mitochondria.<sup>23</sup> Again there was excellent agreement between the Cl content of PAMV smooth muscle measured with electron-probe analysis and independent bulk chemical measurements of the same tissue.<sup>23,38</sup>

The composition of the cell nucleus has also been compared with that of the cytoplasm in smooth muscle,<sup>23</sup> and the results of these analyses and those of several laboratories on

a variety of cell systems converge to the same general conclusion that the nucleus is not a site of Na or Ca sequestration.<sup>23</sup> Mitochondrial Ca has been measured in resting PAMV smooth muscle and in preparations frozen after a maintained contracture of 30 min. In neither of these conditions was the Ca concentration in the mitochondria significantly higher than in the adjacent cytoplasm, which indicates that, unlike the SR, the mitochondria (at least in PAMV smooth muscle) are *not* major sites of calcium sequestration.<sup>23</sup> However, given the comparatively high minimal concentration detectable by electron probe analysis (approximately 2mmol/kg dry weight with the parameters used) and the fact that we are measuring total rather than free Ca, the electron-probe studies do not exclude the possibility that there is a higher concentration of *free* Ca in the mitochondrial matrix than in the cytoplasm. Nevertheless, if the mitochondria were able to accumulate Ca with an apparent affinity notably higher than the 17 $\mu$ M value measured *in vitro*,<sup>40</sup> a detectable increase in mitochondrial Ca content would have been expected after a 30min maintained contraction during which cytoplasmic free Ca is thought to rise to micromolar levels. This is an example of the usefulness of electron-probe analysis in determining whether an apparent  $K_m$  measured after isolation of mitochondria *in vitro* is significantly different from that present in the intracellular environment. The fact that mitochondria can accumulate high concentrations of Ca *in situ*, if cytoplasmic  $Ca^{++}$  rises to abnormally high levels, has also been verified. Mitochondria in damaged PAMV smooth muscle cells, like in a variety of other damaged cells, contained granules consisting of large amounts of Ca (up to 1.8 mole/kg) and P.<sup>23</sup> The significance of such mitochondrial Ca granules cannot be evaluated without quantitative analysis of the cytoplasmic concentration of diffusible elements (Na, Cl, K). We consider that, unless proven otherwise, such mitochondrial granules are evidence of cell damage either prior to or during preparation of the tissues. Indeed, although preliminary studies in this laboratory have previously demonstrated mitochondrial granules in cultured vascular smooth muscle cells thought to be normal,<sup>41</sup> more recent studies showed that the presence of such granules is associated with abnormally low cytoplasmic K levels suggestive of cell damage.<sup>42</sup> However, mitochondrial calcium is high in mitochondria isolated from apparently normal bovine arteries, and the Ca and Mg content is further increased in atherosclerotic bovine vessels.<sup>43,44</sup> Therefore, variations in mitochondrial Ca content related to tissue, species, and pathological processes still remain to be clarified.

We conclude that electron-probe analysis of cryosections has been uniquely suitable for obtaining information about the subcellular composition of muscle and its organelles during rest and contraction.

## References

1. M. Endo, "Calcium release from the sarcoplasmic reticulum," *Physiol. Rev.* 57: 71, 1977.
2. A. Fabiato and F. Fabiato, "Calcium release from the sarcoplasmic reticulum" *Circ. Res.* 40: 119, 1977.
3. D. H. MacLennan and P. C. Holland, "Calcium transport in sarcoplasmic reticulum," *Ann. Rev. Biophys. Bioeng.* 4: 377, 1975.
4. A. P. Somlyo et al., "Vertebrate smooth muscle: Ultrastructure and function," *Cell Motility, Cold Spring Harbor Laboratory*, 3: 165, 1976.
5. A. Weber and J. M. Murray, "Molecular control mechanisms in muscle contraction," *Physiol. Rev.* 53: 612, 1973.
6. A. P. Somlyo, "Vascular smooth muscle," in T. Narahashi, Ed., *Cellular Pharmacology of Excitable Tissues*, Springfield, Ill.: Thomas, 1975, p. 360.
7. L. L. Costantin, "Contractile activation in skeletal muscle," *Prog. Biophys. Biol.* 29: 197, 1975.
8. A. V. Somlyo, "Bridging structures spanning the junctional gap at the triad of skeletal muscle," *J. Cell Biol.* 80: 743, 1979.
9. S. Ebashi and M. Endo, "Calcium ion and muscle contraction," in J. A. V. Butler and D. Noble, Eds., *Progress in Biophysics and Molecular Biology*, New York: Pergamon Press 1968, pp 123-183.
10. S. Winegrad, "Intracellular calcium movements of frog skeletal muscle during recovery from tetanus," *J. Gen. Physiol.* 51: 65, 1968.
11. R. J. Podolsky, T. Hall, and S. L. Hatchett, "Identification of oxalate precipitates in striated muscle fibers," *J. Cell Biol.* 44: 699, 1970.



12. P. F. Duggan and A. Martonosi, "Sarcoplasmic reticulum: IX. The permeability of sarcoplasmic reticulum membranes," *J. Gen. Physiol.* 56: 147, 1970.
13. D. McKinley and G. Meissner, "Evidence for a  $K^+$ ,  $Na^+$  permeable channel in sarcoplasmic reticulum," *J. Memb. Biol.* 44: 159, 1978.
14. H. E. Huxley, "Evidence for continuity between the central elements of the triads and extracellular space in frog sartorius muscle," *Nature* 202: 1067, 1964.
15. S. G. Page, "The organization of the sarcoplasmic reticulum in frog muscle," *J. Physiol.* 175: 10P, 1964.
16. E. Rogus and K. L. Zierler, "Sodium and water contents of sarcoplasm and sarcoplasmic reticulum in rat skeletal muscle: Effects of anisotonic media, ouabain and external sodium," *J. Physiol.* 233: 227, 1973.
17. A. V. Somlyo, H. Shuman, and A. P. Somlyo, "Elemental distribution in striated muscle and the effects of hypertonicity: Electron probe analysis of cryo sections," *J. Cell Biol.* 74: 828, 1977.
18. A. V. Somlyo and A. P. Somlyo, "Strontium accumulation by sarcoplasmic reticulum and mitochondria in vascular smooth muscle," *Science* 174: 955, 1971.
19. B. Johansson, "Processes involved in vascular smooth muscle contraction and relaxation," *Circ. Res.* 43: I-14, 1978.
20. C. E. Devine, A. V. Somlyo, and A. P. Somlyo, "Sarcoplasmic reticulum and excitation-contraction coupling in mammalian smooth muscle," *J. Cell Biol.* 52: 690, 1972.
21. A. V. Somlyo, Henry Shuman, and A. P. Somlyo, "The composition of the sarcoplasmic reticulum *in situ*: Electron probe x-ray microanalysis of cryo sections," *Nature* 268: 556, 1977.
22. H. Gonzales-Serratos et al., "The composition of vacuoles and sarcoplasmic reticulum in fatigued muscle: Electron probe analysis," *Proc. Natl. Acad. Sci.* 75: 1329, 1978.
23. A. P. Somlyo, A. V. Somlyo, and H. Shuman, "Electron probe analysis of vascular smooth muscle: Composition of mitochondria, nuclei and cytoplasm," *J. Cell Biol.* 81: 316, 1979.
24. A. V. Somlyo and J. Silcox, "Cryoultramicrotomy for electron probe analysis," in C. Lechene and R. Warner, Eds., *Microbeam Analysis in Biology*, New York: Academic Press (in press).
25. B. L. Gupta and T. A. Hall, "Electron microprobe x-ray analysis of calcium," in A. Scarpa and E. Carafoli, Eds., *Ann. N.Y. Acad. Sci.*, New York: New York Academy of Sciences, 1978, pp. 28-51.
26. C. P. Lechene, "Electron probe microanalysis: Its present, its future," *Amer. J. Physiol.* 232: F391, 1977.
27. T. E. Hutchinson, D. E. Johnson, and A. P. Mackenzie, "Instrumentation for direct observation of frozen hydrated specimens in the electron microscope," *Ultramicroscopy* 3: 315, 1978.
28. M. J. Costello and J. M. Corless, "The direct measurement of temperature changes within freeze-fracture specimens during rapid quenching in liquid coolants," *J. Microsc.* 112: 17, 1978.
29. H. Shuman, A. V. Somlyo, and A. P. Somlyo, "Quantitative electron probe microanalysis of biological thin sections: Methods and validity," *Ultramicroscopy* 1: 317, 1976.
30. H. Shuman, A. V. Somlyo, and A. P. Somlyo, "Theoretical and practical limits of ED x-ray analysis of biological thin sections," *Scan. Elect. Micros., IIT Res. Inst.* 1: 663, 1977.
31. T. A. Hall, "The microprobe assay of chemical elements," in G. Oster, Ed., *Physical Techniques in Biological Research*, New York: Academic Press, 1971, vol. 1A.
32. A. P. Somlyo et al., "Electron probe analysis of muscle and x-ray mapping of biological specimens with a field emission gun," *Scan. Elect. Micros.* (in press).
33. H. Shuman and A. P. Somlyo, "Electron probe x-ray analysis of single ferritin molecules," *Proc. Natl. Acad. Sci.* 73: 1193, 1976.
34. A. V. Somlyo et al., "Changes in sarcoplasmic reticulum composition in activated frog skeletal muscle," *Biophys. J.* 25: 25a, 1979.
35. C. Franzini-Armstrong et al., "T-tubule swelling in hypertonic solutions: A freeze substitution study," *J. Physiol.* 283: 133, 1978.
36. R. Casteels, "The distribution of chloride ions in the smooth muscle cells of the guinea pig's taenia coli," *J. Physiol.* 214: 225, 1971.

37. A. W. Jones, A. P. Somlyo, and A. V. Somlyo, "Potassium accumulation in smooth muscle and associated ultrastructural changes," *J. Physiol.* 232: 247, 1973.
38. A. W. Jones and L. A. Miller, "Ion transport in tonic and phasic vascular smooth muscle and changes during deoxycorticosterone hypertension," in B. F. Bohr and F. Tanenaka Eds., *Blood Vessels, Molecular and Cellular Aspects of Vascular Smooth Muscle in Health and Disease*, Berne (Switzerland): S. Karger, 1978, pp. 83-92.
39. C. Y. Kao and A. Nishiyama, "Ion concentrations and membrane potentials of myometrium during recovery from cold," *Amer. J. Physiol.* 217: 525, 1969.
40. J. Vallieres, A. Scarpa, and A. P. Somlyo, "Subcellular fractions of smooth muscle. Isolation, substrate utilization and  $Ca^{++}$  transport by main pulmonary artery and mesenteric vein mitochondria," *Arch. Biochem. Biophys.* 170: 659, 1975.
41. R. E. Garfield and A. P. Somlyo, "Ultrastructural basis for vascular smooth muscle reactivity," in S. Shibata and O. Carrier, Eds., *Factors Influencing Vascular Smooth Muscle Reactivity*, Tokyo: Igaku-Shoin Ltd., 1977, pp. 1-25.
42. M. R. James, H. Shuman, R. Karp, and A. P. Somlyo (in preparation).
43. B. F. Sloane et al., "Calcium and magnesium content of isolated vascular smooth muscle mitochondria," *Proc. 6th Intl. Biophys. Cong.*, p. 233, 1978 (abstract).
44. A. P. Somlyo et al., "Electron probe analysis of calcium compartments in cryo sections of smooth and striated muscles," in A. Scarpa and E. Carafoli, Eds., *Ann. N.Y. Acad. Sci.*, New York: New York Academy of Sciences, 1978, pp. 523-544.

## ELECTRON PROBE MICROANALYSIS OF BULK-FROZEN HYDRATED BIOLOGICAL SAMPLES

Claude Lechene

Analysis of unbound elements in biological tissues is of prime importance in cell physiology. Three main different approaches exist: that of the Hall's group in Cambridge, analyzing frozen hydrated sections approximately  $1\ \mu$  thick<sup>1</sup>; that of Somlyo analyzing ultrathin (approximately 100nm) cryosections of muscle, subsequently freeze dried<sup>2</sup>; and the analysis of frozen bulk specimens, approached by Marshall,<sup>3</sup> Fuchs,<sup>4</sup> and our group.<sup>5</sup>

The analysis of frozen bulk biological specimens is of prime importance in renal physiology, where large spaces (tubular lumens) contain no organic matrix, which leads to important ion translocations during drying. The principle we follow to justify electron-probe analysis of frozen hydrated bulk biological specimens is that at liquid-nitrogen temperature, a biological tissue is similar to a geological sample and could be prepared and analyzed as if it were a piece of rock. Analysis of volumes of a few cubic microns would bring important information to cell physiology and particularly to renal physiology.

Towards this aim the biological sample should be quenched, prepared under liquid nitrogen, transported into the probe column without rewarming and without trapping frost, and maintained in the probe stage at very low temperatures during analysis.

We have now developed the following steps. The sample is quenched in solid nitrogen, which contrary to the report by Costello and Corless<sup>6</sup> (who used a slush of liquid/solid nitrogen) freezes faster than any freon. (We have observed, on bulk samples, contamination by chlorine after using freon 13 and contamination by bromine after using freon 13B.) When frozen, the sample is transferred to a working station, where it is prepared under liquid nitrogen. It is trimmed by means of dental tools. It is mounted in a copper holder by means of a mixture of glycerol and ammonium acetate. The surface to be analyzed is exposed by a special diamond cutting saw (Red Blazer,  $4 \times 012 \times 021 \times 518$ , Raytech Industries, Inc., Stafford Springs, Conn.), immersed in the liquid nitrogen. When the surface to be analyzed is exposed, the copper holder with the sample is placed in the bottom of a special copper container filled with liquid nitrogen, which is transferred from the working station to an interlock chamber located on the probe column of the Camebax instrument. The interlock chamber is closed and the small chamber is evacuated with a sorption pump. The copper holder is then inserted under a vacuum into the frozen stage of the probe column. The entire operation takes less than 2 min. When in the interlock chamber the sample is under liquid nitrogen. When the chamber is pumped, the sample is in an environment of cold nitrogen. In the electron probe, the copper holder is kept cold ( $-190^\circ\text{C}$ ) in the instrument stage cooled by circulation of liquid nitrogen.

The system we use is a modified Camebax electron probe made in France by Cameca, with three wavelength-dispersive spectrometers and one energy-dispersive spectrometer. The photomicroscope attached to the probe column has proved invaluable for sample monitoring.

We have modified the vacuum of the probe to be oil free. Rough pumping is done by a membrane pump (KNF Neuberger, NV770-3-7E, Princeton, N.J.) down to 2 Torr. From 2 Torr to 0.01 Torr a sorption pump (Vac Sorb 941-6501, Varian, Palo Alto, Calif.) is used. Below 0.01 Torr the column is pumped with a cryogenic pump (Cryo-Torr model T, CTI Cryogenics, Waltham, Mass.). All vacuum grease has been eliminated. O-rings are made in Viton. Vacuum below  $9 \times 10^{-8}$  Torr at room temperature and of  $5 \times 10^{-8}$  Torr when the stage is cold are reached. No contamination was observed, even when observing ultrathin sections with the true transmission electron microscope attachment. Return to atmospheric pressure is made with ultra clean nitrogen.

---

The author is director of the National Biotechnology Resource in Electron Probe Microanalysis at the Harvard Medical School. This work has been supported by National Institutes of Health under grant RR-00679.

We have recently observed an important contamination containing chlorine appearing when the stage is cold. This contamination is attributed to a leak between the column and the space containing the coil of the objective lens, which is cooled by circulation of freon.

As liquid-droplet analysis has become a routine method for analysis of picoliter volumes of micropunctured samples, it is hoped that frozen-hydrated bulk sample analysis will provide a general method for elemental analysis of femtoliter volumes of cells and extracellular spaces in biological tissues *in situ*.

#### References

1. B. L. Gupta, T. A. Hall, and R. B. Moreton, "Electron probe x-ray microanalysis," in B. L. Gupta, R. B. Morton, J. L. Oschman, and B. J. Wall, Eds., *Transport of Ions and Water in Animals*, London: Academic Press, 1977, 83-143.
2. A. V. Somlyo, H. Shuman, and A. P. Somlyo, "Elemental distribution in striated muscle and the effects of hypertonicity: Electron probe analysis of cryosections," *J. Cell Biol.* 74: 828, 1977.
3. A. T. Marshall, "Electron probe--x-ray microanalysis of frozen-hydrated biological specimens," *Microscopica Acta* 79(3): 254-266, 1977.
4. W. Fuchs, B. Lindemann, and J. D. Brombach, "Instrumentation and specimen preparation for electron beam x-ray microanalysis of frozen hydrated bulk specimens," *J. Microscopy* 112(1): 75-87, 1978.
5. C. Lechene, J. V. Bonventre, and R. R. Warner, "Electron probe analysis of frozen hydrated bulk tissues," in C. Lechene and R. Warner, Eds., *Microbeam Analysis in Biology*, New York: Academic Press, in press.
6. M. J. Costello and J. M. Corless, "The direct measurement of temperature changes within freeze-fracture specimen during rapid quenching in liquid coolents," *J. Microscopy* 12: 17-37, 1978.

## SECONDARY ION MASS SPECTROMETRY: APPLICATIONS TO BIOLOGICAL PROBLEMS

Margaret S. Burns

Many biological problems require localization and measurement of elements in tissue. Each problem has individual requirements for localization (spatial resolution) and measurement (limits of sensitivity). To choose an analytical method consonant with the requirements of the specific problem, one needs to understand the basic capabilities of the instrumentation.

Secondary ion mass spectrometry (SIMS) is an analytical method that detects the secondary ions produced by bombardment of a sample surface with primary ions such as oxygen, nitrogen, argon, or cesium. The secondary ions are formed within the sample surface as the surface is eroded by sputtering; the secondary ions thus reflect the surface composition. These sputtered ions are separated in a mass spectrometer, a mode of detection with a high signal-to-background ratio. Because the secondary ions arise from the sample surface an analysis in time can yield three-dimensional information on the sample composition. The secondary ions may be analyzed in four different modes: (1) a mass spectrum; (2) ion images, (3) quantitative ion counts, or (4) depth profiles.<sup>1</sup>

The advantages of a mass-spectrometric detection method are its universality and high signal-to-background ratio. Thus all isotopes from mass/charge = 1 (H) to  $m/e = 300$  may be detected; that includes isotopes such as deuterium, and light elements that are otherwise difficult to detect such as lithium and beryllium.<sup>2</sup> The background noise is less than 3 cps, so that low signals are readily detected. Mass spectra of different classes of organic chemical compounds show similar peaks. The spectra of different types of tissue areas also have a general similarity, which suggests that the process of secondary-ion formation is similar for biological structures known to be composed of different macromolecules. The relative yield of secondary ions (the number of secondary ions produced per incident primary ion) is a complex variable but is high for many elements of biological interest such as Na, Ca, K, and Mg. Improved instrumentation has increased the available mass resolution to a resolving power of 5000, sufficient for separation of most hydrocarbon interferences.

Ion images may be formed by direct imaging by means of an ion optical system, or by the collection of signal from a scanned primary-ion beam. The spatial resolution of an ion image is about  $0.5 \mu$ . The ion image is useful because the composition of a relatively large area (25 to  $250 \mu$  in diameter) can be observed in pictures taken in a few seconds and because images from exactly the same specimen can be compared. The rate of sputtering is a few Angstroms per second so that compositional information may be obtained by sputtering as little as tens of Angstroms. The exact parameters depend upon both instrumental operating conditions and tissue composition. Images of ocular tissue show a completely different distribution depending on the mode of tissue preparation.

Quantitation of ion counts by SIMS is difficult to do from a theoretical basis because a satisfactory theoretical model for secondary-ion emission is lacking. However, empirical standards for analysis of biological tissues can be used for quantitation. A model using water-soluble elements in gelatin films has given good empirical standards for Li, Rb, and Sr.<sup>3</sup> Since the secondary ion spectra of different compounds and tissues are generally similar, these protein standards may be suitable for all tissue areas. Standards

---

The author is in the Department of Ophthalmology and Biochemistry of Montefiore Hospital and Medical Center/Albert Einstein College of Medicine, 111 East 210th St., Bronx, NY 10467. This work was sponsored in part by Grant EY 02093 and a Research Career Development Award EY 00104-01 from the National Institutes of Health; and grants from the National Society for the Prevention of Blindness, Inc., and from Research to Prevent Blindness, Inc., both in New York, N.Y.

of apatites have been used for mineralized tissue, although recent studies of geochemical samples may indicate that quantitation is more complex in these minerals.<sup>4,5</sup>

SIMS has been used for depth profiles of biological tissues in the study of fluorine deposition in teeth.<sup>6</sup> This potentially powerful use of surface analysis has two problems: (1) preparation of a flat tissue surface to present to the primary ion beam in order to achieve maximum depth resolution, theoretically 50-100 Å; (2) differential sputtering rates due to tissue interaction with the primary ion beam. Scanning electron microscope studies of sputtered tissues may be used to gauge the severity of the ion-etching process.

SIMS, in common with other microanalytical methods that achieve localization and measurement, has advantages and disadvantages. The optimum method for any biological problem depends upon two factors: (1) the exact parameters of the problem being investigated, and (2) the exact instrumental operating conditions used. A comparative study can demonstrate this point.

#### References

1. J. A. McHugh, *Methods of Surface Analysis*, Amsterdam: Elsevier, 1975.
2. J. L. Abraham and T. A. Whatley, "Ion microprobe analysis of beryllium containing particles *in situ* in human lungs," *Fed. Proc.* 36: 1090, 1977.
3. M. Bellhorn, and D. File, "Secondary ion mass spectrometry (SIMS) standards for analysis of soft biological tissue," *Analytical Biochemistry* 92: 213, 1979.
4. A. Lodding et al., "Aspects of quantitative determination by ion probe of fluorine concentrations in apatites," *Zeit. Z. Naturf.* 29A: 897, 1974.
5. G. Slodzian and A. Havette, "Quelques résultats d'analyse quantitative sur des silicates," *J. Microsc. Spectrosc. Electron.* 2: 77, 1977.
6. L. G. Petersson et al., "Secondary ion microanalysis of fluorine in apatites of biological interest," *Z. Naturf.* 20C: 417, 1974.



## RECENT ADVANCES OF LASER MICROPROBE MASS ANALYSIS (LAMMA) AS APPLIED TO BIOLOGICAL AND ENGINEERING SPECIMENS

R. L. Kaufmann, H. J. Heinen, M. W. Schürmann, and R. M. Wechsung

During the preceding MAS Conference a new laser microprobe mass analyzer (LAMMA) for biomedical purposes was introduced. An extensive description of the principle and of the LAMMA instrument, as well as some examples of its application, were given in the proceedings of that conference<sup>1</sup> and in several other papers.<sup>2-5</sup> During the past year the following improvements of the LAMMA instrument have been achieved:

- Detection limits for many elements, especially for heavy trace elements such as Pb, Ba, or U, could be further improved and have reached sub-ppm levels in many cases (Table 1).
- Mass resolution has been increased to  $M/\Delta M \approx 850$  by means of a "time focusing" ion reflector in the TOF (time of flight) mass spectrometer which compensates for the spread of initial ion energies (see also Fig. 1).
- Reproducibility from shot to shot was improved to  $\pm 5\%$  SD in standard specimens.
- For sampling bulk specimens a modified version of the LAMMA instrument has been developed. First preliminary results are promising.

TABLE 1.--Detection limits of LAMMA instrument (Dec. 1978). Data refer to analyzed volume (about  $3 \times 10^{-13}$  g) of organic-matrix material and to the condition that polyatomic fragments of matrix do not interfere with atomic mass signals to be measured. Data in parenthesis refer to standard reference specimens prepared by Spurr's low-viscosity medium. Here organic "background" peaks interfere with Cu and Sr signal.

	Absolute (g)	Relative (ppmw)
Li	$2 \times 10^{-20}$	0.2
Na	$2 \times 10^{-20}$	0.2
Mg	$4 \times 10^{-20}$	0.4
Al	$2 \times 10^{-20}$	0.2
K	$1 \times 10^{-20}$	0.1
Ca	$1 \times 10^{-19}$	1.0
Cu	$2 \times 10^{-18}$ ( $10^{-17}$ )	20.0 (200)
Rb	$5 \times 10^{-20}$	0.5
Cs	$3 \times 10^{-20}$	0.3
Sr	$5 \times 10^{-20}$ ( $10^{-19}$ )	0.5 (5.0)
Ag	$1 \times 10^{-19}$	1.0
Ba	$5 \times 10^{-19}$	0.5
Pb	$1 \times 10^{-19}$	0.3
U	$2 \times 10^{-19}$	2.0

Authors Kaufmann and Schürmann are at the Institute of Physiology of the Department of Clinical Physiology at Düsseldorf University; authors Heinen and Wechsung, at Leybold-Heraeus Co., Cologne. The support of this work by grants from Stiftung Volkswagenwerk and the German Federal Ministry of Science and Technology is gratefully acknowledged.

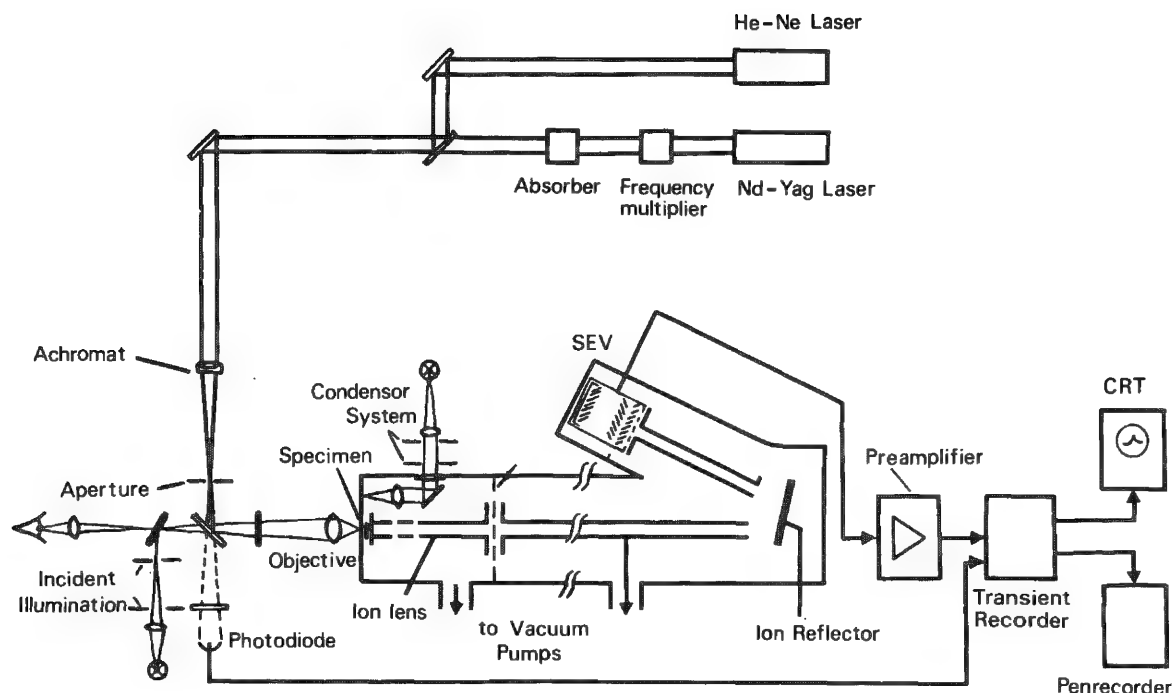


FIG. 1.--Schematic drawing of modified LAMMA instrument. Time-focusing ion reflector has been introduced into time-of-flight (TOF) spectrometer to compensate for spread of initial ion energy.

#### *Quantitative Analysis; Comparison of LAMMA and SIMS*

Linear signal intensity-concentration plots and comparably fair reproducibility (Fig. are the basic prerequisites for a quantitative analysis. For absolute quantitation, however, data such as the evaporated volume, ion yield, and the (mass-dependent) ion/electron

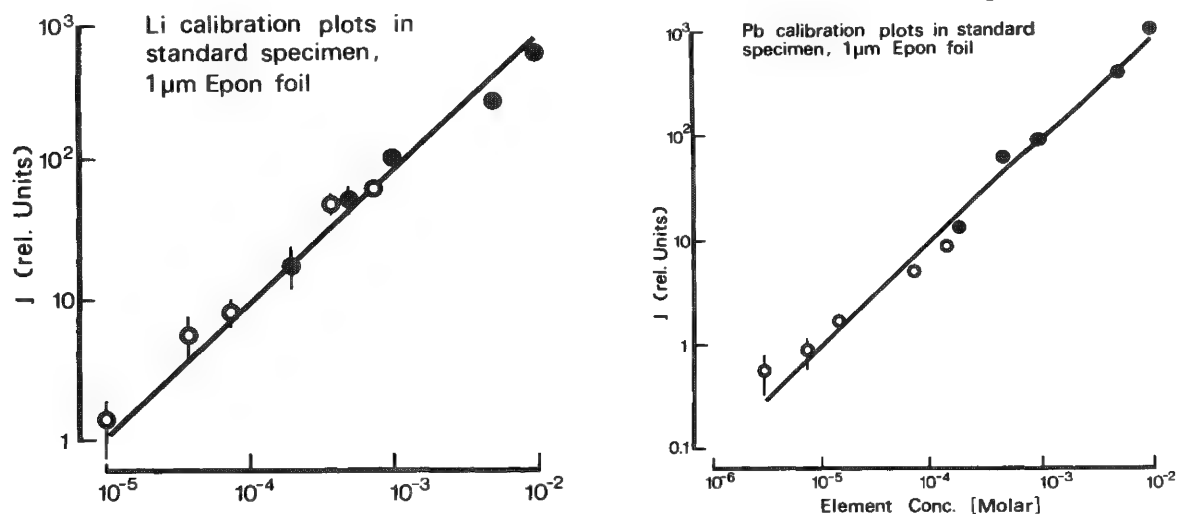


FIG. 2.--Calibration plots determined for Li and Pb in epoxy resin standard specimen.

conversion efficiency of the SEM must be known. For variations of the evaporated volume one may correct by referring to an internal standard which, in the simplest case, might be the integrated organic background, whereas the other variables require either the introduction of element-specific sensitivity factors (as in the ion microprobe) or the use of appropriate standard reference materials.

When comparing LAMMA and SIMS one must bear in mind that the formation of ionized particles is basically different in the two instruments. In the laser probe, electron-atom collisions seem to be the dominating ionizing processes, whereas in SIMS ionization energy is directly transferred from the primary ions to the surface lattice atoms.

That is why in LAMMA-analysis the ionization potential (positive ions) or electron affinity (negative ions) are practically the sole determinants for ion yield. Also, in SIMS, ion yield is related to the ionization level by an inverse exponential function but the main determinants are chemical bondings and matrix composition such that ion yield can vary over three to five orders of magnitude depending on matrix composition.<sup>6</sup> Ion yield of heavy elements in SIMS is further influenced by the mass ratio of primary and secondary ions, such that sensitivity basically tends to decline with increasing Z-number. First comparative studies indicated that with LAMMA absolute and relative sensitivity for heavy trace metals such as Pb, Ba, or U are better than in ion microprobe mass analysis (Table 2).

TABLE 2.--Semiquantitative guide to relative SIMS and LAMMA sensitivities for various elements (normalized to Na = 1). The numbers in brackets are approximated minimum detection levels in ppm.

	Li	Na	K	Sr	Ba	Pb
SIMS*	1.7 (0.15)	1 (0.25)	0.9 (0.30)	$8 \times 10^{-2}$ (8.0)	$6 \times 10^{-2}$ (4.0)	$2.5 \times 10^{-3}$ (100)
LAMMA	0.27 (0.2)	1 (0.2)	1.55 (0.1)	0.55 (0.5)	0.30** (0.6)**	0.70 (0.3)**

\*Taken from G. R. Sparrow.<sup>6</sup>

\*\*Preliminary estimates.

#### *Recent Applications*

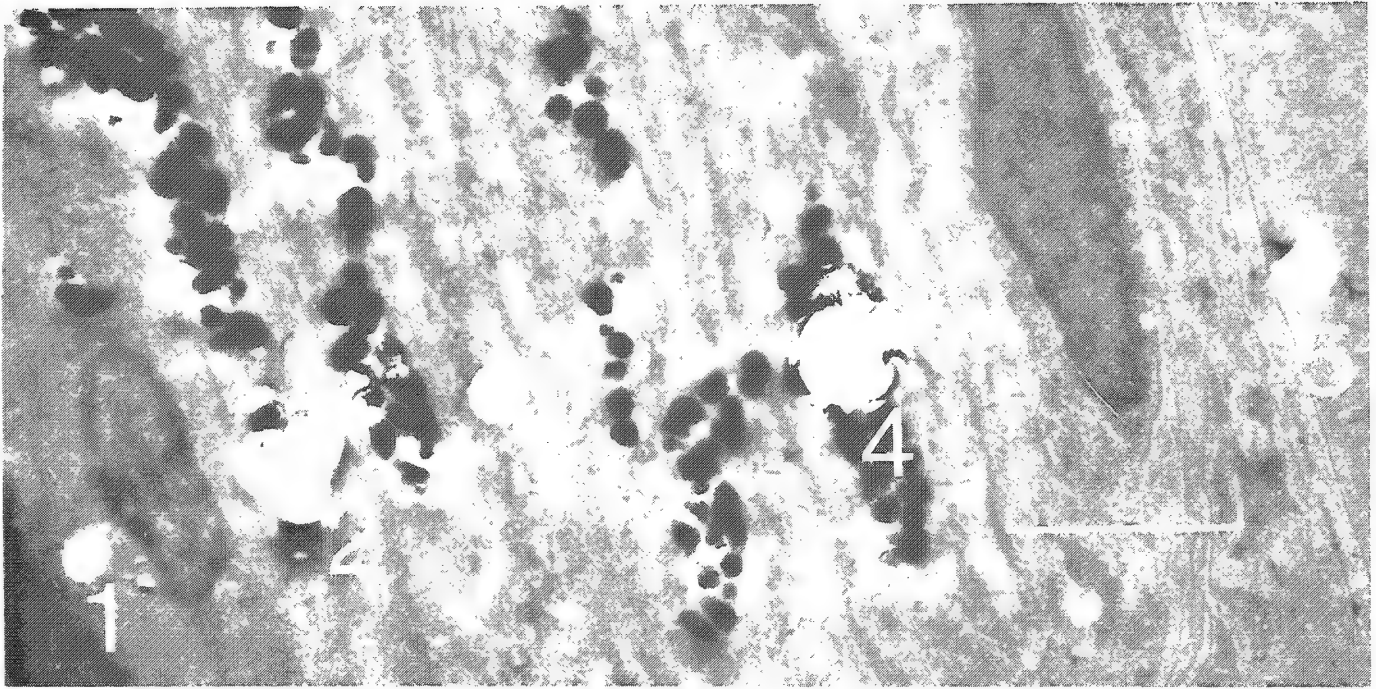
The work done on biological materials is much beyond the scope of this paper. Some representative examples may suffice.

*Retina Tissues.* In a recent ion-probe study M. Burns-Bellhorn unexpectedly detected rather large amounts of barium in the retinas of cats and cows.<sup>7</sup> In collaboration with the present authors, a cross check study was done by means of LAMMA analysis in human, cat, and frog retina tissues that consistently demonstrated the presence of Ba (in association with Ca and Mg) in all three species. As shown in Fig. 3, the barium is strictly localized to the pigment granula of the pigment epithelium and the choroid. (See also the ionic profiles of Fig. 4b.) A first quantitative approximation by reference to Ba standards gave an estimate of 20-50 mM Ba in the pigment granula, whereas only trace amounts of Ba were found in other cell layers of the retina. Nothing is known so far about the physiological significance of Ba.

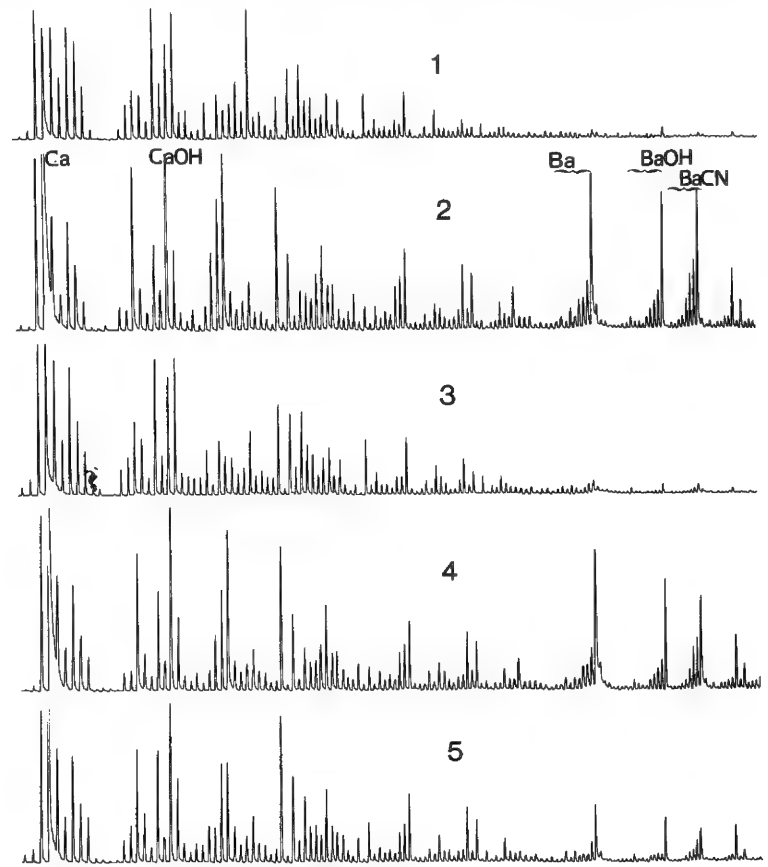
*Airborne Particles.* Owing to the increasing pressure for environmental controls, a new branch of microprobe analysis centers interest on the microchemical identification of aerosols. Analysis of single particles has been attempted by all microprobe systems available so far including EPXM,<sup>8</sup> SIMS,<sup>9</sup> Auger spectroscopy,<sup>10</sup> and laser Raman microprobe analysis.<sup>11</sup> With respect to the highly nonhomogeneous nature of most airborne particles, surface sensitive methods (SIMS, Auger spectroscopy) are of limited use. On the other hand, methods allowing bulk analysis (EPXM, Raman probe) are not always sensitive or selective enough to provide the desired analytical information.

Here, LAMMA may fill in a gap, since it analyzes the whole volume of a microparticle at once and provides analytical information about the atomic and molecular constituents with high sensitivity and selectivity.

In a first systematic study, Wieser et al.<sup>12</sup> used the LAMMA instrument for microprobe analysis of atmospheric particles (0.5-5  $\mu$ m in size; see Fig. 5) collected from the airborne state near the ground. Because of the unique "high-speed analysis," in which a particle is analyzed in the time it takes to focus the microscope and ink-write the mass spectrum (about 30 sec for an experienced operator), some hundreds of particles were an-



(a)



(b)

FIG. 3.--(a) Transmission electron micrograph of human retina tissue showing five laser probed areas of interest. Calibration bar corresponds to 1  $\mu\text{m}$ . (b) LAMMA spectra obtained from the five areas of interest of (a). Note appearance of Ba signals in records 2, 4, and 5 (pigment granula).

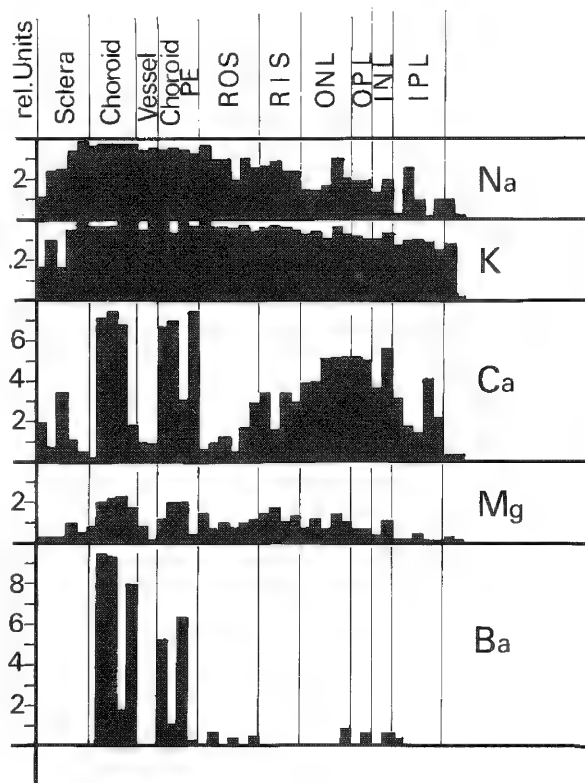
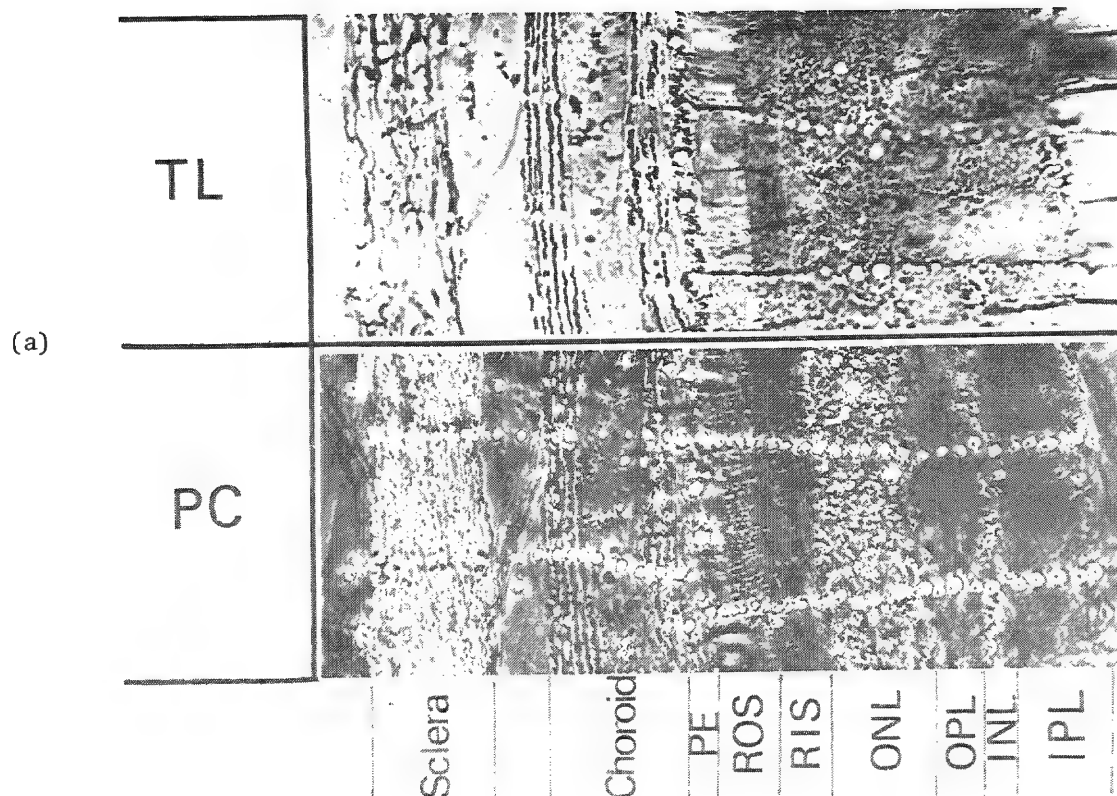


FIG. 4.--(a) Light micrograph of unstained section through ocular wall of cat eye featuring two rows of laser impacts. Top, transmitted light (TC); bottom, phase contrast (PC). Mean diameter of probed areas, 2  $\mu$ m. PE = pigment epithelium, ROS = rod outer segment, RIS = rod inner segment, ONL = outer nuclear layer, OPL = outer plexiform layer, INC = inner nuclear layer, IPC = inner plexiform layer. (b) Concentration profiles for Na, K, Mg, and Ba obtained from specimen shown in (a).

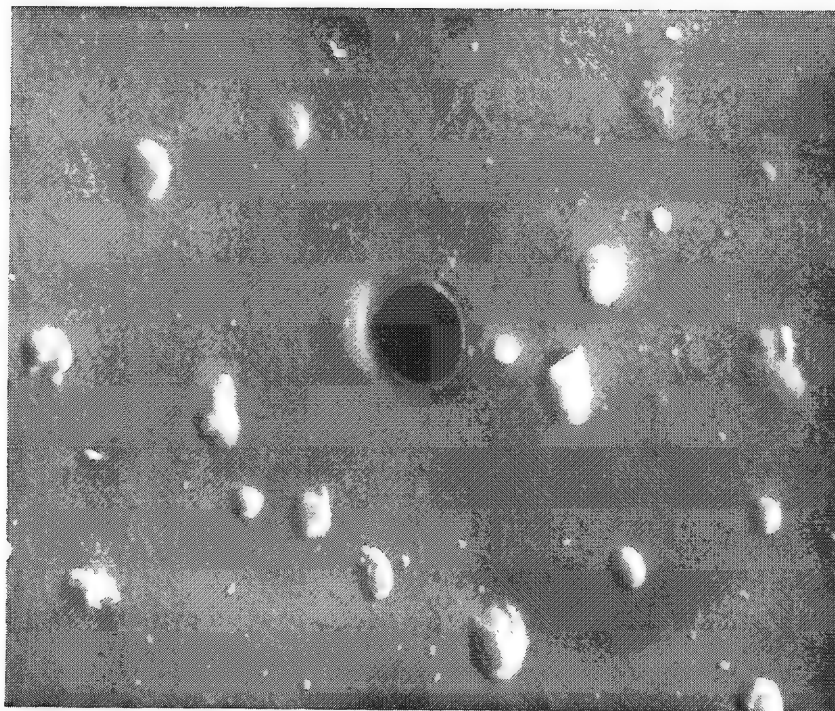


FIG. 5.--REM micrograph of airborne particles deposited on thin formvar film. Note laser-probed area (diameter about  $0.8\ \mu\text{m}$ ) at center (where one of the smaller particles had been located). (Courtesy of Wieser et al.<sup>12</sup>)

alyzed to determine whether classification histograms give meaningful information about mixed aerosols, which turned out to be possible. The high yield of (mostly organic) negative ions typical for the LAMMA principle proved to be of great advantage in characterizing the organic constituents of the airborne particles. Typical molecular fragments were  $\text{OH}^-$ ,  $\text{C}_2\text{H}^-$ ,  $\text{C}_2\text{H}_2^-$ ,  $\text{CN}^-$ ,  $\text{C}_2\text{H}_3^-$ ,  $\text{NO}_2^-$ ,  $\text{CO}_3^-$ ,  $\text{NO}_3^-$ ,  $\text{HNO}_3^-$ ,  $\text{SO}_3^-$ ,  $\text{HSO}_3^-$ , and  $\text{SO}_4^-$ , whereas inorganic (metallic) constituents usually show up in the spectrum of positive ions [as atomic or metal (hydr)oxide ions] (Fig. 6). In 30% of the particles trace amounts of Pb could be detected.

In another study the present authors attempted to classify airborne particles (collected in a coal mine) that were taken up by human lymphocytes after preincubation *in vitro*. (The specimens were provided by Prof. Bruch of the Institute of Hygiene and Occupational Medicine at the University of Essen.) We were able to show that the lymphocytes preferred to take up, by phagocytosis, particles of predominantly organic (pit coal) composition; whereas particles of basically inorganic chemical nature (containing mainly Na, Al, K, Fe, and Ca) were found to remain to a significantly higher extent in the extracellular space.

#### *LAMMA Analysis of Organic Compounds*

Two aspects have been investigated further, one of which is unique to the LAMMA principle:

1. Microprobe analysis of labelled organic compounds.
2. Mass spectrometry of pure crystalline organic materials.

As to the first point, the sensitivity of the LAMMA-instrument should be sufficiently high to make a search for trace amounts of labelled organic compounds or drugs possible. For labeling, any covalently bound atom of high ion yield may be a suitable candidate. No efforts have been made so far to produce compounds especially designed for this purpose.



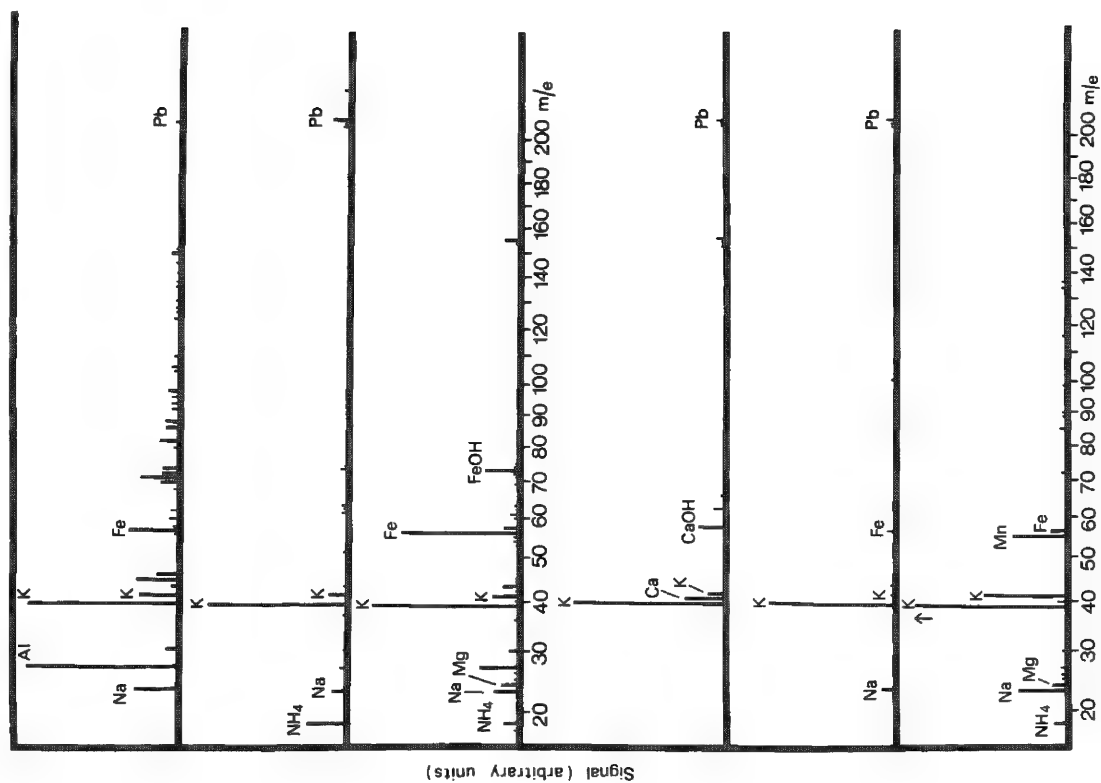


FIG. 6.--Examples of LAMMA mass spectra (positive ions) obtained in airborne particles by Wieser et al.<sup>14</sup>

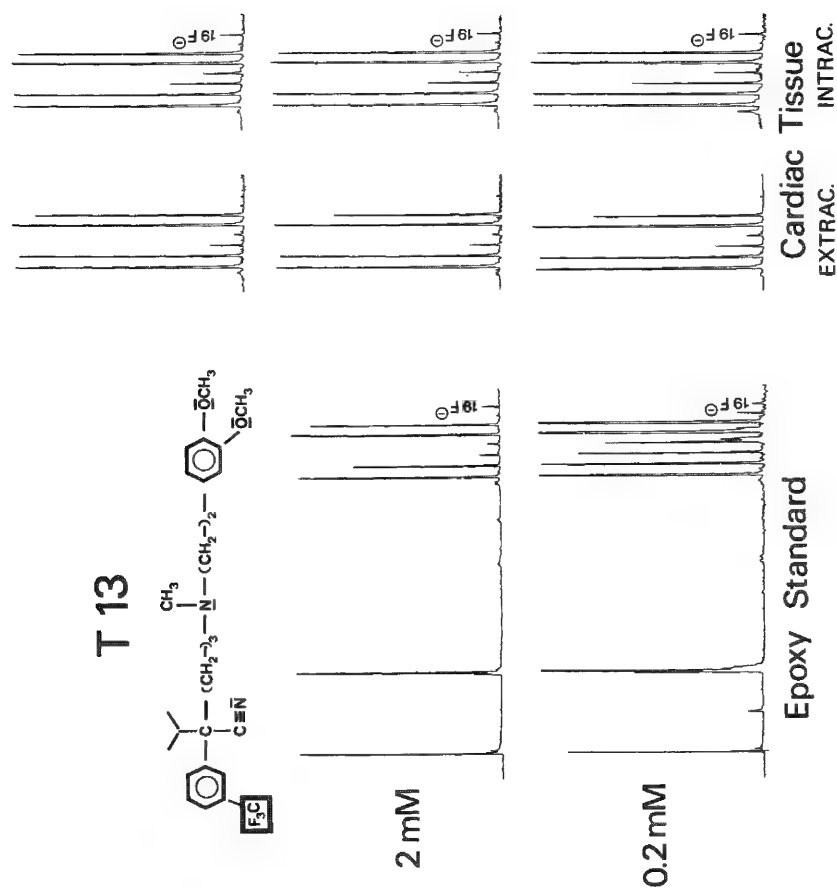


FIG. 7.--Detection of fluorinated cardioactive drug in epoxy standard specimen and in preincubated cardiac tissue (papillary muscle superfused with 0.2 mM for 1 hr). Note relatively high F- signal from inside cell; whereas outside cell, F signal is barely detectable.

However, in a preliminary attempt, fluorinated derivatives of cardioactive drugs were tested in the form of standard specimens (the drugs were dissolved in an epoxy resin at known concentrations) and in cardiac tissue sections. In the LAMMA-spectrum of negative ions (Fig. 7), an F-signal was recorded down to detection limits in the range of  $10^{-4}$  molar with respect to F. In cardiac tissue sections, intracellular accumulation of one of these drugs was evidenced. Since F is certainly not the best choice for this purpose, a systematic search for a more appropriate label (for instance Si instead of C) will probably end up with much lower detection limits and may thus possibly produce a new tool for the study of subcellular pharmacokinetics.

As to the second point, the LAMMA principle--much to our own surprise--turned out to be rather advantageous in mass spectrometry of pure organic compounds. First, it is a very easy-to-handle ion source for any kind of solid organic material otherwise difficult to ionize. One simply needs a few very small (1-10 $\mu$ m) crystals visibly deposited on a thin supporting foil. Second, nanograms to picograms of material, rather than the micrograms usually required for conventional organic mass spectrometry, are sufficient for a full analysis. Third--and this is the most exciting point--LAMMA mass spectra will be extremely simple if the laser power in the focus is reduced. As shown in the example of Fig. 8 the LAMMA spectrum of a heterocyclic organic compound obtained with a "smooth laser shot" consists only of a few lines (including the parent molecule and some larger fragmentation products). However, with increasing laser power fragmentation increases drastically although the signals of the parent molecule and other larger fragments still persist. The last and also rather unique feature of organic LAMMA analysis is the occurrence of about equal amounts of negatively and positively charged ions. In electron-impact ion sources, negative-ion yield is only about 0.01-0.001 of the positive-ion yield, which is considered to be too low for useful analysis; but laser-induced ionization opens an easy access to this hitherto rather neglected field of organic mass spectrometry. All that has been done so far indicates that the mass spectrum of negative molecular ions provides us with a great deal of complementary information not contained in the mass spectrum of positive ions. In the LAMMA instrument, recording either ion group is simply a matter of actuating a single pushbutton.

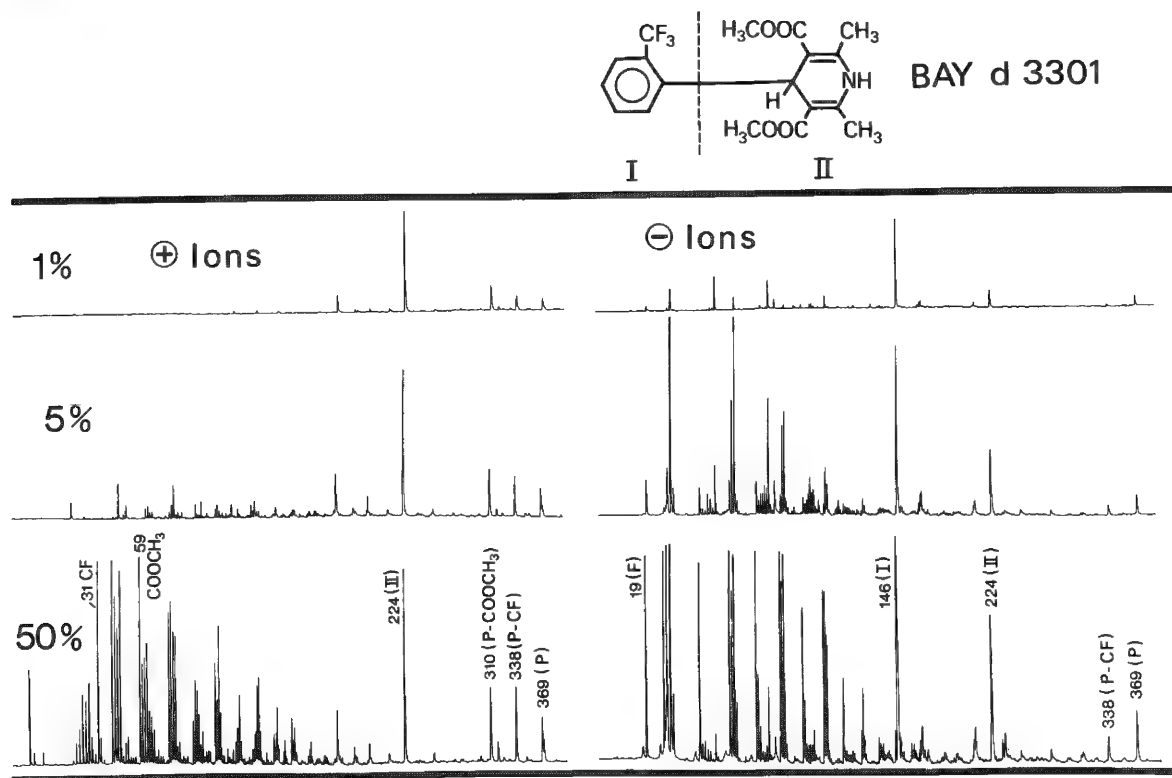
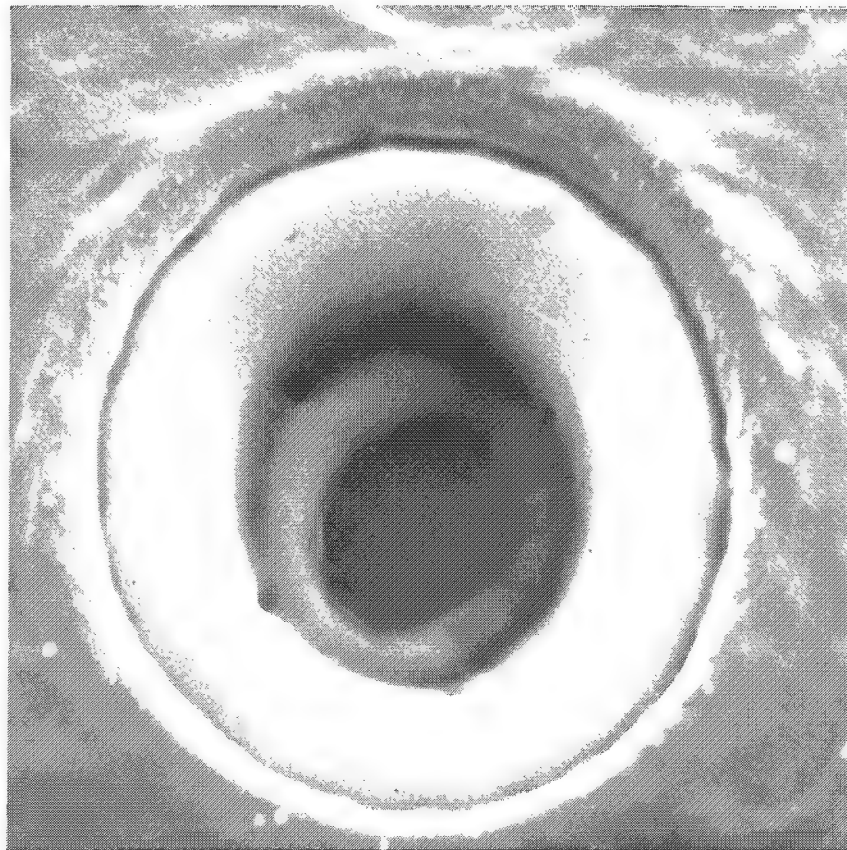
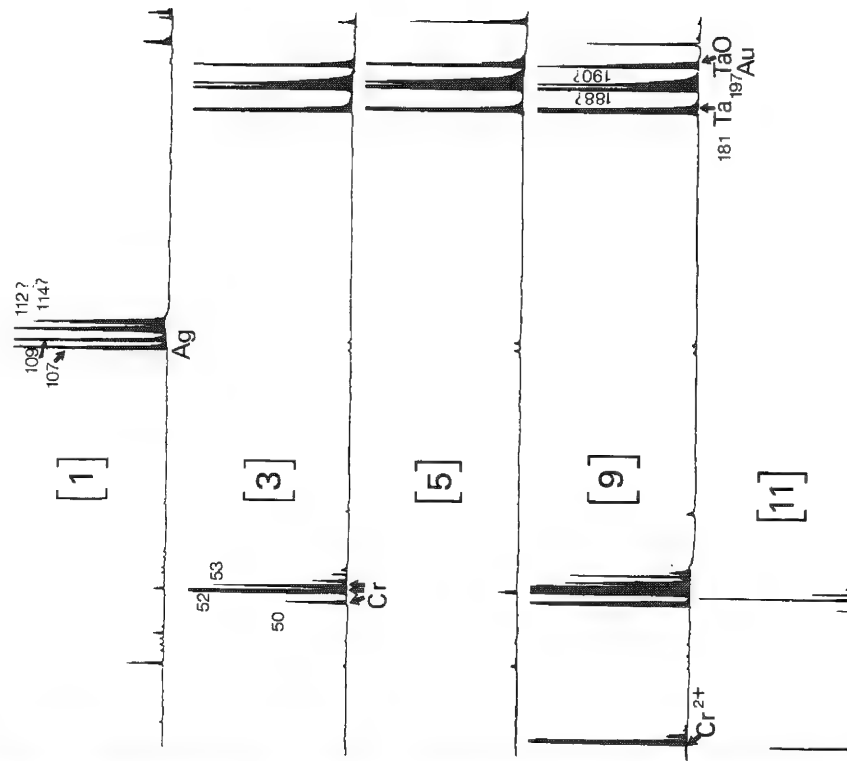


FIG. 8.--LAMMA spectra of positive and negative ions obtained from small (1-2 $\mu$ m) crystals of heterocyclic organic compound. Note simplicity of mass spectra recorded at reduced laser power.



(a)



(b)

FIG. 9.--(a) REM micrograph of a hole "drilled" by eleven consecutive laser impacts in multilayered sandwich of metallic and dielectric materials (total thickness 1.4  $\mu\text{m}$ ). Task was to remove enough layered material to expose "sensitive" spot in gold layer for micro- $\text{pO}_2$  measurements. Crater diameter is 4  $\mu\text{m}$  at surface, 1.2  $\mu\text{m}$  at bottom. (b) LAMMA spectra recorded during laser "drilling" of hole shown in (a). Thin film cover to be perforated consisted of successive layers of metallic silver, chromium, tantalum oxide ( $\text{Ta}_2\text{O}_5$ ), gold, and chromium, all deposited on quartz substrate.

### *LAMMA Applications in Nonbiological Materials*

Although primarily developed for biomedical purposes, the LAMMA instrument has already been used for microprobe analysis of numerous technical and geological materials, ranging from dust particles of cosmic origin in the depth of the Rhône glacier to fragments of a Roman amphora.

To give just one example that may possibly have some general implications for future microprocessing of thin films of dielectric materials or of layered sandwiches of conducting and nonconducting materials, a LAMMA application is shown in which the problem was to produce "sensitive spots" of 2-3  $\mu\text{m}$  in diameter on the surface of a  $\text{pO}_2$ -sensitive micro-electrode (Fig. 9). The electrode consisted of a needle-like quartz substrate on which thin films of gold, tantalum oxide, silver, and an organic insulator had been deposited. Mechanical processing to produce a small  $\text{pO}_2$ -sensitive spot at the tip of this electrode failed. So we attempted localized removal (over an area of about  $10 \mu\text{m}^2$ ) of the silver/tantalum oxide layers by repetitive focused laser irradiation with the LAMMA instrument. The depth of this "laser drilling" could be nicely controlled and monitored by the mass spectra recorded with each laser shot. Laser parameters could be adjusted such that  $10 \pm 1$  shots were needed to arrive on the (inner) gold layer (which had to be freed of superimposed material to become the  $\text{pO}_2$ -sensitive spot).

### *References*

1. R. Kaufmann et al., "The LAMMA instrument: A new laser microprobe mass analyzer for biomedical purposes," *Proc. 13th MAS Conf.*, 1978, 16A.
2. F. Hillenkamp et al., "A high sensitivity laser microprobe mass analyzer," *Appl. Physics* 8: 341-348, 1975.
3. R. Wechsung et al., "LAMMA: A new laser-microprobe-mass analyzer," *Microscopica Acta Suppl.* 2: 281-296, 1978.
4. R. Kaufmann et al., "The third choice: Laser microprobe mass analysis, achievements and aspects," in O. Johari, Ed., *SEM*, AMF O'Hare: SEM, Inc., 1979.
5. R. Kaufmann, F. Hillenkamp, and R. Wechsung, "Laser microprobe mass analysis," *ESN-European Spectroscopy News* 20: 41-44, 1978.
6. R. Sparrow, "Quantitative SIMS approximations for general applications in surface analysis," *25th Ann. Conf. Mass Spectrom.*, 1977.
7. M. S. Burns-Bellhorn and R. K. Lewis, "Localization of ions in retina by secondary mass spectrometry," *Exp. Eye Res.* 22: 505-518, 1976.
8. T. J. Armstrong, "Methods of quantitative analysis of individual microparticles with electron beam instruments," *SEM* 1978, 1, 485-497.
9. D. E. Newbury, "Secondary ion mass spectrometry for particle analysis," *Proc. 13th MAS Conf.*, 1978, 65A.
10. H. Malissa, *Analysis of Airborne Particles by Physical Methods*, Cleveland: CRC Press, 1978.
11. E. S. Etz et al., "Particle analysis with the laser Raman microprobe," *Proc. 13th MAS Conf.*, 1978, 66A.
12. R. Wieser, R. Wurster, and H. Seiler, "About the identification of airborne particles by laser-induced mass spectrometry," *Atmospheric Environment*, 1979, in press.

## MINIMUM DETECTABLE CONCENTRATIONS WITH THE LIQUID-DROPLET TECHNIQUE

P. M. Quinton, R. R. Warner, and Claude Lechene

The liquid-droplet technique,<sup>1,2</sup> developed to measure element concentrations in small biological fluid samples, has been applied primarily to physiological elements ranging in concentration from Na at 0.15M to Mg at 0.0006M.<sup>3</sup> The technique has been shown to be applicable for elements at high concentrations approaching 0.5M,<sup>8</sup> but systematic studies have not been reported that establish lower limits of element detection for the liquid-droplet technique in wavelength-dispersive spectroscopy. Since concentrations as low as 0.20 ( $\pm$  0.03 [SE]) mM for P<sup>9</sup> and 0.28 ( $\pm$  0.19 [SD]) mM for Mg<sup>10</sup> have been reported in the literature, the minimum detectable concentrations are presumably lower than 0.2 mM and have been estimated to be 0.1 mM;<sup>11</sup> for a 0.5mM solution, peak-to-background ratios of 1.0 can be obtained.<sup>2</sup> These determinations have been made, however, on samples placed upon thick Be block substrates in which a large fraction of the sample background is contributed by the substrate. If this substrate were removed or diminished, minimum detectable concentrations might be considerably reduced. Procedures for minimizing this substrate background have been developed in modifications of the liquid droplet technique for EDS,<sup>7,22,13</sup> where a large background contribution would intolerably limit the detection sensitivity. These procedures utilize thin organic films such as parloidin mounted over metal grids to minimize substrate contributions to the sample background. EDS analysis<sup>7</sup> by use of this procedure on 0.5mM solutions yields peak-to-background ratios that are approximately 0.1, an order of magnitude less than with WDS. Adaptation of this procedure for mounting droplets on thin organic supports to WDS analysis might make it possible to lower the detection sensitivity significantly; although electron-probe analysis has not been regarded as being directly suited for biological trace element analysis,<sup>14</sup> there remains a possibility that trace elements such as Si, Zn, and Br could be routinely analyzed with these procedures.

### Methods

Using the liquid droplet technique,<sup>2</sup> we placed a series of five solutions containing 150 mM NaCl but decreasing concentrations of Ca, Mg, SO<sub>4</sub>, and PO<sub>4</sub> either on Be blocks or on thin carbon-coated formvar films mounted over nickel grids. After freeze drying, the preparations were analyzed using a Cameca MS46 microprobe at 11 kV and 200 nA. Pipette size was 64.7 pL and beam diameter was generally 70 $\mu$ . Cl, S, Ca, and P were analyzed with a PET crystal; Na and Mg were analyzed with a TAP crystal. Analysis time was 50 sec per sample. Background was measured on each sample by detuning of the spectrometers and averaging of the intensity measured above and below the characteristic wavelength. With the Be blocks, background was also measured on peak but off the sample on pure Be, which is the customary procedure for background measurement by the liquid droplet technique.<sup>2</sup> Solutions S1-S5 were prepared to contain 150 mM NaCl plus either 10 mM (S1), 2 mM (S2), 1 mM (S3), 0.4 mM (S4), or 0.1 mM (S5) Ca, Mg, SO<sub>4</sub>, and PO<sub>4</sub>. Solution composition was confirmed by macroscopic techniques for all elements except SO<sub>4</sub> and PO<sub>4</sub>. Results are reported as mean x-ray counts, not normalized, with their standard deviations.

### Results

Background measurements for the five samples deposited on Be blocks are shown in the left columns of Table 1. The backgrounds measured off peak are equivalent for the differ-

---

This work was done at the National Biotechnology Resource in Electron Probe Microanalysis, Harvard Medical School, Boston, MA 02115. (Author Quinton is now at the Division of Biomedical Sciences of the University of California, Riverside, CA 92521.) The support of this work by National Institutes of Health grants AM-00324, AM-20356, and RR-00679 is gratefully acknowledged.

ent samples, which indicates that the background is generated primarily from the substrate, a conclusion that is supported by the similarity of the off-peak backgrounds with backgrounds measured on peak on pure Be (B0) (Table 1 and Ref. 15). Background measurements for the five samples deposited on formvar films are shown in the right columns of Table 1. Backgrounds measured off peak are no longer equivalent for the different samples, with the S1 background being statistically higher ( $P < 0.05$ ) than the S5 background for S, Ca, Mg, and Cl, which indicates that the samples themselves are now significantly contributing to the background. The backgrounds are one order of magnitude lower than those measured on Be blocks, whereas the sample counts are similar as indicated in Table 2 for sample S2, which results in an improvement in the signal/background ratio ( $P-B/B$ ) by approximately one order of magnitude.

The conventional criterion for the minimum detectable concentration, that concentration for which the peak x-ray count exceeds three standard deviations of the background measurement, is given by<sup>16</sup>

$$C_{\min} = 3\sqrt{B} \cdot C_{st}/(P - B)_{st} \quad (1)$$

in which "st" denotes a standard of known concentration. An alternative criterion for the minimum detectable concentration based on the use of "n" multiple measurements as was done in this study is given by<sup>17</sup>

$$C_{\min} = (4.5/n) + 3[(1.5B/n) + (2.25/n^2)]^{1/2} C_{st}/(P - B)_{st} \quad (2)$$

Minimum detectable concentrations based on these equations and the data of Table 1 and 2 are shown in Table 3. Minimum detectable concentrations calculated from Eq. (2) are approximately half the values calculated from Eq. (1). In either case minimum detectable concentrations measured on formvar films are a quarter to a half of those obtained from samples mounted on Be blocks. The use of formvar grids with the liquid-droplet technique decreases the background by an order of magnitude and improves the minimum detectable concentrations by a factor of two, which could allow trace elements such as Zn, Br, and Si to be routinely measured in plasma.

## References

1. C. Lechene, "The use of the electron microprobe to analyze very minute amounts of liquid samples," *Proc. 5th Nat'l Conf. Electron Probe Analysis*, New York, 1970, 32A-32C.
2. C. Lechene, "Electron probe microanalysis of picoliter samples," in T. Hall, P. Echlin and R. Kaufmann, Eds., *Microprobe Analysis as Applied to Cells and Tissues*, New York: Academic Press, 1974, 351-367.
3. C. Le Grimellec, N. Roinel, and F. Morel, "Simultaneous Mg, Ca, P, K, Na, and Cl analysis in rat tubular fluid," *Pflügers Arch.* 340: 181-210, 1973.
4. C. Lechene, E. Abraham, and R. Warner, "Effect of sulfate loading on ionic distribution along the rat nephron," *Clin. Res.* 23: 432A, 1975.
5. R. M. Borland, J. D. Biggers, and C. P. Lechene, "Studies on the composition and formation of mouse blastocoele fluid using electron probe microanalysis," *Dev. Biol.* 55: 1-8, 1977.
6. S. K. Peterson, L. S. Frishkopf, C. Lechene, C. M. Oman, and T. F. Weiss, "Element composition of inner ear lymph in cats, lizards and skates determined by electron probe microanalysis of liquid samples," *J. Comp. Physiol.* 126: 1-14, 1978.
7. P. M. Quinton, "Ultramicroanalysis of biological fluids with energy dispersive x-ray spectrometry," *Micron* 9: 57-69, 1978.
8. N. Roinel, M. Champigny, L. Meny, and J. Henoc, "Quantitative analysis of lyophilized solutions: Experimental and theoretical evaluation of the limits of linearity of the calibration curves," *Proc. 13th MAS Conf.*, 1978, 62A-62D.
9. K. Baumann, C. de Rouffignac, N. Roinel, G. Rumrich, and K. J. Ullrich, "Renal phosphate transport: Inhomogeneity of local proximal transport rates and sodium dependence," *Pflügers Arch.* 356: 287-297, 1975.
10. Y. Murayama, F. Morel, and C. Le Grimellec, "Phosphate, calcium and magnesium transfers in proximal tubules and loops of Henle, as measured by single nephron microperfusion

TABLE 1.--Background measurements.

	S		Ca		P		Mg		Cl		Na	
	BLOCK	FILM	BLOCK	FILM	BLOCK	FILM	BLOCK	FILM	BLOCK	FILM	BLOCK	FILM
S1	18.1 $\pm$ .9	1.8 $\pm$ .4	117 $\pm$ 7	10.7 $\pm$ 3	17.2 $\pm$ .7	2.3 $\pm$ .5	99 $\pm$ 4	7.5 $\pm$ 2	27.6 $\pm$ 1	4.0 $\pm$ .4	55.6 $\pm$ 2	6.3 $\pm$ 0.9
S2	18.3 $\pm$ .6	1.5 $\pm$ .5	113 $\pm$ 4	8.2 $\pm$ 3	16.4 $\pm$ .7	1.9 $\pm$ .5	100 $\pm$ 3	5.6 $\pm$ 2	27.1 $\pm$ 1	3.8 $\pm$ 1.	56.2 $\pm$ 2	5.3 $\pm$ 1.3
S3	18.1 $\pm$ .5	1.4 $\pm$ .4	114 $\pm$ 4	7.4 $\pm$ 3	16.8 $\pm$ 1.	2.0 $\pm$ .5	100 $\pm$ 3	5.2 $\pm$ 2	27.1 $\pm$ 1	3.6 $\pm$ .9	55.5 $\pm$ 2	5.3 $\pm$ 1.7
S4	17.8 $\pm$ .9	1.3 $\pm$ .5	114 $\pm$ 4	6.7 $\pm$ 3	17.0 $\pm$ 1.	1.6 $\pm$ .5	101 $\pm$ 4	4.9 $\pm$ 3	27.6 $\pm$ 1	3.7 $\pm$ .8	57.0 $\pm$ 2	5.4 $\pm$ 2.0
S5	18.0 $\pm$ .6	1.3 $\pm$ .4	114 $\pm$ 4	7.0 $\pm$ 2	16.8 $\pm$ .8	2.0 $\pm$ .4	102 $\pm$ 3	4.9 $\pm$ 2	27.8 $\pm$ 1	3.5 $\pm$ .4	55.9 $\pm$ 1	5.4 $\pm$ 1.4
BO	22.4 $\pm$ 3		109 $\pm$ 3		16.4 $\pm$ .8		107 $\pm$ 1		35.4 $\pm$ 8		55.8 $\pm$ 1	

Values are x-ray counts/10 sec ( $\pm$ SD); n = 8 (blocks); n = 6 (films).

TABLE 2.--Peak-background (P-B) measurements (per 10 sec) for S2.

	S		Ca		P		Mg	
	P-B	P-B/B	P-B	P-B/B	P-B	P-B/B	P-B	P-B/B
Block	61.9	3.4	180	1.6	48.4	3.0	136	1.4
Film	37.2	24.8	176	21.5	43.0	22.6	127	22.7

TABLE 3.--Minimum detectable concentrations (mM).

	S		Ca		P		Mg	
	eq 1	eq 2	eq 1	eq 2	eq 1	eq 2	eq 1	eq 2
Block	0.19	0.08	0.16	0.07	0.22	0.10	0.20	0.09
Film	0.09	0.05	0.04	0.02	0.09	0.05	0.05	0.03

Values are for 50sec counting time.



experiments in the rat," *Pflügers Arch.* 333: 1-16, 1972.

11. C. Lechene, "Analysis of ultra small volumes in physiology with electron probe microanalysis," *Microsc. Acta*, Supplement 2; in P. Echlin and R. Kaufmann, Eds., *Microprobe Analysis in Biology and Medicine*, Stuttgart: Hirzel Verlag, 1978, 228-235.

12. P. M. Quinton, "Energy dispersive x-ray analysis of picoliter samples of physiological fluids," *Proc. 10th MAS Conf.*, 1978, 50A-50B.

13. R. Rick, M. Horster, A. Dorge, and K. Thureau, "Determination of electrolytes in small biological fluid samples using energy dispersive x-ray microanalysis," *Pflügers Arch.* 369: 95-98, 1977.

14. P. S. Ong, P. K. Lund, and W. M. Conrad, "Trace metal analysis of human serum with an electron probe microanalyzer," *Proc. 7th Nat'l Conf. Electron Probe Analysis*, 1972, 46A-46C.

15. C. Lechene and R. Warner, "Electron probe analysis of liquid droplets," in C. Lechene and R. Warner, Eds., *Microbeam Analysis in Biology*, New York: Academic Press, in press.

16. L. S. Birks, *X-ray Spectrochemical Analysis*, New York: Interscience, 1969.

17. Z. Kotrba, "The limit of detectability in x-ray electron probe microanalysis," *Mikrochim. Acta* 11: 97-106, 1977.

# INSTRUMENTAL FACTORS AFFECTING THE ACCURACY OF MICROPROBE QUANTITATION OF ELECTROLYTE CONCENTRATIONS IN FROZEN SECTIONS

John McD. Tormey and Robert M. Platz

Biological tissues consist of multiple aqueous phases that contain electrolytes at widely varying concentrations. The possibility of rapid diffusion between phases has presented an unique challenge to the preparation of biological specimens for microprobe analysis. To prevent such diffusion, it is now common practice to freeze tissue specimens rapidly and then to cut thin frozen sections at low temperature. The resulting sections must be freeze-dried before they can be handled at room temperature.

Before one accepts results from complex, unknown biological systems, it is prudent to validate methods on a simple, well-characterized specimen. With that in mind, we have been using microprobe x-ray analysis to quantitate electrolyte concentrations in freeze-dried frozen sections of red blood cells. These small cells have the advantage not only of structural homogeneity, but also of the ease and accuracy with which their electrolyte concentrations can be determined by wet chemical analysis. Validation entails obtaining agreement between microprobe and wet chemical measurements.

Using methods described previously,<sup>1,2</sup> we obtained 0.5 $\mu$ m thick freeze-dried frozen sections mounted on carbon films on Cu grids. The sections included two types of red blood cell: (a) high potassium (HK) cells, containing approximately 100 mM K and 10 mM Na; and (b) low potassium (LK) cells, containing approximately 10 mM K and 100 mM Na. (The above, and all subsequent, concentrations are expressed as millimoles/ $10^3$  cm<sup>3</sup> of tissue volume.) The remainder of the section (about 75% of its area) consisted of an extracellular phase, which was a dextran-containing physiological saline that contained 140 mM Na and 6 mM K. Chemical analyses were performed on aliquots of cells and extracellular fluid at the time the cell suspensions were frozen. Thus we had a well-characterized three-phase system.

Microprobe quantitation of intracellular concentrations of Na and K was obtained by several methods that yielded similar results.<sup>1,2</sup> Most of the results presented here used intracellular Fe as an internal standard.

Table 1 show typical results obtained at 20 kV accelerating voltage in a scanning electron microscope equipped with an energy-dispersive x-ray spectrometer. Excellent agreement

TABLE 1.--Comparison between microprobe and wet chemical analyses of Na and K in HK and LK red blood cells. Results obtained at 20 kV, and expressed as concentrations in millimoles/ $10^3$  cm<sup>3</sup> of cell volume  $\pm$  standard error; n = 18-20.

	HK		LK	
	Na	K	Na	K
Microprobe Analysis	64.5 $\pm$ 4.8	89.8 $\pm$ 2.2	133.2 $\pm$ 7.5	12.1 $\pm$ 1.0
Chemical Analysis	17.5	88.7	97.0	10.4
Microprobe-Chemical	47.0 $\pm$ 4.8	1.1 $\pm$ 2.2	36.2 $\pm$ 7.5	1.7 $\pm$ 1.0

between microprobe and chemical analyses of K was found. However, microprobe measurements of Na were too high by about 40 mM in both types of cell. The rest of this abstract is concerned with the origin of this excess Na.

The pattern of results cannot be due to a partial melting of the sample which has allowed ions to diffuse down their respective concentration gradients. Otherwise, consider-

The authors are at the Department of Physiology, UCLA School of Medicine. This work was supported in part by Research Award 510 from the American Heart Association, Greater Los Angeles Affiliate, and by Program Project Grant HL-11351 from the National Institute of Health.

able amounts of K would have been lost from the HK cells, and the excess Na in the HK cells would be nearly three times greater than in the LK cells, since the concentration gradient favoring its entry was nearly three times greater.

The results *are* consistent with the possibility that the intracellular measurements are contaminated by x-ray signals related to the extracellular fluid. For instance, the Na excess in Table 1 is that which would be expected if approximately 20% of the electrons impinging on the cells were deflected into the extracellular phase; this process would cause a large error in Na but a negligible one in K, since the concentration of Na in this phase is 23 times larger than that of K.

Such an effect could be caused by one of several forms of stray radiation within the microprobe itself, or it could be an artifact of specimen preparation in which part of the extracellular matrix is smeared over the cells during microtomy. Experiments were therefore carried out to distinguish among these alternatives.

Both electron beam "tailing" and hard x rays originating from the column were ruled out by use of a 5  $\mu$ m diameter Pt aperture over a Faraday cup. When a line raster was positioned about 0.2  $\mu$ m inside the edge of the aperture, the intensity of the Pt M peak was only 0.5% of that when the Pt was directly irradiated. Such stray radiation is nearly two orders of magnitude too small to explain our results.

If the excess Na were due to microtomy, it should be affected by a lowering of the cutting temperature. For instance, if there were local melting, reduction of temperature should alter the nature of the cutting process from melting towards cleaving.<sup>3</sup> Alternatively, if the dextran-containing matrix has a plastic quality that allows it to be deformed and smeared by the knife, this property should also be affected by temperature. However, when sections cut at -110°C were analyzed and compared with those cut at -80°C (our usual cutting temperature), no differences were found.

The degree to which smearing affects results should also be a function of section thickness. If cutting should cause a zone of local melting, each section would consist of a region that has remained frozen faced on both sides by transiently melted zones. The ratio of unmelted to melted (or smeared) material increases as section thickness increases, so that there should be an inverse relation between section thickness and excess Na. However, when section thickness was varied over a three-fold range, a *direct* linear relationship between thickness and Na error was found.

This result and the cutting-temperature experiment argue strongly against a microtomy artifact, and direct attention to the likelihood of stray radiation within the microprobe. Since the primary beam has been shown to be essentially "clean," this stray radiation would have to come from interaction between the beam and specimen.

Scattering by the specimen is implicated by three pieces of evidence. (1) There is a direct linear relationship between section thickness and excess Na. The Rutherford model of elastic scattering predicts the same relationship between target thickness and scattering through a given angle. (2) Examination of the same section at both 10 and 20 kV revealed that the excess Na concentration was doubled at the lower voltage, whereas K remained unchanged. This finding is compatible with the well-known inverse relationship between scattering and accelerating voltage. (3) When samples were studied at 80 kV in a transmission electron microscope in the STEM mode, microprobe estimates of Na became equal to those determined chemically.

Two forms of scattering must be considered. One is scattering from the cells directly into the extracellular phase. The other is scattering from the section into the specimen chamber followed by scattering back to the section. However, it is unlikely that enough radiation could be scattered back to explain our results. Not only is the backscattering coefficient for specimen chamber material only about 0.3, but also, based on purely geometrical considerations, only a small fraction of the electrons scattered by the specimen chamber could return to the sections. Therefore, scattering within the section itself is the more likely cause of excess Na.

If this interpretation is correct, we need a model that predicts it quantitatively. Doubtless a fraction of the electrons passing through the cells are elastically scattered over sufficiently wide angles to enter the extracellular matrix. Those which do so have much longer trajectories through the section than those in the unscattered primary beam and have correspondingly higher probability of exciting x rays. Simple application of an

expression based on the Rutherford model suggests that too little scattering would occur<sup>1,4</sup> Monte Carlo calculations will probably have to be carried out to determine whether our explanation is reasonable.

Whatever the outcome, it is obvious that proper attention to instrumental factors can control an artifact that is liable to occur in the study of an element at low concentration in a small phase surrounded by another where it is present at high concentration. With this limitation in mind, microprobe x-ray analysis is proved to be capable of yielding valid quantitation of diffusible elements in biological systems.

#### References

1. J. McD. Tormey, "Validation of methods for quantitative x-ray analysis of electrolytes using frozen sections of erythrocytes," *Scanning Electron Microscopy/1978/2*, Chicago: SEM, 1978, 259-266.
2. J. McD. Tormey and R. M. Platz, "Origin of artifactual quantitation of electrolytes in microprobe analysis of frozen sections of erythrocytes," *Scanning Electron Microscopy/1979*, Chicago: SEM, in press, 1979.
3. R. G. Kirk and G. H. Dobbs, "Freeze fracturing with a modified cryo-ultramicrotome to prepare large intact replicas and samples for x-ray microanalysis," *Science Tools, LKB Instrument J.* 23: 28-31, 1976.
4. J. I. Goldstein et al., "Quantitative x-ray analysis in the electron microscope," *Scanning Electron Microscopy/1977/1*, Chicago: IIT Res. Inst., 1977, 315-324.

## ULTRASTRUCTURAL ANALYSIS OF BILIARY CALCULI

B. E. McConville

Underlying factors of stone formation can be elucidated by determination of the composition of biliary calculi, since the stones contain a record of changes in the body that influence the function of the liver and gallbladder; and since 60 000 people in Britain alone are treated in hospital for gallstones each year, investigation leading to a better understanding of the disease is essential, as agreed in the specific recommendations of priority areas by the work group report of the NIH committee on research on Digestive Diseases in 1975. In an attempt to obtain more precise analytical evidence regarding the composition of calculi, SEM and associated x-ray analysis has been undertaken on a number of gallstones.

Selected stones have been subjected to simultaneous electron microscopic studies and autoradiographic analysis with the use of charged-particle activation. Cross sections of stones are mounted and irradiated in Birmingham University's 60 in. cyclotron using 2.2MeV deuterons and 5MeV protons. Correlation of results is achieved with particular attention to the ultrastructure of stones in the region of the nidus.

Results of the investigations are discussed in the light of present-day theories of nucleation and growth mechanisms in stone formation. It is believed that any fibrous mass at the center of the stone could support the theory of nucleation by entrapment on debris or mucus-type material. The theory of epitaxy is also shown as a possible contributory factor to the growth mechanism.

Distinct differences of the composition and ultrastructure across individual calculi are clearly shown to indicate different mechanisms of growth within the gallbladder during the deposition of layers of calculus. The technique has also been used successfully with investigations on urinary calculi.

---

The author is in the Department of Physics of the University of Birmingham in Birmingham B15 2TT, England.

## ELECTRON IRRADIATION PRODUCTS FROM ORGANIC MATERIALS AND IMPLICATIONS FOR MICROANALYSIS OF BIOLOGICAL SECTIONS

J. W. Edie and P. L. Glick

The damage to organic specimens as a result of electron bombardment are widely reported.<sup>1-3</sup> These effects impose limitations on the potential image resolution within transmission electron microscopes and the validity of analytical data acquired from electron-optical instrumentation. Any analyst attempting quantitative measurements on light-element matrices must consider the effects of irradiation on the results.

It has been previously reported that characteristic count rates from thick specimens undergo variations with electron dose whenever organic content is present in the analyzed matrix.<sup>4</sup> Valid quantitative results are shown to be possible only if count rates are obtained at initial exposure or the same dynamic response occurs in both the standard and the unknown.

The loss of light-element content is the primary reason for the count rate variations--which continue until further losses from the specimen are terminated. These light-element losses may be observed by means of a quadrupole mass spectrometer in close proximity to the specimen during the irradiation period.<sup>5</sup> Consider, for example, the effects of electron irradiation on methacrylate when 30keV electrons at a current density of about  $10^{-11}$  A- $\mu\text{m}^{-2}$  bombard the sample. Figure 1(a) displays the mass spectra ( $1 \leq m/e \leq 45$ ) of the residual gas within the column just prior to electron irradiation, Fig. 1(b) displays the instantaneous mass spectra as the electron beam is made incident on a methacrylate specimen, and Fig. 1(c) shows the net peak heights for masses detected as a result of electron bombardment. Of the many masses observed, the more probable identifications exist for  $m/e = 2$  ( $\text{H}_2$ ), 12 (C), 14 (N), 15 ( $\text{CH}_3$ ), 16 (O), 28 (CO and  $\text{N}_2$ ), 32 ( $\text{O}_2$ ), and 44 ( $\text{CO}_2$ ). The light-microscopical observation of "gases bubbling" through the coating of the specimen when irradiated is supported by these masses. The other fragments are probably the result of H-bond ruptures due to irradiation and/or heating effects which release molecular fragments that are characteristic of the matrix.

The irradiation products are dependent upon the material irradiated, the operating conditions employed and the temperature of the specimen. The dependence on type of plastic is illustrated in Fig. 2(a), where net peaks relative to methacrylate (expressed in %) are shown for the masses representing the organic constituents and  $\text{CO}_2$ . The same operating conditions were used for each specimen. Similar relative net peaks are displayed for materials of biological origin in Fig. 2(b). The extensive variation in mass products from matrices of differing organic composition are apparent in these figures. A different characteristic x-ray count rate variation of an included heavier element could be anticipated for each matrix.

A simplified model is advanced to describe the variation of characteristic x-ray count rate. Prior to electron irradiation, a heavier element to be detected in the low density matrix is assumed uniformly distributed. In Fig. 3(a), the electron beam (for given operating conditions) is made incident upon the specimen, an initial excitation volume is established, and light-element fragments are ejected from the surface. The maximum range  $R_i$  for electrons is characteristic of the original matrix. After prolonged irradiation (Fig. 3b) the density of the excitation volume increases due to loss of light element fragments, but physically recesses from the surface. The concentration of the heavy element increases within this volume, which accounts for the increased characteristic x-ray count rate. The maximum range  $R_f$  from the surface is material dependent and assumes both the recession from the surface and the new range in the denser medium. These ranges would have

---

The authors are with Dows Institute for Dental Research of the University of Iowa in Iowa City. The support of this work by the Veterans Administration is gratefully acknowledged.

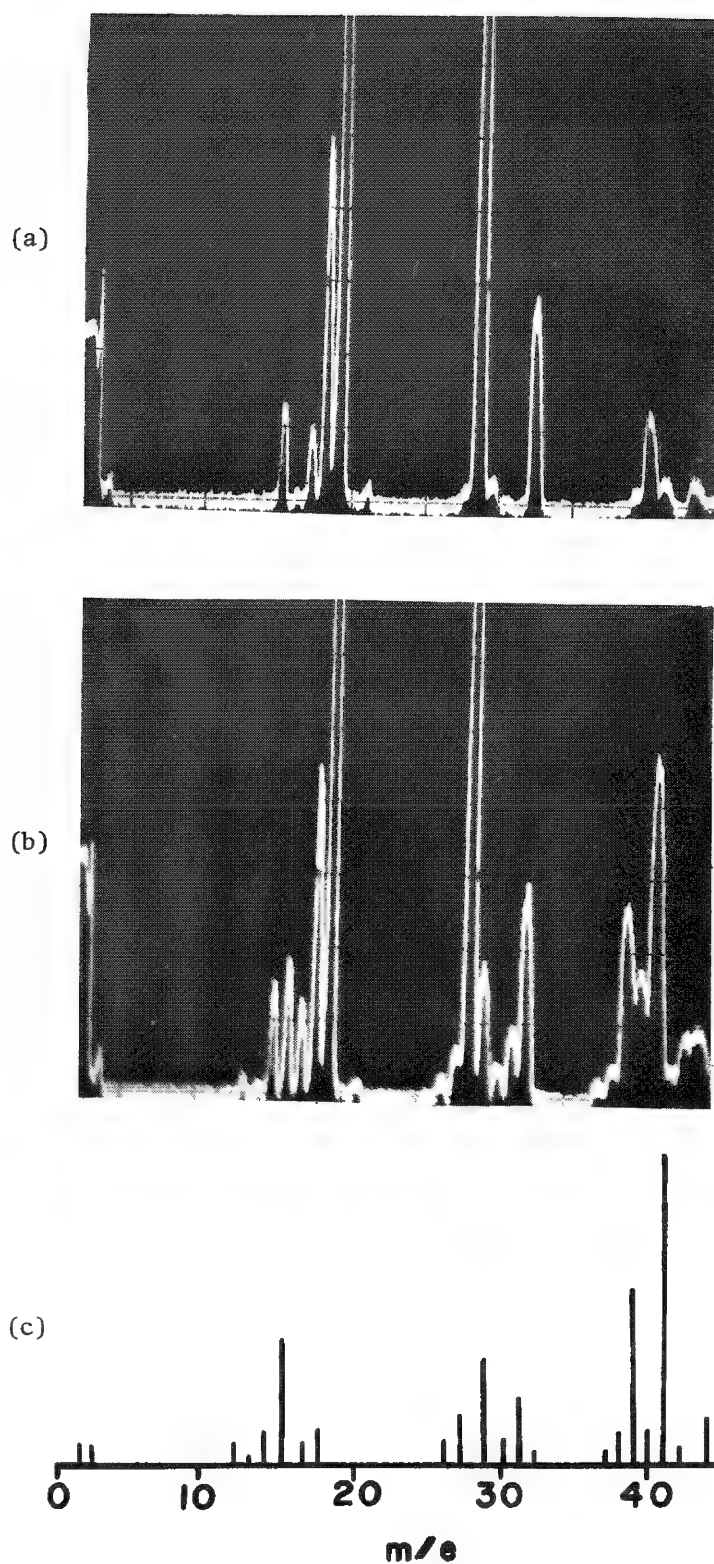


FIG. 1.--Mass spectra ( $1 \leq m/e \leq 45$ ) for (a) residual gas within microprobe column just prior to electron irradiation of sample; (b) residual gas plus ejected masses upon irradiating methacrylate specimen with 30keV electrons at current density of  $\sim 10^{-11}$  A- $\mu\text{m}^{-2}$ ; and (c) net mass peak heights resulting from electron irradiation.



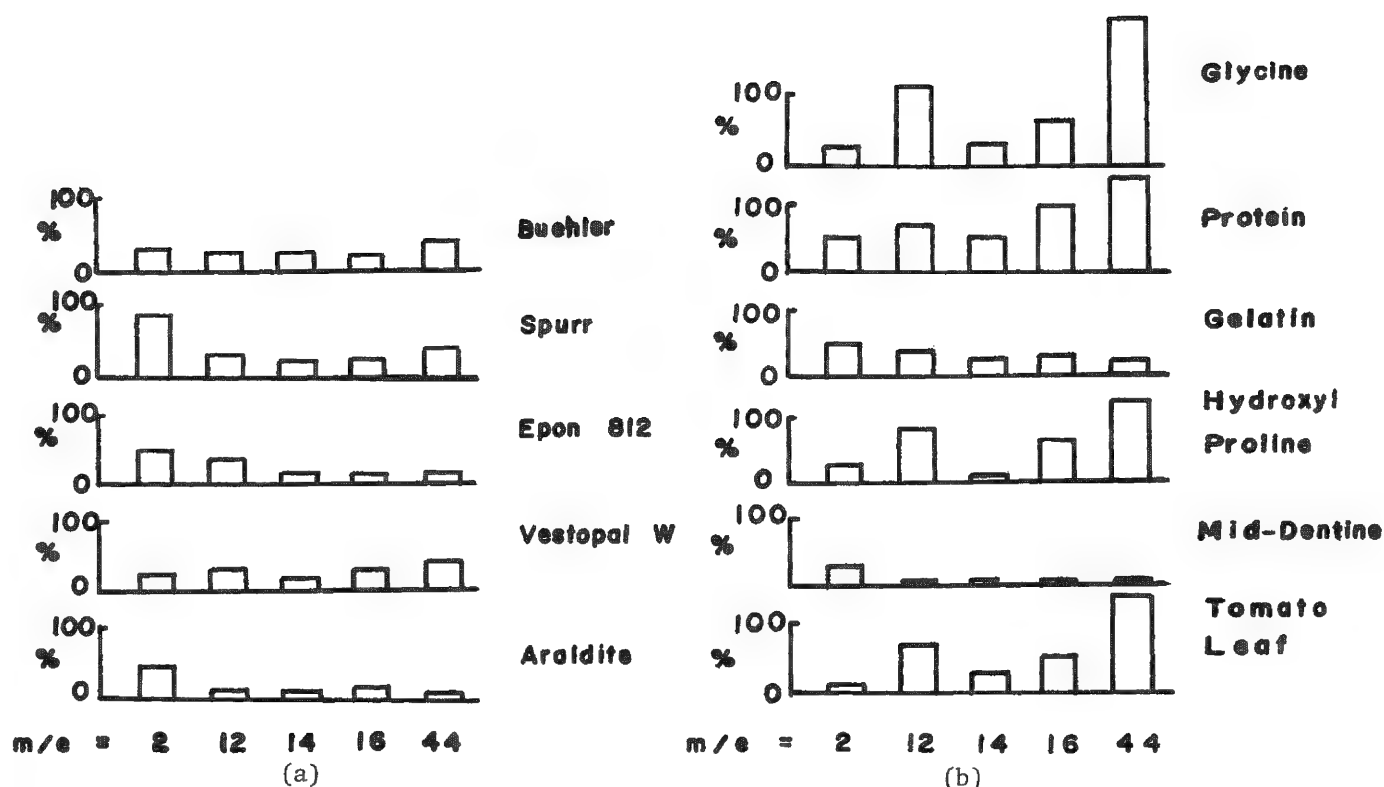


FIG. 2.--Selected mass peak heights relative to methacrylate (expressed in %) for (a) different plastic specimens and (b) different biological specimens. Operating conditions were maintained constant.

strong beam energy and matrix density dependences.

Ignoring the effect electron irradiation would have on stopping power and mean ionization potentials or the possible removal of the element to be analyzed by bombardment, it would be argued that no characteristic x-ray count rate variation would result if the section thickness  $t$  was less than  $R_i$ , since no additional heavy-element content would be analyzed with prolonged electron irradiation. Similarly, if  $t > R_f$ , the sample is infinitely thick to the electron beam and the magnitude of count rate variation would be maximized for the operating conditions employed. A transition zone between these extremes would exist.

To illustrate this phenomenon, we prepared a plastic block with about 8 wt.% sulfur by mixing the LP-3 polysulfide (Thiokol) with Epon 812. Sections were cut in about 1, 2, 4, 6, 8, 10, and 12  $\mu\text{m}$  thicknesses and placed on a carbon substrate. A crystal spectrometer was used to monitor the S characteristic x-ray intensity as a function of electron dose when 20keV electrons at a current density of about  $10^{-11} \text{ A-}\mu\text{m}^{-2}$  were made incident on the specimen. The percentage increase in count rate from the initial count rate is shown in Fig. 4 as a function of section thickness. These variations would occur for electron doses on the order of  $10^{-10} \text{ C-}\mu\text{m}^{-2}$ ;  $R_i$  is estimated to be about 4  $\mu\text{m}$  and  $R_f$  is about 10  $\mu\text{m}$ . However, these results are characteristic of the operating conditions employed and of this particular matrix.

## References

1. R. M. Glaeser, "Radiation damage and biological electron microscopy," *Physical Aspects of Electron Microscopy and Microbeam Analysis*, New York: Wiley, 1975, 205.
2. M. S. Isaacson, "Specimen damage in the electron microscope," *Principles and Techniques of Electron Microscopy*, New York: Van Nostrand Reinhold, 1977, 7: 1.
3. L. Reimer, "Review of the radiation damage problem of organic specimens in electron microscopy," *Physical Aspects of Electron Microscopy and Microbeam Analysis*, New York: Wiley, 1975, 231.

4. J. W. Edie and P. L. Glick, "Dynamic effects on quantitation in the electron probe analysis of mineralized tissues," *Proc. 11th MAS Conf.*, 1976, 65.

5. J. W. Edie and P. L. Glick, "Some effects of electron irradiation of biological specimens," *Proc. 13th MAS Conf.*, 1978, 19.

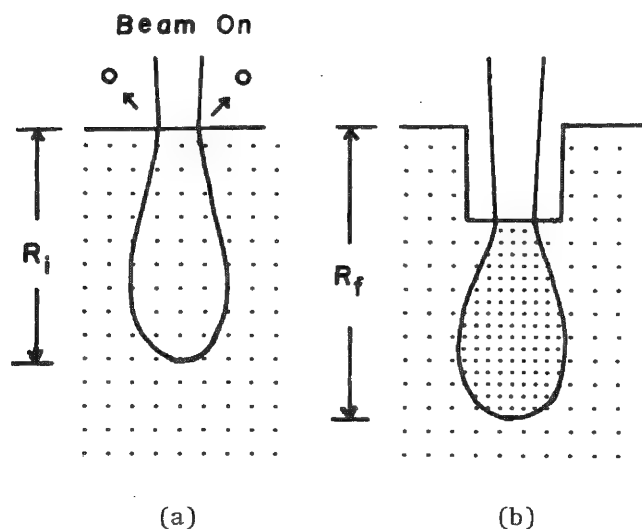


FIG. 3.--Excitation volume within light-element medium in which heavy element to be analyzed is uniformly distributed (a) at onset of electron irradiation and (b) after prolonged irradiation when stable conditions exist. Depth of penetration  $R_i$  at initial exposure increased to maximum value  $R_f$  and depends strongly on electron energy and matrix characteristics.

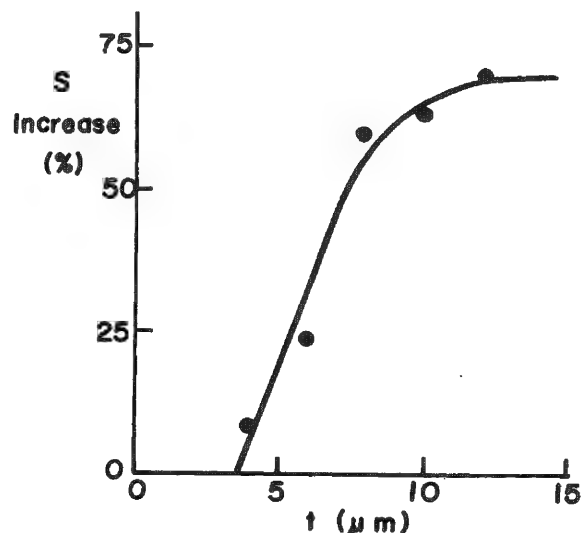


FIG. 4.--Percentage increase in sulfur characteristic x-ray intensity as function of section thickness for 8 wt.% sulfur in Epon 812 sections. Beam energy is 20 keV and electron dose to reach final stable count is about  $10^{-10} C-\mu m^{-2}$ .

## MICROANALYSIS OF ELEMENTAL DISTRIBUTIONS IN MINERALS AND CELLS PERFORMED WITH A PROTON MICROPROBE

Bernd Martin

X-ray emission spectroscopy has been widely used for qualitative and quantitative determinations of trace elements in recent years, largely because of the rapid development of high-resolution Si(Li) detectors. The electron-microprobe technique allows quantitative analysis of micrometer-sized particles, inclusions in solids, and biological samples. However, because of the high bremsstrahlung background from the electrons this method is limited to a sensitivity of 1 part in 10 000, so that only the major elements (with concentrations > 1000 ppm) in the sample can be quantitatively determined. To obtain information on elements with concentrations < 1000 ppm, one is forced to use other techniques such as x-ray fluorescence or neutron activation analysis. Yet the last two methods are not applicable to microscopic objects. Trace elements in such small areas can be analyzed with the ion probe<sup>1</sup> or laser mass spectrometer,<sup>2</sup> but these techniques are destructive because material is sputtered from the samples surface. Nondestructive trace-element analysis can be achieved by use of a charged-particle beam of, for example, protons or alpha particles to induce the emission of characteristic x rays of the elements present in the specimen.<sup>3</sup>

The accelerators used are capable of producing beams of charged particles with energies and intensities that are continuously variable over a wide range. The beams can be tightly focused so that x-ray emission is restricted to the small sample of interest.<sup>4</sup> The penetration depth and the detection limits<sup>5</sup> can be chosen by varying the particle energy. It has been shown experimentally<sup>3</sup> that a combination of x-ray excitation by protons and detection of the emitted x rays by a Si(Li) detector provides a powerful method for multielemental, nondestructive analysis of major and trace elements with atomic number  $Z \geq 12$ .

The proton microprobe roughly described in this paper was constructed jointly by physicists from the Physikalisches Institut der Universität Heidelberg and the Max-Planck-Institut für Kernphysik in Heidelberg. The facility (Fig. 1a), located at the 6MV EN Tandem Van de Graaff accelerator of the Max-Planck-Institut, consists of two major parts: a collimator system to produce an ion beam of micro-dimensions, and a focusing unit. A schematic view of the beam profile of the proton scanning microprobe is shown in Fig. 1b. The collimator consists of two pairs of crossed slits (collimators 1 and 2 in Fig. 1) mounted in two vacuum chambers. These slits are made of stainless steel with highly polished sharp edges (surface roughness  $\leq 0.1 \mu\text{m}$ ) for optimal definition of the beam; their width is varied by piezoceramic drives. The collimated beam is then focused by a small magnetic quadrupole doublet at the target located about 100 mm behind the second quadrupole. The quadrupoles have air-cooled coils, an outer yoke diameter of 170 mm, and an aperture diameter of  $2r_a = 5 \text{ mm}$ . Each has a field 40 mm long. A maximum field gradient of 500 T/m at 3 A can be obtained, sufficient for focusing protons or heavier ions (e.g.,  $^{16}\text{O}^{4+}$ ) from the 6MV Tandem Van de Graaff accelerator. The lens, as well as the collimator slits, are adjustable in both x and y directions. In addition, the lens can be rotated around the x and y axis. Adjustments of the beam during the experiment, as well as an accurate selection of a specific spot for analysis, is easily accomplished with an optical microscope fastened to the target chamber. This arrangement allows a view of nearly the entire sample. The sample holder can be moved in both x and y directions by a step motor,

---

The author is with the Max-Planck-Institut für Kernphysik, P. O. Box 103 980, D-6900 Heidelberg, Federal Republic of Germany. The paper is based on work performed in collaboration with F. Bosch, H. Döbbeling, A. El Goresy, R. Nobiling, D. Pelte, B. Povh, D. Schwalm, and K. Traxel (Max-Planck-Institut für Kernphysik Heidelberg and Physikalisches Institut der Universität Heidelberg), C. Petzelt (Institut für Zellenlehre, Deutsches Krebsforschungszentrum, Heidelberg), and W. Herth and H. D. Reiss (Zellenlehre, Universität Heidelberg).

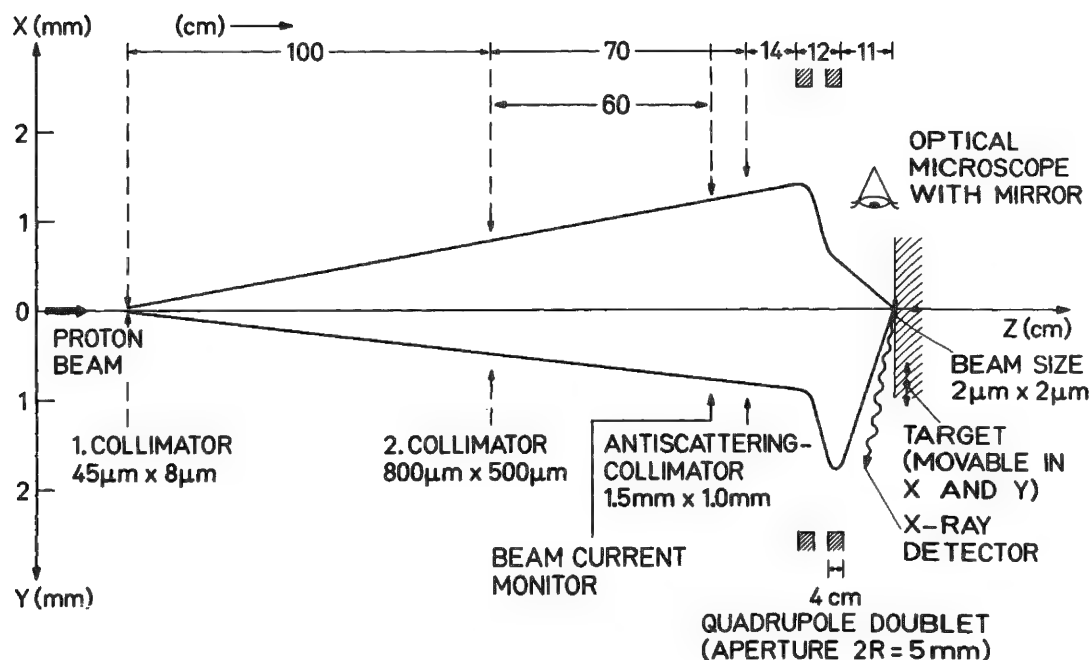
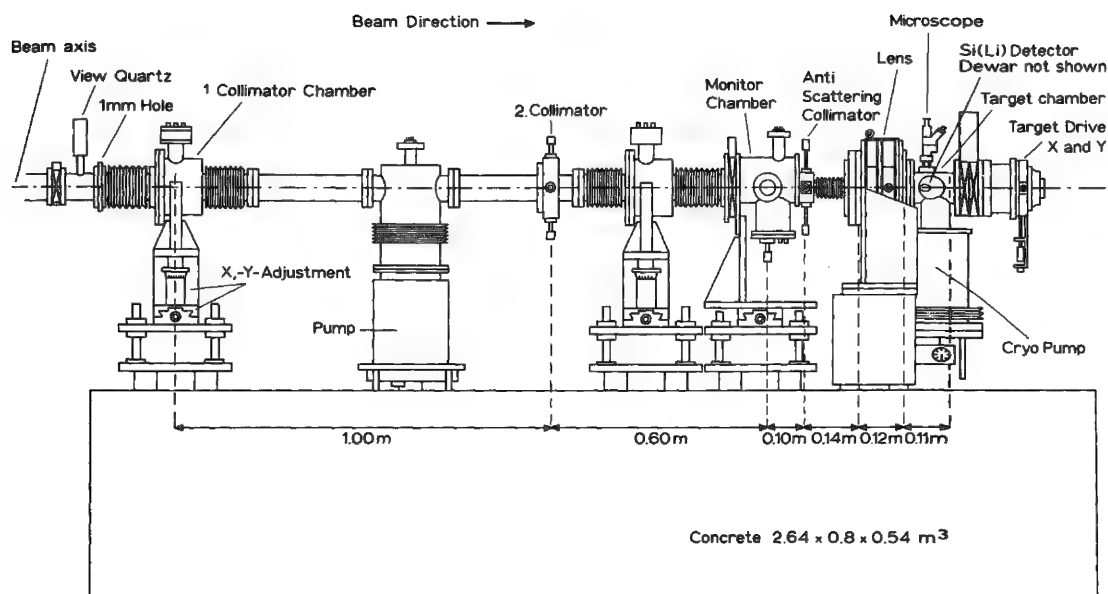


FIG. 1.--Proton microprobe facility connected to the 6MV EN Tandem Van de Graaff accelerator of the Max-Planck-Institut für Kernphysik, Heidelberg: (a) technical drawing, (b) beam profile.

so that a scan of the specimen can be performed without breaking the system's vacuum. The minimum size of a proton beam achieved so far is about  $2 \times 2 \mu\text{m}^2$  with an approximately rectangular intensity distribution.<sup>6</sup> The proton current density obtained in the measurement ranged from 5 to 20 pA/ $(\mu\text{m})^2$  at initial beam currents between 0.3 and 1  $\mu\text{A}$ . This density is sufficient for reaching relative detection limits of the order of 1-10 ppm for elements with proton numbers  $Z \geq 12$ , even for specimens with volumes of the order of microns cubed.

To demonstrate the performance of the proton microprobe we used it to determine trace elements and trace element distributions in some mineral grains in a lunar basalt (Apollo 17, sample No. 75015) and in biological samples like sea urchin eggs (*Sphaerechinus granulosus*).

*laris*) during mitosis and pollen tubes (*Lilium longiflorum*) during growth.

Two minerals, ilmenite ( $\text{FeTiO}_3$ ) and baddeleyite ( $\text{ZrO}_2$ ) were chosen to search for trace elements that had not been detected by the electron microprobe so far.<sup>7</sup> The grains were analyzed with the proton microprobe at excitation energies of 2 and 4 MeV with the results shown in Fig. 2. A typical recording took 2 hr. The  $K_\alpha$  and  $K_\beta$  lines of Y ( $60 \pm 20$  ppm), Zr ( $1600 \pm 300$  ppm), and Nb ( $40 \pm 15$  ppm) are well developed in the spectra of ilmenite (Fig. 2a). Note the absence of the L lines of these elements in the spectra taken at

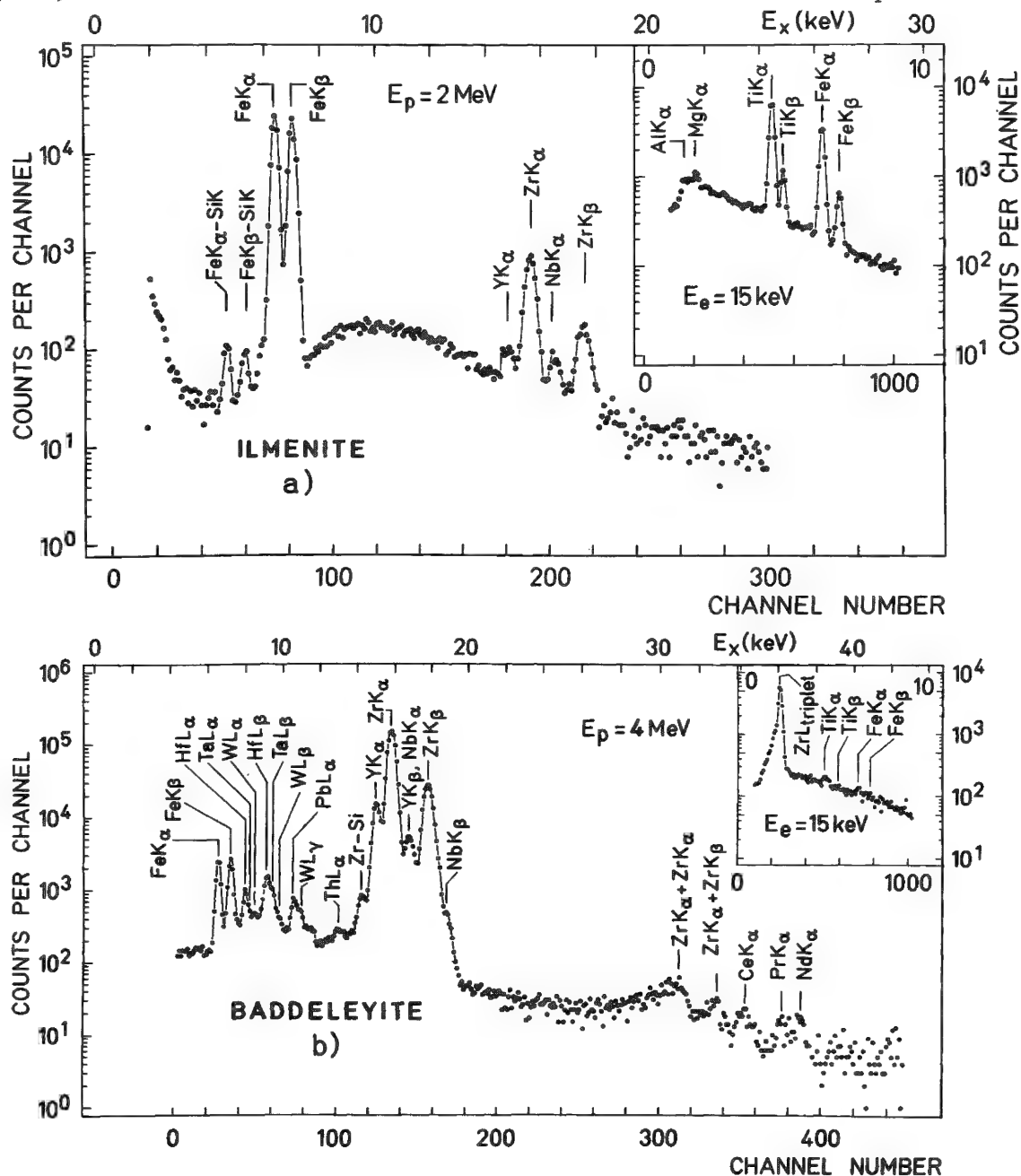


FIG. 2.--(a) X-ray spectrum of ilmenite obtained with proton excitation at 2 MeV. The inset displays the spectrum taken with the electron microprobe at 15 keV for the same grain. (b) X-ray spectrum of baddeleyite obtained with proton excitation at 4 MeV. The inset shows the spectrum taken with the electron microprobe at 15 keV for the same grain. The lines  $\text{ZrK}_\alpha + \text{ZrK}_\beta$  and  $\text{ZrK}_\alpha + \text{ZrK}_\beta$  indicate the Zr pile-up peaks.

15keV electron energy because of the high bremsstrahlung background (insets in Fig. 2a). The spectrum of baddeleyite (Fig. 2b) revealed the presence of K lines of trace elements which were not detected with the electron microprobe, such as Ta, Pb, Th, W, Y, Nb, Ce, Pr, and Nd. Because of the small grain size of the baddeleyite crystal and its intimate intergrowth with the zirconolite grain, we cannot exclude the possibility that the x rays of the elements measured by the proton microprobe in the baddeleyite were excited in both baddeleyite and zirconolite. In the geological sciences the technique should thus allow determination of the partitioning of trace elements among coexisting minerals and phases in natural rocks and in multicomponent synthetic material.

For the investigation of biological samples we studied the Ca distribution and gradient in sea urchin eggs and pollen tubes. In mitosis a spindle-like structure is formed for the distribution of the chromatids to the daughter cells. Since Ca is probably the main regulator of this process,<sup>8</sup> we sought to determine its distribution in the spindle and in the cytoplasm as well. The measurements were performed on glutaraldehyde-fixed, dehydrated, and air-dried eggs (diameter after drying about 50  $\mu$ m). The spindle visible before dehydration was photographed through a light microscope and the pictures obtained were used for identification and orientation. In this way it was possible to scan the dehydrated egg along and perpendicular to the spindle. The scan was accomplished by a motion of the egg through the proton beam (3 MeV) focus in steps of 0.5  $\mu$ m. At each step a constant charge was accumulated. The charge was monitored by a thin gold foil switched into the beam periodically. The protons elastically scattered from the foil were recorded by a surface barrier detector. The accumulated counts per step correspond to the beam intensity along the scanned direction. The egg was glued to a thin scintillator foil by polylysine<sup>9</sup> and carbon was evaporated onto the sample, which avoided charge-up effects. The x-ray spectrum and the scans are shown in Fig. 3(a)-(c). With 3MeV protons, which have a range of about 80  $\mu$ m in biological material, a sea urchin egg can be analyzed in its entire depth without substantial depreciation of the lateral resolution, something that cannot be accomplished with an electron microprobe. Figures 3(b) and (c) show Ca distributions of one egg recorded parallel (b) and perpendicular (c) to the spindle. In the middle of the egg (c), at 25  $\mu$ m, the Ca is enhanced by about 40% with respect to an isotropic distribution. Since the sea urchin eggs were air dried, only insoluble Ca could be detected.

For other biological processes calcium also seems to be essential. It is often hypothesized<sup>10</sup> that pollen tubes need a Ca gradient for growth. Such Ca distributions in pollen tubes have not yet been measured quantitatively. In our investigations the samples were fixed with glutaraldehyde, washed, and air dried. Parallel samples were treated with chlorotetracycline (CTC) before fixation for better preservation of the membrane-bound calcium.<sup>11</sup> Figure 3(e) displays a scan along a CTC-pretreated pollen tube starting from the pollen corn. In the last 20-30  $\mu$ m of the tip region the amount of Ca rises steeply from a concentration of 220 ppm to 3000 ppm. These values were obtained from the single spectrum (Fig. 3d) according to the method described in Ref. 12. Five additional scans on other pollen tubes gave similar results. Figure 3(f) displays a characteristic cross scan of a pollen tube without CTC pretreatment. Well-defined peaks with a half width of about 2.5  $\mu$ m could be detected. The absolute amount of Ca varies from 250 to 450 ppm, with the highest amount in the cortical region of the pollen tubes.

Before drawing any final biological conclusions we have to collect more statistics on different samples, and above all we have to analyze possible correlations between the experimental results and the preparation techniques used. However, the results reported on so far demonstrate that a proton beam focused to a few square microns is suited well for the trace-element analysis in biological samples. Its features are particularly advantageous for improving the investigations in diverse fields, e.g., the determination of the trace element profiles of healthy and malignant tissues.

## References

1. H. Liebl, "Ion probe microanalysis," *J. Phys.* [E]8: 797, 1975.
2. F. Hillenkamp, E. Unsöld, R. Kaufmann, and R. Nitsche, "A high sensitivity laser microprobe mass analyzer," *Appl. Phys.* 8: 341, 1977.
3. S. A. E. Johansson and T. B. Johansson, "Analytical application of particle induced x-ray emission," *Nucl. Instr. Meth.* 137: 473, 1976, (and references cited therein); "Proceedings of the International Conference on Particle Induced X-Ray Emission and Its

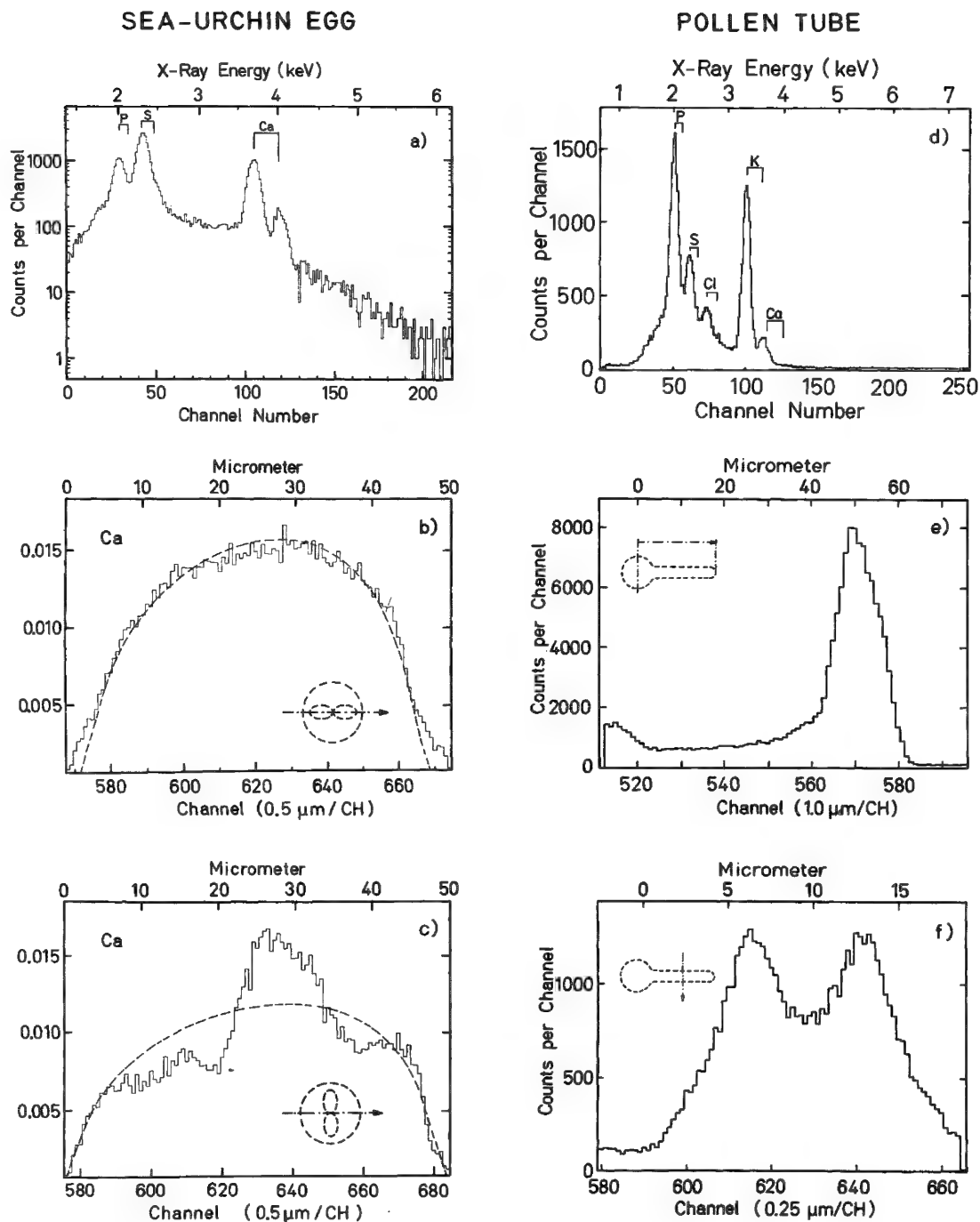


FIG. 3.--Spectra of a sea urchin egg ( $\approx 50 \mu\text{m}$  in diameter) and a pollen tube obtained with proton excitation at 3 MeV. The insets show the measurements schematically. (a) X-ray single spectrum of a sea urchin egg. (b) and (c) Ca distribution of a sea urchin egg measured parallel (b) and perpendicular (c) to the spindle (histogram). The calculated spectra for isotropically distributed Ca are shown by the broken line. These lines correspond to an absolute Ca amount of 600 ppm. (d) X-ray spectrum of a pollen tube. (e) Ca distribution along a CTC-treated pollen tube starting in the middle of the corn. The Ca amount varies from 200 to 3000 ppm. (f) Ca distribution perpendicular to the pollen tube axis. The half-widths of the peaks are  $\approx 2.5 \mu\text{m}$ .



Analytical Applications," Lund 1976, *Nucl. Instr. Meth.* 142: 1, 1977.

4. F. Bosch, A. El Goresy, B. Martin, B. Povh, R. Nobiling, D. Schwalm, and K. Traxel, "The proton microprobe: A powerful tool for nondestructive trace element analysis" *Science* 199: 765, 1978 and references cited therein; B. Martin and R. Nobiling, "High energy ion microprobes," in A. Septier, Ed., *Focusing of Charged Particles*, New York: Academic Press, to be published.

5. F. Folkmann, "Analytical use of ion-induced X rays," *J. Phys.* [E]8: 429, 1975.

6. F. Bosch, H. Döbbling, B. Martin, C. D. McKenzie, R. Nobiling, D. Pelte, B. Povh, K. Traxel, C. Petzelt, W. Herth, and H. D. Reiss, *Microanalysis of Elemental Distribution in Cells Performed with a Proton Microprobe*, Max-Planck-Institut für Kernphysik Report MPIH-1979-V3.

7. A. El Goresy, P. Ramdohr, O. Medenbach, and H. J. Bernhardt, "Taurus-Littrow  $\text{TiO}_2$ -rich basalts: Opaque mineralogy and geochemistry," *Proc. Fifth Lunar Conf., Geochem. Acta* 1: 627, 1974.

8. C. Petzelt, "Calcium activated ATPase during the cell cycle of the sea urchin *Strongylocentrotus purpuratus*," *Exptl. Cell Res.* 70: 333, 1972; C. Petzelt and D. Auel, "Synthesis and activation of myofibrillar calcium ATPase during the cell cycle of mouse mastocytoma cells," *Natl. Acad. Sci., USA* 74: 1610, 1977; H. Timourian, M. M. Jotz, and G. E. Clothier, "Intercellular distributions of calcium and phosphorus during the first cell division of the sea urchin egg," *Exptl. Cell Res.* 83: 380, 1974.

9. D. Mazia, G. Schatten, and W. Sale, "Adhesion of cells to surfaces coated with polylysine: Application to electron microscopy," *J. Cell Biol.* 66: 198, 1975.

10. W. Herth, "Ionophore A23187 stops tip growth but not cytoplasmic streaming in pollen tubes of *Lilium longiflorum*," *Protoplasma* 96: 275, 1978.

11. H. D. Reiss and W. Herth, "Visualisation of the calcium two plus gradient in growing pollen tubes of *Lilium longiflorum* with chlorotetracycline fluorescence," *Protoplasma* 97: 373, 1979.

12. Y. J. Uemura, Y. Kuno, H. Koyama, T. Yamazaki, and P. Kienle, "A new way of determining concentrations in PIXE trace element analysis," *Nucl. Instr. Meth.* 153: 573, 1978.

## AUTOMATED WDS QUALITATIVE AND QUANTITATIVE MICROANALYSIS IN GEOSCIENCES

R. Giraud, G. Remond, D. Pajon, J. Henoc, C. Conty, and M. Tong

### *Introduction*

Automation of the various steps of quantitative microprobe analysis permits the statistical evaluation of big numbers of chemical data. The microprobe thus becomes a powerful analytical tool for quantitative analysis on a routine basis in a similar way to that of optical emission spectrometry in geochemistry applications.

A microprobe with four wavelength-dispersive spectrometers (WDS) is managed by a PDP 11/05 minicomputer with two cartridge disks; data processing is executed on line. The original software written with an interpreter language was quite slow even when a matrix correction according to Bence and Albee was used.<sup>1-3</sup> This approach has been adopted because chemical composition of the specimen is needed before the strategy of analysis of a sample set can be conducted; uncorrected values are quite insufficient for this purpose. The substitution of FORTRAN for the former permits a faster execution and the introduction of a full ZAF treatment into the procedure.<sup>4,5</sup>

Potential output exceeds the amount of information the operator can manage during data acquisition; these outputs are saved on files to be processed further by appropriate programs, which give the final report to the customer. For instance, this paper will describe the programs we use for petrological applications.

A perfect qualitative knowledge of the specimen is assumed in the above treatment, as is generally the case with major components of silicates. For ore studies (sulfide) qualitative and quantitative compositions may vary by large amounts, even inside the same deposit, owing to the presence of many impurities, which are the most significant characteristics for these compounds. Rather than checking the presence of every hypothetical element we have developed a program that permits a rapid exploration of the entire spectrum. We use WDS spectrometers, which have much better resolution than the energy-dispersive spectrometer (EDS) and a greater ratio peak to background. For this purpose, display and identification of the spectrum has been programmed to be the output on a DEC VT 55 video terminal; the computer is under the control of the foreground-background monitor.

### 2. *Final Report for Quantitative Analysis of Silicates*

2.1. *Quantitative Analysis.* The MBXCOR package written in FORTRAN includes the analytical CORREX and QUANTI programs.<sup>6,7</sup> CORREX is the more general treatment applied for sequential quantitative microanalysis, including data acquisition and processing. QUANTI is a shortcut for quantitative analysis of specimens belonging to the same family as those already studied in a former problem by means of CORREX. Some output files of CORREX are then input files for QUANTI. Prior to the execution of QUANTI the coordinates of the points of interest may be stored by means of the store function of the CDMBX program for the control of the instrument. A full ZAF routine is included in both CORREX and QUANTI analytical programs. To be corrected, all elements have to be analyzed under the same accelerating voltage.

An incident energy of 15 keV has been chosen for major and minor element analysis. A new CORREX version can accommodate multiple excitation conditions. It will be used for trace elements.<sup>8</sup>

All parameters concerning instrumental configuration are saved on the GFGEXP.DAT file.

---

Authors Giraud, Remond, and Pajon are at the Bureau de Recherches Géologiques et Minières, Service Géologique National, BP 6009, 45018 Orléans Cedex; Henoc is at the Centre National d'Etudes des Télécommunications, 196 rue de Paris, 92220 Bagneux; and Conty and Tong are with Cameca, 103 Boulevard St-Denis, 92400 Coubevoie; all in France.

Experimental conditions are given at the beginning of a CORREX run. The PHYS.DAT file contains all this information. Moreover, the possibility of saving all parameters leads to a reduction in the dialog between the operator and the computer, so that a new analysis under previous conditions can be started more quickly.

Thirteen to fourteen elements are frequently encountered in silicate analysis. A run is performed in about 2 min, so that 300 points can be easily analyzed each day. The results are saved on the CONCOR.DAT file in order to process the results for specific applications.

**2.2. Report for Petrological Application.** In practice, the operator may call up each individual set of experimental data because they are permanently printed on the terminal. All intermediate results of significance only for the microprobe operator must be eliminated from the output. Moreover, the data stored on the files are used as input for special routines necessary for the petrologist's final report. The following programs have been developed for this purpose in the case of silicate analysis performed on a routine basis.

**BISON** (Fig. 1). This program gives the result list of all sequentially analyzed points. The data saved on the CONCOR.DAT file are expressed in terms of oxide weight concentrations. It offers a rapid overview of the entire set of results.

RT-11FB V03-02

.SET TT:WIDTH=132

.RUN RK1:BISON

NA= 10 NEL= 11

	1	2	3	4	5	6	7	8	9
NA	0.0330	0.0563	0.0572	0.0598	0.0624	0.0616	0.0596	0.0590	0.0032
SI	0.2239	0.5712	0.5791	0.5900	0.5934	0.5915	0.5830	0.5831	0.5237
FE	0.0011	0.0002	0.0017	0.0018	0.0020	0.0006	0.0014	0.0042	0.1036
CA	0.0373	0.0903	0.0872	0.0735	0.0741	0.0802	0.0823	0.0814	0.2159
MG	0.0000	0.0000	0.0000	0.0002	0.0000	0.0000	0.0001	0.0003	0.1363
AL	0.2821	0.2685	0.2597	0.2523	0.2562	0.2586	0.2617	0.2661	0.0164
MN	0.0000	0.0000	0.0006	0.0000	0.0000	0.0000	0.0002	0.0000	0.0029
K	0.0048	0.0051	0.0049	0.0067	0.0049	0.0048	0.0054	0.0051	0.0000
CR	0.0001	0.0000	0.0000	0.0000	0.0000	0.0000	0.0000	0.0001	0.0001
TI	0.0007	0.0000	0.0000	0.0007	0.0001	0.0002	0.0000	0.0002	0.0012
	0.5830	0.9916	0.9903	0.9849	0.9932	0.9975	0.9937	0.9994	1.0034
	10	11	12	13	14	15	16	17	18
NA	0.0000	0.0000	0.0036	0.0026	0.0603	0.0614	0.0000	0.0000	0.0000
SI	0.5282	0.5259	0.5232	0.5244	0.5868	0.5890	0.3777	0.3804	0.0000
FE	0.2564	0.2450	0.1086	0.1152	0.0013	0.0018	0.1620	0.1620	0.4974
CA	0.0095	0.0082	0.2189	0.2156	0.0799	0.0800	0.0000	0.0000	0.0000
MG	0.2011	0.2040	0.1332	0.1328	0.0000	0.0000	0.1479	0.1476	0.0064
AL	0.0083	0.0084	0.0158	0.0162	0.2580	0.2605	0.1415	0.1424	0.0000
MN	0.0078	0.0068	0.0037	0.0047	0.0000	0.0000	0.0003	0.0012	0.0050
K	0.0000	0.0000	0.0000	0.0000	0.0066	0.0065	0.1044	0.1063	0.0000
CR	0.0009	0.0010	0.0000	0.0003	0.0000	0.0000	0.0000	0.0000	0.0017
TI	0.0005	0.0007	0.0017	0.0023	0.0003	0.0000	0.0468	0.0486	0.4912
	1.0127	0.9999	1.0087	1.0141	0.9932	0.9991	0.9806	0.9886	1.0017
	19	20	21	22	23	24	25	26	27
NA	0.0000	0.0620	0.0634	0.0632	0.0637	0.0000	0.0000	0.0000	0.0002
SI	0.0000	0.5944	0.5962	0.6017	0.5940	0.5326	0.5289	0.0000	0.0000
FE	0.5275	0.0000	0.0016	0.0020	0.0022	0.2612	0.2620	0.5106	0.5183
CA	0.0000	0.0791	0.0729	0.0719	0.0770	0.0089	0.0079	0.0000	0.0003
MG	0.0067	0.0002	0.0000	0.0000	0.0000	0.2072	0.1989	0.0103	0.0101
AL	0.0000	0.2570	0.2500	0.2540	0.2575	0.0080	0.0081	0.0000	0.0004
MN	0.0059	0.0006	0.0000	0.0000	0.0000	0.0054	0.0077	0.0037	0.0029
K	0.0000	0.0056	0.0079	0.0061	0.0080	0.0000	0.0000	0.0000	0.0000
CR	0.0000	0.0000	0.0000	0.0006	0.0003	0.0000	0.0004	0.0008	0.0003
TI	0.4568	0.0000	0.0000	0.0000	0.0003	0.0006	0.0013	0.4772	0.4501
	0.9967	0.9988	0.9920	0.9995	1.0032	1.0239	1.0153	1.0027	0.9827

FIG. 1.--Output from BISON: oxide weight fractions.

**STRUC.** This program successively allows the calculation of:

- the chemical formula according to the number of cations normalized to the number of oxygen atoms contained in each defined species
- the  $\text{Fe}^{3+}$  content based upon the relation given in Table 1 for magnetite, chromite, ilmenite, and garnet
- the  $\text{H}_2\text{O}$  content in case of hydrous minerals
- the relative molecular content of each end member making the analyzed solid solution

TABLE 1.--Fe<sup>3+</sup> calculation.

Magnetite, Chromite	$\frac{2}{3} (\text{Fe} - (\text{Al} + \text{Cr})/2 - 2 (\text{Ti} - (\text{Mg} + \text{Mn})/2))$
Ilmenite	$\text{Fe} - ((\text{Al} + \text{Cr})/2 - (\text{Ti} + \text{Mn} + \text{Mg}))$
Garnet	$4 - (\text{Al} + \text{Ti} + \text{Cr})$

For instance, Fig. 2 relates to plagioclase phases characterized by the [(Na,Ca)(Al,Si)<sub>3</sub>O<sub>8</sub>] theoretical composition. Row 1 corresponds to weight concentration. Row 2 gives the number of cations calculated on a basis of eight oxygen atoms. Row 3 indicates the percentage of each end member successively made of albite (NaAlSi<sub>3</sub>O<sub>8</sub>), orthose (KAlSi<sub>3</sub>O<sub>8</sub>), and anorthite (CaAl<sub>2</sub>Si<sub>2</sub>O<sub>8</sub>).

RUN RK1:VTLEC

BUREAU DE RECHERCHES GEOLOGIQUES & MINIERES  
SERVICE GEOLOGIQUE NATIONALDEPT.: MGA LE 8/ 2/79  
LAB. MIXTE BRGM/CNRSDEMANDEUR : BRGM  
ETUDE M.1256RESULTATS D ETUDES  
ANALYSES A LA MICROSONDE ELECTRONIQUE

PLAGI/FELDS.

	2	3	4	5	6	7	8	39	40
NA	0.0563	0.0572	0.0598	0.0624	0.0616	0.0596	0.0590	0.0529	0.0517
SI	0.5712	0.5791	0.5900	0.5934	0.5915	0.5830	0.5831	0.5615	0.5548
FE	0.0002	0.0017	0.0018	0.0020	0.0006	0.0014	0.0042	0.0012	0.0013
CA	0.0903	0.0872	0.0735	0.0741	0.0802	0.0823	0.0814	0.0993	0.0985
MG	0.0000	0.0000	0.0002	0.0000	0.0000	0.0001	0.0003	0.0001	0.0003
AL	0.2685	0.2597	0.2523	0.2562	0.2586	0.2617	0.2661	0.2815	0.2813
MN	0.0000	0.0006	0.0000	0.0000	0.0000	0.0002	0.0000	0.0000	0.0000
K	0.0051	0.0049	0.0067	0.0049	0.0048	0.0054	0.0051	0.0036	0.0029
CR	0.0000	0.0000	0.0000	0.0000	0.0000	0.0000	0.0001	0.0000	0.0000
TI	0.0000	0.0000	0.0007	0.0001	0.0002	0.0000	0.0002	0.0009	0.0002
	0.9916	0.9903	0.9849	0.9932	0.9975	0.9937	0.9994	1.0011	0.9910
NA	0.4928	0.5006	0.5240	0.5427	0.5338	0.5199	0.5118	0.4599	0.4538
SI	2.5788	2.6155	2.6668	2.6598	2.6440	2.6206	2.6080	2.5189	2.5127
FE	0.0009	0.0063	0.0066	0.0077	0.0021	0.0052	0.0155	0.0045	0.0049
CA	0.4369	0.4220	0.3560	0.3559	0.3839	0.3964	0.3902	0.4773	0.4781
MG	0.0000	0.0000	0.0016	0.0000	0.0000	0.0004	0.0019	0.0010	0.0023
AL	1.4286	1.3823	1.3439	1.3533	1.3623	1.3867	1.4026	1.4884	1.5014
MN	0.0001	0.0022	0.0000	0.0000	0.0007	0.0000	0.0000	0.0000	0.0000
K	0.0292	0.0283	0.0386	0.0282	0.0274	0.0311	0.0290	0.0206	0.0167
CR	0.0000	0.0000	0.0000	0.0000	0.0000	0.0000	0.0004	0.0000	0.0000
TI	0.0000	0.0000	0.0023	0.0004	0.0007	0.0000	0.0005	0.0030	0.0007
	4.9674	4.9573	4.9398	4.9480	4.9542	4.9610	4.9599	4.9737	4.9707
FM	0.9984	0.9998	0.8061	0.9998	1.0000	0.9392	0.8933	0.8226	0.6779
AB	0.5139	0.5265	0.5704	0.5856	0.5647	0.5487	0.5497	0.4802	0.4784
OR	0.0305	0.0297	0.0420	0.0304	0.0290	0.0328	0.0312	0.0215	0.0176
AN	0.4556	0.4438	0.3876	0.3840	0.4062	0.4184	0.4191	0.4983	0.5040

FIG. 2.--Output from VTLEC: plagioclase analysis (STRUC data saved on CONCOS.DAT file).

The same approach is available for other species. In practice, the operator has only to indicate the name of the mineral of interest and to input the corresponding quantity of oxygen atoms involved in the chemical formula. STRUC calculation is then applied to the quantitative results selected by their sequential identification number in the list of analyzed points. Data being processed by the use of STRUC program are then stored on the CONCOS.DAT file. The VTLEC routine prints out all the results as they appear in Fig. 2 for plagioclase minerals.

CALMO (Fig. 3). For each analyzed species, this program gives the mean value of all results previously calculated by the use of STRUC program. For instance, Fig. 3 summarizes the mean value of eleven analyzed plagioclase minerals and three amphibole minerals. Oxide weight concentrations are given in row 1; the quantity of cations and the end-member ratios are given in rows 2 and 3, respectively.

RUN RK1:CALMO

BUREAU DE RECHERCHES GEOLOGIQUES & MINIERES  
SERVICE GEOLOGIQUE NATIONAL

DEPT.: MGA LE 8/ 2/79  
LAB. MIXTE BRGM/CNRS

DEMANDEUR : BRGM  
ETUDE M.1256

RESULTATS D ETUDES  
MOYENNES D ANALYSES DE LA M.S.E.

MOYENNE SUR LES PLAGI/FELDS. : MOY. SUR 11 ANALYSES.  
=====

	①	②
NA	0.0568	0.4960
SI	0.5739	2.5843
FE	0.0014	0.0054
CA	0.0886	0.4277
MG	0.0001	0.0007
AL	0.2680	1.4226
MN	0.0001	0.0003
K	0.0046	0.0264
CR	0.0000	0.0001
TI	0.0002	0.0007
	0.9939	4.9643

	③
FM	0.9214
AB	0.5228
OR	0.0279
AN	0.4493

MOYENNE SUR LES AMPHIBOLES : MOY. SUR 3 ANALYSES.  
=====

	①	②
NA	0.0081	0.2353
SI	0.4872	7.1536
FE	0.1516	1.8723
CA	0.1002	1.5854
MG	0.1379	3.0031
AL	0.0763	1.3503
MN	0.0030	0.0370
K	0.0013	0.0255
CR	0.0009	0.0103
TI	0.0010	0.0112
OH	0.0204	1.0000
	0.9878	16.2839

	③
FM	0.4037

FIG. 3.--Output from CALMO: Mean value for plagioclase and amphibole analysis.

Figure 4 illustrates the flow chart of available programs for the processing of quantitative results saved on the CONCOR.DAT file during silicate analysis. Calculated values according to the STRUC program make a new CONCOS.DAT file permanently available. The content of this file may be printed to give individual (VTLEC) or mean value (CALMO) of a large number of point quantitative data.

### 3. Automated WDS qualitative analysis

3.1 Basis. The range of every spectrometer, from  $\sin \theta = 0.224$  to  $\sin \theta = 0.824$  is divided into 600 channels of 0.001 width. The four spectrometers are respectively equipped with LIF, PET, TAP, and ODPb crystals, so as to cover the whole wavelength domain. All the monochromators are scanned simultaneously, so that we get an energy range corresponding to a 2400-channel multichannel analyzer. Radiation intensity integrated over one step is stored in a matrix WDS(I,J) where I and J are respectively the channel and the spectrometer subscripts. This matrix is saved in the WDS.DAT file. Data acquisition for one scan is about 3 min.

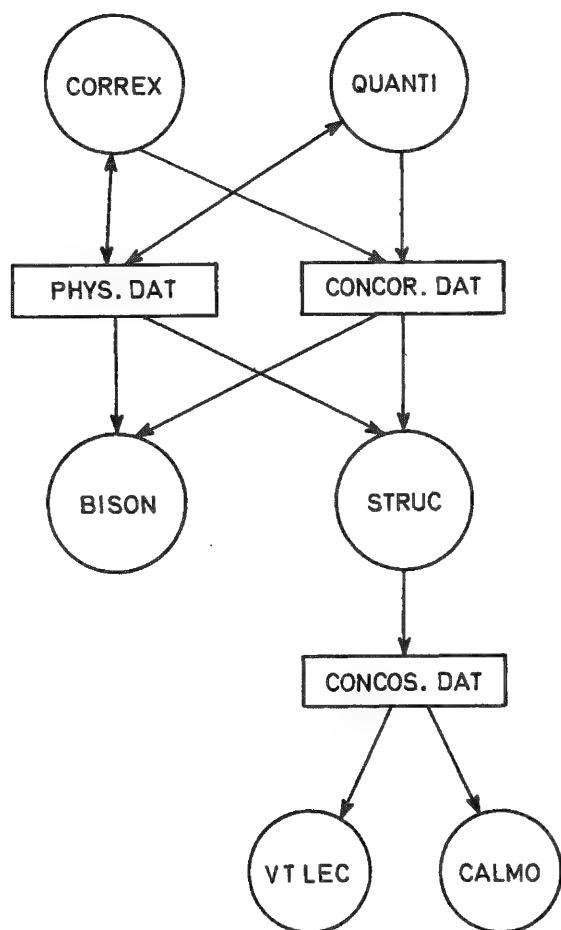


FIG. 4.--Schematic organization of the silicate treatment.

Resolution obtained on the displayed spectrum is twice as good as that we obtain with an EDS system for high energy (LiF crystal). It is increased by a factor of 4-6 for the medium energy range (PET and TAP crystals), in which many overlaps might occur. Moreover, light elements are detectable. We have developed four programs allowing the operator to identify elements associated with each line displayed on the screen.

**MARKER.** A "bug" is moved gradually channel by channel (or every 10 channels) by depressing of the carriage return key (CR) and the corresponding value of  $\sin \theta$  is written on the screen. If we assume the bug is set on peak maximum that is supposed to correspond to a first-order radiation, it can be sent automatically to the second-order position upon operator request by typing of 2 and (CR).

**PEAK.** This program generates a number of bars superposed on the spectrum to show radiation position and relative intensity for one element (Fig. 6). The operator selects a particular element by typing its atomic symbol. If a reasonable agreement is observed between the experimental peaks and the bars, the result is saved on a file for further use. Another option allows some sequential search by starting from the first element available on the monochromator in question. In case a coincidence between peaks and bars occurs the name of the corresponding element is saved. When the exploration of

The data can be accessed by one of two programs. The first, QUALI, gives a list of all detected radiations with their identification when it is possible (Fig. 5). An early version of this procedure consists in looking for the coincidence between the detected radiations and the best known theoretical values contained in a table. The execution of this routine was fast because no correlation was made between the characteristic lines of each element. A more sophisticated routine that attempts to use these correlations between positions and relative intensity ratios still leads to some ambiguities. Automatic identification may be too rich or too poor according to the degree of peak selection. That is why the operator should intervene to decide whether the element is present or not. The second program, VTQUAL was specially written to help the operator in this task.

**3.2. The Program VTQUAL.** This program allows the processing of data stored in WDS.DAT file and the display of the spectrum on the screen of the DEC VT 55 video terminal. Figure 6 shows the spectrum corresponding to the PET crystal, when the probe impinges on the same  $\text{PbCuSbS}_3$  mineral as was qualitatively analyzed by the QUALI program (Fig. 5). Energy resolution defined by half width at full maximum (HWHM) is clearly apparent on this record. The channel width quoted in energy corresponding to a step  $\Delta \sin \theta = 10^{-3}$  is  $dV(\text{eV}) = 12\,398/(2d \sin^2 \theta)$ .

Table 2 below gives the order of magnitude of the resolution obtained on the displayed spectrum, with the different number of channels included in HWHM of peaks for each available monochromator taken into account.

# QUALITATIVE ANALYSIS #

ACQUISITION BY WDS-SCANNING ?

DO YOU WANT A NEW HIGHER LEVEL IDENTIFICATION ? Y

SPECTR. NO : 1 & XTAL : TAP

SYMB	LAMBDA	SIN(A)	COUNT
PTMA	6.046	0.23446	188.
YLA	6.449	0.25036	694.
CARE	6.716	0.26173	148.
SRGR	6.863	0.26705	1053.
SIKA	7.125	0.27749	123.
ASLA	9.671	0.37659	235.
GELB	10.175	0.39495	230.
	10.318	0.40162	305.
2PBM	10.570	0.41142	619.
	10.750	0.41846	1481.
CULA	13.376	0.51915	722.
2SIK	14.250	0.55488	50.
CUMN	15.289	0.59248	84.
2ALK	15.919	0.61637	137.
COLA	15.970	0.62694	311.

SPECTR. NO : 2 & XTAL : LIF

SYMB	LAMBDA	SIN(A)	COUNT
KRKA	0.980	0.24370	1672.
ASKA	1.176	0.29171	4556.
IRLA	1.351	0.33456	277.
CUDS	1.392	0.34560	972.
CUKA	1.541	0.38269	6818.
FEKA	1.836	0.48741	244.
2ASK	2.352	0.58310	451.
2CUK	2.784	0.69116	95.
2ZNK	2.870	0.70803	76.
CUSC	3.031	0.75075	154.
2CUK	3.082	0.76578	484.
ILA	3.148	0.78282	81.
	3.192	0.79288	53.
2COK	3.242	0.80116	568.

SPECTR. NO : 4 & XTAL : PET

SYMB	LAMBDA	SIN(A)	COUNT
LALA	2.665	0.30766	375.
2ZNK	2.870	0.32545	722.
CUSC	3.031	0.34504	1142.
2CUK	3.082	0.35070	140.
ILA	3.148	0.35970	468.
2COK	3.242	0.36837	2565.
K/SB	3.439	0.39271	5897.
2FEK	3.872	0.44279	92.
CLKA	4.728	0.53440	87.
SKB	5.032	0.57531	216.
BITC	5.115	0.58012	2117.
PBMA	5.285	0.60438	2666.
SKA	5.372	0.61450	6068.
YLA	6.449	0.73831	73.
3CRK	6.870	0.78738	95.

SPECTR. NO : 1 & XTAL : TAP

SYMB	LAMBDA	SIN(A)	COUNT
	10.750	0.41846	1481.

SPECTR. NO : 2 & XTAL : LIF

SYMB	LAMBDA	SIN(A)	COUNT
CUKA	1.541	0.38269	6818.
2CUK	3.082	0.76578	484.
2COK	3.242	0.80116	568.

SPECTR. NO : 3 & XTAL : ODPB

SYMB	LAMBDA	SIN(A)	COUNT
------	--------	--------	-------

SPECTR. NO : 4 & XTAL : PET

SYMB	LAMBDA	SIN(A)	COUNT
2COK	3.242	0.36837	3312.
K/SB	3.439	0.39271	5897.
BITC	5.115	0.58012	2117.
PBMA	5.285	0.60438	2666.
SKA	5.372	0.61450	6068.

DO YOU WANT A NEW HIGHER LEVEL IDENTIFICATION ? N

FIG. 5.--QUALI automated WDS qualitative analysis: peak detection and identification. Specimen: natural bournonite ( $\text{PbCuSbS}_3$ ).  $E_p = 20 \text{ kV}$ ,  $I_{sp} = 30 \text{ nA}$ .

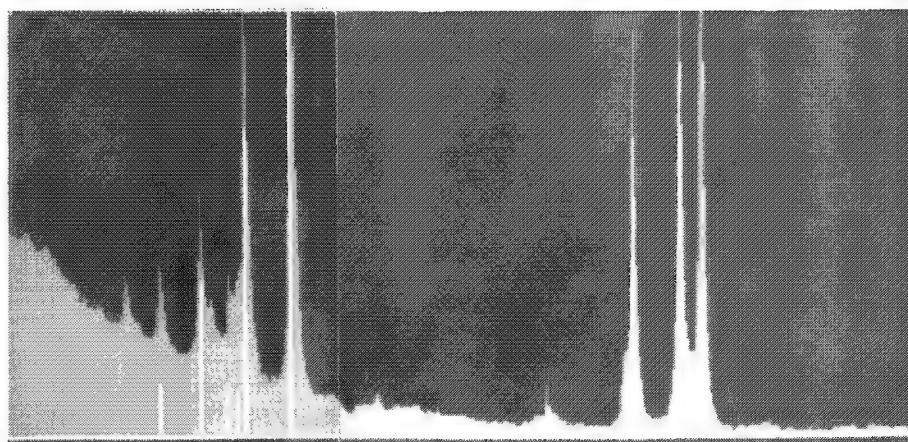
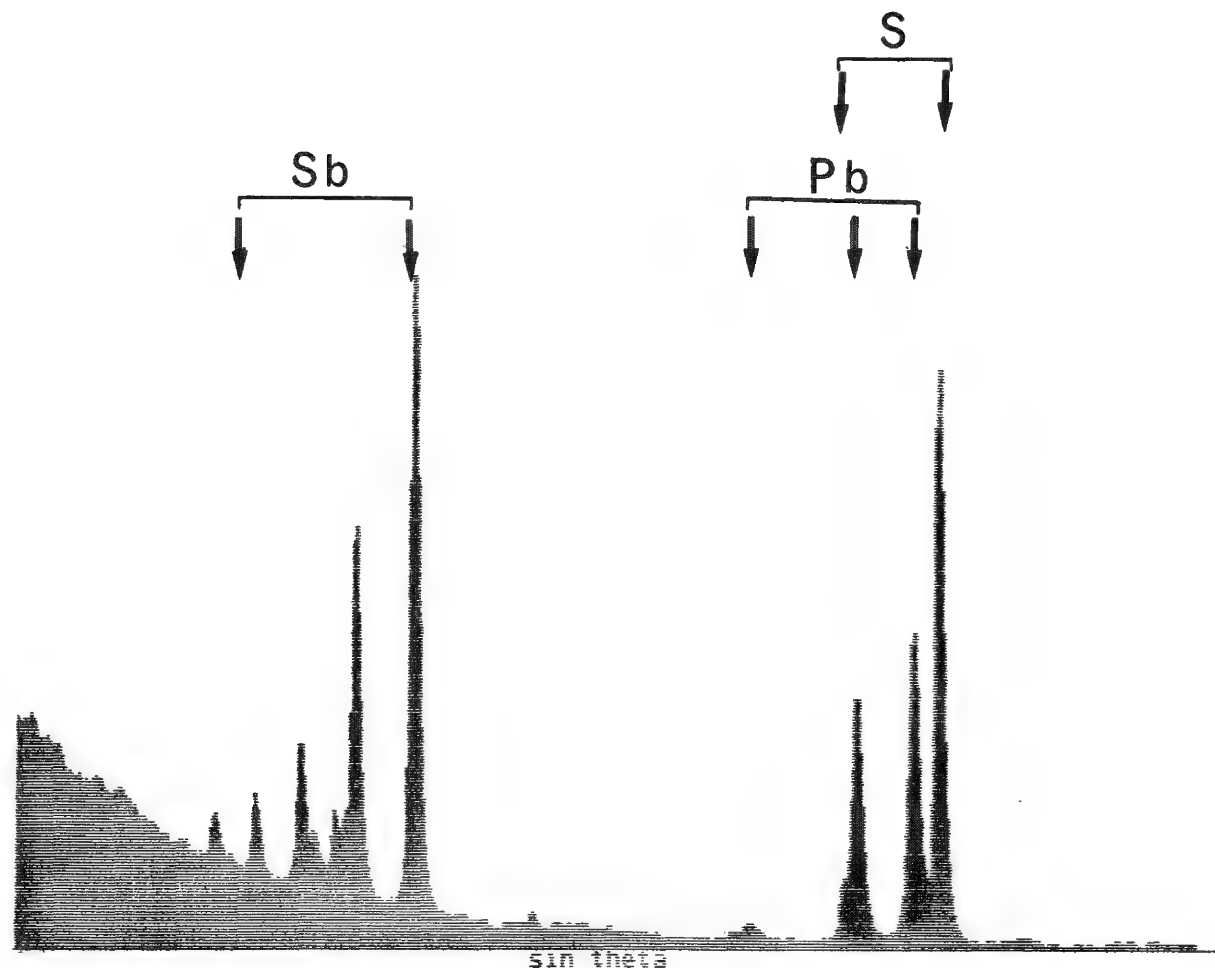


FIG. 6.--PET monochromator spectrum displayed on DEC VT 55 video terminal (VTQUAL). Same specimen as in Fig. 5. Brighter bars superimposed on spectrum indicate theoretical peak position and relative intensity for each detectable element (PEAK).



TABLE 2.--Characteristics of spectrum displayed by VTQUAL program for WDS automated qualitative analysis.

Monochromator	Analyzed Energy Range	Channel width (ev)	Mean HWFM (ev)
ODPb	0.560-0.170	0.8	
TAP	2.1-0.66	3	20
PET	6.40-1.95	9	35
LIF	13.8-4.22	20	80



CRISTAL PET

ELEMENTS DECELES

2D ORDRE

			KB1		KA1			KB1	KA1
			0.57514		0.61402			0.00000	0.00000
LG1	LB3	LB4	LB1	LB2	LA1	LL1		LB1	LA1
SB 0.32589	0.36029	0.36458	0.36865	0.34552	0.39367	0.44437		0.00000	0.00000
MG1			MB1		MA1			MB1	MA1
PB 0.53430			0.57999		0.60393			0.00000	0.00000

FIG. 7.--Hardcopy output from VTQUAL: PET monochromator spectrum. Same specimen as in Figs. 5 and 6.

the whole spectrum is performed, results are shown on the video screen and a hard copy of both spectrum and list of recognized elements may also be printed to keep track of the experiment (Fig. 7).

*LOG.* This option just displays the spectrum intensity on a logarithmic scale. It is particularly useful in case of large variations of peak intensities on the same displayed data.

*ZOOM.* This program allows a region of interest to be enlarged. This region is 150 channels wide and its origin can be moved along the energy axis upon the operator's request. These regions are sequentially displayed and marked by a brighter band at the lowest part of the spectrum image. Between two successive possible regions of interest there is an overlap of 50 channels. For instance two distinct regions have been selected and superposed on the same photograph in Fig. 8. An extended view corresponding to the highest energy range shown on the previous record is given in Fig. 9. A shaped mark bar is then available that allows the value of  $\sin \theta$  associated with each channel to be known (Note the distance between  $SK\alpha$  and  $PbM\alpha$  lines, which are completely resolved.) A second example showing the energy resolution obtainable with the sequential WDS qualitative exploration and display is shown in Fig. 10, illustrating the silicon K spectrum with a TAP crystal.

Figure 11 summarizes the general flowchart of the VTQUAL program included into the WDS qualitative analysis package. The latter similar to the quantitative CORREX routine used in point quantitative analysis is written in FORTRAN language.

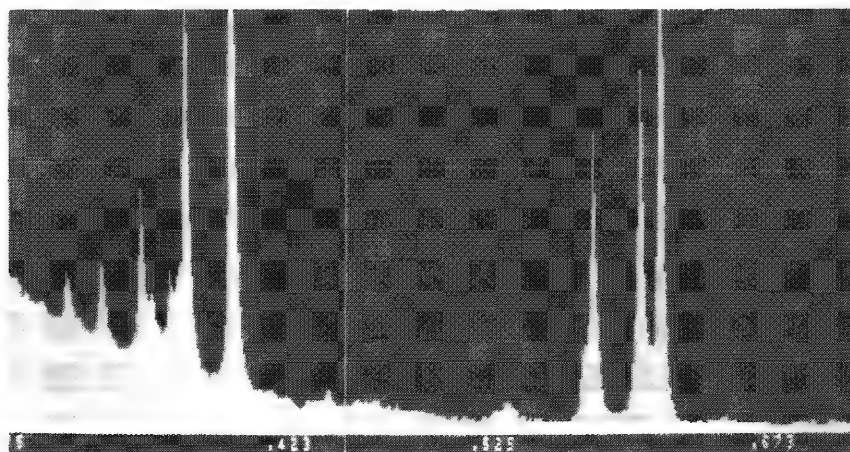


FIG. 8.--ZOOM option of VTQUAL. Parts of spectrum to be enlarged are indicated by brighter bands along wavelength axis of displayed spectrum.

### *Conclusion*

In setting an automated microprobe for geological applications our first aim was to offer a powerful software that would allow the operator to perform quantitative analysis of silicate on a routine basis. The use of FORTRAN allows us to reach this aim. The analytical capability of the equipment led us to develop new programs that meet the needs of the geoscientist. The automated WDS qualitative-analysis program that has been developed provides all the information the operator needs to prepare a quantitative procedure for unknown or unusual materials. This program is particularly useful for silicates because these materials contain many impurities. The next step in developing software for geological applications will concern trace elements and digital quantitative x-ray image analysis.

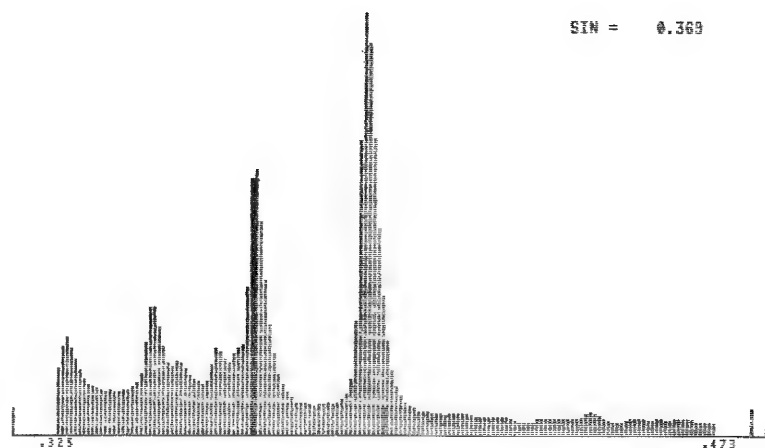


FIG. 9.--ZOOM option of VTQUAL:  
enlarged view of regions of  
interest selected in Fig. 8.

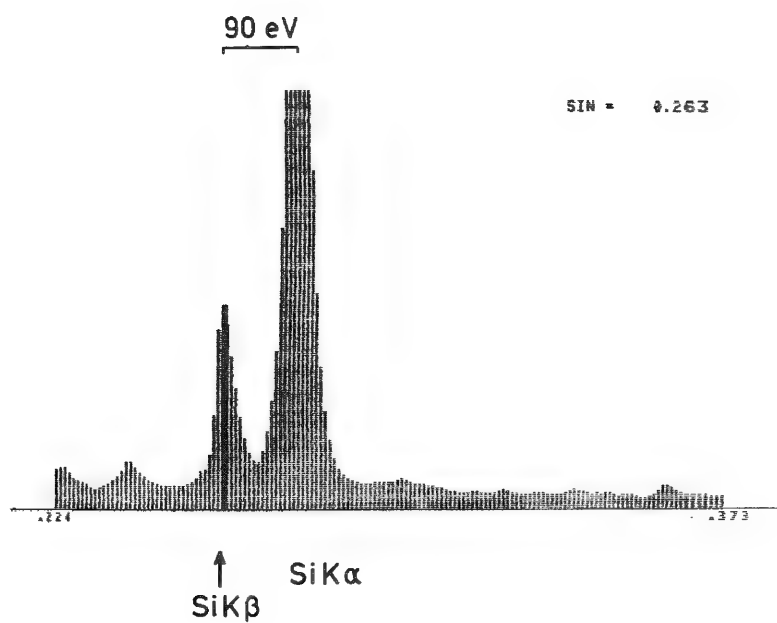
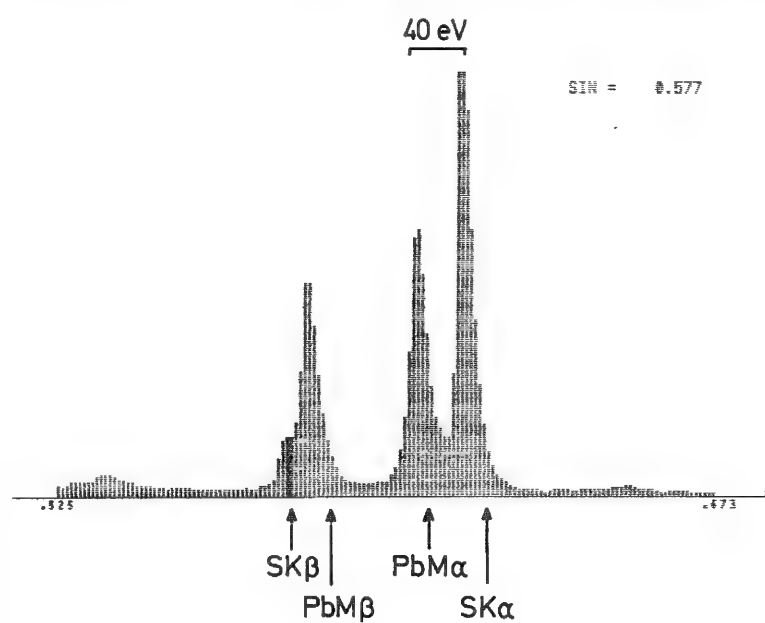
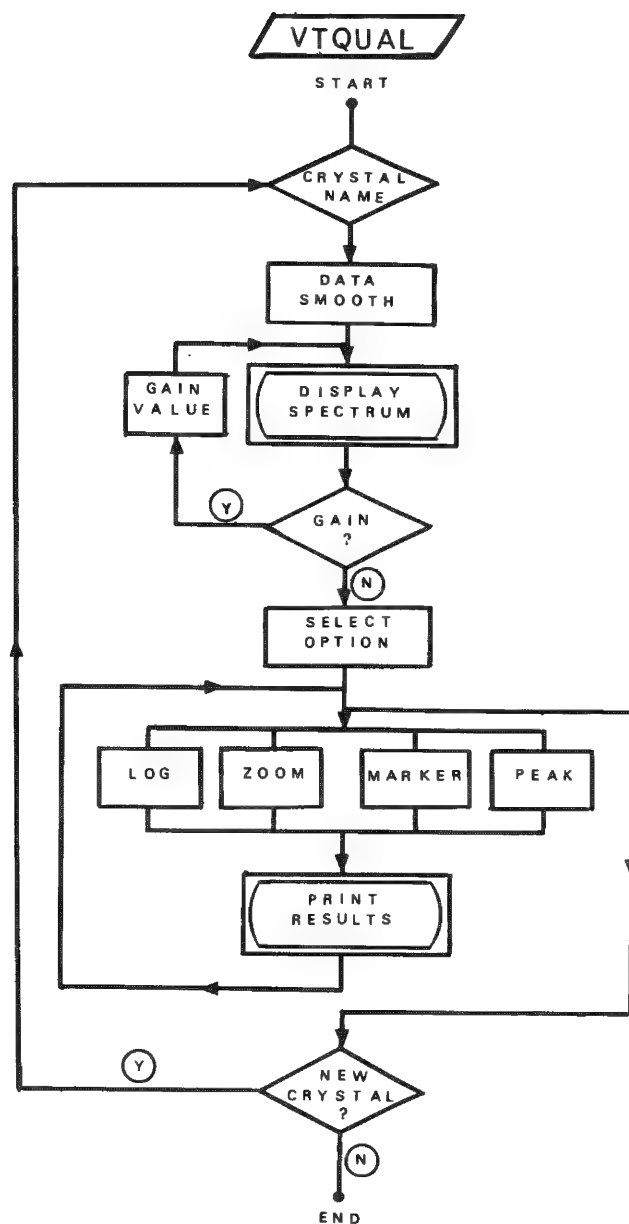


FIG. 10.--ZOOM option of VTQUAL:  
enlarged silicon K spectrum (TAP  
crystal).

FIG. 11.--Schematic flowchart of VTQUAL program.



### References

1. A. E. Bence and A. L. Albee, "Empirical correction factors for electron microprobe analysis of silicates and oxides," *J. Geol.* 76: 382-403, 1968.
2. R. Giraud, Z. Johan, G. Remond, J. M. Rouberol, and M. Tong, "Recherche des formules de corrections applicables aux analyses quantitatives réalisées à la microsonde électronique sur des matériaux naturels," Report 77 SGN 150 MGA, Bureau de Recherches Géologiques et Minières, Orléans, France, 1977.
3. G. Remond, R. Giraud, C. Conti, and M. Tong, "The use of an automated microprobe in geosciences applications," *Proc. 8th Intern. Conf. X-ray optics and Microanalysis; Proc. 12th MAS Conf.*, 1977, 186.
4. G. Remond, R. Giraud, and M. Tong, "Evolution des méthodes et moyens d'analyses quantitatives ponctuelles: Utilisation dans les géosciences de la microsonde électronique automatisée," *J. Micros. Spectrosc. Electron.* 3: 165-168, 1978.
5. G. Remond, "Tendances actuelles pour l'exploitation d'un laboratoire de microanalyse et de microscopie à balayage," Report 78 SGN 490 MGA, Bureau de Recherches Géologiques et Minières, Orléans, France, 1978.
6. J. Henoc and M. Tong, "Automation of the electron microprobe," *Proc. 8th Intern. Conf. X-ray Optics and Microanalysis; Proc. 12th MAS Conf.*, 1977, 46.
7. J. Henoc and M. Tong, "Automatisation de la microsonde," *J. Micros. Spectros. Electron.* 3: 247-254, 1978.
8. C. Conti, J. Henoc, and M. Tong, "New topics about an on-line correction procedure," *Proc. 14th MAS Conf.*, 1979, 281.

## AUTOMATED ELECTRON MICROPROBE IDENTIFICATION OF MINERALS IN STREAM SEDIMENTS FOR THE NATIONAL URANIUM RESOURCES EVALUATION PROGRAM

W. C. Mosley Jr.

The National Uranium Resources Evaluation (NURE) program was begun in 1973 to improve the assessment of uranium resources in the continental U.S. and to identify areas favorable for commercial exploration. The Grand Junction Office of the Department of Energy administers and coordinates NURE efforts. The Savannah River Laboratory (SRL) has responsibility for hydrogeochemical and stream sediment reconnaissance in 37 eastern and western states. A scanning electron microprobe quantometer (SEMQ), purchased from Applied Research Laboratories, is used to identify minerals in anomalous NURE sediment samples.

These anomalous sediment samples have high values of the ratio:

$$\frac{\ln(\text{U content})}{\ln(\text{Th content}) + \ln(\text{Hf content}) + \ln(\text{Dy content})}$$

as determined by neutron activation analysis.<sup>1</sup> This ratio is higher for ore-type minerals than for weather-resistant uranium-bearing minerals such as monazite ( $\text{Ce, ThPO}_4$ ), xenotime ( $\text{Y, DyPO}_4$ ), and zircon ( $\text{Zr, HfSiO}_4$ ). The SEMQ, with six automated x-ray spectrometers and on-line data reduction, provides the rapid, quantitative analyses needed for good geochemical characterization of sediments.<sup>2</sup>

When NURE stream sediment samples are collected, they are wet-sieved through a 40-mesh screen, and particles less than 420  $\mu\text{m}$  in diameter are retained for analysis. In the laboratory, the samples are dried and sieved through a 100-mesh screen. Some of the particles less than 149  $\mu\text{m}$  in diameter are analyzed by neutron activation analysis. Based on the results of this analysis, samples may be selected for SEMQ analysis.

If SEMQ analysis is desired, a fresh portion of sample is used. The particles are separated by suspension in tetrabromoethane (density = 2.96  $\text{g/cm}^3$ ) to remove light quartz and feldspar particles. The dense particles that settle out have different magnetic susceptibilities. A strong magnet recovers highly magnetic particles (MSI), and the remaining particles are separated by a Frantz Isodynamic Magnetic Separator Model L-1<sup>®</sup> (S. G. Frantz Co., Inc) into four fractions (0.3A, 0.55A, 1.0A, and HSI) with decreasing magnetic susceptibilities. For SEMQ analyses, particles from each fraction are embedded in 1.0in.-dia. Kold-Weld TM<sup>®</sup> mounts (Precision Dental Manufacturing Co.), ground, polished, and coated with a thin layer of carbon.

Mounted samples are examined in the SEMQ with the 300X optical microscope. About twenty particles on each mount are randomly selected, and their coordinates are filed in the computer. These particles are then automatically repositioned under the electron beam for SEMQ analyses. The electron beam is rastered over a 20  $\times$  20 $\mu\text{m}$  area to average out local inhomogeneities in the mineral particles.

Several schemes were developed for analysis of NURE sediments. The most useful scheme analyzes 17 elements in about 7 min (Table 1). The peak-seeking capability of the SEMQ is used to determine spectrometer settings during standardization, and the same settings are used for particle analyses. Backgrounds are calculated from the average intensities measured at spectrometer settings above and below the peak settings. Pulse height analyzers are used to eliminate higher-order x-ray interferences at the peak and background settings. The Bence-Albee method,<sup>3</sup> which empirically corrects for adsorption, fluorescence, and atomic number, is used for data reduction. Detection limits for all elements measured, except boron and oxygen, are < 0.05wt%. Detection limits for boron and oxygen are 1.0 and 1.9wt%,

---

The author is a staff physicist in the Analytical Chemistry Division of the Savannah River Laboratory, Aiken, SC 29801, which is operated for the U.S. Department of Energy by E. I. du Pont de Nemours & Co., under Contract AT(07-2)-1.

TABLE 1.--Seventeen-element analysis scheme used to analyze NURE stream sediments. The beam voltage is 15 keV and current is 30 nA. Counting time for both peak and background is 10 sec.

Spectrometer Crystal	1 LiF	2 APD	3 RAP	4 PbSD	5 PET	6 LiF
Element, Line (Cycle 1)	Ca, K $\alpha$	Y, L $\alpha$	Mg, K $\alpha$	B, K $\alpha$	Nb, L $\alpha$	Ce, L $\alpha$
Element, Line (Cycle 2)	Ti, K $\alpha$	P, K $\alpha$	Al, K $\alpha$	O, K $\alpha$	Th, M $\alpha$	Cr, K $\alpha$
Element, Line (Cycle 3)	La, L $\alpha$	Zr, L $\alpha$	Si, K $\alpha$	O, K $\alpha$	U, M $\alpha$	Fe, K $\alpha$

Standards: Apatite (Ca, P); Rutile (Ti, O); Chromite (Cr, Fe, Mg, Al);

Zircon (Zr, Si); Sintered Rare Earth Oxide (La, Ce, Y);

Lithium Niobate (Nb); ThO<sub>2</sub> (Th); UO<sub>2</sub> (U); and NBS Glass SRM K495 (B).

respectively. Analyses of reference materials showed that the calculated compositions are accurate enough for mineral identification.

To facilitate identification of minerals in stream sediments,<sup>4</sup> the reported compositions of about 200 rock-forming minerals were cataloged according to composition. Over 500 stream sediment particles have been analyzed. About 96% have been identified as distinct minerals. Most of the others appeared to be mixtures. Table 2 lists the 17 minerals identified in sediment samples. Only zinc-bearing gahnite had to be analyzed further for positive identification.

TABLE 2.--Minerals identified in NURE stream sediments. Monazite and zircon are the only minerals with uranium concentrations significantly above detection limits.

Ilmenite	Almandine	Magnetite
Amphibole	Monazite	Epidote
Tourmaline	Rutile	Sphene
Clinozoisite	Quartz	Hornblende
Staurolite	Zircon	Ferrohypersthene
Kyanite or Sillimenite		Gahnite

Monazite and zircon were the only minerals with concentrations of uranium significantly above the detection limit. The Frantz Isodynamic Magnetic Separator<sup>®</sup> isolated the monazite into the 1.0 fraction. Monazite particles in anomalous sediments contained up to 3.7wt% uranium. This uranium concentration is unusually high for monazite, which normally has about 0.5wt% uranium, and may be the cause of the anomaly.

#### References

1. *Hydrogeochemical and Stream Sediment Reconnaissance: Eastern United States*, Savannah River Laboratory Semi-Annual Report, April-September 1978 (DPST-78-138-2).
2. W. J. Hamilton et al., "Automated electron microprobe analysis: A system for the ARL-SEMQ based on mass storage and speed capabilities of the flexible-magnetic disk," *Proc. 12th MAS Conf.*, 1977, 52A.
3. A. E. Bence and A. L. Albee, *J. Geol.* 76: 382, 1968.
4. W. A. Deer, R. A. Howie, and J. Zussman, *Rock-Forming Minerals*, London: Longman, 1975, vols. 1-5.

## INTERACTIONS OF SIMULATED WASTE RADIONUCLIDES AND ROCKS

Paul F. Hlava and Thomas E. Hinkebein

In order to predict the long-term sorptive properties of common rock minerals in the vicinity of a radioactive waste repository, it is necessary to understand the mechanism of sorption and to know which are the active sorptive minerals. This paper describes the results of an electron microprobe study designed to further understanding of these processes and materials. Ion exchange is usually assumed to be the most important mechanism of sorption; therefore, radionuclides are assumed to be associated with minor clay constituents. However Jenne has questioned the role of ion exchange in many geological sorption processes.<sup>1</sup> Wet chemical studies do not easily lend themselves to the discovery of the active sorptive minerals without the destruction of the rock and the possible altering of the sorption properties. This study is nondestructive and has sought correlations between concentrations of test ions on the surface of the rocks and the associated mineralogy in elemental distribution photomicrographs obtained with the automated electron microprobe. Although individual clay particles are usually smaller than the resolution of the electron microprobe, we have seen that active clays are frequently found in clusters or exist as detrital grains which lend themselves to examination. A more complete description of the work described here may be found in Ref. 2.

Four rock samples were chosen for this study: a core sample of argillite taken from the Eleana formation in the Nevada Test Site at a depth of 1805 ft, and three core samples from AEC #8 in the Los Medanos area of Southeastern New Mexico. The New Mexico samples are Bell Canyon Sandstone from a core depth of 4823.4 ft, Magenta Dolomite from the Rustler Formation at 749.5 ft, and a halite sample from the Salado Formation at 2186 ft, which contained 7.8% by weight of clay. Four rock chips from each of the core samples were ground to flatness with No. 600 carborundum paper and then were equilibrated as follows: the first chip with a Cs solution, the second with a Sr solution, the third with a Gd solution, and the fourth with a U solution. Relatively concentrated solutions (Cs was 0.19 M, Sr was 0.00057 M, Gd was 0.064 M, and U was 0.0042 M) were used for each of the test ions to insure that the microprobe could detect test ions on the rock surface. The rocks were then flushed to remove excess ions from the surface and then examined with the electron microprobe, operated in the wavelength dispersive mode, to find accumulations of the test ions on the surface. Elemental distribution photomicrographs were then taken for key elements in the minerals given by an x-ray analysis of each of the rock samples. Matching of the qualitative information given in the elemental distribution photomicrograph with tabulated mineral analyses made it possible tentatively to identify many mineral phases and at the same time to tell whether those mineral phases had affinity for the test ions.

It was found that Cs was detectable only on the Eleana shale sample and was probably associated with illite-vermiculite; Sr formed insoluble carbonates and sulfates on the Magenta, Bell Canyon, sandstone and the clay-bearing halite; U was sorbed by both the Magenta and the dirty salts where it is likely that U entered a sample exchange reaction with either dolomite or magnesite to form  $\text{UO}_2\text{CO}_3$ . In the case of Sr and U, the carbonates and sulfates are too soluble to be of importance for tracer migration unless the ions participate in a co-precipitation reaction. Gd was sorbed on all four rock samples. The Gd sorbing mineral present on each of the rocks was possibly chamosite or chlorite, although some hydrolysis of Gd occurred on the dolomite.

The distribution of Gd on the Bell Canyon sandstone is shown in Fig. 1, and is used to illustrate the method of analysis performed on other specimens. There is a strong preference of Gd for the assemblage of elements, Fe, Mg, Al, and Si, indicative of chlorite. An

---

The authors are with Sandia Laboratories, Albuquerque, N.M., a facility of the U.S. Department of Energy (DOE). This work was supported by DOE under contract DE-ACO4-76-DP00789.



area of dolomite at coordinates (3 right, 1 up), where (0,0) is the center of the grid, shows a slight Gd affinity as a result of hydrolysis. Subsequent to the analysis performed on chips of material, geologic thin sections were prepared without cover slides and then examined with the petrographic microscope and the electron microscope operated in a quantitative mode. This analysis lends further support to the original suggestion that chlorite is an active mineral for Gd.

### Summary

Although the solution concentrations used in this study were relatively high and in some cases led to the formation of compounds that are unlikely to form at tracer levels, the study has shown that the underlying mineralogy is amenable to investigation with the electron microprobe. The methods presented here may be adapted to tracer level work by using autoradiography in conjunction with microprobe analysis. This technique should be helpful in determining not only the active sorptive minerals but also the mechanism of sorption.

### References

1. "Trace element sorption by sediments and soils: Sites and processes," in W. Chappel and K. Peterson, Eds., *Symposium on Molybdenum in the Environment*, New York: Marcel Dekker, 1977, 2: 423-553.
2. T. E. Hinkebein and P. F. Hlava, *Microstructural Interactions of Geologic Media with Waste Radionuclides*, Report SAND 78-0108, Albuquerque, N.M. Sandia Laboratories, 1978. (Available from National Technical Information Service, U.S. Department of Commerce, 5285 Port Royal Road, Springfield, VA 22161; \$4 printed copy, \$3 microfiche.)

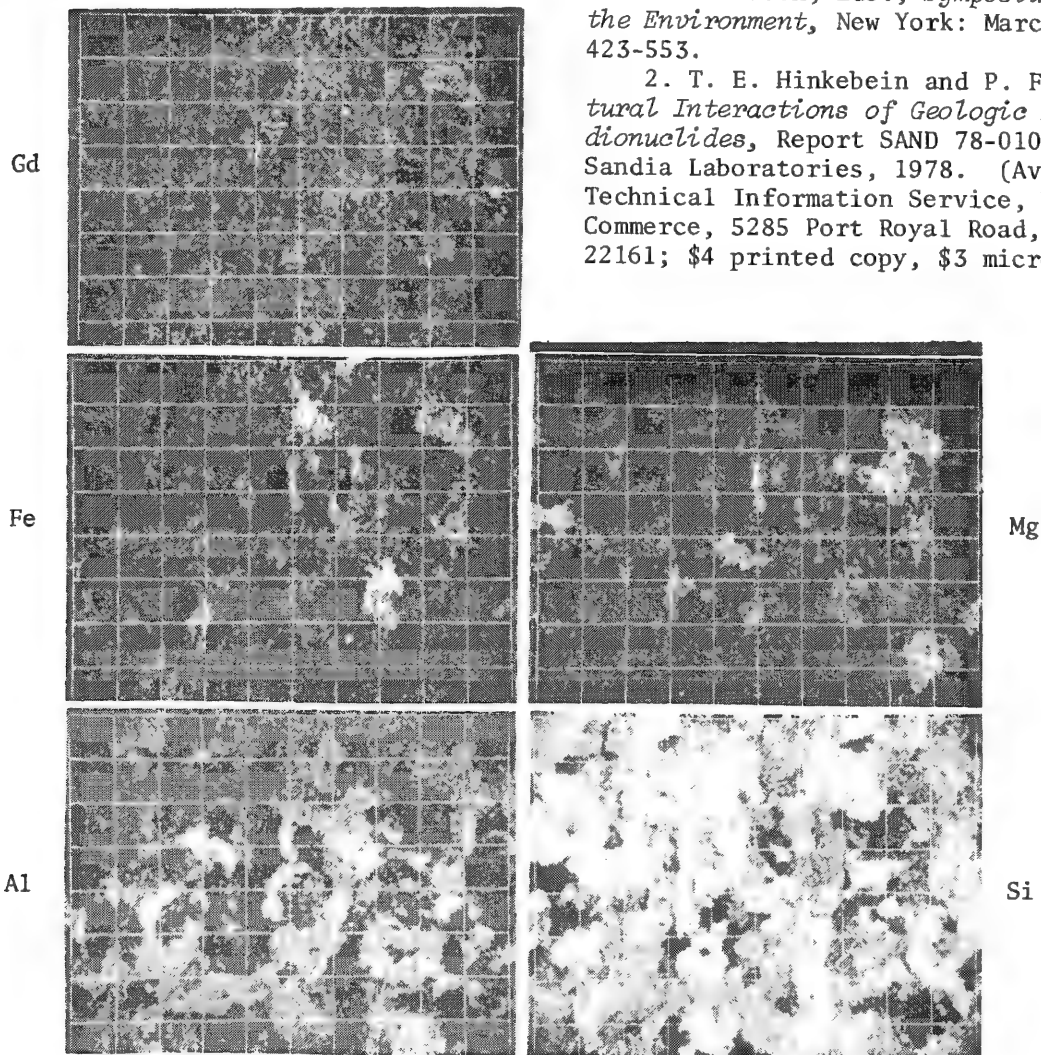


FIG. 1.--Elemental distribution photomicrographs of gadolinium-contaminated Bell Canyon sandstone. Gd is associated with assemblage of elements Fe, Mg, Al, and Si, indicative of chlorite. Grid size, 50  $\mu\text{m}$  per division.

## RELATIVE ABUNDANCES OF COMMON ELEMENTS IN COAL MACERALS

Robert Raymond Jr.

Macerals in coal are the organic equivalent of minerals in rock. They are microscopically observable units and in some cases can be correlated to original plant material. Within coals, common elements can be so finely dispersed as micromineral inclusions or as organically bound components that potential for their removal prior to coal processing is negligible. The electron probe microanalyzer (EPM) was used to determine how Na, Mg, Al, Si, S, K, Ca, Ti, and Fe are distributed throughout macerals on a submicron scale. Eight types of macerals were examined: vitrinite (V), psuedovitrinite (Pv), fusinite (F), semi-fusinite (Sf), macrinite (Ma), micrinite (Mi), sporinite (S), and resinite (R). Analyzing a variety of coal samples elucidated several trends correlating the distribution of common elements with macerals.

### *Sample Preparation and Analysis*

Coal samples were provided by the Coal Section of the Pennsylvania State University. The samples are from 18 localities within the USA and range in rank from low-volatile bituminous to subbituminous C, and in age from Pennsylvanian to Paleocene. Proximate and ultimate analyses performed by the Pennsylvania State University Coal Section further suggest the 18 samples are a random grouping.

The samples had previously been ground to -20 mesh size. Upon receipt, they were split, potted in epoxy, and made into polished 2.5cm rounds, approximately 120  $\mu$ m thick. The rounds were mounted on 27  $\times$  46 mm glass slides, and photomicrograph mosaics of portions of the samples were prepared at approximately 400 $\times$  magnification. Mosaics are necessary since the samples must be carbon coated for conductance during electron bombardment. Once the samples are carbon coated, reflectance levels are obscured and maceral identification is extremely difficult. I identified coal macerals present in the mosaics by oil-immersion reflected-light techniques. Where possible, five examples of all maceral types within each section were located. In most cases fewer than five examples of some macerals could be found; fewer than five were therefore analyzed. Our EPM has a 400 $\times$ -magnification optical system, and I used morphology of the various coal grains in conjunction with the mosaics to locate exactly the points of analysis.

To minimize errors in the measurement of low-level concentrations, oxygen and carbon contents defined by specific rank of the coal samples were included in matrix (ZAF) corrections, and background factors were computed on coal samples. The low-level concentrations measured in these analyses cannot be considered entirely quantitative, but consistency of measurements for particular samples shows that the results are quantitative on a relative basis. Therefore, comparisons of elemental concentrations within macerals of an individual sample and between samples appears justified.

Since the intent of this research was to determine how various common elements are distributed within coals on a submicron scale, visible mineral assemblages were avoided during analyses. Data were not accepted when sulfur and iron increased proportionally (as a result of unobserved FeS<sub>2</sub> or FeS<sub>0.4</sub> minerals), or where element concentrations were so high that an analysis was apparently dominated by some other unobserved mineral.

### *Results*

Figure 1 is a compilation of sulfur concentrations of macerals. Of all the common ele-

---

The author is with the Geological Research Group of the Los Alamos Scientific Laboratory, Los Alamos, NM 87545. The work was supported by the U.S. Department of Energy under Contract W-7405-ENG-36.

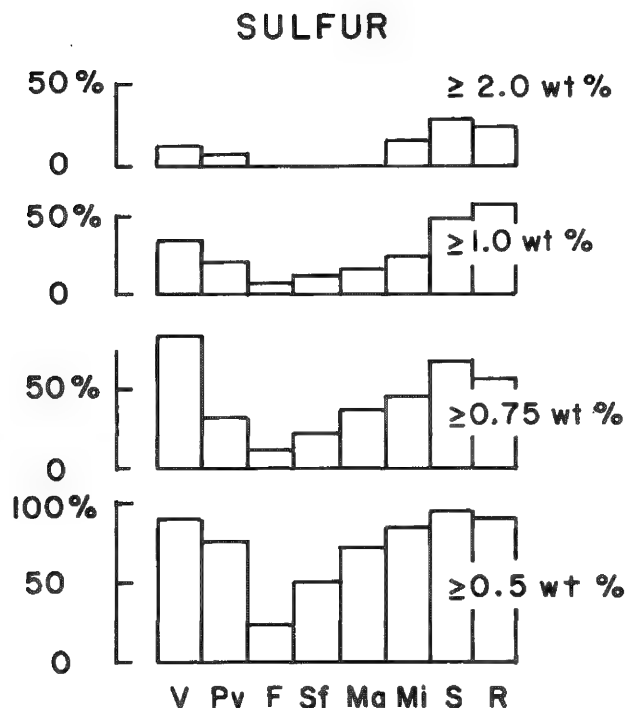


FIG. 1.--Percentages of samples for which the 8 maceral types contain more than 0.5, 0.75, 1.0, and 2.0wt%S.

ment of the element ( $\geq 1.0\text{wt}\%$ ). As can be seen, a large percentage of the micrinite sample contained abundant K, Ti, Al, Si, Na, and Fe. In fact, these elements are more commonly found associated with micrinite than any other maceral, with the exception of Ti's affinity for vitrinite. Al and Fe are also associated with vitrinite, but not as commonly as with micrinite. Vitrinite commonly contains Ca in low concentrations, but possibly more important is Ca's very strong affinity for fusinite. Mg likewise has a strong affinity for fusinite. Semifusinite and sporinite contain relatively high concentrations of K, Al, and Si.

Additional trends concerning relative concentrations of elements were also apparent. Si only increases with increasing Al concentration, though in four coals Al concentration increases whereas Si did not. K increases with increasing Al, Si, and Fe. With increasing Ca concentrations, Mg likewise increases. Fe is associated with a variety of other elements, although it is most commonly found with Al and/or Si. In some cases, whereas Si remains low, Fe increases as does Ca, Mg, Al, and Na. In a few coals certain elemental concentrations were high in all macerals: (1) Na, Mg, Al, Ca, and Fe in PSOC 529, a subbituminous B coal from Wyoming; (2) Ti in PSOC 408, a low-volatile bituminous coal from Oklahoma; and (3) Na in PSOC 458, a high-volatile bituminous coal from Utah.

### Discussion

A previous study<sup>1</sup> employing a recently developed method based on the EPM<sup>2</sup> has correlated organic sulfur content of coals to depositional environments. The study showed that coal samples with nonmarine overburden contain the least weight percent organic sulfur, whereas those with marine overburden contain the greatest weight percent organic sulfur. Furthermore, it showed that although the organic sulfur content of a coal deposited in a nonmarine environment may be low during deposition, later saturation by marine waters may increase organic sulfur content to concentrations greater than those resulting solely from a marine origin of coal. In the 18 samples reported in the present study, organic sulfur

ments studied, the most consistent relationship exists between sulfur and the various macerals; the ranking of sulfur contents is: vitrinite, micrinite, sporinite and resinite > pseudovitrinite  $\geq$  macrinite  $\geq$  semifusinite > fusinite. These sulfur contents are interpreted to be organic since no correlation exists between sulfur and iron contents. Another possibility is elemental sulfur, but it is unlikely that sulfur would be homogeneously distributed throughout each maceral in elemental form. Indeed, R. T. Greer (personal communication, 1979) measured the elemental sulfur contents of many of these samples by means of gas chromatography; he reports concentrations are well below the levels measurable with the EPM. The four histograms in Fig. 1 show that as organic sulfur content of coals increases, the concentrations of organic sulfur in various macerals also increases relative to each other maintaining the consistent relationship discussed above (see also Table 1).

Figures 2a and 2b are compilations of the analytical data on the other elements with respect to coal macerals. The wt% values in the histograms were chosen objectively to represent a concentration greater than background ( $\geq 0.02\text{wt}\%$ ), a substantial presence of the elements measured at two different concentration levels ( $> 0.05\text{wt}\%$  and  $> 0.10\text{wt}\%$  and the presence of a relatively large compo-

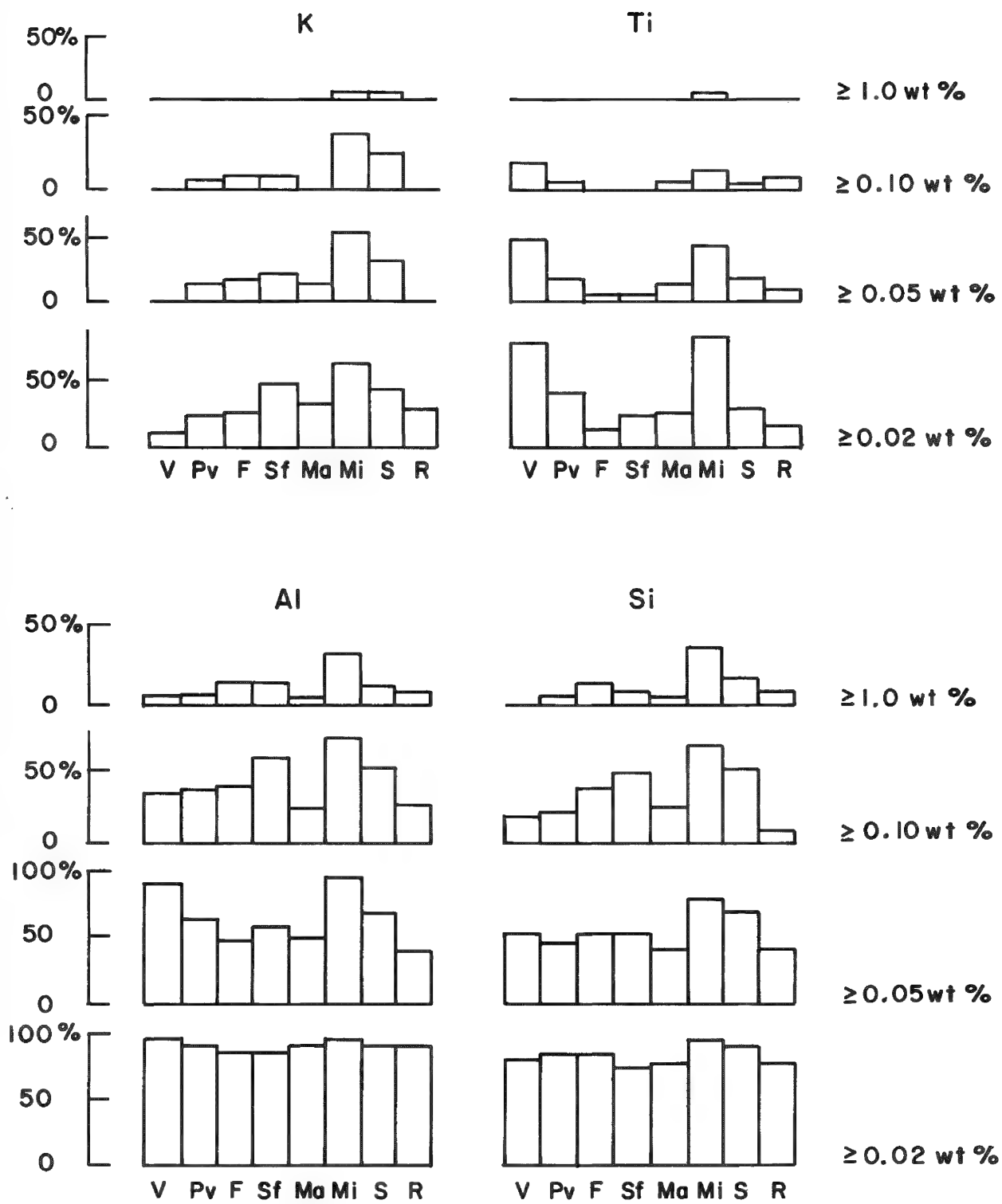


FIG. 2a.--Percentages of samples for which the eight maceral types contain more than 0.02, 0.05, 0.10, and 1.0wt% of K, Ti, Al, and Si.



values vary from 0.32 to 3.07wt%, suggesting depositional environments ranging from non-marine to marine, respectively. (Concentration and morphology of primary pyrite substantiate that.) But even though alterations in water chemistry have affected the total organic sulfur contents of the coals, the concentration of organic sulfur in various macerals increased relative to each other and maintained a consistent relationship (Table 1). Therefore, it appears that organic structure controls to what degree specific coal macerals can and will absorb organic sulfur. In other words, by studying the relative organic sulfur contents of macerals, we should be able to aid our understanding of their chemical structures.

TABLE 1.--Percentages of organic sulfur present in the eight maceral types for coals containing relatively high and low wt% of organic sulfur.

	V	Mi	S	R	Pv	Ma	Sf	F
PSOC 287	3.52	3.87	4.07	4.99	2.81	**	1.03	0.75
PSOC 270	1.52	1.07	1.23	**	1.30	0.83	0.71	0.57
PSOC 506	0.87	0.80	0.65	0.61	0.62	0.50	0.55	0.45
PSOC 458	0.50	0.55	0.79	0.60	0.46	0.34	0.34	0.30

\*\*None of this particular maceral was present in the sample for analysis.

With respect to the data on other common elements and their relationships to macerals, there are several possible interpretations. First, since micrinite is an aggregate of sub-micron grains, analyses of micrinite must of necessity include both the grains and any material in intergranular spaces. One should thus expect the presence of the common rock-forming elements in the analyses, which implies that with an increase of micrinite in coal, there would likewise be an increase in the presence of many common elements that would not be separable prior to processing.

The strong affinity of Ca for fusinite is substantiated by L.A. Harris (personal communication, 1979), who observed submicron, rhombohedral crystals in fusinite. The close relationship between Ca and Mg might suggest that in many cases the rhombohedral crystals are dolomite.

Numerous various relationships between Al, K, Si, and Fe, and possibly Na, Mg, and Ca, suggest that a spectrum of clay minerals are present: kaolinite (Al and Si); illite (K, Al and Si); and montmorillonite/nontronite (Na, Ca, Al, Mg, Si, and Fe). A wide range of possible solid solutions within the clay mineralogies makes specific correlations between individual elements for all coals very tenuous.

The presence of Al and Fe without the presence of Si are suggestive of diaspore and siderite. Where various elements are commonly found in all macerals of a coal, that coal's depositional environment probably contained high concentrations of those elements. The elements would have been absorbed into the lattice structures of the macerals, in a way very much similar to that suggested for organic sulfur.

The views reflected here are based on a preliminary interpretation of data resulting from more than 500 analyses. Further statistical analysis of the data, as well as analysis of additional samples, is needed before more specific conclusions can be drawn concerning the presence of common elements in coal macerals.

## References

1. R. Raymond Jr., "Correlating organic sulfur in coal to depositional environments by electron probe microanalysis," (abs.) *Ninth International Congress of Carboniferous Stratigraphy and Geology* (in press).
2. R. Raymond Jr. and R. Gooley, "A review of organic sulfur analysis in coal and a new procedure," in Om Johari, Ed., *Scanning Electron Microscopy*, Chicago: SEM, Inc., 1978, 1.

## EPMA--SEM AS TOOLS IN THE INVESTIGATION OF HYDROCRACKING PROCESSES

R. H. Packwood, J. F. Kriz and D. J. Patmore

As conventional petroleum reserves become depleted it is good sense to develop such technology as may be required to insure their replacement by less conventional sources, such as Tar Sands Bitumen and Heavy Oil. CANMET has developed a hydrocracking process for the upgrading of these high-sulfur materials that has considerable advantages in terms of fluid yield over the "coking processes" used at present.

Various advanced techniques of analysis are being used at present to help research and development efforts in this area. The microprobe and SEM coupled with Energy-Dispersive X-ray Spectroscopy (EDXS) have been used to investigate catalyst behavior, reactor solids, solids in the starting bitumen, and candidate alloys for reactor construction. By way of illustration, two investigations are described here that touch on problems in catalytic and thermal hydrocracking.

### *Catalytic Hydrocracking*

Previous work on the fouling of some Co-Mo/Al<sub>2</sub>O<sub>3</sub> catalyst pellets indicated that the elements in the deposition which caused greatest concern (V, Ni, and Fe) were distributed in a radial fashion as shown schematically in Fig. 1.<sup>1</sup> Evidently, the poisons when distributed in this manner can block off the remainder of the catalyst material and thus

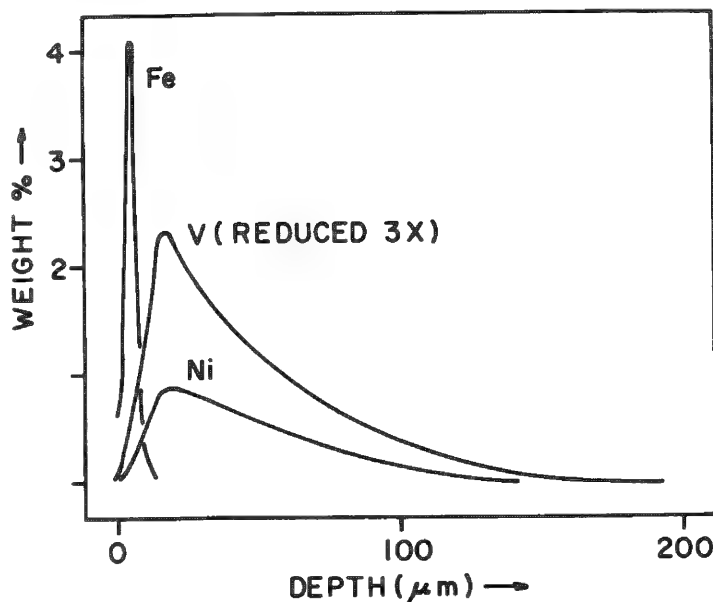


FIG. 1.--Schematic distribution of Fe, V, and Ni in outer layers of Co-Mo/Al<sub>2</sub>O<sub>3</sub> catalyst after 120 hr of use. Surface at zero of distance scale.

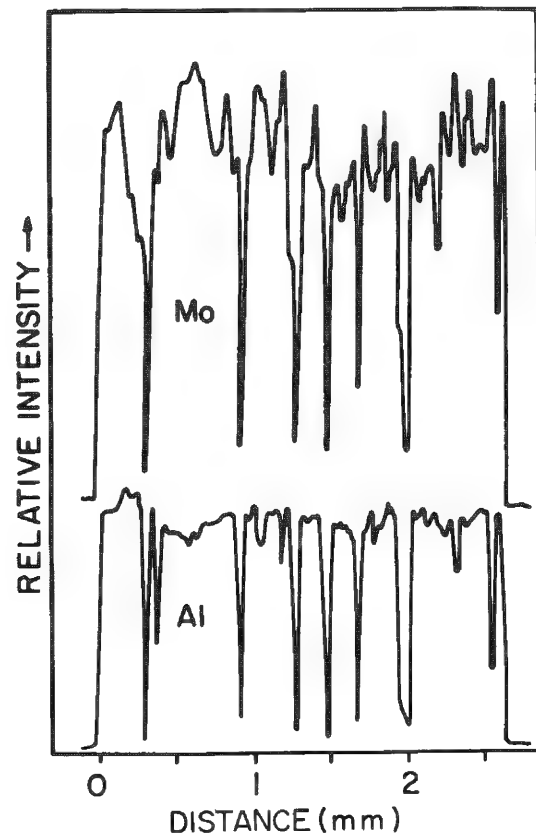


FIG. 2.--Elemental line profiles for Mo and Al across used catalyst extrudate.

The authors are at the Canada Centre for Mineral and Energy Technology (CANMET), Ottawa, Ontario, Canada. Crown copyright reserved.



greatly reduce its overall effectiveness. This behavior has led to the search for cheap and/or fouling resistant catalysts.

A variety of catalyst/substrate combinations were tested in the form of extrudate, which is quick and economical to produce. However, unlike conventional catalyst pellets, extrudates are often very fragile. Attempts to strengthen the extrudates by vacuum impregnation with epoxy resin met with limited success; frequently the resin had only penetrated the outermost layers of the extrudate.

Accordingly, a high-pressure method was devised for driving epoxy or any other fluid mounting medium into the catalyst at pressures reaching 100 MPa (circa 15 000 psi). A heavy-walled aluminum sample cup, 2.5 cm in diameter, with 3mm-thick walls, was used to hold the extrudate and resin. The resin is contained and pressurized via a 2.5mm-thick neoprene rubber washer by squeezing of the assembly in a metallurgical mounting press. Once the resin had cured, the base was turned down in a lathe and standard techniques were employed in preparing polished cross sections for microprobe analysis. Typical x-ray line profiles obtained from such samples are shown in Fig. 2. The sharp dips in the traces are due to drying cracks that traverse the material. The epoxy resin must absorb some of the generated x-ray intensity, but that is a slight effect and much more acceptable than the artifacts produced by a nonflat surface. When Sn-containing catalysts were examined for their activity, a notable sintering effect was observed in used catalyst samples.<sup>2</sup>

Figure 3 gives some indication of the reason. The cross section in Fig. 3a shows bright "metallic" precipitates along grain boundaries and cracks. The microprobe showed these to be Sn and S in equal atomic proportions. Figure 3b is an SEM micrograph of a broken extrudate, unfilled with resin. The crystals seen covering the old crack walls were shown with the EDXS system to be Sn- and S-rich. Evidently the Sn, originally highly dispersed, has been concentrated into these precipitates with a corresponding loss in active surface area.

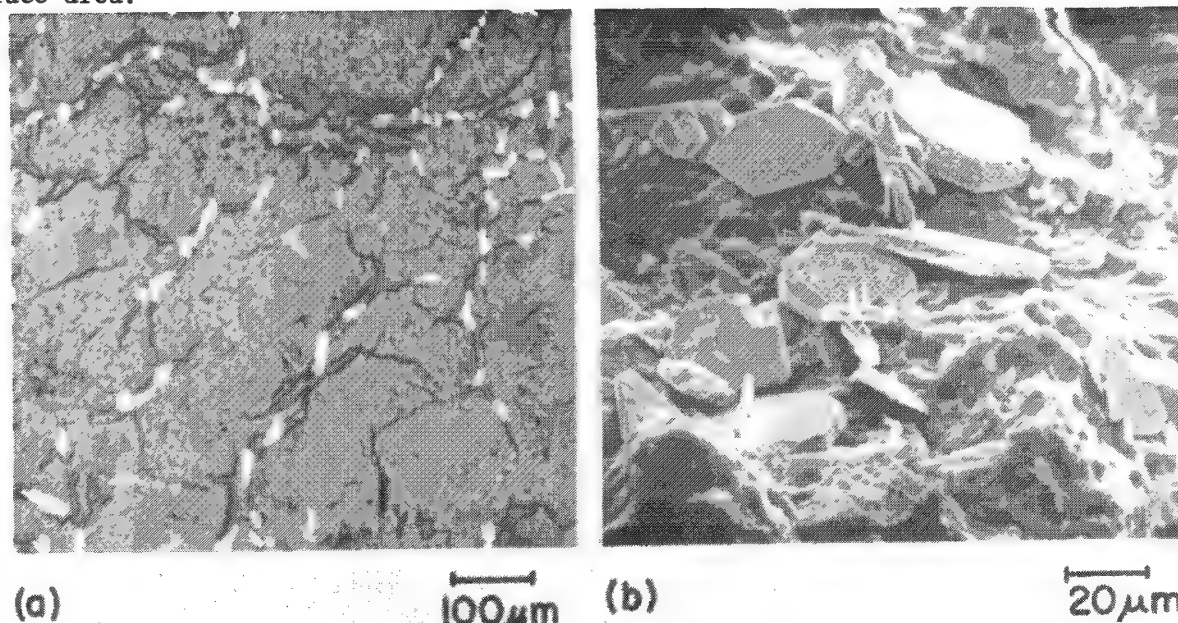


FIG. 3.--(a) Cross section through used Sn/Al<sub>2</sub>O<sub>3</sub> catalyst extrudate (epoxy impregnated). Bright regions are SnS. (b) SEM micrograph of broken section through used Sn/Al<sub>2</sub>O<sub>3</sub> catalyst extrudate. Crystals are SnS.

Work reported elsewhere has focused on the distribution of catalyst fouling agents as a function of mean pore size.<sup>3</sup>

#### *Thermal Hydrocracking*

During thermal hydrocracking, such as with the 1-barrel/day pilot plant at CANMET, it is very important to prevent the deposition of coke on vessel walls and lines. Such deposits can cause premature plant shutdown. During the course of a run, which may last up

to 21 days, a suspension of solids builds up in the reactor. To determine the role played by this material in the deposition of coke in the system one must identify the nature of these solids, which are separated by toluene extraction from liquid samples taken from the reactor during the run.

A sample of these deposits was prepared for examination by mixing with an equal volume of acrylic resin and polymerizing the mixture after it had been thoroughly stirred. Standard preparation techniques were used to obtain cross sections through the samples. X-ray mapping was used as a preliminary examination, followed by EDXS of typical particles and line traces across those thought to be most interesting. The EDXS spectra were quantified with our own computer program. Figure 4 shows a montage of x-ray maps together with an SEM micrograph. It is evident that V- and S-rich agglomerates are prominent. Hollow par-

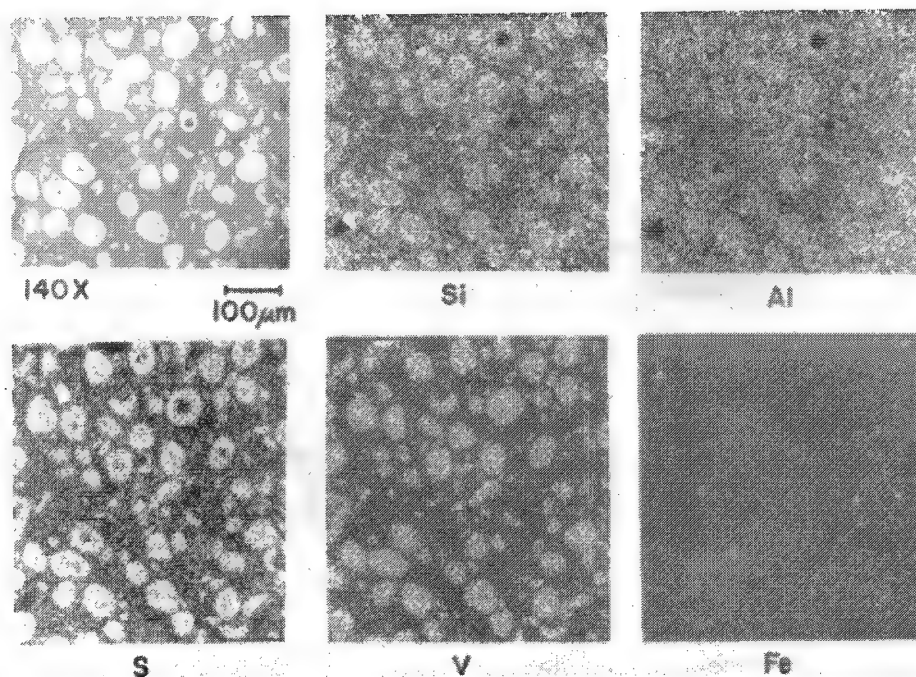


FIG. 4.--X-ray maps of toluene-insoluble particles found in CANMET thermal hydrocracking process.

ticles can be seen that probably contained loose agglomerations lost during polishing. Traces across particles with inclusions at their centers give line profiles like those seen in Fig. 5.

#### Acknowledgments

We should like to thank Mrs. V. E. Moore and Mr. V. C. Chartrand for their assistance in this work.

#### References

1. R. H. Packwood, M. Ternan, and B. I. Parsons, "A preliminary investigation of the fouling of catalyst pellets by residual oils and tars," *Proc. 11th MAS Conf.*, 1976, 55.
2. J. F. Kriz, K. Belinko, and B. N. Nandi, "The effect of tin catalysts on hydrotreating of Athabasca oil sand bitumen and coal hydrogenolysis," *Am. Chem. Soc., Div. Fuel Chem.*, Preprint 23(4), 72, 1978.
3. A. H. Hardin, R. H. Packwood, and M. Ternan, *Effects of Median Pore Diameters in Co-Mo/Al<sub>2</sub>O<sub>3</sub> catalysts on the conversion of Athabasca bitumen*, CANMET Report ERP/ERL 38-78 (J), 1978.

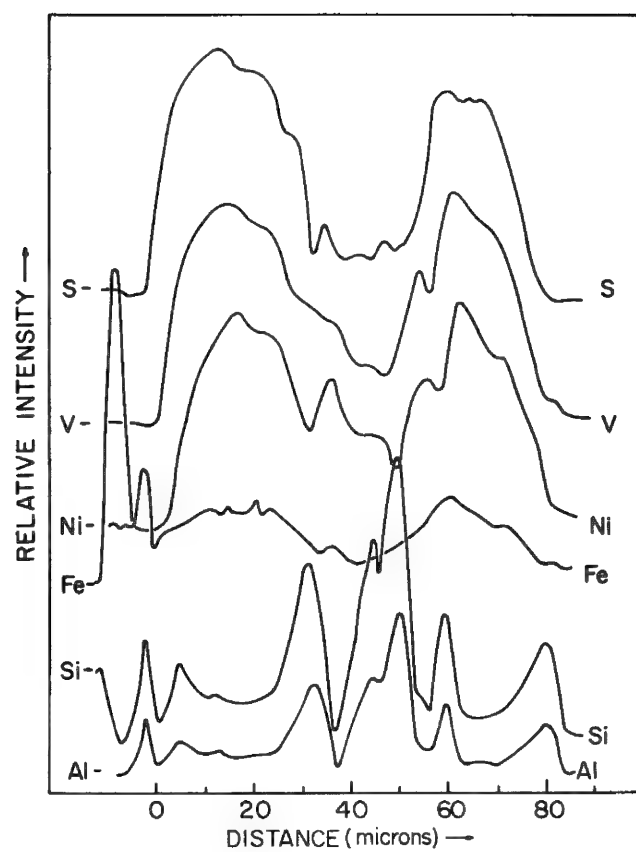


FIG. 5.--Elemental line profiles for V, Fe, Ni, Al, and Si through particles with included material seen in Fig. 4.

## MICROPROBE EXAMINATION OF NITROGEN AND OXYGEN CONTAMINATION IN ZIRCONIUM ALLOYS

J. E. Bohning

The examination of defects in metallic samples for nitrogen and/or oxygen content by microprobe analysis is often hampered by the usual problems encountered in quantitative probe analysis for these elements. Low peak intensities and low peak-to-background ratios are especially pronounced for light element (atomic number below 11) content levels in the range of 0.5 to 10.0 wt.%. Analyses for nitrogen and oxygen in hard spot defects in Zircaloy-4 have been successfully performed in our microprobe laboratory for several years. The techniques and equipment used are described in the following report along with the results of an analysis performed on a typical defect in Zircaloy-4.

The quality of analyses for nitrogen or oxygen is directly related to the physical characteristics of the spectrometer system and the chemical composition of the standards used. The microprobe used in our laboratory is a Hitachi XMA-5. The spectrometer used for nitrogen or oxygen analysis is equipped with a lead stearate pseudocrystal and a thin-window flow proportional detector. The detector gas used is argon-10% methane (P-10), flowing at approximately one-quarter of atmospheric pressure.

Standards used in the analysis of nitrogen or oxygen should be selected with care after consideration of the anticipated composition of the samples to be analyzed. Standards similar in composition to the samples analyzed have been found to be the best choice for the quantitative analysis of light elements.<sup>1</sup> The use of such standards minimizes atomic number, absorption, and fluorescence (ZAF) effects when x-ray intensity ratios of sample count rates to standard count rates are calculated for most light element characteristic lines. We have used ZrN as the standard for the analysis of nitrogen and ZrO<sub>2</sub> as the standard for the analysis of oxygen in zirconium alloys. We have found in the calculation of theoretical x-ray intensity ratios (k-values) for a variety of zirconium-tin-nitrogen compositions that the ZAF correction factors for the nitrogen K-alpha (NK $\alpha$ ) line are essentially constant for a range of nitrogen concentration from 0.5 to 13.3 wt.%. This finding confirms the statement made above about the minimization of ZAF effects for the analysis of nitrogen in zirconium alloys with ZrN used as the standard. The program used in these calculations was the HP-6 microprobe data-correction program written for use on small desk calculators.<sup>2</sup> This program is based on classical ZAF correction techniques.

Nitrogen has been found to be one of the primary sources of hard spot defects in Zircaloy-4. These areas are usually found in metallographic examination to be alpha-phase zirconium; regions of twinned structure are also occasionally detected. Microprobe examination of these defects is routinely performed for nitrogen, zirconium, and tin. Samples are prepared by typical metallographic techniques. The final polish is a light-attack polish with a solution of 8% HNO<sub>3</sub>, 1% HF, balance water and 0.05 $\mu$ m alumina polishing compound. Samples are cleaned in an ultrasonic bath prior to microprobe analysis. The standards used are ZrN for nitrogen and pure-element standards for zirconium and tin. Electron beam accelerating voltages used are usually in the range of 15.0 kV. A constant accelerating voltage is used in our laboratory for NK $\alpha$ , ZrL $\alpha$ , and SnL $\alpha$  microprobe analysis performed on the same sample, as our HP-6 correction program accepts only one accelerating voltage for each set of either k-values or true concentrations used as input. The problems of peak wavelength shifts with changes in composition and the presence of higher-order interference lines usually encountered in analyses for NK $\alpha$  x rays are found to be of little difficulty in zirconium alloys if spectrometer positioning and alignment, pulse height shaping, and gain selection are carefully performed prior to analysis. The problem of carbon contamination on the region of analysis due to decomposition of vacuum-pump oil va-

---

The author is with Teledyne Wah Chang Albany Corp., Box 460, Albany, OR 97321.

pors by electron bombardment is minimized by the taking of readings on a variety of positions in the defect area while keeping the number and duration of the readings to a statistically acceptable minimum. Unfortunately, we have found the cold-plate anticontamination device in our microprobe to have little or no effect on the rate of contamination buildup.

These techniques were used to analyze a defect in a Zircaloy-4 sample showing both the alpha-phase zirconium structure and the twinned structure typical of nitrogen contamination. The distributions of  $NK\alpha$  x-ray count-rate intensity  $I$  as a function of wavelength  $\lambda$  taken from ZrN, pure Zr, and a Zircaloy-2 standard (NBS SRM360a), and the matrix, alpha-phase, and twinned structure defects in the Zircaloy-4 sample are shown in Fig. 1. The readings were taken at 0.1 Å intervals for 50 sec each. Background levels can be determined by linear interpolation between positions at equal distances on either side of the line peak.<sup>3</sup> Owing to the lack of extreme curvature of the background levels seen on pure Zr and the SRM360a Zircaloy-2 standard, a correction for nonlinearity of the background is not necessary in this case. The well-defined  $NK\alpha$  peaks in both the alpha-phase defect grain and the twinned defect grain show the certain presence of nitrogen in each. The results of quantitative microprobe point analyses taken on the Zircaloy-4 sample matrix, alpha-phase defect grains, and twinned defect grains are given in Table 1 as calculated weight % concentrations of N, Zr, and Sn. These values were calculated from k-values

TABLE 1.--Calculated weight % concentrations of nitrogen, zirconium, and tin in the Zircaloy-4 sample matrix, alpha-phase grains, and twinned structure grains.

Region of Analysis	C, %		
	N	Zr	Sn
Matrix	--	98.4	1.55
Alpha Phase Grains	2.73	97.1	0.21
Twinned Grains	7.90	92.1	--

by means of the HP-6 data-correction program mentioned above. The analyses were performed at an accelerating voltage of 13.4 kV, an electron beam diameter of less than 2  $\mu$ m, and a counting time of 50 sec per reading with four readings taken on each standard and sample area.

The ability to obtain accurate and reliable results in the microprobe analysis of nitrogen in zirconium has been shown here. Similar techniques can be used for oxygen or other light-element microprobe analyses in zirconium with comparable levels success in most cases.

#### References

1. J. I. Goldstein et al., *Practical Scanning Electron Microscopy*, New York: Plenum Press, 1977, 3d ed., 437.
2. M. P. Krug and P. A. Romans, private communication.
3. A. J. Mardinly and W. C. Bigelow, "Accurate quantitative analysis of oxy-nitrides using Sialon as a standard," *Proc. 12th MAS Conf.*, 1977, 155B.

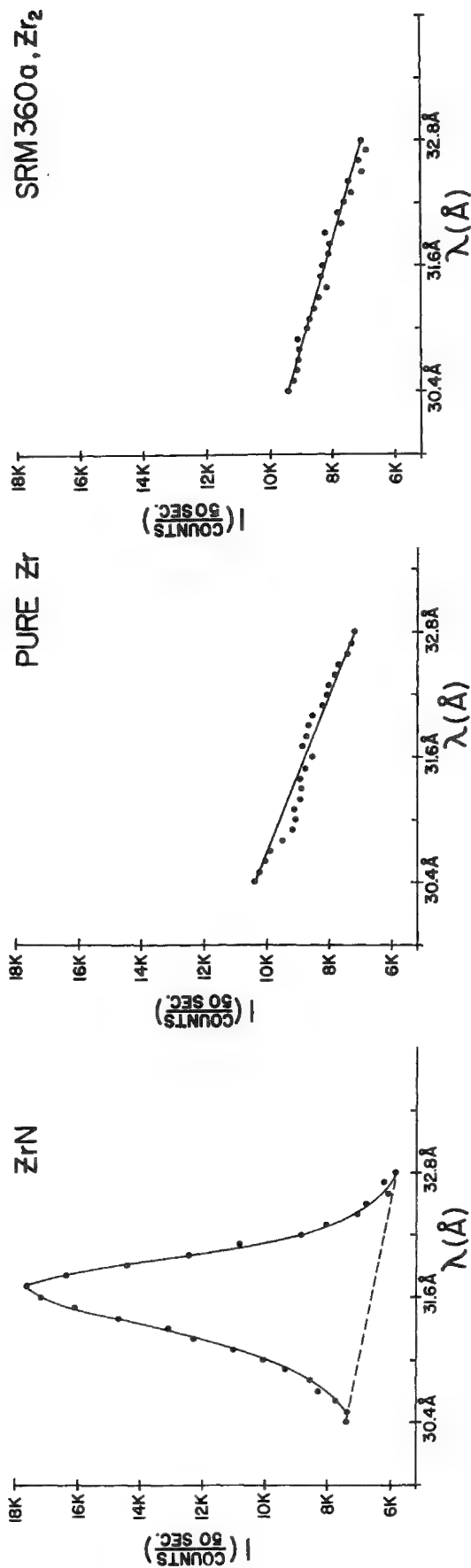


FIG. 1.--Total x-ray intensity vs  $\lambda$  at 0.1Å intervals over N K $\alpha$  x-ray spectral region on ZrN standard.

FIG. 2.--Total x-ray intensity vs  $\lambda$  at 0.1Å intervals over N K $\alpha$  x-ray spectral region on pure Zr standard.

FIG. 3.--Total x-ray intensity vs  $\lambda$  at 0.1Å intervals over N K $\alpha$  x-ray spectral region on Zircaloy-2 standard NBS SRM360a.

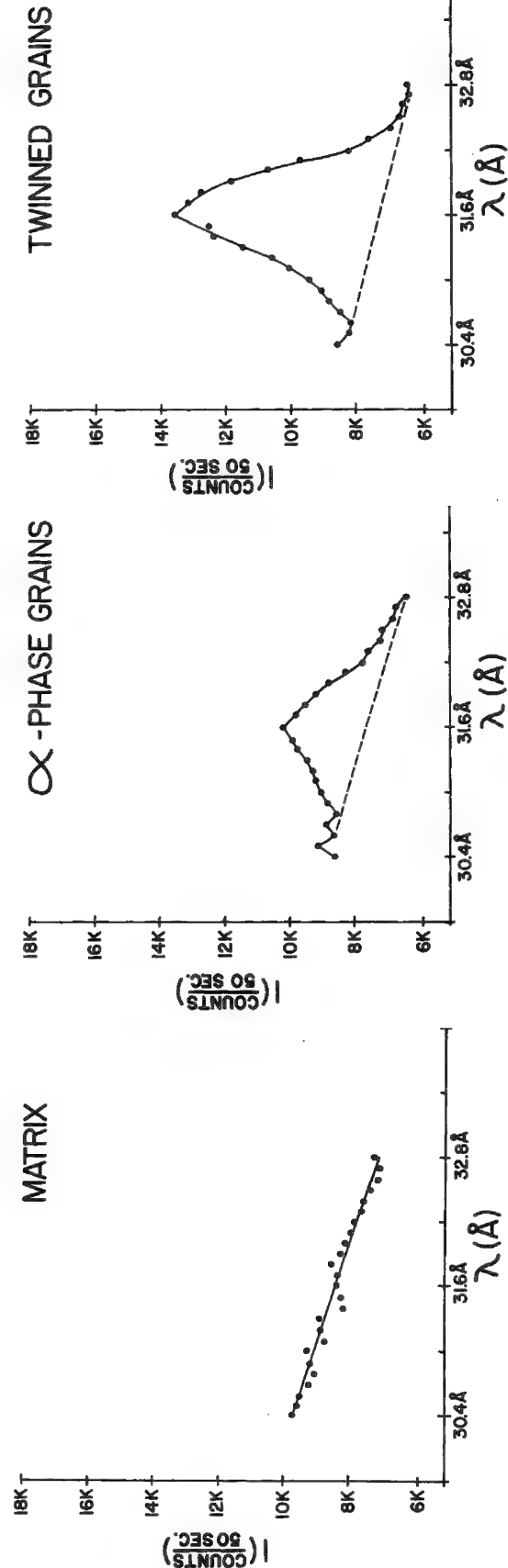


FIG. 4.--Total x-ray intensity vs  $\lambda$  at 0.1Å intervals over N K $\alpha$  x-ray spectral region on Zircaloy-4 sample matrix.

FIG. 5.--Total x-ray intensity vs  $\lambda$  at 0.1Å intervals over N K $\alpha$  x-ray spectral region on Zircaloy-4 sample alpha phase defect grain.

FIG. 6.--Total x-ray intensity vs  $\lambda$  at 0.1Å intervals over N K $\alpha$  x-ray spectral region on Zircaloy-4 sample twinned structure defect grain.

## Analytical Electron Microscopy

### MULTIPLE SCATTERING OF FAST ELECTRONS IN THIN SPECIMENS

Peter Rez

Multiple scattering of fast (0.1-3MeV) electrons in transmission electron microscopy has important consequences for various aspects of microanalysis. The multiple scattering in the energy loss spectrum can have effects on edge visibility and quantitative results. The spreading of the beam due to multiple scattering is important for determining the spatial resolution of x-ray microanalysis.<sup>1-3</sup> The aim of this paper is to show that one can take all these effects into consideration by solving the transport equation assuming small angle scattering. If diffraction and all coherent scattering phenomena are ignored (not a good assumption for transmission microscopy but implicit in any Monte Carlo treatment), the behavior of the electrons in the solid is governed by the Boltzmann equation with the appropriate boundary conditions:

$$v_z \frac{df}{dz} + v_x \frac{df}{dx} + v_y \frac{df}{dy} = \int \sigma'(v, v') f(v', r) d^3 v' - \int \sigma'(v', v) f(v, r) d^3 v' \quad (1)$$

where  $f(v, r)$  is the probability of finding an electron traveling with velocity  $v$  at position  $r$ . In transmission microscopy, the scattering angles and energy losses are small compared to the incident beam energy. Equation (1) can be rewritten as

$$\frac{df}{dz} + \theta_x \frac{df}{dx} + \theta_y \frac{df}{dy} = \int \sigma(\theta - \theta', E - E') f(\theta', E') d^2 \theta' dE' - \int \sigma'(\theta' - \theta, E' - E) f(\theta, E) d^2 \theta' dE' \quad (2)$$

where  $\theta$  is a scattering angle and  $E$  is the electron energy; the  $z$  direction is normal to the specimen. As in all transport equations the first term on the right represents scattering into a given state from all other states (a state refers to a velocity, i.e., a given energy and direction of motion), whereas the second term represents scattering from a given state to all other states, and can be thought of as an "absorption." If spatial variation is neglected, the equation is much simplified:

$$f(\theta, E, t) = \exp(-\mu t) \text{FT}^{-1}[\exp\{\text{FT}[\sigma(\theta, E)]t\} \text{FT}[f_0(\theta, E)]] \quad (3)$$

where  $\mu = \int \sigma(\theta, E) d^2 \theta dE$ ,  $t$  is the specimen thickness, and FT denotes Fourier transformation. Effects of beam tilt or divergent incident beams are included in the incident beam distribution  $f_0(\theta, E)$ . If only the energy variation is of interest then a one-dimensional Fourier transform is sufficient. For the angle scattering the cylindrical symmetry can be used and a Bessel transform replaces the double Fourier transform.<sup>4</sup> These equations can be inverted to give single scattering profiles.<sup>5-7</sup> We can handle the spatial variation in a straightforward manner by taking the Fourier transform with respect to  $x$  and  $y$ . The solution, when the energy variation is neglected, is given by<sup>8,9</sup>

$$f(r, \theta, t) = \text{FT}^{-1}\{\exp[-\int_0^t \{\mu - [\sigma(\tilde{\theta} + z\tilde{R})]dz\}] f_0(\tilde{R}, \tilde{\theta})\} \quad (4)$$

where the variables  $\tilde{R}$  and  $\tilde{\theta}$  are defined from the Fourier transforms

$$f(\tilde{R}, \tilde{\theta}) = \iint f(r, \theta) \exp(ir\tilde{R}) \exp(i\theta\tilde{\theta}) \quad (5)$$

If only a projection along one axis is required then the solution is required then the solution is that given by Snyder and Scott.<sup>10</sup> The form of the cross section for the in-



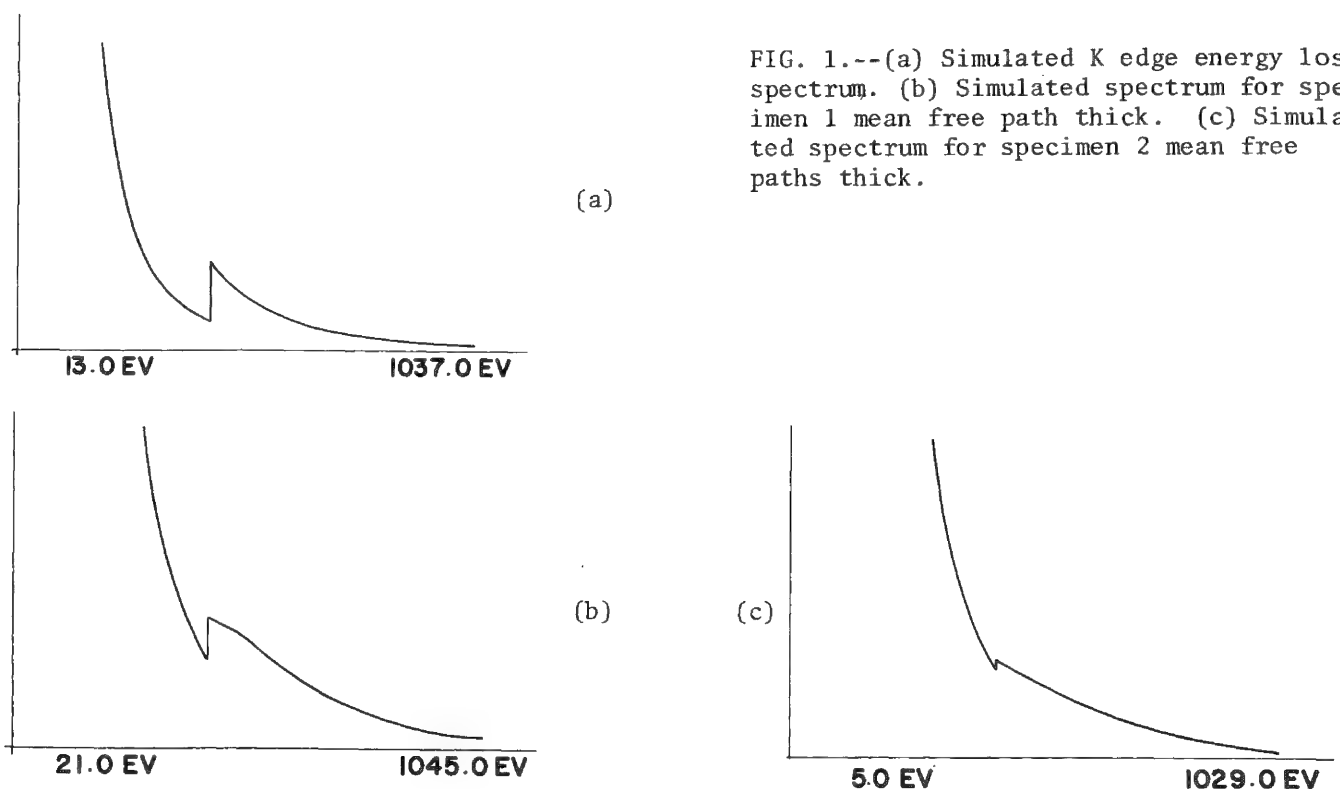
elastic scattering is not well characterized so a spectrum of the form  $1/[E^3 + 1.25 \times 10^5]$  was chosen with an edge at 300 eV. Figure 1 shows the effect of multiple scattering on the edge for thickness of one and two inelastic mean free paths. The gradient after the edge changes and the edge gets weaker, almost disappearing for a crystal two-mean free paths thick. Any quantitative procedure based on the correction of Isaacson and Johnson<sup>11</sup> would give divergent answers for these cases. For elastic scattering a cross section based on the electron scattering factor (as defined by the Mott formula) should be used.

$$\sigma(\theta) = p \left[ \frac{e^2}{4\pi\epsilon_0} \right]^2 \frac{[Z - f_x(\theta)]^2}{E_0^4 \theta^4} \quad (6)$$

where  $p$  is the density,  $E_0$  the electron energy, and  $f_x(\theta)$  the x-ray scattering factor. In the limit of large scattering angle the cross section becomes the same as the Rutherford cross section. For small angles any screening is properly treated as the electron charge density is incorporated in the x-ray scattering factor. Results show the effect of multiple scattering on beam broadening and angular distribution of transmitted electrons.

### References

1. D. Kyser and R. Geiss, *Proc. 12th MAS Conf.*, paper 110, 1977.
2. R. G. Faulkner and K. Norrgard, *X-Ray Spectrometry* 7, 148, 1971.
3. D. E. Newbury and R. L. Myklebust, *Anal. Elect. Micros. Conf.* Cornell, 130, 1978.
4. W. T. Scott., *Rev. Mod. Phys.* 35, 231, 1963.
5. P. E. Batson, Ph.D Thesis, Cornell University, 1976.
6. D. W. Johnson and J. C. H. Spence, *J. Phys.* [D]1, 771, 1976.
7. J. C. H. Spence, *Ultramicroscopy*, (to be published).
8. H. Rose, *Ultramicroscopy* 1, 167, 1978.
9. T. Groves, *Ultramicroscopy* 1, 15, 1975.
10. H. S. Snyder and W. T. Scott, *Phys. Rev.* 76, 220, 1949.
11. M. Isaacson and D. E. Johnson, *Ultramicroscopy* 1, 33, 1975.



# DETERMINATION OF CLIFF-LORIMER $k$ CALIBRATION FACTORS FOR THIN-FOIL X-RAY MICROANALYSIS OF Na, Mg, AND Al IN THE STEM

Sudhir Mehta, J. I. Goldstein, D. B. Williams, and A. D. Romig Jr.

## Introduction

In the scanning transmission electron microscope (STEM) quantitative x-ray microanalysis can be performed if the specimen satisfies the thin-film criterion proposed by Cliff and Lorimer.<sup>1</sup> This criterion states that if primary x rays are neither absorbed nor cause x ray fluorescence, a simple ratio technique may be used for quantitation. The ratio technique uses the expression

$$\frac{C_A}{C_B} = k_{AB} \frac{I_A}{I_B} \quad (1)$$

where  $I_A$  and  $I_B$  are the simultaneously measured characteristic x-ray intensities, and  $C_A$  and  $C_B$  are the weight fractions of two elements A and B in the thin film. The constant  $k_{AB}$  can be experimentally determined from thin-film standards or it can be theoretically derived from expressions that consider x-ray production in thin film and appropriate characteristics of EDS detector.<sup>2</sup> The constant  $k_{AB}$  varies with operating voltage but is independent of sample thickness and composition as long as the thin-film criterion is satisfied.

Using an EMMA-4 instrument at 100kV operating voltage with specimen normal to the electron beam and x-ray detector placed at a take-off angle of 45°, Cliff and Lorimer<sup>1</sup> experimentally determined values of  $k_{AB}$  for a series of elements A, relative to Si. These values are compared with calculated  $k$  values of Goldstein et al.<sup>2</sup> in Fig. 1. The calculated val-

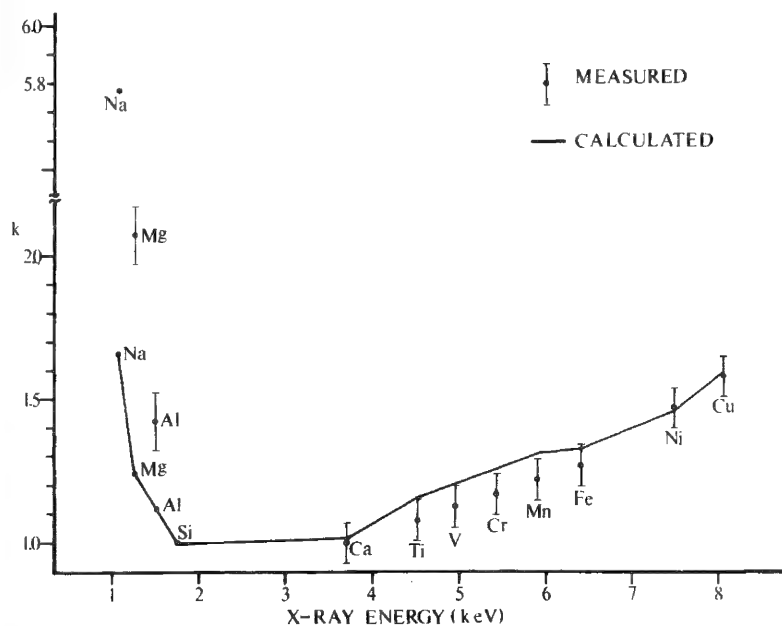


FIG. 1.--Calculated and experimentally measured  $k$  values at 100 kV as function of energy of the  $k_{\alpha}$  lines. (Error limits for measured Na  $k$  value were not reported.) Solid curve represents calculated  $k$  values.

The authors are affiliated with the Department of Metallurgy and Materials Engineering of Lehigh University in Bethlehem, PA 18015. This work was supported by NASA Grant NGR 39-007-056.

ues appear to fit the experimental values best above x-ray energies of 1.7 keV. However, for elements whose characteristic x-ray energies are less than 1.6 keV, e.g., Na, Mg, and Al, the fit is poor. Lorimer et al.<sup>3</sup> report newly measured k values for Na, Mg, and Al that are lower than the original values; nonetheless, the new values are significantly higher than the calculated values (Table 1), and no explanation was proposed to account for the differences. Zaluzec and Fraser<sup>4</sup> have shown that absorption of generated x-rays

TABLE 1.--Comparison of the calculated k values of Goldstein et al.<sup>2</sup> with the measured k values of Cliff and Lorimer<sup>1</sup> and Lorimer et al.,<sup>3</sup> 100 kV.

Element	Calculated k Value (Goldstein et al. <sup>2</sup> )	Measured k Value (Cliff and Lorimer <sup>1</sup> )	Measured k Value (Lorimer et al. <sup>3</sup> )
Na	1.66	5.77	3.2
Mg	1.25	2.07	1.6
Al	1.12	1.42	1.2

due to carbon accumulation on the specimen during the analysis can have a significant effect on the characteristic x-ray intensity ratio. This effect could also explain the differences between the calculated and the measured k values. The present paper presents the results of a study aimed at understanding this discrepancy by remeasuring Na, Mg, and Al k values in an instrument different from the EMMA-4 (namely the Philips EM300 TEM/STEM) as a function of surface contamination, specimen absorption, and detector variables.

#### *Experimental Procedure*

The calibration factors, simply termed k values, were determined by measurement of the ratio of the  $k_{\alpha}$  radiation from Na, Mg, and Al relative to Si from three well-characterized mineral samples, namely Albite Na [AlSi<sub>3</sub>O<sub>8</sub>], orthoclase K [AlSi<sub>3</sub>O<sub>8</sub>], and Forsterite [Mg<sub>2</sub>SiO<sub>4</sub>]. For each element X the expression

$$k_X = \frac{C_X}{C_{Si}} \frac{I_{Si}}{I_X} \quad (2)$$

was used. The mineral samples were crushed under methanol and the slurry containing very fine particles was allowed to evaporate on formvar/carbon-coated beryllium microscope grids. The samples were subsequently coated with approximately 30 nm of carbon to prevent charge buildup under the electron beam.

The x-ray microanalysis was performed by means of an NSI rear-entry retractable Si(Li) detector interfaced to a Tracor Northern NS 880 computer-controlled system. Specially designed condenser apertures were inserted in the microscope column to minimize any spurious x-ray contribution to the detected spectrum.<sup>5</sup> The specimens were held in a beryllium "low background" holder to minimize background x-ray emission from specimen-generated bremsstrahlung. X-ray count rate from the specimen was optimized by tilting the specimen through 36° towards the detector. Point analyses using an electron beam spot size of about 32 nm at 100kV operating voltage and at 10, 60, and 120sec counting times were carried out on thin edges of crushed samples. The thickness of these edges, determined by measuring the relative separation of the carbon contamination marks on the upper and lower surfaces of the foil<sup>6</sup> when tilted back through 36°, ranged from 150 to 250 nm. The determination of peak areas above continuum background was done using Tracor Northern's Super ML (Multiple Least Squares) program.<sup>7</sup> This program uses the principle of least squares to fit the experimental data to a number of model functions, one for each peak, obtained from a reference standard under identical excitation condition, i.e., beam intensity, take-off angle, and excitation energy. We obtained Na, Mg, Al, and Si peak intensities in the complex mineral spectra by performing a ML fit to "pseudo-pure-element" Na, Mg, Al, and Si thin-film reference spectra acquired from reagent grade Na<sub>2</sub>CO<sub>3</sub>, MgO, Al<sub>2</sub>O<sub>3</sub>, and SiO<sub>2</sub>. Since Na, Mg, Al, and Si spectral lines are closely spaced and occur in the low-energy region of the spectrum, where the underlying background changes rapidly with energy, special diagnostic commands in the program

were used to test the performance of the ML fit in determining the peak intensities.

## Results

TABLE 2.--Measured k values as function of x-ray counting time, 100 kV.

Element	X-ray Counting Time (sec)		
	10	60	120
Na	3.4	4.3	5.6
Mg	1.48	1.53	1.58
Al	1.25	1.32	1.34

Table 2 shows the results of k value measurements for Na, Mg, and Al as a function of x-ray counting time. The average error in these values is about  $\pm 5\%$ , derived from the uncertainty in  $I_X/I_{Si}$  intensity ratio computed by the ML program.

With an increase in x-ray counting time a nonlinear increase in k values was observed. The change was most noticeable in the case of Na, whose k value increased from 3.4 to 5.6 (a 65% increase) for a corresponding increase in counting time from 10 to 120 sec; however, Mg and Al k values increased from 1.48 to 1.58 and from 1.25 to 1.34, respectively (a 7% increase) when x-ray counting time was increased from 10 to 120 sec.

## Discussion

1. *Experimental and Theoretical k Factors.* The experimental k factors may be compared with those determined theoretically by Goldstein et al.<sup>2</sup> from the equation

$$k_{XSi} = \frac{A_X(Q_K \omega_K a)_{Si} e^{-\mu/\rho|_{Be}^{Si} \rho Y}}{A_{Si}(Q_K \omega_K a)_X e^{-\mu/\rho|_{Be}^X \rho Y}} \quad (3)$$

where  $A_X$  and  $A_{Si}$  are atomic weights,  $Q_K$  is the Green and Cosslett<sup>8</sup> value of the k shell ionization cross section,  $\omega_K$  is the fluorescence yield,  $a$  is the  $K_\alpha/(K_\alpha + K_\beta)$  ratio and  $\mu/\rho|_{Be}^{Si}$  and  $\mu/\rho|_{Be}^X$  are the mass absorption coefficients of Si and the element X in the Be window of the detector,  $\rho$  is the density, and  $Y$  is the thickness of the Be window. Since window absorption is particularly significant for elements of low atomic number, Goldstein et al.<sup>2</sup> calculated the k values for Na, Mg, and Al after taking into consideration the absorption of their characteristic x-rays by 7.5  $\mu$ m-thick Be window of the EDS detector. (The Be window thickness of most EDS units is  $7.5 \pm 3 \mu$ m). When these values are compared with 10sec x-ray counting time measured values of Table 3, it is apparent that the measured values are significantly higher than the calculated values. (The 10-sec measured k values

TABLE 3.--Comparison of calculated k values of Goldstein et al.<sup>2</sup> with 10sec measured k values, 100 kV.

Element	Calculated k value (Goldstein et al. <sup>2</sup> )	Measured k value (10 sec, 100 kV)
Na	1.66	3.4
Mg	1.25	1.48
Al	1.12	1.25

were chosen for comparison because they are least affected by surface carbon contamination and therefore represent the best measured values.) The cause of discrepancy between the measured and the calculated values is clearly not entirely one of window absorption, but it also depends on factors such as (1) the uncertainty in fluorescence yield and ionization cross section values in Eq. (3); (2) lack of precise information on Be window thick-

ness, needed to determine the exact amount of window absorption; (3) absorption due to carbon buildup on the sample and the Be window; and (4) absorption within the specimen itself.

2. *Absorption Effects.* (a) Surface Contamination. The increases observed in the measured k values of Na, Mg, and Al with longer x-ray counting time (Table 2) is attributed mainly to the absorption of low energy x-rays within carbon contamination layer which accumulates on the sample as a function of time. From the expression<sup>9</sup>

$$k_A' = k_A \frac{e^{-\mu/\rho|_C^{Si} \rho_c X}}{e^{-\mu/\rho|_C^A \rho_c X}} \quad (4)$$

where  $k_A'$  and  $k_A$  represent 120sec and 10sec counting time measured values,  $\rho_c$  is the density of the carbon contamination film,  $X$  is the x-ray path length through the carbon film, and  $\mu/\rho|_C^A$  is the mass absorption coefficient for element A in carbon, the thickness  $X$  of a carbon contamination layer that would give rise to the increased k value was calculated. The results indicate that a 500nm buildup of surface carbon per 60sec x-ray counting time would give rise to the observed changes in Mg and Al k values. However, it would require a 2 $\mu$ m layer of surface carbon contamination to reconcile the increase in the Na k value. Actual observations of carbon contamination spots in the microscope indicate that the carbon layer is no more than 500 nm thick after 60 sec of counting time. It would therefore appear that in the case of Na other factors besides surface carbon contamination could affect the analysis, such as operating voltage, beam intensity, absorption both in the Be window of the ED detector and within the sample, and mass volatilization.

(b) Specimen Absorption. Degradation of measured k values by absorption within the specimen for Na, Mg, and Al x rays relative to Si x rays was calculated from the modified thin-film criterion proposed by Goldstein et al.<sup>2</sup> This criterion states that for any set of two elements A and B considered in the ratio method the absolute value of  $(x_B - x_A) \rho t/2 < 0.1$  or an absorption correction is necessary. The term  $x_A$  is equal to  $\mu/\rho|_{Spec}^A \csc \alpha$  where  $\mu/\rho|_{Spec}^A$  is the mass absorption coefficient for the characteristic x ray of element A in specimen composed of elements A, B, C..., and  $\alpha$  is the angle between the specimen and the X-ray detector,  $\rho$  is the specimen density, and  $t$  is the x-ray path length through the specimen thickness.

The results of these calculations show that for a specimen foil thickness of up to 500 nm the Mg and Al x rays are absorbed almost to the same extent as the Si x rays and hence the intensity ratios with Si remain unaffected, causing no significant differences in their k values. In the case of Na, however, a specimen-induced absorption correction is needed for  $I_{Na}/I_{Si}$  intensity ratio for a foil thickness greater than 250 nm. It may be pertinent to note that even when a good image is apparent in TEM-STEM, the thin film criterion for accurate analysis, may not be satisfied.

(c) Detector Variables. If in Eq. (3) the thickness of Be window is changed from 7.5 to 12  $\mu$ m, the newly calculated k values for Mg and Al are in excellent agreement with the 10-sec measured k values (Table 4), but the Na k value is still considerably lower than the

TABLE 4.--Calculated k values as function of Be window thickness compared with 10sec measured k values, 100 kV.

Element	Calculated k Value (Goldstein et al. <sup>2</sup> ) 7.5 $\mu$ m Be window	Calculated k value 12.0 $\mu$ m Be window	Measured k value (10 sec, 100 kV)
Na	1.66	2.17	3.4
Mg	1.25	1.42	1.48
Al	1.12	1.18	1.25

measured value. However, if the window thickness was actually 7.5  $\mu\text{m}$ , then using Eqn. (4) it can be calculated that absorption by 2-3  $\mu\text{m}$  of carbon buildup on the Be window can also cause the observed differences in the measured and the calculated k values. Since the EDS detectors are always kept at the liquid  $\text{N}_2$  temperature, it is possible that the Be window of the detector acts as a getter of carbon contamination, which in time can build up sufficiently to cause significant absorption of the light-element x rays.

### Conclusion

Analyses of Na, Mg, and Al in thin foils present special problems because their characteristic x rays are easily absorbed. It has been shown that absorption in (1) the Be window of the EDS detector, (2) carbon buildup on the Be window, and (3) surface carbon contamination layer can cause significant differences between the measured and the calculated k values. The calculated values, on the other hand, could be erroneous if in Eq. (3) parameters such as exact Be window thickness, fluorescence yield, and ionization cross section for element X are not accurately known. It is therefore recommended that k values for Na, Mg, and Al should be calibrated for a specific instrument, and it may not be surprising if we find that the values differ for different instruments.

### References

1. G. Cliff and G. W. Lorimer, "The quantitative analysis of thin specimens," *J. Microscopy* 103: 203, 1975.
2. J. I. Goldstein et al., "Quantitative x-ray analysis in the electron microscope," O. Johari, Ed., *SEM/1977*, Chicago: IITRI, 1977, 315.
3. G. W. Lorimer, S. A. Al-Salman, and G. Cliff, "The quantitative analysis of thin specimens: Effects of absorption, fluorescence, and beam spreading," in D. L. Misell, Ed., *Developments in Electron Microscopy and Analysis*, Inst. Phys. Conf. Ser. No. 36, The Institute of Physics, 1977, 369.
4. N. J. Zaluzec and H. L. Fraser, "On the effects of contamination in x-ray microanalysis," *Analytical Electron Microscopy, Report of a Specialist Workshop*, Ithaca, N.Y.: Cornell University, 1978, 122.
5. J. I. Goldstein and D. B. Williams, "Spurious x-rays produced in the scanning electron microscope," O. Johari, Ed., *SEM/1978/I*, O'Hare, Ill.: SEM Inc., 1978, 427.
6. G. W. Lorimer, G. Cliff, and J. N. Clark, "Determination of the thickness and spatial resolution for the quantitative analysis of thin foils," in J. A. Venables, Ed., *Developments in Electron Microscopy and Analysis, EMAG 75*, London: Academic Press, 1976, 153.
7. F. H. Schamber, "A new technique for deconvolution of complex x-ray energy spectra," *Proc. 8th Nat. Conf. on Electron Probe Analysis*, 1973, 85A.
8. M. Green and V. E. Cosslett, "The efficiency of production of characteristic x-radiation in thick targets of a pure element," *Proc. Phys. Soc.* 78: 1206, 1961.
9. J. I. Goldstein, "Principles of thin film x-ray microanalysis," in J. J. Hren, D. C. Joy, and J. I. Goldstein, Eds., *Principles of Analytical Electron Microscopy*, New York: Plenum Press, 1979.

## DETECTABILITY LIMIT AND SPATIAL RESOLUTION IN STEM X-RAY ANALYSIS: APPLICATION TO Fe-Ni ALLOYS

A. D. Romig Jr. and J. I. Goldstein

When performing x-ray analysis of thin films in the scanning transmission electron microscope (STEM) one must be aware of the limiting factors of spatial resolution and analytical sensitivities or detectability limits. A series of experiments were undertaken to determine detectability limits and spatial resolution in a "typical" metallurgical thin film of an FeNi alloy. This study was performed on a first-generation Philips 300 TEM/ST (transmission electron microscope/scanning transmission electron microscope) equipped with a rear entry NSI-EDS detector. The sensitivity limits are a function of several variables. One group of variables is instrument dependent and includes the efficiency and collection configuration of the x-ray detector, the spurious x-ray counts, the current in the primary electron beam, and the contamination characteristics of the microscope. The last variable directly limits the total time one can collect x-rays from a given point. These variables have been optimized in our instrument. The second group of variables includes the electron probe size, foil thickness, and number of repetitions of the analysis, all of which can be controlled by the experimenter.

### *Spatial Resolution*

The spatial resolution for x-ray analysis in a thin foil is a function of atomic number, specimen thickness, and accelerating voltage. Goldstein et al.<sup>1</sup> have estimated the effective beam broadening  $b$  by assuming that scattering takes place at the center of the thin film, that the dominant process causing beam spreading is elastic scattering by atomic nuclei, and that the electron beam is a point source. This development yields an equation for broadening:

$$b = 625 \frac{Z}{E_0} \sqrt{\rho/A} t^{3/2} \quad (1)$$

where  $b$  is in cm,  $Z$  is the atomic number,  $A$  is the atomic weight,  $E_0$  is in keV,  $\rho$  is in g/cm<sup>3</sup>, and  $t$  is the film thickness in cm. The broadening varies inversely as  $E_0$  and increases with film thickness. For example, in a pure Fe foil  $b$  equals approximately 190, 350, and 540 Å for foils 1000, 1500, and 2000 Å thick, respectively. The broadening equation assumes the electron beam impinges the sample at a point. The beam is not a point probe; it has a finite diameter. Hence, the total x-ray spatial resolution is approximately equal to the sum of the broadening  $b$  and the size of the electron beam  $d$  impinging on the sample.

Monte Carlo calculations of beam broadening have been performed by Kyser and Geiss.<sup>2</sup> These calculations should be expected to provide the best estimates because they include such effects as the electron beam size, electron back scattering, multiple scattering, etc. In general, the relatively good agreement between the results of the simple scattering model and the Monte Carlo model tend to validate Eq. (1).

Few experimental measurements of x-ray resolution are available in the literature. One of the most successful methods used in electron probe microanalysis (EPMA) is to move the electron beam point by point across an interface between two phases, which shows a concentration discontinuity.<sup>3</sup> The finite volume from which x-rays are excited in a sample causes the true concentration profile to appear "smeared." One can determine the width of the x-ray excitation region by drawing a tangent to the measured concentration profile at the midpoint of the discontinuity and measuring the intercept on the distance axis at

---

The authors are with the Department of Metallurgy and Materials Engineering, Lehigh University, Bethlehem, Pa. This research was supported by NSF contract EAR74-22518-A01.



the composition of each phase.

In the STEM the foil must be tilted so that the  $\alpha/\gamma$  interface is parallel to the incident electron beam. If one phase overlays another, it would be impossible to determine the interface compositions accurately. Figure 1 shows a typical  $\alpha + \gamma$  assemblage in a Fe-34.7 Ni alloy. This is the ideal structure for measuring concentration profiles with STEM techniques.

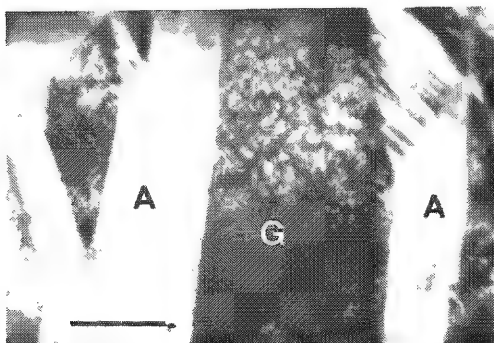
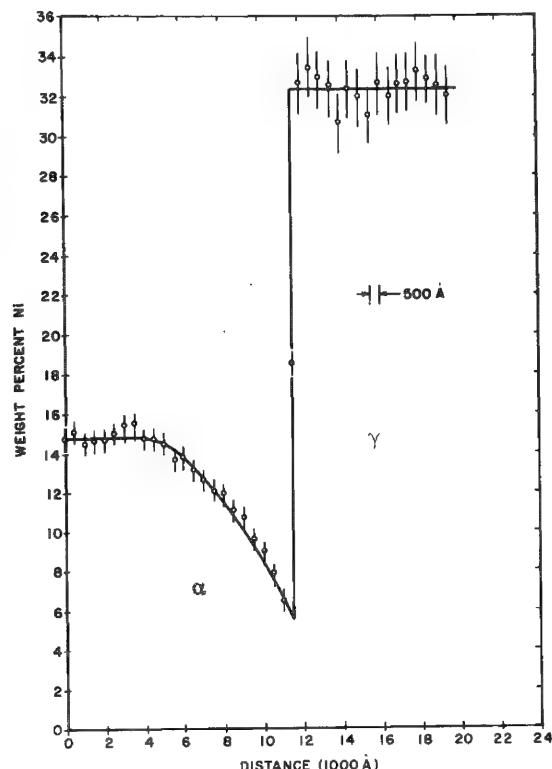


FIG. 1.--TEM micrograph of  $\alpha/\gamma$  structure in Fe-34.7wt%Ni alloy: A-- $\alpha$ (bcc), G-- $\gamma$ (fcc), scale bar = 1  $\mu\text{m}$  (10 000  $\text{\AA}$ ).

FIG. 2.--Ni profile across an  $\alpha/\gamma$  interface in Fe-14.7wt%Ni alloy.



A concentration profile measured in 500 $\text{\AA}$  steps across a two phase interface of  $\alpha$  and  $\gamma$  in a 14.7 wt%Ni-Fe alloy heat treated at 500 $^{\circ}\text{C}$  for 127 days is shown in Fig. 2. Contamination prevented smaller steps from being used. The operating conditions are 100 kV with a 200 $\text{\AA}$ -dia. electron beam. The foil is about 1500  $\text{\AA}$  thick. The total width of the x-ray excitation measured from Fig. 2 is about 500  $\text{\AA}$ . Several other investigators have reported similar spatial resolutions in other ferrous alloy systems. Table 1 summarizes the experimental data currently available. The validity of Eq. (1) is demonstrated by these experimental data.

#### Detectability Limits

One determines the detectability limit ( $C_{DL}$ ) for a given element in a sample of interest by collecting the appropriate data from the sample thin foil. The analysis requirement is to detect significant differences between the intensity of the element of interest and the continuum background generated in the sample. For the detection of Ni in an FeNi alloy<sup>3</sup> the peak intensity  $I_{Ni}$  is significantly larger than the background  $I_{Ni}^b$  when

$$I_{Ni} - I_{Ni}^b \geq 3 (2I_{Ni}^b)^{1/2} \quad (2)$$

This x-ray count criterion for detectability limit ( $C_{DL}$ ) can be converted to wt% using the Cliff-Lorimer thin foil equation<sup>9</sup>

$$\frac{C_{Fe}}{C_{Ni}} = k_{FeNi} \frac{I_{Fe}}{I_{Ni}} \quad (3)$$

TABLE 1.--Selected summary of calculated and measured x-ray resolution for ferrous materials.

Reference	System	Foil Thickness (Å)	E <sub>o</sub> (kV)	Beam Size d(Å)	Spatial Resolution b(Å) Eqn. (1)	Total Broadening (Å)	
						calculated (d + b)	measured
Lyman, et al. <sup>4</sup>	Stainless Steel	1500	100	10-50	350	360-400	~ 300
Rao and Lifshin <sup>5</sup>	Stainless Steel	1000-1200	200	50	100-270	150-320	~ 500
Williams and Goldstein <sup>6</sup>	Fe-Ni	1500	100	200	350	550	~ 500
Romig <sup>7</sup>	Fe-Ni	~ 1500	100	200	350	550	~ 500
Pande et al. <sup>8</sup>	Stainless Steel	1000-1500	100	100	190-350	290-450	~ 500

where  $k_{FeNi}$  is the Cliff-Lorimer constant, which varies with operating voltage but is independent of foil thickness and composition.

Substitution yields

$$\frac{I_{Ni} - I_{Ni}^b}{I_{Fe} - I_{Fe}^b} \geq \frac{3 (2I_{Ni}^b)^{1/2}}{I_{Fe} - I_{Fe}^b} = (k_{FeNi}^{-1}) \frac{C_{DL}}{C_{Fe}} \quad (4)$$

or

$$C_{DL} = \frac{3 (2I_{Ni}^b)^{1/2}}{I_{Fe} - I_{Fe}^b} C_{Fe} k_{FeNi} \quad (5)$$

where  $C_{Fe}$  and  $k_{FeNi}$  are known quantities and  $C_{DL}$  is the detectability limit of Ni in the FeNi alloy. The x-ray intensities  $I_{Ni}$ ,  $I_{Fe}$ ,  $I_{Ni}^b$ , and  $I_{Fe}^b$  are measured experimentally. Unfortunately, the peak and background intensities are functions of foil thickness. Thinner foils produce greater intensities and therefore smaller detectability limits. Furthermore, x-ray intensity is linearly proportional to thickness, so long as the thin-film criterion is not violated. Once absorption effects become significant, the linear relationship is no longer valid. Figure 3 demonstrates the relationship between x-ray intensity and foil thickness for a pure Ni foil analyzed by a STEM operated at 100 kV with a 200Å probe size and a counting time of 60 sec. Foil thickness was determined by tilting of the foil following the STEM analysis and measurement of the separation of the contamination spots on the top and bottom of the foil. Given the spot separation, amount of tilt, and magnification one can calculate the foil thickness from simple geometry. Figure 4 shows the calculated detectability limits from Eq. (5) for a Fe-5.13 wt%Ni alloy as a function of foil thickness. Typical ion thinned metallurgical thin foils of Fe about 1500 Å thick yield a detectability limit of approximately 0.5 wt%Ni. Similar data were obtained from homogeneous Fe-14.5 wt% alloy and yielded the same detectability limit. In all cases, peak intensities were obtained by integrating the region of the peak defined by 1.2 full width at half maximum to optimize the peak intensity and peak-to-background ratio. Backgrounds were determined by averaging the integrated continuum intensities taken on both the high- and low-energy sides of the characteristic  $FeK_{\alpha}$  and  $NiK_{\alpha}$  peaks.

High-brightness guns (LaB<sub>6</sub> or field emission) improve the detectability limits since they increase the x-ray intensity. A larger counting time increases the x-ray intensity but the counting time is limited in practice by contamination and/or specimen drift. Opelzer and Knauer<sup>10</sup> analyzed a metallic glass (B, P, Cr, Fe, Ni) foil which was about

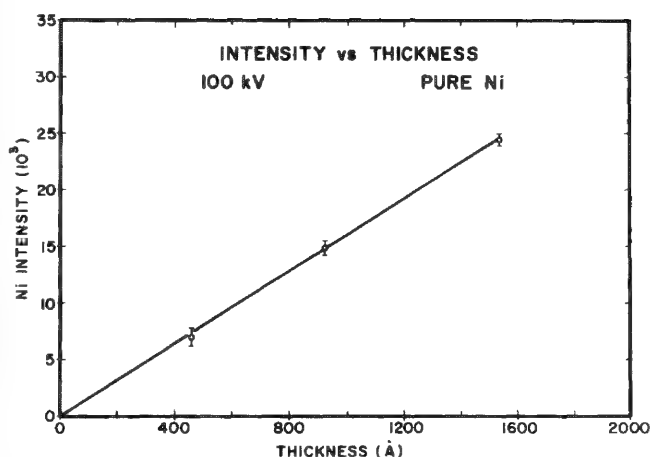


FIG. 3.--Intensity versus thickness relationship measured on a pure Ni foil. Operating conditions: 100 kV, 200Å probe diameter, 60sec counting time, 36° specimen tilt. Thickness determined by the measurement of the distance between contamination spots on the top and bottom of the foil after further tilting.

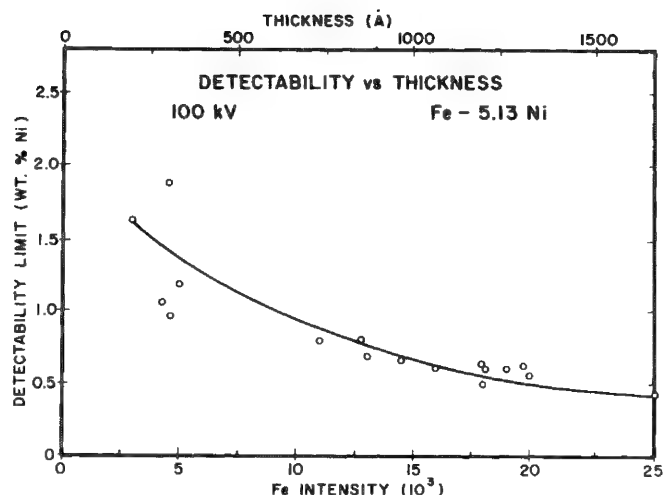


FIG. 4.--Detectability limit of Ni in Fe-Ni as a function of foil thickness and integrated Fe-intensity. Operating conditions: 100 kV, 200Å probe diameter, 60sec counting time, 36° specimen tilt.

500 Å thick with a STEM equipped with a field-emission gun. The data were taken at 100 kV with a 50Å-dia. electron probe. Use of their data in Eq. (5) gives detectability limits for all elements (except B) of approximately 0.15 wt%.

Attempts have been made to predict detectability limits from first-principle equations. Joy and Maher<sup>11</sup> have calculated the detectability limit of Fe in silicon to be approximately 4 wt% using a STEM with a LaB<sub>6</sub> gun operated at 100 kV, with a 100Å-dia. electron probe. This detectability limit can be reduced to approximately 2 wt% by use of a field-emission gun. For a STEM operated at 100 kV and equipped with a thermal emission gun, with a 200Å diameter probe, this theoretical approach gives a detectability limit of 4.8 wt%Ni in an Fe-Ni alloy. It is not clear why experimentally measured detectability limits are so much smaller than calculated limits.

#### Independent Determination of $k_{FeNi}$

To perform a STEM x-ray analysis using Eqn. (3), one needs to know precisely the value of  $k$ . The value of  $k_{FeNi}$  can be calculated from first principles as shown by Goldstein et al.<sup>1</sup> or obtained from the  $k_{FeSi}/k_{NiSi}$  experimental values.<sup>12</sup> At 100 kV, the calculation technique of Goldstein et al. yields  $k_{FeNi} = 0.92$ . The Cliff-Lorimer values yield  $k_{FeNi} = 1.27/1.47 = 0.86$ . The best method is to measure  $k_{FeNi}$  on a homogeneous one-phase-alloy thin foil. Several alloys were used in this series of experiments. Nine separate  $k_{FeNi}$  measurements were made on a Fe-14.5 wt%Ni alloy thin foil, 500-200 Å thick, with a 200Å diameter probe and a counting time of 60 sec. The measured  $k_{FeNi}$  was  $0.88 \pm 0.04$  at the 95% confidence level. Seventeen measurements were made similarly in an Fe-5.13 wt%Ni alloy. At the 95% confidence level  $k_{FeNi} = 0.85 \pm 0.08$ . The calculated  $k_{FeNi}$  and original Cliff-Lorimer  $k_{FeNi}$  agree, within experimental error, with the value determined directly in this study. When this value of  $k_{FeNi}$  is used in later data reduction, any error in the measurement of the Ni content of the homogeneous alloy must be added to the measured uncertainty.

#### Summary

For a Philips 300 TEM/STEM operating at 100 kV (with a 200Å probe diameter and a thermal emission gun):

1. the spatial resolution, as determined by measuring concentration profiles across

$\alpha/\gamma$  interfaces in Fe-Ni alloys, is 500 Å in thin foils which are approximately 1500 Å thick;

2. the detectability limit of Ni in an Fe-Ni matrix is about 0.5 wt%Ni in a thin foil sample 1500-2000 Å thick; and

3.  $k_{\text{FeNi}} = 0.88 \pm 0.04$  at 95% confidence level.

#### References

1. J. I. Goldstein et al., "Quantitative x-ray analysis in the electron microscope," O. Johari, Ed., *SEM/1977*, 1: 315.
2. D. F. Kyser and R. H. Geiss, "Spatial resolution of x-ray microanalysis in STEM," *Proc. 12th MAS Conf.*, 1977, 110.
3. J. I. Goldstein and H. Yakowitz, *Practical Scanning Electron Microscopy*, New York: Plenum Press, 1975, 457.
4. C. E. Lyman et al., "STEM microanalysis of duplex stainless steel weld metal," O. Johari, Ed., *SEM/1978*, 1, 213.
5. P. Rao and E. Lifshin, "Microchemical analysis in sensitized austenitic stainless steel," *Proc. 12th MAS Conf.*, 1977, 118.
6. D. B. Williams and J. I. Goldstein, "STEM/X-ray microanalysis across  $\alpha/\gamma$  interfaces in Fe-Ni meteorites," *9th Intl. Cong. on Elect. Micro.*, Toronto, 1978, 1: 416.
7. A. D. Romig Jr., *Low Temperature Phase Equilibria in Fe-Ni Alloys*, Ph.D. Dissertation, Lehigh University, Bethlehem, Pa; 1979.
8. C. S. Pande et al., "Direct evidence of chromium depletion near the grain boundaries in sensitized stainless steels," *Scripta Met.* 11: 681, 1977.
9. G. Cliff and G. Lorimer, "The quantitative analysis of thin specimens," *J. of Microscopy* 103: 203, 1975.
10. H. Oppolzer and U. Knauer, "Advantages of a STEM with a field emission gun for x-ray analysis of inhomogeneities in metals and ceramics," O. Johari, Ed., *SEM/1979*, to be published.
11. D. Joy and D. Maher, "Sensitivity limits for thin specimen x-ray analysis," O. Johari, Ed., *SEM/1977*, 1: 325.

## A COMPARISON OF PROCEDURES FOR QUANTITATIVE X-RAY ANALYSIS IN THIN FILMS

R. L. Sabatini and C. S. Pande

X-ray microanalysis of thin films is finding increasing use in the analysis and characterization of materials. In many cases, it supplements the wealth of information already obtained on the same film by such techniques as conventional electron microscopy (TEM), scanning transmission electron microscopy (STEM), and electron diffraction. In recent years, the quantitative aspect of the x-ray microanalysis (in which thin-film technique is used not only to identify the elements in a given region of the foil, but also to obtain a quantitative measurement of the various elements present in that region) has acquired great significance, with applications to such important fields as corrosion<sup>1</sup> and phase transformations.<sup>2</sup> It is therefore of some interest to ascertain the accuracy of the procedures by which the quantitative values are obtained from the x-ray spectra. Furthermore, the basic assumptions inherent in this procedure need careful evaluation.

Several techniques have been developed for quantitative thin film analysis. An early review of these techniques was given by Hall.<sup>3</sup> More recently these procedures have been summarized by Goldstein and Williams.<sup>4</sup> For metal films, the three main techniques are (1) analysis using bulk standards, (2) analysis using thin film standards and (3) analysis without standards. We have used all three techniques for the analysis of the same spectra from 304 stainless steel. The advantage of using this material is that the composition for certain regions in the thin films was known independently, so that these techniques could be checked against each other and also with the regions of known composition. It was surprising to find that in some cases significantly different results were obtained, which indicates the need for great caution in the derivation of quantitative values from the x-ray spectra.

Another point of interest in such an analysis is the validity of the basic assumptions often used, namely that below a certain specimen thickness, the characteristic x-ray intensities of the elements present are directly proportional to their local elemental masses,<sup>5</sup> because the matrix corrections (due to fluorescence, absorption, and atomic-number differences) are expected to be negligible. Although there is some experimental evidence to support this assumption,<sup>5-8</sup> the assumption may not be universally true for all materials.<sup>9</sup> It is thus important to ascertain that the composition of the thin film is independent of the film thickness, at least for the range of specimen thicknesses used in the analyses. This assumption is also experimentally checked in this paper.

The experimental setup for obtaining the x-ray spectra from the stainless-steel films was essentially similar to that described by Pande et al.<sup>1</sup> The samples were thinned by a standard of ion milling technique.

The experiments were performed on a JEOL-100C electron microscope with scanning and energy-dispersive attachments. When the scanning electron beam was made stationary it acted as an electron probe and x rays generated were detected by an NSI Si(Li) detector mounted on the electron microscope column. In order to improve spatial resolution and yet obtain sufficient counts it was necessary to optimize various parameters, such as the accelerating voltage of the electrons (120 kV), the detector area (30 mm<sup>2</sup>), the beam size (about 5 nm), a constant counting time (30 sec), and a tilt of 45°. The spectra collected were stored on cassettes for later analysis.

Electron microprobe analysis gave the bulk composition of the sample as 70.3 wt%Fe, 19.0 wt%Cr, 8.6 wt%Ni, 1.6 wt%Mn, 0.06 wt%Si. Independent chemical analysis showed that it also contained 0.07 wt%C.

Three types of stainless steel specimens were analyzed:

- a. Homogenized specimens (1100°C for 3 hr) in which there is not a significant variation of composition throughout the specimens.
- b. Sensitized specimens (1100°C for 3 hr and then at 650°C for 24 hr) consisting of Cr-rich carbide precipitates at the grain boundary and a resulting chromium depletion adjacent to the grain boundary.

---

The authors are with Brookhaven National Laboratory, Upton, N. Y. The work was performed under the auspices of the U.S. Department of Energy.

c. Overaged specimens (1100°C for 3 hr and then at 650°C for 7 days) in which there is a lower chromium depletion adjacent to the grain boundary.

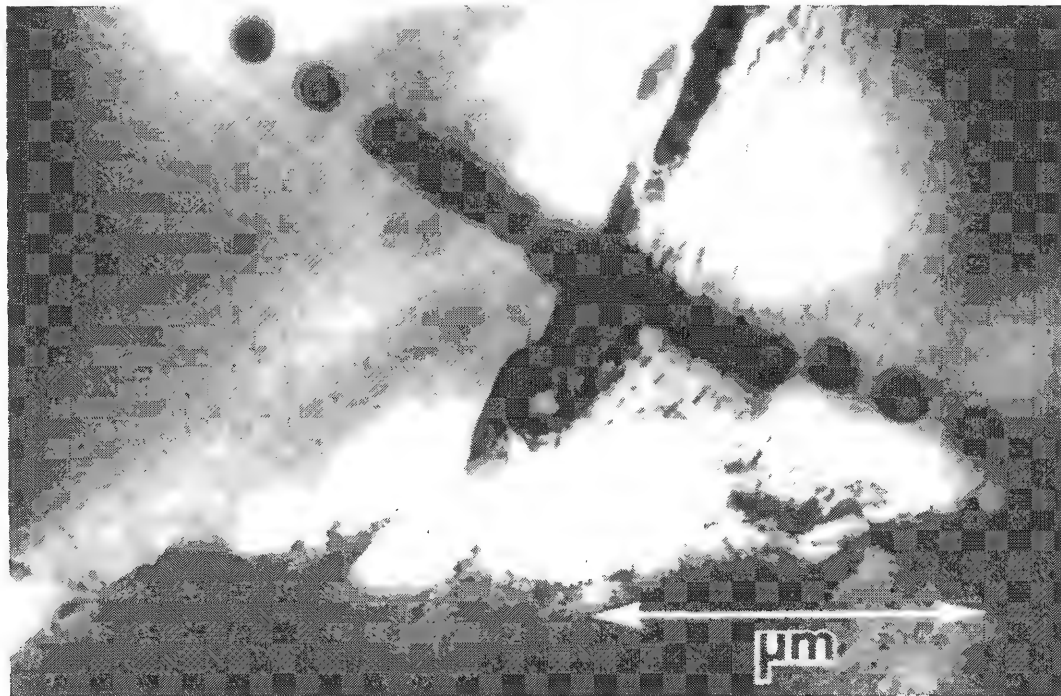


FIG. 1.--Typical electron micrograph of a stainless-steel specimen (sensitized) showing precipitates on grain boundary and path of microanalysis.



FIG. 2.--TEM micrograph of sample that has been rotated back to 0° and then photographed for thickness measurement.

We obtained the thickness of the foil at the point of analysis by turning the foil 45° (back to 0° tilt) and taking a picture of the contamination spots (Fig. 2). If the film is thin enough ( $< 5000 \text{ \AA}$ ) contamination spots are visible at both the top and bottom of the foil, and hence the thickness of the foil at that point could be easily obtained. The thickness was also checked by tilting the foil to a 'two-beam' condition such that only one diffraction beam is strongly excited, and observing the thickness fringes. The thicknesses of the foil by the two methods were in good agreement.

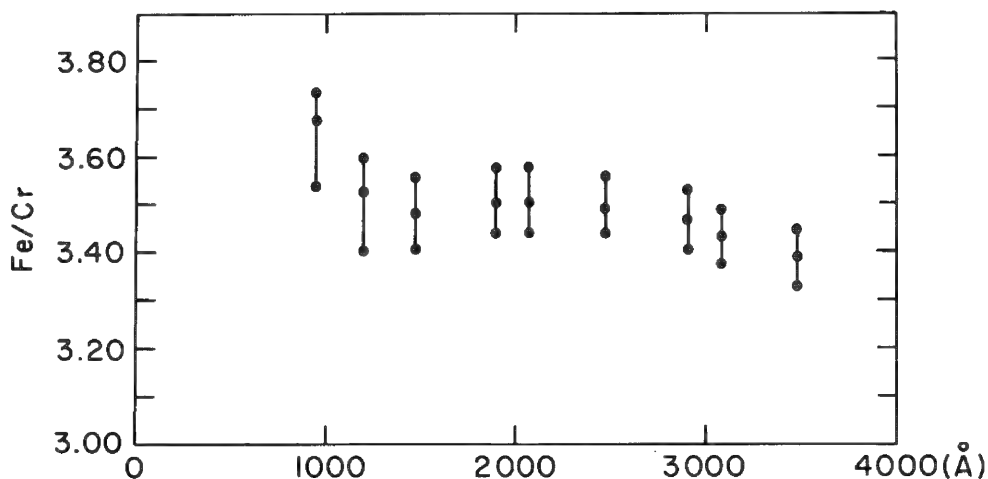


FIG. 3.--Plot of Fe/Cr ratio vs sample thickness.

A series of traces were taken on the homogenized samples, from the edge into thicker areas. The Fe/Cr ratio was then calculated and plotted versus thickness (Fig. 3). The Fe/Cr ratio remains constant over a wide range of thickness of the foil within experimental error of the x-ray counts. A slight increase in the Fe/Cr ratio at lower thicknesses ( $< 1000 \text{ \AA}$ ) was observed; however, the counts from the thin areas were relatively small, which led to a larger error in Fe/Cr measurement. Therefore, for ion-milled stainless-steel specimens used in our experiments, the Fe/Cr ratio can approximately be taken to be independent of the thickness in the range 1000-2000 Å. The specimens analyzed all had a thickness in this range.

The data collected for each sample were analyzed by four different techniques:

1. By the method described by Pande et al.,<sup>1</sup> which is a modified version of the Cliff-Lorimer scheme. According to this scheme,

$$\frac{I_A}{I_B} = (K_{AB})^{-1} \frac{C_A}{C_B} \text{ and } \sum_i C_i = 100\% \text{ (i = A, B, C, ...)}$$

where  $I_A$  = measured intensity of A,  $I_B$  = measured intensity of B,  $C_A$  = concentration of A,  $C_B$  = concentration of B, and  $K_{AB}$  → constant that varies with accelerating voltage but is independent of thickness and composition if the thin-film criterion is satisfied.

A reference spectrum is taken at about 1 μm from the grain boundary. Then the intensity for each element in the unknown spectrum is compared to the intensity in the reference spectrum. This ratio is then multiplied by the concentration for that element in this material and afterwards normalized. The data are normalized because the total number of counts for each element is expected to be proportional to the thickness of the specimen.

2. By a Super ML Fit, with the most distant area taken as a standard; then the results are normalized. The Super ML program employs a multiple least-squares analysis technique to obtain accurate measures of peak intensity in the presence of continuum and peak overlaps. A reference spectrum is obtained at about 1 μm from the grain boundary. Then each unknown spectrum is fitted against this reference. After the Super ML Fit is completed, the K ratios are normalized and then multiplied by the concentration for that element in the standard.



3. By a bulk standard of known Fe, Ni, Cr concentrations; then the ZAF program is run backwards to obtain the correction factors for the three elements. The unknown spectra were then fitted to the corrected bulk standard spectrum and then normalized.

4. By a Metallurgical Thin Film (MTF) program provided by Tracor Northern. The MTF program converts peak-to-peak intensity ratios for elements of interest into concentration ratios for these elements by using the K-factor technique first proposed by Cliff and Lorimer.<sup>5</sup> No absorption correction was made in this technique.

Tables 1 and 2 present the results of these four techniques for comparison. Full details of the composition profile across grain boundaries in both kinds of specimens (i.e., sensitized and overaged) are given in Pande et al.<sup>1</sup>

TABLE 1.--Typical results of microanalysis in sensitized sample by the four different techniques; trace goes across large Cr-rich carbide at grain boundary.

Distance from Grain Boundary (Å)	Composition	Pande et al.	XML Fit	Bulk	MTF
at Grain Boundary	Cr	.471	.473	.379	.526
	Fe	.462	.462	.536	.441
	Ni	.042	.040	.060	.008
-500	Cr	.373	.375	.288	.431
	Fe	.544	.538	.597	.531
	Ni	.058	.062	.091	.012
-1000	Cr	.189	.186	.133	.224
	Fe	.706	.710	.736	.734
	Ni	.080	.079	.107	.017
-2000	Cr	.195	.196	.140	.236
	Fe	.695	.696	.723	.721
	Ni	.084	.083	.112	.018
+2000	Cr	.186	.183	.293	.438
	Fe	.702	.704	.594	.525
	Ni	.087	.088	.088	.012
+3000	Cr	.187	.193	.138	.232
	Fe	.699	.700	.725	.725
	Ni	.089	.082	.112	.018
+4000	Cr	.188	.185	.132	.223
	Fe	.704	.708	.733	.734
	Ni	.083	.082	.110	.018
+7000	Cr	.190	.190	.136	.230
	Fe	.701	.699	.722	.726
	Ni	.084	.086	.117	.019
+8000	Cr	.191	.192	.136	.231
	Fe	.701	.700	.726	.726
	Ni	.087	.083	.112	.018
+10 000	Cr	.187	.186	.134	.226
	Fe	.703	.703	.727	.731
	Ni	.086	.086	.114	.018

TABLE 2.--Typical results of microanalysis in overaged sample by the four different techniques; trace is between the precipitates.

Distance from Grain Boundary (Å)	Composition	Pande et al.	XML Fit	Bulk	MTF
at Grain Boundary	Cr	.193	.189	.140	.212
	Fe	.700	.713	.708	.741
	Ni	.083	.073	.127	.021
-500	Cr	.166	.164	.119	.188
	Fe	.716	.716	.693	.758
	Ni	.093	.097	.163	.029
-1000	Cr	.180	.178	.130	.204
	Fe	.709	.708	.694	.744
	Ni	.086	.089	.151	.026
-3000	Cr	.189	.194	.143	.222
	Fe	.700	.699	.691	.723
	Ni	.086	.082	.141	.024
-6000	Cr	.187	.186	.137	.213
	Fe	.700	.698	.685	.735
	Ni	.088	.091	.153	.027
-10 000	Cr	.187	.187	.139	.216
	Fe	.703	.703	.690	.733
	Ni	.086	.086	.147	.025
+1000	Cr	.214	.214	.158	.242
	Fe	.678	.677	.672	.708
	Ni	.083	.084	.145	.024
+2000	Cr	.186	.183	.137	.210
	Fe	.703	.713	.706	.742
	Ni	.086	.080	.132	.023
+7000	Cr	.186	.185	.134	.212
	Fe	.700	.704	.684	.736
	Ni	.089	.086	.157	.027
+10 000	Cr	.185	.183	.136	.208
	Fe	.702	.707	.698	.742
	Ni	.088	.085	.141	.025

For the sensitized sample we obtained nearly identical results by the modified Cliff-Lorimer technique and the Super ML Fit. The bulk standard technique gave us consistently lower Cr concentrations, higher Fe concentrations, and higher Ni concentrations, probably owing to the uncertainty in the ZAF corrections at 120 kV. The MTF program gave us consistently higher Cr concentrations and very low Ni concentrations, probably owing to the Cr fluorescing.

For the overaged sample, the Cliff-Lorimer technique and Super ML Fit give comparable results. The bulk standard technique also once again gives low Cr and high Ni concentrations. The MTF program still gives high Cr and very low Ni concentrations.

In summary, we have tried to show that:

1. For the case of microanalysis of 304 stainless steel, the Cliff-Lorimer technique and the Super ML Fitting technique seem to give equally reliable results. Part of the reason for this good agreement is that the specimen provides a small region where the concentrations of the elements of interest are well known. In our case, the reference point was taken at a distance approximately  $1\ \mu$  from the grain boundary, where one could assume the concentrations of these elements to be the same as in the bulk.

2. The bulk standards present a problem: if a standard is not a pure element, the correction factors from ZAF at 120 kV could be very large. The absorption effect for pure elements has to be either measured or calculated for the operating conditions. It is also difficult to duplicate the exact operating conditions over a long period of time, so that the bulk standards would have to be run either before or after each run. One solution is to use bulk standards at an accelerating voltage much lower than that used in the thin-film analysis.

3. The MTF program did not yield as reliable results as the first two. The most likely explanation is that the Cr in the sample is fluorescing; since the MTF program assumes no fluorescence we should not expect very reliable results in this case.

4. Thicknesses of more than 1000 Å do not seem to affect the relative x-ray intensities. However, in the thicker films matrix corrections may be significant. Hence the most suitable specimen thickness range for ion-milled stainless-steel specimens appears to be 1000-2000 Å.

#### References

1. C. S. Pande et al., "Direct evidence of chromium depletion near the grain boundaries in sensitized stainless steels," *Scripta Metallurgica* 11: 681, 1977.
2. N. A. Razik, G. W. Lorimer, and N. Ridley, "An investigation of Mn partitioning during the austenite-pearlite transformation using analytical electron microscopy," *Acta Metallurgica* 22: 1249, 1974.
3. G. W. Lorimer et al., "Analysis of the composition of  $\alpha$ , plates precipitated from  $\beta'$  Cu-Zn using analytical electron microscopy," *Scripta Metallurgica* 9: 271, 1975.
4. T. A. Hall, *Advances in Analysis of Microstructural Features by Electron-beam Techniques*, The Chameleon Press for the Metal Society, 1974, 120.
5. J. I. Goldstein and D. B. Williams, "X-ray analysis in the TEM/STEM," *Scanning Electron Microscopy*, Chicago: IIT Research Institute, 1977, 315.
6. G. Cliff and G. W. Lorimer, "Quantitative analysis of thin metal foils using EMMA-4 the ratio technique," *Proc. 5th European Congress of Electron Microscopy*, London: Institute of Physics, 1972, 140.
7. P. Duncumb, "EMMA, combinaison d'un microscope électronique et d'une microsonde électronique," *J. Microscopie* 7: 581, 1968.
8. M. H. Jacobs and J. Baborovska, "Quantitative microanalysis of thin foils with a combined electron microscope-microanalyzer (EMMA-3)," *Proc. 5th European Cong. on Electron Microscopy*, London: Institute of Physics, 1972, 136.
9. G. W. Lorimer and P. E. Champness, "Combined electron microscopy and analysis of an orthopyroxene," *Am. Min.* 58: 243, 1973.
10. M. N. Thompson et al., "The influence of specimen thickness on x-ray count rates in STEM-microanalysis," *Phil. Mag.* [8]35: 1537, 1977.

## SULFUR AND PHOSPHORUS SEGREGATION IN DUPLEX STAINLESS STEEL WELD METAL

C. E. Lyman

Detection of sulfur and phosphorus segregation in steels is difficult because of the low levels of these elements usually present. However, if S and P partition or segregate to small regions in the metal, the local concentration of these elements increases. An analytical technique of sufficiently high sensitivity and high spatial resolution can detect such segregation. The present investigation employed a field-emission scanning transmission electron microscope (STEM) and energy-dispersive x-ray spectroscopy.

Austenitic stainless steels are susceptible to hot cracking when cooling from the melt in welding operations. Early experience with these steels showed that retention of 5-10 vol% of the high-temperature delta ferrite phase after welding, in a previously fully austenitic structure, eliminated the hot cracking problem.<sup>1</sup> The cause of hot cracking has been shown to be sulfur and phosphorus segregation at austenite interdendritic regions and grain boundaries.<sup>2</sup> Sulfur in excess of 0.01wt% in these locations combines with iron to form a mixture of austenite and liquid which does not solidify until 989°C, about 400°C below the usual solidus temperature predicted by the FeCrNi ternary phase diagram.<sup>3</sup> The beneficial effect of retained delta ferrite has been attributed to its effect on the manganese distribution in the alloy and to more uniform distribution of sulfur and phosphorus by structural refinement.<sup>2</sup> However, the Fe-S and Fe-P binary phase diagrams indicate that S and P are from 2 to 15 times more soluble in bcc delta ferrite than in fcc austenite, depending on the temperature.<sup>3</sup> The purpose of this investigation was to determine whether increased solubility of S and P in retained delta ferrite could also contribute to the elimination of hot cracking.

The major microanalysis problem in duplex austenite plus delta ferrite microstructures is the shape and size of the delta ferrite regions, usually long and thin and less than 1 µm wide. The field-emission gun of the STEM provided the necessary beam current in a small electron probe to analyze areas within a delta ferrite region less than 1 µm wide.

To improve chances of detecting segregation of sulfur to delta ferrite, the weld metal analyzed was enriched in sulfur by the use of special high-sulfur welding rods supplied by Chemetron Corp. The compositions of the base metal (Type 304) and welding rod are shown in Table 1. Specimens were thinned by conventional dual-jet electropolishing with 10% perchloric acid in methanol. Specimens were then ion-beam cleaned for 5 min by means of 6kV

TABLE 1.--Compositions of base metal and welding rod in weight per cent.

	C	Cr	Ni	Mn	Si	Mo	S	P
Base metal (Type 304)	0.055	18.28	8.55	1.56	0.61	0.18	0.015	0.027
Welding rod (Type 309 + S)	0.093	23.15	12.35	1.68	0.56	0.05	0.195	0.019

The author is in the Materials Engineering Department of Rensselaer Polytechnic Institute in Troy, New York. The author thanks Prof. J. B. Vander Sande and Dr. E. L. Hall of the Massachusetts Institute of Technology for use of the Vacuum Generators HB5 STEM. The author gratefully acknowledges financial support from the U.S. Department of Energy under Contract EY-76-5-02-2462\*000.

argon ions. Analyses were obtained in 500 sec at 200 000 $\times$  magnification with a Vacuum Generators HB5 STEM at 100 kV. The probe size was about 1-5 nm and the probe current was in the range  $10^{-9}$ - $10^{-8}$  A.

Results are shown in Figs. 1 and 2. Figure 1 shows the four areas of the specimen analyzed: the austenite ( $\gamma$ ) matrix, the  $\gamma/\delta$  boundary, the delta ( $\delta$ ) ferrite region, and the  $\gamma/\gamma$  grain boundary. Diameters of the marking circles indicate the size of the contamination spots built up during the 500sec counting time. The thickness of the foil was about 115 nm from contamination spot measurements. Figure 2 shows x-ray spectra from three of the analyzed areas. The large peak running offscale at 5.41 keV is the  $\text{CrK}_\alpha$  line. The x-ray analysis system generated Si escape peaks for Cr and Fe and subtracted them from the spectra. The remaining background appears to be separable into two components. The background due to the "hole count" is shown in Fig. 3. Experiments similar to those of Goldstein and Williams<sup>4</sup> indicate that this hole count is caused largely by uncollimated electrons. The second component of background is generated in the specimen and exhibits the usual hump of continuum x rays from thick or bulk specimens.

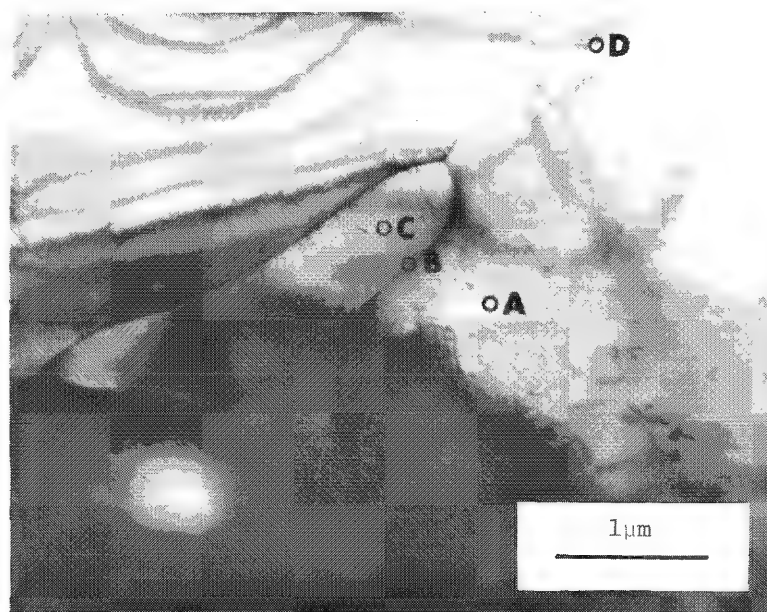
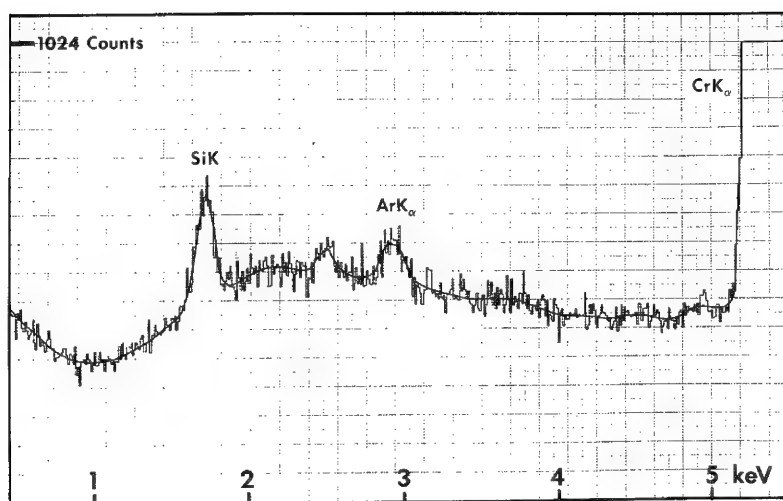


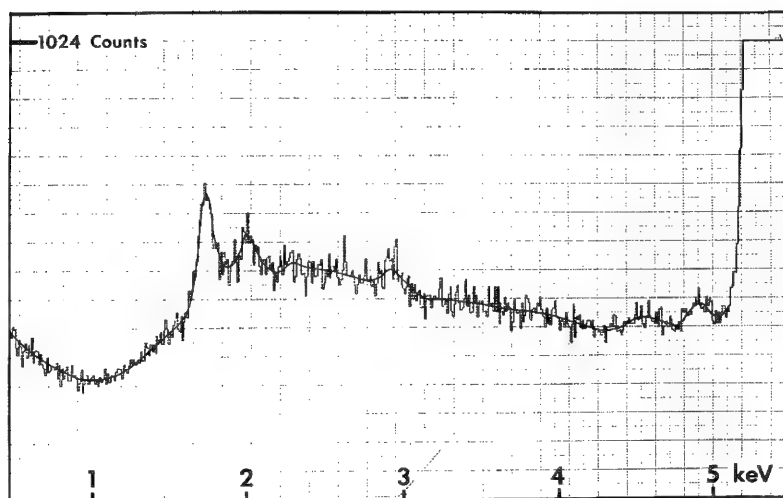
FIG. 1.--STEM micrograph of analysis areas in stainless steel weld metal: A = austenite( $\gamma$ ) matrix, B =  $\gamma/\delta$  boundary, C = delta( $\delta$ ) ferrite, and D =  $\gamma/\gamma$  grain boundary.

The spectrum from delta ferrite (Fig. 2c) shows the presence of phosphorus; this element was not detected above background in the austenite (Fig. 2a). The peak labeled SK (2.31 keV) in Fig. 2c is likely to arise from  $\text{MoL}_\alpha$  (2.29 keV) since the base metal contained nearly 0.2wt% Mo. Thus, for the present case an unambiguous measurement of sulfur is not possible. To a spatial resolution of about 50-100 nm, limited by drift and probe location uncertainty, the  $\gamma/\gamma$  boundary itself (Fig. 2b) does not appear to be enriched in P or S (or Mo) over the interior of the delta ferrite region. Other elements shown in the spectra are from electropolishing (Cl) and ion-beam cleaning (Ar).

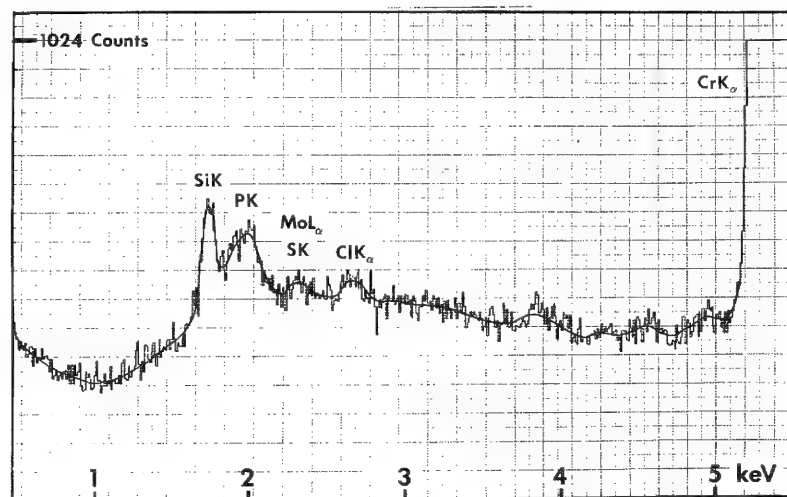
A computer-generated background was manually adjusted to the shape of the spectrum in the region analyzed, normalized to selected channels at each analysis point, and subtracted from the spectrum. Changes in specimen thickness and emission from the field-emission gun require the peaks above background to be given as ratios. Windows set on each peak were slightly larger than full width at half maximum for each element: 150 eV for SiK, 160 eV for PK, 130 eV for SK ( $\text{MoL}_\alpha$ ), and 170 eV for  $\text{FeK}_\alpha$ . Contributions to the  $\text{FeK}_\alpha$  peak from the  $\text{MnK}_\alpha$  were ignored since most of the Mn is tied up in inclusions. Table 2 shows background subtracted peak ratios for Si, P, and (S + Mo) at each location marked in Fig. 1. Relative increases in P and (S + Mo) between austenite and delta ferrite depend critically on the background level subtracted. For the analysis shown in Table 2, the background was matched manually and may be in error. However, a large increase in P is clearly indicated, where:



(a)



(b)



(c)

FIG. 2.--Energy dispersive x-ray spectra from three analysis areas: (a) austenite ( $\gamma$ ) matrix, (b)  $\gamma/\delta$  phase boundary, and (c) delta ( $\delta$ ) ferrite. Counting time = 500 sec.

TABLE 2.--Ratios of Si, P, and (S + Mo) peaks to the FeK $_{\alpha}$  peak for analysis areas shown in Fig. 1. Counting time = 500 sec.

Analysis point in Fig. 1	Integrated intensity ratios			Integrated FeK $_{\alpha}$ peak
	SiK/FeK $_{\alpha}$	PK/FeK $_{\alpha}$	(SK+MoL $_{\alpha}$ )/FeK $_{\alpha}$	
A. $\gamma$ -austenite	$3.47 \times 10^{-3}$	$0.38 \times 10^{-3}$	$0.25 \times 10^{-3}$	407950 counts
B. $\delta/\gamma$ boundary	$4.35 \times 10^{-3}$	$2.76 \times 10^{-3}$	$1.20 \times 10^{-3}$	395080
C. $\delta$ -ferrite	$5.98 \times 10^{-3}$	$6.05 \times 10^{-3}$	$1.53 \times 10^{-3}$	362550
D. $\gamma/\gamma$ boundary	$3.28 \times 10^{-3}$	$1.20 \times 10^{-3}$	$0.81 \times 10^{-3}$	226740

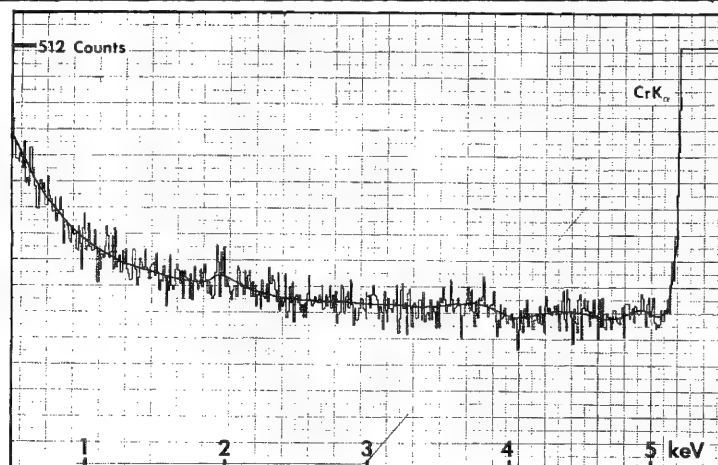


FIG. 3.--Background from "hole count" measured while directing beam through hole in specimen. Counting time = 500 sec.

the Si counts increased by a factor of less than two. One may conservatively estimate the sensitivity of the analysis by assuming that all the phosphorus in the alloy is partitioned to the delta ferrite and no P is tied up in inclusions. For this case, then, assuming 7vol% delta ferrite and a nominal 0.03wt% P for the alloy, 0.43wt% P was measured within the delta ferrite. The sensitivity for phosphorus must be several times better than that.

In summary, this paper shows that phosphorus, and possibly sulfur, partitions to the delta ferrite phase in duplex stainless steel welds. This partitioning probably contributes to the elimination of hot cracking in welded austenitic stainless steels containing retained delta ferrite.

#### References

1. R. Scherer, G. Riedrich, and G. Hoch, *Arch. Eisenhut.* 13: 53, 1939-40.
2. H. Astrom et al., "Hot cracking and micro-segregation in 18-10 stainless steel welds," *Metal Science* 10: 225, 1976.
3. *Metals Handbook*, Metals Park, Ohio: American Society for Metals, 1973, vol. 8.
4. J. I. Goldstein and D. B. Williams, "Spurious x-rays produced in the scanning transmission electron microscope," *Scanning Electron Microscopy/1978*, AMF O'Hare, IU.: SEM Inc., 1978, I-427.



## THE USE OF TEM AND SEM FOR THE DETECTION OF INDIVIDUAL SUBMICROMETER-SIZE SULFATE AND NITRATE PARTICLES

Y. Mamane and R. Pueschel

A quantitative method for the analysis of individual submicrometer size sulfate and nitrate particles has been developed in which a scanning electron microscope (SEM) equipped with an x-ray analyzer and a transmission electron microscope (TEM) are used. The method is based on the reaction of the sulfate and nitrate ions with barium chloride and nitron, respectively, and can be applied to soluble particles. The method is specific reproducible and quantitative for sulfates and nitrates. The result of the reaction is a characteristic halo easily recognized under the TEM. Later the sample with the reaction spots is transferred to the SEM. The reaction spots are relocated and an x-ray spectrum of the reaction spot is obtained, which gives the elemental content of the sulfate or nitrate particles.

The method has been applied to atmospheric samples collected in the plume of a coal-fired power plant. The analysis provided (besides the size of the particles) information about the nature of the sulfate and nitrate particles. Especially, it was possible to observe, for the first time, the existence of submicron fly ash particles (containing mainly Si, Al, Fe, and Ca) coated with a very thin layer (about 0.01  $\mu\text{m}$  deep) of sulfate, which could be the result of the heterogeneous nucleation of sulfur dioxide on foreign particles. In this aspect, it is one of the few (if not the only) technique to provide such information. As with any other method that employs the microscopes for counting and sizing, our method requires time and patience to perform the analysis.

Typical photomicrographs obtained in the TEM and the SEM with the x-ray spectrum of common particles found in the plume of a coal-fired power plant are shown in Fig. 1, which suggests that most of the particles in this size range are sulfates and some are mixed particles, i.e., fly ash particles coated with a thin layer of sulfate.

---

Author Mamane is in Environmental Engineering at the Technion in Haifa, Israel; Pueschel is at the National Oceanic and Atmospheric Administration's Atmospheric Physics and Chemistry Laboratory in Boulder, Colo.

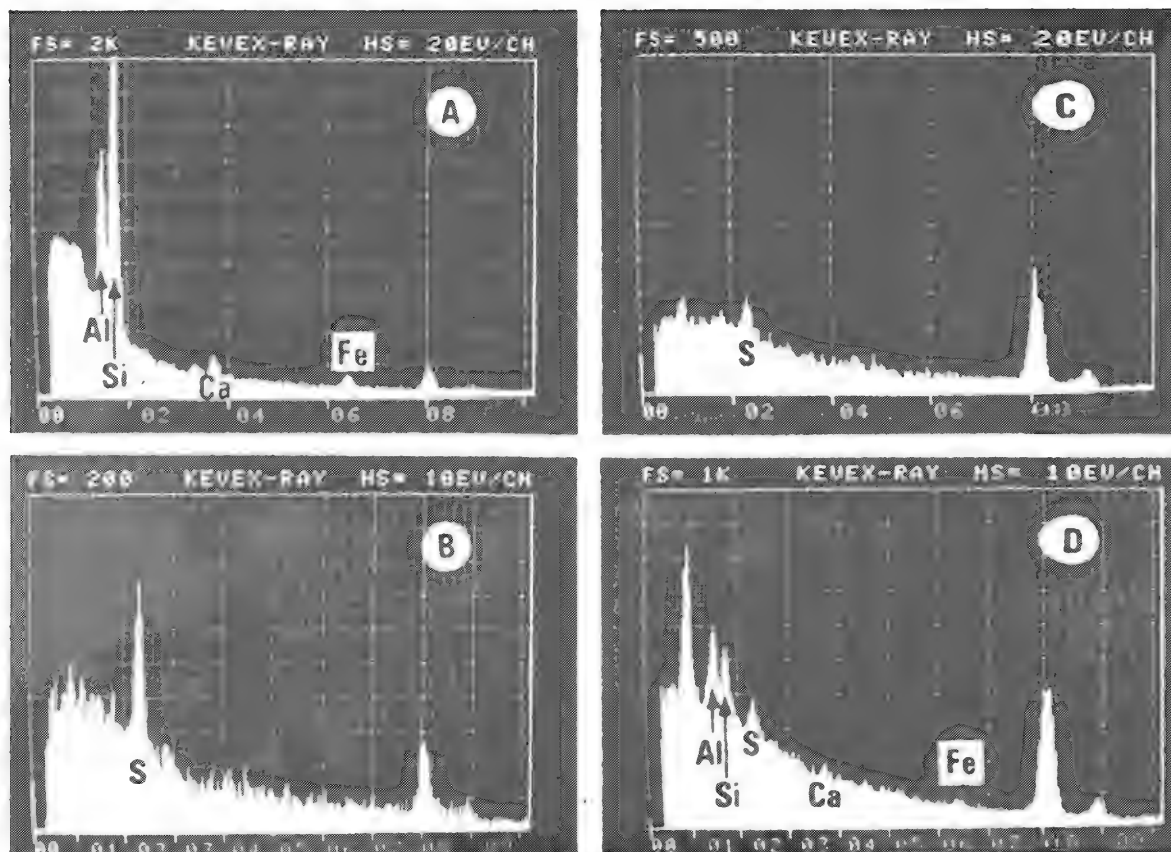
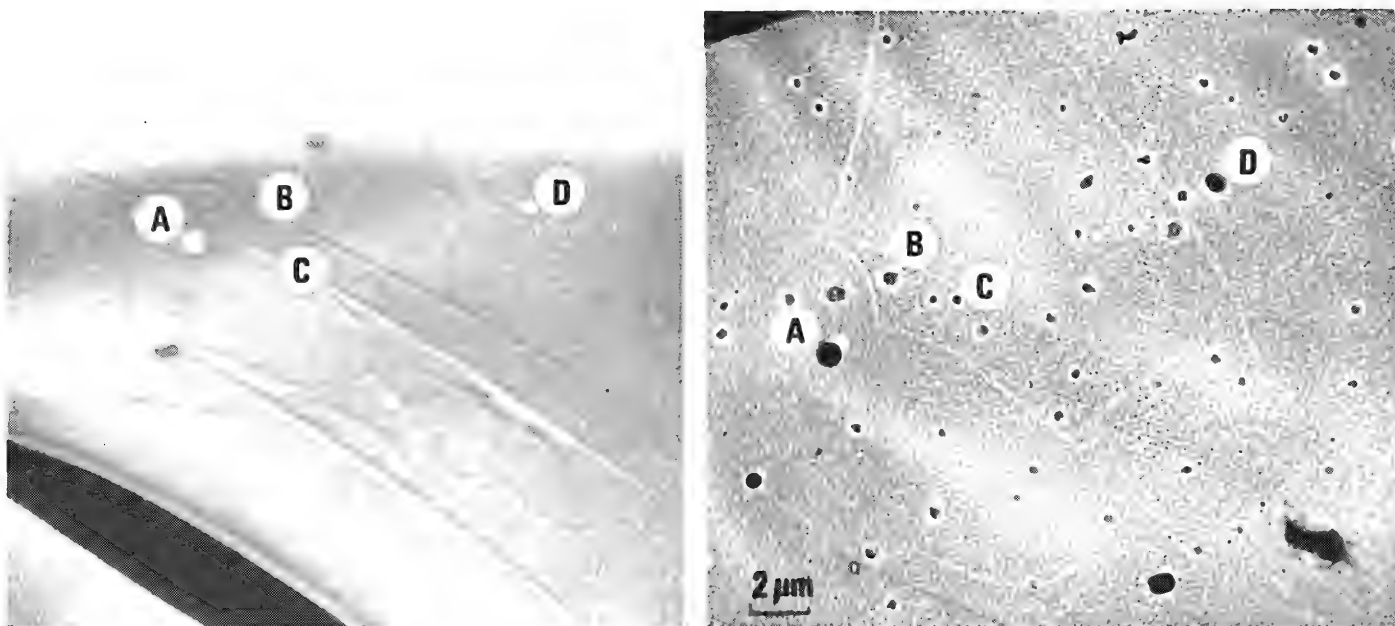


FIG. 1.-- Top right: BaCl<sub>2</sub>-treated sample shows that almost all particles are sulfates (Particles B and C); however, few are fly ash particles: one is not coated (A), other is coated with thin layer of sulfate (D). Top left: SEM photomicrograph of same field of view. Below: X-ray spectra of individual particles A, B, C, and D.

## CALCULATIONS OF INSTRUMENT RESPONSE TO PLASMON EXCITATIONS IN EELS

R. C. Farrow, D. C. Joy and D. M. Maher

We have developed a theoretical model for the plasmon excitation spectrum and the response of an electron energy-loss spectrometer. These theoretical functions have been convoluted under various conditions in order to simulate a range of actual experimental conditions. The results predict the quantitative affects of instrument response on the plasmon spectrum. We relate these results to the error associated with sample thickness determinations by using the ratios of the areas under the plasmon spectrum. It is concluded that this method for calculating the sample thickness can introduce large errors ( $> 30\%$ ) when the sample is very thin ( $< 100 \text{ \AA}$ ) and the resolution of the spectrometer and the separation of the plasmon peaks are not at optimum values.

In recent years the study of electron energy loss with the aid of the transmission electron microscope has led to important developments in elemental microanalysis. For the most part elemental identification does not require very high resolution from the energy loss spectrometer (a value of 5-10 eV is adequate).<sup>1</sup> As we progress to using EEL for quantitative materials analysis, we must be able to characterize the quantitative effects of instrumental factors, such as spectrometer resolution, on the results. When spectral data are used for quantitative materials analysis, an accurate measurement of the sample thickness is needed for certain calculations.<sup>2</sup> The simplest method for its determination involves an analysis of the energy loss spectrum in the plasmon excitation region. In this paper we discuss calculations that demonstrate how the instrument response modifies the answers obtained from such measurements. This study was performed as a prelude to an attempt to understand the quantitative effects of instrument response and plasmon excitations on the inner-shell excitations. That study is in progress and will be reported in a separate publication.<sup>3</sup>

In Fig. 1 we show a typical EEL plasmon spectrum for silicon with 100keV incident elec-

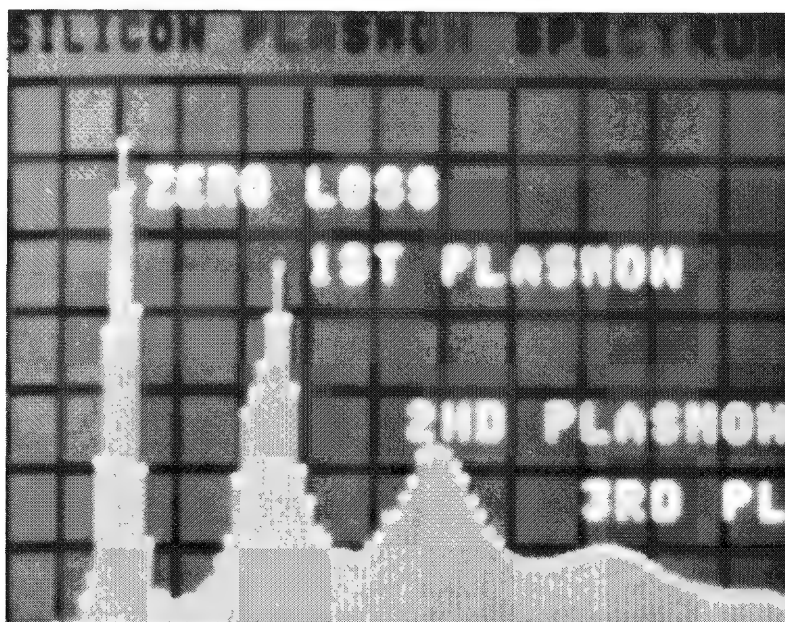


FIG. 1.--Experimental plasmon spectrum from Si with 100keV incident electrons,  $E_{pL} = 17 \text{ eV}$ , spectrometer resolution = 5 eV,  $\lambda_p = 1430 \text{ \AA}$ , and  $x = 1610 \text{ \AA}$ .

The authors are with Bell Laboratories, Murray Hill, NJ 07974.

$$f(E) = \int_{E-\Delta/2}^{E+\Delta/2} F(E - E')G(E')dE' \quad (6)$$

where the interval  $\Delta$  is large enough to include all non-vanishing contributions. The integral in Eq. (6) was approximated by a sum; a typical result is shown in Fig. 2.

### Results

By comparing the convoluted spectrum to the ideal spectrum (Fig. 2) we are able to infer certain general effects of the instrument response: (1) the width of the convoluted

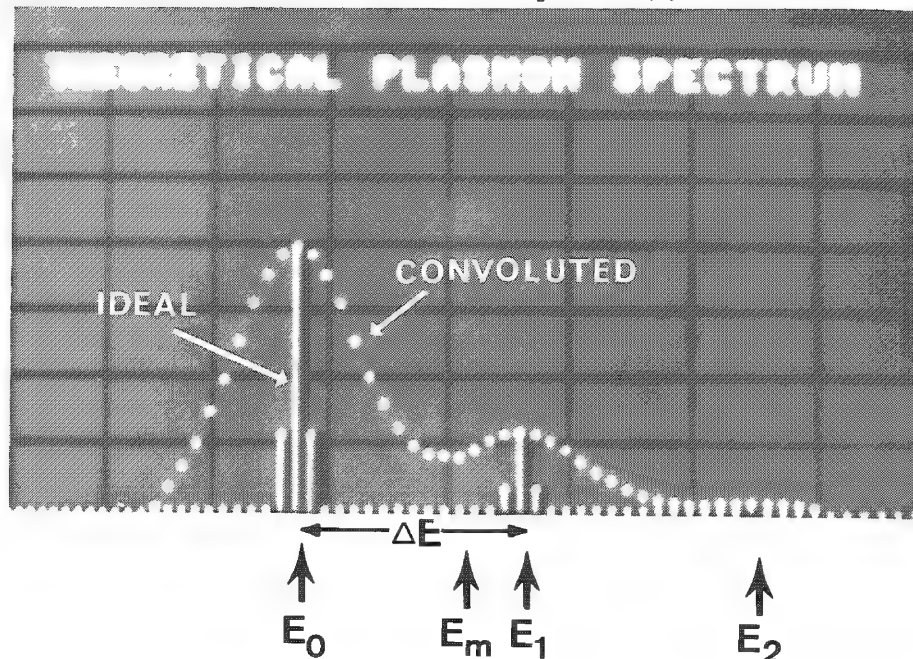


FIG. 2.--Theoretical plasmon spectrum with an ideal ratio of  $A_1/A_0 = 0.3$  and  $\Delta E = 15$  eV. The ideal spectrum (the narrow peaks) is shown along with the convoluted spectrum. The instrument response function has a resolution of 10 eV.

zero-loss peak is equal to the resolution of the spectrometer; (2) there is no apparent shift in the position of the plasmon peaks in the spectrum; and (3) there is a slight shift upwards in the minimum energy  $E_m$  between the peaks.

At first glance it might seem that the peak height ratio would be a good measure of the sample thickness. This method in practice is the least reliable since the peaks may be asymmetrical and may not be smooth enough to define the position of the peak sufficiently well.

In Fig. 3 we show the ratio of the areas of the first plasmon and zero-loss peaks from a convoluted spectrum using our theoretical model with an ideal ratio of 0.1. We compare the values of  $A_1/A_0$  at various peak separations  $\Delta E$  as a function of spectrometer resolution. These area calculations were performed by a computer by summing over 1eV energy increments in order to simulate the actual integrations as they are performed on a multi-channel analyzer. In these calculations the integration limits must be consistent with the theoretical model of the ideal plasmon spectrum. The integration limits of  $E$  for  $A_0$  and  $A_1$  are  $E_0 - \Delta E/2 \leq E \leq E_0 + \Delta E/2$  and  $E_1 - \Delta E/2 \leq E \leq E_1 + \Delta E/2$ , respectively.

The deviation of  $A_1/A_0$  from the ideal ratio increases (Fig. 3) as  $\Delta E$  gets smaller. This error is seen to be large ( $> 15\%$ ) at a modest resolution of 10eV for peaks separated by 18 eV. This deviation is affected in a systematic way by changes in the integration limits. If the limits are reduced equally in  $A_0$  and  $A_1$  while they remain symmetric about the energies of the peaks  $E_0$  and  $E_1$ , the deviation in the plasmon ratio is reduced signifi-

trons. This measurement was made with a JEOL JEM 100B microscope that had been fitted with a scanning attachment and a magnetic prism spectrometer. The largest peak corresponds to zero loss, that is, electrons that have been unscattered or elastically scattered in passing through the sample. From left to right the second, third, and fourth peaks correspond to the first, second, and third plasmon excitations. At higher energies (not shown in Fig. 1) are contributions from inner-shell excitations. We shall concentrate on the plasmon part of the spectrum in our discussion.

### Theory

Plasmon excitations occur at energies  $E_{pL} \approx 15\text{--}30$  eV;  $E_{pL}$  depends on the density  $N$  of free electrons, such that  $E_{pL} \propto N^{1/2}$ . The energy loss  $E_{pL}$  in each plasmon excitation is fixed for any material and the  $n$ th plasmon has an associated energy loss  $nE_{pL}$ . The probability  $P(n)$  of exciting  $n$  plasmons is given by Poisson statistics as

$$P(n) = \frac{1}{n!} \left( \frac{x}{\lambda_p} \right)^n \exp\left(-\frac{x}{\lambda_p}\right) \quad (1)$$

where  $x$  is the sample thickness and  $\lambda_p$  is the mean free path for excitation.<sup>4</sup> From this expression the probabilities for exciting no plasmon and one plasmon are, respectively,

$$P(0) = \exp(-x/\lambda_p) \quad (2a)$$

and

$$P(1) = (x/\lambda_p) \exp(-x/\lambda_p) \quad (2b)$$

The area  $A_0$  beneath the zero-loss peak in the spectrum represents the number of electrons that passed through the sample and did not excite a plasmon. If  $A_{\text{tot}}$  is the total area beneath the spectrum, then

$$A_0 = A_{\text{tot}} P(0) = A_{\text{tot}} \exp(-x/\lambda_p). \quad (3)$$

Likewise,  $A_1$ , the area beneath the first plasmon peak is just

$$A_1 = A_{\text{tot}} P(1) = A_{\text{tot}} \frac{x}{\lambda_p} \exp(-x/\lambda_p). \quad (4)$$

Dividing Eq. (4) by Eq. (3) we get

$$\frac{A_1}{A_0} = \frac{x}{\lambda_p} = \frac{P(1)}{P(0)} \quad (5)$$

Therefore, by measuring the ratio  $A_1/A_0$ , and knowing the mean free path  $\lambda_p$ , we can calculate the thickness of the sample  $x$ . The accuracy of evaluating  $A_1/A_0$  depends on the energy separation  $\Delta E$  of the plasmon peaks and the resolution of the spectrometer, as we shall show.

A reasonable model of an ideal plasmon spectrum is a series of narrow peaks with relative heights governed by Eq. (1). For our purposes it is assumed that the peaks are symmetrical and have the same full widths as the zero-loss peak. This approximation is appropriate for small  $x$  where the actual shape of the plasmon peak is less important. The energy spread of the zero-loss electrons is governed by the stability of the accelerating voltage and the thermal fluctuations of the electron gun filament. We have assumed that the zero-loss peak is Gaussian with a full width of 1.5 eV. This narrow line width is broadened as the spectrum is convoluted with the instrument response.

The instrument response function is assumed to be Gaussian, where the full width is the resolution of the spectrometer; so that the total plasmon spectrum  $f(E)$  is the ideal spectrum  $F(E)$ , convoluted with the instrument response function  $G(E)$ :

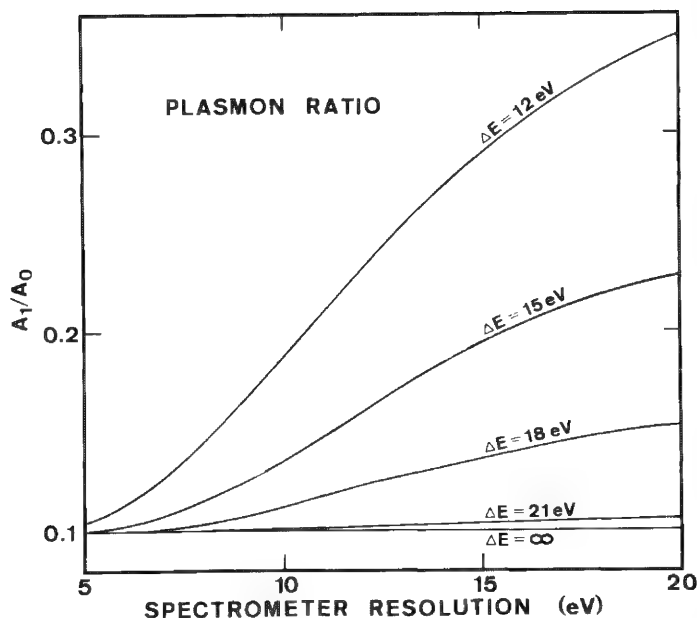


FIG. 3.--Calculated plasmon ratio ( $A_1/A_0$ ) as a function of spectrometer resolution for various  $\Delta E$  values. The ideal spectrum has  $A_1/A_0 = 0.1$ .

This method consists of calculating the logarithm of the ratio of the area under the entire spectrum to the zero-loss peak,

$$\frac{x}{\lambda_p} = \ln(A_{\text{tot}}/A_0) \quad (7)$$

which follows directly from Eq. (3). This method yielded results similar to those in Fig. 3 when the limits for  $A_0$  were  $E_0 - E/2 \leq E \leq E_0 + \Delta E/2$ . The deviations from the ideal value were more sensitive to the limits on  $A_0$  than the former method and there was no systematic way to reduce the deviation. Except for that difference there is little reason to prefer either method over the other if the limits of integration are carefully chosen.

### Conclusion

The present analysis demonstrates that the use of the plasmon peaks to determine sample thickness can produce answers with a substantial error unless proper account is taken of the effects introduced by the instrumental response of the electron spectrometer. In some unfortunate combination of circumstances, e.g., closely spaced plasmon peaks as occur in Al ( $E_{pL} = 15$  eV), and moderate spectrometer resolution, small changes in resolution of the kind that can result from drift in the system or poor focusing can have a significant effect on the thickness calculated.

### References

1. D. C. Joy and D. M. Maher, "A practical electron spectrometer for chemical analysis," *J. Microscopy* 114: 117-129, 1978.
2. D. C. Joy, R. F. Egerton, and D. M. Maher, "Progress in the quantitation of electron energy-loss spectra," *Proc. 12th Annual SEM Symp.*, Chicago: SEMINC, to be published, 1979.
3. R. C. Farrow, D. C. Joy, and D. M. Maher, to be published.
4. B. Jouffrey, "Electron energy losses with special reference to HVEM," in *Short Wave Length Microscopy*, New York: New York Academy of Sciences, 1978, 29-46.

cantly. The minimum deviation was achieved when the range of the integral was  $2(E_1 - E_m)$ . That is true at 10 eV and becomes less important at larger resolutions or very small  $\Delta E$ .

The absolute deviation of the plasmon ratio  $A_1/A_0$  from the ideal ratio depends only slightly on the ideal ratio used in the calculation. This fact causes a significant difference in the relative error for different plasmon ratios. At  $\Delta E = 15$  eV the absolute deviation increased nonlinearly by 14% when the ideal ratio was decreased from 0.5 to 0.05. The difference was less than 1% when the decrease was from a ratio of 0.1 to 0.05. The relative systematic error introduced by the spectrometer resolution to  $A_1/A_0$  thus increases drastically for small ratios, which implies that for very thin samples the estimation of the thickness from  $A_1/A_0$  can be most unreliable. As an example for  $\lambda_p = 1000$  Å, a 100 Å film might give a plasmon ratio as much as 35% higher than 0.1 (the result predicted from the theory) if the peaks were spaced 15 eV apart and the resolution of the spectrometer was 10 eV. On the other hand, a 300 Å film would give a 10% error and a 500 Å film would only give a 6% error.

Another method for calculating  $x/\lambda_p$  has been suggested by Joy, Egerton, and Maher.<sup>2</sup>



## ELECTRON ENERGY LOSSES AND ASSOCIATED SECONDARY-ELECTRON EMISSION OF CARBON, OXYGEN, AND HYDROGEN ON METALS

F. Pellerin, J. M. Fontaine, C. Le Gressus, and J. P. Duraud

Elements of low atomic number can be studied by electron energy loss, secondary-electron emission, or Auger emission. Auger electron spectroscopy is correlated with the inner-shell ionization mechanism and atomic relaxation. Electron energy loss spectrometry is related either to collective phenomena such as plasmon excitations, or to the excitation of molecular electronic states. The secondary electron emission of contaminated layers results from the de-excitation of these excited states. Using these results, we characterized graphite, carbon segregated on aluminum, and organic layers by excitation of  $\pi$  (6 eV) and  $\sigma$  (25 eV) orbitals. Molecular hydrogen, adsorbed on Pt, Ta, and Al, produces a 13 eV electron energy loss which is attributed to the excitation of the transitions  $^1\Sigma_g^+ \rightarrow ^1\Sigma_u^+$ ,  $^1\Pi_u$ . Adsorbed oxygen on clean aluminum produces an electron energy loss at 7 eV which has been reported as due to the 2p O level ionization. The cross section of  $\sigma \rightarrow \sigma^*$  orbital excitation is about 100 times higher than the inner K-level carbon ionization cross section. Molecular electronic level de-excitation produces a secondary-electron emission at an energy equivalent to that of the electron energy loss value.

### Introduction

After separate developments, SEM and AES were combined in an ultrahigh-vacuum apparatus. This evolution was necessary to make analysis of light elements and thin films possible. However, the interactions between the electron beam and the observed samples limit the capabilities of AES to studying the trace elements, because on one hand, the Auger cross section is very low and on the other, radiation effects appear since the current density is higher than  $10^{-3} \text{ A}\cdot\text{cm}^{-2}$ .<sup>1</sup>

On technological samples, the study of the electron energy losses and secondary-emission spectra shows clearly several peaks at 6, 7, 13, and 20 eV. The purpose of this work is to identify one origin of these peaks and to apply it to the elementary microanalysis.

### Experimental

We use a CMA electron spectrometer mounted on an ultrahigh vacuum apparatus with a tungsten hairpin electron gun. The signal detection is based on beam brightness modulation. The FWHM of the primary electron beam is 750 meV.

The analyzer energy window width was measured between 12 eV and a few keV on a carbon layer. A postacceleration (about 300 V) was applied between the CMA outlet slit and the first dynode of the electron multiplier in order to avoid a drop of the gain below 100 eV. Figure 1 presents a typical spectrum recorded with  $E_p \approx 30 \text{ eV}$ ,  $I_p \approx 10^{-10} \text{ A}$ , on a clean polycrystalline aluminum sample.<sup>2</sup> This spectrum, which must be taken as a test for a correct use of the CMA spectrometer, is characterized as follows:

1. A lack of secondary electrons between 0 and about 4 eV; this energy range measures the work function  $\phi$  of aluminum, as no electron can be emitted with an initial energy below  $\phi$ . In this experiment, the energy zero of the electron spectrometer is adjusted at the Fermi level.<sup>3</sup>
2. A symmetrical elastic peak of FWHM about 1 eV, which represents mainly the energy spread of the incident beam.

---

The authors are with the Division of Chemistry of the Physical Chemistry Section at the Centre d'Etudes Nucléaires de Saclay, B.P. 2, 91190 Gif-sur-Yvette, France.



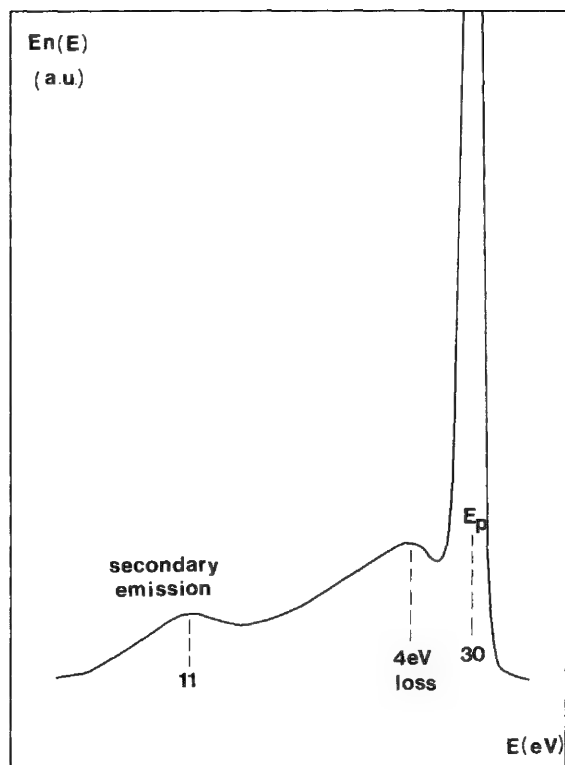


FIG. 1.-- $En(E)$  energy distributions at  $E_p = 30$  eV.

3. An energy loss peak at  $\Delta E \approx 4$  eV, attributed<sup>1</sup> to the aluminum interband transition. No loss peaks relative to surface and volume plasmon exists at this accelerating voltage.

These three features correspond to a good spectrometer reliability.

### Results

Our main results relate to electron energy losses and secondary-electron emission of carbon, oxygen, and hydrogen on metals.

1. *Carbon.* When a clean polycrystalline aluminum sample becomes gradually contaminated with C, the electron energy loss peak corresponding to the Al surface plasmon excitation ( $\Delta E \approx 10$  eV) decreases very quickly and disappears for a low coverage<sup>2</sup> ( $\theta \leq 0.01$ ) while electron energy losses appear at 6 and 20 eV, and secondary emission increases at 20 eV.

For graphite and organic monolayer (Allyl cyanid), we observed with both samples peaks of secondary emission at 6 and 20 eV, whereas the electron energy loss peaks are observed at 6 and 24 eV for graphite and 6 and 25 eV for the organic layer.<sup>9</sup>

2. *Oxygen.* The tabulation below summarizes the results obtained on a clean polycrystalline sample exposed to oxygen.

$E_p$ (eV)	Al		Al + O <sub>2</sub>	
	SE	ELS	SE	ELS
50	11	4,10,15	7,11	4,7,15
250	11	4,10,15	7,11	4,7,15
30	11	4	7,11	4,7

3. *Hydrogen.* Electron energy loss spectra recorded at increasing pressures of H<sub>2</sub> on various metals show the development of a peak at 13 eV (Fig. 2).

### Discussion

Electron energy losses on a clean metallic substrate have been reported previously by other authors. In contrast with their results, when a clean metal becomes contaminated with C, O, or H, the first noteworthy feature is the fast decrease of the electron energy loss intensity peak corresponding to the surface plasmon excitation. Furthermore, the energy value of the electron energy loss that develops during the contamination seems to depend essentially on the adsorbed element, without correlation with the electronic structure of the material.

The electron energy loss observed with C has been attributed previously either to the transition between a high density of state zones in the band structure of graphite<sup>4,5</sup> or to excitation of  $\pi$  and  $\sigma$  bonds.<sup>6</sup> As the electron energy loss values are roughly the same for carbon-contaminated metal, graphite, and organic layer, we prefer the molecular electronic excitation model.

The electron energy loss due to oxygen contamination has been attributed to excitation of a resonance level of chemisorbed oxygen (2p O level).<sup>7</sup> But that does not explain why

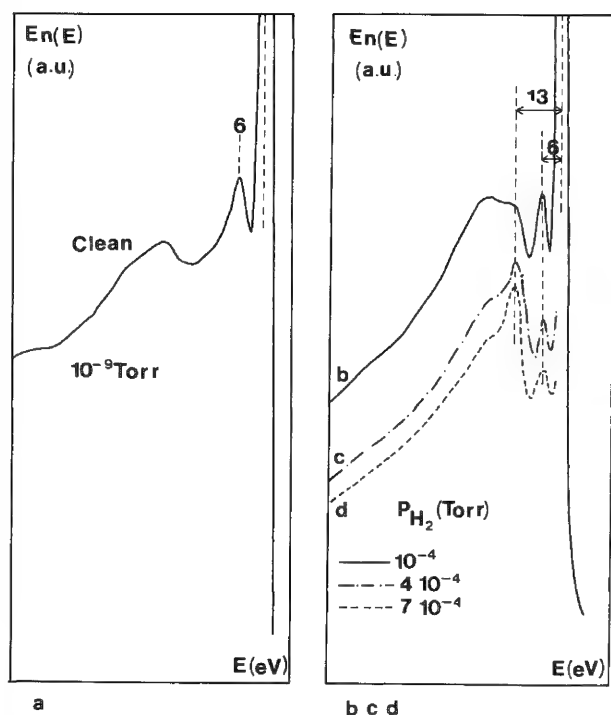


FIG. 2.--Electron energy loss spectrum (a) on clean Pt; (b)-(d) under various partial pressures of  $H_2$ .

### Conclusion

Segregated and adsorbed elements can be characterized by electron energy losses at 6 and 25 eV for carbon, 7 eV for oxygen, 13 eV for hydrogen. These electron energy losses for C and  $H_2$  are attributed to molecular electronic level excitations. This de-excitation results in secondary-electron emission. These emissions are used to make secondary electron micromappings of the adsorbates on a surface.

### References

1. C. Le Gressus, D. Massignon, and R. Sopizet, *Surf. Sci.* 68: 338, 1977.
2. D. Massignon, F. Pellerin, J. M. Fontaine, C. Le Gressus, and T. Ichinokawa, submitted to *J. Appl. Phys.*
3. K. O. Sevier, *Low Energy Electron Spectrometry*, New York: Wiley, 1972.
4. R. F. Willis, B. Fitton, G. S. Painter, *Phys. Rev. [B]* 9: 1926, 1974.
5. B. Lang, *Surf. Sci.* 60: 325, 1976.
6. M. Isaacson, *J. Chem. Phys.* 56: 1803, 1972.
7. C. Colliex, M. Gasgnier, and P. Trebbia, *J. de Physique* 37: 397, 1976.
8. T. E. Everhart, N. Saeki, R. Shimizu, and T. Koshikawa, *J. Appl. Phys.* 47: 2941, 1976.
9. F. Pellerin and C. Le Gressus, *Surface Science* (in press).

this loss is developed at the same value for every studied case.

With regard to the hydrogen contamination, studies have been conducted on silicon and rare earth hydrides.<sup>8</sup> No loss was observed at 13 eV. Then we assign the 13eV observed electron energy loss on Pt, Ta, and Al, to the excitation of hydrogen molecular electronic levels  $^1\Sigma_g^+ \rightarrow ^1\Sigma_u^+$ ,  $^1\Pi_u$ .

As this process is not fully reversible with pressure (we had to heat tantalum at 300°C to return to the initial state), we consider that the contribution of gas molecules to the 13eV loss peak is negligible. On the other hand, the physically adsorbed hydrogen molecules or the molecules trapped in clusters of vacancies could produce this loss peak.

In every case, the secondary-electron emission developed was roughly at the same energy value as the characteristic electron energy loss, and could be the result either of ion neutralization near the surface, or of molecules de-excitation by an Auger-like mechanism. The intensity of the electron energy loss and that of the secondary-electron emission have the same value, for C and O.<sup>9</sup>

For carbon, comparison between the electron energy loss intensity and that of KLL carbon Auger transition shows that these processes have a cross section greater than the inner shell ionization cross sections.

## Raman Microanalysis

### RAMAN MICROPROBE CHARACTERIZATION OF SOUTH POLE AEROSOL

W. C. Cunningham, E. S. Etz, and W. H. Zoller

There has been concern whether it would be possible for man to alter the earth's climate by injecting excessive amounts of particulate material into the atmosphere.<sup>1</sup> To determine the relative contributions of the major particle sources to the global aerosol covering, the University of Maryland and the University of Rhode Island are conducting a joint study on atmospheric aerosols collected at the South Pole. The remoteness and isolation from any major particle source make this an ideal location to study composition and concentrations of the global particulate burden typical of the upper troposphere or lower stratosphere.

The South Pole is at an elevation of 2800 m and the tropopause is lower in altitude in the polar regions than at other latitudes.<sup>2</sup> There are also catabatic wind flows at the South Pole that hinder the transport of lower tropospheric aerosol from the margin of the Antarctic continent to the interior and make possible strong stratospheric contribution to the aerosol in the South Pole air.

A major thrust of stratospheric aerosol studies has been in the physical and morphological characterization of the aerosol.<sup>3-5</sup> Chemical spot tests have shown sulfate to be a principal component of the aerosol.<sup>6</sup> Results of scanning electron microscopy (SEM), energy-dispersive x ray, x-ray diffraction, and wet chemical studies have implicated the existence of  $\text{H}_2\text{SO}_4$ ,  $(\text{NH}_4)_2\text{SO}_4$ , and  $(\text{NH}_4)_2\text{S}_2\text{O}_8$ .<sup>7-10</sup>

South Pole aerosol samples collected by the University of Maryland have been analyzed principally for their elemental composition by bulk methods<sup>11</sup> (e.g., instrumental neutron activation analysis) and single particle methods<sup>12</sup> (principally SEM/x-ray analysis). The results obtained from bulk sample collections indicate high sulfur concentrations and SEM/x-ray studies show sulfur to be present in virtually all particles.<sup>13,14</sup>

A major limitation of conventional single-particle analysis techniques has been their inability to furnish direct evidence of molecular composition. However, with the advent of Raman microprobes it has become possible to obtain vibrational Raman spectra from microscopic samples frequently of mass as low as 1 picogram.<sup>15,16</sup> These spectra allow one to identify the major molecular components and often obtain additional information on the crystalline state of the solid phase.

The Raman microprobe developed at the National Bureau of Standards (NBS) has been shown to be an effective tool for the identification of single particles in airborne dust samples.<sup>17</sup> Its ability to identify specific sulfates as major constituents of aerosol samples has been demonstrated in the case of various types of aerosol collections. In the work reported here we have employed the NBS Raman microprobe to obtain vibrational spectra from single microparticles and subnanogram amounts of submicrometer aerosol particles collected at the South Pole. Described are the sample requirements for micro-Raman analysis, the measurement procedures employed, and the interpretation of the spectra obtained. The results on the molecular identity of the aerosol have been correlated with x-ray results obtained in parallel investigations for a more complete chemical characterization of the aerosol. Modeling experiments consisting of the micro-Raman study of laboratory-generated sulfate aerosols have been performed to answer questions concerning particle transformations observed for the field-collected samples.

---

Authors Cunningham and Zoller are with the Chemistry Department of the University of Maryland; Dr. Etz is at the Center for Analytical Chemistry of the National Bureau of Standards. The support of this research by the National Science Foundation is gratefully acknowledged. The work presented is from a dissertation to be submitted to the Graduate School, University of Maryland, by W. C. Cunningham, in partial fulfillment of the requirements for the Ph.D. degree in chemistry.

## *Experimental*

1. *Sampling Site.* The samples investigated in this study were collected during two research expeditions to the South Pole. The first took place during the period from November 1975 through January 1976; the second, from November 1977 through January 1978.

During each period the samples were collected at a site located 3 miles northeast of the U.S. Scientific Research Station at the South Pole. By sampling at this location, particulate contamination from activities at the research station were minimized as much as possible, since prevailing winds keep this site upwind essentially all the time. Air temperatures varied between  $-20$  and  $-35^{\circ}\text{C}$  during sampling. Thus, any liquid-phase aerosol observed in our laboratory can be assumed to have been in the solid phase during sampling.

2. *Aerosol Sampling.* For characterization of the airborne particulate material, size-segregating impactors were employed as well as conventional high-volume air samplers. All samples intended for micro-Raman analysis were collected by a five-stage Battelle-type impactor. The collection stages were modified to hold micro-Raman sample supports (i.e., substrates). This modification permitted aerosol collection directly onto the substrates and eliminated the need for any kind of transfer of the collected material. For this study, two substrate materials were chosen on the basis of spectral and physical properties,  $\text{Al}_2\text{O}_3$  (sapphire) and LiF. The flow rate during collection was approximately one liter per minute and sampling duration was varied between one and five days, so that a wide range of aerosol loading densities was obtained.

3. *Sample Storage and Handling.* Immediately after collection, the samples were transferred to storage containers inside a clean hood and sealed in polyethylene bags. During sample transfer the relative humidity was less than 5%. All samples were then stored outdoors (at ambient temperatures) to prevent possible aerosol transformations. The samples were then transported to the University of Maryland laboratories and stored in a dessicator at room temperature. They were unpackaged and exposed to ambient laboratory conditions just prior to measurement.

4. *Characterization by Microscopy.* a. *Light Microscopy.* Each sample was initially characterized in a polarizing light microscope. As expected, particle loading increased and particle size decreased with each successive impaction stage; the vast majority of particles was of submicrometer size and deposited on the last two stages. The deposit was also such that some areas on each stage were more densely covered than others. The reactive nature of the aerosol was indicated by areas in which aerosol had reacted with the aluminum particle-finder grids (thin films of Al, about 10-20 nm thick) that had been evaporated onto the substrate prior to sampling. The aerosol was also noted to be hygroscopic at high relative humidities ( $\sim 65\%$ ). In the extreme case of moisture absorption the particles transformed into microdroplets, which recrystallized at low relative humidities.

b. *SEM Characterization.* Following Raman microprobe investigation, the samples were coated with carbon films for SEM/x-ray analysis. Regions where Raman measurements had been made were relocated in a Cambridge SEM equipped with an energy-dispersive x-ray detector. The SEM investigations were limited to regions in which Raman microprobe measurements had been performed; no extensive sample characterization was conducted. In the regions investigated (principally on the fourth and fifth stages), three distinct morphologies were observed, namely aggregates; needlelike crystals; and flat, rounded particles. X-ray measurements were made on many particles of each morphology. The single most striking result of the x-ray analysis is that sulfur ( $Z \geq 11$ ) is the only element detected and found to be associated with these particles. Figure 1 shows a typical region of a collection of aerosol on a LiF substrate. This region contains both aggregates and needlelike crystals. An x-ray spectrum typical of those obtained from all three identifiable morphologies is shown in Fig. 2. This spectrum was taken from one of the aggregates seen in Fig. 1. Two peaks are observed. The right-hand peak at 2.32 keV arises from the  $K\alpha$  emission from the sulfur present. The other peak at 0.7 keV is attributed to the  $K\alpha$  emission from fluorine of the LiF substrate.

5. *Laboratory Aerosol Studies.* Sulfate aerosol was generated under controlled conditions into a chamber, then sampled with a cascade impactor identical to the one used in the field sampling. Aerosol size was varied between  $0.2\ \mu\text{m}$  and  $\sim 10\ \mu\text{m}$  in diameter. Aerosol

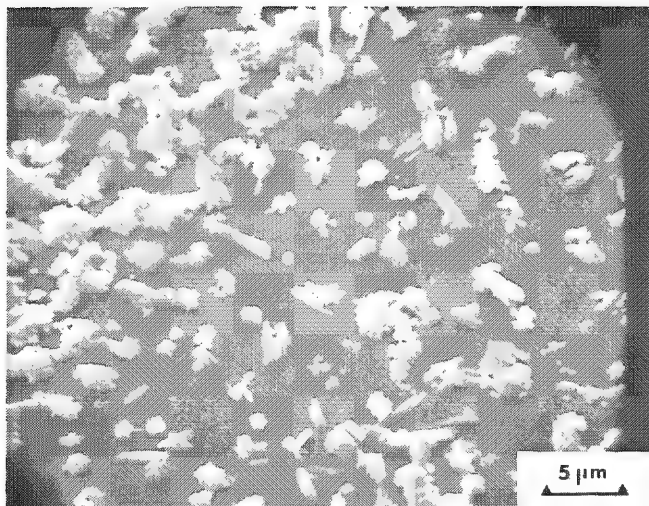


FIG. 1.--SEM micrograph of South Pole aerosol collected on fourth stage of cascade impactor. Substrate is lithium fluoride.



FIG. 2.--X-ray spectrum obtained with SEM of aggregate of microcrystals in impactor sample of South Pole aerosol (cf. Fig. 1).

concentration was adjusted such that a suitable collection was obtained in less than 1 min of sampling time. Aerosols prepared from solutions of sulfuric acid, of ammonium sulfate, and mixtures of the two have been studied. Although these aerosol collections are not identical in all respects to the samples brought back from the South Pole, there is a strong resemblance (with respect to physical appearance and chemical identity) between them. The principal interest in these experiments was to learn more about substrate reactions with these kinds of aerosols.

6. *Raman Microprobe Analysis.* Raman microprobe analysis furnishes spectra characteristic of the molecular and crystal vibrations of the sample. Spectra are obtained by analysis of the inelastically scattered light from the sample subjected to a beam of focused laser light. The microprobe is basically a Raman spectrometer consisting of an exciting laser, beam focusing and scattered light collection optics, a sample stage, a monochromator, and a photomultiplier detector. Details on instrument configuration are given in the literature.<sup>16</sup> The sample stage is enclosed by a sample chamber purged with dry nitrogen to prevent exposure of hygroscopic samples to ambient conditions of high relative humidity.

The laser excitation wavelength that is most often used is 514.5 nm (green). However, when appreciable absorption or sample fluorescence is encountered at this wavelength the spectrum is excited with 647.1nm (red) radiation. Both excitation wavelengths were used for the analysis of South Pole aerosol. Irradiance levels from several kilowatts/cm<sup>2</sup> to fractions of a megawatt/cm<sup>2</sup> were employed by variation of the beam spot size between 20 and 2 μm in diameter. The size of the laser spot in the focal region roughly determines the spatial resolution with which the microprobe measurement is made. Measurement times necessary to obtain analytical-quality spectra may vary from tens of minutes to several hours depending on the detected scattering intensity.

The relative humidity within the sample chamber can be held to ~20% to protect hygroscopic samples. However, the samples are exposed to ambient laboratory air during transfer to the spectrometer sample stage and during observation in the light microscope. A number of the South Pole samples have been inadvertently exposed to relative humidities high enough for moisture absorption to have taken place. In these cases, microscopic droplets were seen to have formed and coalesced with ones nearby to form larger microdroplets. Raman measurements have also been made on particles formed by the recrystallization of such droplets when samples were returned to conditions of low relative humidity.

### *Results and Discussion*

This paper presents results from a larger study with some work still in progress. The

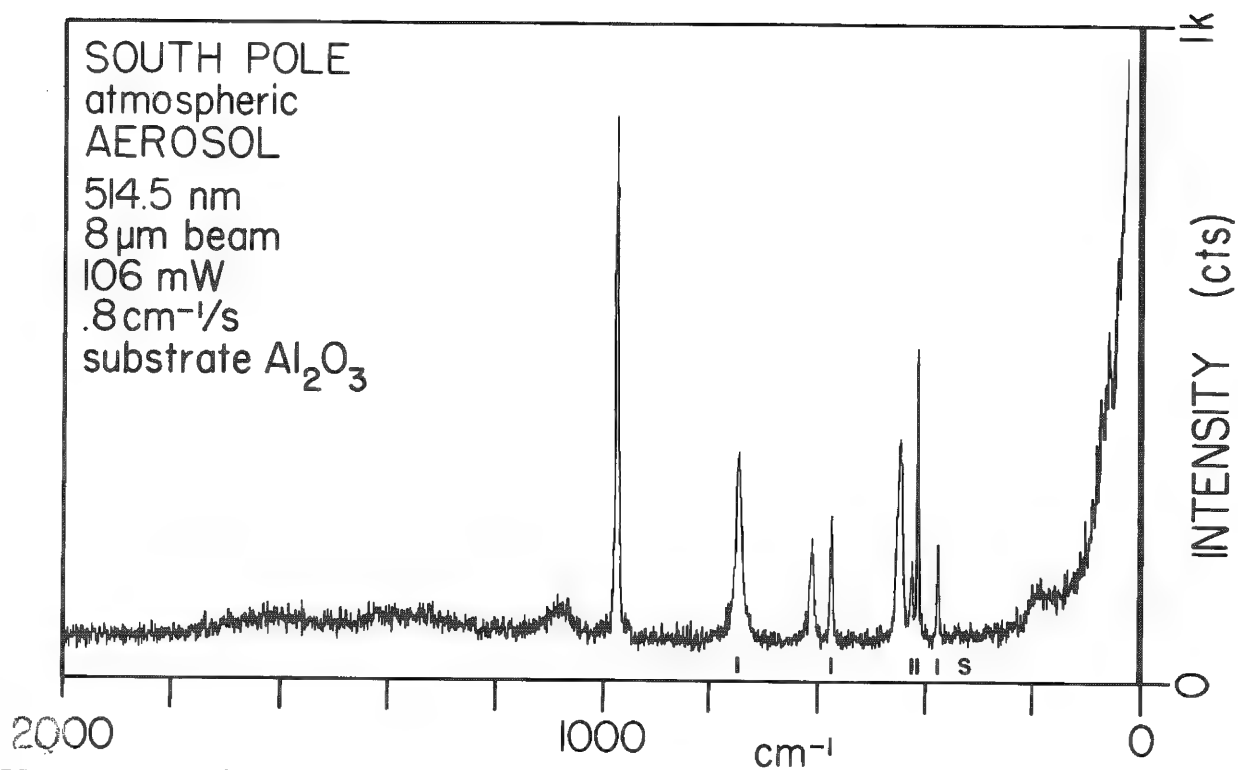


FIG. 3.--Raman microprobe spectrum of impactor-collected South Pole aerosol, Stage 5. Indicated are excitation wavelength, size (diam.) of laser spot, laser power (at sample), scan rate, and sample support. Measurement time constant 1.3 s, spectral slit width 3 cm⁻¹.

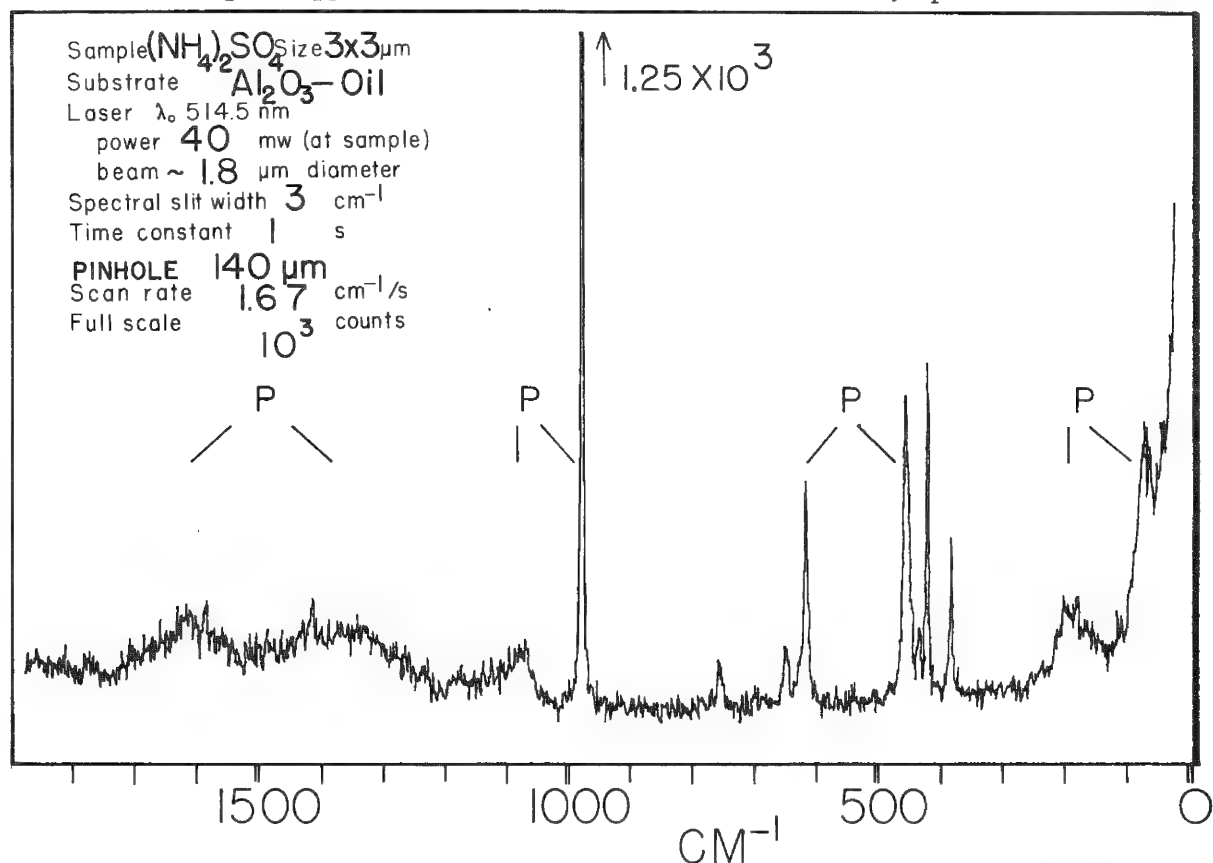


FIG. 4.--Reference spectrum of microparticle of ammonium sulfate. Measurement conditions are indicated. Pinhole in path of collected scattered light serves to minimize spectral interference from substrate.<sup>16</sup>



discussion presented here highlights the results of these investigations and a more complete account of this research is presented elsewhere.<sup>18</sup> In some cases, the interpretation of the results is tentative with work yet to be done. All spectra presented below are plots of scattered intensity versus Raman shift ( $\text{cm}^{-1}$ ).

Figure 3 is a Raman spectrum obtained from a recrystallized particle located on the fifth stage (sapphire substrate) of an impactor-collected sample. Examination of the positions, intensities, and shapes of the observed Raman bands indicates that this particle principally consists of  $(\text{NH}_4)_2\text{SO}_4$ .<sup>19</sup> The bands arising from  $\text{SO}_4^{2-}$  vibrations are seen centered at frequencies 452, 614, 977, and  $1080\text{ cm}^{-1}$ . Relative to the band intensities observed for the  $\text{SO}_4^{2-}$  vibrations, we do not expect to detect the bands due to the internal vibrations of the  $\text{NH}_4^+$  ion because of their comparatively much weaker scattering intensity. These bands have shifts centered at 1429 and  $1669\text{ cm}^{-1}$ . The weak, broad features centered at  $1350\text{ cm}^{-1}$  and  $1600\text{ cm}^{-1}$  are indicative of carbonaceous material associated with the particle.<sup>20-22</sup> The origin of this material is unknown but the appearance of "carbon bands" from environmentally collected samples is not uncommon.<sup>22</sup> The bands centered at 187 and  $73\text{ cm}^{-1}$  arise from lattice vibrations and are characteristic of the crystal structure of the solid phase. The bands marked *S* arise from the sapphire substrate. SEM analysis shows this particle to be flat, with rounded edges containing sulfur as the only observable element.

Figure 4 is a reference spectrum obtained with the Raman microprobe from a small  $(\text{NH}_4)_2\text{SO}_4$  crystal. All the sulfate vibrations seen in Fig. 3 are also seen in this spectrum. The two broad features above  $1200\text{ cm}^{-1}$  derive from internal modes of the  $\text{NH}_4^+$  ion and are not the carbon bands referred to above. The oil overcoat, as noted in the legend, was applied to this reference sample to protect it from moisture in the ambient air.

A marked difference between samples collected on LiF substrates and those collected on sapphire is that the needlelike crystals mentioned above appear only on LiF. Figure 5 is a Raman spectrum obtained from a microscopic sample region on a LiF substrate in an area

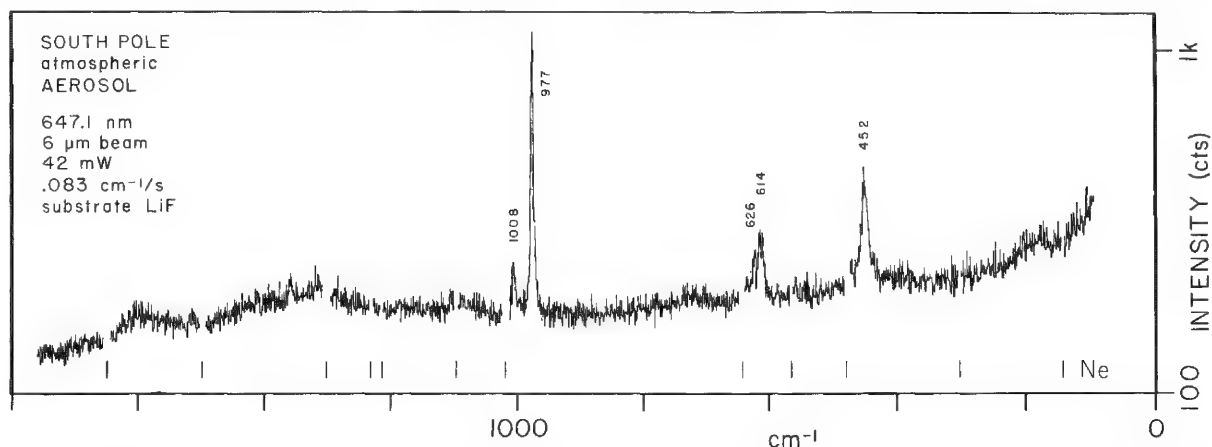


FIG. 5.--Raman microprobe spectrum of South Pole aerosol collected on Stage 5. Measurement conditions are indicated. Scan time constant 10 s, spectral slit width  $3\text{ cm}^{-1}$ .

containing some needlelike crystals but predominantly aggregates. In this measurement the beam spot covered a large aggregate as well as part of a needlelike crystal nearby. The spectrum shows the sample to contain predominantly  $(\text{NH}_4)_2\text{SO}_4$ .<sup>19</sup> The most prominent features expected from  $(\text{NH}_4)_2\text{SO}_4$  are seen and the Raman shifts for the major bands are indicated. The shoulder at  $626\text{ cm}^{-1}$  does not appear in Fig. 4 but is present in other reference spectra of the salt. We attribute this observation to particle orientation effects. Frequency assignments were made against neon calibration lines omitted from the spectrum but marked with bars labeled *Ne*. The band at  $1008\text{ cm}^{-1}$  is attributed to the symmetric stretch of  $\text{SO}_4^{2-}$  in lithium sulfate (presumably  $\text{Li}_2\text{SO}_4 \cdot \text{H}_2\text{O}$ ).<sup>23</sup> As LiF contributes no spectral interference, sample impurity and some degree of heating from absorption of the exciting laser cause a moderate background. Other bands characterizing  $\text{Li}_2\text{SO}_4$  are much weaker and not seen here. The broad bands above  $1200\text{ cm}^{-1}$  again indicate the presence of carbonaceous material. Interrogation of other aerosol regions showed lithium sulfate to be associated with  $(\text{NH}_4)_2\text{SO}_4$  to varying degrees.



Figure 6 is a Raman spectrum from a microsample on a LiF substrate in an area noted in the SEM to contain a relatively high abundance of needlelike crystals. The spectrum

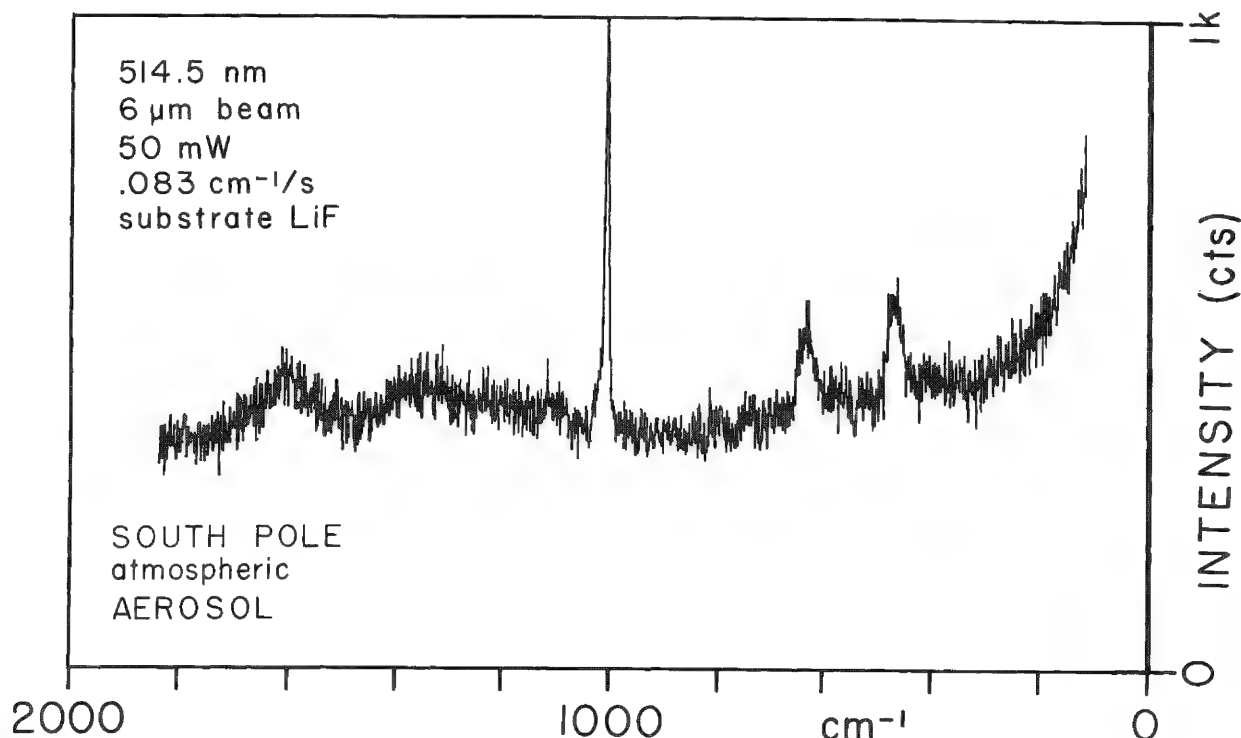


FIG. 6.--Raman microprobe spectrum of South Pole aerosol collected on Stage 4. Measurement conditions are indicated. Scan time constant 12 s, spectral slit width 3  $\text{cm}^{-1}$ .

has many of the characteristics of that of  $\text{Li}_2\text{SO}_4 \cdot \text{H}_2\text{O}$ ; however, we are not excluding the possibility that it is a double sulfate.<sup>24</sup> Further work on the more definitive interpretation of this and other such spectra is in progress. The bands observed at around 471, 636, 1008, and 1115  $\text{cm}^{-1}$  are from this material. Again, carbonaceous bands are present at 1350 and 1600  $\text{cm}^{-1}$  and the background is quite high. SEM investigation shows that the LiF substrate is pitted in the regions where needlelike crystals are found. This is interpreted to be the result of interaction of the aerosol with the LiF. Sulfuric acid aerosol generated in the laboratory and collected on LiF substrates reacted instantaneously to produce needlelike crystals similar in morphology to those seen in the South Pole samples. Raman microprobe measurements show these to be  $\text{Li}_2\text{SO}_4$  microcrystals. Ammonium sulfate aerosol was also collected on LiF substrates and stored under ambient laboratory conditions for as long as 3 days with no discernible aerosol-substrate interaction.

### Conclusion

We have shown that the new technique of Raman microprobe analysis can furnish unique results in the study of atmospheric aerosol of this type. The results presented here show direct evidence for the existence of sulfate species in the South Pole aerosol but further studies are needed to clarify many remaining questions concerning the *in situ* nature of the aerosol. Foremost are questions pertaining to sampling effects, the likely reactions of atmospheric sulfate aerosol with other aerosol components, and the collection substrate, as well as transformations that may have occurred during sample storage and handling.

### References

1. J. B. Pollack et al.; "Volcanic explosions and climatic change; A theoretical assessment," *J. Geophys. Res.* 81: 1071, 1976.
2. H. R. Byers, *General Meteorology*, New York: McGraw Hill, 1974, 4th ed., 56.
3. C. E. Junge, C. W. Chagnon, and J. E. Manson, "Stratospheric aerosols," *J. Meteor.* 18: 81, 1961.

4. E. K. Bigg, "Size distribution of stratospheric aerosols and their variations with altitude and time," *J. Atmos. Sci.* 33: 1080, 1976.
5. R. D. Cadle, *The Measurement of Airborne Particles*, New York: Wiley, 1975.
6. C. E. Junge, *Air Chemistry and Radioactivity*, New York: International Geophysics, 1963, 192.
7. C. E. Junge and J. E. Manson, "Stratospheric aerosol studies," *J. Geophys. Res.* 66: 2163, 1961.
8. J. P. Friend, "Properties of the stratospheric aerosol," *Tellus* 18: 465, 1966.
9. A. L. Lazrus, B. Gandrud, and R. D. Cadle, "Chemical composition of air filtration samples of the stratospheric sulfate layer," *J. Geophys. Res.* 76: 8083, 1971.
10. E. K. Bigg, "Stratospheric particles," *J. Atmos. Sci.* 32: 910, 1975.
11. W. H. Zoller, E. S. Gladney, and R. A. Duce, "Atmospheric concentrations and sources of trace metals at the South Pole," *Science* 183: 198, 1978.
12. E. J. Mroz, private communication, 1976.
13. W. Maenhaut et al., "Concentration and size distribution of particulate trace elements in the South Polar atmosphere," *J. Geophys. Res.*, in press, 1979.
14. E. J. Mroz et al., "Physical and chemical analysis of particles collected with impactors at the South Pole," in preparation, 1979.
15. P. Dhamelincourt et al., "Laser Raman molecular microprobe (MOLE)," *Anal. Chem.* 51: 414A, 1979.
16. G. J. Rosasco and E. S. Etz, "The Raman microprobe: A new analytical tool," *Research and Development* 28: 20, 1977.
17. E. S. Etz, G. J. Rosasco, and E. C. Cunningham, "The chemical identification of airborne particles by laser Raman spectroscopy," in G. W. Ewing, Ed., *Environmental Analysis*, New York: Academic Press, 1977.
18. W. C. Cunningham, *A Study of Trace Elements on Particles in the South Pole Atmosphere*, University of Maryland: Department of Chemistry, Ph.D. thesis, 1979.
19. P. Venkateswarlu, H. D. Bist, and Y. S. Jain, "Laser excited Raman spectrum of ammonium sulfate single crystal," *J. Raman Spectrosc.* 3: 143, 1975.
20. F. Tuinstra and J. K. Loenig, "Raman spectrum of graphite," *J. Chem. Phys.* 53: 1126, 1970.
21. H. Rosen and T. Novakov, "Raman scattering and the characterization of atmospheric aerosol particles," *Nature* 266: 708, 1977.
22. J. J. Blaha, G. J. Rosasco, and E. S. Etz, "Raman microprobe characterization of residual carbonaceous material associated with urban airborne particulates," *Appl. Spectrosc.* 32: 292, 1978.
23. C. Vassas-Dubuisson, "Vibrational spectrum of a single crystal of lithium sulfate monohydrate," *Compt. Rend.* 233: 374, 1951.
24. V. Ananthanarayanan, "Raman spectra of crystalline double sulfates: Part II. Ammonium double sulfates," *Z. Phys.* 166: 318, 1962.

## DEVELOPMENTS AND APPLICATIONS OF THE MOLE LASER RAMAN MICROPROBE

P. Dhamelincourt

Physical analytical methods--electron microscope and microprobe, ion microprobe--have provided the analyst with powerful investigating means that permit the determination of morphology and elemental composition of samples in the micrometer size range. But these techniques use the emission of secondary electrons, x rays, or secondary ions caused by a primary electron or ion beam focused on the sample so that, based on atomic properties, they only provide indirect information about the polyatomic structures present in the sample. To come closer to the ultimate goal of microanalysis--positive identification of the molecular constituents of microsamples and their distribution in the solid state--it was necessary to turn to techniques that provide data on molecular structure (x-ray diffraction, neutron scattering, NMR, and infrared and Raman vibrational spectroscopy). With the advent of the laser, by which the energy of a light beam can be concentrated into a very small volume, Raman spectroscopy appeared to be a choice method for the analysis of very small amounts of matter. Normal (spontaneous) Raman scattering<sup>1-3</sup> relates to the change of frequency observed when a monochromatic light beam ( $\nu_0$  frequency) is scattered by polyatomic molecules. The scattered light contains, near the  $\nu_0$  radiation (Rayleigh scattering without change in frequency), much weaker radiations ( $10^{-6}$  to  $10^{-9}$ ) at frequencies  $\nu_0 - \nu_i$  (Stokes lines) and  $\nu_0 + \nu_i$  (anti-Stokes lines). All these lines form the Raman spectrum. The  $\nu_i$  frequencies, expressed in wave number  $\bar{\nu} = \nu/c(\text{cm}^{-1})$ , characterize the scattering media and are independent of the incident radiation frequency. They correspond to the frequencies of the atom oscillations in polyatomic structures. They are directly read on the Raman spectrum recording, which usually consists only of the more intense Stokes part and whose origin is the  $\nu_0$  frequency. Raman spectra can be used to characterize and identify the chemical species (inorganic, organic, and biological molecules) and precisely determine their structure in all phases of matter. Thus, the vibrational Raman spectra can be regarded as unique fingerprints and often contain information on the local molecular environment.

Raman analysis is relatively rapid (spectrum recording usually takes less than 1 hr) and nondestructive; it may be conducted in air under a controlled atmosphere or even inside transparent media and does not generally require special preparation of the sample. These facts have led two laboratories--the U.S. National Bureau of Standards (NBS) and the Centre National de la Recherche Scientifique (CNRS) at Lille in France--to pioneer the use of Raman spectroscopy as a microanalytical tool,<sup>4,5</sup> and to develop independently in recent years two types of advanced, first-generation microprobe instruments.<sup>6-9</sup> Despite the major limitations of the technique (mainly, the inherent weakness of the Raman effect, the possible fluorescence interferences, and the lack of quantitation), enough problems have been successfully solved by the two pioneering laboratories so far in a wide range of application areas to demonstrate the practical use and the unique capabilities of this technique.<sup>10-13</sup>

The purpose of this paper is to review the development of the MOLE (Molecular Optical Laser Examiner) Raman microprobe/microscope and discuss some results on the application of this instrument to diverse problems in microanalysis.

### *MOLE Raman Microprobe/Microscope*

Some years ago, several arrangements were studied at CNRS-Lille to obtain not only the Raman spectrum of microsamples but also images of very small objects by means of a characteristic Raman frequency. From experience gained in this preliminary work we came to the

---

The author is at the Laboratoire de Spectrochimie Infrarouge et Raman--CNRS, Université des Sciences et Techniques de Lille, C5--B.P. 36, 59650 Villeneuve d'Ascq, France.

conclusion that a good way to study microsamples was to start from the tool of the microscopist--the optical microscope--to create an instrument specially designed for the use of the Raman effect for analyzing such samples. Two prototypes were built and described in earlier published work<sup>7,14</sup> and in patents.<sup>15-17</sup> This instrument is now commercially available under the name of MOLE (Instruments S.A., Inc., J-Y Optical Systems Division).

MOLE assembles in the same instrument (Fig. 1) a conventional optical microscope (with

## DOUBLE CONCAVE HOLOGRAPHIC GRATING FILTER

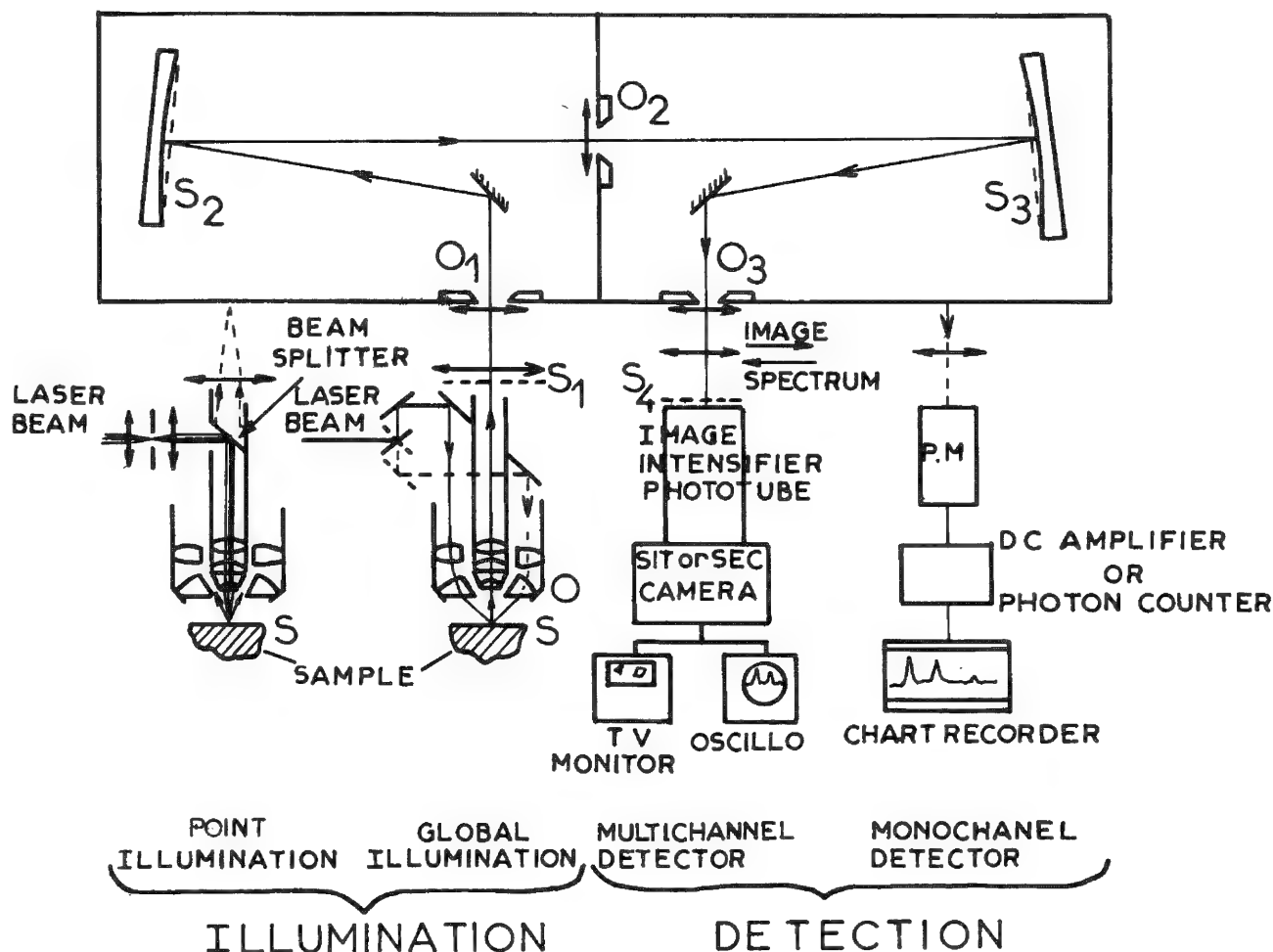


FIG. 1.--Diagram of Raman microprobe/microscope (MOLE) developed at CNRS-Lille, illustrating modes of sample illumination and signal detection.

bright- and dark-field illumination), an optical filter possessing a very low stray light level (built with two concave holographic gratings), and two detection systems (monochannel and multichannel). This association results in a very versatile instrument because it permits two different modes of operation:

(1) Point Illumination with Monochannel or Multichannel Detection (Spectral Mode). By means of the bright-field illumination system of the microscope, the same objective (of high numerical aperture) is used to focus the laser beam into a spot on the component of the sample to be identified and to collect the scattered light at the focal point. The scattered light is sent on the entrance slit of the optical filter, which can work as a micro-Raman spectrometer when the detector is a photomultiplier followed by an amplifier (or a photon counter) and a chart recorder (monochannel detection); or as a micro-Raman spectrograph when the detector is an intensifier phototube followed by a low light level spectrograph when the detector is an intensifier phototube followed by a low light level TV camera. In this case the spectrum is visualized on a TV monitor or a CRT screen. An

adjustable image-field iris diaphragm placed in the image plane of the sample permits the elimination of light (Raman light of support or host material, fluorescence) that does not originate from the focal point and to monitor the depth resolution of the probe (spatial filtering).

(2) Global Illumination and Raman Imaging System (Imaging Mode). In this mode, a larger circular area (150 or 300  $\mu\text{m}$  in diameter) is illuminated with a rotating laser beam feeding the objective annular illuminator (dark-field illuminator device). In this case, the top aperture of the microscope objective (O) is optically conjugated with the three slits ( $O_1$ ,  $O_2$ ,  $O_3$ ) of the optical filter and the image ( $S_1$ ) of the sample (S) given by the objective is formed on the gratings ( $S_2$ ,  $S_3$ ) and from there transferred through the aperture of the exit slit ( $O_3$ ) to the photocathode of the intensifier tube ( $S_4$ ) (multichannel detection).

By selecting, in the Raman spectrum, a radiation characterizing one particular component in the sample and by tuning the optical filter to this frequency, one obtains a micrographic image on the TV monitor which indicates the distribution of this component throughout the illuminated area. The spatial resolution of the image is about 1  $\mu\text{m}$ .

Finally, the imaging system can also be used with point illumination of the sample, so that one may rapidly and easily determine, from the observation of the Raman image of the focus point at the surface or inside the sample, the best conditions for recording spectra (maximum of Raman signal, adjustment of the image field diaphragm).

#### *Applications of Raman Microprobe Analysis*

Many problems were submitted to us. In order to illustrate how the method may be adapted to various problems, we present a few illustrative examples in totally different domains.

*Geology: Inclusions in Minerals.* (1) Solid Inclusions. Raman microprobe permits the localization and analysis of solid inclusions in natural rocks. Figure 2 shows the analysis of inclusions of sulfur ( $S_8$ ) in a natural sample of celestite ( $\text{SrSO}_4$ ). The inclusions are localized by Raman images in the strong  $473\text{cm}^{-1}$  line of sulfur. Isolation of the characteristic strong  $1000\text{cm}^{-1}$  band in the spectrum of  $\text{SrSO}_4$  furnished the image of the host mineral. These images can be compared with that obtained with white light.

(2) Fluid Inclusions. In most cases mineralogic reactions in the earth's crust occur in the presence of a fluid phase which may be trapped in the crystal defects. These fluid inclusions are real witnesses of the genesis of minerals and their compositions are of great interest for the geochemist. A great improvement in the chemical study of fluid inclusions is provided by the Raman microprobe,<sup>18-19</sup> which permits the nondestructive analysis *in situ* of the gas, liquid, or solid in an individual inclusion within transparent media. However, attention must be paid to the irradiance level because local overheating can modify the equilibrium between the phases inside the inclusion. Figure 3 shows the analysis of gas inclusions in the  $\text{N}_2$ - $\text{CO}_2$  system. These inclusions are found inside host quartz and dolomite from Central Tunisian diapsirs.<sup>20</sup> Raman microprobe investigation shows fossil fluids of variable  $\text{N}_2/\text{CO}_2$  ratio. These results agree with microcryoscopic data,<sup>21</sup> but Raman analysis supplies more information since the ratio  $\text{N}_2/\text{CO}_2$  can be obtained directly from the relative cross sections of these gases and the spectral response of the instrument. This ratio lies between 0.5 and 9, depending on the inclusions. In the same samples (quartz and dolomite), some monophasic liquid inclusions (of about 50  $\mu\text{m}$  in linear dimension) containing aliphatic or aromatic hydrocarbon (Fig. 4), have been disclosed. The simultaneous presence, inside the same crystal, of these different inclusions (hydrocarbons and nitrogen) may be related to the superficial signs of oil fields in the same region of Central Tunisia and leads to the supposition that the nitrogen is of organic origin.<sup>20</sup> Similarly, very small solid phases inside fluid inclusions can be identified from their Raman spectrum.<sup>19</sup> Figure 5 shows the spectrum obtained when the laser beam hits the daughter crystal of a liquid  $\text{CO}_2$  inclusion inside a quartz from Bancroft, Ontario. The peaks marked S arise from the crystal and the remainder from  $\text{CO}_2$  and host quartz. The solid phase was identified as Nacholite ( $\text{NaHCO}_3$ ). These studies also include the analysis of dissolved species ( $\text{SO}_4^{2-}$ ,  $\text{CO}_3^{2-}$ ,  $\text{CO}_2$ ,  $\text{CH}_4$ ).<sup>18,19</sup>

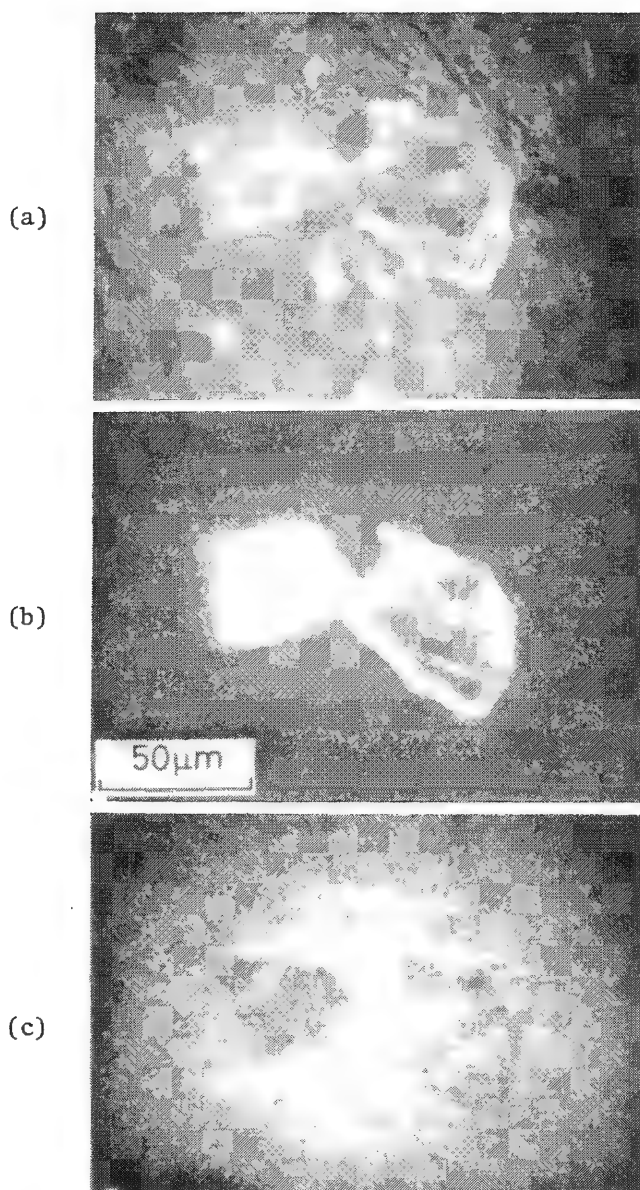


FIG. 2.--Analysis of sulfur inclusions in mineral sample of celestite ( $\text{SrSO}_4$ ): (a) white light image of analyzed area (dark field illumination); (b) Raman image of sulfur crystals obtained from  $473\text{ cm}^{-1}$  line of  $\text{S}_8$  (-S-S-bond stretch); (c) Raman image of same area obtained from  $1000\text{ cm}^{-1}$  line of mineral host  $\text{SrSO}_4$  (S-O bond stretch).

**Geology; Micropaleontology.** Hitherto no method has been available for the direct mineralogical characterization of the two crystalline forms of calcium carbonate (calcite-aragonite) in biomineralized material, a characterization of great importance in the solution of numerous genetic or diagenetic problems posed by the coexistence of the two forms of  $\text{CaCO}_3$ . Raman microprobe is well adapted to this type of problem because lines at  $207\text{ cm}^{-1}$  (calcite) and at  $282\text{ cm}^{-1}$  (aragonite) make the unambiguous characterization of these compounds possible. Figure 6 presents results obtained in the study of cells of triassic *Solenopora* algae.<sup>22</sup> Despite the strong fluorescence due to an inadequate sample preparation for Raman analysis, calcite-aragonite alternations were directly evidenced. These results confirm secondary-ion microanalysis that showed a chemical zonation in Sr and Mg and x-ray diffraction patterns on sample grinding which showed a calcite-aragonite mixture.

**Industrial Material Control; Investigation of Defects.** Formation of defects is a problem currently encountered in the production of materials. The chemical identification of these defects is of particular interest because it can lead to properly selected materials and processes. Many problems have been successfully solved, such as analysis of defects in ceramics and content of bubbles in glass, identification of small particles, contaminants in electronic microcircuits, and defects inside synthetic fibers or films.<sup>23</sup> Figure 7 shows *in situ* analysis of defects observed in polyethylene terephthalate (PET) fibers that are responsible for their breaking. In the high-frequency range ( $> 100\text{ cm}^{-1}$ ) spectra of the fiber and defect are identical but in the low-frequency range significant differences appear, which are characteristic of a local difference of crystallinity. Another example is the *in situ* analysis of small particles (10 to  $20\text{ }\mu\text{m}$  in linear dimension) inside a PET film used for photographic support (Fig. 8). Though these particles were almost transparent they impaired the clarity of the film. They were polytetrafluoroethylene (PTFE) particles whose origin was found to be PTFE gaskets in the ethylene circuit.

**Microanalysis of Biological Tissues.** Interesting information unobtainable by electron or ion microprobe can be obtained on biological tissues (i.e., organic microanalysis in standard histological thin sections ( $\approx 7\text{ }\mu\text{m}$  thick)). In our laboratory various animal organs have been analyzed in a study of bioaccumulation resulting from the degradation of nucleic acids and proteins in cells and tissues (natural or pathological process).<sup>24</sup> Sections of the following animals were investigated: *Blattella* (cockroach), *Schistocerca*



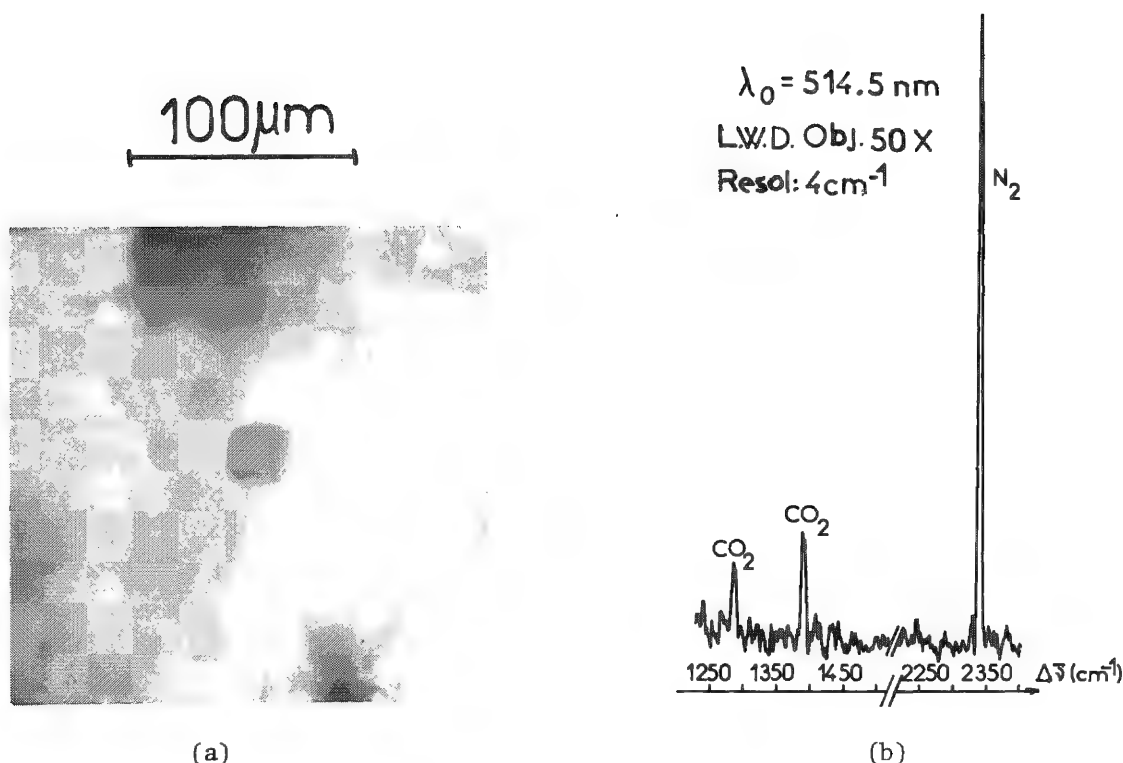


FIG. 3.--Analysis of gas inclusions in the  $N_2$ - $CO_2$  system: (a) white-light image of one  $N_2$ - $CO_2$  inclusion (bright field illumination); (b) Raman spectrum of the inclusion obtained with long-working-distance objective (inclusions are about 200  $\mu m$  below the surface of the quartz host).

(locust), *Epeira* (garden spider), *Promatias* (mollusc), *Helix* (snail), and *Morone* (fish). Figure 9 shows the results of the analysis of single concretions (size 1-2  $\mu m$ ) in the interstitial tissue under the skin of *Epeira*. These results demonstrate that the concretions are made of pure guanine. Figure 10 shows the results obtained from a section of *Schistocerca* by analysis of integument spherocrystals (size 1  $\mu m$  or less). Raman spectrum reveals the presence of uric acid, potassium urate, and some sodium urate.

Thus, a single nondestructive method gave within a few hours as many or more indications than the comparison of results of several different techniques (histochemical reactions, chromatographic studies, x-ray diffraction, and use of electron and ion probes). Moreover, the studies are performed directly at the microscopic level, with very small samples.

**Evolutionary Samples.** In favorable cases, the multichannel detection system permits to follow the evolution of the sample. We have followed the evolution of an equimolecular mixture  $HNO_3$ - $H_2O$  from the glassy to the crystalline state.<sup>25</sup> The glassy state is obtained by temper at 90°K and then the sample is slowly heated. The change of state is followed by means of the imaging mode by observing the appearance of the first crystal ( $31 \times 13 \mu m$ ) (Fig. 11). This result proves that in solid state  $HNO_3$ - $H_2O$  is the oxonium nitrate  $H_3O^+$ ,  $NO_3^-$ . Photochemical reactions have been also followed by the same technique.<sup>26</sup>

### Conclusion

With routine detection limits under the nanogram, Raman microprobe techniques represent here and now a breakthrough in microanalysis. In the future, with more and more laboratories entering the field and a better understanding of phenomena observed in the Raman scattering from microsamples, Raman microprobe techniques are expected to become rapidly major microanalytical techniques yielding new or more precise answers to problems left unsolved or incompletely solved by conventional techniques.



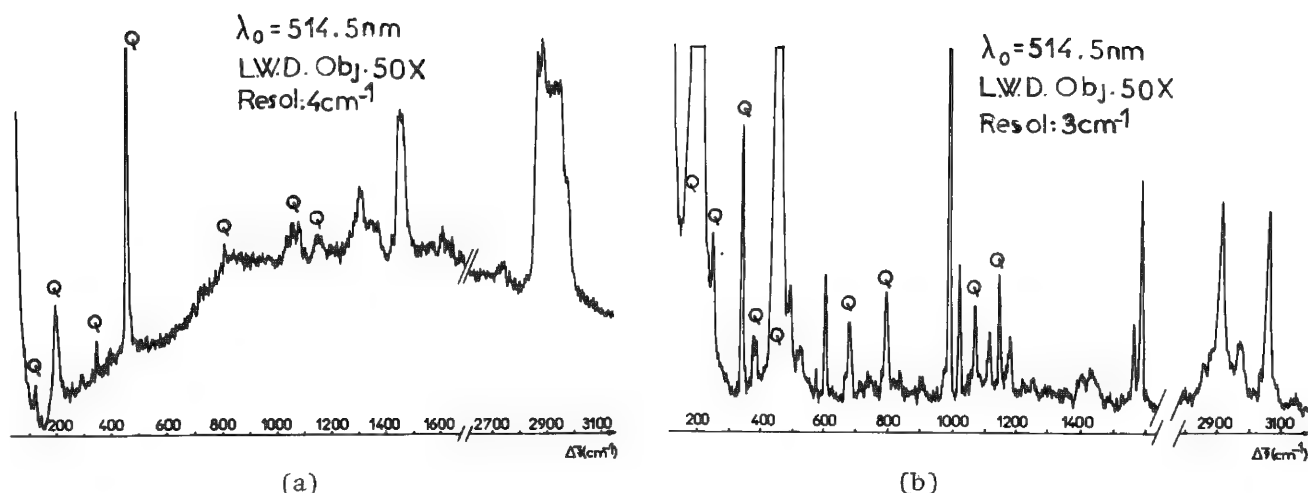


FIG. 4.--Evidence of hydrocarbon fluid inclusions in minerals: (a) Raman spectrum of aliphatic hydrocarbon; (b) Raman spectrum of aromatic hydrocarbon. These spectra were obtained with long-working-distance objective. (Inclusions are about 150  $\mu\text{m}$  below surface of quartz host.)

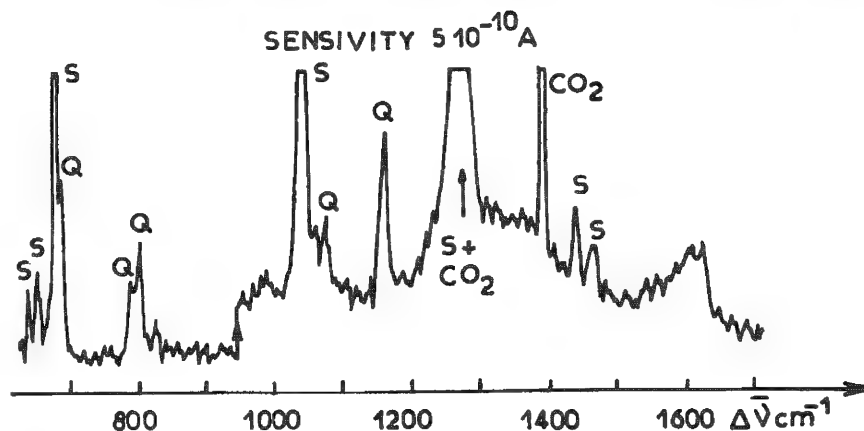
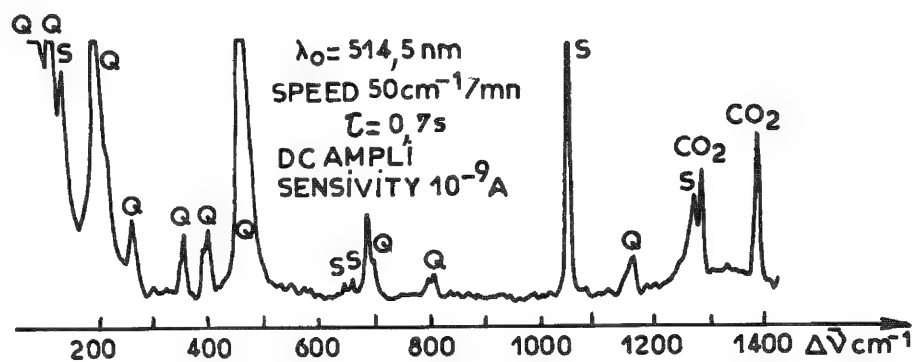
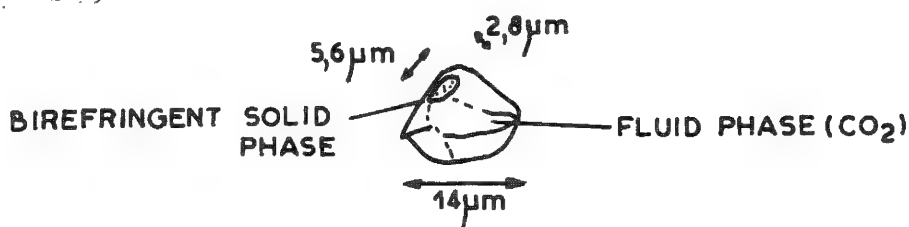


FIG. 5.--Analysis of daughter crystal inside  $\text{CO}_2$  fluid inclusion in host quartz. Direct characterization of Nacholite ( $\text{NaHCO}_3$ ).

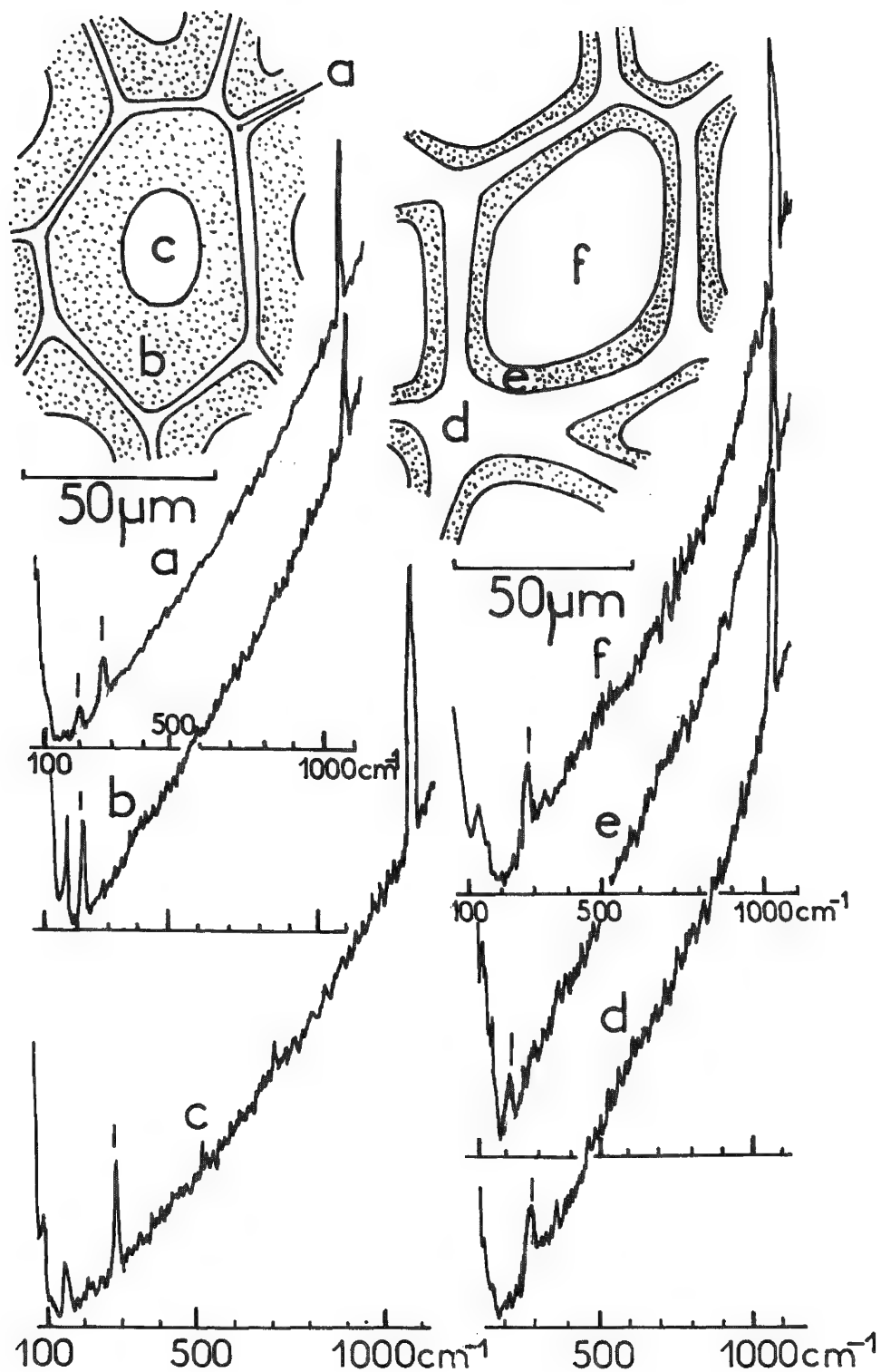


FIG. 6.--Analysis of cells of triassic *Solenopora* algae showing directly calcite-aragonite alternations: (a), (d) peripheral cellular frame: calcite; (b), (e) diagenetic layer: aragonite; (c), (f) central part of cells: calcite.

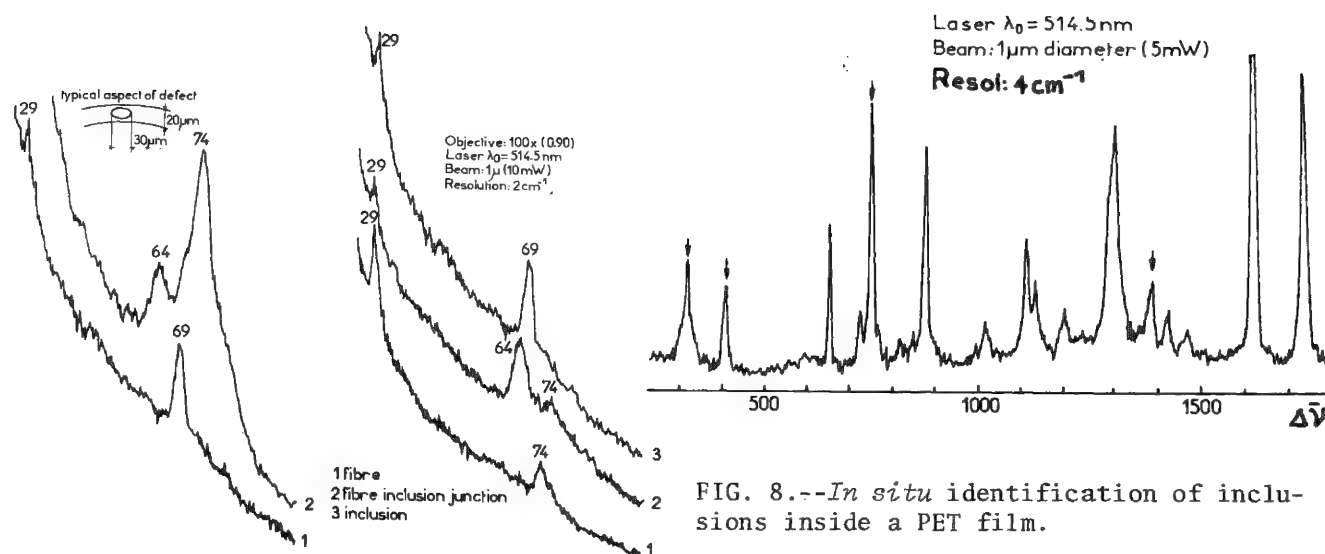


FIG. 8.--*In situ* identification of inclusions inside a PET film.

FIG. 7.--*In situ* characterization of local defects of crystallinity in synthetic PET fibers.

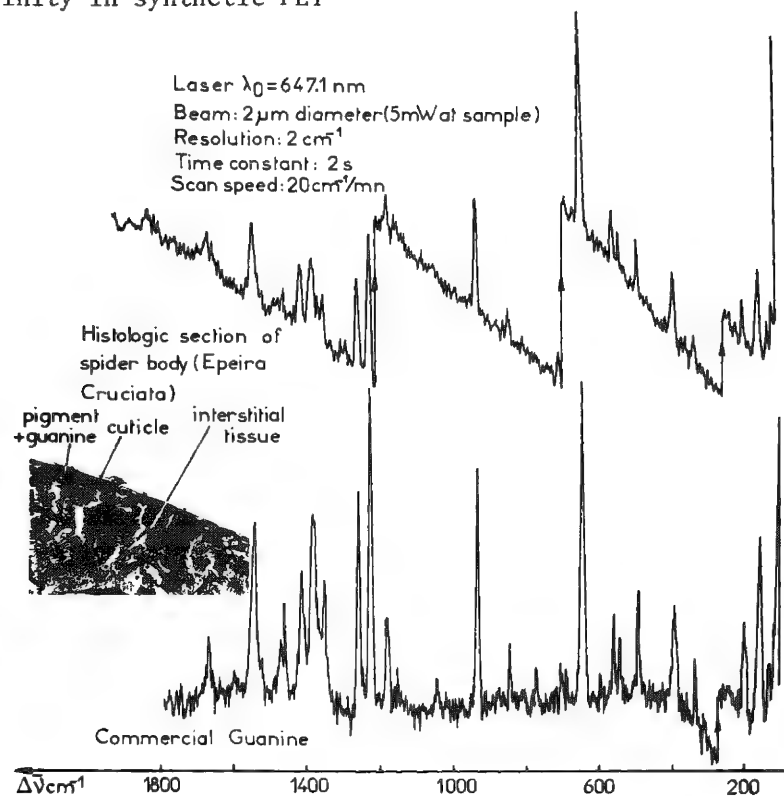
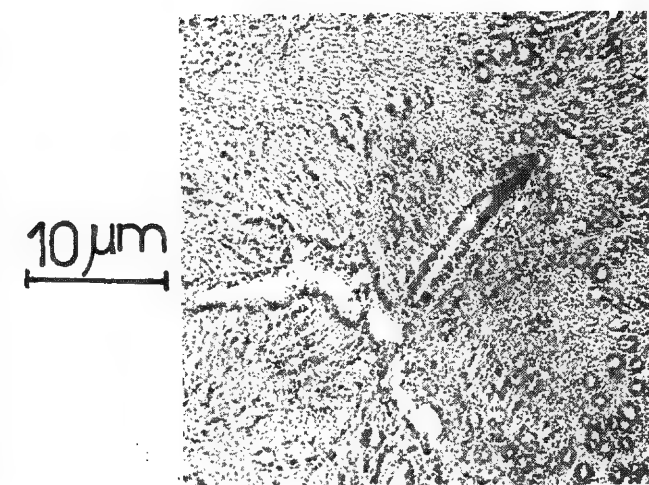
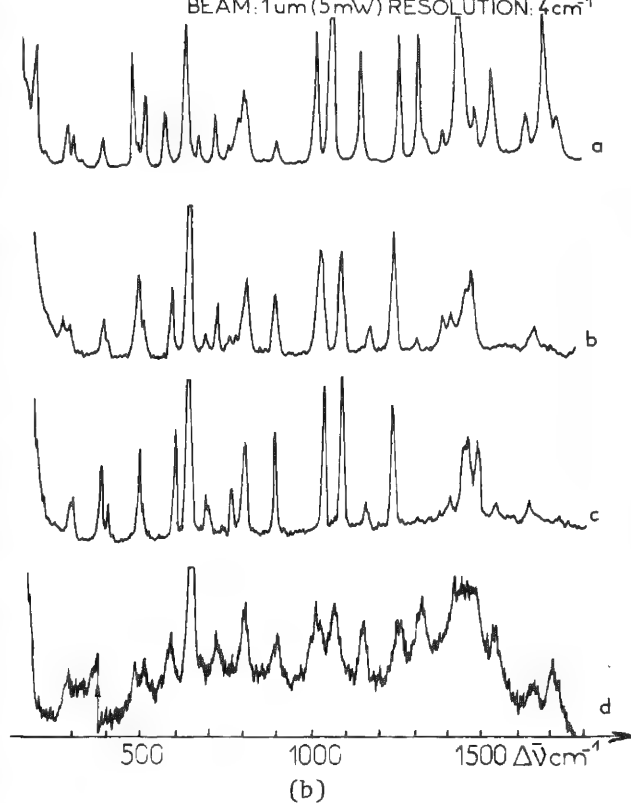


FIG. 9.--Microanalysis of a histological section of *Epeira* (spider). Direct identification of guanine in interstitial tissue.



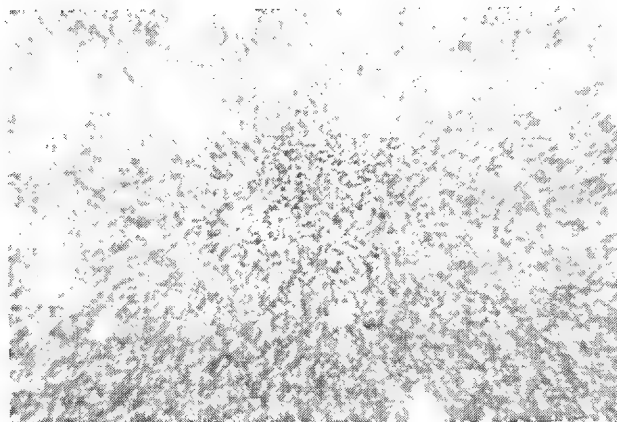
(a)

OBJECTIVE: 100x(0.90) LASER  $\lambda_0=514.5\text{nm}$   
BEAM:  $1\mu\text{m}$  (5mW) RESOLUTION:  $4\text{cm}^{-1}$

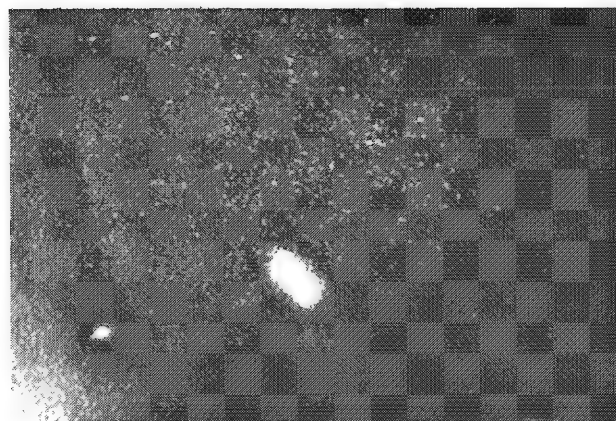


(b)

FIG. 10.--Microanalysis of a histological section of *Schistocera* (locust). Identification of purines in integument: (a) White-light micrograph of a portion of the histological section showing spherocrystals; (b) Raman spectra of a--uric acid, b--potassium urate, c--sodium urate (reference material), and d--spherocrystals.



(a)



(b)

FIG. 11.--Evolution of equimolar mixture  $\text{HNO}_3\text{-H}_2\text{O}$  from the glassy to the crystalline state: (a) glassy state is characterized by diffuse image ( $1000\text{cm}^{-1}$  band); (b) Raman image of the first crystal of oxonium nitrate ( $1060\text{cm}^{-1}$  line).

## References

1. M. C. Tobin, *Laser Raman Spectroscopy in Chemical Analysis*, New York: Wiley-Interscience, 1961.
2. N. B. Colthup, L. H. Daly, and S. E. Wiberly, *Introduction to Infrared and Raman Spectroscopy*, New York: Academic Press, 1975, 2d ed.
3. D. A. Long, *Raman Spectroscopy*, London: McGraw-Hill, 1977.
4. G. J. Rosasco, E. S. Etz, and W. A. Cassatt, "The analysis of discrete fine particles by Raman spectroscopy," *Appl. Spectrosc.* 29: 396, 1975.
5. M. Delhaye and P. Dhamelincourt, "Raman microprobe and microscope with laser excitation," *J. Raman Spectrosc.* 3: 33, 1975.
6. G. J. Rosasco and E. S. Etz, "The Raman microprobe: A new analytical tool," *Research and Development* 28, 20 June 1977.
7. P. Dhamelincourt and P. Bisson, "Principe et réalisation d'un microscope optique utilisant l'effet Raman," *Microscopica Acta* 79: 267, 1977.
8. P. Dhamelincourt, "Laser molecular microprobe," in M. A. West, Ed., *Lasers in Chemistry*, Amsterdam: Elsevier, 1977.
9. M. Delhaye, E. Da Silva and G. S. Hayat, "The molecular microprobe," *American Laboratory*, April 1977.
10. E. S. Etz, G. J. Rosasco, and W. C. Cunningham, "The chemical identification of airborne particles by laser Raman spectroscopy," in *Environmental Analysis*, New York: Academic Press, 1977.
11. J. J. Blaha, G. J. Rosasco, and E. S. Etz, "Raman microprobe characterization of residual carbonaceous material associated with urban airborne particulates," *Appl. Spectrosc.* 32: 292, 1978.
12. P. Dhamelincourt, "Raman microprobe techniques: Some analytical applications," in E. D. Schmid et al., Eds., *Proc. 6th Intern. Conf. Raman Spectroscopy*, London: Heyden, 1978, vol. 1.
13. G. J. Rosasco, "Microanalysis by Raman spectroscopy," *ibid.*
14. E. Da Silva and G. S. Hayat, "New instrumentation for Raman spectroscopy," *Ann. Meet. Opt. Soc. Am.*, October 1976.
15. M. Delhaye, P. Dhamelincourt, and Y. Moschetto, "Dispositif d'étude non-destructive de surfaces hétérogènes," French Patent ANVAR, 2 253 410, 1973.
16. M. Delhaye, P. Dhamelincourt, and E. Da Silva, "Microsonde optique à laser," French Patent ANVAR, 7 621 539, 1976.
17. M. Delhaye, P. Dhamelincourt, and Y. Moschetto, "Apparatus for the nondestructive examination of heterogeneous samples," U.S. Patent 4 030 827, 1977.
18. G. J. Rosasco and E. Roedder, "Application of a new laser excited Raman spectrometer to nondestructive analysis of sulfate in individual phases in fluid inclusions in minerals," *25th Int. Geol. Cong. Abstracts* 3: 812, 1976.
19. J. Dubessy, P. Dhamelincourt, and B. Poty, "Analyse par spectrométrie Raman d'inclusions fluides," *Abstracts Coll. Minéraux et Minerais*, Nancy, France, September 1978.
20. V. Perthuisot, Doctoral Thesis, Paris VI University, France, 1978.
21. N. Guilhaumou et al., "Analyse à la microsonde à effet Raman d'inclusions gazeuses du système  $N_2$ - $CO_2$ ," *C. R. Acad. Sci. Paris* 287: D-1317, 1978.
22. R. Lefevre et al., "Caractérisation mineralogique directe, par microsonde laser à effet Raman, des alternances calcite-aragonite mises en évidence chimiquement par micro-analyse ionique dans une algue solenopore triasique," *C.R. Acad. Sci. Paris* 288: D-19, 1979.
23. P. Dhamelincourt, "Etude et réalisation d'une microsonde moléculaire à effet Raman: Quelques domaines d'application," Doctoral Thesis, Lille University, France, 1979.
24. C. Ballan-Dufrançais, M. Truchet, and P. Dhamelincourt, "Identification of purines in histological sections by laser Raman microprobe (MOLE)," *Biol. Cell.*, to be published.
25. M. H. Herzog-Cance et al., "Association moléculaire et paire ionique dans le verre et le liquide du monohydrate de l'acide nitrique," *J. Raman Spectrosc.* 7: 303, 1978.
26. P. Bisson, "Contribution à l'étude d'une microsonde à effet Raman," Third Cycle Thesis, Lille University, France, 1977.

## RAMAN MICROANALYSIS OF SiO SOURCE MATERIALS BY MEANS OF MOLE

Fran Adar, M. J. Mitchell, and J. N. Ramsey

The molecular optical laser examiner (MOLE) has been successfully utilized in characterizing source materials from which SiO films are deposited on semiconductor integrated circuits. The Raman spectra gathered from  $1\mu\text{m}$ -sized regions indicate that the two source materials examined are different. The spectrum from one material matched that of a 27 000 Å SiO film; the other resembled the Raman spectrum of fused silica. In addition, both source materials contained minority species with well-defined Raman spectra. These data support the existence of SiO (rather than a mixture of Si and SiO<sub>2</sub>) in the solid phase. However, since the MOLE spectrum of one of the source materials is definitely different from that of the film, it is possible to conclude that the characteristics of the film are determined by the mode of deposition as well as the starting material.

Layers of silicon monoxide are routinely deposited on semiconductor integrated circuits because of their electrical insulating and optical properties. Although elemental analysis indicated that silicon and oxygen occur in these films in a 1-to-1 stoichiometric ratio, there was doubt as to whether a well-defined SiO solid species really exists. However, data from Electron Spectroscopy Chemical Analysis (ESCA) indicated that the electronic structure on the silicon in these films is easily differentiated from that of crystalline silicon and fused silica<sup>1</sup> and that the SiO has a cross linked polymeric structure varying between O<sub>3</sub>-Si-O-Si-O<sub>3</sub> and Si<sub>3</sub>-Si-O-Si-Si<sub>3</sub>. However, thermodynamic phase diagrams indicated that SiO, if present, might be unstable.<sup>2</sup> It was therefore proposed that the MOLE be used to characterize the film, compare it to reference materials (crystalline silicon, fused silica, and  $\alpha$ -quartz), and examine the source materials used to make the films.

### *Experimental*

Two source materials of SiO were examined in the MOLE. One was a dull gray material with conchoidal surfaces. The other was a porous, shiny black material. Because of the short working distance of the MOLE objective and undulations on the surfaces of the second material, it was necessary to examine small particles of this material in the MOLE. When examined in incident light, these particles appeared highly reflective. In addition, materials remaining after evaporation were examined in the MOLE. Microscopically this material consisted of several components whose spectra were recorded individually.

The SiO film examined on the MOLE was 27 000 Å (or 2.7  $\mu\text{m}$  thick. Because the depth of focus of the 100 $\times$  lens is of the order of a micron, most scattering observed from the film was from the film itself.

Reference spectra from crystalline silicon, fused silica, and a Herkimer diamond ( $\alpha$ -quartz) were also recorded.

A schematic layout of the MOLE is shown in Fig. 1. A research-grade microscope serves as a sample mount and positioner. In punctual illumination, the objectives permit laser illumination of a microscopic region of sample whose dimensions are determined by diffraction-limited optics (the 100 $\times$  dry objective produces a  $1\mu\text{m}$  spot on the sample). In spectral mode, the monochromator is scanned, the scattered light is detected by a photomultiplier, and a spectrum from the laser-illuminated spot is recorded. (The MOLE also has a multichannel detector consisting of an image intensifier and a high-sensitivity vidicon. In the spectrograph mode, 200  $\text{cm}^{-1}$  can be viewed simultaneously either on a TV monitor or on an oscilloscope. In the image mode, a large field of view is illuminated by a rotating mirror system used in conjunction with a dark-field illuminator; in this case, an image of

---

F. Adar is with Instruments S.A. in Metuchen, NJ 08840; M. J. Mitchell is at the New Mexico Institute of Technology, Socorro, NM, 87801; J. N. Ramsey is with IBM in Hopewell Junction, NY 12533.

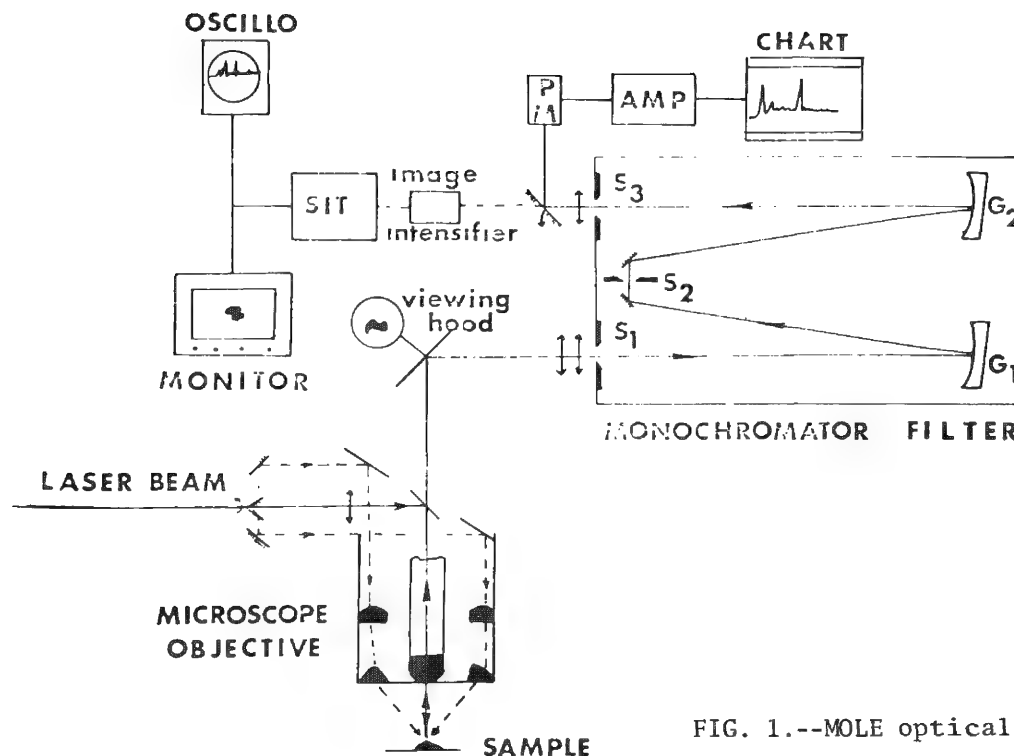


FIG. 1.--MOLE optical schematic.

a heterogeneous sample can be formed by the Raman scattered light. A full description of the MOLE can be found elsewhere.<sup>3)</sup>

### Results

Figure 2 shows the MOLE spectra from the  $2.7\mu\text{m}$   $\text{SiO}_2$  layer and the fused silica,  $\alpha$ -quartz and crystalline silicon reference materials. The  $\text{SiO}_2$  film has a relatively sharp band at  $493\text{ cm}^{-1}$  (full width at half height =  $20\text{ cm}^{-1}$ ); silicon has a very intense, sharp band at  $520\text{ cm}^{-1}$  (full width at half height =  $5\text{ cm}^{-1}$ ). The most intense band in the spectrum of  $\alpha$ -quartz occurs at  $465\text{ cm}^{-1}$  (full width at half height =  $10\text{ cm}^{-1}$ ). Fused silica is a highly amorphous material with a broad band between 200 and  $500\text{ cm}^{-1}$ , and a second weaker broad feature centered between 750 and  $800\text{ cm}^{-1}$ . The Raman spectra of these silicon oxides are easily distinguishable from each other and from crystalline silicon.

Figure 3 shows the MOLE spectra of the first source material. The spectrum of the majority species, the dull gray material, is identical to that of the  $\text{SiO}_2$  film. Microscopic examination revealed numerous white inclusions whose Raman spectrum consisted almost exclusively of a peak at  $508\text{ cm}^{-1}$  and did not match any of the other spectra recorded.

MOLE spectra from the second source material are shown in Fig. 4. The majority species in this case appeared reflective and glassy when viewed in incident light even though the material itself was shiny black and porous when examined visually. Its Raman spectrum was broad and similar to that of fused silica except that the bands tended to have more structure on them. In this case, microscopic examination revealed small yellow inclusions whose Raman spectra matched that of the  $\text{SiO}_2$  film.

Figure 5 shows the MOLE spectra obtained from various microscopically identifiable components of material remaining after evaporation. The spectra vary somewhat from species to species, but all show a single band near  $500\text{ cm}^{-1}$  and a doublet between  $660$  and  $710\text{ cm}^{-1}$ .

### Discussion

The MOLE data shown above give evidence to two facts. The first is that the Raman spectrum of  $\text{SiO}_2$  clearly distinguishes it from crystalline silicon and from other oxides of silicon. The fact that the principal band of  $\text{SiO}_2$  is somewhat broader than those of crystalline



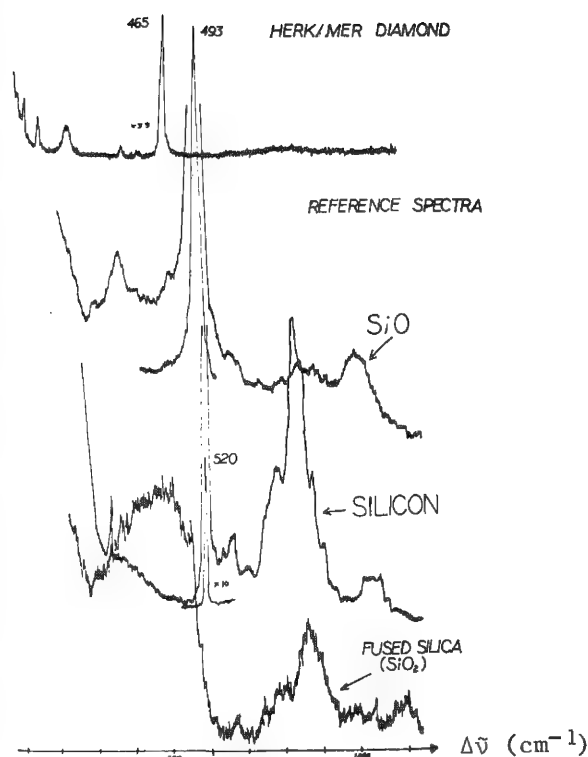


FIG. 2.--MOLE spectra of  $\alpha$ -quartz (Herkimer diamond),  $2.7\mu\text{m}$  SiO layer, crystalline silicon, and fused silica. Conditions for spectrum of  $\alpha$ -quartz:  $\lambda_{\text{Ex}} = 4800 \text{ \AA}$ , 600 mW at laser, 600 m slits,  $100\times$  objective,  $\tau = 3 \text{ sec}$ ,  $50 \text{ cm}^{-1}/\text{min}$ ; for other samples,  $\lambda_{\text{Ex}} = 514.5 \text{ \AA}$ , 400 mW at laser.

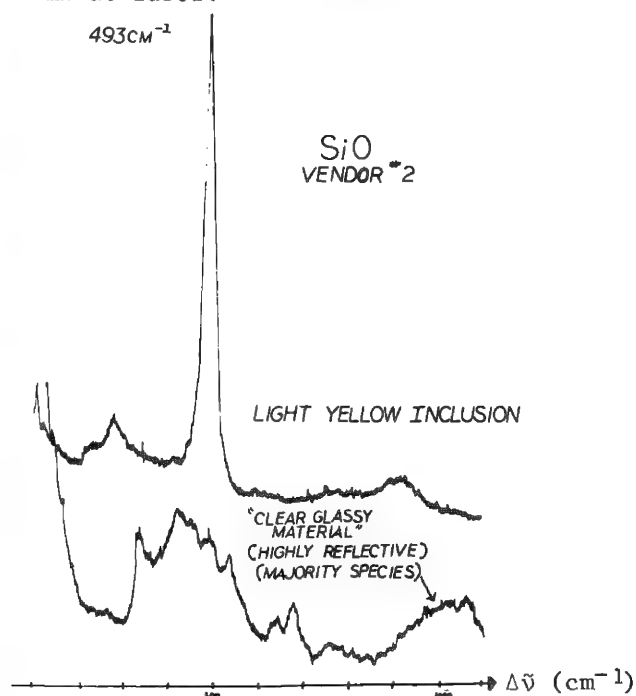


FIG. 4.--MOLE spectra of source material from Vendor 2. Same conditions as Fig. 3.

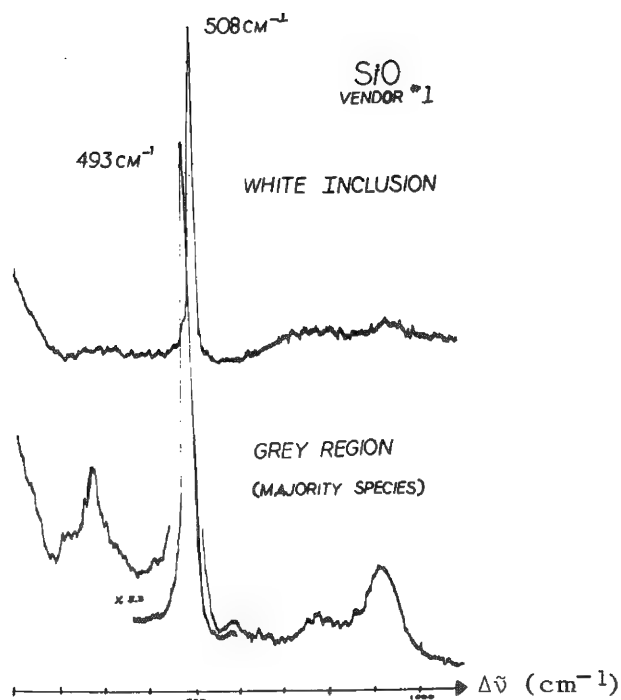


FIG. 3.--MOLE spectra of source material from Vendor 1:  $\lambda_{\text{Ex}} = 5145 \text{ \AA}$ , 400 mW at laser,  $600 \mu\text{m}$  slits,  $100\times$  objective,  $\tau = 3 \text{ sec}$ ,  $50 \text{ cm}^{-1}/\text{min}$ .

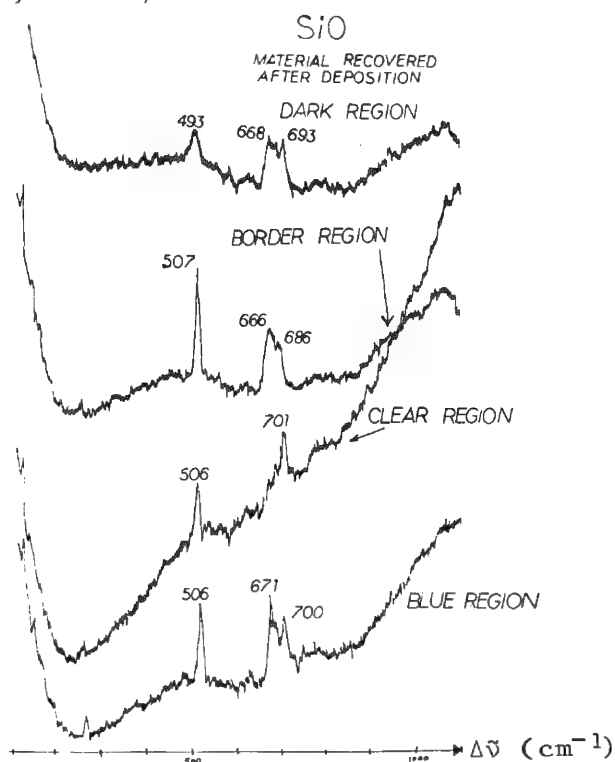


FIG. 5.--Mole spectra of silicon oxide material remaining after deposition. Spectra were produced from more than one region of each morphological species identified in microscope. Same conditions as Fig. 3.

silicon and of  $\alpha$ -quartz is consistent with the supposition based on ESCA results that there is a "distribution of species ranging from  $O_3-Si-O-Si-O_3$  to  $Si_3-Si-O-Si-Si_3$ ."<sup>1</sup>

The second conclusion to be drawn from these data is that the two sources of SiO starting material are not equivalent. The MOLE spectrum of the majority species of one matches that of the SiO film, whereas the spectrum of the other most closely matches that of fused silica (amorphous  $SiO_2$ ). One could thus infer that the characteristics of the SiO film are determined by the mode of evaporation and deposition as well as the stoichiometry of the starting materials.

The data recorded from the material remaining after evaporation are somewhat anomalous. In addition to a band in the  $500\text{cm}^{-1}$  region, there consistently appeared a doublet at  $700\text{cm}^{-1}$ . It is curious that in reference spectra of polydimethylsiloxane, hexamethyldisiloxane and octamethylcyclotetrasiloxane, the strongest bands appear at  $500$  and  $700\text{cm}^{-1}$ , whereas silicic acid tetramethylester and tetramethylsilane show only single bands in these regions. One can infer that the structure observed in the recovered material is indicative of "polymerization" of the siloxane bonds.

### Conclusion

The Raman spectra of an SiO film and source materials used in depositing this film derived in the MOLE provide characterization of these silicon oxides. The spectrum of the SiO film is readily distinguishable from crystalline silicon, fused silica, and  $\alpha$ -quartz. The linewidth of the strongest Raman band is broader than the strongest bands of silicon and quartz which is consistent with the model and Raider and Flitsch,<sup>1</sup> who propose a distribution of silicon tetrahedral linkages. The spectra of the two source materials are not equivalent; only one of them fingerprints the SiO film. That implies that the properties of the film are affected by the method of evaporation as well as the composition of the starting material.

### References

1. S. J. Raider and R. Flitsch, "Silicon monoxide thin films," *J. Electrochem. Soc.* 123: 1754, 1976.
2. L. Brewer and F. T. Greene, "Differential thermal analysis of the Si-SiO<sub>2</sub> System," *J. Phys. Chem. Solids* 2: 286, 1957.
3. M. Delhaye, E. DaSilva and G. S. Hayat, "The molecular microprobe," *Am. Lab.* 9: 83, 1977.
4. B. Schrader and W. Meier, *Raman/IR Atlas*, Weinheim: Verlag Chemie, 1975.

## RAMAN MICROPROBE STUDY OF BIOLOGICAL MINERALIZATION *IN SITU*: ENAMEL OF THE RAT INCISOR

F. S. Casciani and E. S. Etz

The advantages of microprobe methods, especially in the life sciences, are well documented.<sup>1-3</sup> In biological studies, their unique capabilities for the microanalysis of spatially heterogeneous samples permit the determination of the distribution of various components. Unlike conventional (electron- and ion-beam) microprobes, the Raman microprobe,<sup>4-5</sup> through the interpretation of vibrational Raman spectra, permits the identification and localization of molecular species in heterogeneous microregions. A recent application of this technique (which employs the Raman microprobe developed at NBS) to the study of the processes of biomineralization and the identification of molecular species present at the mineralizing front in mineralizing rat enamel and embryonic chick tibia, has been reported.<sup>6</sup>

Enamel mineralization has been described in terms of morphological<sup>7-10</sup> and chemical<sup>10,11</sup> characteristics; these studies suggest that enamel mineralization is a complicated process. Enamel mineralization is characterized by the nucleation of a mineral phase--biological apatite--in an extracellular highly hydrated matrix, during the secretory stage of the ameloblasts. A continuous increase in mineral content occurs until the mineral is approximately 99wt% of the tissue.

The studies reported here were undertaken to determine the initial mineral present at the mineralization front and to elucidate the changes that occur in the mineral content during the early stage of enamel development.

The continually erupting rat incisor contains regions reflecting these stages of enamel development. This type of tissue was chosen for study because with appropriate sample preparation these regions are easily identified and morphologically discernible.

Sprague Dawley rats weighing approximately 100 g were sacrificed with ether. The mandibles were dissected out and the incisors removed; care was taken to avoid damaging the enamel organ. A piece 4 mm long was cut from the apical end of the incisor and positioned in freezing water in such a way that sagittal sections could be cut on the cryostat at -20°C. A mid-sagittal section 10  $\mu\text{m}$  in thickness, with the expected morphological detail, was transferred to a sample substrate (sapphire) and allowed to air dry. This section of the tissue contains a region in which the developing enamel is about 30  $\mu\text{m}$  thick, which reflects the development of inner enamel.

Spectroscopic measurements on these enamel sections were made with the 514.5nm line of an argon-krypton ion laser; the spectra were excited with 20 mW of laser power placed in a beam spot of 7  $\mu\text{m}$  diameter (lateral spatial resolution).

The size of the focal spot and the incident laser power determine the power density or irradiance ( $\text{watts}/\text{cm}^2$ ) incident on the sample. From the laser spot size (7  $\mu\text{m}$ ) and the tissue section thickness (about 10  $\mu\text{m}$ ), we estimate that the spectra were obtained from about 1.5 ng of sample, based on a value of 1.5  $\text{g}/\text{cm}^3$  for developing enamel.

Each spectrum was recorded with  $3\text{cm}^{-1}$  spectral resolution, a time constant of 15 sec (by photon counting detection), and a scan rate of 5  $\text{cm}^{-1}/\text{min}$ . A complete description of the instrument and its microanalytical capabilities has been given elsewhere.<sup>5</sup>

Figure 1 shows typical enamel sections mounted on sample substrates prepared for analysis by the procedures described above.

Figure 2 shows a comparison of the Raman spectra obtained from rat incisor enamel at two distinct stages of development. The spectrum of mineralizing enamel was obtained from area B of the section shown in Fig. 1b. The spectrum of mature enamel was obtained from an erupted rat incisor, fractured and positioned on a sample substrate so that the

---

F. S. Casciani is with the National Institute of Dental Research, Bethesda, MD 20205; E. S. Etz is with the National Bureau of Standards, Washington, DC 20234. This work has been supported by an Interagency Contract Y01-DE-80027 between NBS and NIDR.

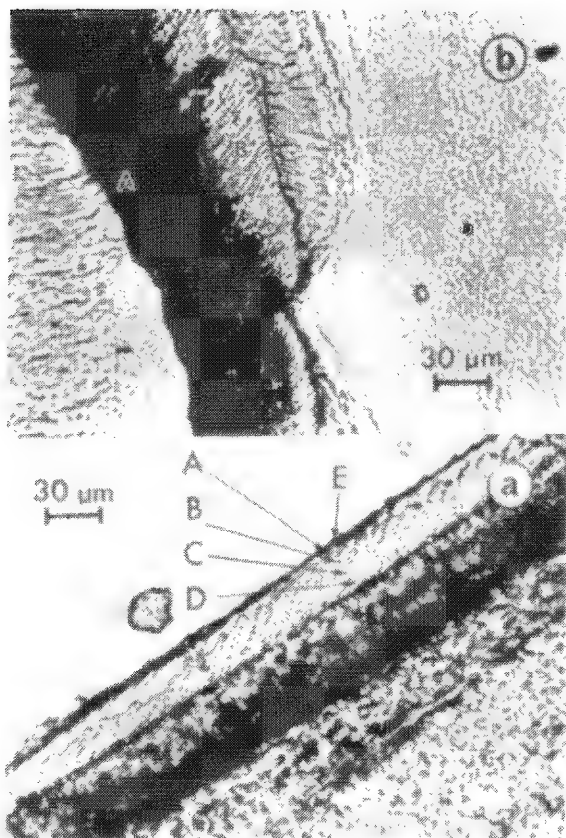


FIG. 1.--Light micrographs of 10µm-thick rat incisor enamel sections on sapphire sample substrates. (a) A, B, C, and D are microregions from which spectra in Fig. 3 were obtained. Micro-region A is at mineralizing front and D is at dentino-enamel junction. (b) B is the microregion from which spectrum of mineralizing enamel (Fig. 2) was obtained.

The spectra in Fig. 3 show the increase in the intensity of the  $960\text{cm}^{-1}$  band from area A to area D. The spectral features associated with the  $\nu_2$ ,  $\nu_3$ , and  $\nu_4$  are observed in spectra C and D. In spectra A and B, the intensity of the  $\nu_1$  ( $960\text{cm}^{-1}$ ) suggests that the  $\nu_2$ ,  $\nu_3$ , and  $\nu_4$  are too weak for these modes to be detected above the spectral background. The  $\nu_2$  in spectra A, B, C, and D is also in the region of the bands associated with the sapphire substrate, which are marked by arrows in Fig. 3. In all analyses of early mineralizing enamel, the spectra indicate that the  $\nu_1$  of the phosphate mineral occurs at  $960\text{cm}^{-1}$ , which suggests that if other phosphate species are present during this early stage of mineralization, they are present in either much lower concentrations than the apatite mineral associated with the  $\nu_1$  mode at  $960\text{cm}^{-1}$ , or a transformation to this apatitic phosphate phase occurs as a result of the measurement or sample preparation. Raman microprobe analyses of several other mineral phosphates (such as octacalcium phosphate, dicalcium phosphate dihydrate, and monocalcium phosphate hydrate) indicate that good Raman spectra are obtained at similar and much higher irradiance levels than those used in this study.

Whether these spectra might also reveal the potential presence of an amorphous calcium phosphate (ACP) is a goal of future research. Such studies, by this technique, require the

spectrum of mature enamel could be obtained. These spectra illustrate the changes in the Raman spectral features associated with the process of mineralization. The lower spectrum in Fig. 2 is a reference spectrum of synthetically prepared hydroxyapatite, and is shown in order that the spectral features associated with the apatite mineral portion of the developing tissue may be compared. The vibrational analysis of hydroxyapatite has been reported and band assignments for the infrared and Raman active modes have been made.<sup>12,13</sup> The Raman spectrum is dominated by the intense  $\nu_1$  band at  $961\text{cm}^{-1}$ , whose intensity is approximately eight times the intensities of the  $\nu_2$  ( $431$  and  $499\text{cm}^{-1}$ ),  $\nu_3$  ( $1030$ ,  $1048$ , and  $1079\text{cm}^{-1}$ ), and  $\nu_4$  ( $581$ ,  $590$ , and  $610\text{cm}^{-1}$ ) internal modes of the  $\text{PO}_4^{3-}$  ion in the apatite structure.

The  $\nu_1$  (P-O symmetric stretch) is readily recognized in the Raman spectrum of the biological apatite. Its observation along with the  $\nu_2$ ,  $\nu_3$ , and  $\nu_4$  modes permits the identification of biological mineral as apatite.

The comparison of the spectra of mineralizing enamel and mature enamel indicates that the differences in the spectra are attributable to the gradual disappearance (or removal) of the organic matrix as the enamel becomes fully mineralized. From the similarities in the spectra of mature enamel and hydroxyapatite the high (about 99wt%) mineral content of the mature tissue is easily recognized.

The regions denoted by A, B, C, and D (Fig. 1a) indicate the location of microscopic sampling volumes analyzed in the microprobe and correlate with the sequential spectra shown in Fig. 3. The region denoted by point E was analyzed after the A-D sequence of analysis was performed, to determine whether measurement-induced changes had occurred during the analysis. The spectra obtained from regions A and E were in excellent agreement.

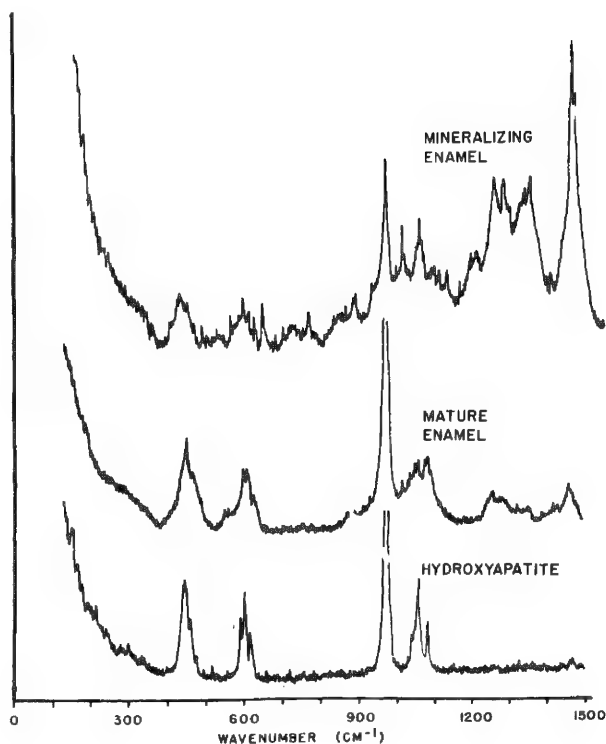


FIG. 2.--Comparison of the Raman microprobe spectra of mineralizing enamel, mature enamel, and synthetic hydroxyapatite  $[\text{Ca}_{10}(\text{PO}_4)_6(\text{OH})_2]$ .

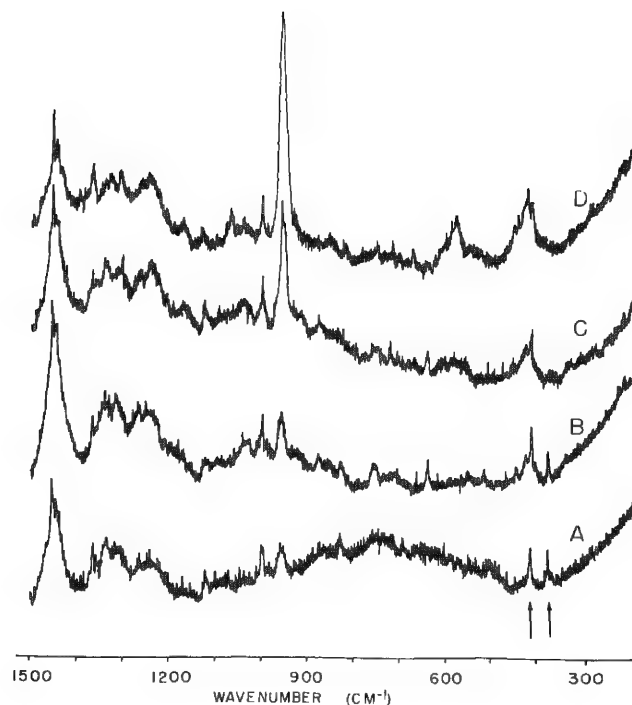


FIG. 3.--Sequential Raman microprobe spectra obtained from tissue section in Fig. 1a.

characterization of ACP and the study of the stability of this material with respect to laser irradiance levels employed.

Figure 4 shows the increase in the relative intensity of the  $960\text{cm}^{-1}$  band from region A to region D in the enamel section of Fig. 1a. Over the  $30\mu\text{m}$  distance from the amelo-blast-enamel junction to the dentino-enamel junction there is approximately an eight-fold increase in intensity. This gradient in phosphate intensity is in good agreement with the elemental calcium analyses performed by Glick<sup>10</sup> by use of electron microprobe for examination of the same regions of developing rat incisor. Hiller has shown, by the microanalysis of samples obtained by microdissection, that in this region of developing rat incisor enamel a sample equivalent to the total thickness of the enamel contains 7-8% phosphorus (corresponding to 23-24% phosphate).<sup>11</sup> Based on the observed changes in the  $\nu_1$  phosphate intensity reported here, we conclude that the outer  $10\mu\text{m}$  region of developing enamel contains approximately 10% of this total phosphate (Fig. 4). This region may therefore contain as little as 2% phosphate mineral by weight, which suggests that early enamel matrix may have more than 95wt% hydrated protein.

At present our efforts are being directed to a more complete understanding of the compositional and structural information obtained in the spectra, especially with regard to this initial mineral in the  $10\mu\text{m}$  region of early developing enamel. Beyond that, we expect that future work will provide more definitive information concerning the conformation of the proteinaceous matrix and any changes in protein structure as mineralization proceeds in the tissue.

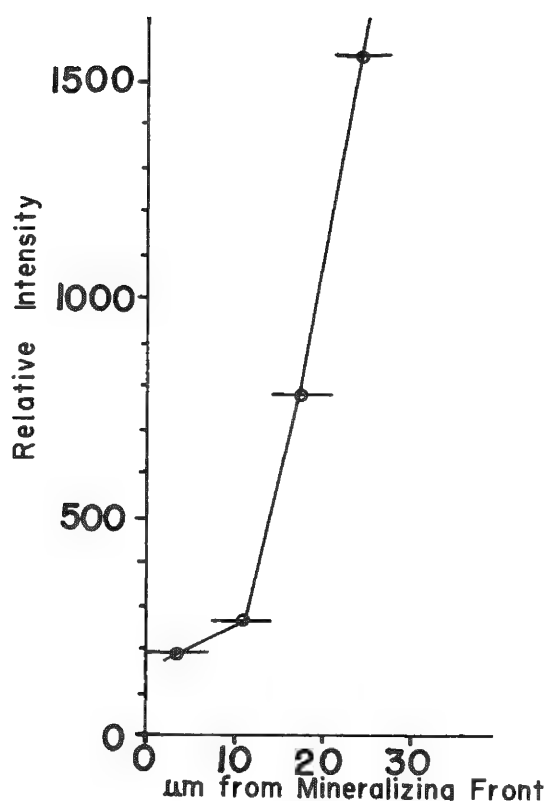


FIG. 4.--Relative intensity of  $\nu_1$  ( $960\text{ cm}^{-1}$ ) phosphate band vs distance ( $\mu\text{m}$ ) from mineralizing front.

#### References

1. T. Hall, P. Echlin, and R. Kaufmann, *Microprobe Analysis as Applied to Cells and Tissues*, London: Academic Press, 1974.
2. J. R. Coleman, "X-ray analysis of biological samples," *SEM/1978/11*, SEM, Inc., AMF O'Hare, IL 60666, 1978, 911-926.
3. M. B. Bellhorn and R. K. Lewis, "Localization of ions in retina by secondary mass spectrometry," *Exp. Eye Res.* 22: 505-518, 1976.
4. M. Delhaye and P. Dhamelincourt, "Raman microprobe and microscope with laser excitation," *J. Raman Spectrosc.* 3: 33-43, 1975.
5. G. J. Rosasco and E. S. Etz, "The Raman microprobe: A new analytical tool," *Res. and Devel.* 28: 20-35, 1977.
6. F. S. Casciani et al., "Raman microprobe studies of two mineralizing tissues: Enamel of the rat incisor and embryonic chick tibia," *SEM/1979/II*, SEM, Inc., AMF O'Hare, IL 60666, 1979.
7. M. U. Nylen, E. D. Eanes, and K. A. Omnell, "Crystal growth in rat enamel," *J. Cell Biol.* 18: 109-123, 1963.
8. K. A. Selvig and A. Halse, "Crystal growth in rat incisor enamel," *Anat. Rec.* 173: 453-468, 1972.
9. P. L. Glick and D. R. Eisenmann, "Electron microscopic and microradiographic investigation of a morphological basis for the mineralization pattern in rat incisor enamel," *Anat. Rec.* 176: 289-305, 1973.
10. P. L. Glick, "Patterns of enamel maturation," in *Proc. of Third International Symposium on Tooth Enamel*, *J. Dent. Res.* 58(B): 883-892, 1979.
11. C. R. Hiller, C. Robinson, and J. A. Weatherall, "Variations in the composition of developing rat incisor enamel," *Calcif. Tiss. Res.* 18: 1-12, 1975.
12. K. C. Blakeslee and R. A. Condrate, "Vibrational spectra of hydrothermally prepared hydroxyapatites," *J. Am. Cer. Soc.* 54: 559-563, 1971.
13. B. O. Fowler, "Infrared studies of apatite: I. Vibrational assignments for calcium strontium, and barium hydroxyapatites utilizing isotopic substitution," *Inorg. Chem.* 13: 194-207, 1973.

## INVESTIGATIONS INTO THE CRITICAL MEASUREMENT ASPECTS OF RAMAN MICROPROBE ANALYSIS

E. S. Etz and J. J. Blaha

At last year's conference we presented a survey of microparticle studies performed with the NBS-developed Raman microprobe.<sup>1</sup> That account was limited to a brief description of the instrument and to a discussion of microsample analyses; no attempt was made to present in detail some of the more important experimental considerations and limitations. We now extend these earlier discussions and focus on what we consider to be critical aspects of Raman microprobe measurements. From our investigations of a broad range of problems in microanalysis, we have gained some insight into several important experimental difficulties and their potential resolution.<sup>2-7</sup> We focus here on (i) instrument design and spatial resolution, (ii) laser-induced sample heating and optical breakdown, (iii) effects due to the chemical reactivity of microparticles, (iv) laser-induced sample fluorescence, and (v) low-signal measurements. These examples are not exhaustive, but point to experimental observations we consider significant.

### *Microprobe Design and Spatial Resolution*

An important experimental goal in microprobe work is to obtain measurements with as precise and well known a spatial resolution as is possible. In Raman microprobe diagnostics, spatial resolution may be defined by the intersection of the incident focused laser beam (i.e., the laser spot) and the field of view or the sampling volume of the collection optics. In the NBS instrument, spatial resolution is determined by the particular configuration (180° backscattering) of the focusing/light collection geometry utilized in the fore-optical system.<sup>8</sup> This design (Fig. 1) has important consequences regarding the effec-

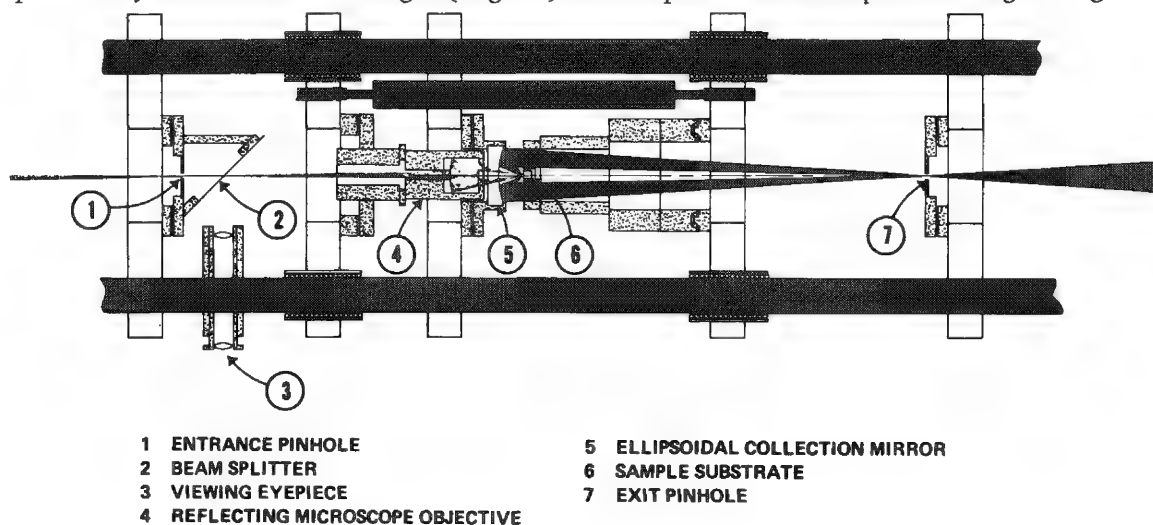


FIG. 1.--Schematic of fore-optical system of NBS Raman microprobe, showing beam focusing, sample viewing, and scattered light collection optics mounted on support rails.

tive spatial resolution of the probe measurement. The schematic shows the optical and mechanical components between the (beam) entrance pinhole and the exit pinhole spatial filter positioned on the optic axis in the path of the collected scattered radiation. The entrance pinhole is at the image point of the beam-focusing objective--either a re-

The authors are with the Center for Analytical Chemistry of the National Measurement Laboratory, U. S. National Bureau of Standards. The partial support of this work by the U. S. Air Force Technical Applications Center (AFTAC) is gratefully acknowledged.



flecting objective (as shown) or a refractive lens--which allows the use of beam spots that may be varied between about 2-20  $\mu\text{m}$  in diameter (lateral resolution). The exciting radiation is focused through a circular opening in the ellipsoidal mirror collector of high numerical aperture ( $\text{NA} = 0.86$ ) that provides efficient, large-solid-angle collection of the scattered light. The size of the exit pinhole (140  $\mu\text{m}$  in diameter for most measurements) determines the degree of spatial filtering and thereby the effectiveness in the rejection of potentially interfering scattering by the substrate or the host material. For the NBS microprobe, the optical and geometrical factors that determine the effective sampling volume and hence the effective spatial (lateral and depth) resolution have been discussed for the case of single microparticles supported by a substrate (typically  $\alpha\text{-Al}_2\text{O}_3$  or LiF) and for microscopic regions localized in or below the surface of a heterogeneous bulk specimen.<sup>9</sup> Calculations show that for discrete microscopic samples larger than 0.9  $\mu\text{m}$  (the diffraction limit of the ellipsoidal mirror collector), the diameter of the exit spatial filter closely determines the dimensions of the collection volume accessed by the ellipsoidal mirror. With a 140 $\mu\text{m}$ -diameter exit spatial filter the collection volume is described by an ellipsoid with axial dimensions of 8 and 9  $\mu\text{m}$ . Owing to spherical aberrations and coma the true depth (along the optic axis) of the collection volume is more like 12  $\mu\text{m}$  (in air). Thus, the Raman signal--in most cases--originates from both the surface and the bulk of the sample. For probe volumes embedded in a host (e.g., a microscopic fluid inclusion) the effective spatial resolution is less well defined owing to several optical effects and aberrations (distortions) of the sampling volume, which reduce the collection efficiency of the ellipsoid.

From the above it is apparent that the performance requirements placed on the illumination/collection geometry call for the optimized collection of the scattered light from the probed region and isolation or minimization of any contributions from the substrate or host. Figure 2 shows Raman spectra obtained under identical irradiance conditions (approx. 1  $\text{MW}/\text{cm}^2$ ) from a thorium oxide particle (a microsphere) of submicrometer size (diam. 0.8  $\mu\text{m}$ ), which illustrate the effects of spatial filtering--with and without exit pinhole--on the extent of spectral interference by the sapphire substrate. The oxide displays a simple Raman spectrum<sup>10</sup> consisting of a single line (marked P) with shift 467  $\text{cm}^{-1}$ . The Raman bands characteristic of sapphire,<sup>11</sup> a relatively weak scatterer, are labeled S. The effect of limiting the collection volume of the ellipsoid by the size of the exit spatial filter is seen by comparison of the signal-to-background ratios of the two spectra.

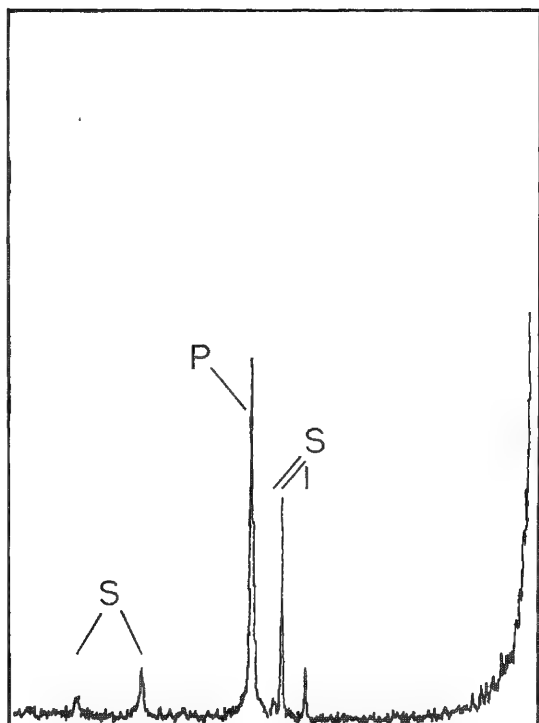
#### *Laser-Induced Sample Heating and Optical Breakdown*

A Raman scattering experiment on a microsample with strongly absorbing properties presents formidable problems. Strong absorption of the focused laser radiation by colored samples heats them and may lead to their thermal decomposition. A 100mW laser beam focused at a particle about 1  $\mu\text{m}$  in size produces a light intensity or irradiance of several megawatts per square centimeter. Thus, measurements must be made at irradiance levels commensurate with preserving the integrity of the sample. The microprobe systems in use have been designed so that the signal-to-background ratio is almost independent of the irradiance level; thus, power density on the sample can be reduced, but measurement times are increased.

The problem of sample heating, for the special case of radiation absorption by (spherical) microparticles, has been considered.<sup>9,12</sup> From model calculations, estimates have been derived for the transient and steady-state temperature reached by optically absorbing spherical particles immersed in a host (e.g., air or  $\text{Al}_2\text{O}_3$ ). Results show that heating effects become less severe as the particle size decreases (which is also borne out by experiment) and that a sapphire host, for example, is three orders of magnitude more efficient as a heat sink than air. The calculations indicate also that destructive heating of microparticles can be attributed to highly localized absorption and large temperature gradients in the particle. In the practical situation, these effects can be brought on by absorbing surface layers or microscopic inclusions. In these cases, the heat-sinking properties of the substrate material (e.g., sapphire) are likely to be relatively ineffective.

Laser-induced sample heating usually leads to noticeable spectral changes that can either be attributed to the rise in sample temperature (bands tend to shift to lower wavenumbers and broaden) or to thermally induced sample changes, such as phase transitions or compositional modifications. Not much is known about real energy density thresholds for

Sample  $\text{ThO}_2$  Size  $0.8 \mu\text{m}$   
 Substrate  $\text{Al}_2\text{O}_3$   
 Laser  $\lambda_0$   $514.5 \text{ nm}$   
 power  $40 \text{ mw}$  (at sample)  
 beam  $\sim 1.8 \mu\text{m}$  diameter  
 Spectral slit width  $3 \text{ cm}^{-1}$   
 Time constant  $2 \text{ s}$   
 PINHOLE  $85 \mu\text{m}$   
 Scan rate  $.83 \text{ cm}^{-1}/\text{s}$   
 Full scale  $10^3 \text{ counts}$



Sample  $\text{ThO}_2$  Size  $0.8 \mu\text{m}$   
 Substrate  $\text{Al}_2\text{O}_3$   
 Laser  $\lambda_0$   $514.5 \text{ nm}$   
 power  $40 \text{ mw}$  (at sample)  
 beam  $\sim 1.8 \mu\text{m}$  diameter  
 Spectral slit width  $3 \text{ cm}^{-1}$   
 Time constant  $1 \text{ s}$   
 PINHOLE OUT  
 Scan rate  $1.67 \text{ cm}^{-1}/\text{s}$   
 Full scale  $10^3 \text{ counts}$

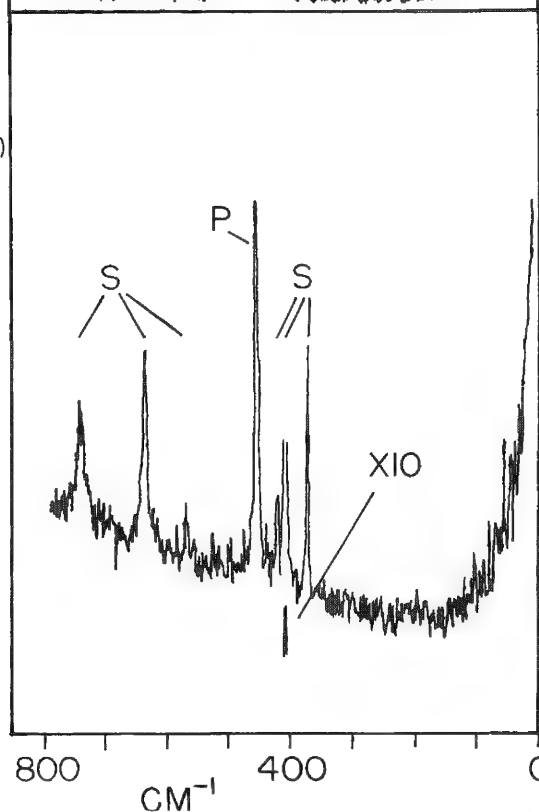


FIG. 2.--Raman spectra of submicron thorium oxide particle showing effect of spatial filtering on spectral interference by sapphire substrate. Bands marked P and S derive from particle and substrate, respectively. Upper spectrum obtained with  $85\mu\text{m}$ -diameter pinhole exit spatial filter, lower spectrum without.

significant absorption-induced perturbations of microsamples. Complete sample breakdown (e.g., melting, vaporization) by simple absorption heating sets an upper limit on the allowable intensity of the focused beam.

We can illustrate the effects of laser-induced sample heating with experimental observations made in the analysis of radiation-absorbing environmental particles (i.e., "unknowns"), as well as by spectral studies of known materials for which the effects of high temperature increases are understood. Figures 3 and 4 show spectra obtained under both low and high irradiance conditions (with 514.5nm excitation) that demonstrate spectral changes brought on by thermally induced sample changes; Fig. 3 shows the result of two successive measurements on a  $3\mu\text{m}$  particle isolated from a bulk sample of airborne dust. The unknown particle is identified as  $\text{NaNO}_3$  with reference to published Raman data for this salt.<sup>13</sup> The upper spectrum was obtained at an irradiance of  $5.7\text{ kW/cm}^2$ ; the lower, at  $0.32\text{ MW/cm}^2$ . The most pronounced difference in the two spectra consists of the two broad bands in the  $1200\text{--}1700\text{ cm}^{-1}$  region and the appearance of a much higher background light or lumi-

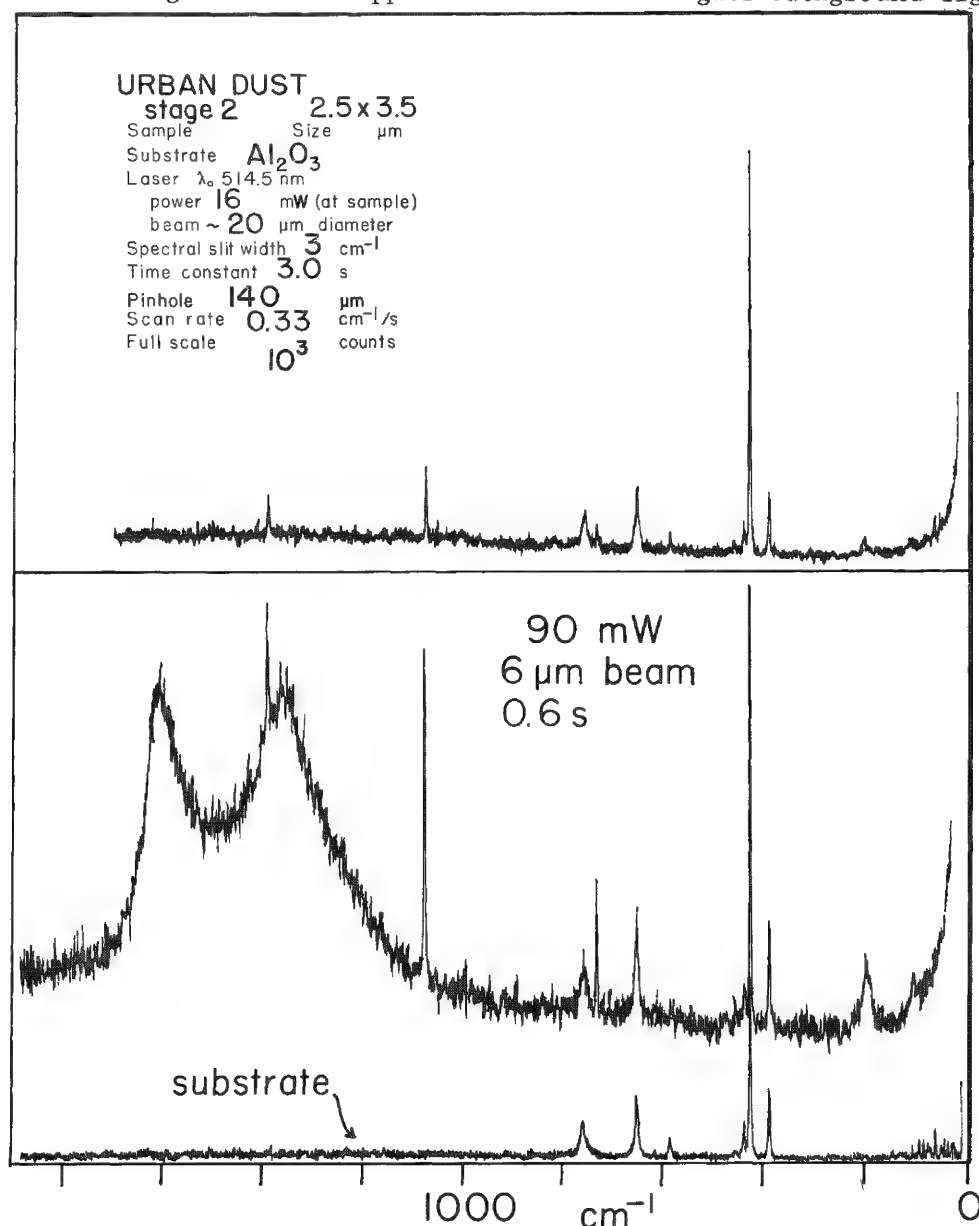


FIG. 3.--Effect of laser irradiance ( $\text{watts/cm}^2$ ) on spectrum of microparticle of sodium nitrate ( $\text{NaNO}_3$ ) in urban air particulate dust. Power density at sample: top,  $5.7\text{ kW/cm}^2$ ; bottom,  $0.32\text{ MW/cm}^2$ . Shown also is (interfering) spectrum of sapphire substrate.

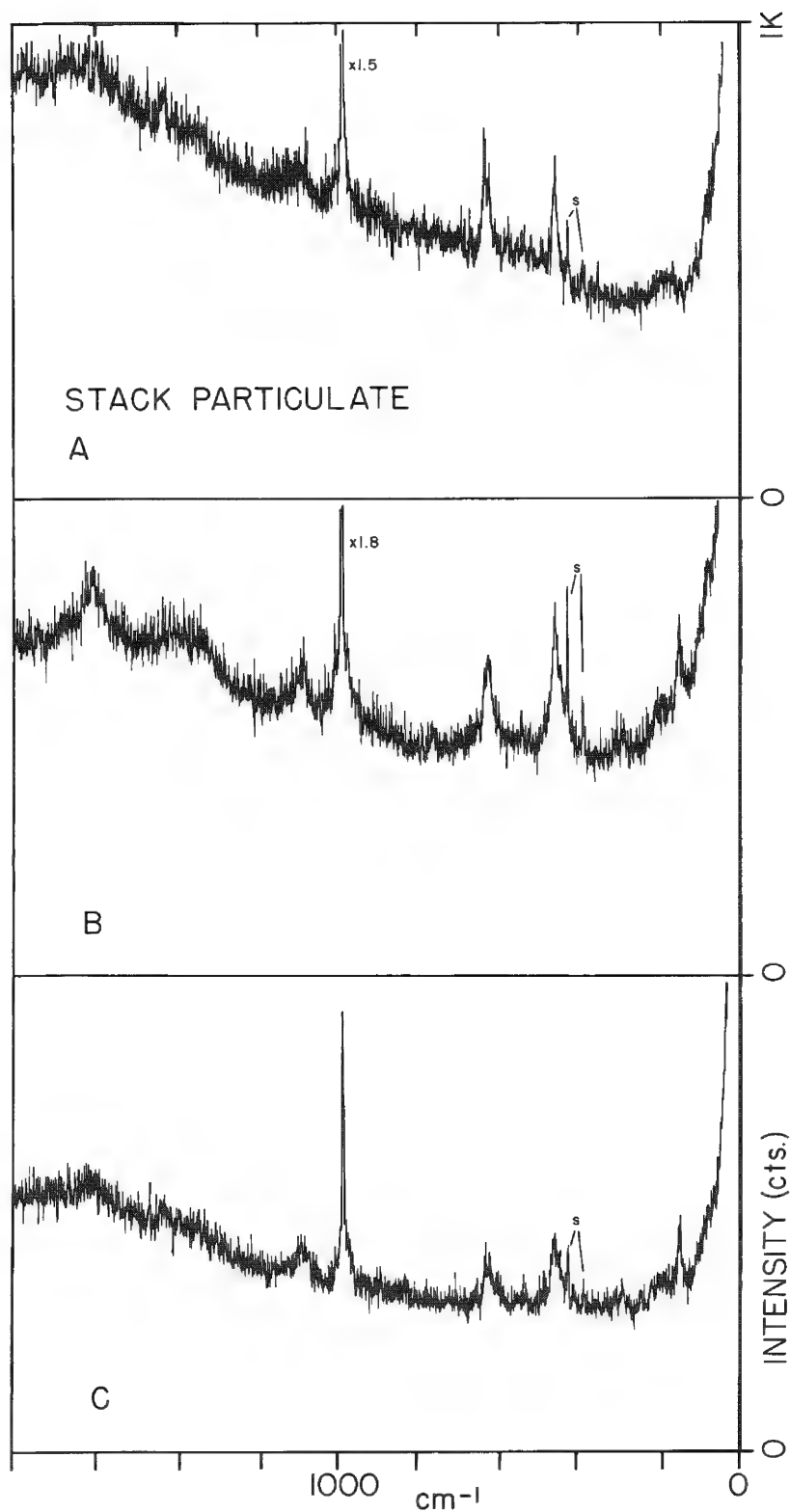


FIG. 4.--Spectra of stack particulate from oil-fired power plant, illustrating measurement-induced effects. Analysis conditions: particle size,  $8 \times 12 \mu\text{m}$ ; substrate,  $\alpha\text{-Al}_2\text{O}_3$ ; laser,  $\lambda_0 = 514.5 \text{ nm}$ ; spectral slit width,  $3 \text{ cm}^{-1}$ ; pinhole,  $140 \mu\text{m}$ ; intensity, 1000 counts full scale. Parameters varied: power (at sample), 25 mW (A,C), 120 mW (B); beam spot, about  $18 \mu\text{m}$  diameter (A,C), about  $8 \mu\text{m}$  (B); time constant, 3.0 sec (A,C), 1.0 sec (B); scan rate,  $20 \text{ cm}^{-1}/\text{min}$  (A,C),  $50 \text{ cm}^{-1}/\text{min}$  (B). Bands marked S arise from scattering by sapphire substrate.

nescence level in the high irradiance spectrum. Other differences are noted in both the intensity and spectral definition of the bands--with frequency shifts 98, 185, 724, 1068 and  $1385\text{ cm}^{-1}$ --attributed to sodium nitrate. The two pronounced, broad bands in the lower spectrum, centered at  $1350$  and  $1600\text{ cm}^{-1}$ , are associated with the presence of a form of polymeric (also called graphitic or elemental) carbon not detected in the low-irradiance spectrum. In the spectra of Fig. 3 we see the result of the absorption-induced conversion of an environmental carbonaceous material (a minor constituent of the particle, most likely surface adsorbed) to a form of polymeric carbon with graphitic structure.<sup>4,14</sup>

In the analysis of stack particulates from oil-fired power plants we have made similar observations of measurement-induced spectral changes.<sup>3</sup> Figure 4 shows results from current investigations of stack aerosol particulates collected by size-separating impaction samplers. The top (A) and bottom (C) spectra of Fig. 4 were obtained under identical, low-irradiance conditions; the middle one (B), at high irradiance. The analysis of these consecutive spectra permits the following interpretation. Nickel ammonium sulfate,  $\text{NiSO}_4 \cdot (\text{NH}_4)_2\text{SO}_4 \cdot 6\text{H}_2\text{O}$ , is the major--and in the top spectrum the only detectable--component of the microparticle, by comparison with Raman data cited in the literature<sup>15,16</sup> and reference spectra of this double sulfate obtained in the microprobe. The crystalline solid has its strongest band (sulfur-oxygen mode) at about  $985\text{ cm}^{-1}$  and other bands of weaker intensity centered around 455, 625, and  $1110\text{ cm}^{-1}$ . The high-irradiance measurement (B) gives evidence of a second (minor) component, with the appearance of a band at  $144\text{ cm}^{-1}$ , the strongest feature in the spectrum of vanadium pentoxide.<sup>17</sup> Other bands characteristic of  $\text{V}_2\text{O}_5$  have assigned Raman shifts of 104, 285, 406, 701, and  $995\text{ cm}^{-1}$ , but (except for the last) are obscured by the high luminescent background of the spectrum. In parallel measurements on microparticles of two other oxides of vanadium,  $\text{V}_2\text{O}_3$  and  $\text{V}_2\text{O}_4$  (or  $\text{VO}_2$ ), we have shown that these lower oxides are transformed by the intense laser radiation (via thermal oxidation) to  $\text{V}_2\text{O}_5$ . The two lower oxides are dark (black/green) colored and highly absorbing at  $514.5\text{ nm}$ . The middle spectrum also shows the graphitic carbon bands (in the region  $1200\text{--}1700\text{ cm}^{-1}$ ) thought to arise from the decomposition of an organic layer or film on the particle. The third measurement furnished a spectrum (C) with better signal-to-background than the first, owing to sample changes that altered the nature, or abundance, of luminescing constituents or contaminants.

Spectral changes induced by laser irradiance are frequently observed in the analysis of organic microparticles. However, these changes cannot always be fully explained by thermally induced modifications of the sample, but may result from photodecomposition (e.g., photooxidation, photolysis), as many molecular solids are unstable to high-intensity visible laser radiation. Optical breakdown is thus a second, laser-induced potential perturbation and can at times be a source of difficulty.

An example of this kind of observation is shown in the spectra of Fig. 5 for two microcrystals of trinitrotoluene (TNT explosive, straw-yellow colored) excited with the yellow ( $568.2\text{ nm}$ ) and red ( $647.1\text{ nm}$ ) line of the laser. Bands in the Raman spectrum of TNT arise from vibrations of the phenyl ( $\text{C}_6$ ) ring; C-H, C-N bonds; and vibrations of the  $\text{NO}_2$  groups. No spectra could be obtained with green line ( $514.5\text{ nm}$ ) excitation owing to instantaneous sample decomposition (melting point  $82^\circ\text{C}$ ). The top spectrum--obtained under low-irradiance conditions--shows a slowly progressing sample modification, evidenced by the changing or developing background during the course of the measurement. This luminescent background can not be attributed to thermal radiation (incandescence), for the microcrystal is still at a low (nonincandescent) temperature well below its melting point. From this observation we cannot exclude, in this and other such examples, the possibility of the optically induced formation of a fluorescing species.

Since this particle is supported by a sapphire substrate, we note in the bottom spectrum the fluorescence interference (R-lines of ruby) from trace amounts of chromium ( $\text{Cr}^{3+}$ ) in the sapphire, appearing as a sharp doublet at  $1050\text{ cm}^{-1}$  and  $1021\text{ cm}^{-1}$  (wavenumber shift with red-line excitation). The TNT spectra then illustrate a form of background interference which is excitation dependent but not necessarily absorption (i.e., thermally) induced.

Since the intensity of vibrational Raman scattering is temperature dependent, we have in some experiments--obtained estimates of the temperature reached by the sample from the determination of Stokes and anti-Stokes Raman intensity ratios.<sup>19</sup>

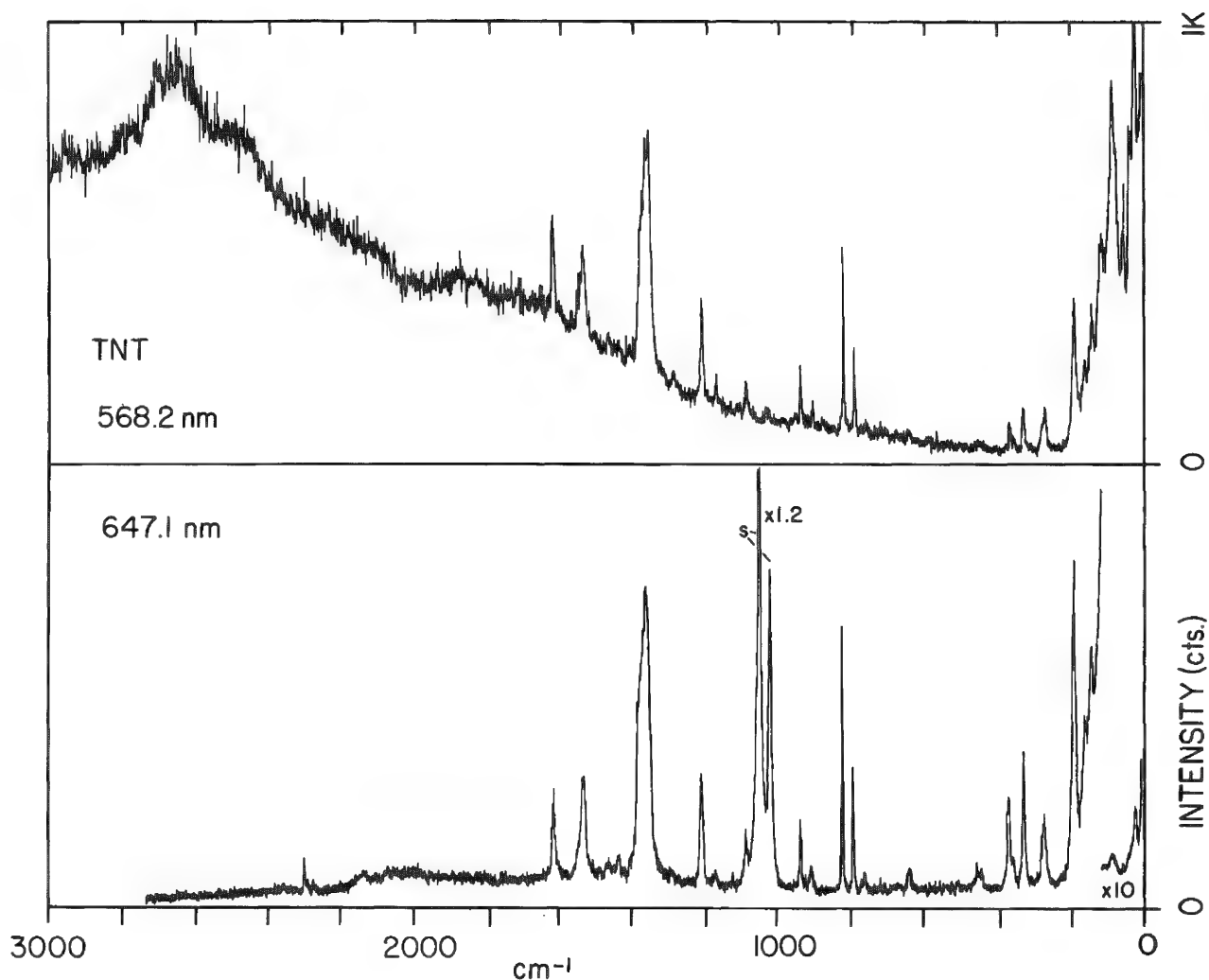


FIG. 5.--Spectra of microcrystals of trinitrotoluene (TNT) excited at two laser wavelengths. Measurement parameters: Top--particle size,  $20 \times 60 \mu\text{m}$ ; power, 8 mW (at sample); beam spot, about  $16 \mu\text{m}$  diameter; time constant, 2.0 sec; scan rate,  $50 \text{ cm}^{-1}/\text{min}$ . Bottom--particle size,  $15 \times 25 \mu\text{m}$ ; power, 30 mW (at sample); beam spot, about  $12 \mu\text{m}$  diameter; time constant, 2.0 sec; scan rate,  $50 \text{ cm}^{-1}/\text{min}$ . For both spectra--spectral slit width,  $3 \text{ cm}^{-1}$ ; pinhole,  $140 \mu\text{m}$ ; intensity, 1000 counts full scale. Particles supported by sapphire substrate. Bands marked S in lower spectrum are due to substrate fluorescence.

#### *Chemical Reactivity of Microparticles*

The pronounced chemical reactivity of microscopic particles of many classes of materials and compounds is well known. This enhanced susceptibility of certain microsamples--as against that of their bulk sample counterparts--to chemical reaction or modification can be a source of difficulties in Raman microprobe studies as the sample is usually exposed to the ambient laboratory atmosphere, rather than being confined to an evacuated sample chamber, as in electron- and ion-beam instruments. Considerations of the reactivity (or, conversely, the instability) of microsamples are particularly pertinent in the characterization of atmospheric aerosols, such as in the speciation of airborne soluble sulfates and nitrates.<sup>20,21</sup> In recent work, as part of a micro-Raman study of the molecular identity of South Pole atmospheric aerosol,<sup>5</sup> we have examined the question of aerosol reactivity and chemical transformation of microparticles more carefully. These measurements made use of a controlled-atmosphere sample chamber, built to enclose the sample stage of the instrument. It permits maintaining samples in a nonambient atmosphere (usually dry nitrogen) to prevent

contamination or alteration of the specimen by (for example) ammonia at ambient levels or by atmospheric moisture. This procedure has allowed us to examine the relationship between chemical composition (solid/aqueous phase) and humidity to Raman scattering by hygroscopic particles.

In these investigations of (submicron) South Pole atmospheric aerosol we needed to be concerned with the hygroscopic nature of microparticulate crystalline sulfates and nitrates [e.g.,  $(\text{NH}_4)_2\text{SO}_4$ ,  $\text{NH}_4\text{HSO}_4$ ,  $\text{LiNO}_3$ ]. For several of these salts we have obtained the spectra under various conditions of relative humidity (RH), to observe (from the spectra) the deliquescence of microsamples, the evaporation rate of liquid microparticles, and the kinetics of crystallization from the solution phase. In the case of these hygroscopic solids, the formation of a deliquescent phase is denoted by rapid spectral changes, such as the disappearance of lattice modes in the low-frequency region. The spectra of Fig. 6 show these changes for a microparticle of lithium nitrate. This salt crystallizes in the calcite

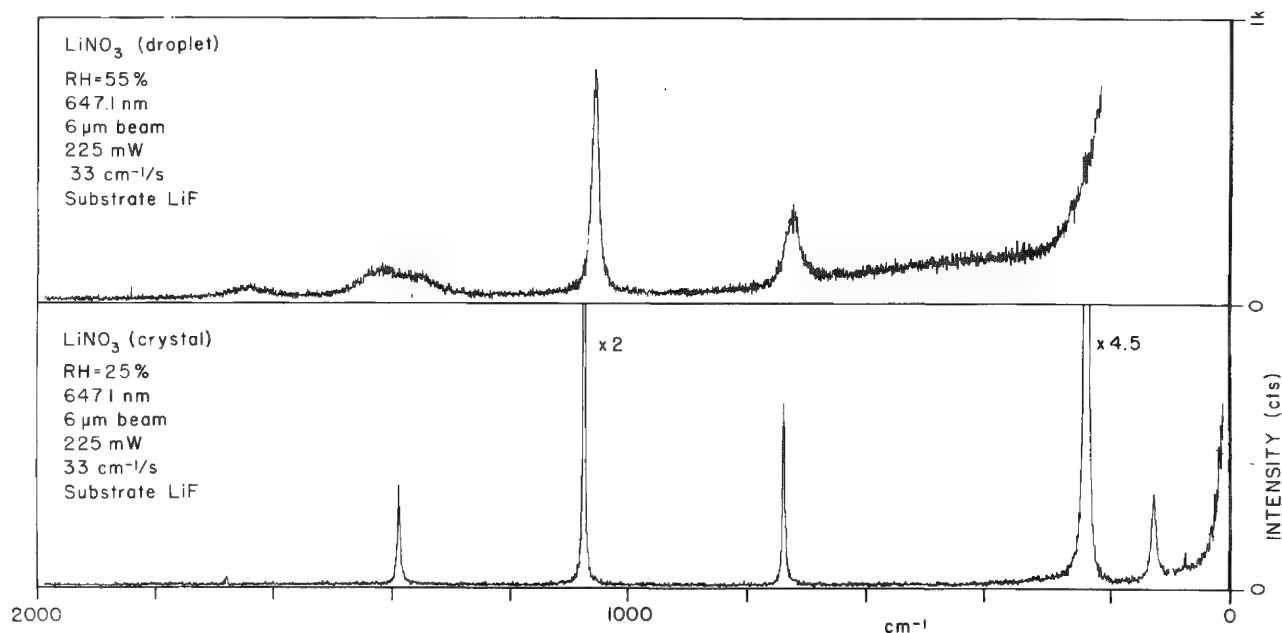


FIG. 6.--Spectra of a microparticle (size about  $20\ \mu\text{m}$ ) of lithium nitrate exposed to differing conditions of relative humidity (RH). Recorded with: time constant, 2.5 sec (top), 0.3 sec (bottom); scan rate,  $20\ \text{cm}^{-1}/\text{min}$  (top),  $200\ \text{cm}^{-1}/\text{min}$  (bottom); spectral slit width,  $3\ \text{cm}^{-1}$  for both.

structure; thus, three Raman-active  $\text{NO}_3^-$  internal vibrations and two lattice modes are expected.<sup>22</sup> The internal frequencies in  $\text{LiNO}_3$  are quite dependent on the amount of water present and the physical state of the sample. Since crystalline  $\text{LiNO}_3$  is highly hygroscopic, this dependency is reflected in shifts for the internal frequencies that are a sensitive function of the extent of hydration of the crystal. (At least two stable hydrates exist,  $\text{LiNO}_3 \cdot \text{H}_2\text{O}$  and  $\text{LiNO}_3 \cdot 3\text{H}_2\text{O}$ .) The top spectrum is that of a microparticle converted to a microdroplet. In the aqueous solution phase the strongest band is the nitrate symmetric stretching vibration ( $\nu_1$ ) at about  $1052\ \text{cm}^{-1}$ , the low-frequency lattice modes are of course absent. The spectrum (bottom) of the microcrystal shows much sharper bands, with shifts at about  $1385\ \text{cm}^{-1}$  ( $\nu_3$ ),  $1072\ \text{cm}^{-1}$  ( $\nu_1$ ),  $785\ \text{cm}^{-1}$  ( $\nu_4$ ),  $238\ \text{cm}^{-1}$ , and  $125\ \text{cm}^{-1}$ , the last two being the lattice modes--all of which have shifted (about  $20\ \text{cm}^{-1}$  for  $\nu_1$ ) to higher frequencies. In this measurement, the exact state of hydration of the microcrystal is not known.

#### *Laser-induced Sample Fluorescence*

Intimately related to excitation and detection of micro-Raman spectra is one other wavelength-related factor--fluorescence--which assumes major importance in the selection of excitation wavelength. Fluorescence occurs when one or more constituents of the ob-



served system (e.g., a single particle or a biological tissue section) absorb part of the incident light and then emit some of this absorbed energy. The fluorescence emission per molecule can be many orders of magnitude stronger than Raman scattering from the sample. Thus, fluorescence from only minor constituents such as sample impurities or contaminants can provide severe background interference to microprobe measurements. In the analysis of environmental particulates, fluorescence can be attributed to absorption by organic combustion residues (present as contaminating films) or other types of adsorbed materials. In certain organic (e.g., PAH) and biological samples, this native fluorescence can be very strong.

The fluorescence problem in these measurements manifests itself as a broad continuum in the Raman spectrum of many samples. With microsamples, there is not much that one can do to reduce the effect of fluorescence background to manageable levels, such as by sample "clean-up" as in macro-Raman work. However, sometimes the fluorescence background decays with time (by quenching processes) to the point at which a suitable signal-to-noise level is reached. In rare cases one can subtract the fluorescence background to obtain a reliable Raman spectrum.

In recent work we have more systematically examined the problem of sample fluorescence. As part of a broader study, the spectra of microsamples of a series of polynuclear aromatic hydrocarbons (PAHs) were obtained.<sup>23</sup> These polyaromatic ring systems represent a class of compounds known to be notorious fluorescers. The PAHs were measured as single microparticles, generally of size 2-10  $\mu\text{m}$ , and include representative members of the 3-ring (e.g., phenanthrene) and 4-ring (e.g., chrysene, pyrene, fluoranthene) systems. The fluorescence levels were examined in the spectra excited at three laser frequencies: 514.5 nm (green), 568.2 nm (yellow), and 647.1 nm (red). Two results from these studies are shown in Fig. 7. In general, excitation with 514.5nm radiation under the lowest practical irradiance conditions (typically 2 mW at sample in 20 $\mu\text{m}$  beam spot), furnishes spectra characterized by high, broadband fluorescence background levels. In these situations, a useful spectrum cannot be obtained. Excitation at 568.2 nm results in spectra that have appreciably lower background levels, which indicates much diminished fluorescence emission at this wavelength. With 647.1nm excitation, the problems of fluorescence from these compounds are virtually nonexistent.

The spectrum of the pyrene microcrystal shows a moderate fluorescence background with 568.2nm excitation. This spectrum could not be obtained with 514.5nm excitation. The spectrum of the microcrystal of phenanthrene, excited at 647.1 nm, has excellent signal-to-background and shows no fluorescence. The micro-Raman spectra of these compounds are consistent with the spectra reported for macroscopic single crystal samples.<sup>24,25</sup>

### *Low Signal Detection*

Micro-Raman scattering is a weak process and frequently the signals are not sufficiently intense for the detection of major or minor species. Limiting the experimental enhancement of signals in normal (spontaneous) Raman scattering are the levels of irradiance that can safely be employed as well as the response (i.e., sensitivity) of the detection devices that have come into use. Resonance Raman scattering<sup>26</sup>--optimally realized with tunable lasers--which has not been explored for microsample analysis, may hold some promise for the detection of weakly scattering species or trace constituents.

Monitoring of Raman scattering signals is by photoelectric detection with optimally cooled and shielded photomultiplier detectors (PMTs). These devices are still the detectors providing lowest noise (typically 1-3 cps in the photon counting mode) for very low light levels. However, important advantages in the detection of weak signals may be realized through the use of multichannel detectors (coupled to a spectrograph) which are composed of one or more optical image intensifiers and a two-dimensional transducer such as a vidicon or diode array.<sup>27,28</sup> These TV-type detectors allow data acquisition times to be significantly reduced and permit the observation of many spectral lines (and spectral points) simultaneously. The most recent versions of these optical multichannel analyzer systems (OMAs) combine the multiplex advantage with signal-to-noise (S/N) ratios approaching those of photomultiplier tubes.<sup>29</sup> Moreover, these detectors can be gated to pulsed excitation sources, prospects that are extremely exciting. Pulsed laser excitation would allow discrimination of Raman scattering against undesirable effects with longer life and decay

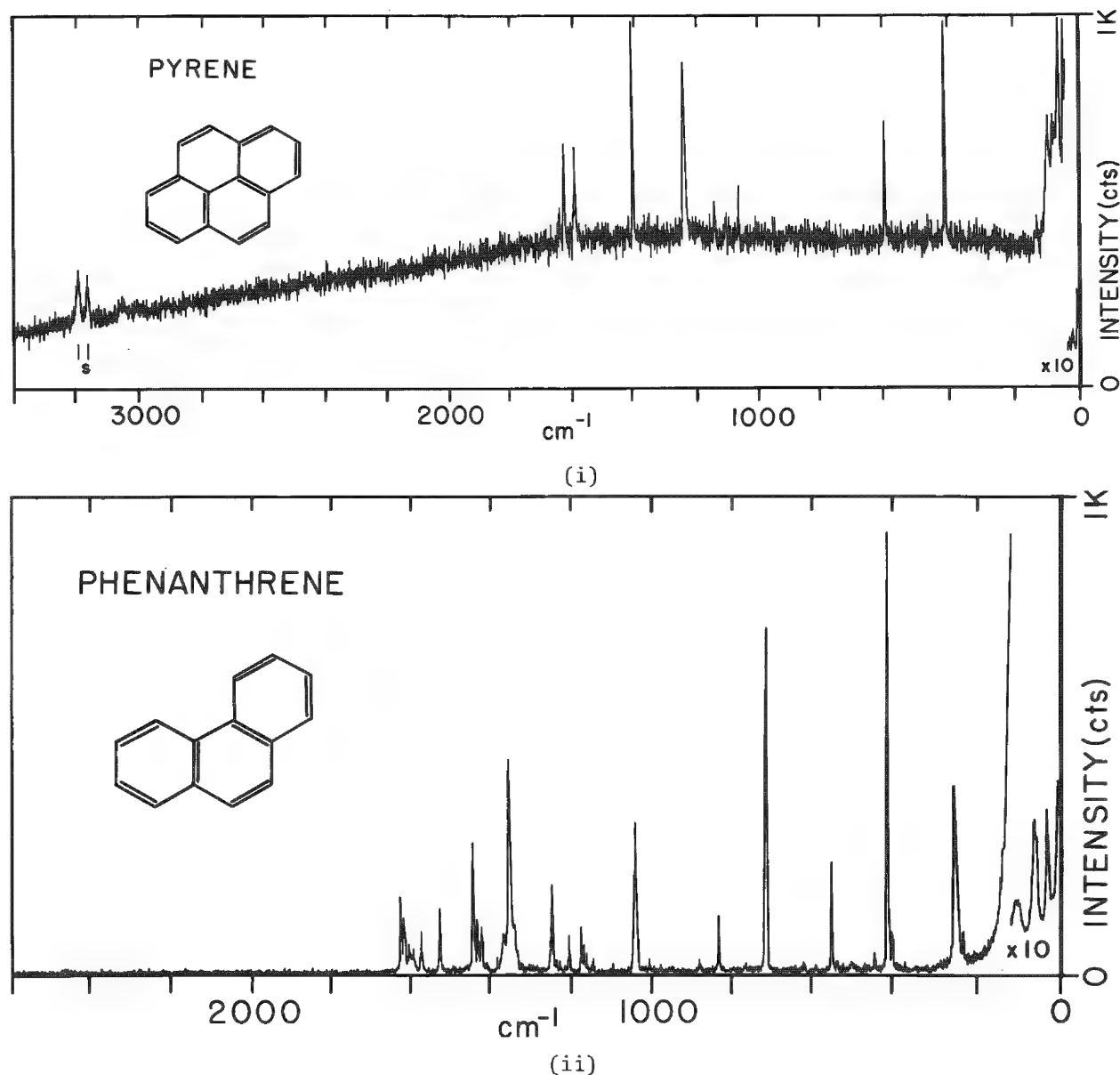


FIG. 7.--Raman microprobe spectra of fluorescence sensitized polynuclear aromatic hydrocarbons (PAHs). (i) Pyrene ( $C_{16}H_{10}$ ): particle size,  $30\text{ }\mu\text{m}$ ; substrate,  $\alpha\text{-Al}_2\text{O}_3$ ; laser,  $\lambda_0 = 568.2\text{ nm}$ ; power,  $4\text{ mW}$  (at sample); beam spot, about  $18\text{ }\mu\text{m}$  diameter; time constant,  $0.2\text{ sec}$ ; scan rate,  $200\text{ cm}^{-1}/\text{min}$ . Bands marked S arise from fluorescence of substrate. (ii) Phenanthrene ( $C_{14}H_{10}$ ): particle size,  $7 \times 7\text{ }\mu\text{m}$ ; substrate  $\text{LiF}$ ; laser,  $\lambda_0 = 647.1\text{ nm}$ ; power,  $20\text{ mW}$  (at sample); beam spot, about  $16\text{ }\mu\text{m}$  diameter; time constant,  $1.0\text{ sec}$ ; scan rate,  $50\text{ cm}^{-1}/\text{min}$ . Spectra recorded with slit width  $3\text{ cm}^{-1}$ , intensity 1000 counts full scale.

times, such as fluorescence. Pulsed excitation with time-gated detection might also improve the peak-to-background (P/B) ratio of weak Raman spectra or of scattering spectra perturbed by either luminescence or fluorescence backgrounds. However, this approach has yet to be explored for microprobe work.

#### *Challenges and Prospects*

We have discussed real and potential limitations to the effective implementation of micro-Raman scattering experiments and have tried to indicate to what extent they can be overcome or minimized by appropriate experimental countermeasures. We have highlighted the areas in which major progress must be made to enhance the capabilities of micro-Raman

scattering experiments, notably detection limits (relative and absolute) for species distributed homogeneously and heterogeneously, sample perturbation thresholds for laser-particle interactions, heat sinking efficiencies of substrate materials and particle embedding media, and advantages of pulsed lasers with gated detection. These and other, related challenges are the ones worth pursuing.

## References

1. E. S. Etz, G. J. Rosasco, J. J. Blaha, K. F. J. Heinrich, and W. C. Cunningham, "Particle analysis with the laser-Raman microprobe," *Proc. 13th MAS Conf.*, 1978, 66A.
2. E. S. Etz, "Raman microprobe analysis: Principles and applications," *SEM/1979*, SEM, Inc., AMF O'Hare, IL 60666.
3. E. S. Etz, G. J. Rosasco, and J. J. Blaha, "Observation of the Raman effect from small, single particles," in T. Y. Toribara, J. R. Coleman, B. E. Dahneke, and I. Feldman, Eds., *Environmental Pollutants: Detection and Measurement*, New York: Plenum, 1978, 413-456.
4. J. J. Blaha, G. J. Rosasco, and E. S. Etz, "Raman microprobe characterization of residual carbonaceous material associated with urban airborne particulates," *Appl. Spectrosc.* 32: 292, 1978.
5. W. C. Cunningham, E. S. Etz, and W. A. Zoller, "Raman microprobe characterization of South Pole aerosol," *Proc. 14th MAS Conf.*, 1979.
6. J. J. Blaha and G. J. Rosasco, "Raman microprobe spectra of individual microcrystals and fibers of talc, tremolite, and related silicate minerals," *Anal. Chem.* 50: 892, 1978.
7. F. S. Casciani, E. S. Etz, D. E. Newbury, and S. B. Doty, "Raman microprobe studies of two mineralizing tissues: Enamel of the rat incisor and the embryonic chick tibia," *SEM/1979*, SEM, Inc., AMF O'Hare, IL 60666.
8. G. J. Rosasco and E. S. Etz, "The Raman microprobe: A new analytical tool," *Res. & Devel.* 28: 20, June 1977.
9. G. J. Rosasco, "Microanalysis by Raman spectroscopy," in E. D. Schmid, R. R. Krishnan, W. Kiefer, and A. W. Schroetter, Eds., *Proc. 6th Intern. Conf. Raman Spectroscopy*, London: Heyden, 1978, 389-398.
10. V. G. Karamidas and W. B. White, "Raman spectra of oxides with the fluorite structure," *J. Chem. Phys.* 59: 1561, 1973.
11. S. P. S. Porto and R. S. Krishnan, "Raman effect of corundum," *J. Chem. Phys.* 47: 1009, 1967.
12. H. S. Bennett and G. J. Rosasco, "Heating microscopic particles with laser beams," *J. Appl. Phys.* 49: 640, 1978.
13. W. P. Griffith, "Raman studies on rock-forming minerals: Part II," *J. Chem. Soc. (A)*: 286, 1970.
14. F. Tuinstra and J. L. Koenig, "Raman spectrum of graphite," *J. Chem. Phys.* 53: 1126, 1970.
15. V. Ananthanarayanan, "Raman spectra of crystalline double sulfates: Part II. Ammonium double sulfates," *Z. Physik* 166: 318, 1962.
16. Y. S. Yain and H. D. Bist, "Optical phonons in  $\alpha$ -NiSO<sub>4</sub>·6H<sub>2</sub>O single crystal," *J. Raman Spectrosc.* 2: 327, 1974.
17. J. R. Gilson, O. F. Bizri, and N. Cheetham, "Single crystal Raman and infrared spectra of vanadium (V) oxide," *J. Chem. Soc. (Dalton)*: 291, 1973.
18. F. R. Dollish, W. G. Fateley, and F. F. Bentley, "Characteristic Raman frequencies of organic compounds," New York: Wiley, 1974.
19. D. A. Long, *Raman Spectroscopy*, London: McGraw-Hill, 1977.
20. R. L. Tanner and L. Newman, "The analysis of airborne sulfate: A critical review," *J. Air Poll. Control Assoc.* 26: 737, 1976.
21. E. S. Etz, G. J. Rosasco, and W. C. Cunningham, "The chemical identification of airborne particles by laser Raman spectroscopy," in G. W. Ewing, Ed., *Environmental Analysis*, New York: Academic Press, 1977, 295-340.
22. R. E. Miller, R. R. Getty, K. L. Treuil, and G. E. Leroi, "Raman spectrum of crystalline lithium nitrate," *J. Chem. Phys.* 51: 1385, 1969.
23. E. S. Etz, S. A. Wise, and K. F. J. Heinrich, "On the analytical potential of micro-Raman spectroscopy in the trace characterization of polynuclear aromatic hydrocarbons," in H. S. Hertz and S. N. Chesler, Eds., *Trace Organic Analysis: A New Frontier in Analytical*

*Chemistry*, Proc. 9th Materials Research Symp., NBS Special Publication 519, Washington, D.C.: National Bureau of Standards, April 1979.

24. A. Bree, R. A. Kydd, T. N. Misra, and V. V. B. Vilkos, "The fundamental frequencies of pyrene," *Spectrochim. Acta* 27A: 2315, 1971.

25. A. Bree, F. G. Solven, and V. V. B. Vilkos, "A vibrational analysis for phenanthrene," *J. Mol. Spectrosc.* 44: 298, 1972.

26. A. Compaan, "Resonance Raman scattering with tunable lasers," *Appl. Spectrosc.* 13: 295, 1977.

27. Y. Talmi, D. C. Baker, J. R. Jadamec, and W. A. Saner, "Fluorescence spectrometry with optoelectronic image detectors," *Anal. Chem.* 50: 936A, 1978.

28. R. Mathies and N.-T. Yu, "Raman spectroscopy with intensified vidicon detectors: A study of intact bovine lens proteins," *J. Raman Spectrosc.* 7: 349, 1978.

29. R. E. Benner, R. Dornhaus, M. B. Long, and R. K. Chang, "Inelastic light scattering from a distribution of microparticles," *Proc. 14th MAS Conf.*, 1979.

## THE DEVELOPMENT OF INSTRUMENTATION FOR MICROPARTICLE ANALYSIS BY RAMAN SPECTROSCOPY

D. O. Landon

In this paper we present a brief history of the highways and byways taken in the development of instruments designed explicitly for the purpose of obtaining Raman spectra of microparticulates (defined as particles smaller than  $10\text{ }\mu\text{m}$  in diameter). The introduction of lasers as light sources for Raman spectroscopy<sup>1</sup> signalled the rebirth of that technique since the laser, in addition to being the long-hypothesized ideal light source for Raman spectroscopy, was also the ideal light source for illumination of microsamples.

A laser beam exhibits a high degree of coherence and little divergence; it is almost perfectly collimated and can be easily focused to a diffraction-limited point<sup>2</sup>; that is, to a spot size limited by the wavelength and the optics used to focus the beam. Table I gives some idea of these dimensions when  $514.5\text{nm}$  radiation is focused with typical microscope objectives. The  $f$  number familiar to photographers is the focal length of the lens divided by its diameter. The numerical aperture (NA) is the microscopists' equivalent;  $\text{NA} = n \sin \theta$ , where  $n$  is the refractive index of the medium in which the lens operates (usually air) and  $\theta$  is the half angle of convergence.

It should be noted that the energy distribution in the spot is not uniform, but Gaussian.

As stated, the potential of focused, intense monochromatic light beams for microanalysis is obvious. Laser Raman spectroscopy began to appeal to analytical chemists, and this microsampling capability became feasible for microvolume analysis of both liquids and gases.<sup>3,4</sup>

With hardly a pause, instrumentalists dreamed of new conquests, and proposals for microparticle analyzers began to appear (circa 1969). The first instrument of this type was built in France, and similar developments occurred in the USA.<sup>5-10</sup> Although we cannot give a comprehensive review of these efforts here, we can touch on enough points to define the problem, present the current state of the art, and peer into the future.

The constraints on a Raman system for microparticle analysis can be summed up simply. The problem is to obtain a Raman spectrum of a particle of microscopic dimensions in a reasonable time and with limited laser power. When we focus large optical powers into small spots, we are forced to consider power density and its effects on the Raman process. McQuillan et al. at the University of Toronto showed that intensity of spontaneous Raman emission from a solid sample increases linearly with increasing laser power up to a threshold above which stimulated Raman emission commences (Fig. 1).<sup>11</sup> For a diamond crystal this threshold was measured at  $1.1 \times 10^9\text{ W/cm}^2$  (laser irradiance), in excellent agreement with a calculated theoretical value of  $1.2 \times 10^9\text{ W/cm}^2$ . Since diamond has a high scattering efficiency, this value of approximately  $10^9\text{ W/cm}^2$  can be taken as a worst case; but if Raman spectra obeying the normal selection rules are to be observed, we must restrict laser power accordingly.

A particle  $0.5\text{ }\mu\text{m}$  in diameter covers an area approximately  $2 \times 10^{-9}\text{ cm}^2$ . If the laser power is kept to  $10^8\text{ W/cm}^2$  (to avoid stimulated scattering) the maximum laser power is approximately 600 mW when focused with an  $\text{NA} = 1$  lens. The Gaussian distribution of energy in the spot makes a further reduction in power advisable; a commonly accepted value is below 200 mW.

All the above ignores any tendency for the sample to heat in the process of being illuminated by the laser. These heating effects are explored by Bennet and Rosasco.<sup>12</sup>

In general, to avoid catastrophic sample heating, or even a temperature rise sufficient to cause a phase transformation, the microparticle must be in good thermal contact with a reasonably good thermal conductor. Sapphire ( $\text{Al}_2\text{O}_3$ ) is such a material; it has become customary to place isolated microparticles on a sapphire rod or disk. Even so, an

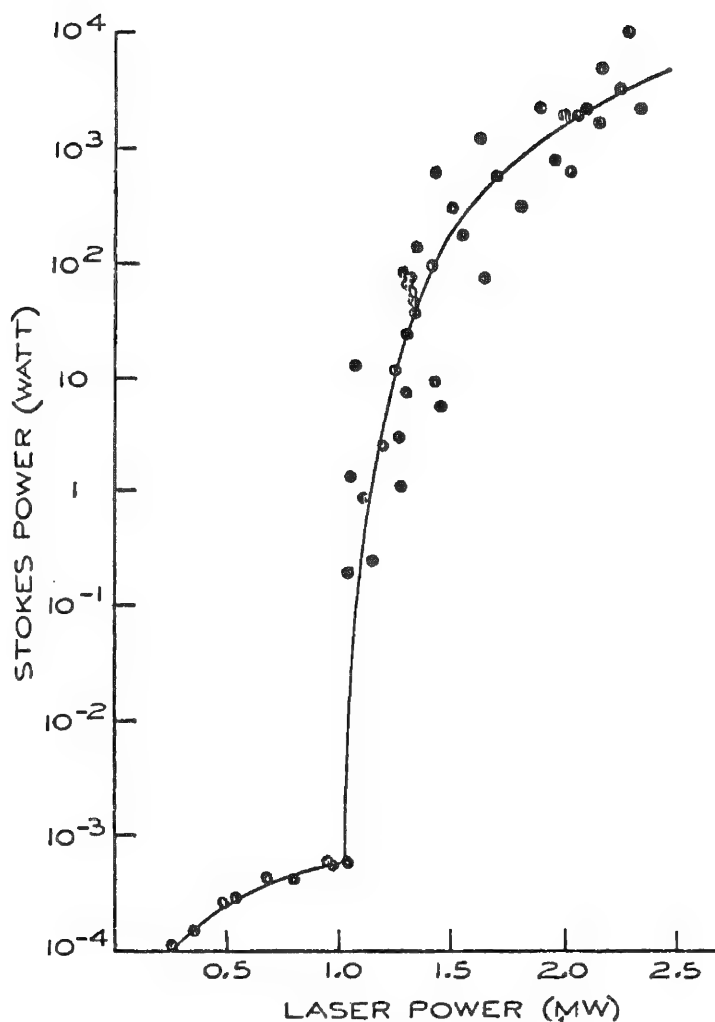


FIG. 1.--Experimental curve of Raman Stokes power vs incident laser power for scattering from diamond crystal (after McQuillan et al.<sup>5</sup>).

Microprobe measurements made on various types of solid particles at the National Bureau of Standards and at Instruments SA, Inc., give Raman signals in substantial agreement with this predicted level of signal intensity, when the obvious differences of Raman cross section and instrument geometry are factored in. Even if we assume that we wish to observe only 0-2000  $\text{cm}^{-1}$  of the Raman spectrum, the implications are disturbing. To obtain a signal-to-noise ratio of approximately 30:1 in the most intense Raman bands, we must record for approximately 10 sec per channel, or  $2000 \text{ cm}^{-1} / 4 \text{ cm}^{-1} \times 10 \text{ sec} = 5 \times 10^3 \text{ sec}$  (about 80 min) when scanning with an ordinary high-performance Raman spectrometer, even under nearly ideal conditions with a good Raman scatterer of adequate size, capable of accepting substantial laser power. Reduce this same particle to approximately 0.3  $\mu\text{m}$  diameter, and the signal will be only 1/64. It now requires nearly 4 days to obtain a Raman spectrum as before.

These problems were well known to those designing microparticle Raman systems; as early as a decade ago there were proposals to make suitable instruments. (Suitable meant a good multichannel Raman spectral recording system.) Fourier-transform infrared analyzers were bringing the advantages of simultaneous multichannel measurement into the analytical laboratory, and Raman spectroscopists desired nothing less. Theory and practice told us that to obtain such advantages in the UV-visible spectrum we could not use the nondispersive

absorbing material with low thermal stability can limit the incident optical power to a few milliwatts. (The previous discussions and those to come assume that the microparticle is spherical, homogeneous, and isotropic.)

Finally, a word about the efficiency of Raman scattering. Scattering phenomena are inherently weak. Skinner and Nilsen<sup>13</sup> measured the Raman scattering cross section of benzene, a relatively strong scatterer, at  $1.05 \times 10^{-29} \text{ cm}^2$  per molecule, per steradian, per wavenumber, per plane of polarization at 488 nm.

For spherical microparticles, Raman signals scale with the third power of the particle diameter and are thus proportional to sample volume. This ignores any resonances that occur in the scattering and absorption processes.<sup>14</sup>

Having described the constraints, we can calculate the time necessary to record a Raman spectrum of a microparticle to any desired signal/noise ratio, assuming that the statistical noise (shot noise) in the signal is the predominant noise source (as is essentially true).

In the course of planning a microparticle Raman system some years ago, some colleagues and I calculated that a 1.16  $\mu\text{m}$ -diameter sphere of benzene, illuminated by 25 mW of 514.5 nm laser radiation, focused with an f 1 lens would generate 138 cps at the peak of the  $992 \text{ cm}^{-1}$  Raman band when viewed with an optical system having a collection geometry of f 1, a transmittance of approximately 0.20, and a spectral bandwidth of  $4 \text{ cm}^{-1}$ .

(interferometric) system, but had to separate the wavelengths. Thus, before it was quite dead, the spectrograph was reinvented.

Much recent work has been devoted to overcoming the limitations of the spectrograph as it applies to recording Raman spectra. The limitations of the classic photographic spectrograph are:

1. Low quantum efficiency (q.e.) detection. Photographic emulsions have typically approximately 0.2% q.e.
2. High stray light. Even with holographically recorded gratings, stray light levels of approximately  $10^{-8}$  are enough to obscure weak Raman radiation.

The obvious antidote for a low-q.e. photographic emulsion is a modern high-efficiency electronic camera;<sup>15,16</sup> whereas the cure for stray laser photons is prefiltering of light. In all modern instruments that is done with gratings, and as we shall see it is best done not with two but with three gratings--hence the usual name "triple spectrograph".<sup>17,18</sup>

To be quite accurate, a two-grating instrument ("double spectrograph") suffices if only a moderate range--approximately  $100\text{ cm}^{-1}$ --of Raman spectrum is needed. Several special instruments have been made; the I.S.A. MOLE<sup>®</sup> is a commercial instrument with this capability.<sup>19</sup> As we shall see, it has some features in common with those dictated by our needs, but diverges in that it is a general-purpose micro-Raman analyzer that is also capable of presenting microscopic images of samples emitting over a bandwidth of only a few wavenumbers, so that various molecular species can be mapped. These double spectrographs have a multichannel advantage of only about  $25\times$  over simplex scanning instruments, which is significant but not sufficient for our particular needs.

The techniques designers use to illuminate samples and collect scattered light have now reached a high state of development in these instruments. The problem of both illuminating the sample at large NA, and collecting the scattered light with equal or greater NA, means that the optics will mechanically interfere if conventional  $90^\circ$  scattering is attempted (Fig. 2). The solution to this problem is some form of coaxial optical system. These design approaches have been used in micro-Raman systems from the beginning.<sup>7,10,20</sup> One such design<sup>7</sup> incorporates a lens system for focusing the laser and a large portion of an ellipsoid of revolution for light collection (Fig. 3).

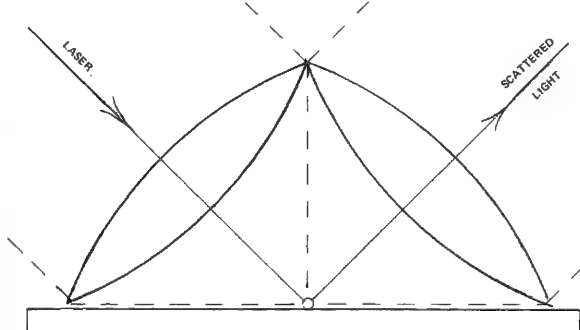


FIG. 2.--Incident and scattered light at  $90^\circ$ , with lenses of numerical aperture NA = 1.

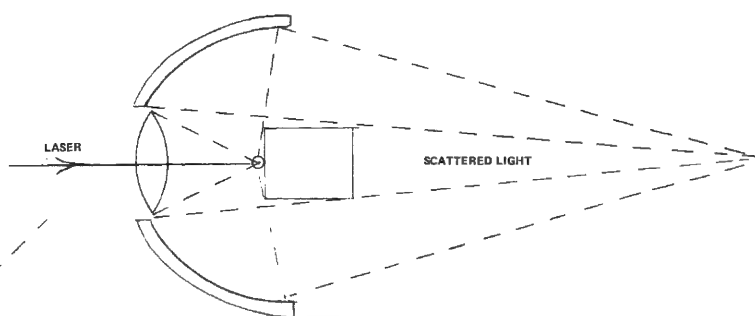


FIG. 3.--Incident and scattered light with co-axial lens/mirror system.

A most ingenious solution to the problem is found in the I.S.A. MOLE.<sup>19</sup> To illuminate and observe at equally large NAs, the same lens is used for both purposes and beam splitters separate the incoming and outgoing radiations. A specifically designed research microscope is used for this purpose in the instrument.<sup>21</sup> This system solves most of the illumination and viewing problems of a microparticle Raman system very well at all but extremely low light levels. Here the problem of using the same optical elements for both illuminating and viewing becomes evident. Even without any sample a small background signal, consisting of diffuse fluorescence and Raman scatter from the lenses and beam splitters themselves, is observed at all wavelengths.

To overcome this problem, we explored the use of commercially available all-reflecting objectives. The results were so encouraging that a special unit is now being fabricated.<sup>22</sup> Its primary (concave) element is a rather large hemispherical piece with a diameter of approximately 80 mm (Fig. 4).



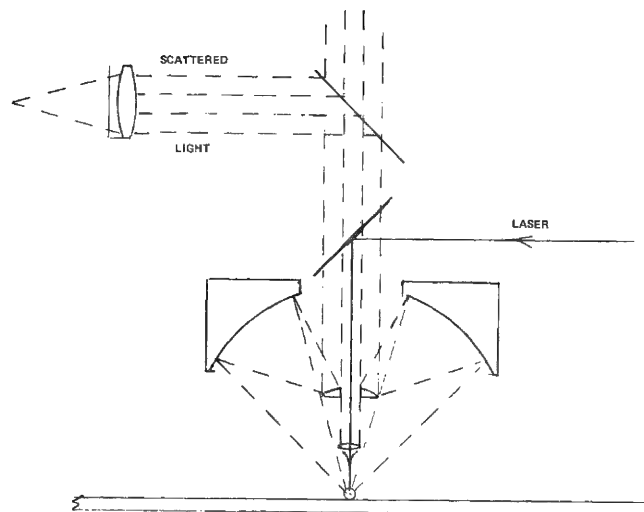


FIG. 4.--Incident and scattered light in monocentric reflecting microscope objective with coaxial lens.

The central obscuration always present in coaxial designs is used to introduce the laser beam to the system and focus it at the sample by means of a small lens. The lens is limited to  $NA \approx 0.25$  ( $f/2$ ), but that only limits power density at the sample, which is already limited by other sample-dependent factors to values lower than those readily obtainable from commercial lasers. The illuminating and viewing optics are totally isolated and should introduce no background Raman signal. This configuration resembles the original elliptical mirror design (Fig. 3) but it is compatible with microscope stands, and the optical quality of these monocentric mirror objectives allows good images to be viewed with standard microscope optics.

This illuminating and viewing system is being combined with a small commercial triple spectrograph (Model DL-203, Instruments S.A., Inc.); its optical scheme is shown in Fig.

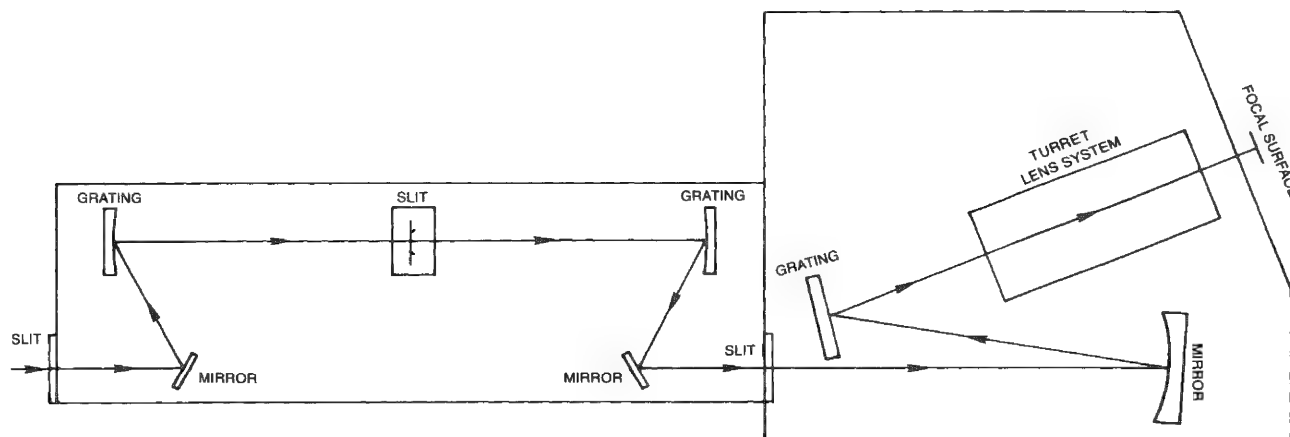


FIG. 5.--Optical schematic of Raman triple spectrograph system.

It was designed to work with commercially available electronic cameras. In general, these cameras limit the user to approximately 25 mm of spectrum in a single strip approximately 3 mm in height and resolve the field up to a maximum of 1728 channels. A unique feature of this triple spectrograph is its turret of three lenses. Classic Hilger and Watts Raman spectrographs--vintage 1958--offered the user several lenses from  $f/6.8$  to  $f/2.5$  to photograph the Raman spectrum.

Electronic cameras also respond to brightness in the image plane, and one can to some extent trade resolution for speed. Table 2 gives a comparison of spectral coverage and

TABLE 1.--Optical properties of microscope lenses used to focus laser beam. Diffraction-limited spot size for focused laser,  $D = 2.44\lambda f/d$ ; where  $\lambda$  = wavelength,  $f$  = focal length,  $d$  = beam diameter.

F number	NA	Diffraction-limited spot for 514.5 nm ( $\mu$ m)
2	0.24	2.5
1	0.45	1.2
0.5	1.0	0.6

TABLE 2.--Lenses in DL-203 triple Raman spectograph: Spectral coverage and recording time.

F number	Spectrum interval, 12.5mm field ( $\text{cm}^{-1}$ )	Relative recording time
4.5	900	14 ×
2.5	1800	4 ×
1.2	3400	1 ×

recording time for the three lenses in the instrument.

The instrument described here as the triple spectrograph has been with us for about a year and has been reasonably well tested. It does what it is supposed to, and is quite compact. It is optically somewhat slower than large 1m- focal length monochromators when both are used as monochannel scanning instruments. It equals any larger instrument in speed (the time needed to record a spectrum) once approximately 300 wavenumbers are recorded. When used as intended, to record between  $900 \text{ cm}^{-1}$  and  $3400 \text{ cm}^{-1}$  of a Raman spectrum, it is 10 to 100 times faster than a scanning spectrometer.

Even this limitation can yield to advanced electronic cameras and computer technology. Without going into the calculation, we can present that an optimum system for multichannel Raman spectroscopy would disperse the spectrum not over 25 mm, but over approximately 250 mm. A diode array of this size is not envisionable, even when segmented. However, there is another way to segment a spectrum. Using the phenomenon of ordered dispersion by a diffraction grating, one can present twenty-five vertically stacked overlapping segments, each approximately 10 mm long, to an electronic camera of rectangular aperture.

This idea was proposed independently by Tomas Hirschfeld and myself about ten years ago. Years later, a successful version for atomic emission was completed at the Bell Laboratories by D. Wood.<sup>23</sup> A Raman version is still a possibility. As we say, it is only a small matter of programming to read and output the data.

## References

1. S. P. S. Porto and D. L. Wood, "Ruby optical maser as a Raman source," *J. Opt. Soc. Am.* 52: 251, 1962.
2. A. Yariv, *Introduction to Optical Electronics*, New York: Holt, Rinehart & Winston, 1971, 35.
3. S. K. Freeman, P. R. Reed Jr., and D. O. Landon, "Microsampling techniques in laser Raman spectroscopy," *Mikrochim. Acta* 1972/3, 288-297.
4. J. J. Barrett and N. I. Adams III, "Laser excited rotation: Vibration Raman scattering in ultra-small gas samples," *J. Opt. Soc. Am.* 58: 311, 1968.
5. M. Delhay and P. Dhamelincourt, "Laser Raman microprobe and microscope," and G. J. Rosasco, E. S. Etz, and W. A. Cassatt, "Investigation of the Raman spectra of individual micrometer-sized particles," abstracts of papers presented at the Fourth International Conference on Raman Spectroscopy, Brunswick, Maine, Aug. 1974.
6. M. Delhay and P. Dhamelincourt, "Raman microprobe and microscope with laser excitation," *J. Raman Spectrosc.* 3: 33, 1975.
7. G. J. Rosasco, E. S. Etz, and W. A. Cassatt, "The analysis of discrete fine par-

ticles by Raman spectroscopy," *Appl. Spectrosc.* 29: 396, 1975.

8. M. Delhaye and P. Dhamelincourt, "Laser microprobe and microscope using Raman effect," *Molecular Spectroscopy of Dense Phases*, Proc. 12th European Congress on Molecular Spectroscopy, July 1975.

9. M. Delhaye, T. Bisson, and P. Dhamelincourt, "Laser microscopy using Raman effect," *Proc. Fifth Intern. Conf. on Raman Spectroscopy*, Freiburg, Germany, September 1976.

10. G. J. Rosasco and E. S. Etz, "The Raman microprobe: A new analytical tool," *Res. & Dev.* 28: 20, June 1977.

11. A. K. McQuillan, W. R. L. Clements, and B. P. Stoicheff, "Stimulated Raman emission in diamond: Spectrum, gain, and angular distribution of intensity," *Phys. Rev. [A]* 1: 628, 1970.

12. H. S. Bennett and G. J. Rosasco, "Heating microscopic particles with laser beams," *J. Appl. Phys.* 49: 640, 1978.

13. J. G. Skinner and W. G. Nilsen, "Absolute Raman scattering cross-section measurement of the  $992\text{ cm}^{-1}$  line of benzene," *J. Opt. Soc. Am.* 58: 113, 1968.

14. G. J. Rosasco and H. S. Bennett, "Internal field resonance structure: Implications for optical absorption and scattering by microscopic particles," *J. Opt. Soc. Am.* 68: 1242, 1978.

15. Y. Talmi et al., "Fluorescence spectrometry with optoelectronic image detectors," *Anal. Chem.* 50: 936A, 1978.

16. R. P. Cooney, G. D. Boutilier, and J. D. Winefordner, "Comparison of image devices vs photomultiplier detectors in atomic and molecular luminescence spectrometry via signal-to-noise ratio calculations," *Anal. Chem.* 49: 1048, 1977.

17. M. Bridoux et al., "New Trends in Rapid Laser Raman Spectroscopy" in R. J. H. Clark and R. E. Hester, Eds., *Advances in Infra-red and Raman Spectroscopy*, New York: Heyden, 1973, 1: 65-69.

18. M. Bridoux et al., "Rapid and ultra-rapid Raman spectroscopy," abstract presented at the Raman workshop, Schenectady, N.Y., 10-11 May 1973.

19. P. Dhamelincourt et al., "Laser Raman molecular microprobe (MOLE)," *Anal. Chem.* 51: 414A, 1979.

20. T. Hirschfeld, "Raman microprobe: Vibrational spectroscopy in femtogram range," *J. Opt. Soc. Am.* 63: 476, 1973.

21. P. Dhamelincourt, "Developments and applications of the laser Raman microprobe (MOLE)," Proc. 14th MAS Conf., 1979, 000.

22. G. J. Rosasco and E. S. Etz, "Raman microprobe spectroscopy," to appear in R. J. Clark and R. E. Hester, Eds., *Advances in Infra-red and Raman Spectroscopy*, New York: Heyden, 1979, 7.

23. D. L. Wood, A. B. Dargis, and D. L. Nash, "A computerized television spectrometer for emission analysis," *Appl. Spectrosc.* 29: 310, 1975.

## INELASTIC LIGHT SCATTERING FROM A DISTRIBUTION OF MICROPARTICLES

R. E. Benner, Ralf Dornhaus, M. B. Long, and R. K. Chang

Molecular species contained within the bulk of microparticles (diameters 0.1-10  $\mu\text{m}$ ) can be identified by inelastic light scattering (fluorescence and Raman) if the product of the particle absorption coefficient and diameter is less than unity at both the incident and scattered wavelengths. The size, shape, and refractive index of the particles do not alter the wavelength dependence of their inelastic emission<sup>1</sup> but can greatly influence the inelastic scattering intensity. Two independent experiments<sup>2,3</sup> and one recent calculation<sup>4,5</sup> seem to indicate that the effective Raman cross sections for molecules embedded in aerosol particles can increase by as much as a factor ten. However, the combination of small Raman cross sections (about  $10^{-30}$   $\text{cm}^2/\text{sr}$  for most molecules) and low aerosol particle densities results in an extremely weak Raman signal. Furthermore, the amount of incident laser power that can be used to increase the Raman intensity is limited by the optical absorption of the particle, which leads to laser-induced heating. To minimize particle heating effects, Raman spectra can be collected from a distribution of particles flowing past the laser focal volume, or by illumination of particles placed on a substrate that serves as a heat sink. In this paper we present preliminary results on (1) a high-sensitivity laser-Raman spectrograph with a vidicon camera to monitor the inelastic radiation from aerosols flowing past the laser focal volume, and (2) internal reflection techniques to enhance the inelastic scattering from particles placed on a substrate.

### *Raman Detection of Flowing Aerosols*

An optical multichannel analyzer (OMA) is formed by the positioning of a low-light-level vidicon camera at the focal plane of a spectrograph. Compared with the conventional single-channel scheme, consisting of a scanning spectrometer and photomultiplier, the OMA has the following advantages: (1) data acquisition time is reduced in proportion to the number of wavelength-resolved intervals simultaneously detected by the OMA (approximately 500 for our system); (2) photocathode dark counts are distributed over the 500 wavelength intervals, which for the OMA with an S-20 photocathode of 12.5mm diameter and 200 counts/sec corresponds to 0.4 counts/sec for each interval (compared to a GaAs photomultiplier having 2-5 counts/sec for each wavelength interval); and (3) short- and long-term stability requirements for the entire laser-Raman system are greatly relaxed if the complete Raman spectrum is detected simultaneously, since optical alignment and laser intensity fluctuations do not give rise to spurious peaks in the observed data.

In the laser-Raman system (Fig. 1), an argon ion laser beam (1 W cw) is deflected by mirror  $M_1$  and focused by lens  $L_1$  into a multipass cell consisting of spherical mirrors  $M_3$ ,  $M_4$ , and  $M_5$ . Aerosols are introduced near the foci of the multipass cell, which gives a gain of 92 over a single-pass configuration. The Raman radiation is collected by camera lens  $L_2$ , passed through interference filter IF (which rejects the elastically scattered laser light), and finally focused by lens  $L_3$  onto the horizontal entrance slit of a single concave holographic grating spectrograph (1m focal length, 2000 grooves/mm). The wavelength-dispersed spectrum (about  $500\text{cm}^{-1}$  range) is deflected by mirrors  $M_6$  and  $M_7$  and focused onto the cooled ( $-50^\circ\text{C}$ ) SIT vidicon camera face (12.5mm diameter). Should single-channel detection be desired, mirror  $M_6$  and lens  $L_4$  can be moved to image the spectrometer exit slit onto the photomultiplier. Advance to the next wavelength range is controlled by an LSI/11 microprocessor, which increments a stepping motor that tilts the grating gimbal

---

The authors are with the Department of Engineering and Applied Science, Yale University, New Haven, CT 06520. The partial support of this work by the Army Research Office (Grant DAAG29-79-G-0008), the National Science Foundation (Grant ENG77-07157), and the Northeast Utilities Service Company is gratefully noted.

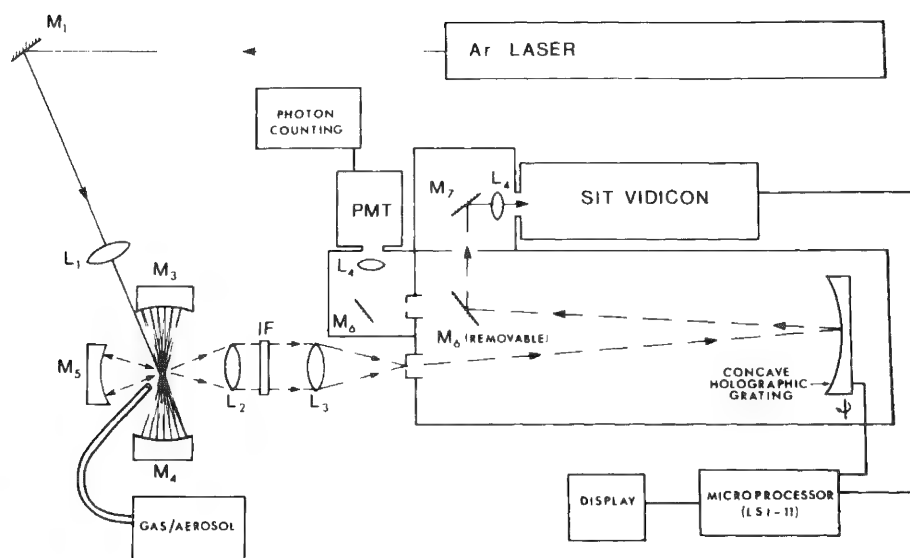


FIG. 1.--Schematic of laser-Raman scattering spectrometer/spectrograph used for detection of molecular species in gases and aerosols flowing past laser focal volume. Conversion from conventional spectrometer to SIT vidicon spectrograph is accomplished by insertion of single mirror  $M_6$  (removable). The Raman signal is enhanced by multipass optical assembly.

mount. Although the throughput of this single-grating spectrograph is about twice that of a double monochromator, its elastic light rejection is not adequate to suppress Mie scattering from particles. Interference filter IF (long-wavelength-pass type) increases the rejection ( $10^{-7}$ ) afforded by the grating by an additional  $10^{-3}$ - $10^{-4}$ .

One obtains optimum signal-to-noise ratio with OMA detection by (1) allowing photoelectrons to integrate (up to several hours if necessary) on the target of the cooled SIT camera without scanning the read beam, (2) shutting off the read beam filament, which generates noise at the photocathode, until 30 sec before the data stored on the target is to be read, and (3) scanning the target multiple times to insure that all the stored data are removed. Summing photoelectrons on the target is vastly superior to digital accumulation of the signal in the computer memory since with the former method electronic noise from the read beam is not added to the data. Vidicon scan format, activation of the read beam filament, and data storage are all controlled by the microprocessor.

A calibration gas of 800 ppb of  $\text{SO}_2$  in laboratory air was used to compare the sensitivity of the OMA to that of the single-channel configuration. The OMA spectrum of  $\text{SO}_2$  (Fig. 2) was found to have a significantly better signal-to-noise ratio than that obtained with single-channel detection. The structure to the right of the  $1151\text{cm}^{-1}$   $\text{SO}_2$  peak is the rotational wing of the ambient  $\text{CO}_2$  vibrational line. OMA spectra of a laboratory-generated  $(\text{NH}_4)_2\text{SO}_4$  aerosol and of  $(\text{NH}_4)_2\text{SO}_4$  dissolved in water (1.0 M) are compared in Fig. 3. The Raman shifts of  $\text{SO}_4^{2-}$  ( $981\text{cm}^{-1}$ ) in both aerosol and in liquid solution could be measured, but an exact calculation of the  $\text{SO}_4^{2-}$  concentration in the aerosol was not possible from the Raman data because the particle size, shape, and refractive index influence the effective Raman cross section. Based on previous results,<sup>3</sup> the  $\text{SO}_4^{2-}$  aerosol concentration was approximately 8 ppm. The broad background associated with the aerosol spectrum is caused by fluorescence emanating from the  $(\text{NH}_4)_2\text{SO}_4$  droplets, as well as from the multipass optical cell.

Two methods remain for improving the sensitivity of the Raman spectrograph. The first is by a deconvolution of the noisy spectra from minor species with their Raman spectra measured at high concentrations. Second, the argon laser could be replaced by a pulsed source such as a frequency-doubled Nd:YAG laser (530.2nm wavelength, 15nsec pulse duration, 200 mJ/pulse, and 10 pulses/sec). Advantages of a Nd:YAG laser include both higher average power than our present 1W cw argon laser and low duty cycle ( $10^{-6}$ ). Since the SIT vidicon

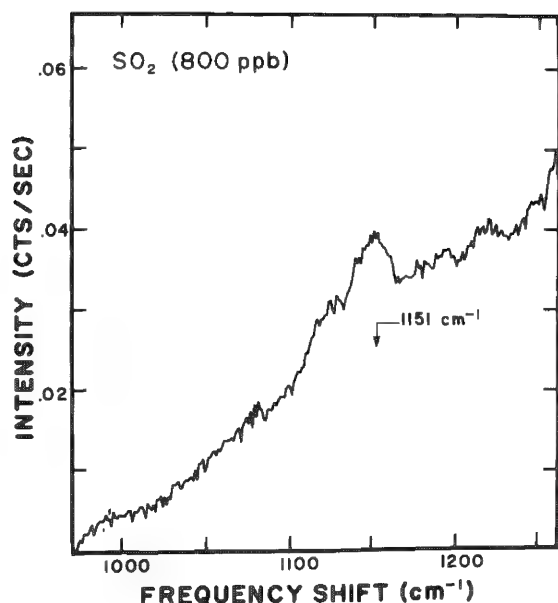


FIG. 2.--Raman spectrum obtained in 60 min with SIT vidicon spectrograph of 800 ppb of  $\text{SO}_2$  gas ( $\Delta\nu = 1151 \text{ cm}^{-1}$ ) mixed with ambient air. Sloping background results from rotational wing of vibrational line of ambient  $\text{CO}_2$  at  $1286 \text{ cm}^{-1}$ .

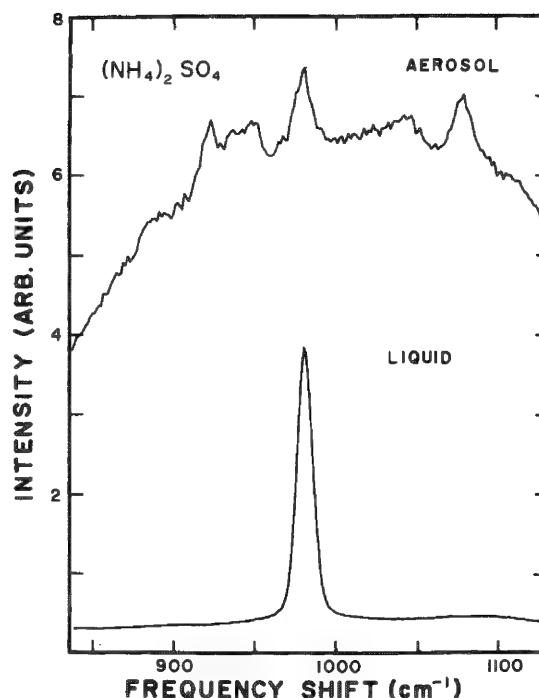


FIG. 3.--Raman spectra of laboratory-generated  $(\text{NH}_4)_2\text{SO}_4$  aerosol (top) and of  $(\text{NH}_4)_2\text{SO}_4$  dissolved in water (bottom). Peaks corresponding to  $\text{SO}_4^{2-}$  ( $981 \text{ cm}^{-1}$ ) are observed in both spectra.

can be electronically gated to accept data during 100nsec intervals, the low duty cycle can be exploited to reduce dark counts and detection of fluorescence emission with a lifetime longer than 100 nsec can be eliminated.

#### *Enhanced Scattering by Use of the Substrate*

When the Raman microprobe approach is used to investigate particulate systems, it is often necessary to position the particles on a substrate with a high thermal conductivity in order to dissipate heat generated by particle absorption at the laser wavelength. This laser-induced heating limitation can be reduced by illumination of a single layer of particles tightly packed on a substrate rather than just a single particle. However, for this multiple-particle geometry the available laser power can limit the particle excitation intensity. Furthermore, a portion of the incident radiation is wasted since it falls in the void regions between particles. To overcome the corresponding decreases in Raman intensity, the optical properties of the substrate can be utilized to increase inelastic scattering signal-to-noise ratios. For example, enhancement of the laser intensity within the particulate layer can be achieved if the laser beam is directed through the substrate before it impinges on the sample layer. The incident angle  $\theta_i$  with respect to the normal of the substrate-particle interface should be greater than the critical angle<sup>6</sup> ( $\theta_i \geq \theta_c$ , total internal reflection condition). An even larger enhancement of the laser intensity within the particles can be obtained if the laser beam is directed through a substrate that is coated with a thin (500Å) silver film. For this configuration,  $\theta_i$  must be adjusted so as to excite a surface plasmon<sup>7</sup> within the silver film ( $\theta_i = \theta_p$ , surface plasmon resonance condition). To improve coupling of the enhanced electric field associated with the surface plasmon excitation to the particles, one should make the sample layer spatially homogeneous by coating the particles with a thin film of refractive-index-matching liquid, which can also serve to increase the heat conduction rate. The electromagnetic wave above

the substrate for  $\theta_i \geq \theta_c$  and for  $\theta_i = \theta_p$  is an evanescent wave (exponentially decaying with distance from the interface) and the electric-field intensity within the particles is larger than that of the incident wave by an amount given by the Fresnel transmission factors.<sup>7-9</sup>

The resultant Raman or fluorescence radiation can be collected on the air side of the substrate-particle interface or through the substrate. On the air side, the radiation pattern is essentially isotropic and conventional large-solid-angle collection of the Raman radiation is appropriate. However, the radiation pattern passing through the substrate (prism) is not isotropic. We have investigated the angular profile of inelastic emission emerging from a hemi-cylindrical  $\text{SrTiO}_3$  prism (Fig. 4) which was coated with a 500 Å film of silver on the top half and not coated on the bottom half. As a function of observation angle  $\theta_o$ , the fluorescence intensity emanating from dye molecules embedded in a uniformly coated sample film is shown in Fig. 5 for  $\theta_i = \theta_p$ . With the unsilvered half of the prism illuminated, the fluorescence from the dye sample is observed to peak at an angle equal to

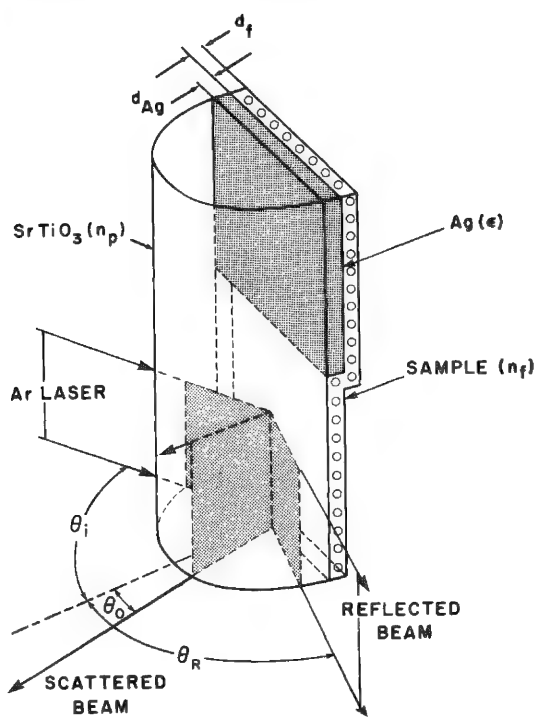


FIG. 4.--Hemi-cylindrical  $\text{SrTiO}_3$  prism configuration used to observe angular distribution of inelastic emission from particulate layers. Fluorescence emission was observed through curved surface with  $0.3^\circ$  angular resolution. Bottom half of prism has no silver film; upper half is coated with 500 Å of silver. Sample film consisted of either dye fluid or dye-containing particles.

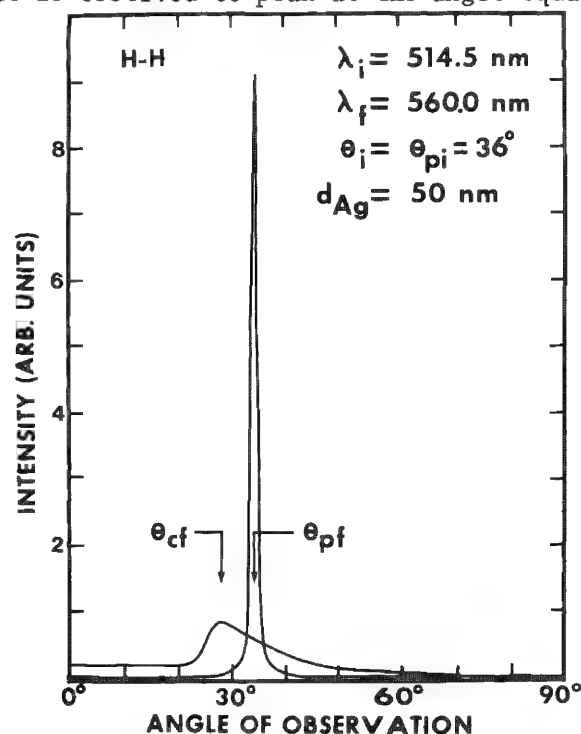


FIG. 5.--Angular distribution of fluorescence intensity emanating from dye molecules embedded in uniformly coated sample film for  $\theta_i = \theta_p$  (geometry of Fig. 4). With bottom half of prism illuminated, fluorescence peak at  $\theta_{cf}$ . With top half illuminated, fluorescence emission is confined to narrow region centered at  $\theta_{pf}$ .

the critical angle  $\theta_{cf}$  for light of the fluorescence wavelength incident on the interface from the prism side.<sup>8</sup> Upon illumination of the silvered half of the prism, the fluorescence is noted to be confined to a narrow angular region (less than the instrumental spatial resolution, which was  $0.3^\circ$ ) centered at  $\theta_o = \theta_{pf}$ , where  $\theta_{pf}$  is the plasmon angle for light of the fluorescence wavelength incident on the silver-sample interface from the prism side.<sup>9</sup> The total enhancement of the inelastic intensity with  $\theta_i = \theta_p$  and  $\theta_o = \theta_{cf}$  for the total-reflection case and with  $\theta_i = \theta_p$  and  $\theta_o = \theta_{pf}$  for the surface plasmon resonance configuration can be expressed as the product of Fresnel transmission factors for the incident and scattered waves. Thus far, we have experimentally observed enhancement factors of 5 for



the total-reflection case and 350 for the surface plasmon case relative to a transmission geometry of  $\theta_i = 0$  and  $\theta_o = \theta_{cf}$ .

Collection of the Raman radiation emerging from particulates from the prism side of the interface has several potential advantages. Since the emission solid angle is very small for the surface plasmon case, one can spatially reject fluorescence generated along the laser track within the substrate by using a small collection solid angle and still collect nearly all the emitted radiation. Furthermore, since at  $\theta_i = \theta_p$  the reflected beam has a minimum in its intensity and is spatially separated from the inelastic emission peak because of refractive-index dispersion, much of the elastic scattering can be suppressed. However, the relative merits of both collection on the air side of the substrate with large solid angle and of collection on the substrate side with narrow solid angle, as well as the maximum attainable enhancement, require further investigation.

### Conclusion

Although the size, shape, and refractive index of aerosol particles do not alter Raman shifts, previous results indicate that the effective Raman cross sections for molecules embedded in aerosol particles can increase by as much as a factor of ten. This increase, along with the sensitivity and data-taking speed of the OMA, may facilitate the chemical speciation of flowing aerosols by Raman spectroscopy. In addition, the sensitivity of the Raman technique for investigating a distribution of microparticles packed as a monolayer on a substrate should be improved by use of the surface plasmon resonance geometry.

### References

1. G. J. Rosasco, E. S. Etz, and W. A. Cassatt, "The analysis of discrete fine particles by Raman spectroscopy," *Appl. Spectrosc.* 29: 396, 1975.
2. M. L. Wright and K. S. Krishnan, *Feasibility Study of in-situ Source Monitoring of Particulate Composition by Raman or Fluorescence Scatter*, Report EPA-R2-73-219, Washington D.C.: Environmental Protection Administration, 1973.
3. R. G. Stafford, R. K. Chang, and P. J. Kindlmann, "Laser Raman monitoring of ambient sulfate aerosols," in *Methods and Standards for Environmental Measurement, Proc. 8th IMR Symposium*, Special Publication 464, Washington, D.C.: National Bureau of Standards, 1977, 659.
4. H. Chew, P. J. McNulty, and M. Kerker, "Model for Raman and fluorescent scattering by molecules embedded in small particles," *Phys. Rev. [A]* 13: 396, 1976.
5. P. J. McNulty and M. Kerker, private communication.
6. N. J. Harrick, *Internal Reflection Spectroscopy*, New York: Interscience, 1967.
7. Y. J. Chen, W. P. Chen, and E. Burstein, "Surface-electromagnetic-wave-enhanced Raman scattering by overlayers on metals," *Phys. Rev. Letters* 36: 1207, 1976.
8. El-Hang Lee et al., "Angular distribution of fluorescence from liquids and mono-dispersed spheres by evanescent wave excitation," *Appl. Opt.* 18: 862, 1979.
9. R. E. Benner and R. K. Chang, "Utilization of optical fibers in remote inelastic light scattering probes," in Bernard Bendow, Ed., *Fiber Optics: Advances in Research and Development*, New York: Plenum Press, 1979, 625.

## DESIGN CONSIDERATIONS IN A MICRORAMAN SPECTROMETER

Tomas Hirschfeld

For a micro Raman spectrometer to detect submicron objects, extreme sensitivities are necessary. To achieve them the following must be done.

1. A high energy density must be delivered into the sample, and the sample made to survive it. For particulate samples, extremely good thermal sinking to a cryogenic holder is the optimum procedure; on large samples, spatially multiplexed scanned illumination can substantially reduce the thermal stress. The steep wavelength dependence of multi-photon damage mechanisms makes wavelength choice more crucial than is usual in Raman spectroscopy.

2. To observe effectively only the sample, diffraction-limited illumination and observation are both desirable, which requires repeated spatial filtering and control of thermal lensing. Vertical-axis resolution can be obtained by focal isolation at high numerical apertures by means of appropriate correction algorithms. At least four monochromators are needed to get rid of the stray light and plasma line background, some of which may be virtual.

3. Adequate sensitivity requires not only multiple detection but also that each element of the multiple detector be made equivalent to a quantum counting photomultiplier. Random-addressed multiplex detectors with a selective integration program allow detective quantum efficiencies approaching that of the cathode. Other data-handling tricks then provide a normalized, corrected Raman spectrum for even very small scatterers.

---

The author is at the University of California's Lawrence Livermore Laboratory. This work was performed at Block Engineering, Framingham, Mass.

## Quantitative X-ray Microanalysis

### PROSPECTS FOR IMPROVED CORRECTION PROCEDURES IN EPMA

G. Love and V. D. Scott

#### *Introduction*

In the last decade the ZAF correction procedures employed in electron-probe microanalysis have remained substantially unchanged. The constituent elements of the correction models have usually been based on the following:

- a. atomic number correction of Duncumb and Reed<sup>1</sup> or Philibert and Tixier<sup>2</sup>
- b. absorption correction of Philibert<sup>3</sup> incorporating values for  $\sigma$  and  $h$  suggested by Heinrich<sup>4</sup>
- c. characteristic fluorescence correction of Reed<sup>5</sup>
- d. continuous fluorescence correction of Henoc<sup>6</sup> or Springer<sup>6</sup>

Since these corrections were formulated, the quality of microanalysis instrumentation has improved; in particular higher x-ray take-off angles, better analyzing crystals and detectors, greater specimen current stability, and fully automated data-acquisition methods have all led to increased precision of measurement. Furthermore, light-element ( $Z < 11$ ) analysis has now become routine and, with the advent of solid-state x-ray detectors, inclined-specimen geometry is now frequently adopted. To exploit the improved instrumentation, new correction models must be more accurate and more flexible than the established theories. The present paper reviews three recent correction methods and assesses their capabilities.

Although it may be possible to criticize a particular model on theoretical grounds, the only real test is its ability to correct microanalysis measurements. For this purpose 430 microanalysis results have been collated,<sup>8,9</sup> together with some oxygen analysis in oxides.<sup>10</sup> We focus here on the atomic-number and absorption-correction factors, since they usually constitute the largest error in corrected data. The following models are assessed.

- a. Anderson-Wittry,<sup>11</sup> which incorporate the analytical expression of Rao-Sahib and Wittry<sup>12</sup>
- b. Ruste-Zeller<sup>13</sup>
- c. Love-Scott<sup>14</sup>

In addition, data obtained by an established method are used for comparison.

The constituent elements of each model are tabulated below; the numbers included in the tabulation correspond to the list of references at the end of this paper.

TABLE 1

Model	At. No. correction	Absorption correction	Char. fluor. correction	Cont. fluor. correction
Established method	1	3	5	7
Anderson-Wittry	1	11, 12	5	7
Ruste-Zeller	2	13	5	7
Love-Scott	20, 14	14	5	7

The authors are at the School of Materials Science of the University of Bath in England.

### Correction Models

*Anderson-Wittry.* In this method the absorption factor  $f(\chi)$  is represented as a function of the product of  $\chi = (\mu/\rho) \csc \theta$  and an effective mean depth of x-ray generation  $\rho z^*$ . In order to obtain an expression for the mean depth  $\bar{\rho z}$ , the electron range  $\rho S_T$  was first calculated by integration of Bethe's formula,<sup>15</sup> since it was expected that  $\bar{\rho z}$  and  $\rho S_T$  would be related. Plots of  $\bar{\rho z}$  determined from Monte Carlo methods<sup>16</sup> versus  $\rho S_T$  confirmed that such a relationship existed. Furthermore, the authors were able to demonstrate that for a fixed value of  $f(\chi)$ , graphs of  $\chi$  versus a modified mean depth  $\rho z^*$  gave a series of straight lines; these lines fitted experimentally determined values<sup>17,18</sup> of  $f(\chi)$  very well, provided  $f(\chi) \geq 0.5$ . Finally, a 'universal curve' was produced from which the appropriate value of  $f(\chi)$  could be read when the product of  $\chi$  and  $\rho z^*$  had been calculated. The method is thus a graphical one, which is probably why it has not been widely used. Recently Rao-Sahib and Wittry have represented  $f(\chi)$  as a polynomial in  $\chi \rho z^*$  so that  $f(\chi)$  values can be computed directly.<sup>12</sup>

*Ruste-Zeller.* The Ruste-Zeller method<sup>13</sup> is essentially an absorption correction (Table 1) and is based on the approach of Philibert.<sup>3</sup> The absorption factor  $f(\chi)$  is given by

$$f(\chi) = \frac{1 + \frac{\phi(o)h}{4 + \phi(o)h} \frac{\chi}{\sigma}}{\left(1 + \frac{\chi}{\sigma}\right) \left(1 + \frac{h}{1 + h} \frac{\chi}{\sigma}\right)}$$

where the terms  $\phi(o)$ ,  $\chi$ ,  $\sigma$ , and  $h$  have their usual meanings. Ruste and Zeller have examined experimental data on the attenuation of electrons in solids<sup>19</sup> and have shown that the Lenard coefficient  $\sigma$  depends on atomic number. In electron-probe microanalysis  $\sigma$  is written as  $\sigma_0/(E_0^n - E_c^n)$ , where  $E_0$  and  $E_c$  are the incident electron energy and the critical ionization potential, respectively. Ruste and Zeller have arbitrarily chosen to represent both  $\sigma_0$  and  $n$  in the general form  $A = A_\infty + a \exp(-bZ^p)$ , which means that  $\sigma_0$  and  $n$  tend towards the values given by Heinrich for elements of high atomic number.<sup>4</sup> The formula for  $h$  proposed by Ruste and Zeller also gives results very similar to Heinrich's values for elements of atomic number above 24. A feature of the Ruste-Zeller method is that although  $\sigma$ ,  $n$ , and  $h$  all depend on atomic number, only  $h$  is averaged for a multicomponent specimen;  $\sigma$  and  $n$  have the appropriate values for the element and radiation being measured.

*Love-Scott.* This method incorporates new atomic-number and absorption corrections. The atomic-number correction employs an empirical electron energy loss expression<sup>20</sup> that should be more accurate than the Bethe equation in the region where the electron energy approaches the mean ionization potential  $J$ . In addition, backscatter factors may be computed for any electron energy or specimen tilt angle.

The absorption correction is based on the 'square' model of Bishop,<sup>21</sup> in which the x-ray depth distribution is approximated to a rectangle. In these circumstances  $f(\chi)$  is represented by

$$f(\chi) = \frac{1 - \exp(-2\chi\bar{\rho z})}{2\chi\bar{\rho z}}$$

The mean depth of x-ray generation  $\bar{\rho z}$  has been determined by means of Monte Carlo calculations<sup>24</sup> and an analytical expression has been deduced in which  $\bar{\rho z}$  is expressed in terms of the electron range, the backscatter coefficient, and overvoltage  $E_0/E_c$ .

### Assessment of Models

Results of applying the correction models to the 430 microanalysis measurements mentioned previously are shown in Table 2. In all cases Heinrich's mass absorption coefficients<sup>22</sup> have been employed. The Love-Scott model is clearly superior to the other methods, both in terms of the RMS error and in the number of results lying within 2.5% of the true value. A problem with the Anderson and Wittry approach is that it is limited

TABLE 2

Model	RMS Error %	% of results within 2.5% of true conc.	% of results within 7.5% of true conc.
Established method	6.8	49	84
Anderson-Wittry*	7.3	47	87
Ruste-Zeller	7.1	44	69
Love-Scott	5.3	54	87

\*In this model four of the microanalysis measurements had  $\chi\rho z^*$  values outside the limits permitted by Rao-Sahib and Wittry and were therefore excluded from the assessment.

to  $f(\chi) \geq 0.06$  and gives highly inaccurate results for lower values. The Ruste-Zeller method, which was developed especially for light-element microanalysis, does not work particularly well for heavier elements; nor did the original full Philibert model,<sup>8</sup> because the peak in the x-ray depth distribution was both too high and too close to the specimen surface. Ruste and Zeller's revised values for  $\sigma_0$ ,  $n$ , and  $h$  do not appear to have substantially improved matters.

Results of applying the corrections to oxide systems (94 measurements) are illustrated in Table 3; oxygen mass absorption coefficients of Love, Cox, and Scott<sup>10</sup> have been used here.

TABLE 3

Model	RMS Error %	% of results within 2.5% of true conc.	% of results within 7/5% of true conc.
Established method	14	24	50
Anderson-Wittry*	14.4	21	49
Ruste-Zeller	9.2	22	57
Love-Scott	5.6	38	82

\*Only 70 results could be analyzed for the reasons stated previously.

Again the Love-Scott model appears to correct the microanalysis results better than the other methods, although the Ruste-Zeller approach seems worthy of further study.

### Conclusions

From an evaluation of three new correction procedures applied to both heavy and light element systems it is clear that the Love-Scott model is superior to both the Anderson-Wittry and the Ruste-Zeller methods. However, the last model merits additional study in connection with light-element analysis; further work will involve the detailed investigation of a wider range of light-element systems and conditions.

Further work will also include the treatment of tilted-specimen geometry, so that correction procedures can be extended to include this factor. Inspection of the proposed models indicates that such extension can be most readily accomplished for the Love-Scott model and has, in fact, already been achieved for the atomic number component;<sup>20</sup> the absorption term merely requires  $\bar{\rho}z$  to be related to the tilt angle. In contrast, it is difficult to see how the approach of Ruste and Zeller could be easily adjusted to take into account inclined-specimen geometry, since three factors ( $\sigma_0$ ,  $n$ , and  $h$ ) may all require alteration. Finally, although in principle the Anderson-Wittry absorption correction might be extended, since  $f(\chi)$  is related to the product of  $\chi$  and  $\rho z^*$ , in view of the limitations of the model this extension would not appear to be a profitable exercise.

### References

1. P. Duncumb and S. J. B. Reed, in K. F. J. Heinrich, Ed., *Quantitative Electron Probe Microanalysis*, NBS Spec. Tech. Publ. 298, 1968; 325-339.
2. J. Philibert and R. Tixier, *ibid.*, pp. 13-33.

3. J. Philibert, in H. H. Pattee, V. E. Cosslett, and A. Engström, Eds., *X-ray Optics and X-ray Microanalysis*. New York: Academic Press, 1963, 379-392.
4. K. F. J. Heinrich, *2nd Nat. Conf. Electron Microprobe Analysis*, Electron Probe Analysis Soc. of America, Boston, Mass., 1967.
5. S. J. B. Reed, *Brit. J. Appl. Phys.* 16: 913-926, 1965.
- J. Henoc, in K. F. J. Heinrich, Ed., *Quantitative Electron Probe Microanalysis*, NBS Spec. Tech. Publ. 298, 197-214.
7. G. Springer, in G. Shinoda, K. Kohra, and T. Ichinokawa, Eds., *X-ray Optics & Microanalysis*, Tokyo: University of Tokyo Press, 1972, 141-146.
8. G. Love, M. G. C. Cox, and V. D. Scott, *J. Phys.* [D]8: 1686-1702, 1975.
9. G. Love, M. G. C. Cox, and V. D. Scott, *ibid.*, 9: 7-14, 1976.
10. G. Love, M. G. C. Cox, and V. D. Scott, *ibid.*, 7: 2131-2141, 1974.
11. C. A. Anderson and D. B. Wittry, *ibid.*, 1: 529, 1968.
12. T. S. Rao-Sahib and D. B. Wittry, *J. Appl. Phys.* 45: 5060-5068, 1974.
13. J. Ruste and C. Zeller, *C. R. Acad. Sci.* B284: 507-510, 1977.
14. G. Love and V. D. Scott, *J. Phys.* [D]11: 1369-1376, 1978.
15. G. D. Archard and T. Mulvey, *Brit. J. Appl. Phys.* 14: 626-634, 1963.
16. H. E. Bishop, Ph.D. thesis, University of Cambridge, 1961.
17. R. Castaing and J. Descamps, *C. R. Acad. Sci.* 238: 1506, 1954.
18. R. Castaing and J. Henoc, in R. Castaing, P. Deschamps, and J. Philibert, Eds., *X-ray Optics and Microanalysis*, Paris: Hermann, 1966, 120-126.
19. V. E. Cosslett and R. N. Thomas, *Brit. J. Appl. Phys.* 15: 883-907, 1964.
20. G. Love, M. G. C. Cox, and V. D. Scott, *J. Phys.* [D]11: 7-21, 1978.
21. H. E. Bishop, *ibid.*, 7: 2009-2020, 1974.
22. K. F. J. Heinrich, in T. D. McKinley, K. F. J. Heinrich, and D. B. Wittry, Eds., *The Electron Microprobe*, New York: Wiley, 1966, 296-377.

## THE EFFECT OF THE CRITICAL EXCITATION POTENTIAL ON THE X-RAY ABSORPTION IN ELECTRON PROBE MICROANALYSIS

Kurt F. J. Heinrich and Robert L. Myklebust

The distribution in depth of electron-excited x-ray photon generation is a function of the critical excitation potential of the x-ray line. The available models for absorption factors for primary x rays contain a term which aims to express this effect. Monte Carlo calculations at the National Bureau of Standards, as well as the critical study of experimental information obtained by other investigators, indicate that these algorithms for the absorption correction do not accurately describe the critical excitation potential effect.

The distribution in depth of the sites of primary x-ray generation in a target bombarded by electrons depends on the energy of the penetrating electrons. This energy decreases in a quasi-continuous fashion as the electron travels within the target. When the energy drops below that which corresponds to the critical excitation potential  $q$  for a given orbital level, this level cannot be ionized, and hence the corresponding x-ray lines cannot be emitted. Hence, the mean depth of x-ray generation decreases with increasing critical excitation potential  $E_q$ .

### *Available Models*

Philibert's equation<sup>1</sup> for the x-ray absorption correction is

$$\frac{1}{f_p} = \left(1 + \frac{\chi}{\sigma}\right) \left(1 + \frac{h}{1+h} \frac{\chi}{\sigma}\right) \quad (1)$$

in which  $\chi$  is equal to  $\mu \operatorname{cosec} \psi$ , where  $\psi$  is the x-ray emergence angle and  $\mu$  the corresponding mass absorption coefficient. The parameter  $\sigma$  depends on the initial energy of the electron at the start of the target penetration. The dependence of  $\sigma$  on  $E_q$  was later introduced by Duncumb and Shields:<sup>2</sup>

$$\sigma = 2.39 \times 10^5 / (E_0^{1.5} - E_q^{1.5}) \quad (2)$$

In Philibert's equation with Duncumb's  $\sigma$ ,  $f_p$  converges to one as  $E_q$  approaches  $E_0$ . This result is expected since in the limiting case ( $E_q = E_0$ ) the depth of penetration of the electrons is zero; and therefore, the emerging x rays are not attenuated. Heinrich<sup>3</sup> has proposed changing of the constants in Eq. (1) to

$$\sigma = 4.5 \times 10^5 / (E_0^{1.65} - E_q^{1.65}) \quad (3)$$

and this expression, in conjunction with Eq. (2), is widely used in data-evaluation procedures for electron probe analysis. A similar but simpler expression was later proposed by Heinrich and Yakowitz:<sup>4</sup>

$$f_p = (1 + 1.2 \times 10^{-6} \gamma \chi)^{-2} \quad (4)$$

In this equation,  $\gamma$  is defined as follows:

---

The authors are with the Center for Analytical Chemistry, National Bureau of Standards, Washington, D.C.



$$\gamma = E_0^{1.65} - E_q^{1.65} \quad (5)$$

In Eq. (4), the effect of target composition on the absorption factor is neglected. A somewhat different approach was proposed by Theisen,<sup>5</sup> who defines the energy-dispersive parameter  $\sigma$  as follows:

$$\sigma \propto (E_0 - E_q)^n \quad (6)$$

This algorithm also leads to the appropriate limiting values for  $E_0 = E_q$  and for  $E_q = 0$ , but it fits poorly the available experimental information on the absorption correction.

#### *Verification of the Energy-dependent Parameter*

Although Eqs. (2), (3), and (5) all lead to the correct limiting conditions, there seems to be no theoretical justification for any one of them. Under practical conditions of analysis, the more significant energy term is  $E_0$ . The power 1.65 has been justified in Heinrich's studies<sup>3</sup> of experimental results by Henoc and Castaing,<sup>6</sup> in which the distribution in depth of the generation of Mg K $\alpha$  in Al was investigated. In this case, the effect of the critical excitation potential is small and can be neglected. With a higher excitation potential, such as in the excitation of Cu K $\alpha$  in aluminum, the effect of  $E_q$  on the value of  $\gamma$  increases; at the same time, however, the attenuation of x rays decreases because the absorption coefficients for high-energy x rays are, in general, low. It is for this reason that the models for the energy dependence of  $f_p$  were never critically tested for the effect of variations in  $E_q$ . However, the experimental results on depth distribution in aluminum with a Cu K $\alpha$  tracer<sup>7</sup> provide information of interest in this respect. If the numerical constants in Eqs. (3) and (4) are fitted to the results with the magnesium tracer, a poor fit for the values of  $f_p$  with the copper tracer is obtained, and vice versa. If this discrepancy is real, it must be due to a failure of the model for the effect of  $E_q$ .

We have inserted in Eq. (4) the values of  $f_p$  obtained in the Monte Carlo calculations (Table 1), and then solved the equation for  $\gamma$ . The values so obtained were divided by

TABLE 1.--Conditions used in Monte Carlo calculations;  $E_0 = 29$  kV,  $\chi = 1000$ . Mean ionization potentials from Berger and Seltzer.<sup>8</sup>

<u>Matrix</u> lines	<u>Al</u>	<u>Cu</u>	<u>Au</u>
	MgK $\alpha$	CuK $\alpha$	AuL $\alpha$
	AlK $\alpha$	MgK $\alpha$	MgK $\alpha$
	CaK $\alpha$	CaK $\alpha$	CaK $\alpha$
	MnK $\alpha$	MnK $\alpha$	MuK $\alpha$
	ZnK $\alpha$	ZnK $\alpha$	ZnK $\alpha$
	BiL $\alpha$	BiL $\alpha$	BiL $\alpha$
	ZrK $\alpha$	ZrK $\alpha$	ZrK $\alpha$

the postulated value of  $\gamma$ , according to Eq. (5). The ratios  $r_\gamma$  are a correction factor to be applied to the numerical constant in Eq. (4); they are shown as a function of  $E_q$  and of the target material in Fig. 1. The Monte Carlo value for  $\gamma$  is seen to vary with respect to that defined from Eq. (5) as a function of both matrix and critical excitation energy. These results suggest that an accurate matrix-dependence model can be established on the basis of the Monte Carlo calculations, and also that the conventional model for dependence of  $f_p$  on  $E_q$  will have to be modified. Similarly, the failure of this model is illustrated in Fig. 2 on the basis of the tracer experiments cited previously. In this graph, we plot the value of the parameter  $[(1/f_p) - 1]/\chi$  as a function of  $\chi$ , as explained in Ref. 4. In such a graph, the general forms of Eqs. (1) and (4) produces a straight line, the slope of which depends on the term quadratic in  $\chi$  in these equations. The intercept of this line at the value  $\chi = 0$  depends on the constants in Eqs. (3) or (4). It is impossible to choose the value of these constants so as to satisfy the experimental values with both Mg K $\alpha$  and Cu K $\alpha$  tracers. Hence, the failure of the model for the effect

of  $E_q$  can also be demonstrated by means of these experimental tracer results.

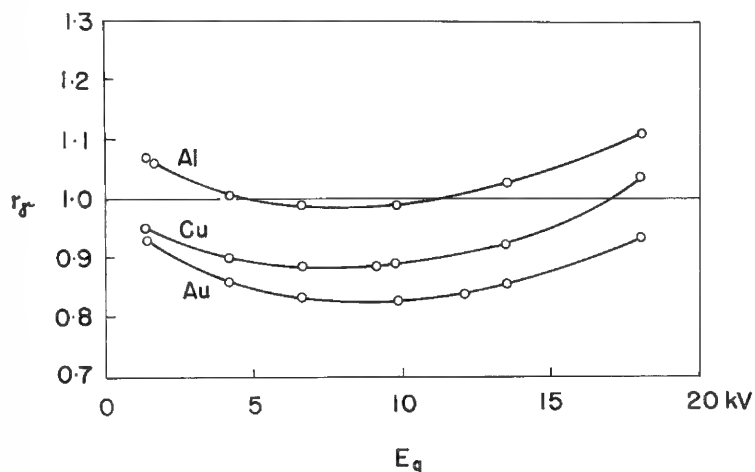


FIG. 1.--Correction factor  $r_\gamma$  as function of critical excitation energy  $E_q$  and of target composition.

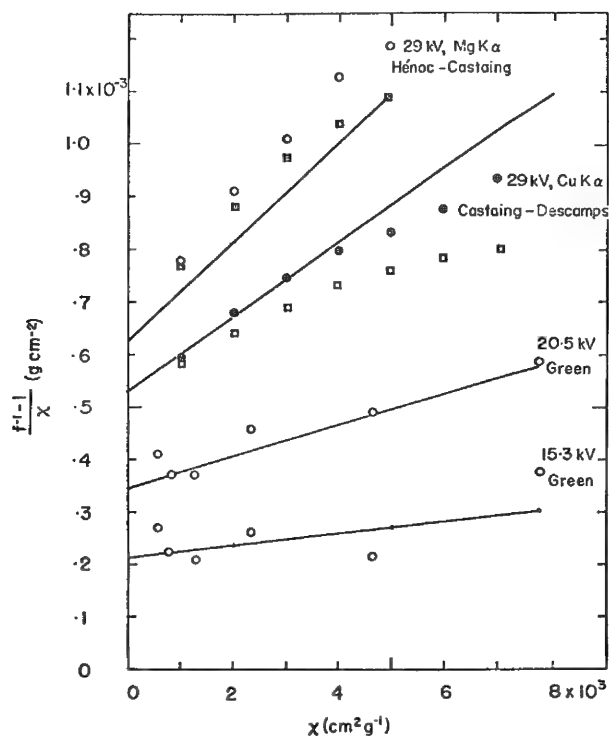


FIG. 2.--Parameter  $(f^{-1} - 1)/\chi$  ( $\text{g-cm}^{-2}$ ) as function of  $\chi$ . Circles are experimental results; straight lines are obtained from Eq. (4); squares are obtained by Monte Carlo calculations.

#### References

1. J. Philibert, *Proc. 6th Int. Symp. on X-ray Optics and X-ray Microanalysis*, New York: Academic Press, 1962, 379.
2. P. Duncumb and P. K. Shields, in T. D. McKinley, K. F. J. Heinrich, and D. B. Wittry, Eds., *The Electron Microprobe*, New York: Wiley, 1966, 284.
3. K. F. J. Heinrich, *Anal. Chem.* 44: 350, 1972.
4. K. F. J. Heinrich and H. Yakowitz, *Anal. Chem.* 47: 2408, 1975.
5. R. Theisen, *Quantitative Electron Microprobe Analysis*, Berlin: Springer, 1965.
6. R. Castaing and J. Hénoc, *Proc. 4th Intern. Congress X-ray Optics and Microanalysis*, Paris: Hermann, 1966, 120.
7. R. Castaing and J. Descamps, *J. Phys. Radium* 16: 304, 1955.
8. M. J. Berger and S. M. Seltzer, Report SP-3012, Washington, D.C.: National Aeronautics and Space Administration, 1964.

## DETERMINATION OF X-RAY WDS EFFICIENCY FOR ABSOLUTE AND RELATIVE INTENSITY MEASUREMENTS

R. B. Bolon, M. D. McConnell, and M. E. Gill

### *Introduction*

*Background.* Relative x-ray line intensities are used in secondary fluorescence corrections and spectral deconvolution procedures in both electron microprobe analysis (EMA) and x-ray emission spectroscopy (XES). Unfortunately, existing tables<sup>1</sup> list relative values based on observed intensities measured with wavelength-dispersive spectrometers (WDS) and do not take into account differences in self-absorption and spectrometer efficiency for the various wavelengths. These problems tend to be more serious for L lines than for K lines because the former involve electron transitions to three energy levels, as opposed to one, and span a much wider range of 20 values.

Although a correction for self-absorption can be directly calculated, the total efficiency of a given crystal spectrometer cannot. Factors such as solid angle subtended, mechanical alignment, crystal perfection, diffraction efficiency, window absorption, and detector efficiency are difficult if not impossible to determine.

An alternate approach is to use energy-dispersive methods. Green<sup>2</sup> used a proportional counter to measure the absolute yield of the integrated emission series for several pure elements. Although the efficiency of the proportional counter can be adequately calculated, its poor resolution (> 20%) precluded separation of the individual lines and hindered subtraction of the continuum background. More recently, Lifshin et al.<sup>3,4</sup> used a Li drifted silicon energy-dispersive spectrometer (EDS) to measure the integrated K series absolute yields for a number of pure elements. In that study, corrections were made for background, self-absorption, detector acceptance angle, and absorption by the Be window, Au contact layer, and Si dead layer. Unfortunately, this approach could not be extended to the L series because the detector resolution (< 2.6%) was still inadequate for resolving the individual lines for assignment to the appropriate L energy level.

*Current Study.* This paper describes a method in which the K series absolute yields<sup>4</sup> were used to determine a calibration curve that describes the overall efficiency of a crystal spectrometer as a function of its position. In this manner, it was possible to employ the same spectrometer, with its high resolving power (about 0.2%), to determine the absolute yields for individual L series lines. These yields were then used to obtain relative line intensities by division of the appropriate values; for example, as in this study, by the yield of the  $L\alpha_1$  line.

### *Theory*

The absolute yield of a line or series of lines is defined as the average number of x rays generated per incident electron per unit solid angle in a flat polished sample with normal electron beam incidence. Thus

$$Y/4\pi = I'_{\text{gen}}/i_0 \quad (1)$$

where  $Y/4\pi$  is the yield,  $I'_{\text{gen}}$  the generated characteristic intensity in counts per second per steradian, and  $i_0$  the beam current in electrons per second. Of the x rays oriented towards the spectrometer, only a fraction are emitted or escape the sample, as defined by

$$I'_{\text{emit}} = I'_{\text{gen}}f(x) \quad (2)$$

---

The authors are at the General Electric Co. (Corporate Research and Development), Schenectady, NY 12301.

where  $f(\chi)$  is the correction for self-absorption. If the spectrometer efficiency is then defined as

$$T = I_{\text{meas}}/I'_{\text{emit}} \quad (3)$$

where  $I_{\text{meas}}$  is the measured intensity in counts per second, it is possible to write

$$T = I_{\text{meas}}/[I(Y/4\pi)i_0f(\chi)] \quad (4)$$

In this manner, all the factors that affect the efficiency of the spectrometer are accounted for by the single parameter  $T$ , which is a function of wavelength and crystal position.

The individual factors on the right of Eq. (4) can either be measured or calculated. For example, the K series yields can be obtained from

$$Y/4\pi = (-3.704 \times 10^{-5} + 4.085 \times 10^{-6}Z)(U_0 - 1)(1.304 + 1.431 \times 10^{-2}Z) \quad (5)$$

which is the result of a least-squares fit to experimental data.<sup>4</sup> In this expression  $Z$  is the atomic number and  $U_0$  the overvoltage ratio obtained when the beam voltage is divided by the excitation potential. Since these data represent the combined  $K\alpha_{1,2}$  and  $K\beta$  lines, the resulting values were multiplied by 0.5882--the nominal fractional contribution of the  $K\alpha_1$  line to the series.

The absorption correction  $f(\chi)$  was calculated according to the expression proposed by Heinrich,<sup>5</sup>

$$f(\chi) = [1 + 3 \times 10^{-6}(E_0^{1.65} - E^{1.65})\chi]^{-1} \quad (6)$$

where  $E_0$  is the beam energy in kV,  $E$  the energy of the line, and  $\chi$  the mass absorption coefficient<sup>5</sup> times the cosecant of the spectrometer take-off angle.

Two assumptions were necessary for this study: first, that the spectrometer efficiency changed in a smooth continuous fashion, and could be adequately described by the points obtained from the pure elements whose  $K\alpha$  lines were measurable; and second, that the efficiency was constant over the short range containing the  $K\alpha_1$  and  $\alpha_2$  lines. The latter assumption was used in the development of a simple method for deconvoluting overlap.

### Experimental

*Instrumentation.* For the purposes of this investigation, a quartz 10 $\bar{1}1$  crystal on a Cameca Model MS46 electron microprobe was selected for calibration. This choice was based on its relatively high resolving power, reflectivity, and wavelength range; the last encompassed the  $K\alpha$  lines of Ca(20) through Ge(32). Figure 1 illustrates the ranges of four common crystals, in terms of atomic number, for the major lines of the K, L, and M series. We see that the quartz 10 $\bar{1}1$  crystal can detect some or all of the L series lines from elements Ag(47) through Ir(77). Through the use of several different crystals, the L and M series lines of most elements can be measured.

*Operating Conditions.* X-ray data were collected at a beam energy of  $20 \pm 0.4$  kV, as determined by the EDS high-energy cutoff method, and a takeoff angle of  $18^\circ$ . A current of  $8 \times 10^{-8}$  A was selected so that sufficient counts could be obtained in a reasonable time (less than 100 sec) with minimum dead-time correction (less than 2%). The current was measured periodically using a Faraday cage, constructed from a 200  $\mu\text{m}$  aperture, coupled to a Keithley model 610A electrometer.

*Data Processing.* All count data were corrected for dead time, background, and peak overlap. Figure 2 illustrates a spectral scan through the Ni  $K\alpha_1$  and  $K\alpha_2$  lines. Although the overlap between the two peaks is only a few per cent at peak centers, we decided to incorporate peak deconvolution for completeness. Since the peaks are not necessarily symmetric and their areas not related to total counts existing EDS deconvolution methods were not used. Instead, we developed a simple scheme (see Appendix) to correct for overlap. Six data points plus two backgrounds were collected by means of a computer-controlled spectro-

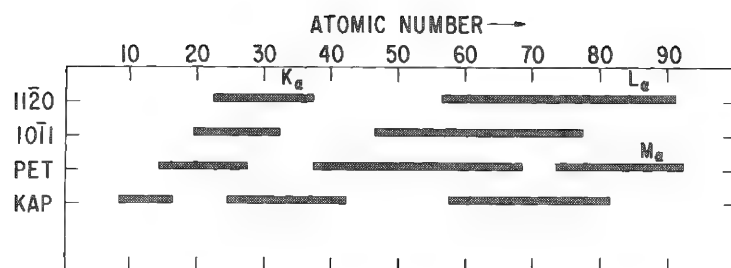
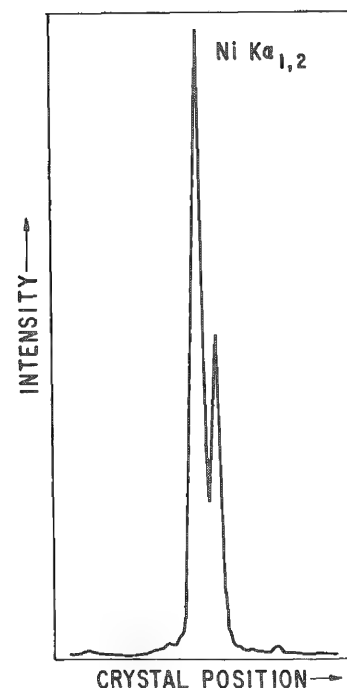


FIG. 1.--Ranges of four common WDS crystals, in terms of atomic number, for major lines of K, L, and M series.

FIG. 2.--WDS scan illustrating small amount of overlap between Ni K<sub>α1</sub> and K<sub>α2</sub> with quartz IOI crystal.



meter. The points included the two peak values and two readings on each side of the overlapped peaks, spaced at intervals equal to the peak separation. The deconvoluted peak values were then determined from

$$I_{p1} = I_3 - R(I_2 - RI_1) \quad (7)$$

and

$$I_{p2} = I_4 - R(I_5 - RI_6) \quad (8)$$

where  $I_1$  through  $I_6$  are the sequentially measured intensities across the two peaks,  $I_{p1}$  and  $I_{p2}$  the deconvoluted peak values, and  $R$  the ratio of the two peaks; i.e.,  $R = I_{p2}/I_{p1}$ .

Following deconvolution, the data were corrected for absorption by Eq. (6) and used in Eq. (4) to obtain the corresponding spectrometer efficiencies. These values were plotted and a smooth curve was fitted to them. This curve was then used to determine efficiencies for the L lines.

### Results and Discussions

Figure 3 shows the efficiency curve for the quartz IOI crystal in spectrometer No. 2. This curve is valid only with the spectrometer for which it was determined and could change if the crystal were realigned. In fact, such a curve could be a useful means for evaluating alignment and performance. Values from this curve were then used in Eq. (4) to obtain absolute yields for the individually measured L lines. A limitation of these results is the uncertainty associated with the original K series yields.<sup>4</sup> This uncertainty includes a 15% systematic difference between two separate experiments and an average random variation of  $\pm 7\%$ , and is unfortunately incorporated into the uncertainty of the resulting L line yields. The problem is fortunately less severe for relative line intensities, which are obtained by dividing one yield by the other. In this case most or all of the systematic uncertainty cancels. Future work on improved K series yields is needed.

Sm(62) was chosen for the initial measurements based on its availability as a pure elemental metal standard and because all its major L lines fall within the range of the spectrometer as illustrated in Fig. 4, which also identifies the lines in relation to their respective absorption edges. The relative intensities associated with transitions into a given L level are independent of the beam voltage. However, this is not the case when lines associated

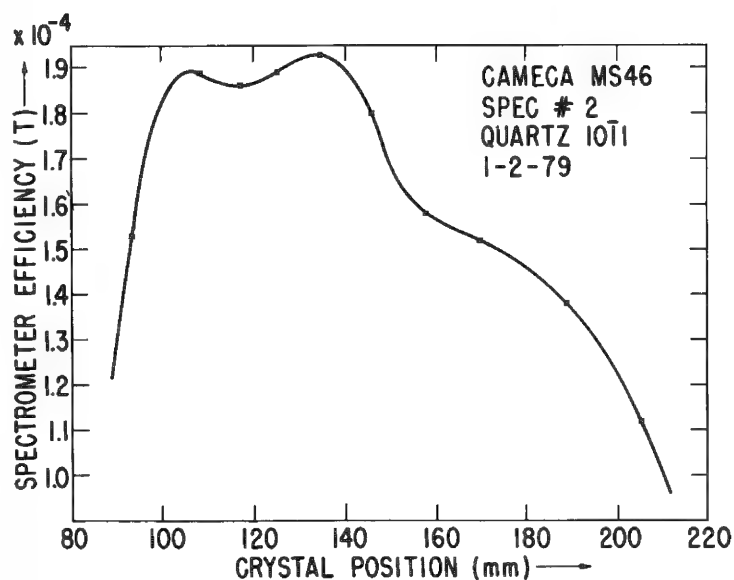


FIG. 3.--Experimentally determined WDS efficiency curve for quartz 1011 crystal used in this study.

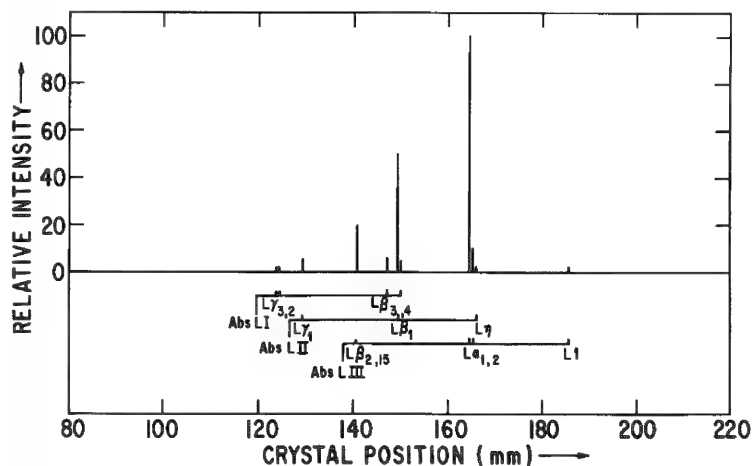


FIG. 4.--Nominal relative intensities as function of spectrometer position for the 11 major lines of the L series of Sm. These lines are also identified by their respective absorption edges.

with transitions into different L levels are compared. In this case, the magnitude of the differences is greatest at low overvoltages, which will be the subject of a future investigation.

Table 1 summarizes some of the data and results from the Sm study. Of the eleven lines, whose nominal relative intensities (compared to  $L\alpha_1$ ) were 1% or more, nine were measured. Included in this table are: the spectrometer efficiencies from Fig. 3; the measured peak intensities in cps; the absorption corrections; the resulting absolute yields; and the relative intensities as determined from (a) measured peak intensities, (b) yield ratios, and (c) existing tabulated values. It can be seen from (a) and (b) that self-absorption and spectrometer efficiency introduce small but significant corrections to the data. The larger discrepancies between (b) and (c) illustrate the magnitude of the uncertainties associated with existing tabulated data.

### Conclusion

We have described a method in which the K series absolute yields, as obtained by EDS, were used to determine an absolute efficiency calibration curve for a quartz 1011 crystal. This curve was in turn used to measure the absolute generation yields for nine of the major L-series lines of Sm. Although these values have a large uncertainty, attributed to uncertainty in the K-series yields, they are believed to give better relative line intensities than previously available. Future improvements in K-series yields are necessary to give better L-line yields.

It is proposed that a similar calibration method can be also developed for x-ray fluo-

TABLE 1.--Summary of data used to determine Sm L line absolute yields and relative line intensities;  $E_0 = 20$  kV,  $\theta = 18^\circ$ ,  $i_0 = 8 \times 10^{-8}$  A.

	$L\gamma_3$	$L\gamma_2$	$L\gamma_1$	$L\beta_{2,15}$	$L\beta_3$	$L\beta_1$	$L\beta_4$	$L\alpha_1$	$L\alpha_2$	$L_n$	$L_1$
Spectrometer efficiency ( $\times 10^{-4}$ )	1.88	1.88	1.92	1.88	1.76	1.68	1.68	1.54	1.54	1.53	1.41
Intensity (cps)	74.37	29.45	267.28	736.68	241.68	1849.28	--	3467.36	392.18	--	41.68
$f(\chi)$	0.660	0.659	0.704	0.845	0.828	0.821	0.820	0.777	0.775	0.773	.713
Absolute yield ( $Y/4\pi$ ) *	1.20	0.476	3.96	9.29	3.32	26.9	--	58.0	6.58	--	0.831
Percentage relative intensity from:											
(a) peak ratios	2.14	0.85	7.71	21.3	6.97	53.3	--	100	11.3	--	1.20
(b) yield ratios	2.07	0.82	6.28	16.01	5.72	46.3	--	100	11.3	--	1.43
(c) Ref. 1	1	1	5	20	6	50	5	100	10	1	2

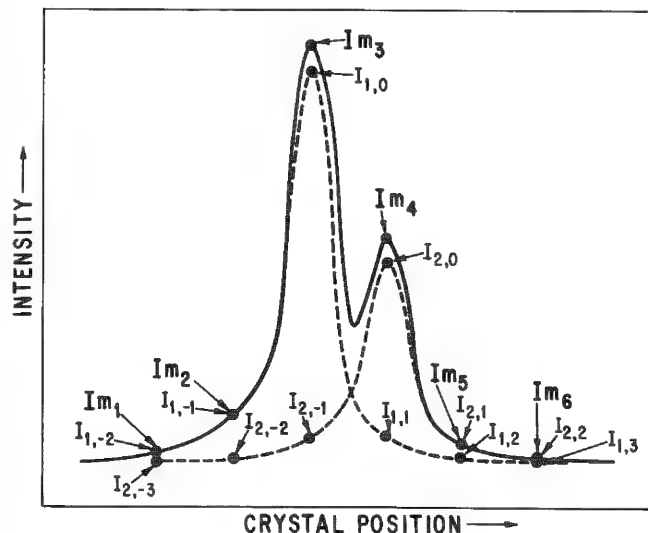
\*( $\times 10^{-6}$  photons/incident electron-steradian).



rescence WDSs by use of a series of carefully calibrated radioactive standards in place of the sample. The measured intensities could then be used to determine an efficiency curve for use in quantitative fundamental parameter methods.

#### APPENDIX

The maximum values of 2 overlapping peaks can be easily deconvoluted from each other provided that the peaks have similar shapes and tails that decrease to negligible values within a distance of no more than 3-4 times the peak separation. Figure 5 illustrates two such peaks with six points to be measured-- $Im_1$  through  $Im_6$ . The points, spaced at intervals equal to the peak separation, can be represented in terms of the contributing peaks by



$$\begin{aligned}
 Im_1 &= I_{1,-2} + I_{2,-3} \\
 Im_2 &= I_{1,-1} + I_{2,-2} \\
 Im_3 &= I_{1,0} + I_{2,-1} \\
 Im_4 &= I_{1,1} + I_{2,0} \\
 Im_5 &= I_{1,2} + I_{2,1} \\
 Im_6 &= I_{1,3} + I_{2,2}
 \end{aligned}
 \tag{A-1}$$

FIG. 5.--Schematic illustration of two asymmetric but similar overlapping peaks. The six points ( $Im_1$ -6), spaced at intervals equal to peak separation, represent values measured and used for deconvolution.

where the subscripts identify the peak (1 or 2) and relative position (-3 to +3). By virtue of their similar shapes we can write the following relationships:

$$\frac{I_{2,0}}{I_{1,0}} = \frac{I_{2,-2}}{I_{1,-2}} = \frac{I_{2,-1}}{I_{1,-1}} = \frac{I_{2,1}}{I_{1,1}} = \frac{I_{2,2}}{I_{1,2}}
 \tag{A-2}$$

where  $I_{1,0}$  and  $I_{2,0}$  are the deconvoluted maximum peak values. Furthermore, if it is assumed that:

$$I_{1,3} = I_{2,-3} = 0
 \tag{A-3}$$

we are left with twelve equations and twelve unknowns, which can be reduced to give

$$\begin{aligned}
 I_{1,0} &= Im_3 - R(Im_2 - RIm_1) \\
 I_{2,0} &= Im_4 - \frac{1}{R}(Im_5 - \frac{1}{R}Im_6)
 \end{aligned}
 \tag{A-4}$$

where  $R$  is the relative peak intensity defined by

$$R = I_{2,0}/I_{1,0}
 \tag{A-5}$$

Equations (A-4) can be solved iteratively if an initial value for  $R$  is assumed. If necessary these equations can be easily extended to include more data points.

#### References

1. ASTM Data Series D5 37A, *X-ray Emission and Absorption Wavelengths and Two Theta Tables*, ASTM, Philadelphia, 1970.

2. M. Green and V. E. Cosslett, *Brit. J. Appl. Phys. (J. Phys.D)* 1: 425-436, 1968.
3. E. Lifshin, M. F. Ciccarelli, and R. B. Bolon, *Proc. 12th MAS Conf.*, 1977, 104A-104C.
4. E. Lifshin, M. F. Ciccarelli, and R. B. Bolon, in D. Beaman, R. Ogilvie, and D. Wittry, Eds., *X-ray Optics and Microanalysis--8th Intern. Conf.*, Princeton, N.J.: Science Press (in press).
5. K. F. J. Heinrich, H. Yakowitz, and D. L. Vieth, *Proc. 7th Nat. EPASA Conf.*, 1972, paper 3.
6. K. F. J. Heinrich, "X-ray absorption uncertainty," in T. D. McKinley, K. F. J. Heinrich, and D. B. Wittry, Eds., *The Electron Microprobe*, New York: Wiley, 1966, 296-377.

## SOME INVESTIGATIONS FOR THE DETERMINATION OF THE SPATIAL DISTRIBUTION OF THE IONIZATION DENSITY

H. J. Dudek

In many modern materials, chemical inhomogeneities of the order of one micrometre and smaller determine their mechanical properties. For electron microbeam analysis of these inhomogeneities, the spatial resolution must be known. The spatial resolution of electron microbeam analysis (X-ray and Auger) is influenced mainly by the spatial distribution of the specific ionization density in the material. Some results concerning the determination of the spatial distribution of ionization density in the material are discussed below.

### *The k-ratio as a Function of Particle Diameter*

In energy-dispersion microbeam analysis in the scanning electron microscope, the effect of the electron-beam diameter on the spatial resolution can be usually neglected.<sup>1</sup> Measurement of the k-ratios of small particles embedded in a matrix of a different chemical constitution as a function of the particle diameter should yield constant values as long as the electron-induced ionization is contained completely inside the particle.<sup>2</sup> The change in the k-ratios at small particle diameters indicates the influence of the matrix and allows conclusions to be drawn about the diameter of the ionization-density distribution.

Figure 1 shows k-ratios of the  $\beta$ -phase of Ti6Al4V alloy as a function of the particle diameter.<sup>3</sup> The decrease in the k-ratios of vanadium and the increase in the k-ratios of aluminum at particle diameters of approximately 0.5  $\mu\text{m}$  indicate that the dimensions of the ionization-density distribution are of the same order of magnitude.

### *X-ray Measurements at Element Couples*

The x-ray intensity measured at an element couple as a function of the distance from the boundary is the spatial integral of the spatial x-ray production function.<sup>4-6</sup> The measurements of the x-ray intensity near the boundary can be used to determine the dimensions of the ionization density distribution. The distance of the two k-ratio plots at 5% of the maximum intensity can be taken as an approximate measure for the dimensions of the ionization-density distribution in the material (and as a measure for the lateral resolution). The 5% distances were determined for various element couples as a function of the accelerating voltage (Fig. 2).<sup>1</sup>

### *Radial Function of the Ionization Density Determined from Measurements of the X-ray Intensity at Element Couples*

With simple assumptions for the radial distribution of the ionization density (normal distribution), it can be shown that the x-ray intensity measured at element couples can be used to determine this radial distribution.<sup>4,6</sup> The radial distribution of the primary ionization density in copper (Fig. 3) and the secondary ionization density in iron (Fig. 4) excited by  $\text{CuK}_\alpha$  was obtained by a graphical differentiation of the x-ray intensity measured at the Cu/Fe couple.<sup>6,7</sup> To assure results without artifacts a special preparation method for element couples was developed.<sup>7</sup>

---

The author is at DFVLR (German Aerospace Research Establishment), Materials Science Laboratory, 5000 K8ln 90, Federal Republic of Germany.

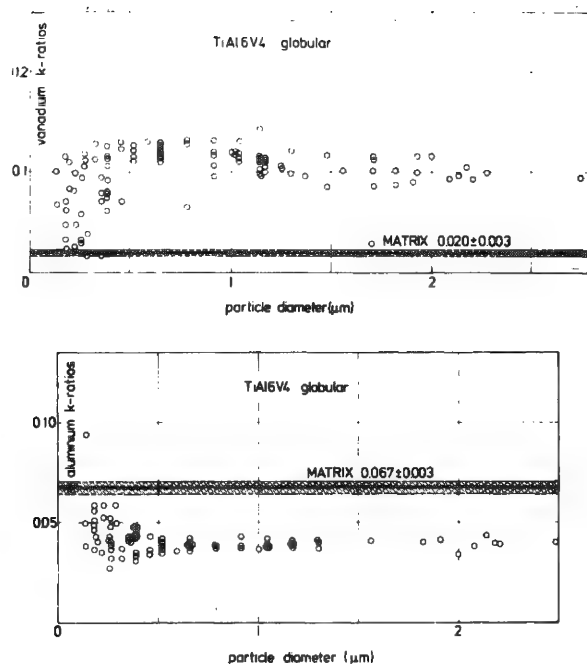


FIG. 1.--EDS-measured k-ratios of  $\beta$ -phase of Ti6Al4V alloy as function of particle diameter for vanadium (top) and aluminum (bottom); 10 kV,  $1.3 \times 10^{-10}$  A.

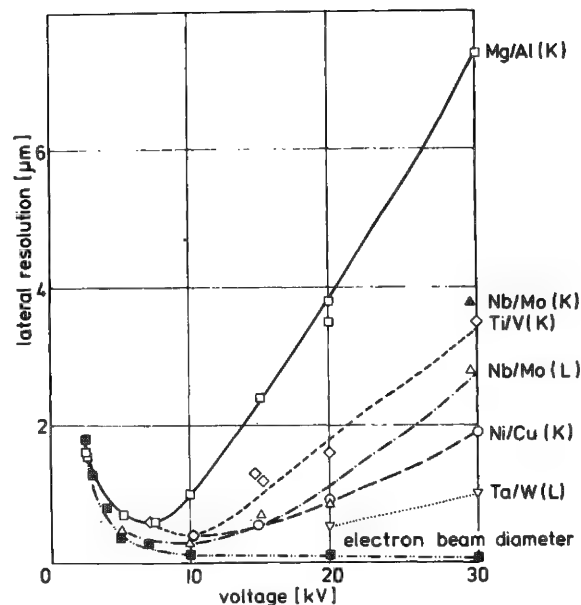


FIG. 2.--Five-percent distances measured in k-ratio plot of element couples as function of accelerating voltage for various element couples.

### Energy Distribution of Escape Electrons

The electrons escaping from the side face of a rectangular edge while the primary electron beam is scanning across the edge can be used to determine the dimensions of the ionization-density distribution in the material.<sup>8</sup> The ionization density is influenced by the intensity and the energy of the escape electrons. For the determination of the influence of these two factors a retarding-field spectrometer for the escape electrons was developed<sup>9</sup> and the intensity of the escape electrons was measured as a function of the retarding field (Fig. 5). The width of the intensity distribution of the escape electrons shows a substantial decrease only at high retarding potentials.

### Model Calculations

For a general formulation of the lateral resolution of the electron microbeam analysis the spatial ionization-density distribution function has to be known as a function of all beam and material parameters.<sup>10</sup> For the depth distribution many such functions were developed, but the radial distribution is not sufficiently known in the general case. For a mathematical formulation of this problem, a scattering model for the determination of the spatial distribution of the ionization density is being developed. Use of a normal distribution for the electron beam permits the computation of the number of monoenergetic electrons that pass through an infinitesimal volume at any point in the material after one scattering event.<sup>11</sup> First computations done with simple assumptions for the scattering and ionization cross section lead to a depth distribution for copper shown in Fig. 6.<sup>11</sup>

### Discussion

For the investigation of materials science problems in aerospace technology by means of electron microbeam analysis, some experimental investigations and calculations have been made that give information about the spatial distribution of the ionization density in the material. These investigations are intended to lead to a general formulation of

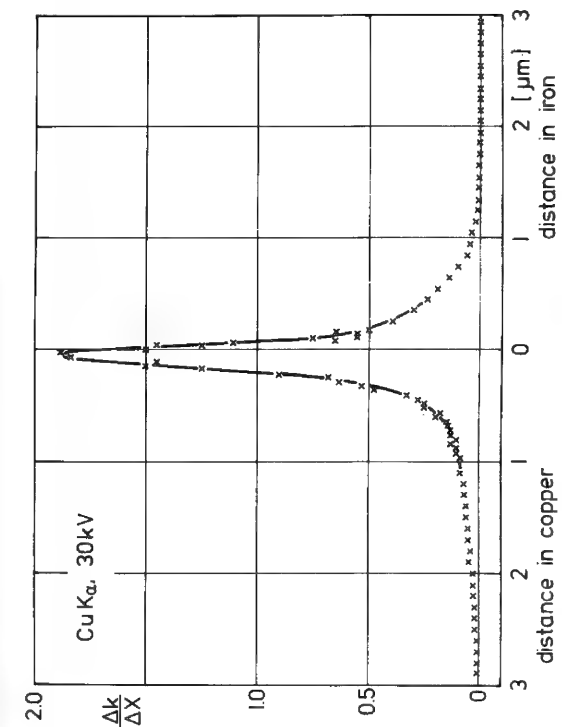


FIG. 3.--Radial distribution of primary ionization density in copper obtained by graphical differentiation of k-ratio measurements near boundary of Cu/Fe couple.

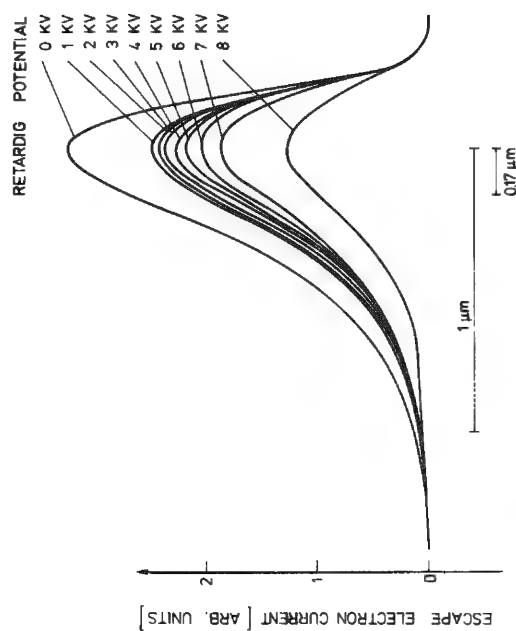


FIG. 5.--Escape-electron intensity measured with retarding field spectrometer as function of distance of primary electron beam from edge at various retarding potentials. Material: aluminum; accelerating voltage 10 kV, beam diameter 0.17  $\mu\text{m}$ , beam intensity  $3 \times 10^{-11}$  A.

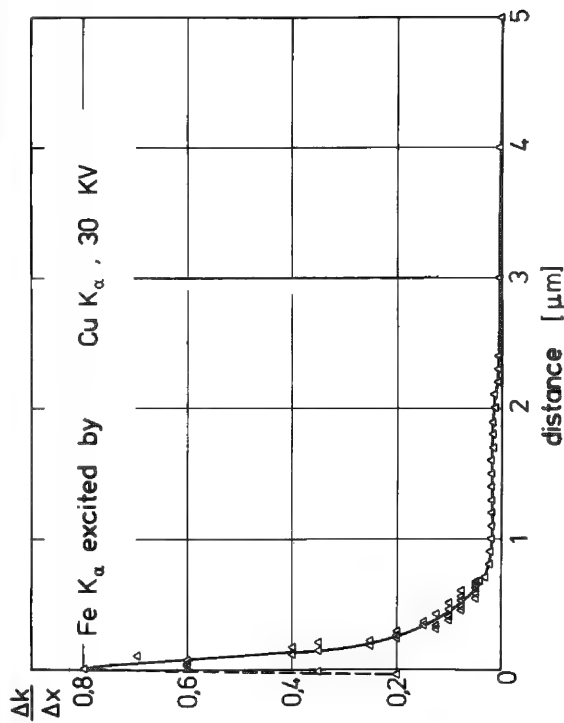


FIG. 4.--Radial distribution of secondary-ionization density in iron excited by Cu  $K\alpha$  obtained by graphical differentiation of k-ratio measurements near boundary of Cu/Fe couple.

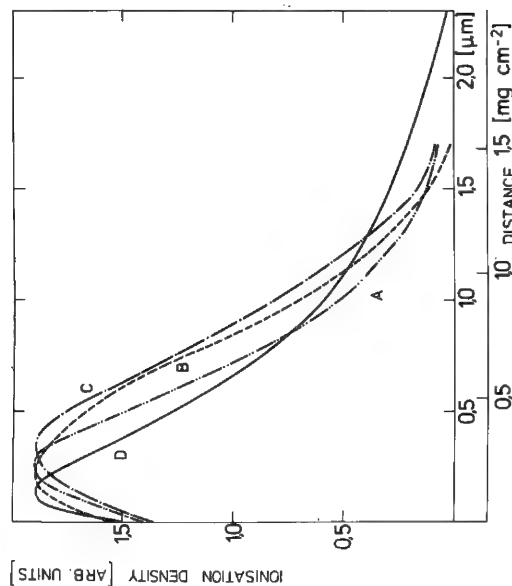


FIG. 6.--Model calculations (plot D) of depth distribution of ionization density in copper at 30 kV compared with experiments (A)<sup>12</sup> and with Monte Carlo calculations<sup>13</sup> (B: single scattering; C: multiple).

of the spatial resolution of the electron microbeam analysis.

#### References

1. H. J. Dudek and G. Ziegler, "Optimum lateral resolution of energy dispersion x-ray microanalysis," *Electron Microscopy* 1: 408-410, 1976.
2. N. J. Page, L. C. Calk, and M. H. Carr, "Problems of small-particle analysis with the electron microprobe," *U.S. Geological Survey Research* 1968, 600C (C31-C37).
3. H. J. Dudek and G. Ziegler, "Optimierung des lateralen Auflösungsvermögens der energiedispersiven Röntgen-Mikroanalyse am Beispiel der Analyse von ( $\alpha$ + $\beta$ )-Titanlegierungen," *Beitr. elektronenmikroskop. Direktabb. Oberfl.* 9: 15-26, 1976; "Methoden der energiedispersiven Elektronenstrahl-Mikroanalyse in der Metallkunde," *Mikrochimica Acta Suppl.* 7: 243-260, 1977.
4. S. J. B. Reed and J. V. P. Long, "Electron-probe measurements near phase boundaries," in H. H. Pattee, Ed., *X-ray Optics and X-ray Microanalysis*, New York: Acad. Press.
5. R. R. Dils, L. Zeitz, and R. A. Huggins, "A suggested secondary fluorescence correction technique for electron-probe analyses in the vicinity of a steep concentration gradient," *ibid.*, pp. 341-360, 1963.
6. H. J. Dudek, "Ordnungszahlabhängigkeit der lateralen Auflösung der Elektronenstrahl-Mikroanalyse," *Beitr. elektronenmikroskop. Direktabb. Oberfl.* 10 (in preparation).
7. H. J. Dudek, "Preparation of a sharply defined boundary between two elements for x-ray microanalysis," *Scanning* 1 (in preparation).
8. R. Shimizu and G. Shinoda, *Electron Diffusion and Determination of Sizes of X-ray Source in X-ray Microanalyser Specimen*, Osaka University Technical Report 14, 1964, 879-935.
9. H. J. Dudek, "Ein Spektrometer für Escape-Elektronen," *Beitr. elektronenmikroskop. Direktabb. Oberfl.* 11: 175-178, 1978.
10. H. J. Dudek, "Lateral resolution of the electron microbeam analysis," *Electron Microscopy*, 1: 542-543, 1978.
11. H. J. Dudek, "Modellrechnungen zur Bestimmung der räumlichen Verteilung der durch Elektronenstrahlen im Material erzeugten spezifischen Ionisierungsdichte," *Beitr. elektronenmikroskop. Direktabb. Oberfl.* 11: 179-186, 1978.
12. R. Casteing and J. Descamps, *J. Physics (Rad.)* 16: 314, 1955.
13. R. Shimizu, "Practicality of Monte Carlo technique to Quantitative Microanalysis," in E. Preuss, Ed., *Quantitative Analysis with Electron Microprobes and Secondary Ion Mass Spectrometry*, Berichte der Kernforschungsanlage Jülich 8: 156-192, 1973.

## EDS k-RATIO DETERMINATION USING A MINIMUM SET OF STANDARDS

A. G. Jackson and M. B. Strobe

Quantitative analysis of energy-dispersive-spectrometry (EDS) data can be accomplished by several methods. Variations of FRAME and other schemes have proved to be very useful in the analysis of spectra. One of the requirements for these schemes is a set of standards from which the counts used to find the k-ratio are generated. As with all quantitative methods, care in obtaining the data is essential to credible results. In particular, the standards must be well prepared and checked frequently to assume that contamination has not occurred. This is a time-consuming process requiring patience and skill.

One way of reducing the time for collecting data is to use fewer standards. An approach to minimizing the use of standards, as well as to check for reliability, is to take advantage of the response of the EDS detector to characteristic radiation over the range 2 kV to about 20 kV.

The integrated intensity measured by EDS peaks is proportional to beam current and to beam energy minus the excitation voltage, to some power, i.e.,

$$I_p \propto i[E - E(1)]^n \quad (1)$$

where usually  $n = 1.7$ .<sup>1,2</sup> Thus, for the same beam current, the ratio of the intensities of two elements is simply

$$\frac{I_p(1)}{I_p(2)} = \left[ \frac{E - E(1)}{E - E(2)} \right]^n \quad (2)$$

When the experimental values of  $\ln(I_1/I_2)$  vs  $\ln \{ [E - E(1)]/[E - E(2)] \}$  are plotted, the expected curve is a straight line with slope  $n$ . If the line is not straight, then the data were collected from a faulty standard produced by carbon or oxygen contamination; instrument problems may also be responsible for the nonlinearity. The critical excitation voltages are well known; the exponent can be found experimentally; and the beam voltage is known. Hence, by measuring the intensity of one element and using it as a reference, one can calculate the intensity of other elements.

The usefulness of this approach lies in the ability to estimate values of integrated intensity from Eq. (2) for a standard which may not be available. Instead of using standards for every element in a specimen one may thus make do with a standard that is available.

This approach as applied to K-lines is discussed in the following sections. Experimental values of  $n$  are given for three operating voltages, and the interpolated values for a Cr-Fe-Ni standard are calculated and compared with actual values.

### *Experimental*

The integrated-intensity data were obtained from a Kevex 5100 EDS system operating on an ETEC Autoprobe. Intensity was corrected for a background by a simple straight-line method. The standards used are listed in Table 1. Most of them have been tested against known compositions and have proved to be the compositions represented. Count rates were kept below 5000 cps in order to minimize dead-time effects, and Be absorption effects were minimized by avoiding excitation voltages below 2 kV.<sup>3</sup> The Cr-Fe-Ni standard with

---

The authors are with Systems Research Laboratories, Inc., 2800 Indian Ripple Road, Dayton, OH 45440. This work was supported by the Air Force Materials Laboratory at the Wright-Patterson Air Force Base, Ohio, under Contract F33615-77-C-5008.



certified concentrations was obtained from NBS. Only K-line data are presented here.

TABLE 1.--Standards used for generating integrated-intensity data.

Element	V	Cr	Mo	Co	Fe	Ni	Cu	Zn	Ge	Se
$E_c$ (kV)	4.952	5.415	5.899	6.930	6.404	7.478	8.048	8.639	9.886	11.22
(K-line)										

### Results

Integrated-intensity data from each standard were obtained at 15, 20, and 30 kV. Ratios of intensity for each combination of two elements were calculated from count data and plotted (Fig. 1) as a function of  $[E - E(1)]/[E - E(2)]$ ; the data fell on a straight line as expected. However, the value of  $n$  was voltage dependent, increasing with increasing voltage. In Table 2 the values of  $n$  obtained from a least-squares fit of the data are listed.

TABLE 2.--Experimental values of  $n$  by least-squares fit of  $\ln I_1/I_2$  vs  $\ln[(E - E_1)/(E - E_2)]$

$E_0$ (kV)	15	20	30
$n$	3.33	3.73	4.55

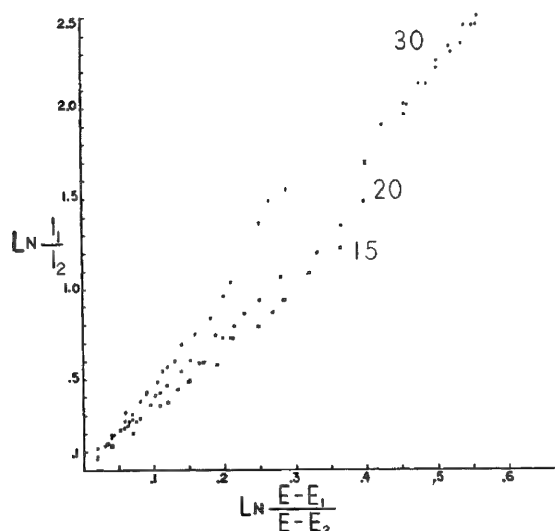


FIG. 1.--Log-log plot of intensity ratio as function of  $(E - E_1)/E - E_1$ , for  $E = 15, 20, 30$  kV. Scatter in 30kV data at center resulted from contaminated standard.

Scatter in the data at 30 kV resulted from data generated by a poor standard--in this case Se. Inspection of the Se standard showed that it was contaminated and was producing too low an intensity. During the investigation, similar results had been obtained for a Ti standard. When the Ti was repolished and new data were generated, they fell on the line as expected.

The procedure--once a value of  $n$  for Eq. (2) had been found--is relatively straightforward. First, counts from a standard for a material present in the unknown are obtained; next, theoretical values of standard counts for the other elements in the unknown are calculated. Once these counts are available, the k-ratios can be found, from which the corrected concentrations are determined using ZAF computation methods.

Intensity data from a Cr-Fe-Ni standard were obtained at 15 kV in order to test the method and the experimental value of  $n$  in Eq. (2). The results are shown in Table 3. The point of interest is the comparison between theoretically calculated intensity and k-ratio and experimentally obtained intensity and k-ratio. In each case, the values compare favorably. Fe was used as the known intensity since the expected concentration was the largest and would thereby be influenced least by background corrections.

TABLE 3.--Comparison of theoretical counts and k-ratio with actual counts and k-ratio for several sets of data from Cr-Fe-Ni reference standard; Fe is basis element from which others are calculated.

Element	$k_{th}$	$k_{act}$	$I_{th}$	$I_{act}$
Cr	0.204	0.206	115 638	114 649
Ni	0.101	0.101	51 593	51 554
Cr	0.208	0.203	71 169	72 840
Ni	0.098	0.097	31 753	32 066
Cr	0.203	0.205	68 192	67 600
Ni	0.104	0.108	30 424	29 100

On the other hand, use of either Cr or Ni as the starting element is also valid. The problem for this case is that both elements have low concentrations. Contributions from the background are therefore larger than those for Fe. This is not a severe problem for Cr-Ni-Fe; however, where low concentrations and varying background are present, errors introduced during background subtraction are relatively larger.

Experimentally this approach works well for the K-line data reported. The case of Cr-Fe-Ni is a simple situation in which no overlap occurs and other complicating factors are at a minimum. For the more complex situations where overlap is present this technique can be applied by use of the  $K_{\beta}$  line intensities and the exponent suitable for these lines. This is the subject of a separate paper.<sup>4</sup>

Application of this technique to L-lines requires considerable care because of the strong background effects. The narrow separation between the  $L_{\alpha}$  and the higher-order lines ( $L_{\beta}$ ,  $L_{\beta 2}$ ) poses an operational problem in the obtaining of reliable integrated-intensity values for the  $L_{\alpha}$  line. Efforts are under way to obtain values of  $n$  for the L-lines.

### Conclusions

A simple method for calculating theoretical standard counts has been presented for K-line intensity. The calculated values correspond well with measured counts for the simple case of Cr-Fe-Ni reference material. Experimental values of the exponent in the intensity equation for three beam voltages have been found. Hence, all parameters in the intensity equation are known, so that calculation of theoretical counts is made possible.

Application to L-lines and to complex cases where overlap occurs is mentioned. Results for these cases and discussion of the variation of  $n$  with beam voltage will be presented elsewhere.<sup>4</sup>

### References

1. J. I. Goldstein et al., *Practical Scanning Electron Microscopy*, New York: Plenum Press, 1975, 77.
2. M. Green and V. E. Cosslett, "The efficiency of production of characteristic x-radiation in thick targets of a pure element," *Proc. Phys. Soc. (London)* 78: 1206, 1961.
3. R. Woldseth, *X-Ray Energy Spectrometry*, Burlingame, Calif.: Kevex Corp., 1973, 28.
4. A. G. Jackson and M. B. Strope, to be published.

## STATISTICAL PARAMETERS USEFUL FOR CHARACTERIZING SAMPLES BY ELECTRON MICROPROBE

W. G. Fricke Jr. and Gary Gray

We microprobists use statistics as a way of evaluating how good our analyses are. We use them, for example, to calculate detectability limits or analytical sensitivity for some element.<sup>1</sup> However, standard statistical techniques are even more useful in describing our *samples* as distinct from our *methods*. A surprising amount of additional information is obtained if statistical parameters are calculated routinely as part of any analysis. Such extension is relatively easy with modern automated probes once the data are in a computer.

*Standard deviation*, for example, is a measure of the scatter in a set of experimental data. In part such scatter would be observed if repeated analyses were made on one point. Standard deviation from this source is the square root of the mean counts. Yet in general the observed scatter is much greater than that because of inhomogeneity of the sample itself. In fact, the observed standard deviation in analyses is a convenient measure of this inhomogeneity.

Whenever more than a few determinations are made on the same sample, for example during a step scan, the standard deviation for each element should be calculated. If there were  $n$  determinations giving an average analysis  $\bar{X}$ , the standard deviation  $S$  is calculated by a summation of the amount by which each analysis  $X_i$  deviates from the mean, according to the formula

$$S = \left[ \sum_{i=1}^n (X_i - \bar{X})^2 / (n - 1) \right]^{1/2}$$

It is then easy to compare samples. For example, Table 1 lists the scatter of analyses seen in X5020 aluminum alloy ingot as it was cast and after heating intended to homogenize the ingot. The preheating did indeed make the material more homogeneous as it eliminated coring in elements such as magnesium and copper. Manganese, on the other hand, became more "inhomogeneous" with heating because particles high in manganese formed out of the solid solution.

TABLE 1.--Homogeneity in X5020 aluminum alloy ingot.

	As-cast Ingot			Preheated 16 hr at 493°C (920°F)		
	Mean	Std. Dev.	Coeff. Varia.	Mean	Std. Dev.	Coeff. Varia.
Mg	2.53	0.91	0.36	2.53	0.10	0.04
Cu	0.61	0.61	0.80	1.68	0.24	0.14
Mn	0.26	0.06	0.21	0.23	0.12	0.53

It is sometimes convenient to express the standard deviation as a fraction of the amount present, that is, as  $S/\bar{N}$ . This parameter is known as the *coefficient of variation* and gives one a better feel for whether there is a little or a lot of scatter. In the above example, it is easy to see that even in the ingot the copper was relatively more segregated than the magnesium, even though in an absolute sense there was less of it there.

Once the standard deviation is calculated, it is relatively easy to compare samples to determine whether they are significantly different through a method such as the Student *t-test*.<sup>1</sup>

The authors are with the Alloy Technology Division, Alcoa Laboratories, Alcoa Center, PA 15069.

Elements do not usually vary independently of each other in a sample. The same mechanism that tends to concentrate one element in a portion of the sample tends to concentrate other elements in the same or in different areas. *Correlation coefficients* are convenient measures of what elements were varying together and, hence, those which had an affinity for each other. If  $X_i$  and  $Y_i$  are the analyses for two elements at the same  $i$ -th point, the correlation coefficient  $R$  between the two elements is given by

$$R = [n\sum X_i Y_i - \sum X_i \sum Y_i] / \{[(n\sum X_i)^2 - (\sum X_i)^2][n\sum Y_i^2 - (\sum Y_i)^2]\}^{1/2}$$

All the summations are for  $i = 1$  to  $n$ , the total number of analyses. In the above expression,  $\sum(X_i Y_i)$  is the sum of the individual  $X$ 's multiplied by the  $Y$ 's, whereas  $\sum X \sum Y$  is the result of totaling all the  $X$ 's and multiplying by the total of the  $Y$ 's. The term  $\sum X_i^2$  means to square the  $X$ 's and total;  $(\sum X_i)^2$  means to total the  $X$ 's and square; etc.

A correlation coefficient near +1.00 indicates that the two elements were varying together and, in fact, were exactly proportional to each other; a coefficient near -1.00 indicates they were avoiding each other perfectly. A coefficient near 0.00 suggests the two elements were indifferent to each other. Of course, in practice, a calculated coefficient will never be exactly zero, so it is necessary to know how small a coefficient can be for a given amount of data and still be real. Tables exist that help answer this question.<sup>2</sup>

An example shows the power of the method. Step scans were being made across two samples of 3003 ingot for the elements Fe, Mn, and Cu. The graphs of the data showed that points high in Fe also tended to be high in Mn (Fig. 1). In this case, the high points in the analyses occurred when the analyzing spot happened to include part of one of the intermetallic particles that are common in this alloy. The correlation coefficients between Fe and Mn were, therefore, close to +1.00 for both samples (Table 2); the particles contained both Fe and Mn. However, the graphs indicated that high points also occurred for Cu and sometimes seemed to coincide for peaks in Fe and Mn. But was the coincidence real?

TABLE 2.--Correlation coefficients between elements.

Element Pairs	Sample A	Sample B
Fe-Mn	+0.92	+0.96
Fe-Cu	+0.39	(+0.05)
Mn-Cu	(+0.06)	(-0.09)

The correlation coefficient calculated between Fe and Cu in Sample A was large enough to be real (Table 2), but in Sample B it was not larger than the 0.14 value needed to be significant (200 analyses, 95% confidence). There was a suggestion, therefore (later confirmed), that Cu was present in the intermetallics in Sample A, but not in Sample B. The low correlation between Mn and Cu in Sample A probably occurs because high points for Mn in the solid solution are low points for Cu.

Sometimes one wants to estimate the composition of submicrometre-sized particles, even though the individual particles are smaller than the analyzed spot and hence cannot be analyzed quantitatively. *Regression* techniques help here. Think of the separate analyses as being diluted by an unknown quantity of matrix of constant composition. If the individual analyses were arranged in increasing order for some element, they could be extrapolated to large particle size (zero dilution by the matrix), which would be the true composition. This is the method of Betzold,<sup>3</sup> and we have written a computer program to facilitate the extrapolation.

However, complex calculations are not always necessary. In the example above, correlation calculations showed that Fe and Mn were both present in the intermetallics. By simply picking off the observed high points for Fe and Mn and calculating a *least-squares straight line* through the data pairs (Fig. 2), we obtained from the slope of the equation a predicted Fe/Mn ratio in the particles of 2.21. Incidentally, the correlation coefficient between Fe and Mn, calculated previously, measured how well the experimental points fit this straight line.

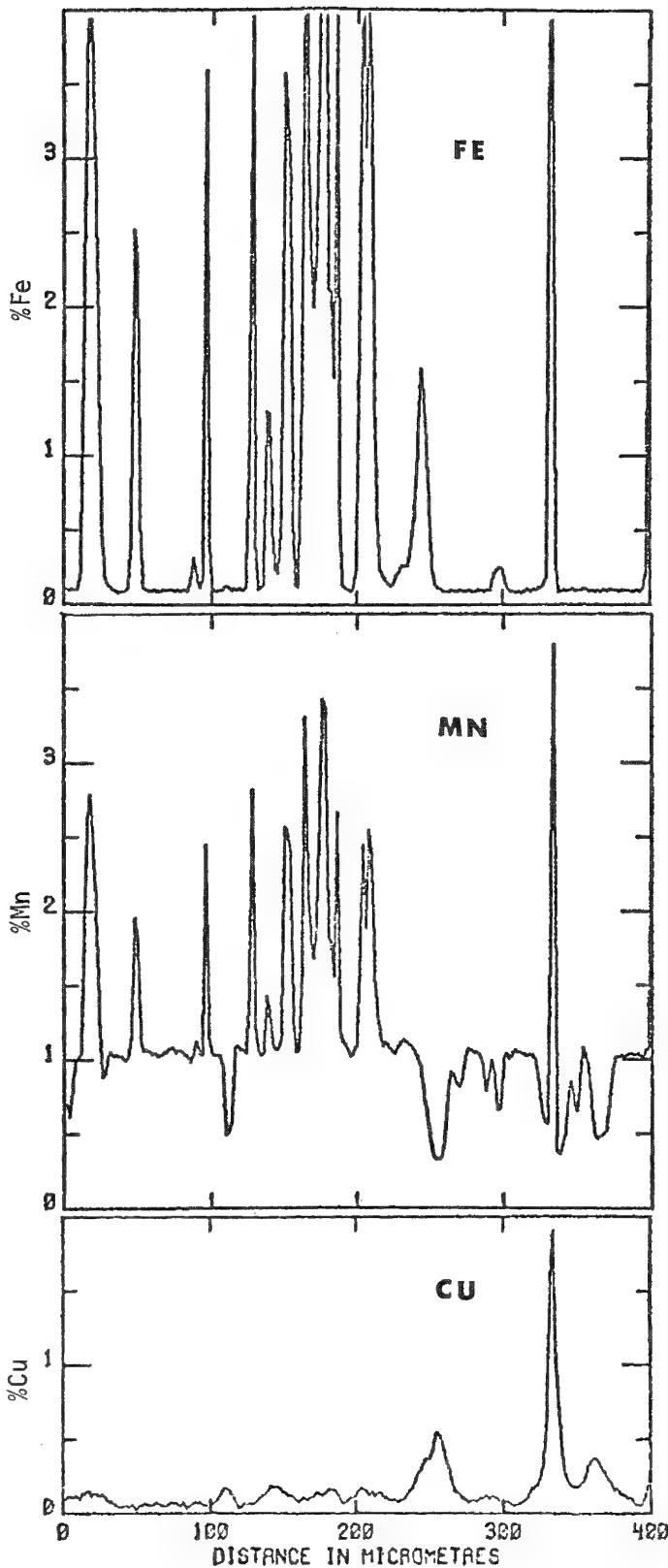


FIG. 1.--Step scans for Fe, Mn, and Cu across 3003 ingot.

Having a computer return such statistical parameters routinely, even when no use is initially visualized for them does help interpret the condition of the samples and occasionally provides surprises that would be missed if one were to look at average analyses alone.

#### References

1. J. I. Goldstein, "Statistics of x-ray analysis," *Proc. 11th MAS Conf.*, 1976, T1.
2. G. W. Snedecor, *Statistical Methods*, Ames: Iowa State University Press, 1956; F. J. Rohlf and R. R. Sokal, *Statistical Tables*, San Francisco: Freeman and Co., 1969.
3. J. Betzold, "Electron microprobe analyses of particles smaller than the region excited by the electron beam," *Pract. Metallogr.* 14: 310-316, 1977.

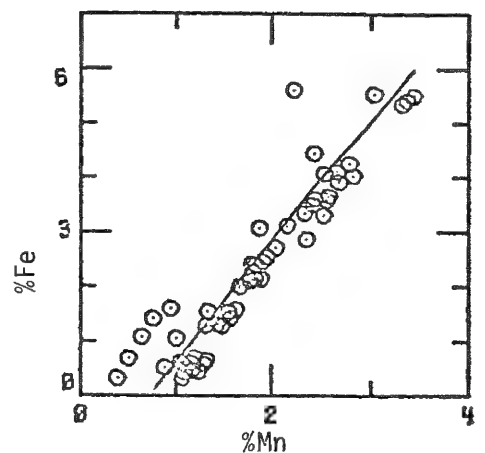


FIG. 2.--Regression plot of Fe vs Mn across this ingot.

## MICROHOMOGENEITY STUDIES OF NBS STANDARDS

R. B. Marinenko, K. F. J. Heinrich, and F. C. Ruegg

We have developed a simple routine procedure for testing the microhomogeneity of specimens. The procedure was described at a previous meeting<sup>1</sup> by one of the authors. Since then, many more samples have been studied and statistical evaluations have been developed.

Several procedures for studying microhomogeneity had been used at NBS before the new procedure was developed. These procedures included random samplings<sup>2,3</sup> that were used to study low-alloy steels (SRMs 461 and 463) and cartridge brasses (SRMs C1102 and 1102) and selective sampling such as quantitative raster scanning (QRS),<sup>4,5</sup> and a program called TOPO,<sup>6</sup> which sampled a region within a defined one- or two-dimensional array. These latter procedures were used to test the microhomogeneity of a tungsten-20 molybdenum alloy (SRM 480) and of gold-silver and gold-copper alloys (SRMs 481 and 482). Other modifications<sup>7,8</sup> of these methods have been used to study an iron-3% silicon alloy (SRM 483) and an iron-chromium-nickel alloy (SRM 479).

The new testing procedure was developed to provide a quick visual display of sample homogeneity on the micrometer scale, with an optional statistical interpretation of the observed signal variations. A periodic integrator as originally proposed by Heinrich<sup>9</sup> but based entirely on digital operations (i.e., a microcomputer) is used. The sample is moved automatically (by a stepping motor on the stage) under the electron beam in steps of one to up to ten micrometers. At each point x-ray counts are accumulated for a preselected time period (usually 10 sec). The total number of counts per time period on the scalars are then shown on a fast strip-chart recorder as an analog signal. The signal on the recorder remains unchanged during any counting period while x-ray counts are accumulated for the next time period display. The same point can be repeatedly sampled for as many as fifteen times before moving on to a new location.

A diagram of the interfacing of the periodic integrator with the electron microprobe and the recorder is shown in Fig. 1. Up to four independent x-ray photon count rates can be simultaneously handled by the scaler assembly. The periodic-integrator outputs from the scalars are transmitted to a teletype and to the strip-chart recorder. The microcomputer also controls the stepping motor on the stage allowing it to advance after one or as many as 15 counting periods. In addition, the signal excursions on the chart can be enhanced by digital multiplication of the signal and by application of a bias to remove unwanted counts.

In Fig. 2 is a typical periodic integrator trace where the homogeneity of molybdenum, chromium, and manganese in the steel SRM 663 are being tested. The sample was moved in 1  $\mu$ m steps under a 1  $\mu$ m electron beam. Visible inclusions were avoided. Counting periods were 10 sec. The operating voltage (30 kV) was chosen so that the effective diameter of the excited area was less than 2  $\mu$ m.

The shaded region through the traces corresponds to a range of  $\pm 3\bar{N}^{1/2}$  around the average number of counts per counting period  $\bar{N}$ . The square root of  $\bar{N}$ , according to Poisson counting statistics, is an unbiased estimate of the standard deviation. Therefore,  $\pm 3\bar{N}^{1/2}$  should provide a 99.7% confidence limit. Deviations outside this range are indicative of inhomogeneity or instrumental variations.

In the figure, chromium and manganese are observably inhomogeneous and show large deviations outside of the  $\pm 3$ -sigma limits. This result truly represents a concentration variation occurring in the sample as confirmed by the trace to the left, where the same area was repeatedly counted with a stationary 20  $\mu$ m beam. Here the signal remains within the  $\pm 3$ -sigma limits and shows variations due only to Poisson counting statistics. According to this interpretation, molybdenum appears to be homogeneous here. Such a conclusion is not valid in this case as the method is not sensitive enough to see such a low concentra-

---

The authors are associated with the Center for Analytical Chemistry, National Bureau of Standards, Washington, DC 20234.

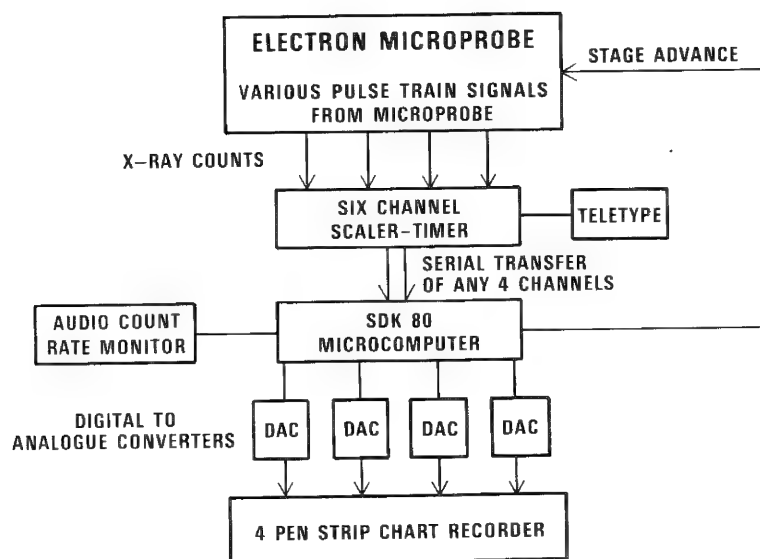


FIG. 1.-- Interfacing of periodic integrator with electron microprobe and recorder.

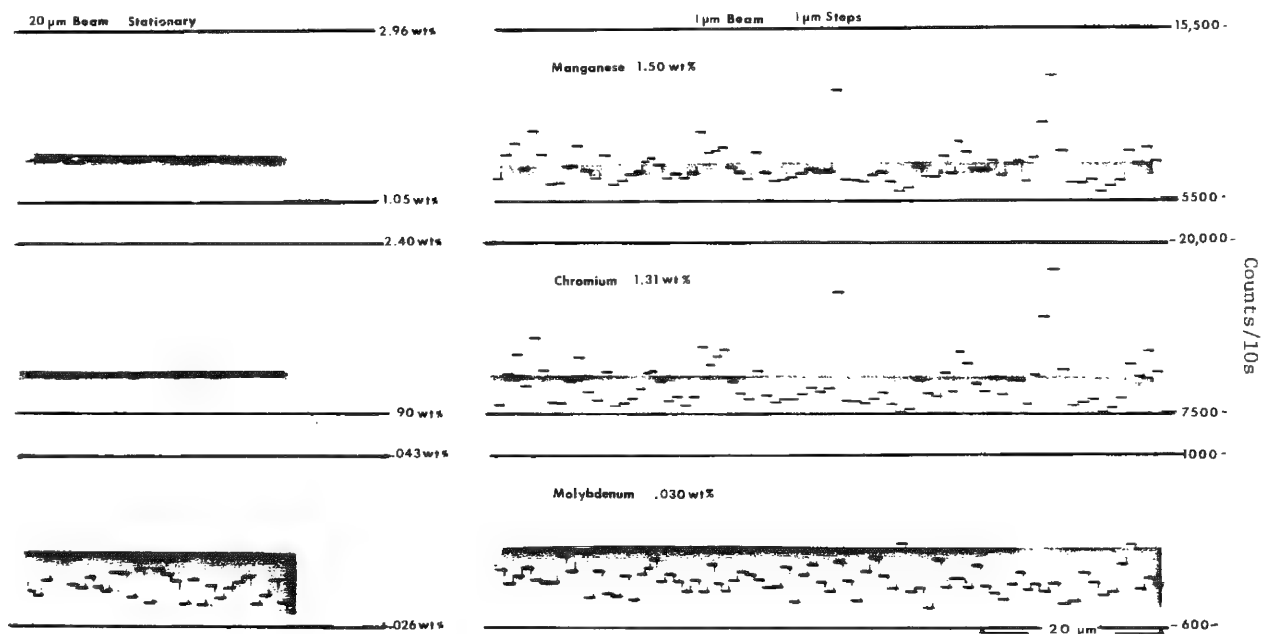


FIG. 2.--Periodic integrator homogeneity traces of manganese, chromium, and molybdenum simultaneously recorded from NBS SRM 663 stainless steel (voltage 30 kV, beam current  $1.3 \times 10^{-8}$  A). In right-hand traces sample was advanced 1  $\mu$ m under a 1  $\mu$ m electron beam after each 10sec counting period. At left, sample was not moved during repeated 10sec counting periods with a 20  $\mu$ m beam. Shaded regions represent range of  $\pm 3\bar{N}^{1/2}$  around average number  $\bar{N}$  of counts per 10 sec for entire trace.



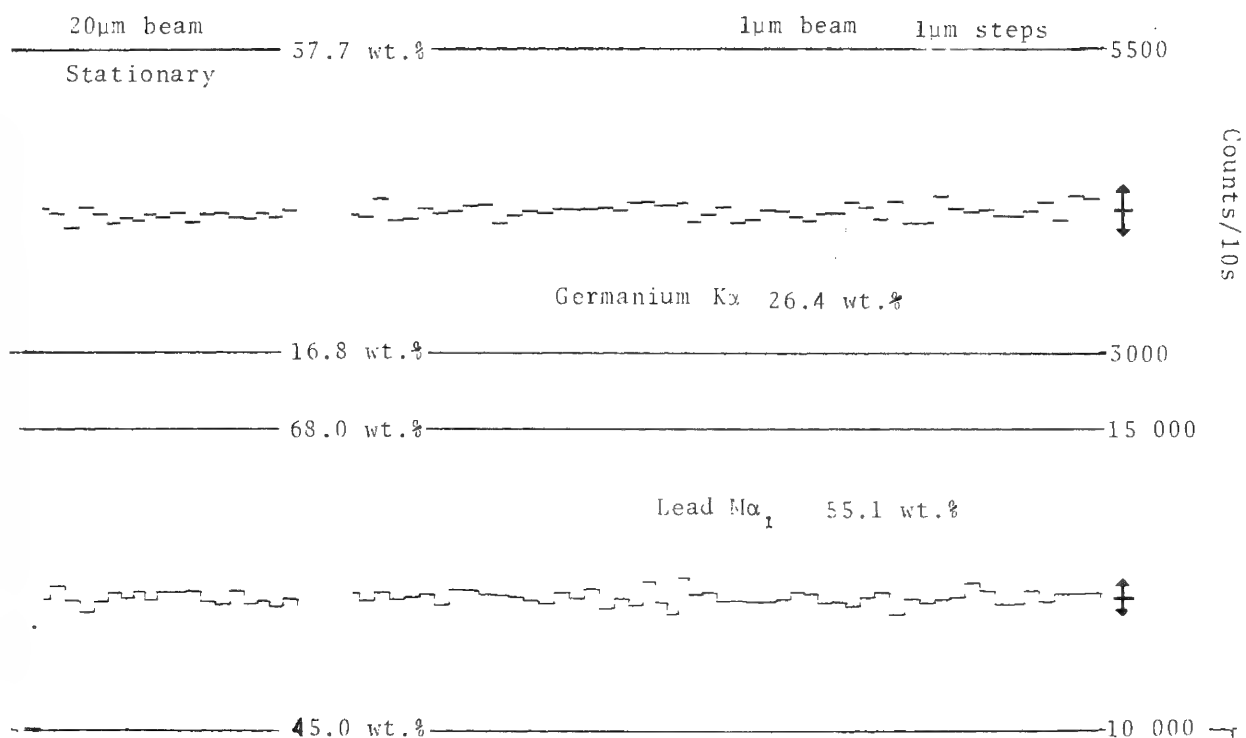


FIG. 3.--Periodic integrator homogeneity trace of germanium and lead simultaneously recorded from NBS RM Glass K-491 (voltage, 15 kV; beam current,  $7.5 \times 10^{-8}$  A). In traces on right, sample was advanced 1  $\mu$ m under 1  $\mu$ m electron beam after each 10sec counting period. To left, sample was not moved during repeated 10sec counting periods with a 20  $\mu$ m electron beam. Double-headed arrows at right represent range of  $\pm 3\bar{N}^{1/2}$  around average number of counts  $\bar{N}$  per 10 sec for entire trace.

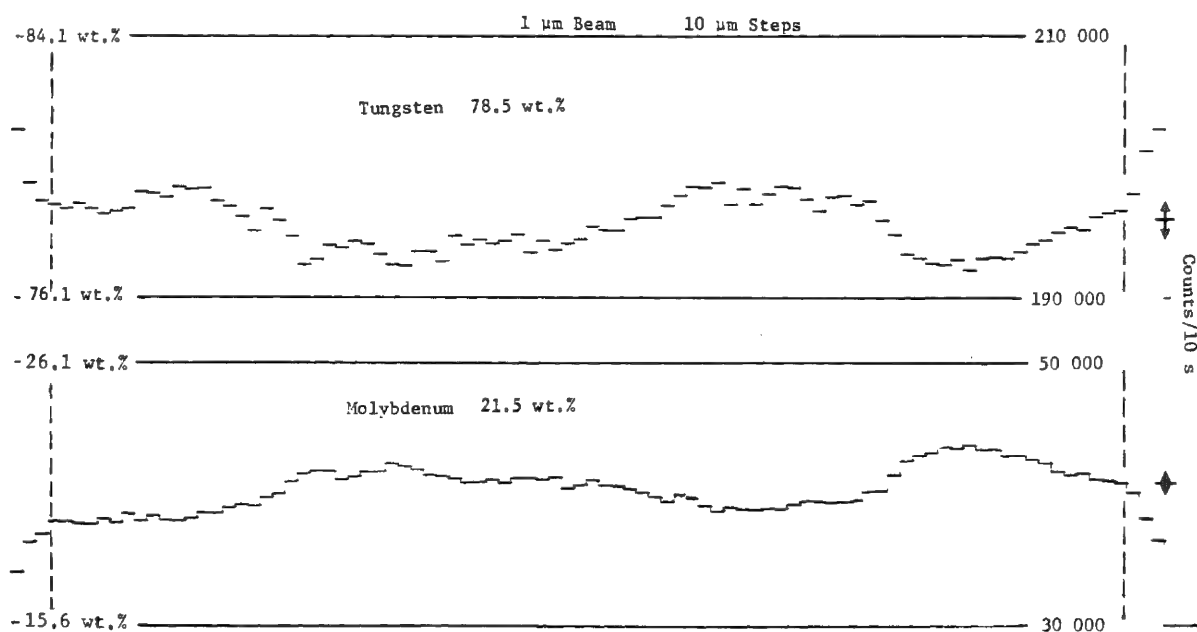


FIG. 4.--Periodic integrator homogeneity trace of tungsten and molybdenum in NBS SRM 480, tungsten-20 molybdenum alloy. Traverse crosses sample from edge to edge in 10  $\mu$ m steps with 10  $\mu$ m electron beam.

tion of molybdenum. The molybdenum signal is hardly discernible above the background.

If desired, a statistical evaluation of the data can be obtained. The standard deviation is separated into two components, one due only to the difference between points or the "between" standard deviation  $\hat{\sigma}_B$ . The other is the "within" standard deviation  $\hat{\sigma}_W$ , which is due only to the variation that occur when the same point is repeatedly measured. To get the latter component, duplicate measurements are taken on each point. This sort of treatment allows one to separate the statistical fluctuations and facilitates identification of inhomogeneities.

Table 1 is a statistical survey of several elements in the steel SRM 662. These are the results of traces we prepared by moving the sample in  $1\mu\text{m}$  steps under a  $1\mu\text{m}$  electron

TABLE 1.--Homogeneity study of stainless steel SRM 662.

Element x-ray Line	Conc. in Wt. %	$\bar{X}$	$\bar{B}$	$\hat{\sigma}_W$	$\hat{\sigma}_B^*$ Counts	$\hat{\sigma}_B^*$ Wt. %	U (wt. %)
CrK $\alpha$	0.30	4769	1000	$\pm 105(2.2)$	$\pm 599(12.6)$	$\pm 0.048$	$\pm 0.023(7.7)$
MnK $\alpha$	1.04	7559	800	$\pm 122(1.6)$	$\pm 560(7.4)$	$\pm 0.086$	$\pm 0.039(3.8)$
NiK $\alpha$	0.59	9943	3000	$\pm 103(1.0)$	$\pm 200(2.0)$	$\pm 0.017$	$\pm 0.014(2.4)$
CuK $\alpha$	0.50	4209	2000	$\pm 68(1.6)$	$\pm 152(3.6)$	$\pm 0.034$	$\pm 0.023(4.6)$
TiK $\alpha$	0.84	1778	900	$\pm 137(7.7)$	$\pm 1295(72.8)$	$\pm 1.239$	$\pm 0.529(6.3)$
V K $\alpha$	0.41	913	650	$\pm 32(8.5)$	$\pm 57(6.3)$	$\pm 0.089$	$\pm 0.067(16)$
CoK $\alpha$	0.30	12433	6300	$\pm 111(0.9)$	$\pm 117(0.9)$	$\pm 0.006$	$\pm 0.012(4.0)$

$\bar{X}$  = Mean intensity, or average of all readings in the scan

$\bar{B}$  = Average background reading

U = Total uncertainty

$\hat{\sigma}_W$  and  $\hat{\sigma}_B$  are expressed as percent in parentheses =  $\sigma/\bar{X}$

beam, taking duplicate readings at each point. The length of each trace was  $50\mu\text{m}$  and each counting period was 10 sec. A quick comparison of  $\hat{\sigma}_W$  and  $\hat{\sigma}_B$  in counts shows that except for cobalt all elements appear to be inhomogeneous in this sample. Titanium is probably the most inhomogeneous element. To the right  $\hat{\sigma}_B$  is expressed in weight percent and U is the total uncertainty (in weight percent) which includes both components of the standard deviation, the background, and the uncertainty from the SRM certificate.

Even though the steel SRMs 661-664 are not completely homogeneous, they can still be used as standards with the electron microprobe. In such cases it would be necessary for each analyst to determine the extent of inhomogeneity of his own specimen. The easiest way to make such a determination is by random sampling.

To check the validity of such an approach, random sampling tests were made on the steel SRMs. Nickel, chromium, and manganese were analyzed with wavelength spectrometers. Duplicate tests were made of ten random samplings on each steel with a  $1\mu\text{m}$  electron beam. Table 2 shows the results where the standard deviation (in weight percent) from both tests are compared to the  $\hat{\sigma}_B$  (in weight percent) calculated from the homogeneity traces. As can be seen both methods give similar results.

We have completed a study of all NBS standards that are sold at present for electron probe microanalysis. Table 3 is a list of these standards. The SRMs in this list had been previously studied for microhomogeneity by the best methods available at the time, but they had not been studied from micron to micron as can be done by the new method.

Figure 3 shows a homogeneity trace of one of the glasses in RM-30. The major constituents in eight of the glasses were studied. This trace is typical of a homogeneous material. All points fall within the  $\pm 3$ -sigma limits indicated on the right by the double-headed arrow. Eight glasses in RM-30 and the gold-silver and gold-copper alloys had similar traces. In samples such as these, statistical evaluations are not necessary, since

TABLE 2.--Comparison of random sampling with homogeneity traces for iron and steel SRMs.

Sample			Ni	Element Cr	Mn
661	Conc (wt%)		1.99	0.69	0.66
	$\sigma_B$ (wt%)	RS <sup>a</sup>	0.046	0.120	0.089
		RS <sub>b</sub>	0.041	0.093	0.067
		HT <sup>b</sup>	0.034	0.110	0.083
662	Conc (wt%)		0.59	0.30	1.04
	$\sigma_B$ (wt%)	RS	0.021	0.045	0.087
		RS	0.018	0.040	0.089
		HT	0.017	0.048	0.086
663	Conc (wt%)		0.32	1.31	1.50
	$\sigma_B$ (wt%)	RS	0.014	0.110	0.075
		RS	0.011	0.198	0.155
		HT	0.009	0.250	0.180
664	Conc (wt%)		0.14	0.07	0.26
	$\sigma_B$ (wt%)	RS	0.024	0.021	0.101
		RS	0.020	0.028	0.064
		HT	0.018	0.011	0.058

<sup>a</sup>RS = Random Sampling<sup>b</sup>HT = Homogeneity Trace

TABLE 3.--Standard Reference Materials and Research Materials which are tested for microscopic homogeneity (taken from "NBS Standard Reference Materials for Electron Probe Microanalysis and Scanning Electron Microscopy," 1976, brochure published by NBS).

No.	Type	Form	Elements (nominal wt %)
SRM 478	Cartridge Brass	Cube and Cylinder	Cu-73; Zn-27
SRM 479	Fe-Cr-Ni Alloy	Wafer	Fe-71;Cr-18;Ni-11
SRM 480	Tungsten-20% Molybdenum	Wafer	W-78;Mo-22
SRM 481	Gold-Silver	Six Wires	Au-100;80;60;40; 20;0 Ag-0;20;40;60; 80;100
SRM 482	Gold-Copper	Six Wires	Au-100;80;60;40; 20;0 Cu-0;20;40;60; 80;100
SRM 483	Iron-3% Silicon	Platelet	Fe-97;Si-3
RM 30	Glasses for Microanalysis	Slices	10 Compositions of Various Oxides
RM 31	Glass Fibers for Microanalysis	Fibers	10 Compositions of Various Oxides

there is no evidence of inhomogeneity, as may be seen from the comparison of  $\hat{\sigma}_W$  and  $\hat{\sigma}_B$  for 80Au20Cu in Table 4.

TABLE 4.--Homogeneity study of gold-copper alloy SRM 482.

Element x-ray Line	Conc. in Wt. %	$\bar{X}$	$\bar{B}$	$\hat{\sigma}_W$	$\hat{\sigma}_B^*$ Counts	$\hat{\sigma}_B^*$ Wt. %	U (wt. %)
AuM $\alpha_1$	80.20	28328	1000	$\pm 166(0.6)$	$\pm 91(0.3)$	$\pm 0.27$	$\pm 0.244(0.3)$
CuK $\alpha$	19.80	28731	1000	$\pm 224(0.8)$	0(0.0)	0.0	$\pm 0.118(0.6)$

$\bar{X}$  = Mean intensity, or average of all readings in the scan

$\bar{B}$  = Average background reading

U = Total uncertainty

$\hat{\sigma}_W^*$  and  $\hat{\sigma}_B^*$  are expressed as percent in parentheses =  $\hat{\sigma}/\bar{X}$

SRM 480, the tungsten-20 molybdenum alloy, on the other hand, was somewhat different. A homogeneity trace of this sample is shown in Fig. 4. The sample was moved in 10 $\mu$ m steps under a 1 $\mu$ m electron beam. The wave-like trends were not observed in the original homogeneity study of this sample. The coefficients of variation in the SRM certificate are 2.5% for molybdenum and 1.5% for tungsten. In terms of  $\pm 3$ -sigma limits, these variations are  $\pm 1.6$  wt% for molybdenum and  $\pm 3.6$  wt% for tungsten. Such deviations are within the variations that occur on the trace.

Cartridge Brass, SRM 478, also showed fluctuations similar to SRM 480 but not as extreme. And the other SRMs showed no significantly large inhomogeneities.

#### References

1. K. F. J. Heinrich, R. B. Marinenko, and F. C. Ruegg, 8 ICXOM and *Proc. 12th MAS Conf.* 1977.
2. R. E. Michaelis, H. Yakowitz, and G. A. Moore, *J. Res. NBS A-68A*(No. 4): 1, 1964.
3. H. Yakowitz, D. L. Vieth, K. F. J. Heinrich, and R. E. Michaelis, *NBS Misc. Pub.* 2010, 1965.
4. H. Yakowitz, R. E. Michaelis, and D. L. Vieth, *NBS Spec. Pub.* 260-16, 1969.
5. *Ibid.*, *Adv. X-ray Anal.* 12: 418, 1969.
6. K. F. J. Heinrich, R. L. Myklebust, S. D. Rasberry, and R. E. Michaelis, *NBS Spec. Pub.* 260-28, 1971.
7. H. Yakowitz, C. E. Fiori, and R. E. Michaelis, *NBS Spec. Pub.* 260-22, 1971.
8. H. Yakowitz, A. W. Ruff, and R. E. Michaelis, *NBS Spec. Pub.* 260-43, 1972.
9. K. F. J. Heinrich, *Adv. X-ray Anal.* 7: 382, 1963.

# AN EMPIRICAL INVESTIGATION INTO POSSIBLE NONLINEARITIES OF THE MICROPROBE CORRECTION FACTORS IN THE SYSTEM $\text{MgO-CaO-Al}_2\text{O}_3\text{-SiO}_2$

H. F. Shaw and A. L. Albee

The use of the  $\alpha$ -factor approach in electron microprobe analysis is based on the empirical observation<sup>1</sup> that curves of  $C_{AB}^A/K_{AB}^A$  as a function of  $C_{AB}^A$  are nearly linear, that is,

$$C_{AB}^A/K_{AB}^A = \alpha_{AB}^A + (1 - \alpha_{AB}^A)C_{AB}^A \quad (1)$$

where  $C_A^A$  is the weight fraction of element or oxide A in a binary mixture AB, and  $K_{AB}^A$  is the measured x-ray intensity of A relative to the pure element or oxide. The parameter  $\alpha_{AB}^A$  is equal to the ratio  $C_{AB}^A/K_{AB}^A$  in the limit as  $C_{AB}^A$  approaches zero. The  $\alpha$ -factors can be determined empirically for systems in which enough standards of intermediate composition are available,<sup>2,3</sup> or it can be calculated by the atomic number-absorption-fluorescence (ZAF) method.<sup>4</sup> Multicomponent systems are treated by the use of compositionally weighted  $\alpha$ -factors. Thus for each element in the mixture  $AB \dots N$ , an equation of the form

$$C_{AB \dots N}^A/K_{AB \dots N}^A = \sum_{X=A}^N C_{AB \dots N}^X \cdot \alpha_{AX}^A / \sum_{X=A}^N C_{AB \dots N}^X \quad (2)$$

is generated.<sup>1</sup> In practice, these equations are solved by iteration, with  $K_{AB \dots N}^A$  used as a first approximation to  $C_{AB \dots N}^A$ . This technique has gained widespread acceptance among mineralogic microprobe laboratories around the world, and has been applied with great success to a variety of problems in many chemical systems.

In some systems, however, the relationship between  $C_{AB}^A/K_{AB}^A$  and  $C_{AB}^A$  is markedly nonlinear.<sup>1,4</sup> The nonlinearity is largest in systems with large characteristic fluorescence corrections (in particular, heavy, adjacent elements for which  $K_\alpha$  radiation is used in analysis). Less significant nonlinearities arise in systems with large absorption corrections. Several authors have proposed the inclusion of higher order terms in the expression for  $C_{AB}^A/K_{AB}^A$  as a function of  $C_{AB}^A$ .<sup>6,7</sup> The simplest assumption is to let  $\alpha_{AB}^A$  in Eq. (1) be a linear function of  $C_{AB}^A$ :

$$\alpha_{AB}^A = a_{AB}^A + b_{AB}^A C_{AB}^A \quad (3)$$

The basic relationship between  $C_{AB}^A/K_{AB}^A$  and  $C_{AB}^A$  is then

$$C_{AB}^A/K_{AB}^A = a_{AB}^A + (1 - a_{AB}^A + b_{AB}^A)C_{AB}^A - b_{AB}^A(C_{AB}^A)^2 \quad (4)$$

We have conducted an empirical investigation in the important mineral forming system  $\text{MgO-CaO-Al}_2\text{O}_3\text{-SiO}_2$ . It has been previously noted that empirically determined  $\alpha$ -factors in the subsystem  $\text{MgO-Al}_2\text{O}_3\text{-SiO}_2$  are significantly different from those calculated using ZAF procedures,<sup>4</sup> and recent work has suggested that there may also be significant nonlinearities in this subsystem.<sup>5</sup>

Multiple analyses of 23 synthetic and natural minerals and glasses (Table 1) in the system  $\text{MgO-CaO-Al}_2\text{O}_3\text{-SiO}_2$  were obtained over a period of one month using an MAC-5 electron probe (effective takeoff angle  $38.5^\circ$ ) operating at 15 keV with a sample current of 0.05  $\mu\text{A}$  measured on brass. The resulting background and deadtime corrected x-ray intensities relative to the endmember oxides used as standards (K values) were then used to calculate empirical  $\alpha$ -factors for each binary in the quaternary system. The  $\alpha$ -factors were evaluated from the least-squares solution to a set of equations of the form of

The authors are with the Department of Geological and Planetary Sciences, California Institute of Technology, Pasadena, CA 91125. This work has been supported by NASA Grant NGL-05-002-338. Dan Weill provided the carefully synthesized glasses that made this study possible.

TABLE 1.--Compositions of the minerals and glasses used in calculating empirical alpha factors in the system MgO-CaO-Al<sub>2</sub>O<sub>3</sub>-SiO<sub>2</sub>.

	Composition (wt %)			
	MgO	CaO	Al <sub>2</sub> O <sub>3</sub>	SiO <sub>2</sub>
Pyrope	30.00	0	25.28	44.72
Enstatite	40.15	0	0	59.85
Enal-5 Glass	38.16	0	5.00	56.84
Enal-10 Glass	36.14	0	10.00	53.86
Enal-20 Glass	32.13	0	20.00	47.87
Spinel	28.34	0	71.66	0
Forsterite	57.30	0	0	42.70
Kyanite	0	0	62.91	37.09
Wollastonite	0	48.27	0	51.73
Anorthite	0	20.15	36.65	43.20
Grossularite	0	37.35	22.63	40.02
Ca-Al Pyroxene	0	25.71	46.74	27.55
Diopside	18.62	25.89	0	55.49
Glass P-721	11.05	23.15	16.07	49.72
Glass P-722	13.99	20.97	16.05	48.99
Glass P-723	16.93	16.96	13.98	52.13
Glass P-724	17.97	16.00	20.96	45.07
Glass P-725	6.00	5.04	8.99	79.97
Glass P-726	10.07	6.94	30.93	52.06
Glass P-727	32.69	2.89	3.31	61.12
Glass P-728	5.22	21.97	41.90	30.91
Glass P-729	19.03	26.01	2.01	52.95
Glass P-730	1.01	36.99	19.02	42.98

Eq. (2). Each equation was weighted according to the observed variance in C/K for the multiple analyses for each of the analyzed elements.<sup>8</sup> Least-squares solutions were obtained for 2 different assumptions: (1)  $\alpha_{AB} = \text{constant}$ ; (2)  $\alpha_{AB} = a_{AB} + b_{AB}C_{AB}$ . In order to eliminate physically unreasonable solutions and to reduce the estimated errors on the parameters, ZAF-calculated  $a_{AB}$  and  $b_{AB}$  values were included as weak constraints<sup>8</sup> on the solution obtained under assumption (2). The results of these calculations are listed in Table 2. The value of the reduced chi square statistic for assumption (1) is less than unity in all cases. This result indicates that the data are adequately described by constant  $\alpha$ -factors and, although we show compositionally dependent factors in Table 2, one is not justified in including these higher order terms given the present observed scatter in the C/K values. This observation has its practical expression in the fact that the average difference between the theoretical compositions of the minerals and glasses and the compositions calculated using constant alpha factors is not significantly different from the average difference obtained using the compositionally dependent alpha factors.

For comparison,  $\alpha$ -factors calculated by means of a ZAF correction program<sup>9</sup> are also listed in Table 2. Constant  $\alpha$ -factors were computed at a 1:1 molar ratio of oxides.<sup>4</sup> Compositionally dependent alpha factors were evaluated by fitting a straight line to  $\alpha$ -factors calculated at intervals of 10 wt% across each binary. An examination of Table 2 shows that the theoretical and empirical slope terms (the b's) all agree in sign and generally agree in magnitude. However, as noted above, there is serious disagreement between the absolute magnitude (a's or  $\alpha = \text{constant}$ ) of the empirical and theoretical factors in three instances (SiO<sub>2</sub> in MgO, SiO<sub>2</sub> in Al<sub>2</sub>O<sub>3</sub>, and Al<sub>2</sub>O<sub>3</sub> in MgO). These differences are larger than any probable variation due to compositional dependence of the  $\alpha$ -factors. This discrepancy is probably due to either the breakdown of the Philibert absorption correction at small values of  $f(x)$ ,<sup>10</sup> or errors in the values for basic constants (absorption coefficients, fluorescence yields, etc.), particularly for the lighter elements.

Compositionally dependent  $\alpha$ -factors were also calculated for each binary in a system of 25 important mineral forming oxides. As expected, nonlinearities are most significant

TABLE 2.--Empirical and theoretical alpha factors for the system MgO-CaO-Al<sub>2</sub>O<sub>3</sub>-SiO<sub>2</sub>, 15 keV, takeoff angle 38.5°. Errors are 1σ errors of the least-squares solution.

	Empirical			Theoretical		
	α = const.	α = a + bC		α = const.	α = a + bC	
	α	a	b	α	a	b
α MgO	1.086	1.089	.008	1.111	1.109	.005
α MgO-SiO <sub>2</sub>	±.006	±.009	±.006			
α MgO	1.049	1.036	.043	1.036	1.032	.011
α MgO-Al <sub>2</sub> O <sub>3</sub>	±.016	±.016	±.027			
α MgO	1.300	1.305	.011	1.336	1.330	.015
α MgO-CaO	±.030	±.027	±.018			
α SiO <sub>2</sub>	1.395	1.417	-.039	1.474	1.493	-.033
α SiO <sub>2</sub> -MgO	±.003	±.016	±.021			
α SiO <sub>2</sub>	1.452	1.466	-.031	1.539	1.552	-.036
α SiO <sub>2</sub> -Al <sub>2</sub> O <sub>3</sub>	±.006	±.011	±.025			
α SiO <sub>2</sub>	1.075	1.070	.009	1.078	1.073	.008
α SiO <sub>2</sub> -CaO	±.006	±.007	±.006			
α Al <sub>2</sub> O <sub>3</sub>	1.008	.996	.024	1.038	1.030	.014
α Al <sub>2</sub> O <sub>3</sub> -SiO <sub>2</sub>	±.017	±.015	±.016			
α Al <sub>2</sub> O <sub>3</sub>	1.702	1.747	-.114	1.767	1.832	-.092
α Al <sub>2</sub> O <sub>3</sub> -MgO	±.038	±.039	±.081			
α Al <sub>2</sub> O <sub>3</sub>	1.194	1.196	.008	1.187	1.182	.007
α Al <sub>2</sub> O <sub>3</sub> -CaO	±.026	±.022	±.009			
α CaO	1.092	1.091	-.001	1.093	1.095	-.005
α CaO-SiO <sub>2</sub>	±.008	±.008	±.008			
α CaO	1.010	1.015	-.003	1.070	1.072	-.003
α CaO-MgO	±.027	±.024	±.009			
α CaO	1.062	1.063	-.003	1.067	1.069	-.004
α CaO-Al <sub>2</sub> O <sub>3</sub>	±.015	±.014	±.009			

in systems in which characteristic fluorescence was a major effect or absorption was large. Many of the binary systems showing nonlinearity consist of unlikely combinations of elements. Even in nonlinear systems that do occur in geologic materials, the use of compositionally dependent α-factors does not make a large difference in the calculated compositions, particularly in light of the possible errors in the theoretically calculated alpha factors, as discussed above.

In summary, it has been shown that the present empirical data do not justify the inclusion of higher-order terms in the α-factor correction procedure for the system MgO-CaO-Al<sub>2</sub>O<sub>3</sub>-SiO<sub>2</sub>, and that some of the theoretically calculated alpha factors do not agree with those found empirically. In these cases, the empirical alpha factors are clearly to be preferred in the reduction of data. Finally, it appears that the use of compositionally dependent α-factors has in general an insignificant effect on the calculated compositions of most geologic materials, especially when simple silicates are used as standards.

#### References

1. T. O. Ziebold and R. E. Ogilvie, "An empirical method for electron microanalysis," *Anal. Chem.* 36: 322, 1964.
2. R. J. Traill and G. R. Lachance, "A practical solution to the matrix problem in x-ray analysis. II. Application to a multicomponent alloy system," *Can. Spectroscopy* 11: 63, 1966.



3. A. E. Bence and A. L. Albee, "Empirical correction factors for the electron microanalysis of silicates and oxides," *J. Geol.* 76: 382, 1968.
4. A. L. Albee and L. Ray, "Correction factors for electron probe microanalysis of silicates, oxides, carbonates, phosphates, and sulfates," *Anal. Chem.* 42: 1408, 1970.
5. A. E. Bence and W. Holzwarth, "Nonlinearities of electron microprobe matrix correction of the matrix effect in x-ray fluorescence analysis," *Proc. 12th MAS Conf.* 1977, 38.
6. F. Claisse and M. Quintin, "Generalization of the Lachance-Traill method for the correction of the matrix effect in x-ray fluorescence analysis," *Can. Spectroscopy* 12: 129, 1967.
7. D. Laguitton, R. Rousseau, and F. Claisse, "Computed alpha coefficients for electron microprobe analysis," *Anal. Chem.* 17: 2174, 1975.
8. M. J. Reid, A. J. Gancarz, and A. L. Albee, "Constrained least-squares analysis of petrologic problems with an application to lunar sample 12040," *Earth Planet. Sci. Letters* 17: 433, 1973.
9. J. W. Colby, "MAGIC IV: A new improved version of MAGIC," *Proc. 6th Nat. Conf. on Electron Probe Anal.*, 1971, 17A.
10. J. Philibert, "A method for calculating the absorption correction in electron probe microanalysis," *Proc. 3rd Intern. Conf. X-ray Optics and Microanalysis*, 1963, 379.

## THE USE AND ABUSE OF A QUANTITATIVE ANALYSIS PROCEDURE FOR ENERGY-DISPERSIVE X-RAY MICROANALYSIS

R. L. Myklebust and D. E. Newbury

The development of quantitative x-ray microanalysis procedures specially adapted to the use of electron excited energy-dispersive x-ray spectrometry (EDS), such as the National Bureau of Standards procedure FRAME C, has extended microanalysis capabilities beyond the classic electron probe microanalyzer (EPMA) to the EDS-equipped scanning electron microscope (SEM).<sup>1,2</sup> In employing a quantitative x-ray microanalysis procedure, the prospective analyst must always be aware of the particular limitations placed on the sample and the instrument within which the procedure is constrained to operate. The extraordinary ease with which an EDS spectrum can be obtained tends to mask the danger of errors that can arise if the required analytical conditions are compromised. It has been our experience that, despite their apparent simplicity, energy-dispersive spectrometers require as much attention to proper operation as wavelength-dispersive spectrometers. In this paper, we shall examine the errors actually observed in practical EDS analyses as a result of incorrect analytical techniques. Error propagation from a theoretical point of view has been treated previously by other authors.<sup>3,4</sup> As a starting point, we shall review the analysis conditions for FRAME C, and then consider the consequences of deviation from or inaccuracy in these conditions.

### *Use of FRAME C*

FRAME C performs the following spectral manipulations and matrix corrections: (1)  $k$  values, the ratio of characteristic intensities in the unknown and standard, are extracted from the spectra after corrections for the bremsstrahlung background and for the overlap of neighboring peaks.<sup>1,5</sup> (2) Matrix corrections are made for the effects of (a) atomic number differences between the unknown and the standards ("Z"); (b) absorption of x rays within the target ("A"); and (c) fluorescence generation of x rays by other characteristic x-rays ("F"). The FRAME C procedure is limited to x rays with an energy of 1 keV or more and is thus restricted to elements with  $Z \geq 11$  (sodium). The use of the procedure requires that the sample must be polished flat (the typical "mirror finish" of the classic EPMA specimen) and that the beam incidence angle and x-ray emergence angle are well known. In the optimal case, the sample is set normal to the electron beam, and the x-ray emergence angle is 30° or more. This condition is often difficult to obtain in an SEM where tilting is required, so the procedure includes a provision for correction for non-normal electron incidence. For tilted specimens, the detector-specimen vector, the specimen normal, and the beam vector must be co-planar; i.e., the specimen must tilt toward the EDS detector. In addition to the spectra as input, the procedure requires only the beam energy and the x-ray emergence angle. All other necessary parameters are generated during the calculations from fitted equations.

The accuracy of FRAME C applied under the specified analytical conditions is demonstrated by the analyses of the NBS Standard Reference Material (SRM) 482 gold-copper alloys, Table 1.<sup>6</sup> The spectra used for these reference analyses contained integrated peak counts whose estimated standard deviation ranged from 0.1% to 1% of the peak count. In Table 1, the average relative error (determined from the summation of the magnitudes of the individual relative errors divided by the number of elemental determinations) from the certified composition is 0.8% for analyses with the gold  $L\alpha$  x-ray line for which the absorption parameter is near unity and 1.3% for analyses with the gold  $M\alpha$  x-ray line, which suffers higher absorption. These analyses are comparable to the errors observed

---

The authors are members of the Microanalysis Group, Center for Analytical Chemistry, National Bureau of Standards, Washington, DC 20234. The authors are grateful to K. F. J. Heinrich, C. E. Fiori, and J. A. Small for many helpful suggestions.

TABLE 1.--Analysis with FRAME C under suitable conditions. Samples: NBS SRM Gold Copper Alloys. Beam: 20 keV, normal to the specimen. X-ray emergence angle: 40°.

Analysis with Cu K $\alpha$  and Au L $\alpha$

Alloy	wt% Cu certified	wt% Cu measured	relative error, %	wt% Au certified	wt% Au measured	relative error, %
20Cu80Au	19.8	19.8	0.0	80.1	79.0	-1.4
40Cu60Au	39.6	39.9	+0.8	60.3	59.4	-1.6
60Cu40Au	59.9	60.5	+1.0	40.1	40.2	+0.1
80Cu20Au	79.8	79.7	-0.1	20.1	19.9	-1.0

average relative error 0.8%

Analysis with Cu K $\alpha$  and Au M $\alpha$

20Cu80Au	19.8	19.8	0.0	80.1	80.1	0.0
40Cu60Au	39.6	29.9	+0.8	60.3	61.5	+2.0
60Cu40Au	59.9	60.5	+1.1	40.1	41.2	+2.8
80Cu20Au	79.8	79.7	-0.1	20.1	20.8	+3.5

average relative error 1.3%

by wavelength-dispersive x-ray microanalysis in an EPMA.<sup>7</sup>

*Abuse of FRAME C*

To demonstrate the consequences of improper use of FRAME C, we have chosen to examine the influence of spectral quality, uncertainty in user-supplied variables (beam energy, x-ray emergence angle, location of the background regions), and specimen condition.

1. *Spectral Quality.* The quality of the EDS spectrum for analysis can be degraded by three common problems: (a) poor statistics resulting from inadequate counting time; (b) artifacts such as pulse pile-up or failure in the deadtime correction which can appear at high count rates; and (c) errors in the energy calibration.

(a) *Poor Statistics.* The gold-copper alloys were analyzed with spectra containing peaks with an estimated standard deviation as high as 10% of the peak count. The results, given in Table 2(a), show that the quality of the analysis has significantly degraded, with the average relative error increasing by a factor of 4 to 5 compared to the reference analyses of Table 1. Note that, owing to the importance of accurate background subtraction, adequate statistics must be considered for the background regions as well as the peaks.

(b) *High Deadtime.* The analyses listed in Table 2(b) were performed with spectra obtained at high count rates resulting in deadtimes in the range 70-90%. The average error increases by a factor of 3 to 4 over the reference analyses and is slightly greater for the analyses with the low-energy gold M $\alpha$  line. This result is probably due to the greater sensitivity to pulse pile-up errors with low-energy x rays.

(c) *Errors in Spectral Calibration.* An attractive feature of EDS microanalysis is the long-term stability of the spectrometer efficiency, which makes the use of stored library spectra of standards feasible. However, the possibility of drift in the calibration with time must not be overlooked. The analyses in Table 2(c) simulate a situation in which the spectra of the standards are accurately calibrated, whereas the energy calibration of the spectra of the unknowns has been deliberately shifted by 20 eV (peak position, 20 eV low). Compared to the reference analyses, the average relative error increases by a factor of 4 as a result of this miscalibration.

TABLE 2.--Effect of spectral quality on analysis.

(a) Poor Statistics (Analysis with Au L $\alpha$  and Cu K $\alpha$ )

Alloy	wt % Cu measured	relative error, %	wt% Au measured	relative error, %
20Cu80Au	19.9	+0.5	80.8	+0.9
40Cu60Au	41.6	+4.9	62.6	+3.9
60Cu40Au	61.3	2.3	36.8	-8.1
80Cu20Au	81.1	+1.6	19.3	-3.9
average relative error 3.3%				

(Analysis with Au M $\alpha$  and Cu K $\alpha$ )

20Cu80Au	19.5	-1.5	79.2	-1.1
40Cu60Au	41.2	+4.3	59.7	-1.0
60Cu40Au	61.3	+2.3	40.9	+2.0
80Cu20Au	81.1	+1.8	21.6	+7.5
average relative error 2.7%				

(b) High deadtime (Analysis with Au L $\alpha$  and Cu K $\alpha$ )

20Cu80Au	19.4	-2.0	79.9	-0.2
40Cu60Au	37.9	-4.3	61.3	+1.7
60Cu40Au	58.8	-1.8	40.2	+0.2
80Cu20Au	78.3	-1.9	20.9	+4.0
average relative error 2.0%				

(Analysis with Au M $\alpha$  and Cu K $\alpha$ )

20Cu80Au	19.2	-3.0	82.6	+3.1
40Cu60Au	37.9	-4.3	62.8	+4.1
60Cu40Au	58.6	-2.2	42.5	+6.0
80Cu20Au	78.2	-1.9	21.7	+8.0
average relative error 4.1%				

(c) Calibration Error (-20 eV)

(Analysis with Au L $\alpha$  and Cu K $\alpha$ )

Alloy	wt % Cu measured	relative error, %	wt% Au Measured	relative error, %
20Cu80Au	19.1	-3.5	76.1	-5.0
40Cu60Au	38.7	-2.3	57.7	-4.3
60Cu40Au	58.7	-2.0	38.8	-3.2
80Cu20Au	77.2	-3.3	19.3	-4.0
average relative error, 3.5%				

TABLE 2 (Cont'd)  
(Analysis with Au  $M\alpha$  and Cu  $K\alpha$ )

20Cu80Au	19.0	-4.0	84.1	+5.0
40Cu60Au	38.8	-2.0	64.8	+7.5
60Cu40Au	58.7	-2.0	43.6	+8.7
80Cu20Au	77.2	-3.3	21.9	+9.0

average relative error, 4.8%

2. *Influence of Errors in User-supplied Variables.* (a) X-ray Emergence Angle. The results in Table 3(a) illustrate the errors that can arise as a result of the use of an incorrect value of the x-ray emergence angle. In this example, the standards have been calculated with the proper value of the x-ray emergence angle ( $40^\circ$ ), whereas the unknowns have been calculated with an incorrect value ( $30^\circ$ ). Such an error might arise in a laboratory that has several instruments with different values of the x-ray emergence angle. Although the average relative error increases only to 5.8%, the error range extends to 11% with the incorrect angle.

(b) Beam Energy. Errors in the presumed beam energy of several hundred electron volts can easily arise as a result of the difference between the indicated accelerating potential and the actual cathode potential. Table 3(b) contains analyses showing the influence of a 1keV error in the beam energy. The average relative error compared to the reference analyses increases by a factor of 2. At lower values of the overvoltage, an error in the beam energy would have a greater effect on the analysis. Note that an excellent measure of the beam energy can be obtained by determining the Duane-Hunt bremsstrahlung limit (after deconvolution for the detector smearing function).

(c) Selection of Background Regions. In order to fit the bremsstrahlung background properly, FRAME C requires the user to select two background regions clear of peak tails, spectral artifacts, etc. To demonstrate the influence of background selection, NBS SRM Fe-3.22%Si alloy was analyzed. This sample provides a demanding analysis because the Si K peak is a small perturbation on a rapidly changing background due to variations in detector efficiency. Analysis 1 in Table 3(c) demonstrates the high relative accuracy possible with proper background selection (background regions well separated and clear of peaks and spectral artifacts). In analysis 2, the low-energy background region is located on the Fe escape peak, increasing the relative error by a factor of 9. Note that the accuracy of the iron analysis is virtually unaffected, since the iron peak-to-background is very high. In analysis 3, the low energy background region is located in the low-energy roll-off, where uncertainties in the efficiency are most serious. Again, the relative error for the silicon analysis increases by a factor of 8. Finally, in analysis 4, both background regions are placed at high energy above the iron absorption edge. The relative error in the silicon analysis increases by a factor of 10, due to uncertainties in background prediction far away from the measured regions.

3. *Influence of Specimen Condition.* The fact that energy-dispersive x-ray spectra can be easily obtained from rough samples makes it very tempting to apply a quantitative x-ray microanalysis procedure to a rough sample. To study the errors that might be experienced in such a case, samples of the NBS SRM 482 gold-copper alloys were fractured ductilely, producing an irregular surface as illustrated in Fig. 1. Spectra were obtained while scanning regions approximately  $10\text{ }\mu\text{m}$  square and were processed with FRAME C with standards measured at normal incidence. The results, listed in Table 4, show that very large relative errors, up to 60%, can occur due to the geometrical effects (absorption path and electron backscattering) associated with rough targets. Even normalization of the results to force the total analysis to 100% is not a satisfactory procedure. Significant errors in excess of 20% relative are still observed after normalization, and in some cases, the errors actually increase as a result of normalization. Note that even the ratio of the compositional values of gold and copper is in large error.

#### Summary

Significant errors are introduced into energy-dispersive x-ray microanalysis with FRAME C when the required analytical conditions are not fulfilled. Although in many of

TABLE 3.--Errors in user supplied parameters.

(a) Error in x-ray emergence angle  
 (Standards at 40°, unknowns calculated at 30°)  
 (Analysis with Au M $\alpha$  and Cu K $\alpha$ )

Alloy	wt% Cu measured	relative error, %	wt% Au measured	relative error, %
20Cu80Au	20.1	+1.5	80.9	+1.0
40Cu60Au	40.8	+3.0	62.9	+4.3
60Cu40Au	61.3	+2.3	42.9	+7.0
80Cu20Au	80.3	+0.6	22.3	+10.9

average relative error 5.8%

(b) Error in beam energy (1 keV high)  
 (Analysis with Au M $\alpha$  and Cu K $\alpha$ )

20Cu80Au	20.0	+1.0	80.4	+0.4
40Cu60Au	40.4	+2.0	61.8	+2.4
60Cu40Au	61.1	+2.0	41.3	+3.0
80Cu20Au	80.3	+0.6	21.0	+4.5

average relative error 2.0%

(c) Selection of background regions

Sample: SRM Fe-3.22% Si

Beam: 20 keV, normal incidence

X-ray emergence angle: 40°

Analysis	wt% Si measured	relative error, %	wt% Fe measured	relative error, %	Comments on background
1	3.25	+0.9	97.1	+0.3	Good locations, 2.5 keV, 8.0 keV
2	2.97	-7.9	97.0	+0.2	Low region on Fe escape peak High region 8.0 keV
3	2.99	-7.1	97.0	+0.2	Low region on roll-off, 1.3 keV High region 8.0 keV
4	3.51	+9.0	97.2	+0.4	Both regions at high energy, 7.5 and 9.5 keV

the above cases the increase in the relative error caused by improper conditions may not seem excessive, the spectra used in this study are free from significant overlaps and the analyses involved x-ray energies in excess of 2 keV. In cases where significant peak overlap or high absorption occurs, the errors introduced by improper analysis conditions can be expected to be considerably greater.

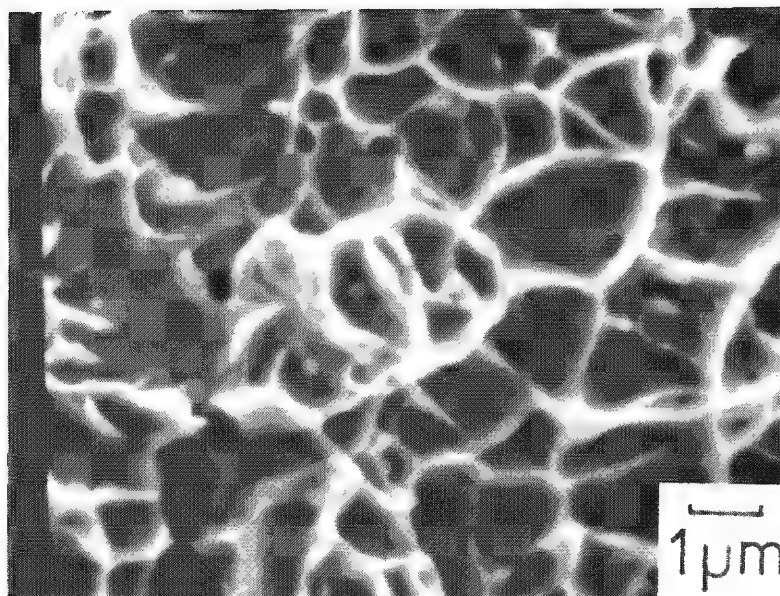


FIG. 1.--Scanning electron micrograph of a typical region on fractured gold-copper alloy.

TABLE 4.--Analysis of rough surfaces.

Beam: 20 keV, normal incidence on standards

Alloy 40Cu60Au

(Analysis with Au L $\alpha$  and Cu K $\alpha$ )

Analysis	wt % Cu measured	relative error, %	wt % Au measured	relative error, %
1	29.9	-24	34.8	-42
2	23.9	-40	22.3	-63
3	18.8	-53	32.9	-45
4	28.2	-29	28.7	-52

Analyses normalized to 100%

1	46.2	+17	53.7	-11
2	51.7	+31	48.2	-20
3	36.3	-8.3	63.5	+5.4
4	49.6	+25	50.5	-16

Alloy 20Cu80Au

(Analysis with Au L $\alpha$  and Cu K $\alpha$ )

1	17.6	-11	36.2	-55
2	39.2	+98	106	+32
3	23.5	+19	50.0	-38
4	25.3	+28	58.0	-28

Analyses normalized to 100%

1	32.7	+65	67.2	-16
2	27.0	+36	73.1	-8.7
3	31.8	+61	67.6	-16
4	30.4	+53	69.6	+13

Each sample was analyzed in four different areas.

## References

1. R. L. Myklebust, C. E. Fiori, and K. F. J. Heinrich, "FRAME C: A compact procedure for quantitative energy-dispersive electron probe x-ray analysis," *Proc. 12th MAS Conf.*, 1977, 96.
2. R. L. Myklebust, C. E. Fiori, and K. F. J. Heinrich, "FRAME C: A compact procedure for quantitative energy-dispersive electron probe x-ray analysis," NBS Technical Note (in press).
3. K. F. J. Heinrich and H. Yakowitz, "Propagation of errors in correction models for quantitative electron probe microanalysis," *Proc. 5th Intern. Conf. X-ray Optics and Microanalysis*, Berlin: Springer-Verlag, 1969, 151-159.
4. K. F. J. Heinrich, "Errors in theoretical correction systems in quantitative electron probe microanalysis: A synopsis," *Analyt. Chem.* 44: 350-354, 1972.
5. C. E. Fiori, R. L. Myklebust, K. F. J. Heinrich, and H. Yakowitz, "Prediction of continuum intensity in x-ray dispersive microanalysis," *Analyt. Chem.* 48: 172-176, 1976.
6. Standard reference materials are available from the Office of Standard Reference Materials, National Bureau of Standards, Washington, DC 20234.
7. K. F. J. Heinrich, R. L. Myklebust, S. D. Rasberry, and R. E. Michaelis, "Preparation and evaluation of SRM's 481 and 482 gold-silver and gold-copper alloys for microanalysis," NBS SP 260-28, Washington, D.C: National Bureau of Standards, 1971.



## QUANTITATIVE ANALYSIS BY $\phi(\rho z)$ CURVES

J. D. Brown and W. H. Robinson

The most popular correction procedure for quantitative analysis in use today is the ZAF technique. A measured intensity ratio is corrected for differences in electron stopping power, backscattering, x-ray absorption, and fluorescence when these phenomena differ in the specimen and the pure element standard. This technique has been obtained from simple physical models which have grown in complexity to account for the available experimental evidence. Many of the parameters involved are not precisely known and models continue to be introduced to increase the accuracy of analysis.

An alternative method for quantitative analysis is available if the depth distribution of primary X-ray production is known. As shown by Castaing,<sup>1</sup> the measured intensity ratio  $K$  for element  $A$  is

$$K_A = W_A \frac{\int_0^\infty \phi_A(\rho z) \exp(-\mu_A^A \rho z \csc \psi) d(\rho z)}{\int_0^\infty \phi_S(\rho z) \exp(-\mu_A^S \rho z \csc \psi) d(\rho z)} \quad (1)$$

where  $\phi_A(\rho z)$  and  $\phi_S(\rho z)$  are the depth distribution of primary x-ray intensity for the specimen and the pure element standard, respectively;  $W_A$  is the weight fraction of  $A$  in the specimen;  $\mu_A^A$  and  $\mu_A^S$  are the mass absorption coefficients for the radiation of  $A$  in the specimen and in the standard; and  $\psi$  is the x-ray take-off angle. The equation above is exact and  $W_A$  may be calculated if  $\phi(\rho z)$  can be determined. An empirical formula (Eq. 2) suggested by Brown and Parobek<sup>2</sup> for low electron energies (less than 15 keV) accurately describes  $\phi(\rho z)$  for utilizing Eq. (1) and shows better agreement between calculated and known concentrations for analysis of standards reported in the literature. This formula for describing  $\phi(\rho z)$  curves has now been extended to higher electron energies of 15-30 keV. Knowledge of four readily available parameters is required to determine the  $\phi(\rho z)$  function: atomic number  $Z$ , atomic weight  $A$ , electron energy  $E_0$ , and the absorption edge energy  $E_c$  for the characteristic line measured.

The formulas that model the  $\phi(\rho z)$  curves are based on experimental evidence obtained with the sandwich sample technique proposed by Castaing and Descamps.<sup>3</sup> A tracer element is deposited at varying depths within a matrix element. The change in intensity from the tracer layer in the matrix as a function of depth when compared to a thick pure element standard indicates the shape of the  $\phi(\rho z)$  curve. The value of  $\phi(\rho z)$  at zero depth is the ratio of the intensity of the tracer layer on the matrix to intensity of an identical tracer layer that is isolated in space. Some experimentally determined values of  $\phi(0)$  are available in the literature as well as several models based on backscatter coefficient and overvoltage. Measured intensity ratios of the tracer in the matrix to a thick pure element standard are adjusted to the proper magnitude on the basis of the  $\phi(0)$  value.

Experimental  $\phi(\rho z)$  data measured by Brown and Parobek consist of the tracer and matrix elements shown in Table 1. The characteristic lines that were employed are indicated. Measurements are at normal incidence for electron energies of 15, 20, 25, and 30 keV. Intensity measurements were corrected for dead time, background, drift, and absorption by the overlying matrix layers.

---

The authors are with the Faculty of Engineering Science and The Centre for Interdisciplinary Studies in Chemical Physics, The University of Western Ontario, London, Canada.

TABLE 1.--Sandwich samples.

	Matrix			
	Au	Ag	Cu	Al
Tracer	Bi	L $\alpha$ M $\alpha$	L $\alpha$ M $\alpha$	L $\alpha$ M $\alpha$
	Cd	L $\alpha$	L $\alpha$	L $\alpha$
	Zn		K $\alpha$	K $\alpha$
	Si	K $\alpha$	K $\alpha$	K $\alpha$

The  $\phi(\rho z)$  curve may be modelled by the equation

$$\phi(R) = DKn(KR)^{n-1} \exp[-(KR)^n] \quad (2)$$

where  $R = \rho z + \rho z_0$ . The parameters  $D$ ,  $K$ ,  $n$ , and  $\rho z_0$  are obtained from an optimizing routine known as Simplex that fits Eq. (2) to the experimental data, so that the differences between the equation and the data are minimized. These parameters  $D$ ,  $K$ ,  $n$ , and  $\rho z_0$  are then solved in terms of  $Z$ ,  $A$ ,  $E_0$ , and  $E_c$  and are described by the following equations:

$$n = \frac{1.95 A}{Z^{1.32}} \quad K = \frac{BF}{(E_0 - E_c)^m}$$

where  $B = 0.5409/E_c^{1.228}$ ,  $F = 1 + [0.05199Z^{0.7}/\exp(0.0002Z^2)]$ , and  $m = (15.6578/E_c)^{0.2505}$ ;

$$D = Q(E_0 - E_c)^P$$

where  $Q = 0.5945 E_c^{1.42} Z^{0.26}$  and  $P = 2.111(1.84/E_c)^{0.325}$ ;

$$\rho z_0 = \frac{24.487 E_0 E_c^{0.428}}{Z^{1.259}} \left[ 1 + \frac{1}{\exp(0.0015Z)} \right]$$

The depth distribution of x-ray production for many systems has been calculated by means of the above equations. When applied to quantitative analysis by Eq. (1), the technique performs well. The parameters  $D$ ,  $K$ ,  $n$ , and  $\rho z_0$  are determined by the average atomic number and atomic weight of the matrix, the electron energy, and the characteristic line measured. The  $\phi(\rho z)$  curve predicted from Eq. (2) may then be numerically integrated and used to predict the concentration  $W_A$ . This procedure has been compared with other methods of analysis compiled by Poole.<sup>4</sup> Typical results are shown in Table 2.

The equations for predicting  $\phi(\rho z)$  curves for electron energies from 15 to 30 keV yield good results when applied to quantitative analysis and provide an attractive alternative to the popular ZAF techniques.

#### References

1. R. Castaing, "Electron probe microanalysis," *Adv. Electron. Electron Phys.* 13:317, 1960
2. L. Parobek and J. D. Brown, "The atomic number and absorption corrections in electron microprobe analysis at low electron energies," *X-ray Spect.* 7:26, 1978; errata 8: v, 1979.

TABLE 2.--Comparison of relative errors of analysis.

Specimen	Analytical	$E_0$	$W_A$	Percentage relative errors using method of					
				This Paper	Z and O	Belk	Thomas	Duncumb	Smith
Cu Au	Cu $K\alpha$	30	.794	+2.8	-3.0	+0.7	+0.8	-1.5	-6.1
			.585	-4.8	-7.7	0	+0.8	-4.5	-10.1
			.386	-4.5	-12.5	-1.0	+1.3	-7.2	-12.6
			.194	-2.0	-16.8	-1.5	+3.0	-10.0	-13.8
Ag Au	Ag $L\alpha$	30	.801	-3.6	-12.1	-11.9	-5.9	-8.2	-11.5
			.595	-6.4	-22.4	-18.6	-10.8	-13.4	-18.4
			.406	-9.1	-31.0	-25.4	-15.0	-19.4	-24.9
			.196	-5.0	-33.0	-26.8	-12.8	-20.0	-25.6
Al <sub>3</sub> Ti	Al $K\alpha$	15	.628	-4.1	-16.2	-10.6	-3.5	-2.4	-11.1
		20	.628	-4.6	-23.6	-19.3	-8.7	-9.1	-18.1
		25	.628	-5.2	-29.7	-26.8	-12.5	-15.3	-23.8
		30	.628	-4.3	-32.3	-30.4	-12.5	-18.3	-25.4
		25	.628	-1.4	-31.2	-29.9	-9.3		-22.5

3. R. Castaing and J. Descamps, *J. Phys. Radium* 16:304, 1960.

4. D. M. Poole, "Progress in the correction for the atomic number effect," in K. F. J. Heinrich, Ed., *Quantitative Electron Probe Microanalysis*, Washington, D. C.: National Bureau of Standards, Special Publication 298, 1968.

## QUANTITATIVE CARBON ANALYSIS FROM $\phi(\rho z)$ CURVES

J. D. Brown, A. P. von Rosenstiel, and T. Krisch

The usual methods of quantitative electron probe microanalysis based on the absorption correction of Philibert<sup>1</sup> and the atomic number correction of Philibert and Tixier<sup>2</sup> or Duncumb and Reed<sup>3</sup> become increasingly inaccurate as the electron energy and the characteristic line energy decrease. The situation is particularly bad for electron energies below 10 keV and wavelengths greater than 1.0 nm. As an alternate approach to quantitative analysis in this region we have used the equation of Parobek and Brown<sup>4</sup> to calculate both the atomic number and absorption corrections in the analysis of carbides.

### Measurements

Carbides of tungsten, iron, titanium, chromium, boron, and molybdenum were prepared as standards by precipitating the known carbide phases from the pure element into which carbon was dissolved at high temperature. The characteristic x-ray intensities were measured in an ARL electron microprobe at 6, 8, 10, and 12.5 keV. An oxygen gas jet was used to prevent the build-up of carbon during the analysis. Pure element standards were used for all elements except for carbon and boron. For the carbon, Fe<sub>3</sub>C was used as standard. No measurements were made on the BK $\alpha$  line. A summary of the relative intensities measured for each carbide is given in Table 1.

TABLE 1.--Measured relative intensities corrected for background and dead time.

Specimen	Line	Relative Intensities			
		6 KeV	8 KeV	10 KeV	12.5 KeV
Fe <sub>3</sub> C	FeK $\alpha$	-	0.888	0.925	0.931
	CK $\alpha$ *	1.0	1.0	1.0	1.0
TiC	TiK $\alpha$	-	-	0.867	0.849
	CK $\alpha$ *	4.151	-	5.149	5.334
Cr <sub>2</sub> C <sub>3</sub>	CrK $\alpha$	-	0.892	0.872	0.876
	CK $\alpha$ *	2.549	2.693	2.859	3.009
MoC	MoL $\alpha_1$	0.958	0.923	0.934	0.922
	CK $\alpha$ *	0.879	0.755	0.775	0.769
WC	WM $\alpha_1$	0.914	0.882	0.910	0.907
	CK $\alpha$ *	1.032	1.010	0.953	0.951
B <sub>4</sub> C	CK $\alpha$ *	1.198	0.965	0.870	0.769

\*CK Measured relative to the intensity from Fe<sub>3</sub>C

J. D. Brown is in Engineering Science at the University of Western Ontario in London; A. P. von Rosenstiel and T. Krisch are with the Metaalinstituut TNO, Apeldoorn, The Netherlands.

### Calculations

A computer program was written in FORTRAN to calculate relative intensities from composition and measurement parameters based on the  $\phi(\rho z)$  equation of Parobek and Brown.<sup>4</sup> The relative intensity for each line is calculated by numeric integration of the  $\phi(\rho z)$  equation over 100 increments of depth in the specimen. To obtain the final concentrations, iterations are performed by means of a hyperbolic approximation<sup>5</sup> to obtain agreement between calculated and measured relative intensities. Features of the program include the provision for up to 10 elements in a specimen, calculations using compound standards, the possibility of determining one element by difference, and internal calculation of mass-absorption coefficients based on the coefficients of Heinrich.<sup>6</sup>

A major problem in any analysis of carbon compounds is the choice of mass absorption coefficients for the  $\text{CK}\alpha$  line. Table 2 lists the values used in this paper. These are taken from the plot of  $\mu/\rho$  versus atomic number in a compilation of published data of Weisweiler.<sup>7</sup>

TABLE 2.--Mass absorption coefficients for carbon  $\text{K}\alpha$  line.

Absorber	$\mu/\rho$ ( $\text{cm}^2/\text{g}$ )
B	33000
C	2280
Ti	6550
Cr	10500
Fe	11500
Mo	12500
W	10000

### Results and Discussion

The results of the calculations show that when the absorption coefficient is very large only x rays generated very near the surface of the specimen manage to escape and the most important factor affecting the observed intensity is the magnitude of the mass absorption coefficient. That is particularly important when considering the calculation for the carbon  $\text{K}\alpha$  line. For the characteristic line of the metallic elements, the absorption in carbon is generally less than in the element itself. On the basis of absorption alone, one expects a relative intensity that is greater than the weight fraction. However, the off-setting factor, which is the atomic number effect, dominates for many of the carbides, as can be seen in Table 1. Good agreement has been obtained between the known stoichiometric concentrations and the calculated concentrations by this approach. The method will be applied to mixed carbides where stoichiometry is unknown as an aid in understanding the formation and composition of carbides in low-alloy steels.

### References

1. J. Philibert, *Proc. 3rd Intern. Congress on X-ray Optics and Microanalysis*, New York: Academic Press, 1963, 379-392.
2. J. Philibert and R. Tixier, Special Publication 298, Washington, D.C: National Bureau of Standards, 1968, 13-33.
3. P. Duncumb and S. J. B. Reed, *ibid.*, 133-154.
4. L. Parobek and J. D. Brown, *X-ray Spectrometry* 7: 27, 1978; errata 8: v, 1979.
5. J. W. Criss and L. S. Birks, in T. D. McKinley, K. F. J. Heinrich, and D. Wittry, Eds., *The Electron Microprobe*, New York: John Wiley, 1966, 217-236.
6. K. F. J. Heinrich, *ibid.*, 296-377.
7. W. Weisweiler, *Mikrochim. Acta* 64: 744, 1970.

# ANALYSIS OF PARTICLES AND ROUGH SAMPLES BY FRAME P, A ZAF METHOD INCORPORATING PEAK-TO-BACKGROUND MEASUREMENTS

J. A. Small, D. E. Newbury, and R. L. Myklebust

The ideal specimen for electron probe microanalysis has the form of a bulk solid with a flat, polished surface. When samples are analyzed that deviate from this condition, such as small particles or specimens with rough surface topography, large errors in the composition calculated from a ZAF method can arise, frequently exceeding 50% relative.<sup>1</sup> Moreover, normalization of the results by forcing of the sum of the elements to 100% can sometimes actually increase the relative errors. Nevertheless, there is great interest in the quantitative analysis of particles and rough samples because of their importance in technology and the environmental sciences.

Providing instrumental conditions are kept constant, the x-ray intensities measured on a flat, bulk sample vary for compositional reasons only. However, for a particle or rough surface geometrical factors, including size and shape of the sample relative to the electron interaction volume and x-ray emergence angle, can also strongly affect the measured signals. Previous attempts to generalize ZAF methods to such objects have generally produced complicated analytical models that require significant subjective operator input, such as estimation of the shape of the object.<sup>2</sup> Recently, a new method for compensation of the geometrical effects has been independently suggested by Small et al.<sup>3</sup> and Statham and Pawley.<sup>4</sup> This method is based on the observation that, to a first approximation, the ratio of a characteristic x-ray peak to the continuum intensity of the same energy for a flat, bulk target is equivalent to the ratio from a particle or rough surface of the same composition:

$$(P/B)_{\text{particle}} = (P/B)_{\text{bulk}} \quad (1)$$

where P is the background-corrected peak and B is the continuum intensity for the same energy window as the peak. We have incorporated Eq. (1) into a standard ZAF method, FRAME C, in the following manner.<sup>3,5</sup> A modified peak intensity P\* is determined that would be the intensity observed in the absence of geometrical effects (i.e., if the particle or rough surface could be transformed into a flat, polished target):

$$P^* = P_{\text{bulk}} = P_{\text{particle}} \times B_{\text{bulk}}/B_{\text{particle}} \quad (2)$$

where  $P_{\text{particle}}$  and  $B_{\text{particle}}$  are measured intensities of the characteristic and continuum x rays at each energy of interest in the spectrum of the unknown.  $B_{\text{bulk}}$  cannot be directly measured since, in general, the analyst has no bulk solid of the same composition of the unknown;  $B_{\text{bulk}}$  is estimated as part of the iterative loop of a ZAF scheme from the current estimate of the concentration  $C_i$ :

$$B_{\text{bulk}} = \sum_i C_i B_{i,E} \quad (3)$$

where  $B_{i,E}$  is the continuum from a pure element standard at the energy, E, of interest. A k value corrected for geometric effects,  $k^*$ , is finally calculated as:

$$k^* = P^*/P_{\text{standard}} = P_{\text{particle}}/P_{\text{standard}} \times B_{\text{bulk}}/B_{\text{particle}} \quad (4)$$

The authors are with the Center for Analytical Chemistry, National Bureau of Standards, Washington, D.C. They would like to thank Dr. K. F. J. Heinrich for his assistance in the development of this method.

Various methods for evaluating Eq. (3) are currently being tested. In the simplest approach, the pure-element continuum spectra are directly measured. In more elaborate and more flexible schemes, mathematical descriptions of the continuum generation as a function of beam energy, continuum energy, and atomic number are being tested.

### Results

Several preliminary results have been obtained that indicate the potential of the peak-to-background method.

*Particles.* Various types of mineral particles have been analyzed with the peak-to-background method. The results of these analyses are reported in Table 1, along with the results determined with the conventional ZAF routine, FRAME C. In all cases the analyses

TABLE 1.--Analysis of mineral particles with FRAME P and FRAME C.

	Talc Particles(15kV 40° Take-Off-Angle)			
	Mg(wt. frac.) $\pm\sigma$	Rel. Error(%)	Si(wt. frac.) $\pm\sigma$	Rel. Error(%)
Stoic*	0.193		0.298	
FRAME C	0.103 $\pm$ 0.057	-47.	0.158 $\pm$ 0.087	-47.
FRAME P	0.185 $\pm$ 0.009	- 4.	0.290 $\pm$ 0.016	- 3.
	FeS <sub>2</sub> Particles(20kV 40° Take-Off-Angle)			
	S(wt. frac.) $\pm\sigma$	Rel. Error(%)	Fe(wt. frac.) $\pm\sigma$	Rel. Error(%)
Stoic*	0.534		0.466	
FRAME C	0.399 $\pm$ 0.081	-25.	0.358 $\pm$ 0.067	-23.
FRAME P	0.529 $\pm$ 0.024	- 0.9	0.464 $\pm$ 0.029	- 0.4
	ZnS Particles(20kV 40° Take-Off-Angle)			
	S(wt. frac.) $\pm\sigma$	Rel. Error(%)	Zn(wt. frac.) $\pm\sigma$	Rel. Error(%)
Stoic*	0.329		0.671	
FRAME C	0.303 $\pm$ 0.046	- 8.	0.551 $\pm$ 0.064	-18.
FRAME P	0.360 $\pm$ 0.027	+ 9.	0.676 $\pm$ 0.049	- 0.7

\*Stoichiometric concentration.

Lines used: Mg K, Si K, S K, Fe K $\alpha$ , Zn K $\alpha$

with FRAME P are within a 10% relative error of the stoichiometric values. In contrast, the errors with FRAME C range from 7.9% for S in ZnS to 47% for Mg and Si in talc. In addition, the standard deviations for individual measurements are less for FRAME P than they are for FRAME C.

*Rough Surfaces.* To test FRAME P on rough surfaces, specimens were needed that were homogeneous on the micrometer scale to eliminate any possible composition variation. To achieve this condition, samples of NBS Standard Reference Material Microprobe Standards (Au-Cu alloys, Fe-3.22%Si) were fractured, which produced rough surfaces such as those shown in Fig. 1. Several analyses from these samples are listed in Table 2. These analyses demonstrate the large errors that can be observed in the analysis of a rough surface with a conventional ZAF routine that does not incorporate geometrical corrections. The errors are still substantial, even after normalization, which occasionally makes the errors greater. Geometrical correction by the peak-to-background method leads to significant improvement.

TABLE 2.--Analysis of fracture surfaces.

	60Au-40Cu (nominal) SRM 482				Rel. Error (%)	FRAME P (wt.%)	Rel. Error (%)
	Actual (wt.%)	FRAME C (wt.%)	Rel. Error (%)	FRAME C (wt.%) Normalized			
Analysis 1							
Au	60.3	28.2	-53.	49.6	-18.	58.0	- 4.
Cu	39.6	28.7	-28.	50.4	+27.	44.0	+11.
Analysis 2							
Au	60.3	1.08	-98.	29.1	-52.	52.0	-14.
Cu	39.6	2.63	-93	70.8	+79.	41.0	+ 3.5
80Au-20Cu (nominal) SRM 482							
Analysis 1							
Au	80.1	95.8	+20.	73.8	- 8.	76.9	- 4.
Cu	19.8	34.0	+72.	26.2	+32.	19.1	- 3.5
Analysis 2							
Au	80.1	43.3	-46.	69.3	-13.	76.7	-4.2
Cu	19.8	19.1	- 3.5	30.6	+55.	20.1	+1.5
Fe-3.22Si (nominal) SRM 483							
Analysis 1							
Fe	96.8	97.5	+ 0.7	97.0	+ 0.2	100.	+ 3.3
Si	3.22	2.97	- 8.	2.95	- 8.2	3.21	- 0.3
Analysis 2							
Fe	96.8	97.5	+ 0.7	96.4	- 0.4	97.7	+ 0.9
Si	3.22	3.61	+12.	3.57	+11.	3.46	+ 7.4

Instrumental conditions: 20kV 40° Take-Off-Angle.

Lines used: Au M $\alpha$ , Cu K $\alpha$ , Si K, Fe K $\alpha$ .

FRAME P consists of a relatively minor alteration to the conventional ZAF routine, FRAME C, and requires no additional input beyond that required for a conventional analysis. The results from the analysis on both mineral particles and rough surfaces are in good agreement with known compositions and in most cases show a definite improvement over the results determined by FRAME C.

#### References

1. R. L. Myklebust and D. E. Newbury, "The use and abuse of a quantitative analysis procedure for energy-dispersive x-ray microanalysis," *Proc. 14th MAS Conf.*, 1979, 231.
2. J. T. Armstrong and P. R. Buseck, "Quantitative chemical analysis of individual microparticles using the electron microprobe: Theoretical," *Anal. Chem.* 47: 2178-2192, 1975.
3. J. A. Small et al., "The production and characterization of glass fibers and spheres for microanalysis," *Scanning Electron Microscopy*, AMF O'Hare, Ill.: SEM Inc., 1978, 1: 445-454.
4. P. Statham and J. Pawley, "A new method for particle x-ray micro-analysis based on peak-to-background measurement," *ibid.*, pp. 469-478.
5. J. A. Small et al., "Progress in quantitation of single-particle analysis with the electron probe," *Proc. 13th MAS Conf.*, 1978, 56.



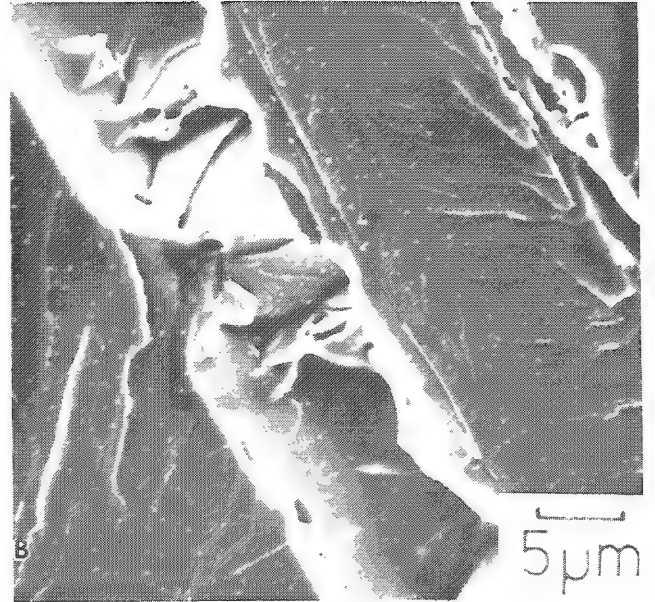
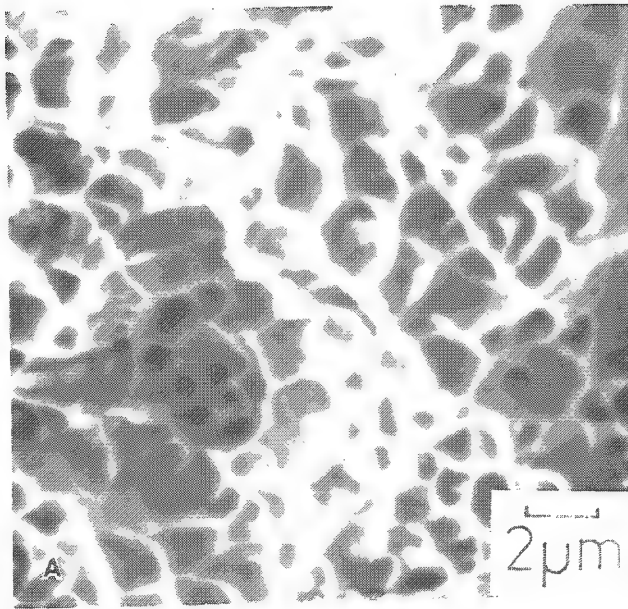


FIG. 1.--Secondary-electron images of rough surfaces analyzed by FRAME P.

## A ZAF PROCEDURE FOR MICROPROBE ANALYSIS BASED ON MEASUREMENT OF PEAK-TO-BACKGROUND RATIOS

P. J. Statham

In conventional microprobe analysis, the atomic number, absorption, and fluorescence (ZAF) corrections applied to characteristic line intensities are subject to uncertainties in both the theory and the fundamental parameters used to evaluate correction formulae. We achieve accuracy by arranging experimental conditions so as to minimize the magnitude of the required correction, or by use of standards similar in composition to the sample. In situations where absorption is severe, or where the topography is complex, detailed investigation can lead to improved correction models,<sup>1,2</sup> but the dependence on fundamental parameters such as absorption coefficients and the necessity to define geometry precisely still remain. With electron-beam excitation, the bremsstrahlung background typically constitutes about 50% of the total emitted intensity and the potential for using this signal in microanalysis has already been recognized.<sup>3-7</sup>

Since the ratio of characteristic to continuous radiation intensity is less sensitive to absorption and backscatter effects than the characteristic intensity alone, a ZAF procedure based on peak-to-local-background ratios (P/B) rather than peak intensities should involve smaller (and therefore less critical) correction factors. As a starting point, an apparent concentration,  $C_i'$  is defined for element  $i$  from measurements on both the specimen and a standard of known composition:

$$C_i' = \frac{(P/B)_i^{\text{Spec}}}{(P/B)_i^{\text{Std}}} C_i^{\text{Std}} \quad (1)$$

$C_i'$  is related to the true concentration  $C_i$  by

$$C_i = C_i' \frac{(f_{\text{ZAF}})_i^{\text{Std}}}{(f_{\text{ZAF}})_i^{\text{Spec}}} \quad (2)$$

where the correction factor  $f_{\text{ZAF}}$  can be considered as the product  $f_Z \cdot f_A \cdot f_F$ , as in the conventional procedure. These factors are discussed below in relation to the analysis of bulk samples.

### Atomic Number Correction

The atomic number correction  $f_Z$  is most significant in the P/B approach because the intensity of the continuum is directly affected by the overall matrix composition, whereas characteristic line intensities are primarily governed by the concentrations of component elements. According to the Sommerfeld theory,<sup>8</sup> the bremsstrahlung intensity from a thin foil is proportional to  $Z^2$ . For every increment of path length in a bulk specimen, the intensity scales in the same way and in a compound is therefore proportional to the mean  $Z^2$ , weighted according to the atomic concentrations of the constituents or equivalently to a "g-factor" defined by

$$g_{\text{spec}} = \sum_i C_i Z_i^2 / A_i \quad (3)$$

---

The author is with Link Systems Ltd., Halifax Road, High Wycombe, Bucks, England HP12 3SE.

where  $A_i$  is the atomic weight of element  $i$ .

The average intensity along an electron path is given by

$$\int_{\text{path}} Q_w dx \approx \int_{E_0}^{E_v} \frac{Q_w}{S} dE \quad (4)$$

where  $Q_w$  is the cross section for continuum generation,  $E_v$  is the energy of the x rays of interest,  $E_0$  is the incident electron energy in keV, and  $S$  is the "stopping power" given by the Bethe expression

$$S = 7.85 \times 10^4 \frac{1}{E} \frac{Z}{A} \ln(1.166E/J) \quad (5)$$

The product  $(Q_w E/Z^2)$  can be fairly well represented by a universal function of  $E_v/E$  which varies quite slowly with energy.<sup>9</sup> Thus, the argument of the integral in Eq. (4) is again a slow function of energy, which suggests that the "stopping power correction" can be simply evaluated at a mean energy  $E = (E_0 + E_v)/2$  as is commonly done in ZAF correction schemes. In the absence of backscatter and absorption effects, Eqs. (3) and (5) imply that the intensity of the continuum for pure elements is thus given by

$$I_w \propto \frac{Z}{\ln(101.4 E/Z)} \quad (6)$$

where the approximation  $J = 11.5Z$  eV has been used for the "mean ionization potential."

In Fig. 1, this formula is compared with experimental measurements of Rao-Sahib and Wittry<sup>10</sup> and an empirical formula proposed by Smith et al.<sup>11</sup> for the case of 11keV continuum radiation excited by a 20kV electron beam. For these conditions, Eq. (6) appears to predict the  $Z$  variation fairly well, and although more results are obviously needed to check the dependence (particularly for  $\bar{E} < Z/10$ , where the formula is more suspect), the use of a simple stopping-power correction seems justified. Therefore, when the ratio of characteristic to continuum radiation is considered, the respective stopping-power factors will be assumed to cancel, leaving only the  $g$ -factor for continuum generation.

For characteristic radiation, electrons of energy  $E$  produce radiation intensity proportional to  $(U - 1)^{1.63}$ , where  $U = E/E_c$ ,<sup>12</sup> whereas for continuum radiation, the same electrons produce intensity proportional to  $(U' - 1)$ , where  $U' = E/E_v$ <sup>13</sup> and  $E_v$  in most cases close to the critical excitation potential  $E_c$ . Therefore, the ratio of fractional losses due to backscattering is given by

$$\frac{1 - R_w}{1 - R_c} = \frac{\left[ \int_{E_v}^{E_0} \frac{dn}{dE} (U' - 1) dE \right] / (U' - 1)}{\left[ \int_{E_c}^{E_0} \frac{dn}{dE} (U - 1)^{1.63} dE \right] / (U - 1)^{1.63}} \quad (7)$$

where  $R_w$  and  $R_c$  are the backscatter correction factors for continuum and characteristic radiation, respectively, and  $(dn/dE)$  is the differential backscattering coefficient. Working from this equation, calculated values of  $R_w$ <sup>10</sup> and  $R_c$ ,<sup>14</sup> and observations made by Love et al.<sup>15</sup> on the backscatter correction, one can derive the following relationship:

$$\frac{1 - R_w}{1 - R_c} = \left( \frac{2}{1 + \eta} \right)^{0.63} (0.79 + 0.44E_v/E) \quad (8)$$

where  $\eta$  is the backscatter coefficient for the specimen. Thus, the ratio  $R_c/R_w$  can be calculated from an estimate of the backscatter correction for characteristic radiation  $R_c$ , and the overall atomic number correction is then given by

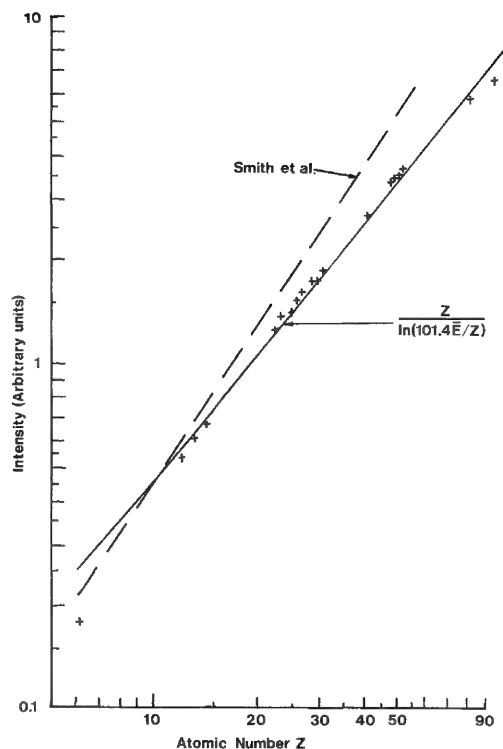


FIG. 1.--Atomic number dependence of continuum intensity for 11keV photons excited by 20kV incident electrons. Experimental data (+) of Rao-Sahib and Wittry<sup>10</sup> are compared with empirical formula  $Z^n$  suggested by Smith *et al.*,<sup>11</sup> where  $n = 1.159 + (0.1239 - 0.02857 \ln E_0)(E_v - 2.044)$ , and the theoretical formula  $Z/\ln(101.4 \bar{E}/Z)$  given by Eq. (6) in text, where  $\bar{E} = (E_0 + E_v)/2 = 15.5$  keV.

or thin film than for a bulk specimen.<sup>5</sup> In terms of the present discussion, this difference is due to the change in  $R_C/R_W$ , since the backscattered electron distribution is drastically altered when electrons are lost by transmission as well as reflection. Ideally, one would attempt to adjust  $R_C/R_W$  according to the mass thickness of the sample, but we can obtain satisfactory results by using particle standards and ignoring the backscatter effect.<sup>5</sup> Both the absorption and fluorescence corrections should also contain terms to accommodate different particle sizes, since no corrections are needed for very small particles. Indeed application of an inappropriate fluorescence correction can give errors as high as 6% relative, as shown by Small *et al.*<sup>4</sup> In summary, the overall correction factor varies from  $1/g \times (R_C/R_W)$  for small particles and thin films to  $f_{ZAF}$  for bulk specimens.

#### Anisotropy

The bremsstrahlung radiation distribution is peaked in the forward beam direction for thin films and small particles, and anisotropy is still likely to be apparent in the radiation from bulk specimens. The  $Z^2$ -dependence of intensity (Eq. 3) arises from consideration of the total radiated continuum; it is likely that the form of the  $Z^2$ -dependence will be a function of the incident-beam/sample/detector configuration. Although it is desirable to view the specimen from the same side as the incident beam to improve the peak-to-background ratio and hence detection limits for trace elements, there may be some justification in placing the detector beneath the specimen in order to accentuate the background for the

$$f_Z = \frac{1}{g_{\text{spec}}} \frac{R_C}{R_W} \quad (9)$$

#### Absorption

The mean depth for production of bremsstrahlung exceeds that for characteristic radiation because the ratio of cross sections is greater for low electron energies. The parameter concerned with electron penetration in the absorption correction formula should therefore be increased<sup>9</sup> and Monte Carlo calculations<sup>16</sup> affirm that the ratio of absorption corrections can be adequately represented by the formula<sup>17</sup>

$$f_A = f(\chi)_C / f(\chi)_W = \frac{1 + 3.34 \times 10^{-6}x + 5.59 \times 10^{-13}x^2}{1 + 3.00 \times 10^{-6}x + 4.50 \times 10^{-13}x^2} \quad (10)$$

where  $x = (\bar{\mu}/\rho) \csc \psi (E_0^{1.65} - E_v^{1.65})$ ,  $\psi$  is the effective take-off angle for x rays, and  $(\bar{\mu}/\rho)$  is the mass absorption coefficient in  $\text{cm}^2/\text{g}$ .

#### Fluorescence

Since there is no fluorescence effect to consider for bremsstrahlung, the fluorescence correction is the same as for characteristic radiation and the formulas suggested by Reed<sup>18</sup> can be used for  $f_F$  when fluorescence by the continuum is negligible.

#### Modifications for Particle Analysis

Because of the difference in cross sections,  $(P/B)$  is greater for a small particle than for a bulk specimen. In terms of the present discussion, this difference is due to the change in  $R_C/R_W$ , since the backscattered electron distribution is drastically altered when electrons are lost by transmission as well as reflection. Ideally, one would attempt to adjust  $R_C/R_W$  according to the mass thickness of the sample, but we can obtain satisfactory results by using particle standards and ignoring the backscatter effect.<sup>5</sup> Both the absorption and fluorescence corrections should also contain terms to accommodate different particle sizes, since no corrections are needed for very small particles. Indeed application of an inappropriate fluorescence correction can give errors as high as 6% relative, as shown by Small *et al.*<sup>4</sup> In summary, the overall correction factor varies from  $1/g \times (R_C/R_W)$  for small particles and thin films to  $f_{ZAF}$  for bulk specimens.

P/B approach.

#### *Iteration Procedure*

Since the major part of the correction involves a scaling of all observed intensities according to the g-factor, a normalized set of apparent concentrations will be very close to the true composition and straightforward substitution of the results of one calculation as input for the next iteration leads to rapid convergence. However, if normalization is not possible because one element is determined by difference, then a little manipulation shows that the concentration of the difference element (subscript m) should be calculated by

$$C_m = \frac{1 - g_{elmt} \sum_i C_i 'f_i'}{1 + (g_m - g_{elmt}) \sum_i C_i 'f_i'} \quad (11)$$

where  $g_{elmt}$  is the average g-factor for the measured elements,  $f_i'$  is the overall correction factor with the  $g_{spec}$  term removed, and the sums are over all measured elements. A further consideration is the propagation of errors: if the specimen is composed of a measured element i and an element to be determined by difference, then

$$C_i \propto (P/B)_i [C_i g_i + (1 - C_i) g_m] \quad (12)$$

to a fair approximation and the relative error in concentration is thus given by

$$\frac{\Delta C_i}{C_i} = \frac{\Delta (P/B)}{(P/B)} \cdot \left[ 1 + C_i \left( \frac{g_i}{g_m} - 1 \right) \right] \quad (13)$$

where the relative error in (P/B) measurement is enhanced or attenuated by a term dependent on the atomic numbers of the two elements. If a heavy element is embedded in a light matrix, (P/B) rapidly approaches the pure element value as  $C_i$  is increased; so it is understandable why a small error in P/B should give a large error in  $C_i$  at large concentrations. The propagation of errors in a general situation is more complicated and will not be discussed here, save to mention that since absolute (rather than normalized) concentration estimates approximately depend on the mean atomic number of the specimen, consideration of error propagation is more important in the (P/B) method than in the conventional ZAF approach where estimates are relatively insensitive to the average composition.

#### *Experimental Measurements*

The P/B approach depends on the measurement of the bremsstrahlung intensity from the specimen alone. In particle analysis, supporting the particles on a thin film essentially removes the interference of continuum from the substrate,<sup>5,6</sup> but the biggest potential problem with any sample is stray radiation produced by backscattered electrons or electrons that fall outside the probe spot.<sup>19</sup> With a crystal spectrometer, measurement of the background near to the characteristic line is facilitated by good resolution and the focusing geometry is an advantage, although stray background can still be significant.<sup>13</sup> With an energy-dispersive spectrometer, the problem of poor resolution can be tackled by spectrum processing,<sup>5,7,20</sup> but the large solid angle for x-ray detection enhances the stray radiation problem. Backscattered electrons can excite bremsstrahlung in the beryllium detector window<sup>16</sup> and can pass through to the active region; an extreme example is given by Fiori and Newbury.<sup>21</sup> Figure 2 shows the effect of placing a 4 $\mu$ m-thick Mylar film in front of a Si(Li) detector with a 7.5 $\mu$ m Be window. At 30 kV roughly half the observed background is due to transmitted electrons, and even at 20 kV enough electrons get through to excite a substantial silicon peak from the dead layer. Since roughly 1000 times as many backscattered electrons approach the detector as do x rays, the detector window cannot be very thin unless an electron trap is used.<sup>22,23</sup>

Measurements on a series of energy-dispersive spectra of ilmenite showed that the (P/B) approach can give analytical accuracies better than  $\pm 10\%$  relative even with a rough surface

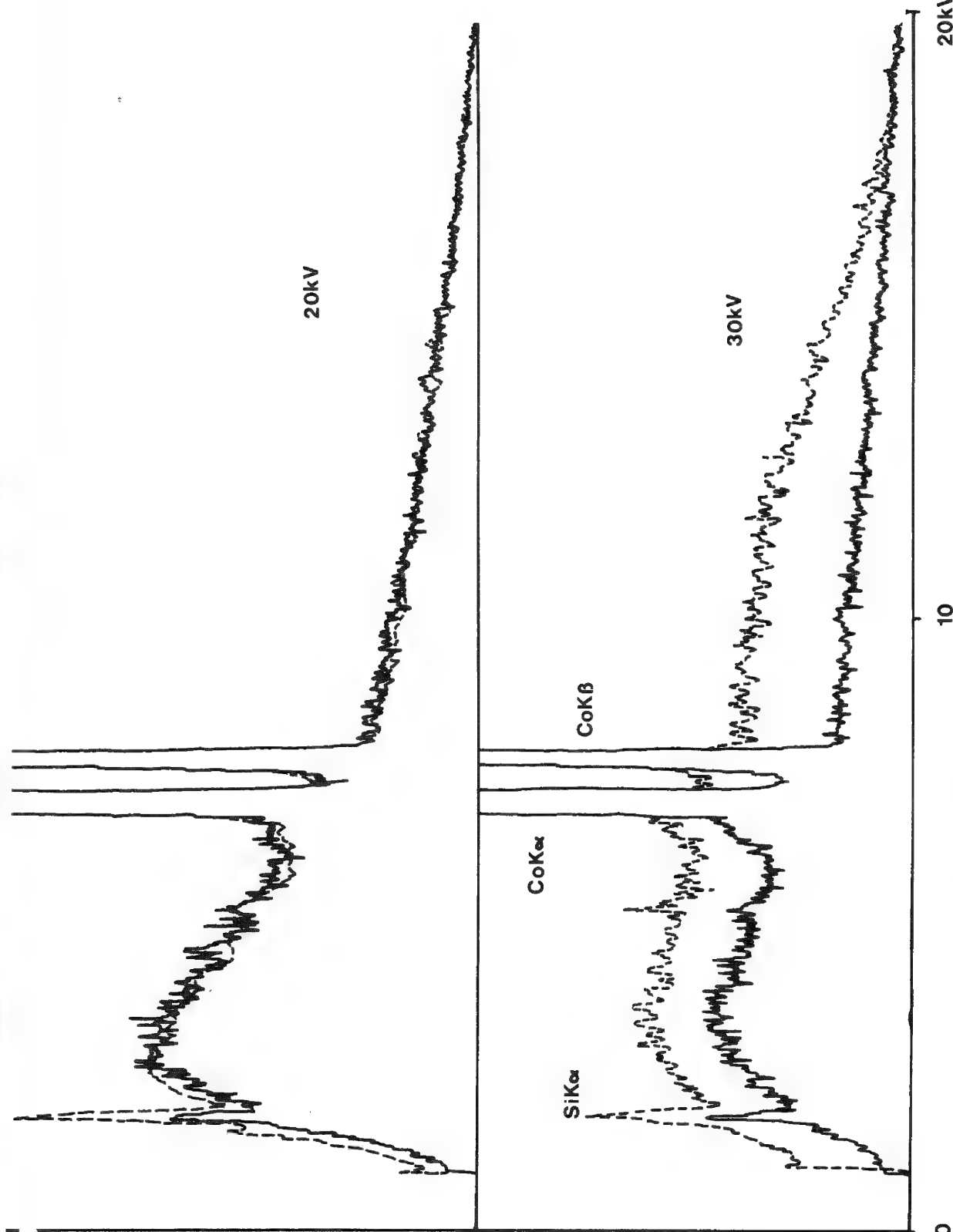


FIG. 2.--Spectra from polished cobalt specimen taken with angle of incidence and take-off-angle of  $45^\circ$  by means of a KeveX Si(Li) detector with nominal  $7.5\mu\text{m}$  Be window and Link Systems 860 x-ray analyzer. The pairs of spectra for 20kV and 30kV incident electrons are offset for clarity; lower curve in each pair shows effect of placing  $4\mu\text{m}$  Mylar in front of detector window.

and undefined geometry when a conventional ZAF approach gives errors of up to 30%.<sup>7</sup> However, the above theory predicts a small increase in (P/B) at low tilt angles, whereas the measurements showed a decrease. This decrease is consistent with a stray component of radiation produced by "beam-tailing"<sup>19</sup> and exemplifies the need for tight collimation and a "clean" electron column when one tries to make measurements of the background.

### Discussion

In Table 1, the correction factors for magnesium in a bulk sample of ilmenite have been evaluated for various tilt angles. The conventional ZAF factors for absorption  $f(\chi)_c$  clearly involve much larger corrections than the equivalent factors for (P/B) ratios.

TABLE 1.--Correction factors for magnesium in a sample of ilmenite. (Mg 4.67%, Ti 29.85%, Fe 30.62%, Cr 0.99%, Mn 0.29%, O 33.6%) excited by 20kV electrons. Tilt is angle between electron beam and normal to specimen surface; detector direction is perpendicular to electron beam. Symbols for absorption and backscatter corrections are described in text.

TILT	$f(\chi)_c$	$\frac{f(\chi)_c}{f(\chi)_w}$	$R_c$	$\frac{R_c}{R_w}$
25	0.19	1.11	0.86	1.02
45	0.29	1.09	0.82	1.01
65	0.35	1.08	0.76	1.00

Therefore, if there was no error in measurement, a ZAF procedure based on (P/B) ratios would be more accurate and less dependent on fundamental parameter values than the conventional ZAF procedure. To date it has been demonstrated that (P/B) measurements can grossly simplify problems where the x-ray distribution cannot be easily defined, as in particle analysis. Since ratios rather than absolute intensities are involved, there is no need to monitor or control the probe current or counting time. Moreover, the ratio of intensities is unaffected by the presence of material between probe spot and detector, be it the beryllium window or a projecting piece of the sample itself. It remains to be seen whether the experimental problems of stray radiation and background measurement can be solved so that these advantages can be exploited.

### References

1. L. Parobek and J. D. Brown, "The atomic number and absorption corrections in electron microprobe analysis at low electron energies," *X-Ray Spectrom* 7: 26-30, 1978.
2. J. T. Armstrong and P. R. Busek, "Quantitative chemical analysis of individual microparticles using the electron microprobe: Theoretical," *Anal. Chem.* 47: 2178-2192, 1975.
3. T. A. Hall, "The microprobe assay of Chemical elements," *Physical Techniques in Biological Research*, New York: Academic Press, 1971, 2nd ed., 1A, 157-275.
4. J. A. Small et al., "The production and characterization of glass fibers and spheres for microanalysis," *Proc. SEM/1978 O'Hare, Ill.*: SEM Inc., 1978, 445-454.
5. P. J. Statham and J. B. Pawley, "A New method for particle x-ray microanalysis based on peak-to-background measurements," *ibid.* 469-478.
6. J. A. Small et al., "Progress in quantitation of single particle analysis with the electron probe," *Proc. 13th MAS Conf.*, 1978, paper 56.
7. P. J. Statham, "Measurement and use of peak-to-background ratios in x-ray analysis," *Proc. Neuntes Kolloquium über metallkundliche Analyse*, Vienna, 1978; *Mikrochimica Acta*, Suppl. 8, 1979; in press.
8. P. Kirkpatrick and L. Wiedmann, "Theoretical continuous x-ray energy and polarization," *Phys. Rev.* 67: 321-339, 1945.
9. S. J. B. Reed, "The shape of the continuous x-ray spectrum and background corrections for energy-dispersive electron microprobe analysis," *X-ray Spectrom.* 4: 14-17, 1975.
10. T. S. Rao-Sahib and D. B. Wittry, "The x-ray continuum from thick targets," *Proc. 6th Intern. Conf. X-Ray Optics and Microanalysis*, 1972, 131-137.

11. D. G. W. Smith, C. M. Gold, and D. A. Tomlinson, "The atomic number dependence of the x-ray continuum and the practical calculation of background in energy dispersive electron microprobe analysis," *X-Ray Spectrom.* 4: 149-156, 1975.
12. M. Green, "The efficiency of production of characterization x-radiation," *X-Ray Optics and X-Ray Microanalysis*, New York: Academic Press, 1963, 185-192.
13. T. S. Rao-Sahib and D. B. Wittry, "X-ray continuum from thick elemental targets for 10-50keV electrons," *J. Appl. Phys.* 45: 5060-5068, 1974.
14. P. Duncumb and S. J. B. Reed, "The calculation of stopping power and backscatter effects in electron probe microanalysis," *Quantitative Electron Probe Microanalysis*, Special Publication 298, Washington D.C.: National Bureau of Standards, 1968, 133-154.
15. G. Love, M. G. Cox, and V. D. Scott, "A versatile atomic number correction for electron-probe microanalysis," *J. Phys.* [D] 11: 7-21, 1978.
16. P. J. Statham, "The generation, absorption, and anisotropy of thick target bremsstrahlung and implications for quantitative energy dispersive analysis," *X-Ray Spectrom.* 5: 154-168, 1976.
17. P. J. Statham, "Reliability in data-analysis procedures for x-ray spectra," *Proc. 8th Intern. Conf. X-Ray Optics and Microanalysis; Proc. 12th MAS Conf.*, 1977, paper 95.
18. S. J. B. Reed, "Characteristic fluorescence corrections in electron probe microanalysis," *Brit. J. Appl. Phys.* 16: 913, 1965.
19. R. B. Bolon and M. D. McConnell, "Evaluations of electron beam tails and x-ray spatial resolution in the SEM," *Proc. SEM/1976*, Chicago, Ill.: ITT, 1976, 164-170.
20. P. J. Statham, "Deconvolution and background subtraction by least-squares fitting with prefiltering of spectra," *Analytical Chemistry* 49: 2149-2154, 1977.
21. C. E. Fiori and D. E. Newbury, "Artefacts observed in energy-dispersive x-ray spectrometry in the scanning electron microscope," *Proc. SEM/1978*, O'Hare, Ill.: SEM Inc., 1978, 401-422.
22. T. A. Hall, "Reduction of background due to backscattered electrons in energy-dispersive X-ray microanalysis," *J. Microscopy* 110: 103-106, 1977.
23. B. Neumann, L. Reimer, and B. Wellmanns, "A permanent magnet system for electron deflection in front of an energy-dispersive x-ray spectrometer," *Scanning* 1: 130, 1978.



## RAPID QUANTITATIVE ANALYSIS OF INDIVIDUAL PARTICLES BY ENERGY-DISPERSIVE SPECTROMETRY

Gary D. Aden and Peter R. Buseck

The analytical scanning electron microscope (SEM) is an extremely powerful tool for the study of particulate air pollutants. The most rapid and efficient means of analyzing small particles (0.05-10  $\mu\text{m}$ ) on the SEM is by energy-dispersive spectrometry (EDS). Quantitative EDS, although still not routine, has been shown to be a potentially accurate method of analyzing thick flat materials.<sup>1</sup> This method has two distinct advantages for particle analysis in that it can be used at low beam currents (about 1 nA), which allows reasonable imaging of the smaller particles (about 0.1  $\mu\text{m}$ ), and the spectra for all elements from Na to U can be collected simultaneously.

The main drawbacks of quantitative analysis by EDS occur in the data processing.<sup>2,3</sup> Accurate background subtraction routines are required in order to remove the large contribution to the spectrum by the bremsstrahlung (BSS). In addition, deconvolution routines must be employed to correct for the severe x-ray line overlaps caused by the relatively poor resolution of the detector. Programs that perform both of these procedures are quite lengthy and can require many minutes of computational time per element per sample, when run on a minicomputer.<sup>4</sup>

These algorithms, though accurate, are too slow to be useful for routine particle analyses. This paper describes a new particle-analysis procedure capable of background subtraction over the entire spectrum and of fitting the x-ray peaks for a 15-element sample in under 2 min. It consists of TWIST, a relatively simple, fast, and yet accurate routine for background subtraction, and QKFIT, a linear least-squares fitting routine that uses simplifications designed to increase the speed of analysis. All data were collected on a JEOL JSM-35 scanning electron microscope with a PGT-1000 detector, analyzer, and 32K computer with four floppy-disk drives.

The TWIST procedure is based on two main approximations. The first assumes that the background for a complex sample can be constructed by addition of the percentage of BSS contributed by its element or oxide components,

$$\text{BSS}_{\text{sample}} = \sum_i X_i \cdot \text{BSS}_{\text{components}} \quad (1)$$

where  $X_i$  is the weight fraction of the component  $i$  in the sample. For example, one can calculate the BSS for the mineral olivine,  $(\text{Fe,Mg})_2\text{SiO}_4$ , by adding the appropriate weight fractions of  $\text{BSS}_{\text{MgO}}$ ,  $\text{BSS}_{\text{FeO}}$ , and  $\text{BSS}_{\text{SiO}_2}$ .

Figure 1 shows a comparison of the theoretically calculated BSS to the 'mixed' oxide BSS for olivine. For particles, the mixed background must also include the BSS contributed by the substrate. Although the calculation of theoretical backgrounds is very slow, a mixed background requires only simple vector additions of precalculated backgrounds and is performed in a few seconds.

Although this procedure is fast and accurate for samples containing few elements, it is impractical to store calculated backgrounds for all elements that might be analyzed. A second approximation is made that avoids this storage requirement. The spectrum can be treated in two parts, below and above 2 keV. The shape of the background at energies below 2 keV is most strongly affected by elements whose absorption edges also lie below 2 keV. A mixed background must thus be used in this region. The background above 2 keV follows a relatively smooth curve, and can be modeled fairly accurately by a linear extrapolation between many background points. One can achieve an even better fit by 'twisting'

---

The authors are with the departments of Chemistry and Geology, Arizona State University, Tempe, Ariz. This work was supported in part by NSF grant AENV 76-17130.

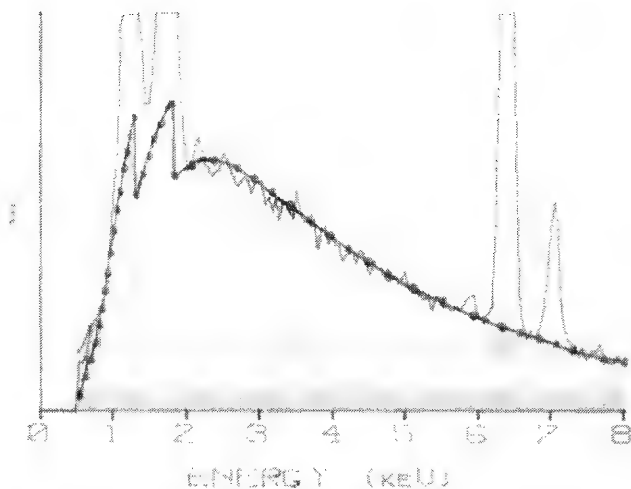


FIG. 1.--Comparison of calculated background (dotted line) to mix background (shaded) for spectrum of springwater divine (dark line)-- 44% MgO, 39% SiO<sub>2</sub>, 17% FeO, by weight.

$$B(E) = [1 - (X_{Mg}' + X_{Al}' + X_{Si}')] \cdot B(E)_{carbon} + [X_{Mg}' \cdot B(E)_{MgO}] + (X_{Al}' \cdot B(E)_{Al_2O_3}) + [X_{Si}' \cdot B(E)_{SiO_2}] \quad (2)$$

where  $B(E)$  is the intensity of the background at energy  $E$  and  $X_i$  is the appropriate weight fraction for component  $i$  defined as

$$X_i = \frac{(P/B)_i \text{ sample}}{(P/B)_i \text{ standard}} \quad (3)$$

This mix background, since it is only an approximation, must be force-fitted (twisted) to the sample spectrum. This fitting is done by choosing three or more background points on the sample spectrum, to be used as comparison points to the mix background. For a given spectrum between pairs of these points  $E_1$  and  $E_2$ , the scale and the slope of the background spectrum is varied in a linear fashion such that  $I(E_1)_{sample}$  is set equal to  $B(E_1)$  and  $I(E_2)_{sample}$  is set equal to  $B(E_2)$ . This adjustment is made by determination of the equation for a line between these two energy points for the sample and then multiplication of the old background  $B$  by this equation. The parameters for the line are

$$\text{Slope: } m = \frac{I(E_1)_{sample}}{B(E_1)} - \frac{I(E_2)_{sample}}{B(E_2)} \quad (4)$$

$$\text{Intercept: } b = \frac{I(E_1)_{sample}}{B(E_1)} - (m \cdot E_1) \quad (5)$$

The new background  $B'$  then becomes

$$B'(E) = [(m \cdot E) + b] \cdot B(E) \quad (6)$$

In effect, this procedure rotates the background spectrum so that the imaginary lines that

an already calculated background to fit to just a few background points. With this 'twisting' procedure (described below) it is necessary to include backgrounds only for significant elements whose x-ray lines fall below 2 keV (Mg, Al, and Si) plus the background from the carbon substrate.

The following procedure is used to carry out the BSS generation. Spectra from four thick flat samples of C, MgO, Al<sub>2</sub>O<sub>3</sub>, and SiO<sub>2</sub> are collected at a given beam current. The peak-to-background ratio (P/B) is determined for the Mg, Al, and Si peaks, and a theoretical background is calculated for each spectrum by a modified Ware-Reed and Lifshin approach.<sup>5,6</sup> The P/B ratio from sample to standard, for a given component  $i$  is then used to estimate the weight fractions of the oxides or, if element standards are used, elements in the sample. If we allow the carbon BSS to make up the remainder of the background, we have for Eq. (1)

can be drawn between points  $E_1$  and  $E_2$  on the sample and background spectra have the same slope (Fig. 2).

The TWIST routine was tested on a variety of oxide, sulfide, and silicate samples with excellent results obtained on most samples (Fig. 3). These tests included both particle and thick flat samples, most of which only contain elements from Na to Zn. It was found that it is unnecessary to perform the 'mix' calculation for particles whose diameter is smaller than  $1\text{ }\mu\text{m}$ , as a 'twisted' carbon spectrum provides sufficiently accurate background. Care must be taken that the background is not being extremely contorted to fit the sample spectrum. The fit can be considered good as long as the slope  $m$  remains within  $\pm 0.0001$  of 0, the best fit value.

The final step in the procedure involves the linear least-squares fitting deconvolution routine.<sup>7</sup> The QKFIT routine utilizes a simple idea to achieve a four-fold reduction in computational time. The linear least-squares fit routine, for  $n$  elements, requires the solving of  $n$  linear equations over  $j$ , the number of x-ray channels in each of  $n$  fitting regions. This process involves iterative matrix inversions until a best fit is determined and takes considerable time even if programed in machine language. However, performing this process for  $n/2$  elements takes little over one-fourth the time because both the number of elements and the number of channels is decreased. Therefore, by performing the least-squares fit by parts, including only those elements in each fit that have significant overlap, one can achieve a major reduction in processing time.

To compare the two procedures, several air-pollution samples were analyzed for fourteen elements--Na, Mg, Al, Si, S, Cl, K, Ca, Ti, Cr, Mn, Fe, Cu, and Zn. A fitting routine for all elements was compared to a routine where the fitting was performed in a 6/4/4 fashion:

6: Na, Mg, Al, Si	-K-overlaps
Na, Cu, Zn	-K, L-overlaps
4: S, Cl, K, Ca	- $K_\alpha$ , $K_\beta$ -overlaps
4: Mn, Fe, Cu, Zn	- $K_\alpha$ , $K_\beta$ -overlaps

The fourteen-element fit requires over 5 min of computation time; the 6/4/4 fit is completed in under 90 sec. A comparison of the k-values returned by the two methods shows that negligible error is produced by fitting in this manner as long as there are truly no unaccounted overlaps. Such overlaps could result from sum peaks, escape peaks, incomplete charge collection, or poor background subtraction.

In summary, two rapid routines for particle analysis have been tested. The TWIST routine for background subtraction works well for the analysis of K-lines of Na to Zn for most particles and some thick flat samples. The QKFIT routine is a simplification of a linear least-squares fitting routine that allows a four-fold reduction in computing time for samples containing large numbers of elements. These routines take an unprocessed EDS spectrum and return element K-values which must then be used in a particle, atomic number, absorption, and fluorescence correction scheme (PZAF). Currently the most flexible PZAF routine is the Armstrong and Buseck program, ARMSTØ,<sup>8</sup> which is written for use on a large computer. Approximations are being investigated that will, it is hoped, allow this program to be used also on a minicomputer.

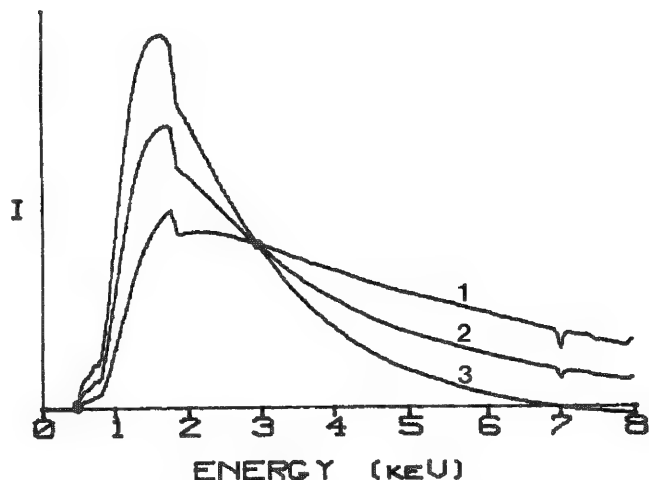


FIG. 2.--The effect of 'twisting' carbon spectrum (curve 2) by changing slope  $m$  around point 2.94 keV, as described in text. (Curve 1:  $m = 0.0003$ ; curve 3:  $m = -0.0003$ .) Note effect that drastic twisting has on Si dead-layer absorption edge (1.84 keV).

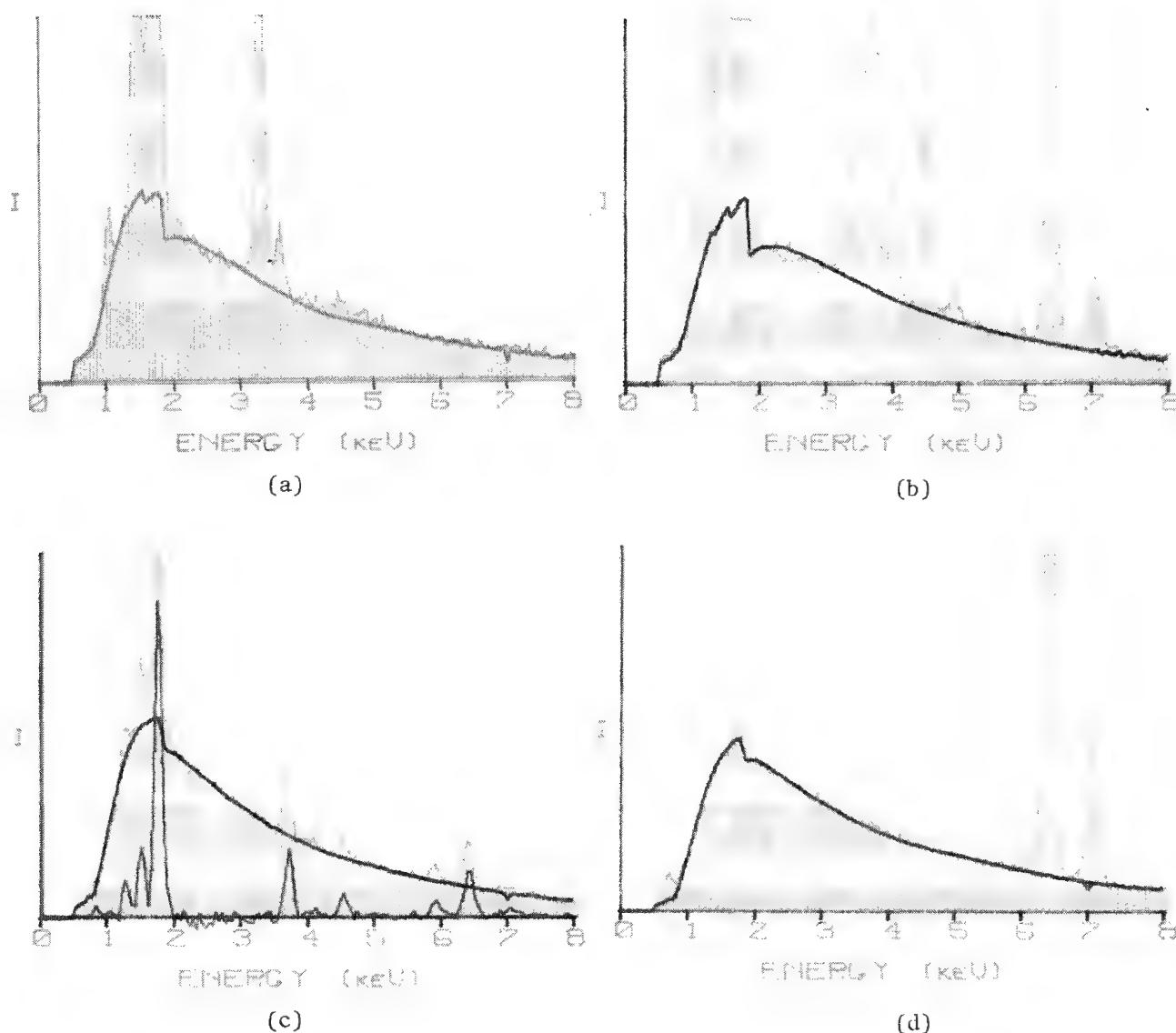


FIG. 3.--Selected examples of TWIST background correction for various particle diameters and compositions. Note close matches between experimental spectra (shaded) and calculated mix backgrounds (solid outline). All samples were run at 15 kV,  $35^\circ$ , with 0.912, 4.24, and 7.5 keV as background points. (a) Orthoclase particle,  $3.1\mu$  dia., containing 3.79% Na, 9.87% Al, 30.2% Si, 7.77% K, 1.43% Ba, 46.4% O by weight; (b) Hornblende, thick flat, containing 2.30% Na, 5.91% Mg, 7.25% Al, 19.0% Si, 0.91% K, 7.22% Ca, 2.82% Ti, 12.1% Fe, 41.1% O; (c) Hornblende particle,  $0.33\mu$  dia.; inset is spectrum after background subtraction; (d) FeO particle,  $2.0\mu$  dia., containing 77.7% Fe, 22.3% O.

#### References

1. C. E. Fiori et al., "Prediction of continuum intensity in energy dispersive x-ray microanalysis," *Anal. Chem.* 48: 172, 1976.
2. P. J. Statham, "Reliability in data analysis procedures for x-ray spectra," *Proc. 8th Intern. Conf. X-ray Optics and Microanalysis; Proc. 12th MAS Conf.*, 1977, 95.
3. S. J. B. Reed, "Quantitative energy dispersive analysis," *Proc. 11th MAS Conf.*, 1976, 4.
4. P. J. Statham, "A comparative study of techniques for quantitative analysis of the x-ray spectra obtained with a Si(Li) detector," *X-Ray Spectro.* 5: 16, 1976.
5. N. G. Ware and S. J. B. Reed, "Background corrections for quantitative electron microprobe analysis using a lithium drifted silicon x-ray detector," *J. Phys. [EL]* 6: 286, 1973.

6. E. Lifshin, M. F. Ciccarelli, and R. B. Bolon, *X-ray Spectral Measurements and Interpretation*, General Electric Tech. Information Series, Report 74CRD159, 1974.

7. R. J. Gehrke and R. C. Davies, "Spectrum fitting techniques for energy dispersive x-ray analysis of oxides and silicates with electron microbeam excitation," *Anal. Chem.* 47: 1537, 1975.

8. J. T. Armstrong and P. R. Buseck, "Quantitative chemical analysis of individual microparticles using the electron microprobe: Theoretical," *Anal. Chem.* 47: 2178, 1975.

## QUANTITATIVE ANALYSIS OF MULTIPHASE SAMPLES

John C. Russ

Quantitative analysis of specimens to determine their average or bulk composition is often carried out by SEM/microprobe techniques, sometimes without regard to the fact that the sample may not be homogeneous. The usual procedure, naively applied, is to scan a large area to average over the various phases. As an example of this case, we were recently asked to perform quantitative analysis for elemental composition on a metal sample. The sample contained Al, V, Ni, Mo, and Re; each of these pure elements was provided along with the unknown in a single, polished mount.<sup>1</sup>

The sample was analyzed at 25 kV, 20° inclination, with the EDAX detector located 16° above the horizontal at an azimuthal angle of 40°. Three widely spaced locations on each pure standard and five widely spaced locations on the alloy specimen were analyzed, and each spectrum was processed by means of software<sup>2</sup> that automatically removes escape peaks, fits a quasi-theoretical background to a series of selected points, and uses simultaneous least-squares fits of generated non-Gaussian peaks for all the major and minor lines of each line for each element (including minor lines down to 1% relative height). The analysis of each location was obtained by a continuous scanning of the beam over an area roughly 20  $\mu\text{m}$  square. The intensity data (in cps) for the standards and unknown are summarized in Table 1, along with the concentrations in weight and atomic percent calculated by the COR2 ZAF program,<sup>3</sup> adapted to run in a minicomputer.

TABLE 1.--Intensities (cps) on pure and alloy specimens, and ZAF calculations.

element:	Al (K)	V (K)	Ni (K)	Mo (L)	Re (L)
pure # 1	2219.00	2365.18	1444.02	1879.31	770.17*
pure # 2	2257.92	2491.39	1506.98	1871.28	1009.56
pure # 3	2232.85	2386.02	1487.68	1839.60	999.15
average	2236.59	2414.20	1479.56	1863.40	1004.36
alloy # 1	36.77	41.60	933.90	423.35	7.32
alloy # 2	35.57	39.55	930.19	422.76	6.13
alloy # 3	35.91	38.06	909.07	411.31	9.76
alloy # 4	36.24	39.63	926.92	424.59	7.06
alloy # 5	35.52	39.39	924.71	425.97	7.12
average	36.00	39.65	924.96	421.60	7.48
weight %	5.46	1.86	62.52	31.96	0.97
atomic %	12.33	2.22	64.85	20.28	0.32
total $\sigma$ (% rel.)	1.7	4.3	2.4	1.8	18.1

note: sum of calculated weight percent = 102.78

\* omitted from average

While data were being taken it was noticed that the samples had a very definite microstructure. Figure 1 shows the typical appearance of the polished surface, with bright areas about 0.75  $\mu\text{m}$  on a side, surrounded by a darker gray phase, each region of which was distinct from its neighbors and sometimes separated by a shallow depression probably caused by differential polishing or etching. The sample, in other words, appeared to be a cross section through a directionally solidified eutectic structure. Clearly, the phases had a different composition. Equally clearly, the inherent assumptions of the ZAF model were not being met--the sample was not homogeneous on a fine enough scale to cause the x rays from each element to pass through a representative mixture of atoms of the other elements, so that absorption and secondary fluorescence depended on average composition. For example, an "average" analysis of a scan covering equal areas of five pure elements should require no ZAF correction at all, and should give 20% of each element.

The author is at EDAX Laboratories, Prairie View, IL 60069.

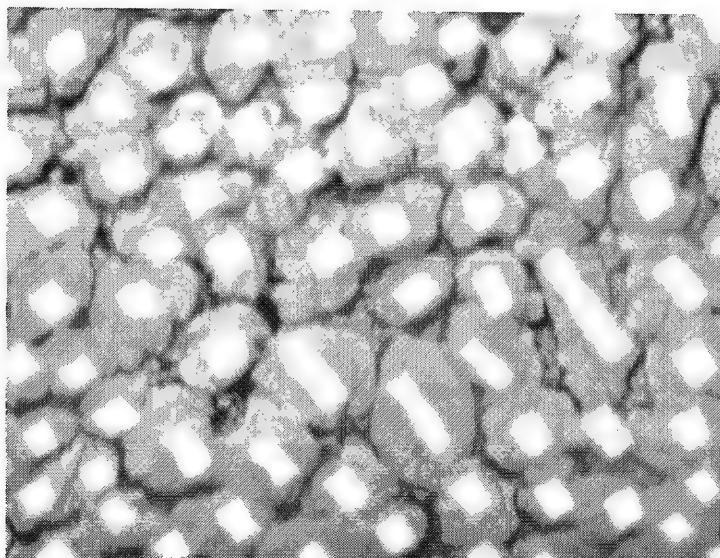


FIG. 1.--SEM micrograph (5000 $\times$ ) of typical region of specimen, showing bright phase surrounded by gray matrix.

Although we reported the data of Table 1 (along with similar data for several other samples, which did appear to be homogeneous), it was not possible to stop there, since the reported concentrations were not meaningful. The correct method to obtain average bulk concentrations on inhomogeneous samples is quantitatively to analyze the composition of each phase, and then add the results for the several phases together in proportion to the respective volume fractions.

To do that, we first measured energy-dispersive spectra on five of the bright squares, carefully centering a stationary beam on each one, and on five matrix regions (avoiding pits and other irregularities). Processing these spectra in the same way as already described, we obtained estimates of composition for each phase (Table 2). For the ZAF calculations using COR2, the pure element intensities from Table 1 were used, multiplied by the ratio of beam current; a smaller spot size (160 Å) was needed to achieve adequate image resolution to select individual phases at magnifications of 10 000 $\times$ . The factor used was 0.2505. Analysis times of 200 sec were used to obtain adequate statistics. Since the excited volume is roughly the same size as the size of the phases, these concentration values cannot be considered fully accurate (as can be seen in the variation of intensities among the five points); however, for our purposes they are preferable to an overall average.

To measure the volume fraction of each phase, we used a program which performs simultaneous least-squares fits of library (stored) spectra.<sup>4</sup> Although this is not the correct technique to obtain net intensities or K-ratios for elements in a homogeneous mixture, the program is a correct way to measure volume fractions. The spectrum measured while the beam is continuously scanning over a large area containing multiple phases is a linear combination of the individual spectra (peaks and background) from each separate phase. Furthermore, the total spectrum can be expressed as a sum of each individual phase's spectrum times a fractional constant, and the constant for each phase is just the area fraction which the phase represents of the total area scanned.<sup>5</sup> The latter equality assumes only that the total system count rate remains essentially the same on the various phases so that the dead time does not change, so as artificially to reduce the relative contribution of the higher count rate phase; in this case the total system count rate was held below 1000 cps by the need to keep the beam small for adequate image resolution, and in any case the count rate on the bright and gray phases was virtually the same. The area fractions of phases on a surface through a random structure is the same as the volume fractions of the phases.

Figure 2 shows representative spectra measured on the bright phase, the gray matrix, and an area. The spectra were fitted over the energy range from 1 keV (below the Al K peak) to 12 keV (above the Re L lines), including all the elemental peaks and continuum

TABLE 2.--Intensities (cps) and calculated concentrations (COR2) for individual phases and average area scan.

element:	Al (K)	V (K)	Ni (K)	Mo (L)	Re (L)
bright phase # 1	4.46	8.65	98.41	281.10	8.27
bright phase # 2	3.61	8.49	87.95	274.87	7.97
bright phase # 3	2.43	7.10	61.61	311.49	7.32
bright phase # 4	3.56	7.14	76.72	290.85	8.20
bright phase # 5	3.54	6.68	84.99	274.18	7.30
average	3.52	7.61	81.94	286.50	7.81
weight %	1.52	1.56	21.65	72.00	3.64
grey matrix # 1	10.02	10.45	269.85	59.24	-0-
grey matrix # 2	12.07	10.82	278.12	57.80	-0-
grey matrix # 3	10.25	10.69	270.73	49.30	-0-
grey matrix # 4	11.11	10.35	272.31	63.84	-0-
grey matrix # 5	11.60	10.51	276.98	51.24	-0-
average	11.01	10.56	273.60	56.28	-0-
weight %	7.36	1.89	74.19	18.12	0.00
area scan # 1	8.92	10.20	235.07	106.25	2.90
area scan # 2	8.52	10.01	235.19	105.44	1.51
area scan # 3	8.68	9.39	233.13	102.67	2.44
area scan # 4	7.94	9.99	234.99	102.04	1.44
area scan # 5	8.79	9.44	231.86	102.13	1.76
average	8.57	9.81	234.05	103.69	2.01
weight %	5.22	1.83	63.14	31.45	0.34

background. The results of least-squares fitting of the spectra from the individual phases are illustrated in Fig. 3 and summarized in Table 3 for five different areas and sets of single-phase spectra. The average of the five individual fitting factors gives a value of 20.6% and 79.4% for the volume fractions of the bright phase and gray matrix, respectively. Particularly significant are the excellent chi-squared values for the fits (which indicate good agreement between the measured average spectra and the summed individual phase spectra) and the fact that each pair of fitting values and the overall average values add up to nearly 1.0, although there is no constraint in the program for them to do so (which indicates that these two phases together do represent 100% of the area analyzed).

As an independent check on the volume fractions obtained by this method, point counting was carried out on micrographs of areas of the sample. Three micrographs, taken at 5000 $\times$ , were each overlaid with a grid of about 4000 points, and the number of points on the bright phase was counted. Points on voids or crevices presumably due to polishing relief were omitted on the basis that those regions did not contribute to the x-ray analysis, either. The percentage of the remaining points lying on the bright phase and the gray matrix, at widely separated points in the sample, are shown in Table 4. The results agree within expected variance with those determined by the spectrum-fitting method. However, the voids that are ignored by this method may originally have contained material, either of the gray matrix phase or some other composition, which is thus not taken into account in determining average composition. It is always essential that the surface used for quantitative phase determination reveal all phases with statistically random probability, and that the plane surface used for microanalysis not have some elements or phases systematically removed.

The individual phase compositions from Table 2 can be multiplied by the volume fraction of each phase, from Table 3 (or 4), to obtain the overall bulk composition. This gives the results shown in Table 5, which are different from the false "average" shown earlier in Table 1.

The "true" bulk composition of this sample was not known to us when this analysis was actually performed and the original report was given to the customer. When these data became available, they showed a very encouraging agreement with the results from the EDAX



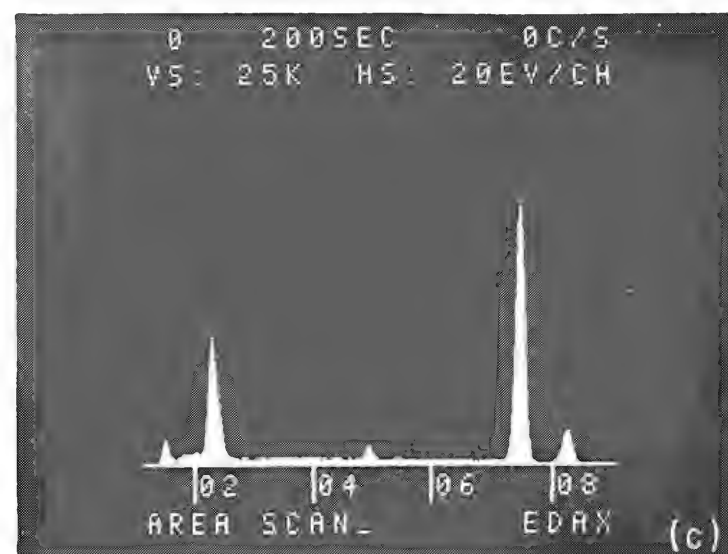
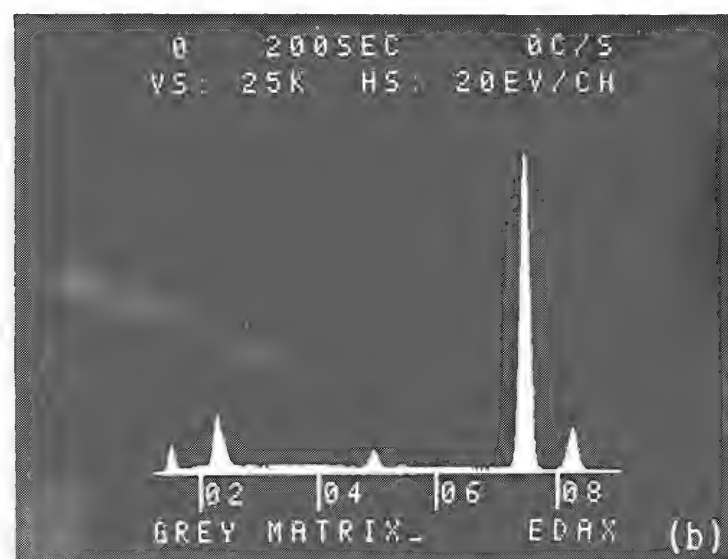
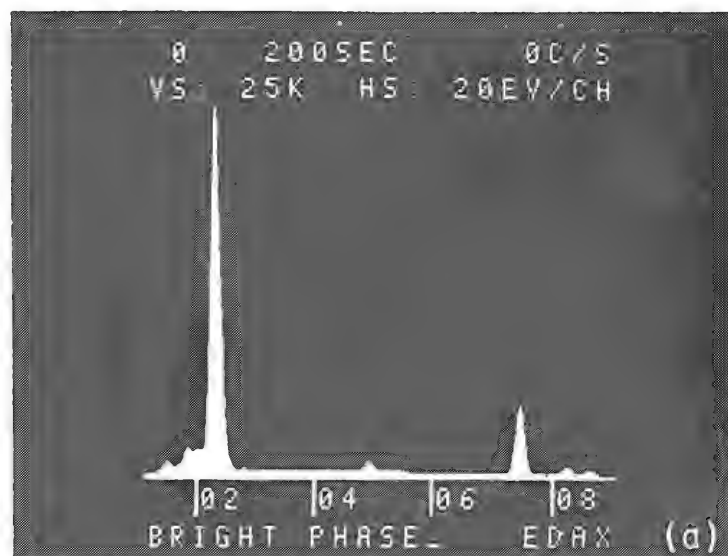


FIG. 2.--Typical spectra measured on bright phase, gray matrix, and large average area.

```

MULTIFIT - KEYBOARD COMMANDS:-
  1      2      3      4      5      6      7
ENTER  DISPLAY  STORE  READ  GEN PKS  LIBRARY  STOP

NEXT ? 1 ENTER ? BRIGHT #1
NEXT ? 3 STORE FILENAME ? BR1
NEXT ? 1 ENTER ? MATRIX #1
NEXT ? 3 STORE FILENAME ? MTX1
NEXT ? 1 ENTER ? AREA #1
NEXT ? 3 STORE FILENAME ? AREA1
NEXT ? 6 LIBRARY FITS-HOW MANY SPECTRA? 2
      APPLY DIGITAL FILTER ? NO
      LIMITS TO FIT: LO=1.0 HI=12.0
      NO. 1 FILENAME ? BR1 BRIGHT #1
      NO. 2 FILENAME ? MTX1 MATRIX #1
SPECTRUM                                FACTOR
  1  BR1                                .207873
  2  MTX1                                .802646
REDUCED CHI-SQUARED FOR FIT= 1.00527
ENTER PEAK/SPECT # FOR DISPLAY, END @ +/- : #.
NEXT ?

```

FIG. 3.--Typical result from Multifit "MF" program showing fitting of spectra from bright phase and gray matrix to area scan.

TABLE 3.--Results of "MF" fitting of single-phase spectra.

area spectrum number	fraction of single phase spectrum		chi-squared for fit
	bright	grey matrix	
1	.20787	.80265	1.00527
2	.22059	.77937	1.00701
3	.20422	.81588	1.00202
4	.17126	.81176	0.99807
5	.22449	.76129	0.99312
average	.20569	.79419	

TABLE 4.--Volume fraction values from manual point counting.

area	percent of points		
	no points	bright phase	grey matrix
<u>total</u>			
1	3545	19.3	80.7
2	3756	17.8	82.2
3	3750	20.8	79.1

TABLE 5.--Calculated bulk composition from phase analysis (compared to directly measured false "average").

element	Al	V	Ni	Mo	Re
bright phase (20.6%)	1.52	1.56	21.65	72.00	3.64
grey matrix (79.4%)	7.36	1.89	74.19	18.12	0.00
overall average	6.16	1.82	63.37	29.22	0.75
directly calculated false "average" from Table I	5.46	1.86	62.52	31.96	0.97

phase-analysis method (Ni was given as "balance"), as shown in Table 6. Note especially the Mo results, which show the effect of having most of the Mo in the bright phase where the concentration is different and hence the matrix absorption is different.

TABLE 6.--Comparison of true and calculated composition.

element:	Al	V	Mo	Re
true bulk %:	5.9	1.8	29.7	0.9
by phase analysis:	6.2	1.8	29.2	0.8
false "average":	5.5	1.9	31.0	0.9

The intensity data in Table 2 for each phase can be also multiplied by the same 20.6% and 79.4% factors to give good agreement with the area scan intensities reported there. In principle one could thus determine the volume fractions by solving a set of overdetermined simultaneous equations using only those intensities, of the form

$$I_{\text{average}_i} = \sum_{n \text{ phases}} I_{\text{phase}_i} V_{\text{phase}}$$

for each element (i). In practice, it is both simpler and potentially more accurate directly to fit the entire spectrum since more individual data points and the information contained in the continuum are then also used.

This method for obtaining quantitative phase analysis information can be used as an adjunct to the normal quantitative elemental analysis capability of a standard EDAX system using existing software, and requiring only knowledgeable interpretation on the part of the user. It offers better quantitative bulk analysis results on inhomogeneous materials; and quantitative volume fraction or phase analysis of phases of different composition, directly from the EDAX measurements, with no need for other special attachments or computer control of the microscope.

#### References

1. Sample obtained by courtesy of D. C. J. Andrews, NASA Lewis Research Center.
2. J. C. Russ, "A fast, self-contained, no-standards quantitative program for EDS," *Proc. 13th Annual MAS Conf.*, 1978, 46.
3. K. F. J. Heinrich and R. L. Myklebust, *A Rigorous Correction Procedure for Quantitative Electron Probe Microanalysis (COR2)*, Technical Note 796, Washington, D.C.: National Bureau of Standards, 1973.
4. J. C. Russ, "Multiple least squares fitting for spectrum deconvolution," *EDAX EDITor* 8(No. 4): 3, 1978.
5. R. E. Ogilvie and M. F. McKittrick, "A new technique for quantitative metallography employing a scanning electron microscope and a solid state x-ray detector," *Proc. 12th Annual MAS Conf.*, 1977, 7.

## COMPUTER EVALUATION OF PHOTON, ELECTRON, AND PROTON-INDUCED X-RAY SPECTRA

Pierre Van Espen, Henri Nullens, and Willy Maenhaut

Photon-excited x-ray energy spectrometry (XES), proton-induced x-ray emission (PIXE), and analytical electron microscopy (EM) are widely used to perform elemental analysis of environmental, geological, and biological samples. The difference in excitation mode results in fairly different analytical features, but the fact that the detection of the characteristic x rays is done with a Si(Li)-detector spectrometer for the three methods results in digitized spectral data which are a convolution of the original spectrum with the same, or a comparable, instrumental function. The common problem then is to obtain reliable net peak areas for the individual characteristic x-ray lines in the spectrum. In recent years computer programs have been developed for the purpose of analyzing XES, PIXE, and EM spectra.<sup>1-3</sup> We report here a program capable of deconvoluting x-ray spectra generated by the three modes of excitation.

To deal with the very complex nature, in particular, of the photon- and the proton-induced x-ray spectra, the deconvolution method is based on the powerful nonlinear least-squares optimization algorithm of Marquardt.<sup>4</sup> However, in using this nonlinear-fitting principle, one must overcome several problems normally associated with the method. The major problems are the number of parameters in the fitting function, the accuracy of the model used, and avoidance of the selection of physically meaningless minima in the  $\chi^2$ -hypersurface.

The first two problems require the use of a suitable fitting function. The model used consists essentially of two cumulative portions: the background function and the function representing the characteristic x-ray spectrum. The background is built up of different components, depending on the excitation mode. In mono-energetic photon excitation the background originates in the detector itself and results from incomplete charge collection of the high energetic excitation x-rays which interact with the detector after scattering onto the sample.<sup>5</sup> In EM and PIXE, the major portion of the background is due to electron bremsstrahlung.<sup>6</sup> This background is radiative, in contrast to the background in XES, and thus becomes affected by absorption in the sample and in the detector entrance windows. For proton excitation this picture is complicated by the presence of a background component caused by Compton interaction of energetic gamma radiation, originating from nuclear reactions in the sample.

As a complete description of the background for all excitation modes, the following relation is used:

$$\text{BACK}(E) = \sum_{i=0}^{n_1} B_{1i} (E - E_0)^i + B_{20} \exp\left\{ \sum_{j=1}^{n_2} B_{2j} (E - E_0)^j \right\} + B_{30} \exp\left\{ \sum_{k=1}^{n_3} B_{3k} (E - E_0)^k \right\} \cdot \text{ABS}(E) \quad (1)$$

in which  $E$  is the energy and  $E_0$  a suitable reference energy. The first term is used to describe the background when only a small energy interval is fitted; for larger fitting regions, when the exponential terms are included in the description, only  $B_{10}$  is retained. The second term represents the background not affected by absorption (XES:  $n_2 = 3$ ; PIXE:  $n_2 = 1$ ). The third term is the bremsstrahlung background, which is affected by an absorption factor  $\text{ABS}(E)$ . This term is disregarded for XES spectra; for PIXE spectra  $n_3 = 2$  or  $3$ . Normally for a number of spectra originating from a group of similar samples, the parameters  $B_{2j}$  for  $j > 0$  and  $B_{3k}$  for  $k > 0$  are determined once from one or more representative spectra. These parameters are then kept constant for the remaining spectra in the set. In this way only three background parameters  $B_{10}$ ,  $B_{20}$ , and  $B_{30}$  are to be optimized.

The second part of the fitting function describes the entire x-ray line spectrum. The emission spectrum of an element consists of a number of x-ray lines; each line is, at

---

Authors Van Espen and Nullens are at the Department of Chemistry of the University of Antwerpen (U.I.A.), 2610 Wilrijk, Belgium; Maenhaut is at the Institute for Nuclear Sciences (I.N.W.), University of Gent, 9000 Gent, Belgium.

a first approximation, represented by a Gauss function:

$$G(x,n,m) = \frac{1}{\sqrt{2\pi} W_{n,m}} \exp\{-(P_{n,m} - x)^2/2W_{n,m}^2\} \quad (2)$$

where  $W_{n,m}$  is the width of the peak number  $m$  of element  $n$ ,  $P_{n,m}$  the position of the peak number  $m$  of element  $n$ ,  $x$  the channel number, and  $W_{n,m}$  and  $P_{n,m}$  are calculated from the relations

$$P_{n,m} = C_1 + C_2 E_{n,m} + \exp\{-C_3 E_{n,m}^2\} \quad (3)$$

$$W_{n,m}^2 = C_4 + C_5 E_{n,m} \quad (4)$$

where the  $C_i$  are the spectrum calibration parameters and  $E_{n,m}$  is the energy of line  $m$  of element  $n$ . This formulation means that in the optimization it is not the individual position and width of every peak that is determined, but only the position ( $C_1 - C_3$ ) and the resolution ( $C_4 - C_5$ ) calibration parameters of the entire spectrum. The term between brackets in Eq. (3) can be used to account for the nonlinearity of the calibration in the low-energy part of the spectrum.

The x-ray emission of an element is then modeled with a single area parameter  $A_n$  and the various transitions are scaled to this area by the use of known relative intensities. This radiative part of the spectrum is again subjected to absorption. The fitting function therefore becomes

$$YFIT = BACK(E) + \sum_n A_n \left[ \sum_m G(x,n,m) \cdot R_{n,m} \cdot ABS(E_{n,m}) \right] \quad (5)$$

The first summation concerns the number of elements;  $A_n$  is proportional to the number of photons emitted towards the detector. The second summation runs over the number of lines for each element;  $R_{n,m}$  is the relative transition probability. The absorption factor  $ABS$ , for a particular x ray with energy  $E_{n,m}$ , is discussed later.

In this way the spectrum description is complete, but not yet accurate. Indeed the use of a simple Gaussian distribution for the representation of the x-ray peaks is a crude approximation. It has been shown that a considerable non-Gaussian contribution is associated with each peak, which is to a great extent due to incomplete charge collection, and thus nonradiative in nature.<sup>7</sup> This deviation is incorporated in the program by means of a numerical correction. The digital correction terms are obtained from single-element spectra with very good counting statistics, by substraction from the original spectrum of all the known Gaussian components and the background. The remaining data are smoothed, normalized to the intensity of the main peak  $K_\alpha$ , and stored together with the calibration of the original spectrum in a library file. The correction term  $S_n(x)$  for intense peaks in each spectrum is calculated from these data by use of the actual spectrum calibration (Eq. 4) and multiplied by the number of  $K_\alpha$  photons detected. The total spectrum function thus becomes

$$YFIT = BACK(E) + \sum_n A_n \left[ \sum_m G(x,n,m) \cdot R_{n,m} \cdot ABS(E_{n,m}) + S_n(x) \cdot R_{n,1} \cdot ABS(E_{n,1}) \right] \quad (6)$$

The last factor to be discussed is the absorption term  $ABS(E)$ . Since the methods are mostly used for the determination of trace constituents in low-Z matrices, absorption edges can be neglected in the calculation of the absorption due to the sample and the x-ray absorption coefficient can be described as

$$\mu(E) = aE^b \quad (7)$$

In XES analysis, absorption is mostly due to the sample itself, with (at low energies) a contribution from the detector beryllium window, the gold contact, and the silicon dead

layer. In PIXE analysis it is common practice to use additional absorbers between sample and detector, with one absorber sometimes containing a small hole as a collimator for part of the low-energy radiation (funny filter).<sup>2</sup> For the three types of absorption we thus have

$$\text{ABS}(E) = [\exp\{-a_1 E^{a_2}\}] \cdot \left[ \frac{1 - \exp\{-a_3 E^{a_4}\}}{a_3 E^{a_4}} \right] \cdot [a_5 + (1 - a_5) \exp\{-a_6 E^{a_7}\}] \quad (8)$$

The first factor represents the absorption by the entrance windows of the detector, including any solid absorber between sample and detector. The second factor is the sample self absorption. The third represents the absorption contribution for an external absorber with a hole;  $a_5$  is the fraction of the detector solid angle subtended by the hole. Detector and external-filter absorption parameters are only optimized at system start up or after alterations have been made to the measurement setup. Self absorption parameters can be kept fixed if a number of comparable samples are being analyzed.

The fitting function as described above can describe the x-ray spectrum completely and accurately, with a limited number of parameters--typically one per element, three for the background, four for the calibration, and two for the radiation absorption.

The third problem, avoiding the selection of undesired minima in the  $\chi^2$ -surface, is dealt with by redefinition of the  $\chi^2$ -function:<sup>8</sup>

$$\chi^2 = \frac{1}{v} \sum_i \left[ \frac{(Y_i - Y_{\text{FIT}_i})^2}{\sigma_i^2} + \sum_j \frac{(A_j - A_{\text{op}_j})^2}{\sigma_{A_{\text{op}_j}}^2} \right] \quad (9)$$

The first term is the normal  $\chi^2$ -function. The second term is added to enhance the curvature of the  $\chi^2$ -surface when the fitting parameter  $A_j$  reaches values strongly different from the expected value  $A_{\text{op}_j}$ . The range for each parameter is controlled by  $\sigma_{A_{\text{op}_j}}^2$ ;  $A_j$  denotes the calibration and absorption parameters.

The program described runs on a PDP 11/45 minicomputer with 32 K words of accessible memory. A typical processing time for a complete spectrum between 2 and 16 keV is 60-200 sec.

## References

1. P. Van Espen, H. Nullens, and F. Adams, "A computer analysis of x-ray fluorescence spectra," *Nucl. Instr. and Meth.* 142: 243, 1977.
2. H. C. Kaufmann, R. Akselsson, and W. J. Courtney, "Rex: A computer programme for PIXE analysis," *ibid.*, p. 251.
3. P. J. Statham, "A comparative study of techniques for quantitative analysis of the x-ray spectra obtained with a Si(Li) detector," *X-ray Spectrometry* 5: 16, 1976.
4. D. W. Marquardt, "An algorithm for least-squares estimation of nonlinear parameters," *J. Soc. Ind. Appl. Math.* 11: 431, 1963.
5. P. Van Espen and F. Adams, "Evaluation of a practical background calculation method in x-ray energy analysis," *X-ray Spectrometry* 5: 61, 1974.
6. F. Folkmann et al., "Proton induced x-ray emission as a tool for trace element analysis," *Nucl. Instr. and Meth.* 166: 487, 1974.
7. P. Van Espen, H. Nullens, F. Adams, "A method for the accurate description of the full-energy peaks in non-linear least-squares analysis of x-ray spectra," *Nucl. Instr. and Meth.* 145: 579, 1977.
8. H. Nullens, P. Van Espen, and F. Adams, "Linear and nonlinear peak fitting in energy dispersive x-ray fluorescence," *X-ray Spectrometry* (in press).

## MODIFICATIONS AND EXTENSIONS TO NBS FRAME C

John C. Russ

The NBS Frame C program<sup>1</sup> for ZAF-corrected quantitative analysis of bulk samples is attractive as a simple, fast, and compact routine for processing EDS spectra. We have modified and extended it in several ways to broaden its range of application. Some of the modifications are instrument-specific and need little discussion; others seek to extend the equations and models used for parameter calculation to gain accuracy over a greater range of energies, and another class of extensions allows the use of unconventional standards or no standards and permits calculations on particles rather than bulk materials.

The original version of the program is a stand-alone program in *BASIC*, actually a simple *BASIC* interpreter for NOVA computers that can handle only numeric inputs and limited array sizes. The program used in our system is rewritten in *FORTRAN*, with user I/O expressed directly in elemental symbols and so on. All user inputs are requested as needed; users can make options by pressing function keys labelled on the keyboard rather than typing in mnemonic codes or numbers from a "menu." Also, data storage is on diskette, so that files of standards data, etc., can be named and re-used as needed. Finally, the use of a high-speed (9600 baud) color video terminal permits extensive data readout (all calculated factors, warnings, propagated errors, etc.) for user examination. The output data are also saved on disk so that hard copies can be printed or passed on to a more sophisticated program such as NBS COR2.<sup>2</sup> These modifications, although important in terms of speed, user interaction, ease of operation and interpretation, etc., are basically trivial and need not be considered further.

### *Parameter Calculation*

One of the important limitations in FRAME has been its restriction to elemental lines between 1 and 12 keV. It is certainly true that difficulties abound when quantitative analysis is performed below 1 keV (e.g., C, O), and errors increase in that range. At higher energies, the elements may not be well excited by the accelerating voltage available in many SEMs. However, in some circumstances a broader energy range would be desirable. A major cause of the limitation appears to be in the equations used to calculate energies of lines and absorption edges, which are of the form

$$\text{energy(keV)} = \exp (A_1 + A_2 \log Z + A_3 \log^2 Z) \quad (1)$$

where  $Z$  is atomic number. The errors in these values became substantial outside the 1-12keV range, and more significant, may cause an emission energy to lie on the wrong side of an absorption edge, even for the element itself. (For example, a carbon emission energy greater than its absorption edge gives rise to a very large value for the carbon mass absorption coefficient.) One solution would be to put a complete table of energies (approximately 3000 for all useful lines and edges) into a diskette file, but the access time and storage space required argue against this approach. We find that by expressing the energies of lines and edges as

$$\text{energy (keV)} = \sum_{j=0}^5 A_j Z^j \quad (2)$$

we can fit all the lines with at least 1% relative intensity and edges in Bearden<sup>3</sup> and Johnson and White<sup>4</sup> to within  $\pm 3$  eV, and that there are no cases of emission/absorption

---

The author is at EDAX Laboratories in Prairie View, IL 60069.

crossover. This approach reduces the storage to an array of 6 numbers  $\times [(5K = 11L + 5M)$  peaks +  $(1K + 3L + 5M)$  edges] = 180 values which cover energies from 0.28 keV (carbon K) to 80 keV (beyond the K lines of Au). The escape peak energies are of course readily obtained from each of these values, with no additional ones needed.

The fluorescenc yield expression used in Frame C also can be improved. The form used is

$$\omega = \exp(A_0 \log Z + A_1) \quad (3)$$

for K and L shells, and

$$\omega = B_1 + B_2 Z + B_3 Z^2 \quad (4)$$

for the M shell. For elements with peaks above 12 keV (e.g., the K lines of elements such as Mo), the values this expression gives are too high ( $\omega = 0.97$ ) and indeed the expression increases beyond 1.0 for higher energies. The Burhop<sup>5</sup> expression

$$\omega/(1 - \omega) = (A_0 + A_1 Z + A_2 Z^3)^4 \quad (5)$$

calculates more reasonable values and so we have incorporated it instead.

#### *Standardization*

Frame allows the use of pure or compound standards; for the latter a ZAF calculation is performed to determine the pure intensities to be stored. This capability is similar to that commonly used for classic microprobe analysis, with every element in the unknown represented in one or another standard, and with standard and unknown analyzed under identical conditions. In addition to this conventional approach, we also have found it extremely useful for amny "real" SEM samples to allow the standards and unknowns to be at different orientations. If that is the case, and the angles of surface tilt and x-ray takeoff are known, the effective current and absorption terms may be adjusted for the difference.

The effective current computed by Frame C omits the term given in Frame B for the effect of inclination, which we have restored:

$$R_{\text{angle } S} = R_{\text{perp}} \cdot \exp\{[\log(0.0753/U) + 0.8994] \cdot [\sec S - 1 - (S/90)]\} \quad (6)$$

where S is the angle of the sample surface (0 = perpendicular to the beam). This appears to be somewhat more accurate than our own earlier expression,<sup>6</sup> but neither is probably adequate at very high (> 45°) tilt angles. Nevertheless, it does permit some difference between the orientation of the standards and unknowns.

Similarly, it is very frustrating to measure a series of standards, have all the data on file, and encounter a beam current change (for example due to a filament burnout). If intensities are expressed as counts (per second) per nanoamp, and beam current is measured with a Faraday cup, this problem can be handled directly. More often, this facility is not present. The user may then see that his results are consistently totaling far from 100%, and elect to allow the program to "renormalize" the standards. That is not the same as renormalizing the answers, i.e., multiplying all the unknown concentrations by a factor to make them total 100%. Rather, we adjust all the pure intensities by a common factor at each iteration in the ZAF process to make the final concentrations total 100%. The method fails, of course, if there is a missing element, and it cannot be used with an element calculated by difference. Also, it forces closure to 100% and so hides some potential error signals from the user. However, it does permit the use of standards data measured with beam current different from that for the unknowns.

To accomodate situations in which not all the elements in the unknown are present in the standard(s), we take advantage of the invariant spectrometer efficiency of the Ed system to interpolate or extrapolate from other elements. Combining the techniques of Blum and Brandt,<sup>7</sup> ourselves,<sup>8</sup> and Barbi,<sup>9</sup> we allow the use of some or no standards. If no standards at all are used, then normalization of the concentrations to 100% as described



above is forced. The relative pure element intensities are calculated for each element as

$$P_i = N_{e1}(U - 1)^{5/3} \omega LTR / (FA) \quad (7)$$

where  $N_{e1}$  is the number of electrons in the shell (2, 8, 18) adjusted for screening effects (the values used are 2, 5.714, 12.857),  $U$  is the overvoltage,  $\omega$  is the fluorescence yield,  $L$  is the fraction of the total shell intensity contained in the integrated region,  $T$  is the spectrometer efficiency,  $R$  is the effective current,  $F$  is the absorption correction, and  $A$  is the atomic weight. The terms  $L$ ,  $T$ ,  $R$ , and  $F$  are calculated by use of existing Frame C subroutines ( $R$  modified as described above);  $\omega$  is calculated as already shown. We have previously used this method in our software for "no standards" and find it quite useful where the speed advantage of not having to run standards outweighs the loss in accuracy from the calculated factors. For major elements (> 5%) all analyzed by the same shell it is unusual to find relative errors exceeding 10% and common to find them less than 5%.<sup>10-12</sup>

When elements covering a broad range of atomic numbers and analyzed by different shells are encountered, better results may be obtained by the use of a few standards (pure or compound) containing convenient nearby elements in the periodic table and of the calculated  $P$  factors to extrapolate from them to the elements in the unknowns. We may conveniently do so by using linear least-squares fitting methods to solve for the constant of proportionality between intensity and calculated  $P$ -factor, and the exponent of the  $(U - 1)$  term. This procedure allows the curve to "tilt" over large  $Z$ -ranges and seems to give better fits than using the nominal  $5/3$  value, but the exponent does not take on consistent values and no physical meaning is implied -- it is an attempt to compensate for many assorted inaccuracies.

With the fitting/interpolation method, it is not necessary to normalize the results, so that deviation from 100% can be used as a warning of error. However, if such normalization is also selected by the user to compensate for unknown beam-current variations, then a few disk files of standard intensities from a set of representative elements measured under typical operating conditions (voltage and topography) can serve for most analysis situations.

#### *Other Extensions*

As a convenience to the user, the program calculates x-ray takeoff angle by the method of Moll<sup>13</sup> and specimen tilt angle from parallax measurements on the SEM screen. The latter requires only that the user measure the change in spacing between two surface features for a known increment of tilt, which makes it fairly easy to analyze locally flat regions on generally irregular surfaces.

Particle analysis is not adequately corrected by classical ZAF calculations, so as a useful approximation we have allowed Frame C to use as input either the intensities for elements or their peak-to-background ratios. The latter are of course readily available since the program calculates the local background intensity under each peak in order to subtract it. The disk files of standards data also preserve that information so that the  $K$  factor used in the ZAF calculation becomes the ratio

$$\frac{P/B|_{\text{unknown}}}{P/B|_{\text{standard}}} \quad (8)$$

rather than the intensity ratio. The assumption that background x rays have a similar depth distribution and absorption effect as characteristic x rays, and therefore that the  $P/B$  ratio is invariant with particle size, shape, and surface texture, is clearly only approximate.<sup>14-16</sup> However, it is expected to be useful until more exact models become practical.

Finally, the original Frame C program requires the user to specify two peak-free regions in the spectrum to be used as background reference points, from which the background intensity at other energies is calculated. This feature can be usefully supplemented by

also allowing the user to default the selection of background reference points to the program. If he does so, the program will begin at 2 keV and proceed up in 0.1keV steps, examining each 0.2keV-wide energy band to see whether it can be used. The criterion<sup>17</sup> is that the average intensity in the energy window must not exceed that in either neighboring window by more than two standard deviations, or it might lie on a peak, and that it must not be lower than that in both neighboring windows by more than the same amount, or it might be a valley between peaks. After a suitable low-energy point has been found, the program begins again at 0.7 times the accelerating voltage, and steps down in 0.1keV steps following the same criteria. The two selected points are then shown to the user for his approval, and unless he rejects them, are used in the background calculation. We have not yet encountered cases in which the points selected by this method are clearly unacceptable, nor give significantly different results from points selected by a knowledgeable operator; the automatic method may thus offer significant advantages for the untrained or insecure operator.

### Summary

Several modifications and extensions to the Frame C program have been added to broaden its range of application. They include

1. Programming in *FORTRAN* and using extensive disk files, input/output formatting, etc., to provide speed, extended output, user convenience, and a permanent database.
2. New parameter models for energy and an improved fluorescent yield expression, to allow use of peaks outside the 1-12keV range.
3. Extended standardization choices in addition to conventional pure or compound standards, to permit renormalization, extrapolation, different geometries, or no-standards.
4. Use of P/B ratios instead of intensities, to compensate partially for finite particle size.
5. Automatic selection of background reference points, to permit the user to default on this selection.

These extensions delete none of the original Frame C capabilities, and in addition allow practical quantitative analysis to be carried out, albeit with reduced accuracy in some cases, in many commonly encountered real situations.

### References

1. R. L. Myklebust, C. E. Fiori, and K. F. J. Heinrich, *A Compact Procedure for Quantitative Energy-Dispersive Electron Probe X-ray Analysis (Frame C)*, Washington, D.C.: National Bureau of Standards preprint, 3 November 1978.
2. K. F. J. Heinrich, R. L. Myklebust, *A Rigorous Correction Procedure for Quantitative Electron Probe Microanalysis (COR2)*, Technical Note 796, Washington, D.C.: National Bureau of Standards, 1973.
3. J. A. Bearden, *X-Ray Wavelengths*, Oak Ridge, Tenn.: U.S. Atomic Energy Commission (Division of Technical Information Extension), 1964.
4. G. G. Johnson Jr. and E. W. White, *X-Ray Emission Wavelengths and keV Tables For Nondiffractive Analysis*, ASTM Data Series DS 46, Am. Soc. for Testing and Materials, 1970.
5. E. H. S. Burhop, *J. Phys. Radium* 16: 625, 1955.
6. J. C. Russ, "A simple correction for backscattering from inclined samples," *Proc. 10th Annual MAS Conf.*, 1975, 7.
7. F. Blum and M. Brandt, *X-Ray Spectrometry* 2: 121, 1973.
8. J. C. Russ, "Quantitative microanalysis with minimum pure element standards," *Proc. 11th Annual MAS Conf.*, 1974, 22.
9. N. C. Barbi, "The calculation of pure element x-ray intensities from empirically derived expressions and its application to quantitative SEM/EDS analysis", *Proc. 13th Annual MAS Conf.*, 1976, 8.
10. A. Hendricks and J. Walinga, "Quantitative analysis of stainless steel with the SEM," *EDAX EDITor* 5(No. 3): 33, 1975.
11. J. C. Russ, "Errors introduced in eliminating or extrapolating standards," *Proc. 13th Annual MAS Conf.*, 1976, 19.

12. J. C. Russ, "A fast, self-contained, no-standards quantitative program for EDS," *Proc. 15th Annual MAS Conf.*, 1978, 46.
13. S. Moll, N. Baumgarten, and W. Donnelly, "Geometrical considerations for ZAF corrections in the SEM," *Proc. 12th Annual MAS Conf.*, 1977, 33.
14. S. J. B. Reed, "The shape of the continuous x-ray spectrum and background corrections for energy-dispersive electron microprobe analysis," *X-Ray Spectrometry* 4: 14-17, 1975.
15. J. A. Small et al., "The production and characterization of glass fibers and spheres for microanalysis," *Scanning Electron Microscopy* 1: 445-454, 1978.
16. P. J. Statham and J. B. Pawley, "A new method for particle x-ray microanalysis based on peak-to-background measurements," *ibid.*, pp. 469-478.
17. J. C. Russ, "Automatic fitting of calculated background in energy dispersive x-ray spectra," *Proc. 12th Annual MAS Conf.*, 1977, 102.

# EDATA2: A FORTRAN IV COMPUTER PROGRAM FOR PROCESSING WAVELENGTH- AND/OR ENERGY- DISPERSIVE ELECTRON MICROPROBE ANALYSES

D. G. W. Smith and C. M. Gold

The development of EDATA2 was stimulated by the proliferation of mixed energy dispersive/wavelength dispersive equipped electron microprobes. For such systems to be operated most efficiently and conveniently, a data reduction program is required that can handle energy-dispersive, wavelength-dispersive, or a mixture of both kinds of data. This requirement has become particularly pressing with the widespread introduction of a high degree of automation, which permits either kind of data to be gathered rapidly and reliably. If the reduction of data to give the compositional information ultimately required is not to present a bottleneck, software must be versatile, running times short, and costs low.

In the development of EDATA2 (Fig. 1) the design philosophy of its predecessor, "EDATA," was retained in that an automatic rather than an interactive program was constructed. In any laboratory where an appreciable part of the operation involves producing large numbers of analyses, it is desirable that minimal intervention be required during data processing. EDATA<sup>1</sup> was developed to process only energy-dispersive analyses, and was limited to handling analytical data for elements of atomic number 11 (Na) to 30 (Zn), plus Zr and Ba. These elements cover the compositions of most silicates, as well as many other minerals. However, EDATA2 permits the specification of any suite of up to 22 analyzed elements (from Z = 9 to 92).

An empirical expression for the relationship of continuum intensity to atomic number, continuum energy, and accelerating potential has now been reinvestigated<sup>2</sup> for an accelerating voltage of 15 kV, continuum energies up to 10 keV, and for atomic numbers up to 92; the following new expression was obtained:

$$I_v = k \sum_i \{ C_i [(E_0 - E_v)/E_v]^{x_i} Z_i^{n_i} \}$$

where  $x_i = a - 0.00145(Z_i/E_v)$  and the constant  $a \approx 1.5$ ,  $Z_i$  = atomic number of element  $i$ ,  $C_i$  is the concentration of element  $i$ ,  $I_v$  = continuum intensity at an energy  $E_v$ , and  $n_i = E_v[(0.0739 - 0.0051)Z_i^{1/2} + p]$ , where  $p$  is a constant. Although this expression differs somewhat from that proposed by Smith,<sup>2</sup> its value is very similar within the atomic-number range then investigated. The new expression is incorporated into EDATA2. It has been tested to date only at one operating voltage (15 kV) and one take-off angle (52.5°), but facilities to test it under various analytical conditions have now been built into the program. The dependence on atomic number of both exponents (that is,  $n$  on  $Z$ , and  $x$  on the energy term) was looked for but not observed by Smith et al. in the more limited atomic number range then investigated,<sup>2</sup> although Rao-Sahib and Wittry suggested such a dependence.<sup>3</sup>

Since spectra can be acquired at different probe currents and for different counting times, the calculated background must be scaled to the sample spectrum. In EDATA2, a new approach has been taken to this scaling: the ratio of calculated background to sample spectrum is determined for each channel, so that a 'histogram' is produced (Fig. 2). The program finds the ratio at the smoothed maximum of this 'histogram' and scales using this factor. A parameter is printed reflecting the histogram peak width--a measure of the success of estimation of background shape.

EDATA used stored values for such parameters as mass absorption coefficients, emission wavelengths, and absorption edge energies. With the extension to  $Z = 92$ , space and data entry requirements become very severe. Expressions published by Springer and Nolan were therefore used to calculate these parameters.<sup>4</sup> Continuum fluorescence corrections used by Springer were also incorporated.<sup>5,6</sup>

The other principal improvement in the capability of EDATA2 over EDATA is its capacity to handle wavelength-dispersive as well as energy-dispersive data. This facility is de-

The authors are at the Department of Geology of the University of Alberta in Edmonton, T6G 2E3. The work was supported by Grant A4254 from the Natural Sciences and Engineering Research Council of Canada. We thank Mr. Desmond Wynne for much programming assistance.

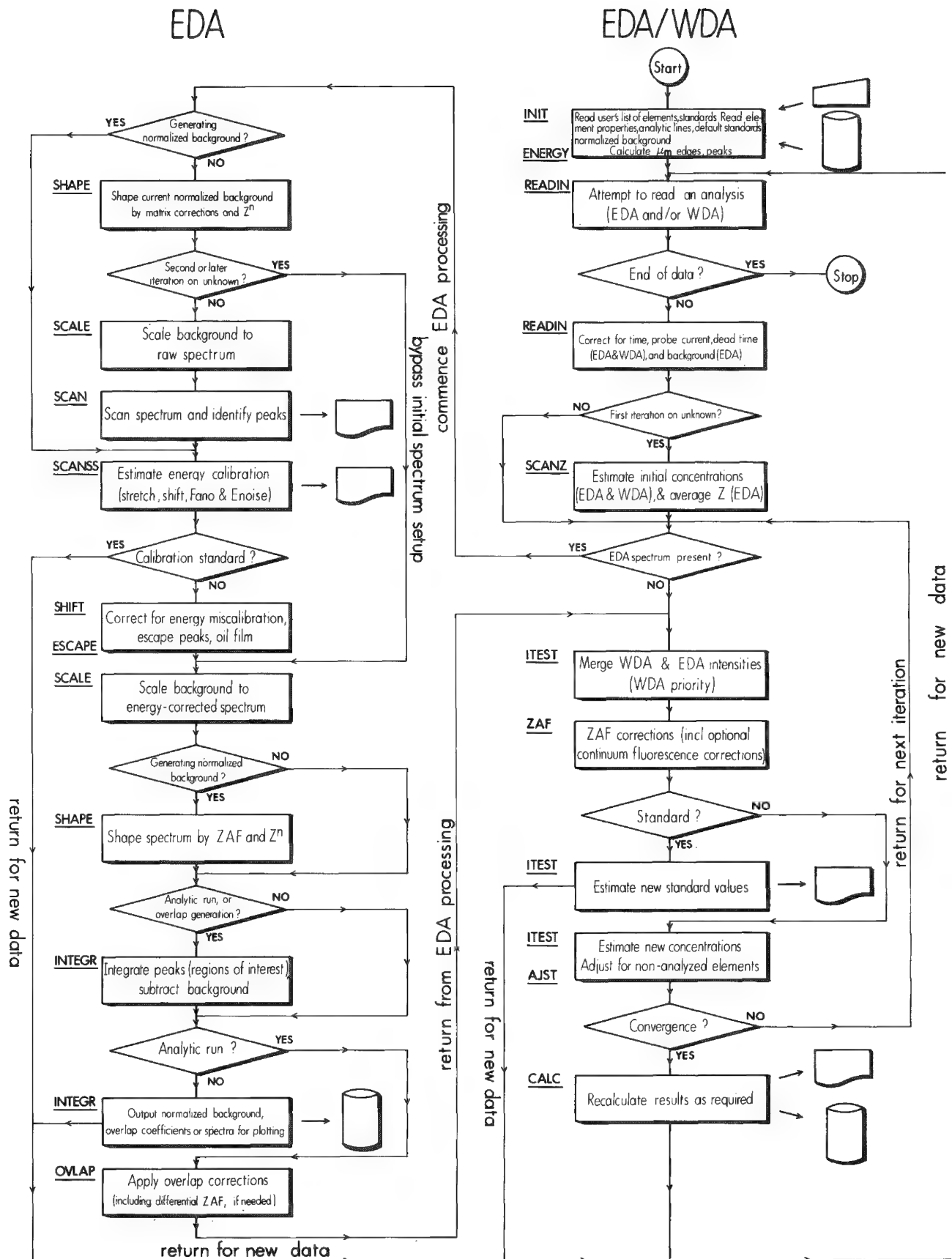


FIG. 1.--Flow diagram for EDATA2. Subroutine names are shown underlined.

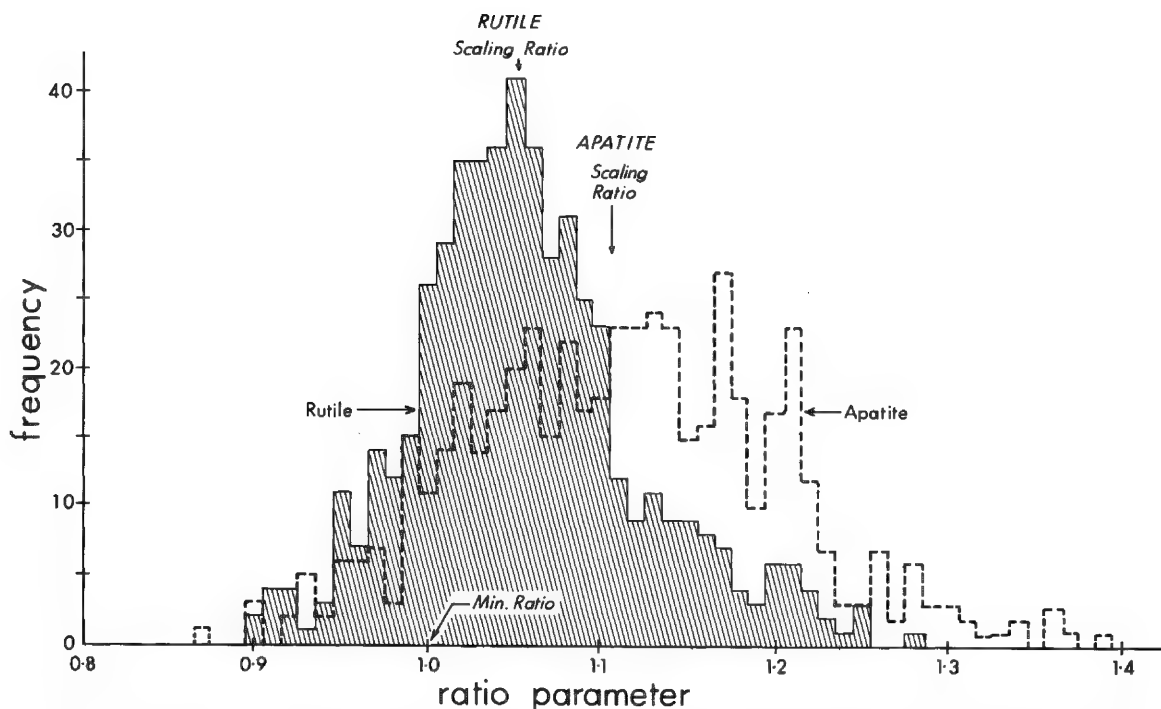


FIG. 2.--Background scaling histograms for rutile (excellent fit) and fluorapatite (poorer fit). "Ratio parameter" is the ratio of sample spectrum to computed background, calculated for each channel as a multiple of the lowest average ratio found for 10 adjacent channels ("min. ratio").

sirable for several reasons.

1. Severe interferences can occur between lines of different elements that may not always be resolvable with sufficient accuracy by EDA. Some examples are: Pb and S, Mo and S, K and U, Si and Sr. These interferences may be resolved by means of WDA.
2. Certain low-Z elements (e.g., B and F) cannot normally be determined, or determined sufficiently accurately, by EDA. However, data for such elements may be obtainable by WDA.
3. Trace elements can be determined with sufficient accuracy only by WDA. It is desirable to be able to merge data on these elements with EDA data.
4. Calculations of matrix corrections in microprobe analysis depend on the concentrations of *all* elements present; in EDA, that also holds true for the estimation of background and overlap. Clearly, the processing of data from the two techniques is greatly simplified if they can be merged.
5. The final presentation of data in a form convenient to the user will normally involve integration of all data obtained by the various analytical techniques used. The data processing program should be therefore able to cope with a wide range of situations, input information (including 'wet chemical' results), and requests for particular kinds of output.

Redesigning EDATA so that it could meet these requirements was fairly straightforward, since the processing of EDA data requires the application of nearly all the corrections needed in WDA (as well as several others). The main requirement is to code wavelength-dispersive data so that they can be recognized and routed appropriately by the program.

In view of the diversity of microprobes in use, the variety of analytical procedures used, and the different formats in which data can be produced, it is practicable to accept, as input to the wavelength-dispersive route through EDATA2, only averaged background and peak intensity readings. Thus, the user must produce, or have produced, a simple custom-designed 'front-end' program that will take the laboratory's data, carry out simple processing such as averaging, and produce an output compatible with EDATA2.

A number of possible conflicts and/or omissions can cause problems when data from the two systems are merged. For example, data for the same element might be obtained from

each system. WDA data are therefore given priority. Furthermore, if an element is specified as having been analyzed by WDA, but no standard information is supplied, the program automatically defaults to EDA. If no EDA standard data were acquired, the program turns to EDA default standard values--values measured previously, corrected for matrix effects, and stored.

The approach to overlap corrections used in EDATA has been retained. Values are obtained for overlap coefficients by using the program itself to determine the extent of overlap of each element into the analytical region for every other element to be analyzed. These coefficients are corrected for background and matrix effects. Overlap coefficients of elements to be determined by WDA must also be included. Comparison of coefficients for elements from F to Zn reported on previously<sup>2</sup> with those obtained recently by means of the revised background correction clearly indicates that minor misfits at the low-energy end of spectra for elements of higher atomic number have largely vanished.

Several other new features have been incorporated into EDATA2. A review of archival tape records of every analytical run between May 1975 and September 1976 revealed a progressive change in the measured ratio of Zn L to Zn K intensities in the Zn<sub>2</sub>SiO<sub>4</sub> calibration standard spectrum, owing to gradual contamination of the detector Be window with pump oil. Based on Zn K : Zn L intensity ratios observed for the calibration standard, EDATA2 now corrects all spectra back to the intensities which would be observed with an ideally clean Be window.

Escape peak stripping is performed by use of a modification of an expression suggested by Statham.<sup>7</sup> However, this modification has been tested only for normal incidence of x rays onto the detector; if variable, non-normal incidence is used, Statham's unmodified expression should be reintroduced together with an opportunity to enter appropriate angles for each analysis.

EDATA2 has retained most of the other features of EDATA, such as automatic measurement of energy miscalibration based on a calibration standard, and correction of all spectra back to ideal calibration. Peak integration ranges are established on the basis of current resolution measured on the calibration standard. A peak-seeking routine locates and identifies peaks. Their FWHM, approximate intensities, peak to background ratios, and identities are reported in the program output.

Although experience suggests that 15 kV is a good accelerating potential for most purposes, any potential may now be used in combination with a chosen width and number of channels. However, when any of these parameters is changed the program must be recalibrated in terms of the background-intensity expression, overlap coefficients, and default standard values. Thus, once values for these parameters have been chosen, the analyst will not wish to change them without good reason.

A feature of EDATA is the presence of two subroutines, AJST and CALC. The former calculates the concentration of elements not analyzed (e.g., oxygen) either on the basis of input information or by difference from 100%. Calculations made in AJST are iterated along with ZAF corrections, etc., until convergence is achieved. On the other hand, CALC is called only once, at the end of data processing, and manipulates corrected data and presents them in whatever form is most useful for the user. In EDATA2 more complex and sophisticated AJST and CALC programs have been incorporated and offer the user a much wider range of options.

The success of the new program can be judged in several ways. For example, background corrections can be tested by plotting the calculated background and the background-subtracted spectrum, as has been done for four substances of varying atomic number and complexity in Fig. 3. In each case residuals are trivial.

Table 1 shows analyses of basaltic glass processed by several options. First, the 'normal' procedure of analyzing samples against standards measured during the same run, with a calibration standard at the beginning and end, was adopted. Second, the same procedure was used except that only one calibration standard was read, at the beginning of the run. Third, standards measured during the run were not used, but sample intensities were measured against 'default' values. In this case, not only were 'default' standard values used, but also no calibration standard was used and samples and standards were made to self-calibrate.

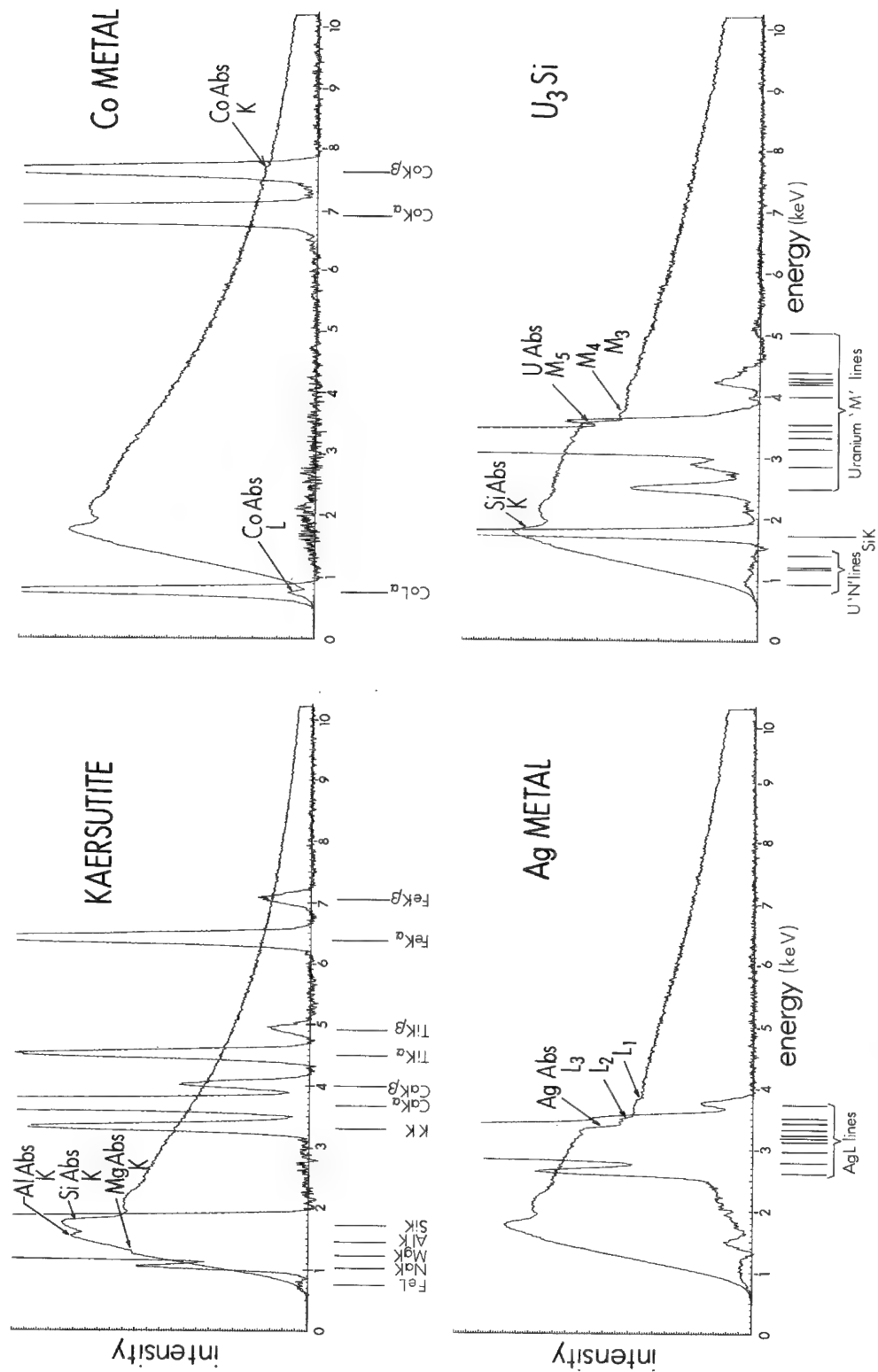


FIG. 3.--Calculated background and background-subtracted spectra for kaersutite  $[\text{Ca}_2(\text{Na},\text{K})(\text{Mg},\text{Fe})_4\text{Ti}(\text{Si}_6\text{Al}_2\text{O}_{22})(\text{O},\text{OH},\text{F})_2]$ , cobalt and silver metals, and uranium silicide  $[\text{U}_3\text{Si}]$ . Note that the small peak centered at about 1.5 keV in the silver spectrum with a small valley on either side may be an artifact of the escape peak correction and result from the different widths of the escape and parent peaks.



TABLE 1.--Composition of basaltic glass. I; best available independent information; II; EDATA2 analytical standards and a calibration standard at the beginning and end of run; III; same as II but without second calibration standard. IV; without either analytical or calibration standards, i.e., using the sample spectrum itself to determine stretch and shift corrections, and 'default' (i.e., stored) values instead of analytical standards. All analyses recalculated H<sub>2</sub>O-free to 100% from analytical totals in parenthesis. Oxygen determined by stoichiometry.

	<u>I</u>	<u>II</u>	<u>III</u>	<u>IV</u>
Na	1.70	1.81	1.81	1.77
Mg	5.67	6.22	6.22	6.38
Al	9.55	9.57	9.59	9.61
Si	22.54	22.25	22.27	22.26
K	0.13	0.10	0.08	0.10
Ca	8.22	8.02	8.02	7.87
Ti	0.41	0.40	0.38	0.39
Mn	0.12	0.10	0.08	0.09
Fe	6.68	6.58	6.58	6.53
O	44.98	44.95	44.97	45.00
TOT.	(98.33)	(98.92)	(98.87)	(99.62)

#### References

1. D. G. W. Smith and C. M. Gold, "A scheme for fully quantitative energy dispersive microprobe analysis," *Advances X-ray Anal.* 19: 191-201, 1976.
2. D. G. W. Smith, C. M. Gold, and D. A. Tomlinson, "The atomic number dependence of the x-ray continuum intensity and the practical calculation of background in energy dispersive electron microprobe analysis," *X-ray Spectrometry* 4: 149-156, 1975.
3. T. S. Rao-Sahib and D. B. Wittry, "The x-ray continuum from thick targets," in G. Shinoda, K. Kohra, and T. Ichinokawa, Eds., *Proc. 6th Intern. Conf. X-ray Optics and Microanalysis*, Tokyo: University of Tokyo Press, 1972; pp. 131-137.
4. G. Springer and B. Nolan, "Mathematical expressions for the evaluation of X-ray emission and critical absorption energies, and of mass absorption coefficients," *Can. J. Spectros.* 21: 134-138, 1976.
5. G. Springer, "Fluorescence by continuous radiation in multi-element targets," in G. Shinoda, K. Kohra, and T. Ichinokawa, Eds., *Proc. 6th Intern. Conf. X-ray Optics and Microanalysis*, Tokyo: University of Tokyo Press, 1972; pp. 141-146.
6. G. Springer, "FEPAC: The Falconbridge procedure for computing electron-probe analysis corrections," Falconbridge Metallurgical Laboratories Internal Report FRL153a, 1976.
7. P. J. Statham, "Escape peaks and internal fluorescence for a Si(Li) detector and general geometry," *J. Phys.* [E]9: 1023, 1976.

## A USER-ORIENTED SOFTWARE SYSTEM FOR ELECTRON MICROPROBES

W. F. Chambers and J. H. Doyle

We have developed a user-oriented software system for electron microprobes. The TASK<sup>1,2</sup> automation program which provides instrument control and data collection is also capable of calling auxiliary programs that can provide quantitative data reduction, editing, plotting, summary, and statistical-analysis capabilities. Qualitative analysis auxiliary capabilities include digital electronic scanning of the beam, mechanical scanning of the stage and the wavelength-dispersive (WDS) spectrometers, identification of energy-dispersive (EDS) peaks, low magnification x-ray mapping (which requires synchronous scanning of the spectrometers and the electron beam), and particle characterization. A disk operating system facilitates loading, exchanging, and saving of programs and data.

Tables 1 and 2 list the items which are under computer control and the accessible data sources. All items in Tables 1 and 2 are software accessible via simple keyboard commands;

TABLE 1.--Items controllable by computer through TASK automation program.

1. Spectrometer position and scanning
2. Crystal selection
3. Detector voltage
4. Pulse height analyzer window
5. Electron beam scanning
6. Electron beam current
7. Camera shutter
8. Film transport
9. Stage
10. Beam blanking
11. Faraday cup

TABLE 2.--Data input available to TASK automation program.

1. Electron beam current (aperture, Faraday cup)
2. Counts from wavelength-dispersive spectrometer
3. Crystal select for wavelength-dispersive spectrometers
4. Counts vs energy from energy-dispersive spectrometer
5. Time
6. Digitized video from secondary-electron detector

for example, POSition X to 28 sets the X-axis of the stage to a position of 28 mm. Much more complex operations are also possible via simple commands; for example, MEASure FE1 will select the lithium fluoride (LiF) crystal in spectrometer 1, set the proper detector voltage and pulse height analyzer window, position the spectrometer to the Fe peak listed in the element table, perform a peak search if the search flag has been set, collect peak data for 5 sec, collect background data if the background flag has been set, compute the counting time required to obtain sufficient data for 1% counting statistics, collect additional data if required, correct the data for background and deadtime, form the probe-ratio (K-ratio) with respect to standard data, apply a correction factor if the standard is not a pure element or oxide, and report the resulting K-ratio along with the 1-sigma variance expected as a result of the counting statistics of both the standard and the unknown.

---

W. F. Chambers is with Sandia Laboratories, Box 5800, Albuquerque, NM 87185. J. H. Doyle is with Rockwell International, Golden, CO 80401. This work was supported by the U.S. Department of Energy under Contract DE-AC04-76DP99789.

These commands can be executed from the keyboard or can be combined into "schedules" for unattended operation. Schedules can also incorporate auxiliary program calls and direct calls to portions of the TASK automation program. PHOTO, a schedule that controls the camera system, has been reported at a previous conference.<sup>3</sup> On line quantitative analyses can be performed by a second schedule, QUANT.<sup>4</sup>

QUANT is initiated by the TASK command RUN QUANT, which can be abbreviated to R.Q. QUANT enters a conversational mode and asks whether an atomic number-absorption-fluorescence (ZAF) or a Bence-Albee<sup>5</sup> analysis is desired. Next, the appropriate element information is requested: number of elements, operating voltage, element names, lines, and references for ZAF; number of elements, element names and references, and number of oxygen atoms for stoichiometry for Bence-Albee. After this information is input, an edit mode permits the correction of any errors. Continuing in the conversational mode, the "setup" section is entered and data collection parameters (EDS collection time, desired standard deviation and maximum counting time for WDS data, flags for peak searches and background collection, label, and desired beam current) are input. The "setup" section also permits selection of stage operating modes (joystick, points table, or trace along lines defined by points in the points table), creation of a disk file for data storage, and editing of the parameters input in the "setup" section. After QUANT has been initialized, detection limits for the current machine operating conditions are calculated and printed and data collection is begun. During the data collection phase the spectrometers are run asynchronously and in their most efficient manner. Once data have been collected for the first point, they are transferred to a buffer so that they can be converted to concentrations and the results printed while the data for the next point are being collected. Data reduction is via one of two auxiliary programs: ZAF78<sup>6</sup> for a ZAF analysis or BA78<sup>7</sup> for a Bence-Albee analysis.

After QUANT has been initialized and executed, it can be re-executed without repetition of the initialization process. If a particular set of elements is to be frequently analyzed, the initialization parameters for the set can be assigned a file number, saved, and later recalled from disk. It is also possible to edit a previously entered set of analysis conditions or element parameters.

The above software has been written in Flextran<sup>8</sup> for a Cameca MBX microprobe with Tracor Northern automation. With minor modifications it is directly applicable to any Tracor Northern automated system. The concepts used in the formulation of the system could be applied to systems that use other hardware or programmed in another language.

#### References

1. J. J. McCarthy and N. F. Wodke, *TASK: Wave Dispersive Spectrometer and Stage Automation Program. Version 3.* Software Dept., Tracor Northern.
2. W. F. Chambers, SANDIA-TASK '78: *An Electron Microprobe Automation Program*, SAND78-1149, 1978.
3. W. F. Chambers, "Computer controlled photography on an electron microprobe," *Proc. 13th MAS Conf.*, 1978, 87.
4. W. F. Chambers and J. H. Doyle, *QUANT. A Quantitative Analysis Schedule for Tracor Northern Automated Electron Microprobes*, SAND78-1836, 1979.
5. A. E. Bence and A. L. Albee, "Empirical correction factors for the electron microprobe analysis of silicates and oxides," *J. Geology* 36: 322-327, 1964.
6. J. H. Doyle and W. F. Chambers, *ZAF78. An Improved Quantitative Analysis Program for Tracor Northern Systems*, Rockwell Rocky Flats Physical Metallurgy report, PMRD-78-006 1979.
7. W. F. Chambers, *BA78. An Improved Bence-Albee Oxide Analysis Program for Tracor Northern Systems*, SAND78-1835, 1979.
8. F. H. Schamber, *FLEXTRAN*, Tracor Northern Report, TN1800M, 1975.

## NEW TOPICS ABOUT AN ON-LINE CORRECTION PROCEDURE

J. Henoc, C. Conty, and M. Tong

We have previously described an automated microprobe<sup>1</sup> with the capabilities of on-line correction procedure when all elements contained in the specimen are analyzed, as is generally the case. In order to conduct a successful experiment an overall strategy has to be planned. We wanted to take advantage of the tricks the operator may use both to save time and to get the most reliable results by eliminating the major sources of uncertainty.

Hardware is similar to that described in the paper given at the Boston Conference,<sup>1</sup> with the memory expanded to 28K.

What we sought to do is to analyze, say, the light elements at a low accelerating voltage in order to minimize the  $f(\chi)$  factor, keeping in mind that excitation of K or L spectra of heavier elements supposes an overvoltage of at least 2. Analysis at *two different voltages* is thus required.

Even when the best experimental conditions are selected, analysis of elements such as oxygen is sometimes difficult, because of the large uncertainty in the mass absorption coefficients. Fortunately, *stoichiometric relationships* allow one to substitute calculation for actual analysis of such elements: The consistency of the material balance (100% check) is preserved, so that a fit of the actual valence values is possible.

A special situation is often encountered when one analyzes semiconductor materials of the type  $(\text{AsGa})_x (\text{SbGa})_{1-x}$ , which behave like a *pseudo binary* system. These materials are very similar to oxide mixtures with valences all equal to unity. In such a compound, analysis of one element is sufficient to characterize the specimen.

Additional elements may be included in a matrix of known composition. If we assume that the composition of the matrix is unchanged, accuracy of measurement of "*trace*" element concentrations is not affected, and the problem is reduced to these elements. In fact, analysis of principal components is not very helpful because of the statistical errors involved.

The various cases listed above are described by the switching within the large NBS COR2 computer program.<sup>2</sup> We have included the same capabilities in the MBXCØR package to achieve the same degree of flexibility with the minicomputer of the microprobe.<sup>1</sup> Some examples of application follow.

In specific fields of application of microprobe analysis (mineralogy, geology, etc.), description of the specimen and of the experimental conditions may be tedious. An update of one compound standard must follow the whole dialog because program execution is sequential. The simplest way to randomize the procedure is to employ an ASCII temporary input file which may be accessed by the RT II EDITOR System. This file is first assembled according to a dialog mode with the possibility of all the safety statements. Further updating is made by means of the EDITOR System as shown in the example. Data processing is based on the classical ZAF approach and the main physical constants are internally computed by means of polynomial fits to the best known experimental or theoretical data. The same is true for the mass absorption coefficients which fit the HEINRICH values.<sup>3</sup> Intensity calculation are very sensitive to the values of these constants. At the request of some of our colleagues who want a personal touch in the processing of their data we have tailored a special version of CORREX that allows them to input values of their own. Every time an absorption coefficient calculation is encountered, its identification and the result (followed by a question mark) are output on the printer. If the operator calls for a carriage return the calculated value is adopted; if he types an actual value, that replaces the calculated value. Once the permanent set of data has been computed (PHYSIC.DAT file) this update is available for further use on this system of elements (see example

---

Authors Henoc and Tong are at the Centre National des Etudes de Télécommunication, 92130 Issy-les-Moulineaux; author Conty is at Cameca, 103 Boulevard Saint-Denis, 92400 Courbevoie, France.

TABLE 1.--Examples of switching 4: (1) use of ACII temporary input file; (2) switching 4; (3) input check; (4) printing of ASCII file data; (5) run of quantitative microprobe analysis for experimental conditions from ASCII file.

```

RUN DX1:ASCIN _____ ①
NEW PROBLEM
  1 OR 2 ACCELERATING VOLTAGE(S) ? 1.
INPUT THE 1TH ACCELERATING VOLTAGE :10.
TOTAL NUMBER OF ELEMENTS CONTAINED IN THE SPECIMEN ?3.
SELECT PROPERLY THE SWITCH
      ALL ELEMENTS ARE ANALYZED      ANSWER
      ONE ELEMENT IS ANALYZED BY STOICHIOMETRY 2
      ONE ELEMENT IS ANALYZED BY DIFFERENCE 3
      THE SPECIMEN IS AN OXYDE-LIKE ONE 4
      TRACE ANALYSIS 5
      K CALCULATION 6

ANSWER ?4. _____ ②
HOW MANY COMPOUND STANDARDS ARE USED ?
TAKE OFF ANGLE (DEFAULT : 40. DEGREES) ?

ELEMENT TO BE ANALYZED NO 1 SYMBOL:LINE ? AL KA
THE SYMBOL OF THE ELEMENT CALCULATED BY STOICHIOMETRY IS THE LAST INPUT
SYMBOL OF THE NON ANALYZED ELEMENT NO: 1 ?GA
SYMBOL OF THE NON ANALYZED ELEMENT NO: 2 ?AS
ENTER VALENCE OF ALL ELEMENTS CONTAINED IN THE SPECIMEN (EX:3,2,1) .
ENTER VALENCE OF :
AL,GA,AS,
1,1,1

STOP --

.RUN DX1:CHEASC _____ ③
STOP --

.TYPE ASCIN.DAT _____ ④

1
10.000000
3
4
0
0.000000
AL KA
GA
AS
1 1 1

RUN DX1:CORASC _____ ⑤
QUANTITATIVE MICROPROBE ANALYSIS
DO YOU WANT TO HAVE THE SAME PHYSICAL CONDITIONS AND THE SAME
STANDARDS AS IN THE PREVIOUS PROBLEM (Y OR N) ? N

NEW PROBLEM
  1 OR 2 ACCELERATING VOLTAGE(S) ? 1.
INPUT THE 1TH ACCELERATING VOLTAGE :10.
TOTAL NUMBER OF ELEMENTS CONTAINED IN THE SPECIMEN ?3.
SELECT PROPERLY THE SWITCH
      ALL ELEMENTS ARE ANALYZED      ANSWER
      ONE ELEMENT IS ANALYZED BY STOICHIOMETRY 2
      ONE ELEMENT IS ANALYZED BY DIFFERENCE 3
      THE SPECIMEN IS AN OXYDE-LIKE ONE 4
      TRACE ANALYSIS 5
      K CALCULATION 6

ANSWER : 4
NUMBER OF COMPUTED ELEMENTS : 1
0 COMPOUND STANDARD(S) USED
TAKE OFF ANGLE IS 40.00 DEGREES

ELEMENT TO BE ANALYZED NO 1 AL KA
ACCELERATION VOLTAGE 10.00 KV
THE SYMBOL OF THE ELEMENT CALCULATED BY STOICHIOMETRY IS THE LAST INPUT
SYMBOL OF THE NON ANALYZED ELEMENT NO: 1 IS GA
SYMBOL OF THE NON ANALYZED ELEMENT NO: 2 IS AS
VALENCE OF :
AL,GA,AS,
1 1 1

UPDATE ABSORPTION COEFFICIENTS (Y OR N) ? N
ELEMENT : AL GA AS
VALENCE : 1 1 1
NEW VALUES OF VALENCE (Y OR N) ?
N
SWITCH(4) ?4.
ARE THE DATA SAVED IN FILE <KRATIO.DAT> ?N
INPUT K OF AL : .1
POINT NO: 1

      K
ELEMENT I.X./I.STD. K.RATIO W.F. CONCN. NORMALIZED ELEM. % AS
      ATOM. C ATOM. C COMP. C
AL : 0.1000 0.1000 0.1655 0.3515 0.6252
GA 0.1807 0.1485 OXYDE-LIKE
AS 0.6538 0.5000 SPECIMEN

TOTAL : 1.0000
ITERATION : 3
MORE ? N
SWITCH(4) ?

```

TABLE 2.--Trace analysis: (1) old problem; (2) new problem.

```

RUN DX1:CORX2 _____ ①
QUANTITATIVE MICROPROBE ANALYSIS
DO YOU WANT TO HAVE THE SAME PHYSICAL CONDITIONS AND THE SAME
STANDARDS AS IN THE PREVIOUS PROBLEM (Y OR N) ? Y
HAVE THESE CONDITIONS TO BE PRINTED OUT (Y OR N) ? Y

      THE COSECANT OF THE TAKE OFF ANGLE IS 1.556
      TOTAL NUMBER OF ELEMENTS : 3
1 ELEMENTS ARE ANALYZED :
THE 1TH STANDARD IS PURE AL LINE:KA AT 10. KV

AL IS ATRACE ELEMENT
SWITCH(5) ?5.
ARE THE DATA SAVED IN FILE <KRATIO.DAT> ?N
INPUT K OF AL : .0003
INPUT C OF AS:1.5179
INPUT C OF GA:1.4821

POINT NO: 1

      K
ELEMENT I.X./I.STD. K.RATIO CONCN. ATOM. C
AL : 0.0003 0.0003 0.0005 0.0014
AS 0.5179 0.4992
GA 0.4821 0.4994

TOTAL : 1.0005
ITERATION : 2
MORE ? N
SWITCH(5) ?

QUANTITATIVE MICROPROBE ANALYSIS
DO YOU WANT TO HAVE THE SAME PHYSICAL CONDITIONS AND THE SAME
STANDARDS AS IN THE PREVIOUS PROBLEM (Y OR N) ? BYE
STOP --

RUN DX1:CORX2 _____ ②
QUANTITATIVE MICROPROBE ANALYSIS
DO YOU WANT TO HAVE THE SAME PHYSICAL CONDITIONS AND THE SAME
STANDARDS AS IN THE PREVIOUS PROBLEM (Y OR N) ? N

NEW PROBLEM
  1 OR 2 ACCELERATING VOLTAGE(S) ? 1.
INPUT THE 1TH ACCELERATING VOLTAGE :10.
TOTAL NUMBER OF ELEMENTS CONTAINED IN THE SPECIMEN ?3.
SELECT PROPERLY THE SWITCH
      ALL ELEMENTS ARE ANALYZED      ANSWER
      ONE ELEMENT IS ANALYZED BY STOICHIOMETRY 2
      ONE ELEMENT IS ANALYZED BY DIFFERENCE 3
      THE SPECIMEN IS AN OXYDE-LIKE ONE 4
      TRACE ANALYSIS 5
      K CALCULATION 6

ANSWER ?5.
NUMBER OF COMPUTED ELEMENTS ?1.
HOW MANY COMPOUND STANDARDS ARE USED ?
TAKE OFF ANGLE (DEFAULT : 40. DEGREES) ?

ELEMENT TO BE ANALYZED NO 1 SYMBOL:LINE ? AL,KA
SYMBOL OF THE NON ANALYZED ELEMENT NO: 1 ?AS
SYMBOL OF THE NON ANALYZED ELEMENT NO: 2 ?GA
HAVE THESE CONDITIONS TO BE PRINTED OUT (Y OR N) ? Y

      THE COSECANT OF THE TAKE OFF ANGLE IS 1.556
      TOTAL NUMBER OF ELEMENTS : 3
1 ELEMENTS ARE ANALYZED :
THE 1TH STANDARD IS PURE AL LINE:KA AT 10. KV

AL IS ATRACE ELEMENT
SWITCH(5) ?5.
ARE THE DATA SAVED IN FILE <KRATIO.DAT> ?N
INPUT K OF AL : .0003
INPUT C OF AS:1.5179
INPUT C OF GA:1.4821

POINT NO: 1

      K
ELEMENT I.X./I.STD. K.RATIO CONCN. ATOM. C
AL : 0.0003 0.0003 0.0005 0.0014
AS 0.5179 0.4992
GA 0.4821 0.4994

TOTAL : 1.0005
ITERATION : 2
MORE ? N
SWITCH(5) ?

```

TABLE 3.--Examples of switching 6, then 1:  
 (1) use of ASCII temporary input file;  
 (2) switching 6; (3) ASCII file data printing;  
 (4) run backward microprobe analysis (experimental conditions from ASCII files;  
 (5) switching 6; (6) optional absorption coefficients; (7) switching 1.

RUN RX1:ASCIN  
 NEW PROBLEM  
 1 OR 2 ACCELERATING VOLTAGE(S) ? 1.  
 INPUT THE 1TH ACCELERATING VOLTAGE :20.  
 TOTAL NUMBER OF ELEMENTS CONTAINED IN THE SPECIMEN ?2.

SELECT PROPERLY THE SWITCH

ALL ELEMENTS ARE ANALYZED	ANSWER
ONE ELEMENT IS ANALYZED BY STOICHIOMETRY	1
ONE ELEMENT IS ANALYZED BY DIFFERENCE	2
THE SPECIMEN IS AN OXYDE-LIKE ONE	3
TRACE ANALYSIS	4
K CALCULATION	5
	6

ANSWER ?6.

NUMBER OF COMPUTED ELEMENTS ?2.  
 HOW MANY COMPOUND STANDARDS ARE USED ?  
 TAKE OFF ANGLE (DEFAULT : 40. DEGREES) ?

ELEMENT TO BE ANALYZED NO 1 SYMBOL/LINE ? FE KA

ELEMENT TO BE ANALYZED NO 2 SYMBOL/LINE ? CR KA

STOP --

.TYPE ASCIN.DAT

1  
 20.000000

2  
 6

3  
 0

4  
 0.000000

FE KA

CR KA

RUN RX1:CORASC

#### QUANTITATIVE MICROPROBE ANALYSIS

DO YOU WANT TO HAVE THE SAME PHYSICAL CONDITIONS AND THE SAME STANDARDS AS IN THE PREVIOUS PROBLEM (Y OR N) ? N

NEW PROBLEM

1 ACCELERATING VOLTAGE(S)

THE 1TH ACCELERATING VOLTAGE IS :20.00 KV

2 IS THE TOTAL NUMBER OF ELEMENTS CONTAINED IN THE SPECIMEN

SELECT PROPERLY THE SWITCH

ALL ELEMENTS ARE ANALYZED	ANSWER
ONE ELEMENT IS ANALYZED BY STOICHIOMETRY	1
ONE ELEMENT IS ANALYZED BY DIFFERENCE	2
THE SPECIMEN IS AN OXYDE-LIKE ONE	3
TRACE ANALYSIS	4
K CALCULATION	5
	6

ANSWER : 6

NUMBER OF COMPUTED ELEMENTS : 2

0 COMPOUND STANDARD(S) USED

TAKE OFF ANGLE IS 40.00 DEGREES

ELEMENT TO BE ANALYZED NO 1 FE KA

ACCELERATION VOLTAGE 20.00 KV

ELEMENT TO BE ANALYZED NO 2 CR KA

ACCELERATION VOLTAGE 20.00 KV

UPDATE ABSORPTION COEFFICIENTS (Y OR N) ? Y

MU(FE:FEKA)= 71.499123 ?

MU(CR:CRKA)= 87.976936 ?

MU(CR:FEKA)= 473.697723 ?

MU(FE:CRKA)= 112.991249 ?

MU(FE:FEKA)= 71.499123 ?

MU(CR:FEKA)= 473.697723 ?

SWITCH(6) ?6.

DIFFUSION OF FE-CR (Y OR N) ?N

INPUT WEIGHT FRACTION OF FE : .9

INPUT WEIGHT FRACTION OF CR : .1

ELEMENT	I.X./I.STD.	K.RATIO	CONCEN.	ATOM. C
FE :	0.8843	0.8843	0.9000	0.8934
CR :	0.1248	0.1248	0.1000	0.1066

TOTAL : 1.0000

ITERATION : 0

MORE ? N

SWITCH(6) ?1.

ARE THE DATA SAVED IN FILE (KRATIO.DAT) ?N

INPUT K OF FE : .8843

INPUT K OF CR : .1248

POINT NO: 1

ELEMENT	I.X./I.STD.	K.RATIO	CONCEN.	ATOM. C
FE :	0.8843	0.8843	0.9000	0.8934
CR :	0.1248	0.1248	0.1000	0.1066

TOTAL : 1.0091

ITERATION : 3

MORE ? N

SWITCH(1) ?

TABLE 4.--Option for updating absorption coefficients: (1) updating.

#### QUANTITATIVE MICROPROBE ANALYSIS

DO YOU WANT TO HAVE THE SAME PHYSICAL CONDITIONS AND THE SAME STANDARDS AS IN THE PREVIOUS PROBLEM (Y OR N) ? N

NEW PROBLEM

1 ACCELERATING VOLTAGE(S)

THE 1TH ACCELERATING VOLTAGE IS :20.00 KV

2 IS THE TOTAL NUMBER OF ELEMENTS CONTAINED IN THE SPECIMEN

SELECT PROPERLY THE SWITCH

ALL ELEMENTS ARE ANALYZED	ANSWER
ONE ELEMENT IS ANALYZED BY STOICHIOMETRY	1
ONE ELEMENT IS ANALYZED BY DIFFERENCE	2
THE SPECIMEN IS AN OXYDE-LIKE ONE	3
TRACE ANALYSIS	4
K CALCULATION	5
	6

ANSWER : 6

NUMBER OF COMPUTED ELEMENTS : 2

0 COMPOUND STANDARD(S) USED

TAKE OFF ANGLE IS 40.00 DEGREES

ELEMENT TO BE ANALYZED NO 1 FE KA

ACCELERATION VOLTAGE 20.00 KV

ELEMENT TO BE ANALYZED NO 2 CR KA

ACCELERATION VOLTAGE 20.00 KV

UPDATE ABSORPTION COEFFICIENTS (Y OR N) ? Y

MU(FE:FEKA)= 71.499123 ?50.

MU(CR:CRKA)= 87.976936 ?100.

MU(CR:FEKA)= 473.697723 ? 500.

MU(FE:CRKA)= 112.991249 ? 150.

MU(FE:FEKA)= 71.499123 ? 50.

MU(CR:FEKA)= 473.697723 ? 500.

SWITCH(6) ?6.

DIFFUSION OF FE-CR (Y OR N) ?N

INPUT WEIGHT FRACTION OF FE : .9

INPUT WEIGHT FRACTION OF CR : .1

ELEMENT	I.X./I.STD.	K.RATIO	CONCEN.	ATOM. C
FE :	0.8823	0.8823	0.9000	0.8934
CR :	0.1266	0.1266	0.1000	0.1066

TOTAL : 1.0000

ITERATION : 0

MORE ? N

SWITCH(6) ?1.

ARE THE DATA SAVED IN FILE (KRATIO.DAT) ?N

INPUT K OF FE : .8823

INPUT K OF CR : .1266

POINT NO: 1

ELEMENT	I.X./I.STD.	K.RATIO	CONCEN.	ATOM. C
FE :	0.8823	0.8823	0.9000	0.8934
CR :	0.1266	0.1266	0.1000	0.1066

TOTAL : 1.0089

ITERATION : 3

TABLE 5.--Output of Physic file before and after updating.

RUN DX1:PHYS12

```

PHYSICAL CONDITIONS OF MICRO ANALYSIS
=====
** THIS IS A 2 ELEMENTS ZAF APPLICATION 1 2 OF THEM ARE ANALYZED
   THE COSECANT OF THE TAKE OFF ANGLE IS 1.556
   0 COMPOUND STANDARDS ARE USED
ACCELERAT. VOLT.= 20.00 REED COEFF.= 0.373892E+04

* THE 1TH STANDARD IS PURE FE
  ATOMIC NUMBER:26
  ANALYZED LINE:KA CODED:11 WAVELENGTH = 1.93636 E0= 20.
  EXCITAT. KEV = 7.110 BACKSC. COEF = 0.8790
  AUTOABSORPTION OF PURE FE ACI= 71.5
  AUTOABSORPTION OF THE STANDARD ACAB= 71.5
  FLUORESCENCE COMPONENT FI= 0.0000
  INTENSITY OF PURE FE FACTI= 0.48863E+00
  INTENSITY RATIO STANDARD/PURE AIRI= 1.000000
  BACKSCATTERING VECTOR
0.8790 0.8896
  ABSORPTION COEFFICIENT VECTOR
  71.50 473.70
  REED VECTOR
0.000000E+00 0.000000E+00
  EXCITING LINE VECTOR
  0
  ABSORPTION COEFFICIENT MATRIX-FLUORESCENCE

* THE 2TH STANDARD IS PURE CR
  ATOMIC NUMBER:24
  ANALYZED LINE:KA CODED:11 WAVELENGTH = 2.28974 E0= 20.
  EXCITAT. KEV = 5.985 BACKSC. COEF = 0.8803
  AUTOABSORPTION OF PURE CR ACI= 88.0
  AUTOABSORPTION OF THE STANDARD ACAB= 88.0
  FLUORESCENCE COMPONENT FI= 0.0000
  INTENSITY OF PURE CR FACTI= 0.74855E+00
  INTENSITY RATIO STANDARD/PURE AIRI= 1.000000
  BACKSCATTERING VECTOR
0.8691 0.8803
  ABSORPTION COEFFICIENT VECTOR
  112.99 87.98
  REED VECTOR
0.980899E-01 0.000000E+00
  EXCITING LINE VECTOR
  1015 0
  ABSORPTION COEFFICIENT MATRIX-FLUORESCENCE
EXCITING ELEMENT NO: 1 LINE:1
  71.50 473.70

  SWITCH IS AT 6
STOP -

```

RUN DX1:PHYS12

```

PHYSICAL CONDITIONS OF MICRO ANALYSIS
=====
** THIS IS A 2 ELEMENTS ZAF APPLICATION 1 2 OF THEM ARE ANALYZED
   THE COSECANT OF THE TAKE OFF ANGLE IS 1.556
   0 COMPOUND STANDARDS ARE USED
ACCELERAT. VOLT.= 20.00 REED COEFF.= 0.373892E+04

* THE 1TH STANDARD IS PURE FE
  ATOMIC NUMBER:26
  ANALYZED LINE:KA CODED:11 WAVELENGTH = 1.93636 E0= 20.
  EXCITAT. KEV = 7.110 BACKSC. COEF = 0.8790
  AUTOABSORPTION OF PURE FE ACI= 50.0
  AUTOABSORPTION OF THE STANDARD ACAB= 50.0
  FLUORESCENCE COMPONENT FI= 0.0000
  INTENSITY OF PURE FE FACTI= 0.49339E+00
  INTENSITY RATIO STANDARD/PURE AIRI= 1.000000
  BACKSCATTERING VECTOR
0.8790 0.8896
  ABSORPTION COEFFICIENT VECTOR
  50.00 500.00
  REED VECTOR
0.000000E+00 0.000000E+00
  EXCITING LINE VECTOR
  0
  ABSORPTION COEFFICIENT MATRIX-FLUORESCENCE

* THE 2TH STANDARD IS PURE CR
  ATOMIC NUMBER:24
  ANALYZED LINE:KA CODED:11 WAVELENGTH = 2.28974 E0= 20.
  EXCITAT. KEV = 5.985 BACKSC. COEF = 0.8803
  AUTOABSORPTION OF PURE CR ACI= 100.0
  AUTOABSORPTION OF THE STANDARD ACAB= 100.0
  FLUORESCENCE COMPONENT FI= 0.0000
  INTENSITY OF PURE CR FACTI= 0.74432E+00
  INTENSITY RATIO STANDARD/PURE AIRI= 1.000000
  BACKSCATTERING VECTOR
0.8691 0.8803
  ABSORPTION COEFFICIENT VECTOR
  150.00 100.00
  REED VECTOR
0.980899E-01 0.000000E+00
  EXCITING LINE VECTOR
  1015 0
  ABSORPTION COEFFICIENT MATRIX-FLUORESCENCE
EXCITING ELEMENT NO: 1 LINE:1
  50.00 500.00

  SWITCH IS AT 6
STOP -

```

of application).

In summary, the package has gained more flexibility without losing the internal consistency of the full treatment. What we must keep in mind is that we have purchased costly equipment to resolve analytical problems in the shortest time; just the kind of service the microprobe, if it is well managed, can insure to match the ease of preparation of microanalysis standards. Perhaps we may enjoy programming our problems one at a time but it is at a cost of lower efficiency. One of us, in charge of an analysis laboratory is glad to find a reliable guide whatever his mood and the pressures are.

#### References

1. J. Henoc and M. Tong, *Eighth Int. Conf. on X-Ray Optics and Microanalysis*, page 46A, Boston, 1977.
2. J. Henoc, K. F. J. Heinrich, and R. L. Myklebust, Technical Note 759, Washington D.C.: National Bureau of Standards, 1973.
3. K. F. J. Heinrich, *The Electron Microprobe*, New York: Wiley, 1966.

## ELEMENTAL DISTRIBUTION MAPS AND LINE PROFILES IN X-RAY ANALYSIS

D. P. Skinner and N. C. Barbi

Two of the most commonly used modes for presenting x-ray microanalysis data are the elemental distribution map (dot map) and the x-ray line profile. Both of these methods are commonly displayed with a corresponding secondary or back-scattered electron image and produce a very graphical presentation of the x-ray data obtained.

### *Elemental Distribution Maps*

The purpose of an elemental distribution map is to display points from the distribution of a particular element over the area of the sample being viewed.

The process is quite similar to obtaining a secondary electron image from the microscope, with the exception that an x-ray signal is being displayed rather than a secondary-electron signal. As the electron beam scans across the sample, x rays are being produced at each point in the raster. The energy-dispersive x-ray spectrometer (EDS) detects these x-rays and sorts them according to their energy. If an x ray of the designated energy is received, the x-ray analyzer generates an appropriate signal to the microscope and produces a bright dot on the microscope cathode-ray tube (CRT). Since the beam on the microscope CRT is scanning in synchronism with the scan of the electron probe, the dot pattern that appears on the CRT reflects the spatial distribution of the element of interest over the scanned area of the sample.

Most EDS x-ray analyzers allow the operator to select the range of x-ray energies that will result in the output of the dot signal to the microscope. This range of energies is commonly called a window and can be set at any position on the x-ray spectrum. If one of these windows is set on a peak from a particular element, the output of dots to the microscope CRT corresponds to the points on the sample where that element is present. Photographing the output of this signal for the entire raster results in the elemental distribution map. Examples of dot maps with the corresponding secondary-electron images can be seen in Figs. 1 and 3.

### *Line Profile Analysis*

A line profile is obtained as follows. The electron probe is scanned across one line of the raster and the signal from a particular element is monitored across that line. As for the x-ray distribution map, to select a range of energy one sets a window on a peak from the element of interest. As the electron probe scans across the selected line on the sample, the signal from the designated window at each point modulates the beam on the microscope CRT in the Y direction. The result is a plot of elemental x-ray intensity as a function of position across the selected scan line on the CRT.

Two kinds of line profile data are in common use: analog and digital. For an analog line profile, the output of pulses from the window is routed to a rate meter whose deflection produces a real-time Y modulation on the microscope CRT. The digital line profile causes the electron probe to move across the scan line in discrete steps, and the number of x rays in a particular energy window is recorded for each separate point and stored in the analyzer memory. Since the digital line profiles are being recorded in the analyzer, profiles for several elements can be collected simultaneously. The profiles are subsequently transferred to the microscope CRT for photographing. Analog line profile capability is generally provided on most SEM/x-ray systems (usually as an optional accessory). However, digital line profile capability is provided only on certain systems, since it requires some method of external control of the microscope scan coils and synchronism with the start of data collection on the x-ray analyzer.

For both analog and digital line profiles, the usual method of presenting data is to obtain the electron image from the area of interest and then to superimpose both the scan line (the line the electron probe was scanning across the sample) and the line profile (the plot of elemental intensity as a function of position on the scan line) on the same

---

The authors are with Princeton Gamma-Tech, Box 641, Princeton, NJ 08540.



photograph. Examples of this type of display are presented in Figs. 1 and 4.

### *Signal Requirements*

The output of pulses from the window when a dot map or x-ray line profile are being generated is not due solely to characteristic x rays from the element of interest but also to background x rays from the continuum that have the same energies as the characteristic peak. Thus, there is a background level of dots in the map even when the element is not present. Dot-map contrast can be defined as the difference in dot density on regions containing the element compared to the density on regions free of the element. In order to produce a dot map of good contrast, the peak being mapped must be significantly above background when the beam is on the concentrated region of the sample. The greater the peak-to-background ratio, the higher the contrast of the map. In general, when the beam is on a concentrated region of the sample, the counting rate in the mapping window should be at least 50% greater than the counting rate from an element-free region in order to produce a map of reasonable contrast with energy-dispersive systems.

Since the pulses from the mapping window are generated in real time, it is impossible to obtain a true background-subtracted dot map or line profile dynamically. However, the background can be kept at a minimum if one uses a narrow window on the center channels of the peak of interest. Since these channels have the highest peak-to-background ratio  $P/B$ , a greater proportion of their counts will be due to characteristic x rays from the element of interest than to background.

To be sure, use of a narrow window decreases the output rate of pulses from the window. This situation can be improved by an increase in the probe current, slower scan speeds, or repeating scans. Indeed, it has been estimated that at least 20 000 pulses are required for an adequate dot map.<sup>1</sup> In view of the count-rate limitations of EDS x-ray systems, analysis scans of anywhere from 1 to 20 min are dictated.

### *X-ray Spatial Resolution*

When the electron beam strikes a bulk sample, the electrons scatter throughout the material both laterally and in depth. Low-energy secondary electrons that escape the material come from a very shallow depth, at which point the primary electrons have not appreciably scattered in the lateral direction. The secondary signal thus comes from a volume with a diameter just slightly greater than that of the incident electron beam.

However, x rays can escape from much greater depths, so that the resultant x-ray analysis volume or x-ray spatial resolution is much larger in diameter (1-10  $\mu\text{m}$ ) than the primary electron beam. The x-ray volume is so great compared to the electron-beam diameter that at normal SEM operating conditions, the spot size has little or no effect on the x-ray spatial resolution. (In thin sections, the x-ray analysis volume more closely approximates the beam diameter.<sup>2</sup>) The smallest discrete point on the sample from which x-ray data can be obtained is limited by the size of the x-ray analysis volume.

For a dot map or line profile analysis, the x-ray signal is being recorded as a function of the position of the electron beam. If the x-ray analysis volume is 2  $\mu\text{m}$  in diameter and the electron probe is approaching a portion of the sample containing the element of interest, x rays are excited from that region when the beam is 1  $\mu\text{m}$  away. For a dot map, this effect causes diffuse, enlarged edges of the region of interest. A line profile shows a slow, increasing gradient as the beam approaches the interface. As the analysis volume decreases, the edges of a distinct elemental interface get sharper in the dot map and line profile.

For bulk materials in the SEM, x-ray spatial resolution is affected by the accelerating voltage, the density of the material, and the energy of the particular x-ray line of interest. The "qualitative" x-ray analysis volume can be approximated by the expression<sup>3</sup>

$$d = 0.077(E_0^{1.5} - E_c^{1.5})/\rho \quad (1)$$

where  $d$  = x-ray spatial resolution,  $E_0$  = accelerating voltage,  $E_c$  = critical excitation energy of the analytical line, and,  $\rho$  = density of material.

The x-ray spatial resolution therefore degrades with increasing accelerating voltage and decreasing sample density. For a given sample, the analyst can minimize the x-ray

analysis volume by selecting an appropriately low accelerating voltage that still provides sufficient excitation of the x-ray line. For an element with several lines in the analytical range, the lowest energy line can be used to allow the minimum accelerating voltage.

Figure 1 illustrates the effect of reducing voltage (and thus improving spatial resolution) for a Mg distribution map and line profile obtained from an Fe/Si/Mg alloy. At an accelerating voltage of 25 kV, the x-ray spatial resolution for the Mg K $\alpha$  x-ray line is approximately 3  $\mu$ m (as estimated from Eq. 1). Reduction of the voltage to 10 kV yields an improved spatial resolution of 0.7  $\mu$ m and still efficiently excites the Mg x rays. The resultant line-profile and distribution map shows a much sharper delineation of the Mg rich phase.

### *Sample-Detector Geometry*

Elemental distribution maps and line-profile analyses are often obtained from non-uniform sample surfaces. When samples with varying topography are being analyzed, the sample/detector configuration must be considered.

The angle defined by the sample surface and the line an emerging x ray travels to strike the x-ray detector is called the x-ray take-off angle. This angle defines the path length that the x-ray had to travel through the material to exit from the sample. The lower this take-off angle, the greater the path length. The absorption of x rays in the material follows Beer's law:

$$I/I_0 = e^{-\mu_m \rho x} \quad (2)$$

where  $I/I_0$  = fraction of x rays transmitted,  $\mu_m$  = mass absorption coefficient for particular x-ray line,  $\rho$  = density of the absorbing material, and  $x$  = x-ray path length through the material; that is, the longer the x-ray path length  $x$ , the greater the absorption. Also, since  $\mu_m$  is different for each elemental line, the absorption depends on the particular element of interest as well.

As the local topography of a sample surface changes, the x-ray take-off angle changes. The result of this change is a difference in x-ray intensity measured at the detector due to increased or decreased absorption path length. The resulting dot map or line profile reflects the relative differences in x-ray signal due to topographical variations, which can easily be misinterpreted as variations in elemental composition.

An even more dramatic effect can occur on rough surfaces as a result of the line-of-sight nature of x-ray detection. In the secondary-electron image, low-energy secondary electrons are pulled into the biased detector from valleys and depressions in the surface. However, x rays (and back-scattered electrons) must travel in a straight-line path to the detector in order to be recorded. On a rough surface, local regions may exhibit a negative take-off angle or be shadowed from the x-ray detector by a nearby topographic feature. The x-ray signal is then suppressed altogether and gives a very distorted elemental distribution map.

Several techniques can be used to determine whether variations in x-ray signal are due to changing topography or true elemental distribution differences. Rotation of the sample 180° and repetition of the dot map or line profile shifts the variations and shadows if the cause is topographic. Another technique is to collect a dot map or line profile that results from the signal from a background region on the low-energy side of the peak of interest. The background distribution map then shows similar intensity variations to that from the characteristic peak, if they are due to topographical rather than compositional variations.

Figure 2 illustrates the use of a background dot map as an aid in interpreting an Fe distribution map obtained from a steel fracture surface. Comparison of the two maps shows the same shadows and variations of intensity. Since the background x rays mapped were close in energy to the Fe x rays (and would therefore experience similar absorption), the similarity of the dot maps indicates that topographic variations are responsible for the variations in dot density. It should be noted that a much longer collection time was used to obtain the background dot map.

It is often possible to orient the sample to minimize topographical shadowing effects,

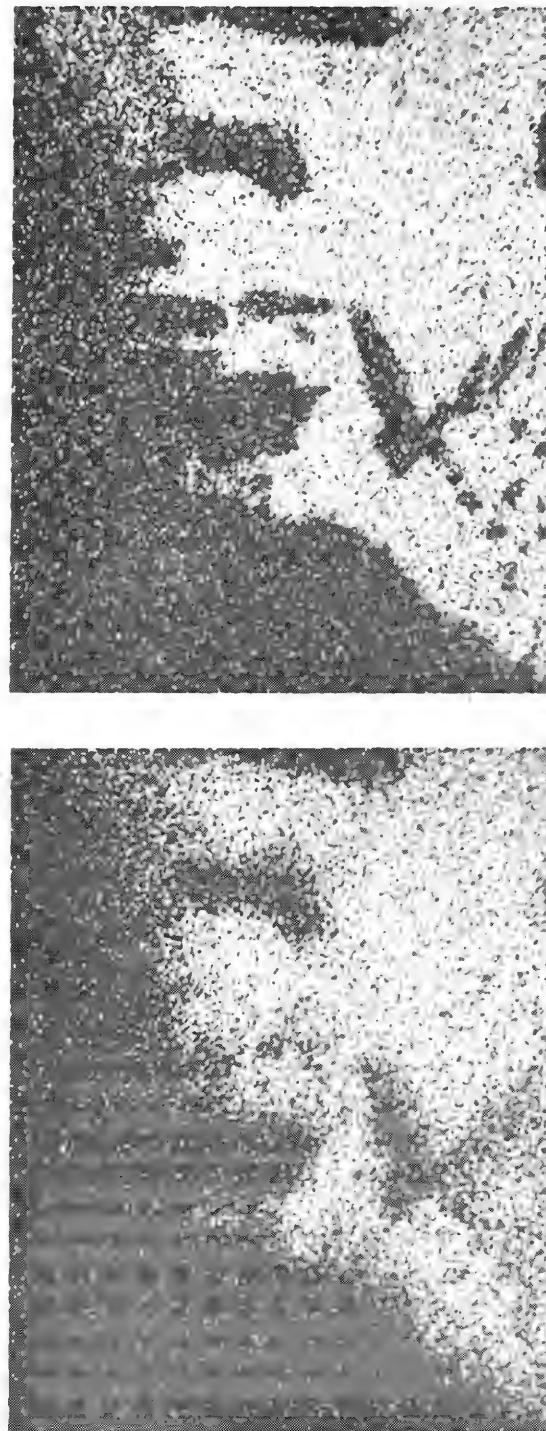
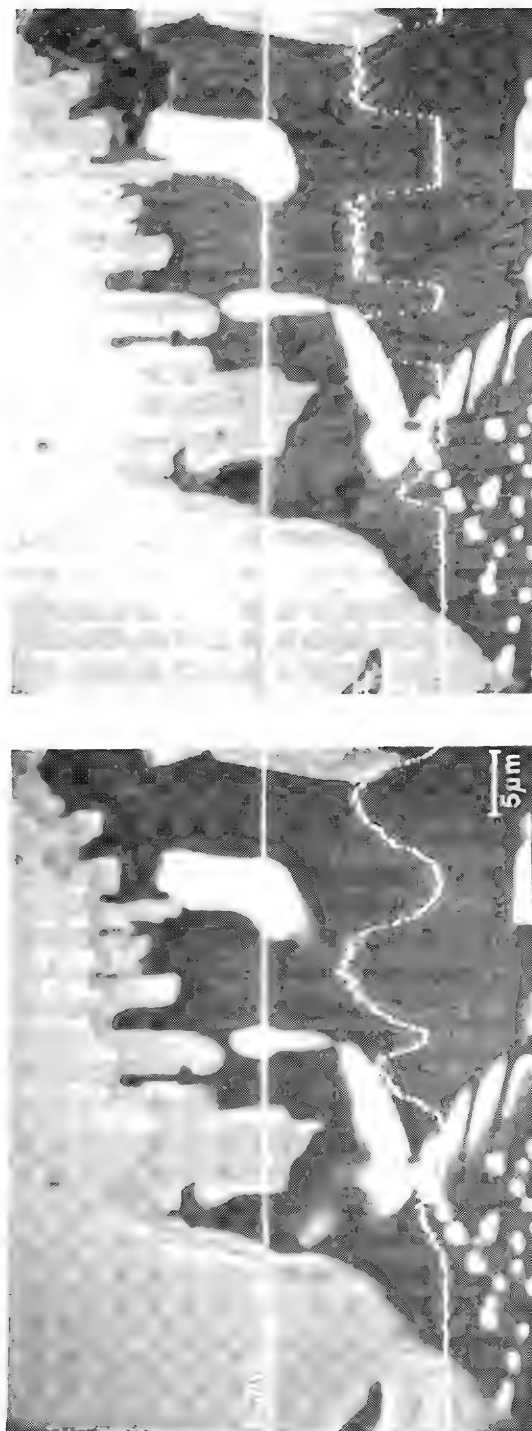


FIG. 1.--Comparison of Mg line profile (top) and distribution maps (bottom) acquired at accelerating voltages of 25 kV (left) and 10 kV (right) illustrating the improved x-ray spatial resolution at the lower voltage.

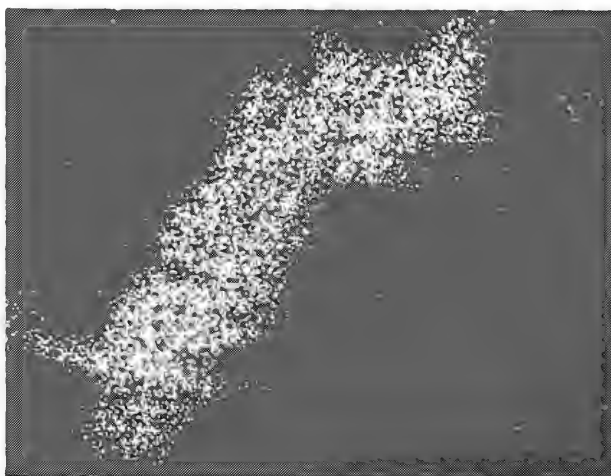
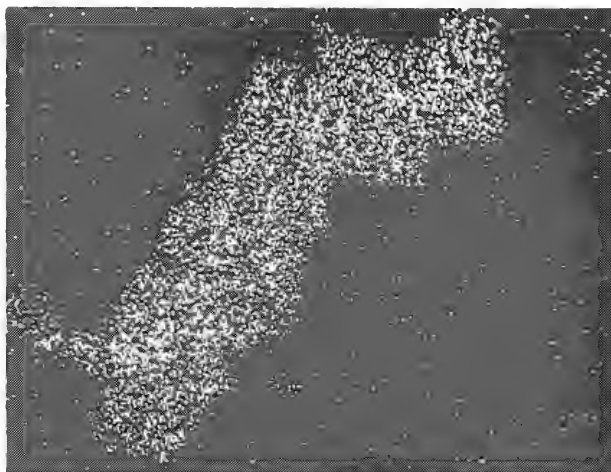
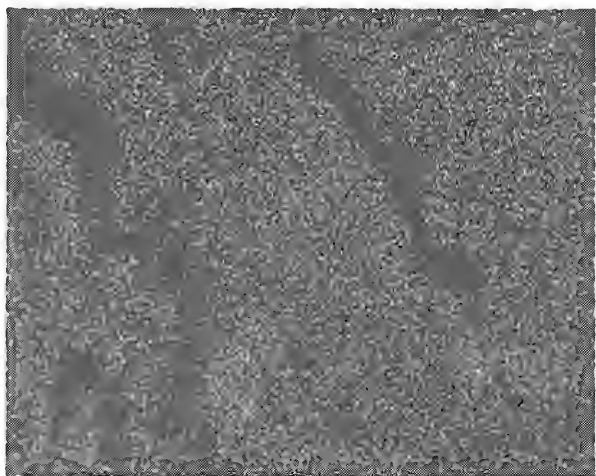
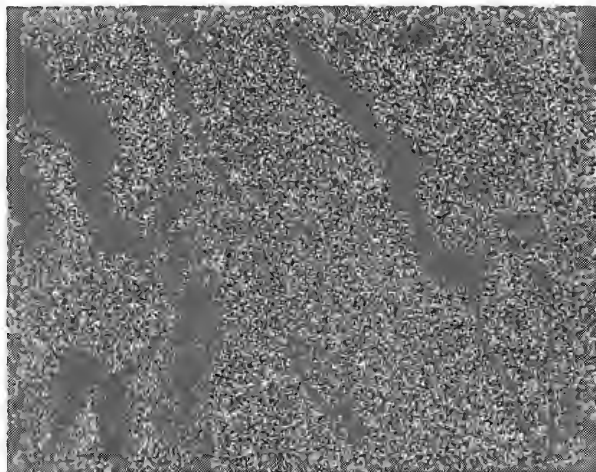
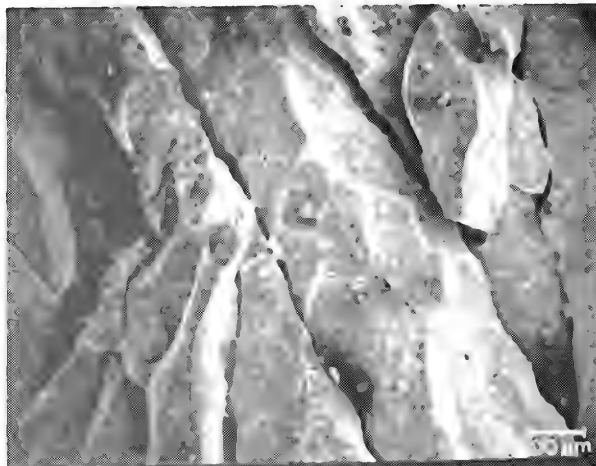


FIG. 2.--Secondary electron image of steel fracture surface (top) with corresponding Fe distribution map (middle) and dot map obtained from background signal (bottom).

FIG. 3.--Secondary electron image of multi-phase material (top) and comparison of the corresponding normal elemental distribution map (middle) with an enhanced elemental distribution map (bottom).



provided the position of the x-ray detector relative to the image on the microscope CRT is known. The orientation of the x-ray detector can often be determined easily by extending the detector inward while imaging the sample at a long working distance and low magnification. When the end-cap or collimator reaches column center line and breaks the beam, its effect will be seen in the image, and its orientation revealed.

#### *Data Processing*

*Enhancement of Elemental Distribution Maps.* As mentioned previously, the output of pulses from a window occurs whenever an x ray of the appropriate energy is detected. This x ray may be a characteristic x ray from the element of interest or a background x ray of the same energy. The result is the presence of a background level of dots in the distribution map. One method of "removing" this background is to impose not only an energy criterion but also a rate threshold that must be exceeded before any pulses are generated. By selection of the appropriate threshold, no dots result until the "background" level is exceeded. Figure 3 compares a normal dot map with an "enhanced" dot map in which the count-rate threshold technique was used.

Artificial enhancement may result in a more pleasing dot map of higher contrast, but important information concerning topography may be lost and artifacts may be introduced. A better procedure for enhancing the elemental distribution map is to use a narrow window set around the center channels of the peak where the peak to background ratio is maximized

*Background Subtraction of Digital Line Profiles.* One advantage of the digital line profile is that the data can be processed after collection, so that a background subtracted line profile can be obtained. A digital line profile is collected for the element of interest; simultaneously, a profile is collected for a background region near and on the low-energy side of the peak. Subtraction of this background line profile, performed digitally in the x-ray analyzer, yields a resultant net intensity profile for the element of interest.

This technique is extremely useful when an intensity profile is being obtained across a region with greatly varying composition, where total x-ray count rate may change significantly from point to point. In the example shown in Fig. 4, a line profile for K shows no significant intensity variation between the contamination particle and the matrix. However, the x-ray energy spectra indicate the presence of K in the particle but not in the matrix. The *total* x-ray count rate from the matrix was so much greater than the count rate from the particle that the intensity in the K window due to background x rays from the matrix was equivalent to both peak and background coming from the particle. However,



FIG. 4.--Digital line profiles for the potassium window (A), for a background window near the peak (B), and the resulting potassium net intensity profile (A - across a contamination particle on solder).

the background-subtracted K line profile gives the correct result.

#### *References*

1. J. I. Goldstein et al., *Practical Scanning Electron Microscopy*, New York: Plenum Press, 1975, 407.
2. J. I. Goldstein et al., *Quantitative X-ray Analysis in the Electron Microscope*, SEM/1977, 1977, vol. 1, 315-322.
3. S. J. B. Reed, *Electron Microprobe Analysis*, London: Cambridge University Press, 1975, 217.

## NEW METHODS TO OBTAIN AND PRESENT SEM X-RAY LINE SCANS

John C. Russ

SEM x-ray line scans have been generally the least used of the modes of x-ray data collection and presentation. The x-ray map has been popularly used because of its obvious pictorial complement to the normal SEM picture, and point (or small-area) analysis has been used for qualitative or quantitative multielement information. The equipment used to produce line scans has not evolved substantially from the earliest microprobes and is widely taken for granted. It suffers from several technical limitations, which have helped to limit the use of the method.

### *Ratemeters*

The most common mode of obtaining and presenting an elemental line scan has been to use an analog or RC ratemeter, whose input is all the signal pulses passed by a single-channel analyzer. That could be a separate analog module with upper and lower level discriminators, as used in most wavelength-dispersive microprobes, but is more often now a digitally set energy "window" or "region of interest" in the multichannel-analyzer memory. The ratemeter uses a resistor-capacitor circuit to time average the rate of pulses continuously. The output voltage, in addition to producing a meter deflection and sometimes an audible signal, can be amplified to drive the vertical deflection axis of the SEM display scope as the beam is slowly scanned along a line across the sample.

This method has the advantage that the information may be readily superimposed (visually or photographically) on the normal SEM picture, so it is easy to judge the correspondence between positions where measured intensity changes occur and features of interest on the specimen. However, there are several common problems with this mode. One lies in the distortion introduced by the RC circuit, which can cause "tailing" following abrupt changes or mask small changes if the time constant of the RC circuit is too great, and allow annoying broadening of the line owing to statistical fluctuations if it is too small. The correspondence between time constant choice and the particular count rate and scanning speed for a given measurement can be difficult to achieve.

Somewhat less obvious but in the long run more serious problems in the analog line scan arise from the fact that it is commonly interpreted as a plot of elemental concentration, but is actually a plot of intensity, and measured intensity at that. Changes in sample surface orientation cause such a large change in intensity as to make the line scan meaningless, yet line scans across large irregular particles resting on a substrate are routinely shown to demonstrate the presence of an element. Since the signal which is counted is not just the characteristic x-rays but the continuum falling in the same energy window, it is sometimes possible to record a visually convincing line scan for an element not present at all, if the particle (either because of its surface orientation or density) produces a larger continuum signal than the substrate.

A similar situation occurs when STEM line scans are attempted, since the changes in specimen density (or sometimes thickness) which produce a viewable transmission image usually are reflected in a change in continuum x-ray production. Conventional line scans on thin sections in STEM or irregular surfaces in SEM are in fact meaningless and potentially misleading (as are, also, x-ray maps) but nevertheless often published.

A more subtle yet no less misleading effect on line scan (mis)interpretation is that of varying count rate. Most modern systems incorporate pulse pileup rejection circuits in the amplifier chain, and make a dead-time correction by slowing down the system's internal clock when high count rates are encountered. Since the line scan is obtained in real time, as the SEM beam is continuously scanned, the measured signal for the count rate at the energy of interest can be altered greatly by a change in overall system count rate. In some cases this effect reduces the apparent change in signal; for example, if a high concentration of the element being measured occurs in a small region of a generally organic sample (or any material emitting few total x rays), the increase in emitted x rays

as the beam crosses this area also produces an increase in dead time, and so fewer of the x rays are actually processed and passed to the ratemeter. In the extreme case, high count rates can actually paralyze the system so that the line-scan signal is reversed, dropping from a low rate due to the continuum to nearly zero in the high concentration-high count-rate region.

In other cases, there may be a change in observed count rate for an element present in an unvarying concentration because of a change in overall count rate, due either to a change in the concentration of another element, or perhaps a topographical change. Finally, any combination of these effects (count rate, geometry, density, etc.) may be present to confuse the unwary microscopist. Figure 1 illustrates some typical effects.

### *Multichannel Scaling*

We can overcome some of the problems inherent in the ratemeter approach by using the multichannel analyzer to store the line-scan data. In this mode the analyzer memory address (channel number) is advanced by an internal time base, and all the counts in an energy window during one time period are summed in one channel. This procedure eliminates any distortion due to RC-circuit time constants. It also makes possible, at least in theory, the use of multiple sweeps of the SEM beam, to build up data on a sample gradually with short beam exposure when a single slow scan might cause damage. In practice, few systems allow this latter mode of operation, which requires some timing link to synchronize the start of the SEM beam scan with the start of the internal MCA address advance.

The problems of confusion arising from configuration, density, and dead-time effects are of course still present in this type of line scan. In addition, it is usually impractical to set a digital energy window to define the x rays to be counted, since the MCA is being used to store the time-base data, so that an analog window is used that is less sharp and more liable to misadjustment. The greatest drawback of the "multichannel scaling" method is the difficulty in relating the stored line scan to the SEM image, since the line appears on a different viewing screen and there is no easy correspondence between channel address (time) and image position because the time bases, physical dimensions, etc. are different. When this mode is used because the SEM has no Y-modulation capability, further distortion may also result, since many of the lower-priced SEMs have not a constant beam-sweep speed. If an analog (ratemeter) scan is directly displayed this lack does not matter, since the same (varying) time base is used for both beam position and display position.

If we consider the continued influence of all the "physical" causes of line-scan distortion plus these additional problems, it is indeed unfortunate that the name "digital" line scan has been applied to this mode of operation, which would seem in current usage to imply a somehow more accurate result.

### *Desired Goals for a New Method*

In approaching the line scan problem anew, we adopted the following goals for a new method, all of which have been achieved.

1. Make the time-base of the data integration exact, to eliminate RC distortion and relieve the operator of concern and trouble in setting time constants for every combination of sweep speed and count rate.
2. Use a digital energy window, which can be seen in the normal spectrum display (and can be set in multiple segments to cover more than one peak of an element in those few cases where improved statistics can be so obtained).
3. Eliminate count-rate/dead-time effects so that the intensities recorded in the line scan are true counts per (live) second.
4. Keep the presentation of the line scan on the SEM display, where it can be superimposed on the normal image for best interpretation.
5. Allow for multiple-sweep recording, particularly for SEMs that have no very slow scan capability and for beam-sensitive materials.
6. Make at least first-order correction for geometry and density effects, and second-element effects.



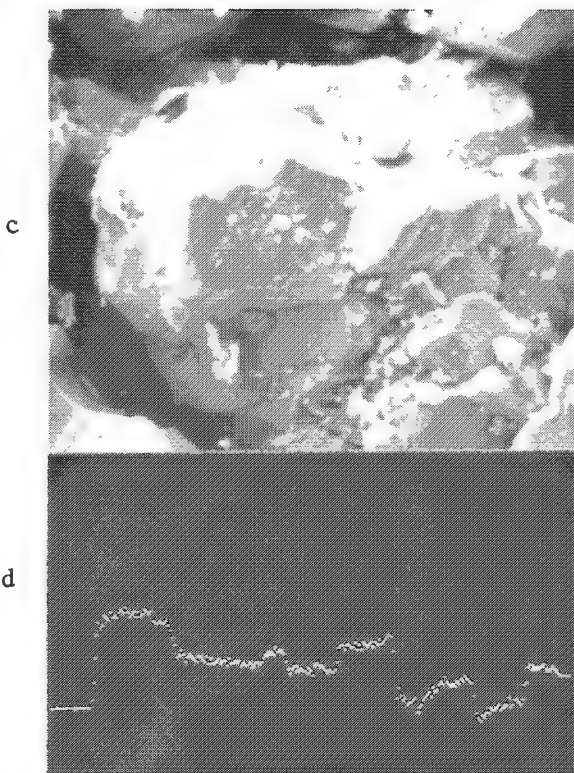
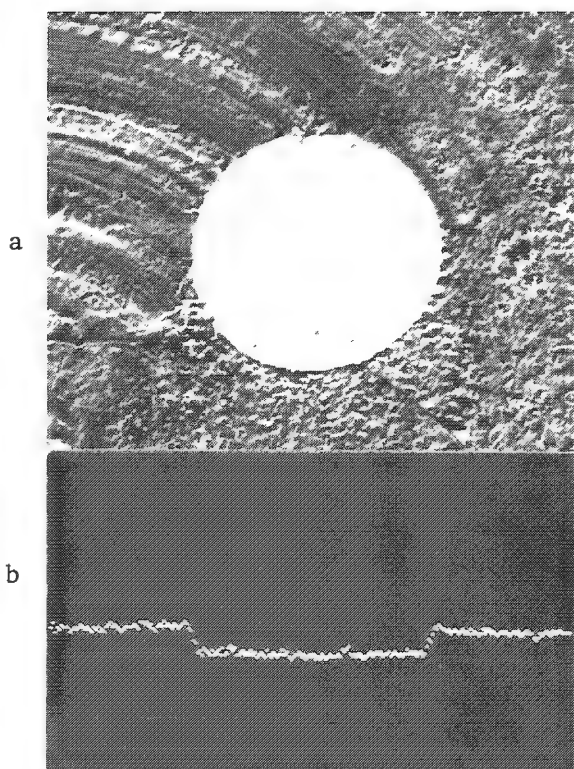
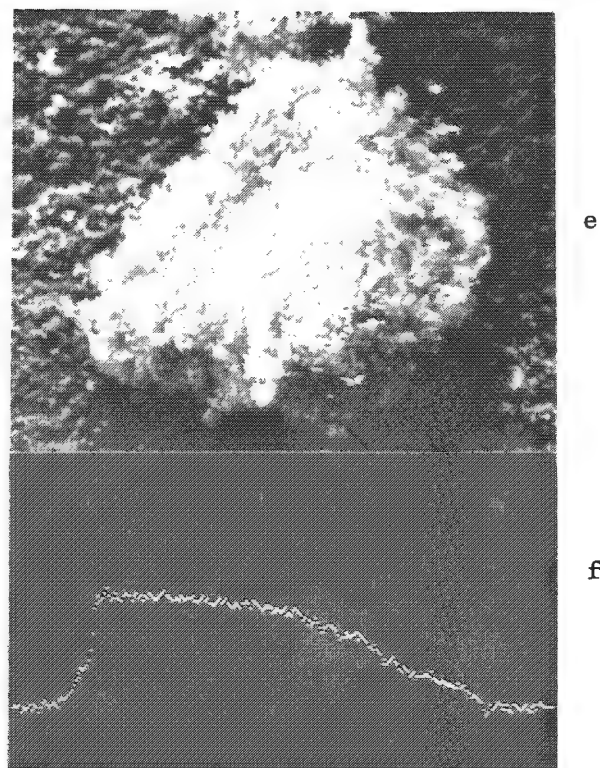


FIG. 1.--Some common line-scan problems. (a), (b) Sample is cross-sectioned Ni wire imbedded in low-Z matrix. Window is set on Ni  $K_{\alpha}$  peak. Total spectral counting rate on wire is above point of maximum stored count rate; count-rate paralysis produces reversed line scan. (c), (d) Sample consists of grains of  $\text{FeS}_2$ . Line scan for S  $K_{\alpha}$  shows variations resulting from topography, not concentration differences. (e), (f) Sample is iron-oxide particle on carbon substrate. Line scan was formed with window set for Ca  $K_{\alpha}$ , although none was present. Increased continuum production when beam is on particle, due primarily to higher atomic number, gives apparent indication that Ca is present.



7. Allow multiple-element scans to be recorded simultaneously, to save time, aid the user in finding correspondence between patterns of distribution or variation for different elements, and provide the database to support item 6 above.

It may seem that some of these items (for example, 4 and 5) are mutually exclusive, but we shall see that this is not the case.

To achieve these goals, we developed several new and novel methods, which are covered by patent applications and which include a new type of ratemeter, a new method for dead-time correction, a method for content mapping along a line or over an area, and a new enhancement method. All are described below.

### *Digital Integrating Ratemeter*

To eliminate the RC analog ratemeter, we use a buffered-output digital integrating ratemeter circuit. In this example it is actually built into the analyzer, for convenience in adjusting the parameters from the main control keyboard. The user-selectable parameters are the integration time (which should usually be set to about 0.002-0.010 of the total line time), the full scale, and a choice of linear or logarithmic scale. The circuit functions by counting all the incoming pulses (from one of the four independent, simultaneous energy windows set on the analyzer spectrum display, each of which can have multiple segments) for the preset integration time. The resulting number of counts is dead-time corrected to obtain counts-per-(live)-second as described below, divided by the selected full scale value (on either a linear or log scale); the result is expressed as a voltage on the buffered output. This voltage is held at the output for the next integration time period, while a new number of counts is obtained. The process is repeated, so that the complete line scan is actually a series of steps across the sample (Fig. 2). Figure 3 shows how this method corrects one fault of conventional line scans. All the line scans shown (except Fig. 2a) simulate stepped or digital scans. In some, such as those of Fig. 1, some of the additional corrections described in this paper have not been incorporated.

The width of each step depends on the beam sweep speed and the integration time. If the user sets the integration time to less than 0.01 of the total sweep time, the individual steps are not usually evident in a photographic recording. We have found integration time settings from 0.01 to 10 sec adequate to cover the useful range. The number of counts still is subject to normal statistical considerations, of course, but the line scan is generally free of the "jitter" seen in RC ratemeter scans with too short a time constant, and eliminates the tailing problem altogether. Finally, since the output voltage is proportional to counts per second, it is independent of scan speed (except for statistical effects), so that the operator can change sweep speed at will with no change in ratemeter settings.

### *Real-Time--Dead-Time Correction*

X-ray analysis of samples produces intensity values, which may be accurately used to compare standard to unknown, or one specimen or location to another, only if they are expressed as counts per (live) second. The "dead" time introduced by the detector itself and the processing electronics have been corrected heretofore in two ways, both of which can provide accurate results but suffer from individual practical limitations. [These methods are in addition to an earlier technique in which the number of counts  $N$  per unit clock (or real or elapsed) time is converted to a "dead-time-corrected" value  $N' = N/(1 - N\tau)$ , where  $\tau$  is a presumed constant time associated with the instrument dead time. This method is inexact because  $\tau$  is not a constant, and because the underlying assumption neglects the statistical variation in  $N$ , which can be quite large for the low number of counts obtained per point in a line scan. It will not be considered further.]

The two accurate methods both make use of a second "fast" analysis channel that amplifies pulses with a short time constant so that events close together in time, which cannot be measured, are rejected (not measured or counted in the stored spectrum). In the Harms method,<sup>1</sup> the total counting time may be fixed (in terms of clock/real/elapsed time). For each pileup event (in which two x rays are lost) the next successfully processed x ray is stored as three x rays instead of one. In other words, the assumption is that the same

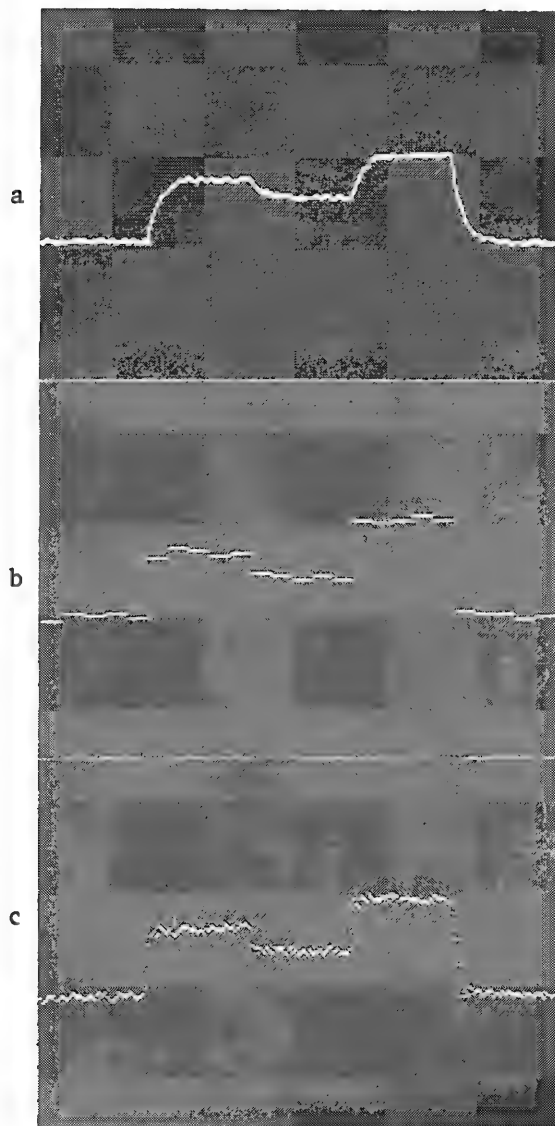
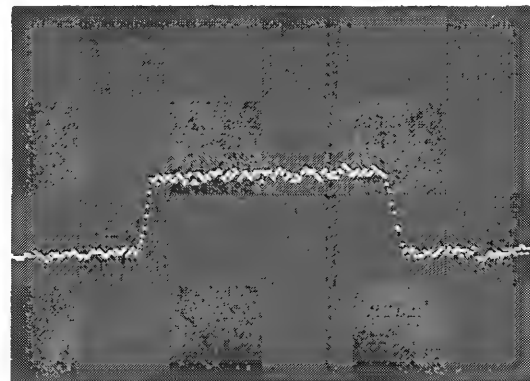


FIG. 2.--Digital nature of new line scan: (a) conventional (RC) analog line scan has tailing when levels change abruptly; (b) same information can be presented as series of steps; (c) with enough finely spaced steps "continuous" scan is obtained.

FIG. 3.--Digital or stepped line scan can incorporate dead-time correction as described in text. Here scan is identical to that shown in Fig. 1a,b except that after dead-time correction profile is intensity (counts per live second) rather than counts, and correct positive indication is obtained



average distribution of x rays is rejected as is successfully processed, and the lost counts are made up as they occur. This method is accurate provided that (1) the number of counts processed is great enough that the two counts that may be lost are insignificant, and (2) there are no cases of triple or higher-order pileup. However, for finite counting times the method suffers from the limitation that the apparent number of stored counts (including the make-up counts) is larger than the number actually processed, but has the actual statistical precision of the (smaller) number actually processed. In other words, it leads to an erroneously good estimate of counting precision unless the percentage dead time is known and used to approximate the actual precision. As the most desirable (high) rates of data collection introduce quite large total amounts of dead time, and multiple pileup does in fact occur, this limitation becomes serious; in fact, the Harms method is now little used.

It has been almost universally supplanted, certainly in commercial instruments, by methods<sup>2,3</sup> based on keeping track of all of the piled-up (rejected) pulses in a separate counter and periodically stopping the system's internal "live time" clock while that many extra x rays are successfully processed. This technique means that the statistical precision of the stored data do obey the normal relationships. However, the "live time" of the system is always less than the actual elapsed time, so that the total clock/real/elapsed time needed to obtain a preset time's worth of data is greater than the elapsed

time.. The method is accurate provided that the distribution of x rays arriving later in time is on the average the same as the earlier ones which were rejected. This relationship may not hold in the case of (for example) a scanning electron microscope in which the beam continuously traverses an inhomogeneous sample. High count rates from high-concentration regions may cause lost pulses from pileup that may be "made up" subsequently in lower concentration or different areas. Similar problems can arise in on-line monitoring situations and can only be overcome if the sampling period is kept short enough to resolve the variation. A more significant problem arises in the unpredictable elapsed time that may be needed to acquire one unit of time's worth of data. In many processes (including on-line monitoring and scanning electron microscopy) the period of analysis must be fixed by external events. In that case, the number of x rays "lost" or "stranded" owing to pulse pileup cannot be made up and so the measured intensity in counts per (live) second is too low.

We have found that the benefits of preset elapsed/real/clock time counting can be combined with accurate dead-time correction and pulse-pileup rejection by a modification of the method just described in the following novel way. If the live time clock is controlled in the usual way so that during a preset elapsed time  $T$  it measures a live time  $t$ , then this value would normally be used to express intensities as the number of counts  $N$  for a given peak or element divided by  $t$ . That is wrong, as described before. However, if the total number of stored counts  $S$  and the number of stranded or rejected counts  $R$  are used to correct the time  $t$  to obtain  $t^* = t\{1 - [R/(S + R)]\}$  then the resulting intensities in counts per live second are exact. One can do that by using either separate counters to keep track of  $R$  and  $S$ , or by using the total stored spectrum to obtain  $S$ , and the same counter used in the normal method to count rejected pulses (to be made up while the clock is stopped) to obtain  $R$ . The mathematical calculation can be carried out either by discrete logic, by a stored-program processor in the system, or by pencil and paper if all the numbers are totalled by the hardware counters and made available to the user. In the case of line scan measurement, the corrected counts-per-(live)-second data are calculated for each integration time period, to form the basis for the output signal.

### *Enhancement and Content Mapping*

The digital-integrating ratemeter with real time-dead time correction by itself satisfies goals 1 through 4 described above. It can also be used in conjunction with the "normal" x-ray-mapping (dot-mapping) mode to produce several novel new displays. First, the user can set a threshold on the ratemeter output (which is displayed on the analyzer TV screen) corresponding to the count rate he associates with background. This threshold can then be used to "gate" the dot output so that in the generation of a map of X-ray dots, any dots occurring in a region where the count rate is below the threshold is not passed to the SEM display. This functions as a flexible image "enhancer," in which the user can directly adjust the threshold or "background" level in cps and the dimension (the ratemeter integration time) of the enhancement.

However, since the multichannel analyzer has four separate, simultaneously active windows, the enhancement (or threshold-gating as it should more properly be described) can be applied from one element to another. As an example, consider a case in which the ratemeter is monitoring the count rate in an energy window set on an iron peak, and the threshold is adjusted to discriminate between the background intensity and the intensity from the region where iron is present. If a second energy window is set for the sulfur peak, the resulting sulfur dot map will show only those regions containing iron *and* sulfur. This result is quite distinct from that obtained when a conventional window is set with multiple segments on the iron and sulfur peaks, which would show places where iron *or* sulfur were present. With the ratemeter output from one element used to discriminate the output of another, an image is obtained that may be interpreted as a map of compounds instead of elements. Figure 4 illustrates this process for a simple case.

Another use to which the digital-integrating ratemeter can be put overcomes the inherent problem of visually integrating an x-ray dot map. Because the human eye/brain combination functions poorly in estimating average dot density, it is usually difficult to see small or gradual intensity changes in a dot map. Only by counting for extremely long times to build up a recorded image with  $10^5$  dots or more, each one so faint as to just be



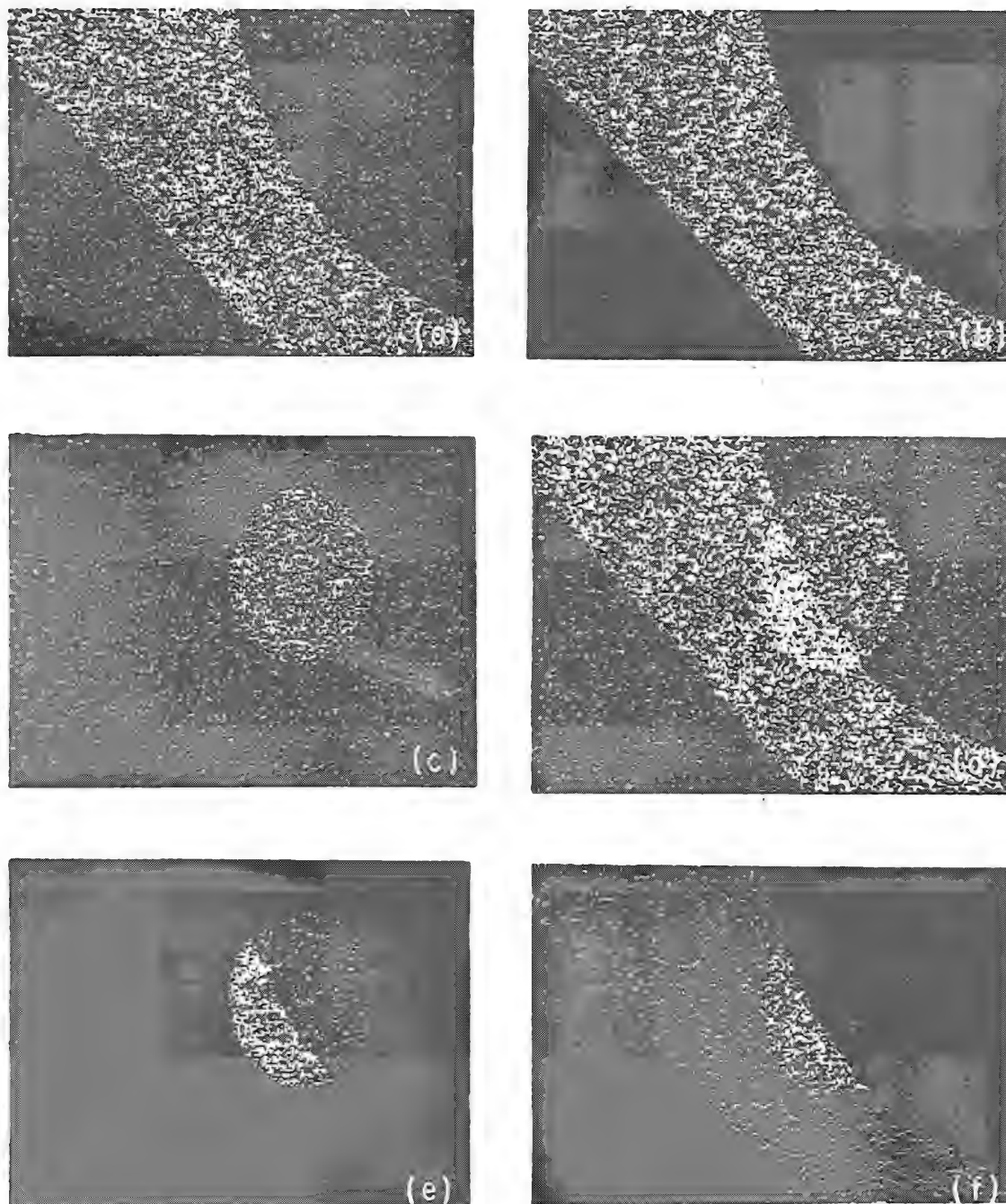


FIG. 4.--Simulated X-ray maps illustrating various logical combinations of elements. (a) "Normal" dot map showing a region of concentration for one element (Ca) and a background dot level where Ca is absent. (b) "Enhanced" dot map showing elimination of background dots, which is done by enabling dots to be shown only where count rate exceeds threshold. (c) "Normal" dot map for a second element (Si), which is concentrated in area that partially overlaps Ca-rich area. (d) Conventional dot map obtained by setting energy windows on both Ca and Si peaks. Logically, this is the image of Ca *or* Si and does not distinguish region rich in both from that containing only one or the other. (e) Map of region containing *both* Ca and Si; image is produced by enabling Ca dots to be shown only in region where Si intensity exceeds threshold. Note that some background dots appear in Si-rich area as well. (f) Map similar to (e) but formed by enabling Si dots to be shown where Ca intensity is high; poorer image results because of dots in the background area.

discernible on the film, can one produce an image with a recognizable gray scale in which brightness variations correspond to intensity variations. Since the digital ratemeter can be set to an integration time short enough to allow reasonable sweep speeds, and the real time-dead time correction allows high count rates to be used, it becomes practical to photograph an image that is intensity modulated by the ratemeter voltage output, so that an x-ray map of brightness rather than discrete dots is obtained. Of course, multiple line scans with deflection modulation are also possible. Both show two-dimensional patterns of element intensity distribution that would be difficult to see in conventional x-ray dot maps. Fig. 5 shows examples of the latter mode of display. Intensity-modulated images are shown in Fig. 6.

#### *Stored Line Scans*

Rather than use the words "analog" and "digital" to describe line scans, as has been previous usage, we prefer "real time" to describe the mode of operation of the buffered-output integrating ratemeter just described. This instrument in a sense replaces the older "analog" or RC ratemeter, though of course it uses digital logic to do so. The other type of line scan mentioned previously, the so-called "digital" or MCS (multichannel scaling) linescan, has been superseded by our new type of stored line scan. In this mode of operation the same ratemeter circuit and same digital energy windows(s) function to produce

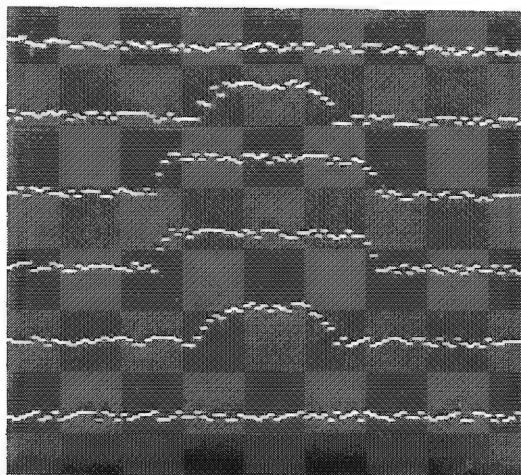


FIG. 5.--Series of line scans displaced vertically across specimen can give two-dimensional distribution pattern.

a dead-time-corrected value of counts-per-(live)-second, but instead of being passed to the SEM display vertical deflection amplifier as a voltage, it is stored in the MCA memory. Unlike the older method, which stored counts, this method stores corrected counts per second. Also, since there are four simultaneously but separately active energy windows in the MCA, we can simultaneously store four line scans for different elements or energy windows (each one with multiple segments if desired).

The resulting display on the multichannel analyzer video screen is particularly effective with color coding, with a different color assigned to the dots of each element's line. Figure 7, reproduced in black and white, loses some of the impact of the color but still shows clearly the correspondence between patterns of element distribution.

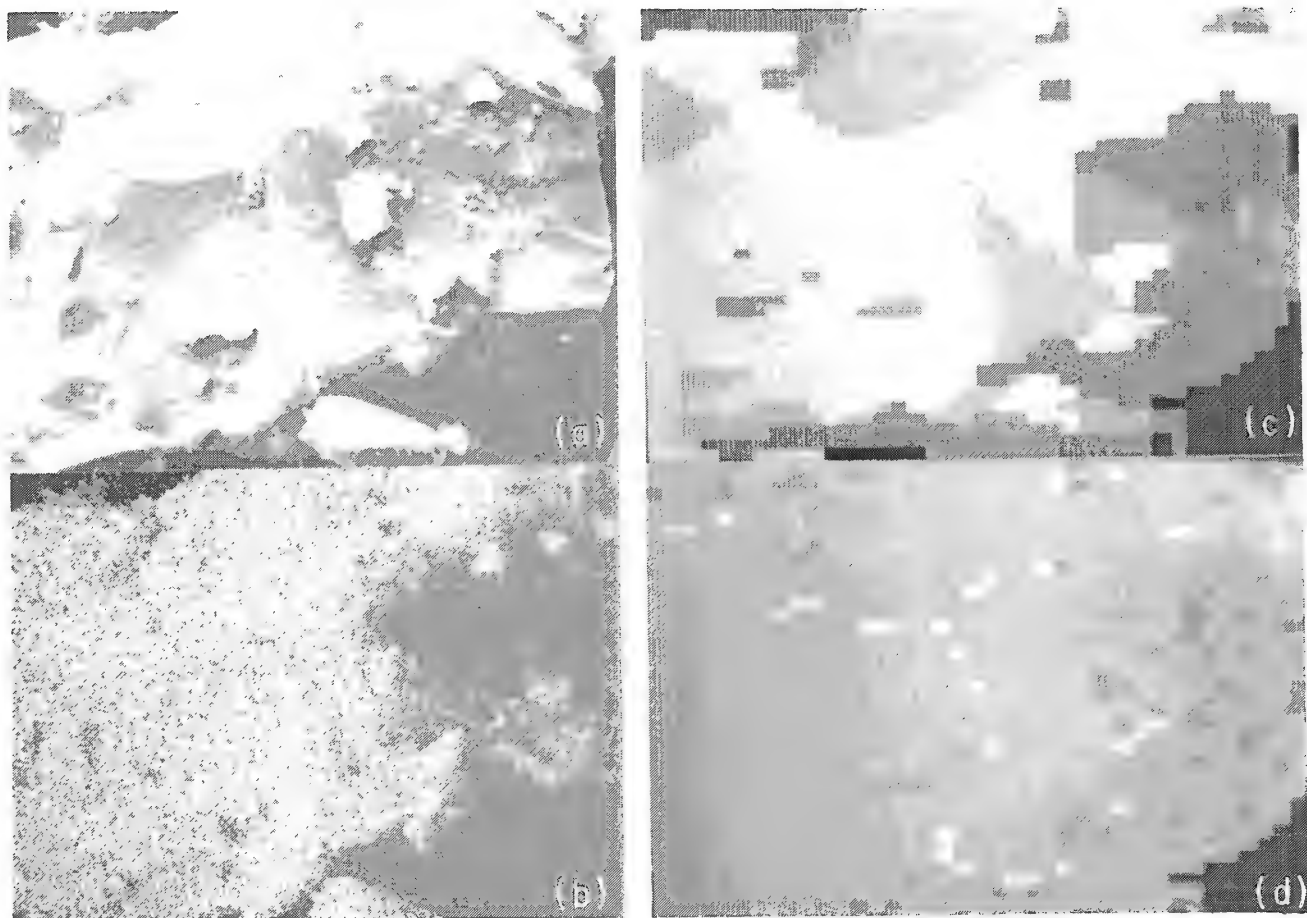


FIG. 6.--Intensity-modulated rather than pulse-modulated images can be formed with series of line scans: (a)  $\text{FeS}_2$  grain; (b) "normal" x-ray map for S; (c) same data as in (b), converted to brightness and very coarse  $40 \times 40$  matrix of points; (d) similar image as in (c) but converted to approximate map of sulfur concentration rather than intensity, obtained from ratio of net peak to background as described in text.

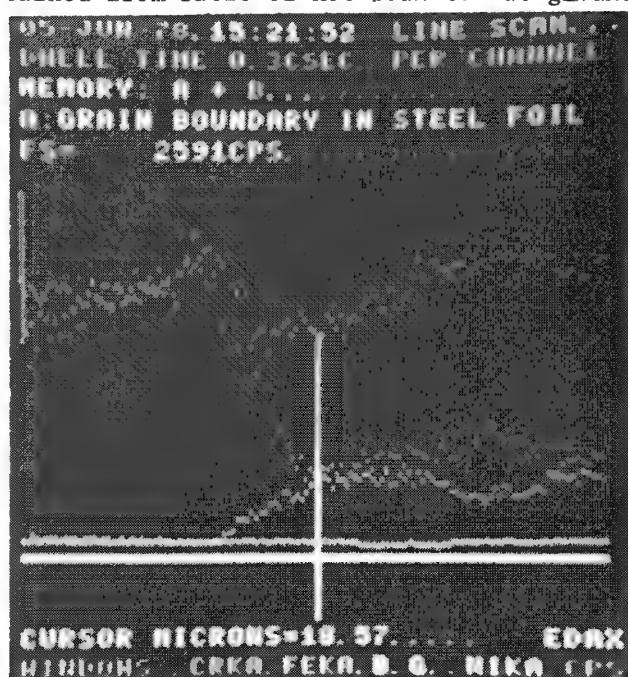


FIG. 7.--Stored line scans for Fe, Cr, and Ni, as well as background in window set below Cr and above Ni, across grain boundary in thin section of stainless steel, examined in STEM. Display actually shows the four profiles with color coding.

Since the data are stored, it requires only a triggering pulse either from analyzer to SEM (to start the beam sweep) or conversely (to start the memory address advance) to make it possible to build up a set of line scans by repetitive scanning. Since the vertical scale of the display is counts per second, the data are signal-averaged so that with each successive sweep the new value is averaged with the old ones, with appropriate weighting based on the number of sweeps. For the  $n$ th sweep, if the previously stored count rate value was  $R_0$  and the new value is  $R_1$ , the subsequently stored value will be

$$\frac{n-1}{n} R_0 + \frac{1}{n} R_1$$

In this way the statistical quality of the stored and displayed line scans improves, but the vertical scale does not change. Since the analyzer memory has a total of 4000 channels, and scans for four elements can be simultaneously stored, it is possible to select a time base for the integration that uses up to 1000 points for the length of the beam scan across the sample. The cursor indicates the position along the horizontal scale if the user has entered the correspondence between time and position, and if that relationship is linear. All four scans are displayed superimposed and color coded.

#### *Displaying Stored Scans*

Although the mode just described can often be viewed and interpreted directly, especially in cases where changes in intensity for one element correspond (positively or inversely) to changes in another, one would still want to view and/or photograph the line scan on the SEM display, where it will be in proper registration with the image. That goal can readily be accomplished by use of the existing buffered output circuitry of the ratemeter, normally used for real-time scans. As the beam scans across the sample, the counts-per-(live)-second data are taken from one of the stored line scans in memory and used to generate the output voltage that is passed to the vertical deflection axis of the SEM display, where it then appears the same as a real-time scan; so multiple-sweep data can be accumulated and then "played out" for viewing, or data can be taken once and then re-played on the display with different full-scale (or linear/logarithmic) selections.

#### *Content Mapping*

If the beam sweep is not confined to a single line, but is allowed to raster over the entire image area, the multiple-sweep storage mode can be used to produce a content map. In this case, the user selects a number of "image points" for the entire picture area, which can practically range from  $100 \times 100$  down to as little as  $25 \times 25$ . All the information in the square area centered around each point of the image can then be automatically averaged and ultimately can be displayed as a content map. Consider for example a beam scanning 1000 lines on the sample, with the horizontal sweep for each line subdivided by the integrative time of the ratemeter and channel address in the MCA into 1000 points. If the first twenty sweeps are signal averaged as described above in the section on Stored Line Scans, and then the contents--which are in counts-per-(live)-second--of each group of twenty channels in the scan for each element are averaged, the result is 50 numbers. They are transferred into computer storage and the process is repeated for the next twenty beam scans, and so on.

The result is an array of  $50 \times 50$  corrected intensity values for each of four elemental energy windows. These data can be "played back" to the SEM display as a brightness-modulated "checkerboard" image for one element at a time, by means of the ratemeter output circuit as described before. Figure 8 illustrates the kind of data obtained, as well as the possibility of recording the data on the printer or other hard-copy device.<sup>5</sup> Displaying the result as a series of deflection-modulated lines produces a result similar to Fig. 5, with a single horizontal line selected for additional display if desired. A brightness-modulated display of this type is similar to Figs. 6 c and d. Not only can various selections of full-scale and log/linear display be used on the stored data, but the content-map image is also quite readily interpretable to the eye, despite its comparatively poor resolution and small number of image points.



### Processed Line Scans

When multiple-element line scans are simultaneously stored, it becomes interesting to use simple modes of data processing to combine them. In many cases we are interested not so much in the variation of one element across the sample as in the relationship between variations of several elements. It is difficult to study this relationship with conventional line scans taken one at a time or even to see in the simultaneous scans presented together (as in Fig. 8). By adding the capability to store the multiple scans and to display any arithmetic combination of them, we introduce the possibility of seeing the relationships more clearly.

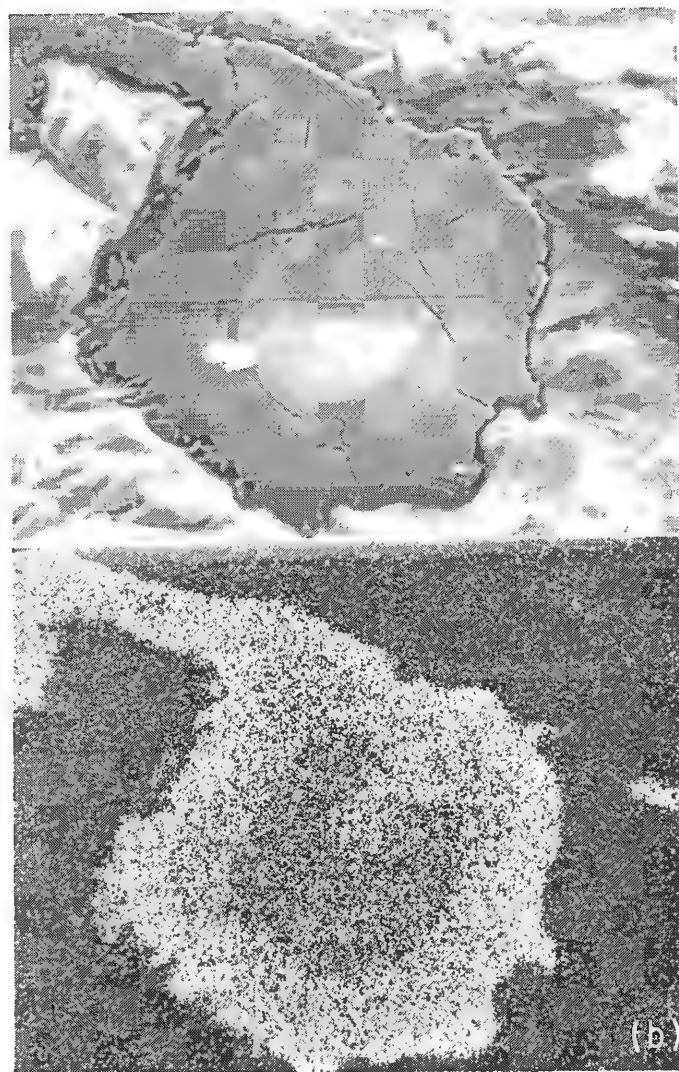


FIG. 8.--Digitized "content map" can be printed as well as photographed. (a) Chromium-bearing mineral; (b) normal dot map for Cr  $K_{\alpha}$ ; (c) digitized array of points in a  $20 \times 32$  matrix, with ten levels (0 - 9) of Cr intensity, corresponding to central portion of image; (d) information in (c) printed to simulate brightness modulation; (e) similar map for Fe/Cr ratio.

```

2 118798887889999771 11 21 1 1
21 177898898777788875 11 11
11 9999877877788879982 1 1111
111879988876556888998871 4 11
11 7999888543344899999888211
2278899777444334898999881 1 1
77299988775433458989988821 11
77 2999787334378898998778 11
1 8999877744478898887788 11 21
1128897843447998887799911 12
C 788798877433898899777889911 1
9988988774334478988433489991 1
9999887744334447893443488999 1 1
8999877743444334433434887889 11
8988777744344343433448999891 12
998887773343344443698989921 1
928989877334344333898889891 1
7 89889883334433898897889 11 1
1 89889997543343898888789961 1
2 89998877743347788988877888 1

```

[illegible][illegible]

FIG. 9.--Processed line scans can show element concentration relationships (derived from measured data in Fig. 7). (a)  $(\text{Fe} - \text{BG})/\text{BG}$  gives iron concentration corrected for density times thickness variation in sample; (b)  $(\text{Cr} - \text{BG})/\text{BG}$  gives Cr profile; (c) Fe/Cr ratio.

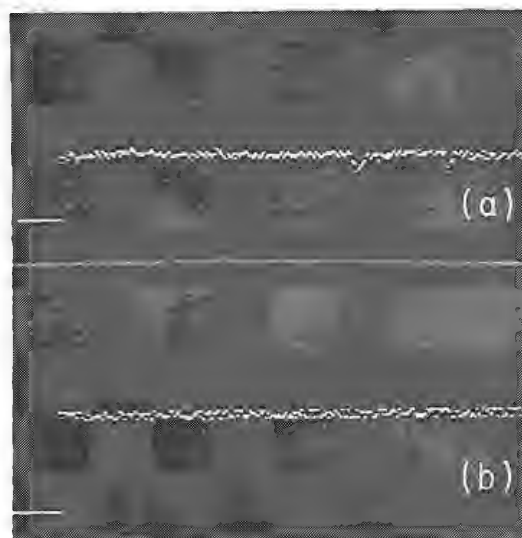


FIG. 10.--Processed line scans can compensate for topographic effects (same specimen and line as shown in Fig. 1c,d). (a)  $(\text{S} - \text{BG}_1)/\text{BG}_1$  where  $\text{BG}_1$  is window set just below sulfur  $\text{K}_\alpha$  peak. Sulfur net peak-to-background ratio remains nearly constant across irregular sample surface. (b)  $[(\text{S} - \text{BG}_1)/\text{BG}_1]/[(\text{Fe} - \text{BG}_2)/\text{BG}_2]$  where  $\text{BG}_2$  is window set between iron  $\text{K}_\alpha$  and  $\text{K}_\beta$ , which approximates S/Fe ratio, shown to be constant despite uneven sample topography.

For example, it may be clear that both Ca and Si increase or decrease in the same grains of a mineral, but by displaying the ratio of Ca/Si (or the inverse) we can see whether the stoichiometry remains essentially the same (apart from second-order effects, which would require a full ZAF computation) or not.

A particularly useful extension of this combination or ratio method results when one of the four energy windows is set on background (typically with several window segments on different portions of the continuum). The background intensity can be used to overcome, to a first-order approximation, many of the topographical and density problems described previously.<sup>4</sup> For example, in a thin section in STEM, the ratio Ca/BG shows real variations in calcium localization independent of the density change associated with the precipitates. Since subtraction can also be easily computed point by point on the line scans, it is even better to display the net calcium variation (Ca-BG)/BG for this case. Figure 9 shows several processed line scans for a thin section.

For bulk samples, one can partially compensate for the effects of surface geometry by setting a background window at an energy near the peak of an element of interest. The effect of changing surface orientation, which particularly changes the absorption path length of the x rays, is similar for the characteristic x rays and for the continuum x rays of nearly the same energy. Hence the problem shown in Fig. 1b can be largely compensated, as shown in Fig. 10 by means of the (S - BG)/BG signal. The ratio of S to Fe in this specimen is also shown to be uniform by the plot of  $[(S_1 - BG_1)/BG_1] / [(Fe - BG_2)/BG_2]$  for the case of two background windows set up at energies near the Fe and S peaks. The system allows any arithmetic combination of terms to be selected. Finally, the same advantages of combining line scans from several elements can also be realized with the stored array of intensities described under content mapping, so that element/element, element/background, and other combinations can be displayed.

These processed line scans thus satisfy goals 6 and 7 on our original list.

### *Conclusion*

Seven goals were established to overcome some of the limitations of line scans as they are presently used. The goals, all of which are met by the new methods set forth, can be summarized as follows:

1. Produce line scans with no "time-constant" RC effects.
2. Use exact (digital) energy windows set on the spectrum display.
3. Correct for count rate and dead-time effects.
4. Present the scans on the SEM, in registration with the image.
5. Allow for multiple sweeps to build up a line scan.
6. Correct for geometry, density, and second-element effects.
7. Collect multiple scans at once.

In addition, the equipment needed to satisfy these goals may be used to extend some of the same features to area scans, in the form of enhanced dot maps, content maps, and "compound" maps. Line scans and area scans contain much information about element distribution, and hence are attractive to the scanning electron microscopist. By making the information contained more accurate and interpretable, these methods will become a valuable tool in conjunction with the SEM and STEM.

### *Acknowledgments*

The author is pleased to acknowledge the invaluable collaboration and contributions of (in alphabetical order) R. Carey, V. Chopra, C. Cwik, W. Rich, and A. Sandborg in inventing and implementing the ideas presented in this paper.

### *References*

1. J. Harms, *Nucl. Instr. & Meth.* 53: 192, 1967.
2. R. Lowes, Kevex Corp., U.S. Patent 3 814 937.
3. M. W. Barnhart, EDAX International, U.S. Patent 3 896 292.
4. J. C. Russ, "X-ray mapping on irregular surfaces," *EDAX EDITor* 9(No. 2): 10, 1979.
5. J. C. Russ, "Digitized x-ray maps," *EDAX EDITor* 8(No. 2): 23, 1978.

## A NEW TECHNIQUE FOR BEAM CURRENT NORMALIZATION IN ENERGY DISPERSIVE ANALYSIS

J. J. McCarthy

An important limiting factor in obtaining accurate and reliable quantitative analysis by energy-dispersive spectrometry (EDS) is the stability of the electron beam current of the scanning electron microscope (SEM). Various techniques seek to minimize the impact of unstable beam current: use of a Faraday cup, use of an isolated aperture for continuous monitoring and current regulation, and monitoring the absorbed current on the specimen itself. Each of these methods has some disadvantages. Faraday cups can be awkward to manipulate and suffer from the inability to monitor the beam during collection of x-ray data, which limits their application to only long-term drifts. Isolated apertures provide continuous monitoring, and can be used with additional circuitry for beam stabilization, but can suffer because of nonlinear response and the difficulty of providing good closed-loop regulation at currents used for EDS. Additional hardware to digitize and scale aperture readings precisely may also be required. More important, some low-cost instruments cannot be fitted with such an aperture at all. Monitoring the specimen current is complicated by the need to separate the atomic number dependence from other beam variations.

The purpose of this paper is to describe a new technique for beam-current normalization that overcomes most of the difficulties described above. (It is the subject of a patent application by Tracor Northern, Inc.)

### *Description*

This technique employs a digital current integrator that combines a current-to-frequency converter with circuitry that is capable of modulating the normal EDS analyzer dead time in a manner directly proportional to the beam current. EDS acquisition is thus based on a fixed beam current integral rather than a fixed acquisition time. Since this beam-current normalization is accomplished entirely by the circuitry of the integrator, the device may be used with any EDS analyzer that provides access to a suitable dead-time signal. The device may be used with an isolated current-measuring aperture or with specimen current.

In order to test the performance of the current integrator over large current ranges, data were collected on both a table-top SEM by monitoring of specimen current, and on another instrument fitted with an isolated aperture. Since the total number of x rays generated in the specimen is directly proportional to the number of absorbed electrons, the total integral of the x-ray spectrum was used to indicate the absorbed current. Results of one set of measurements are shown in Fig. 1. The upper trace represents the total x-ray counts as a function of beam current without use of the digital current integrator. As the current is doubled, so are the total x-ray counts. The lower trace represents the total x-ray counts as a function of beam current when the integrator is used.

In this case, the variation in total x-ray counts is within counting statistics ( $\pm 0.4\%$ ) over the entire current range (100% variation). This absence of dependence on beam current is ideal for quantitative analysis.

Data have been also obtained by monitoring of the specimen current on a table-top SEM (Fig. 2). Note that the vertical axis is a log scale. In this case, the variation of total x-ray counts shows a slight dependence (15%) on specimen current over a wide range of nearly a factor of ten in current. For a current change of a factor of two near the middle of this series of data the variation in total x-ray counts is about  $\pm 0.8\%$ . This figure exceeds the expected statistical variation, but is still acceptable for quantitative analysis.

The use of data obtained by monitoring of the specimen current for quantitative analysis is complicated by the fact that the specimen current depends on the average atomic number of

---

The author, who is with Tracor Northern, Inc., Middleton, Wis., wishes to acknowledge the assistance of Dr. E. Glover of the University of Wisconsin in Madison.

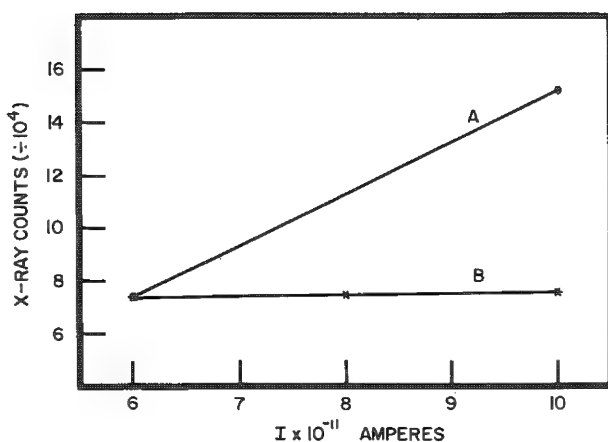


FIG. 1.--Total x-ray counts as function of aperture current. A: digital integrator not used to compensate EDS acquisition; B: with integrator. In this case, x-ray counts are constant within counting statistics over entire current range.

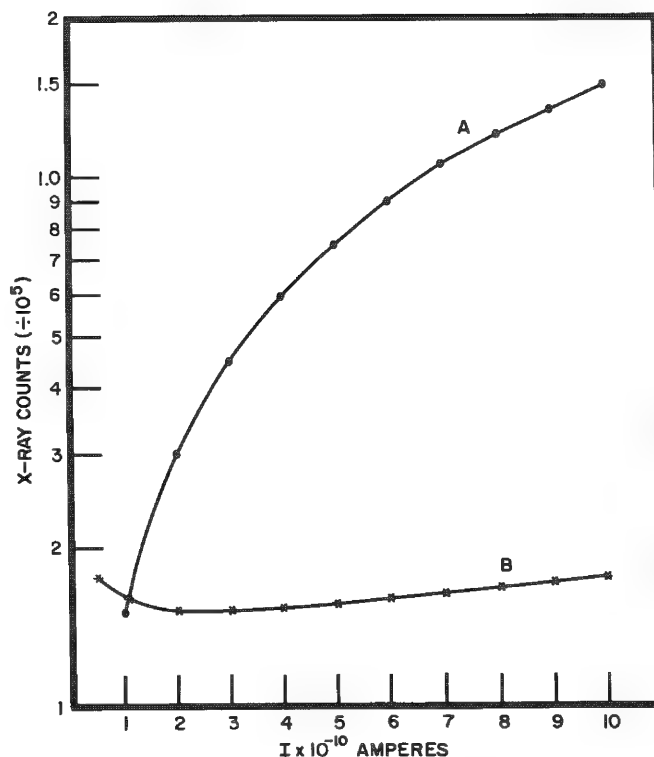


FIG. 2.--Total x-ray counts as function of specimen current for table-top SEM. (Vertical axis has log scale.) A: without integrator; B: with integrator. Trace B shows 15% variation over entire current range.

the specimen. Since most matrix correction procedures require data that are normalized to fixed incident current (not specimen current), data normalized to specimen current must be corrected to the proper incident current values before processing.

### Conclusion

A new technique of beam current normalization for EDS analysis has been described. The method employs a digital current integrator capable of modulating the normal dead-time signal of an EDS analyzer. No additional hardware or software are required. Data have been presented that show this device can efficiently compensate the EDS data for significant changes in the electron-beam current.



## APPLICATIONS OF A DIGITAL SCAN GENERATOR TO EDS ANALYSIS

J. J. McCarthy

As the use of digital computers for automation of wave-dispersive and energy-dispersive operations has become commonplace, interest has been generated for using the computer to control other functions of the electron column. A frequently discussed possibility is to place the beam position under direct computer control. This development has direct impact on many areas of column applications, including improvement in column imaging capability, elemental mapping and profiling, and particle detection and counting. As an example, consider the application of digital beam control to elemental mapping and line profiles.

X-ray detection is inherently rate-limited by the Si(Li) detector electronics. An appropriate counting interval is necessary before a statistically meaningful number of x-ray counts can be acquired. This consideration is crucial when one performs feature enhancement via background subtraction and/or count-rate discrimination.

In conventional scanning electron microscope (SEM) electronics, the electron beam is controlled in a continuous raster scan; longer counting intervals can be achieved only by slowing the sweep rate, which leads to unacceptably long analysis times. In contrast, digital beam control permits direct control of the raster resolution. This procedure allows fewer points to be sampled and acceptable statistical levels to be achieved within a realistic analysis time.

Another advantage of digital beam control is that the SEM beam position is precisely synchronized with the data-processing computer. This feature facilitates computer-controlled point counting and averaging applications. Independent control over CRT intensification permits alphanumeric and graphic information to be superimposed on SEM photos. Secondary-electron (or BSE) discrimination circuitry permits feature recognition and characterization based on both visual contrast and x-ray identification.

It is the purpose of this paper to briefly describe a digital scan generator for electron column instruments and discuss its application to EDS analysis.

### *Scan Generator Hardware*

The basic hardware components of the scan generator are a joystick, time base, a video signal processor, and an X-Y scan controller. These components are contained on several printed circuit boards that are plugged into a single chassis, which contains a common data bus and the computer interface. This chassis may also contain modules to automate other devices on the column, such as stage axes and wavelength-dispersive spectrometers (WDS). The video-signal processor includes circuitry for digitizing the SEM video-signal intensity (normally secondary electron) and presenting these data to the computer, or writing it back to the SEM display screen (CRT). Portions of the digitized signal that fall between two selectable thresholds all intensified for display. The scan controller circuitry includes digital to analog converters (DACs) for X-Y positioning in addition to providing blanking control. The joystick may be used to control the position of an X-Y cursor in the raster image. Cursor positions may be read out for later use in positioning the electron beam.

The scan generator hardware may be used with partial or full software control. For example, under partial software control the computer can initiate raster imaging by loading the time per point and point separation into the scan generator. At this point the raster is carried out without further computer involvement.

### *Beam Control Software*

Software has been written to control the various basic functions of the scan generator.

---

The author is with Tracor Northern, Inc., in Middleton, Wis.

The basic software has been coded as assembly language modules for the PDP-11 series computers. These programs have been designed for use with the Flextran interpreter language available with Tracor Northern analyzer systems, and are denoted Flextran Libraries. The basic library functions include beam and cursor position control, line scan and raster control, character and data display on SEM CRT, and particle detection and location via the video signal.

#### *Application to EDS Analysis*

In addition to the basic software, several Flextran programs have been developed for specific application to digital x-ray line scans, mapping, and particle location and characterization.

#### *Mapping and Line Scans*

Digital line scans and maps may be acquired for up to four elements simultaneously. Separate background regions may be defined for each element, and background is subtracted on a point-by-point basis. Both types of data may be displayed on the SEM CRT after acquisition or stored on floppy disk for later recall and processing. Display data includes magnification, elemental symbols, a calibrated micron bar, number of scans for line scans, and additional label information. Multielement digital maps are displayed for viewing one element at a time, with a different display symbol for each element. This procedure allows total map photographs to be built up with multiple exposures.

The beginning and end points of line scans are conveniently set up with the cursor via the joystick. Single-element line scans may contain up to 1024 points, four-element scans up to 256 points. The path the electron beam traversed during the line scan is displayed in addition to the other data. Figure 1 is an example of a four-element line scan across an interface region of a section of solar cell.

Single-element digital maps are limited to 256 by 256 points, and four-element maps to 128 by 128 points. In addition to background subtraction, digital maps may be enhanced by rejection of counts beneath a threshold level. Digital maps may also be processed after acquisition to obtain the total area covered by each element, the average horizontal chord length for all features containing each element, and the chord length distribution of all features containing each element. Figure 2 is an example of the display of a multielement digital map. The photograph is a multiple exposure taken of the SEM CRT.

#### *Particle Characterization*

Individual particles within a field of view may be detected by a comparison of the digitized SEM video signal to a threshold level on a point-to-point basis. After a particle is detected, the approximate particle center is located, and a series of rotated particle diameters are measured. From these measurements an average diameter and crude particle area and perimeter may be obtained. Figure 3 shows the motion of the electron beam during the location and sizing of several particles in a frame. The technique is limited to simple, well-dispersed particle fields. After the initial sizing has been completed, the beam is repositioned to the particle center and an EDS acquisition is begun for the number of seconds specified by the operator during the setup phase of the program. After the acquisition, up to eight regions of interest may be inspected for net counts so that the particle may be chemically characterized. Up to fifteen chemical types may be defined by the operator by name for comparison to each result from a particle. Multiple-frame average sizes and diameter histograms are accumulated for each of the fifteen types as well as for all types of particles. Individual particle results as well as tabulated averages for all particle types can be typed out.

#### *Conclusion*

A digital scan generator for electron-column instruments and its application to EDS analysis has been discussed. These applications include multielement digital line scans and maps as well as detection and chemical characterization using EDS analysis of individual particles.

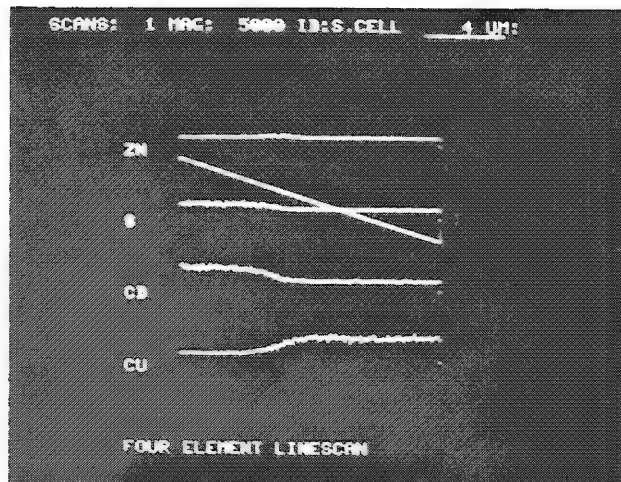


FIG. 1.--Four-element digital line scan display. Diagonal line shows path of beam during line scan acquisitions.

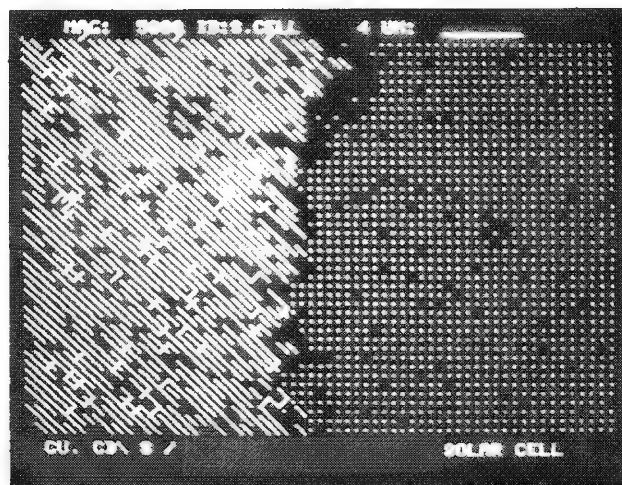


FIG. 2.--Multielement digital map of region where line scan of Fig. 1 was acquired.

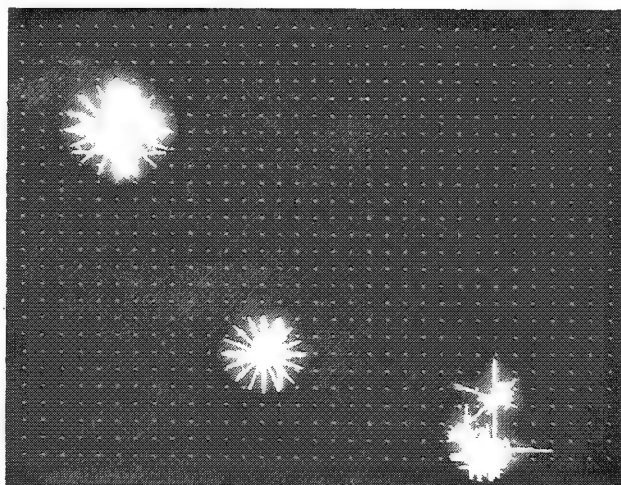


FIG. 3.--Example of motion of electron beam during location and sizing of several particles within raster frame.



## BACKSCATTER ELECTRON DETECTORS ON ENERGY-DISPERSIVE X-RAY SPECTROMETERS

Steven R. Hayashi and Roger B. Bolon

An inexpensive solid-state backscatter electron (BSE) detector has been mounted on the snout of an energy-dispersive x-ray spectrometer (EDS). In this position, the resulting image, from rough surfaces such as fractures, reveals the same shadowing experienced by the x rays. Obscured structures, normally visible with secondary electrons (SE) or BSEs from a different direction, are avoided. This technique can save analysis time and aid in the interpretation of x-ray distribution images. An additional advantage with retractable EDS detectors is that the signal strength can be increased if one moves closer to the sample. Several applications have been developed.

---

The authors are in Corporate Research and Development of the General Electric Co. in Schenectady, NY 12301.

## Surface Microanalysis

### AUGER ELECTRON SPECTROSCOPY (AES) FOR CHARACTERIZATION OF SEMICONDUCTOR MANUFACTURING PROCESSES

E. K. Brandis and H. S. Wildman

With the advent of higher levels of integration of semiconductor circuits, more stringent demands have been placed on the physical characterization of the circuits during manufacturing. The manufacture of integrated circuits consists of a large number of consecutive deposition and etching steps. To obtain a high process yield, a very detailed chemical and physical analysis is often required to insure the integrity of each individual processing step. It is the purpose of this paper to illustrate the use of high spatial resolution AES in achieving this goal. Applications of AES have been grouped into five categories.

#### 1. *Elemental Surface Analysis*

One obvious application of AES is the analysis of residue after a chemical- or plasma-etching step. For example, with submicron spatial resolution it was possible to detect trace amounts of copper residue in an emitter contact area after a rework operation. This small amount of Cu, not detectable by electron microprobe (EMP) analysis, caused a high contact resistance after subsequent metal deposition. Another typical example is the AES surface analysis of a metal film inside a contact hole after the wafer had been subjected to a sputter-cleaning step. AES analysis easily determined the presence of Si due to re-deposition from the surrounding  $\text{SiO}_2$  surfaces.

#### 2. *Measurements of Oxide Thicknesses*

With the use of multilayer structures, contact resistances and diffusion barriers between component layers present potential problems. Therefore, it is necessary to analyze and measure the thickness of surface films at each level. The thickness of thin layers of  $\text{SiO}_2$  and of  $\text{Al}_2\text{O}_3$ , up to a thickness of 120 Å, can be measured with a method described by Chang and Boulin,<sup>1</sup> in which the chemically shifted KLL peak heights from Si and from  $\text{SiO}_2$  (or Al and  $\text{Al}_2\text{O}_3$ ) are measured by means of an electron spectrometer with 0.3% energy resolution. The oxide thickness can be determined from the ratio of the two peaks, since the silicon signal from the substrate is attenuated, whereas the signal from the  $\text{SiO}_2$  grows with increasing oxide thickness, according to exponential laws characterized by the same electron escape distance. This method can be used to measure oxide thickness variations of only a few angstroms, a measurement that is extremely useful in studying the effects of chemical rinses and plasma photoresist stripping on the growth of oxides on metal and silicon surfaces (Table 1).

#### 3. *Chemical Information*

Schottky barrier diodes and some diffusions are sensitive to very thin surface layers on silicon. The Si LVV (55-92eV) transition is sensitive to differences in Si bonding within a 10Å-thick layer. One feature of AES that has not been fully exploited is that it can give Si bonding information within a smaller area than is possible by the use of electron spectroscopy for chemical analysis (ESCA). However, to avoid electron beam damage, very low beam current densities must be used; thus, shifts in the position of the silicon peaks could be used to identify chemically very thin films in contacts.

---

The authors are with IBM Data Systems Division, East Fishkill, Hopewell Junction, NY 12533.

TABLE 1.--AES silicon oxide thickness measurements.

Method of Growth	Temp (°C)	Time (min)	Oxide Thickness (Å)
H <sub>2</sub> SO <sub>4</sub> Rinse	120	10	15.5
O <sub>2</sub> Plasma (Syst. A)* with tunnel	?	5	17.1
O <sub>2</sub> Plasma (Syst. B) with tunnel	?	45	17.3
O <sub>2</sub> Plasma (Syst. B) with tunnel	?	45	19.6
O <sub>2</sub> Plasma (Syst. A) without tunnel	?	5	23.1
Dry O <sub>2</sub>	800	1.7	18.7
Dry O <sub>2</sub>	800	4	20.1
Dry O <sub>2</sub>	800	10	27.4

\*Syst. A and B refers to different models of LFE plasma reactors used for photoresist stripping. The "tunnel" is an Al Faraday cage used to shield the wafers from the plasma.

#### 4. Profiling

AES is frequently used with ion sputter etching to obtain in-depth distribution profiles of thin films, a unique feature not available in other electron-beam analytical techniques. For example, in the analysis of failures in terminal metal vias with high resistances, the electron microprobe related the high resistance to a high oxygen signal from a chromium layer beneath the solder pad; but Auger profiling showed that the chromium had a low oxygen content and that the high oxygen signal came from an oxide-rich layer, a result of Al pitting corrosion present between the Cr and Al layers (Fig. 1).

For profiling of relatively thick films, where ion milling combined with surface analysis would be time consuming and the depth resolution not accurate enough, a taper-section method can be used. A taper section provides a geometrical magnification of the thickness of the deposited film. The shallow escape depth, coupled with the small beam of the high-spatial-resolution AES system, enables one to obtain a composition profile by stepping the beam across the taper section and recording the Auger electron intensity at each point.<sup>2</sup> In Fig. 2, the method is illustrated for the determination of the phosphorus concentration of a phosphosilicate glass film.

#### 5. AES as a Complementary Method

In many instances AES is only one of the methods used in the solution of a semiconductor materials problem. For example, to make rapid measurements of a large number of varying thicknesses of lead/tin oxides, we decided to use the electron microprobe by measuring the x-ray oxygen intensity as a function of oxide thickness. ESCA analysis of a large area of the surface provided information about the type of oxide present, whereas AES analysis, coupled with ion milling, determined the in-depth distribution of the three elements involved. With the AES and ESCA information it was possible to generate reliable oxide-thickness measurements by use of the electron microprobe alone.

Another example of AES application is the characterization of the structure of chromium oxide films.<sup>3</sup> In this work the combined measurements obtained from AES, transmission electron microscope (TEM), and temperature coefficient of resistivity (TCR) on the same films provided the desired understanding of the behavior of the films as a function of a deposition parameters.

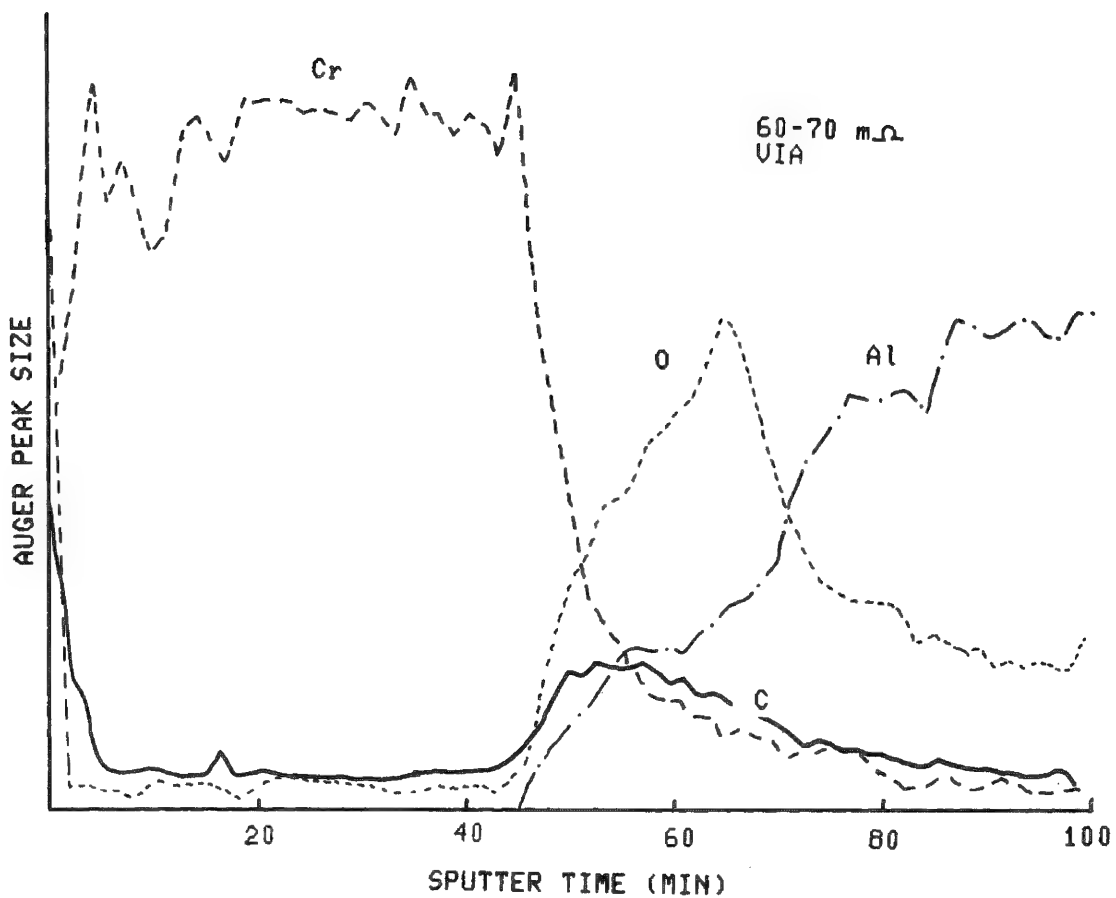
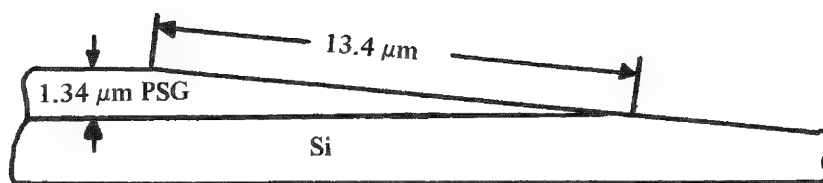


FIG. 1.--In-depth profile of via contact with high resistance.



Taper section of phosphosilicate glass (PSG) layer

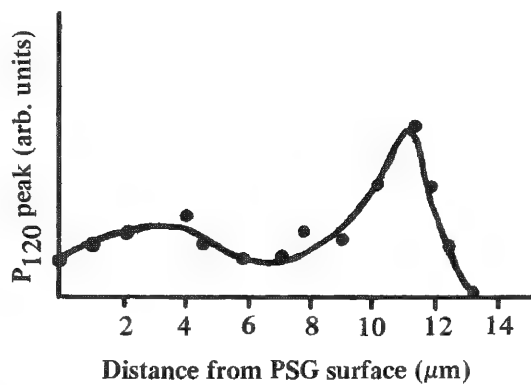


FIG. 2.--P<sub>120</sub> Auger intensities along taper shown in schematic, starting from top of PSG surface.

In summary, AES is a very practical analytical tool for providing unique information about small areas of an integrated circuit. The surface sensitivity of AES in conjunction with sputter etching allows one to determine the elemental composition of the surface and the oxide thicknesses, and to generate in-depth distribution profiles. This type of information complements other analytical instruments, such as TEM and EMP, and gives a more complete characterization of a materials problem.

#### References

1. C. C. Chang and D. M. Boulin, "Oxide thickness measurements up to 120 Å on silicon and aluminum using the chemical shifted Auger spectra," *Surf. Sci.* 69: 385-402, 1977.
2. E. K. Brandis, "High spatial resolution Auger electron spectroscopy in an 'ordinary' diffusion pumped SEM," *Proc. Scanning Electron Microscopy, IITRI* 1975, 141-145.
3. P. J. Smith et al., "Structure of chromium-chromium oxide films," *Proc. 9th Intern. EM Congress*, Toronto, 1978, 650.

## SIMULTANEOUS MULTITECHNIQUE ANALYSIS: SEM, SAM, AND EDX

C. T. Hovland and R. L. Gerlach

Characterization of materials is most effective when combined techniques are used for investigation. The topological information supplied by the scanning electron microscope (SEM) becomes more useful to the analyst when complimentary chemical information is obtained by energy-dispersive x-ray (EDX) analysis and scanning Auger microprobe (SAM) analysis.<sup>1</sup> All three techniques can in fact be performed simultaneously to maximize the information gathering rate per sample.

For chemical characterization of materials, the analyst is concerned with the sensitivity of the technique in absolute elemental concentration and the elemental volume analyzed by the technique. The basis for comparison of the elemental sensitivity of EDX and SAM analysis must include a comparison of the relative analysis volumes for each technique.<sup>2</sup> For such a comparison one finds that EDX analysis and SAM analysis are complementary both in the volume analyzed and the resultant elemental sensitivity. SAM analysis is surface sensitive; a typical analysis depth is the first 10 Å of the surface. Within this depth all elements with  $Z > 3$  are analyzed with relatively uniform sensitivity. Conversely, EDX analysis analyzes a depth of 1 to 3 µm depending on the beam voltage and the selected x-ray line. In general, for  $Z > 10$  EDX analysis can be performed with relatively uniform sensitivity across the periodic table by the use of higher beam voltages or higher-level x-ray transitions.

For both SAM analysis and EDX analysis the volume analyzed for a focused beam is a function of the spot size, the beam voltage, the volume distribution of backscattered electrons, and the escape volume of the x rays or Auger electrons. For a specimen that has a uniform chemistry from surface to bulk, the combined techniques of SAM and EDX analyses provide the analyst with relatively uniform sensitivity to the elements in the periodic table for  $Z > 3$ . For such a uniform sample, the complementary nature of Auger and x-ray emission processes allows the analyst to choose operating parameters such that either the Auger yield or x-ray yield is nearly unity. If we denote the Auger yield for a K-shell excitation as  $a_k$  and the fluorescence yield for a K-shell excitation as  $\omega_k$ , then<sup>2</sup>

$$\omega_k = 1 - a_k \quad (1)$$

For a K-shell excitation the two techniques strictly complement each other in yield across the periodic table. The relationship described by Eq. (1) is also valid for higher level transitions. Figure 1 shows the variation of the fluorescence yield and the Auger yield as a function of atomic number and illustrates the complementary nature of Auger and x-ray yields. Furthermore, Fig. 1 shows that by judicious selection of the Auger transition used for the analysis (i.e., the Auger peak energy) the analyst can always work in a region in which the Auger yield is nearly uniform for all  $Z > 3$  elements.

The absolute yield, particles per incident electron, is a function of the beam voltage and the contribution of backscattered electrons produced in the analysis volume. To achieve high-sensitivity EDX analysis, the beam voltage is usually increased to operate in a region of high fluorescence yield. The increased beam voltage results in a larger analysis volume and consequently may complicate the analysis of layered specimens or the analysis of particles on a substrate. However, the larger analysis volume of EDX has the advantage of "seeing below the surface" without specimen erosion or special sample preparation. A complementary SAM analysis uniquely identifies the surface chemistry and minimizes the contribution of the substrate to the analysis.

---

The authors are at the Physical Electronics Division of Perkin Elmer Corp., 6509 Flying Cloud Dr., Eden Prairie, MN 55343.

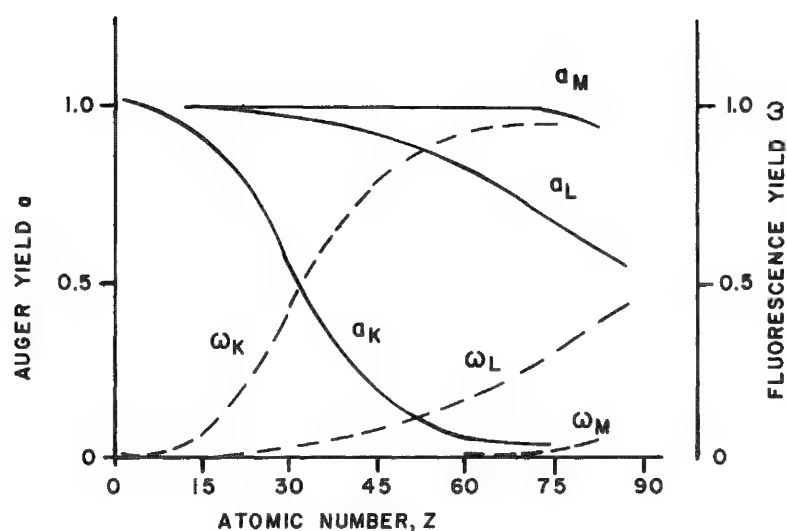


FIG. 1.--Auger yield and fluorescence yield vs atomic number.

For microprobe analysis the analyst is usually interested in the characterization of three-dimensional chemistry and topography of the specimen. SAM analysis combined with EDX analysis, when used in conjunction with sample-etching techniques such as *in situ* ion sputter etching, also can yield chemical information on the transition region between the surface region and the bulk of the specimen. Furthermore, EDX can "see below the surface" to identify elements of interest for performing in-depth SAM elemental analysis. In this way EDX analysis is utilized to select not only the elements of interest for thin-film analysis but also provides the analyst with the information required to set sensitivity levels, analysis time, and sputtering rate.

In summary, SEM analysis combined with SAM and EDX analysis provides the analytical chemist with a multitechnique approach to solving complex materials characterization problems.

#### References

1. J. Kirschner and H. W. Etzkorn, "Thin film analysis: From 'sputter profiles' to 'depth profiles' by combined Auger/x-ray analysis," *Proc. 7th Intern. Vac. Congr. and 3rd Intern. Conf. Solid Surfaces*, Vienna, 1977, 2213.
2. N. C. MacDonald, "The third dimension in scanning electron microscopy: Scanning Auger microscopy," in B. M. Siegel and D. R. Beaman, Eds., *Physical Aspects of Electron Microscopy and Microbeam Analysis*, New York: Wiley, 1975, 431.



## APPLICATIONS OF SURFACE ANALYTIC TECHNIQUES TO MATERIALS SCIENCE

H. L. Marcus

Several applications of surface-sensitive measuring techniques to problems in materials science have been reviewed and compared: AES, SIMS, IMMA, microprobe, ESCA, and UPS, with the main emphasis on the first four approaches. Topics in metallurgy, ceramics, corrosion, and some engineering applications have been included. The dominant application in metallurgy has been to fracture studies. Several aspects of these studies can be described for a range of systems, including temper embrittlement of steels, interface chemistries related to fatigue, and strength of metal-matrix composites. Corrosion and oxidation studies have also been covered. Studies of the influence of free surfaces on the local chemistry of metals and ceramics have been discussed. In ceramics they are related to the valence states of the atoms. Where appropriate, comparisons of the results obtained with different surface analytic methods are made.

---

The author is in the Departments of Mechanical Engineering and of Materials Science and Engineering at the University of Texas in Austin, TX 78712. This work is supported by the Office of Naval Research under contract N00014-78-C-0094.

## ACCURACY OF QUANTITATIVE AUGER ANALYSIS OF Cr-Fe-Ni ALLOYS

Fredrick Bacon and W. G. Morris

Auger electron spectroscopy (AES) is a well-established technique for qualitative analysis of elements on the topmost few atom layers of solids.<sup>1</sup> However, quantitative analysis by AES is still in its infancy since many of the parameters on which the Auger current depends have not been measured or cannot be assessed *a priori*.<sup>2</sup> Many of the uncertainties in quantifying Auger data can be overcome by normalizing measured Auger currents of elements (Z) to the measured Auger current of a standard element, silver, by which a set of relative elemental Auger sensitivity factors  $S_{Ag}(Z, eV)$  is generated.<sup>1</sup> For identical experimental conditions and surface textures, the elemental sensitivity factors represent a ratio of mainly atomic parameters; i.e., the electron-impact ionization cross section and the probability of Auger electron emission.

It is conventional to measure the derivative of the Auger current; it has been established that the peak-to-peak height of the differentiated Auger current  $I$  is proportional to the atomic concentration  $C$ .<sup>3</sup> Therefore, provided appropriate standards are used, the sensitivity factor approach towards quantifying Auger data should still give reasonable accuracy by use of expressions of the form

$$C_i = I_i [S_{Ag}(i, eV)]^{-1} / \sum_j I_j [S_{Ag}(j, eV)]^{-1}$$

Since the relative elemental sensitivity factors are mainly ratios of atomic parameters and do not necessarily and accurately account for matrix effects, a detailed study of alloy systems to assess matrix effects on the accuracy of Auger quantitation by sensitivity factors would be useful. Accordingly, the intent of this paper is three-fold:

1. to compare the accuracy of compositions calculated by sensitivity factors measured from elemental standard with those measured from alloy systems for Fe-Cr-Ni alloy;
2. to evaluate possible variations in composition from grain to grain in Fe-Cr-Ni alloys with a grain size of approximately 10  $\mu$ ; and
3. to correlate the accuracy of calculated compositions with possible secondary and impurity phases present in Fe-Cr-Ni alloys.

Measured elemental sensitivity factors relative to a silver standard for metallographically polished samples of iron, nickel, and chromium, and alloy sensitivity factors for polished 35Fe-35Ni-30Cr alloys, have been obtained. Alloy compositions calculated for sputter cleaned surfaces from both types of sensitivity factors have been compared with compositions obtained by quantitative x-ray fluorescence analysis. Preferential sputtering during *in situ* ion sputter cleaning has been checked by comparison of sputter cleaned surface compositions with those obtained from *in situ* fracture surfaces. The inter- and intra grain variation in calculated compositions for the alloys have been evaluated by means of high-spatial-resolution scanning Auger microscopy. In addition, the effects of distribution and types of phases on the accuracy of calculated compositions have been determined. Transmission electron microscopy is used to characterize the distribution and types of phases in the alloy.

### References

1. L. W. Davis et al., *Handbook of Auger Electron Spectroscopy*, Eden Prairie, Minn. Physical Electronic Industries, 1976, 2nd ed.
2. P. W. Palmberg, "Quantitative auger electron spectroscopy using elemental sensitivity factors," *J. Vac. Sci. Technol.* 13: 214, 1976.
3. R. E. Weber and A. L. Johnson, "Determination of surface structures using LEED and energy analysis of scattered electrons," *J. Appl. Phys.* 40: 314, 1969.

The authors are at General Electric Co.'s Research and Development Center in Schenectady, NY 12301.

## HIGH-RESOLUTION SCANNING AUGER ELECTRON MICROSCOPE EQUIPPED WITH A FIELD-EMISSION GUN

H. Todokoro, Y. Sakitani, S. Fukuhara and Y. Okajima

A scanning Auger electron microscope has been developed which is equipped with a field emission gun (FE-gun). The emission current of 100  $\mu$ A can be obtained for more than 8 hr. A schematic diagram of the microscope is shown in Fig. 1. This microscope has a simple optical system, which is composed of an FE tip, Butler type anodes, and a single magnetic lens. The probe diameter is varied from 20 to 500 nm by selection of the aperture size. Electron beam voltage can be chosen in the range 3-10 kV. The Auger signal is detected by the differential-mode operation of a Cylindrical Mirror Analyzer (CMA). The pressures in the FE gun and the specimen chamber are  $6 \times 10^{-8}$  Pa and  $1 \times 10^{-7}$  Pa, respectively. Secondary-electron images can be observed by the slow-scanning CRT mode and also by the TV-scanning-rate CRT mode. The TV-scanning-rate imaging provides easy focusing and easy selection of analyzing points.

The secondary-electron image of an evaporated gold film on carbon plate is shown in Fig. 2. The arrow shows the crack in the film, which demonstrates spatial resolution of 20 nm.

The spatial resolution of Auger electron image is measured by line scanning at the Si-Al boundary. The specimen was prepared by selectively etching of an aluminum layer (20 nm) evaporated on Si substrate. The secondary electron image and the Si (LMM) signal profile at the boundary are shown in Fig. 3. The profile indicates that the spatial resolution is approximately 20 nm.

As an application of the analysis with this microscope, deposits in a high-temperature alloy were observed and analyzed. The results are shown in Fig. 4. The construction of the alloy is iron (54%), chromium (25%), and nickel (20%), with additions such as titanium (0.4%) and niobium (0.4%). Two different deposits are observed in the absorbed-current image. Auger spectra were taken on the substrate (A) and on the deposits (B and C). It was found that deposit B contains titanium and niobium; and deposit C, chromium. Carbon is detected in both deposits. Auger signal maps of titanium, chromium, and carbon taken from the same area were depicted as shown in the bottom micrographs. The figures clearly indicate that deposit B is titanium and carbon and that deposit C is chromium and carbon.

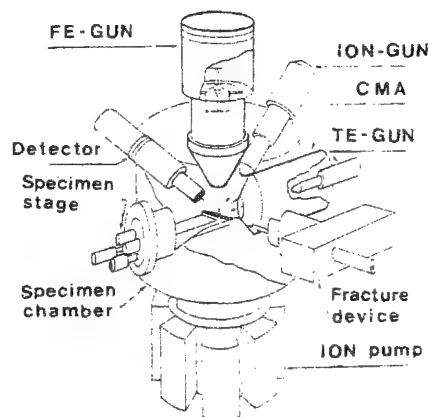


FIG. 1.--Schematic diagram of scanning Auger electron microscope.

Authors Todokoro, Sakitani, and Fukuhara are at the Central Research Laboratory of Hitachi Ltd., Kokubunji, Tokyo; author Okajima is at the Hitachi Research Laboratory in Omika Ibaraki, Japan.

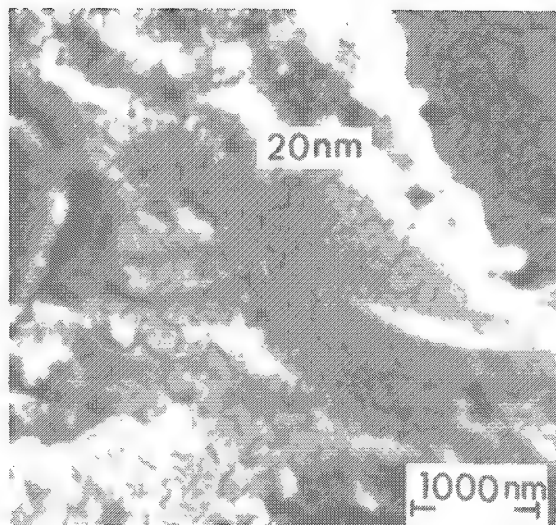


FIG. 2.--Secondary electron image of evaporated gold film. Arrow shows 20nm-wide crack in film.

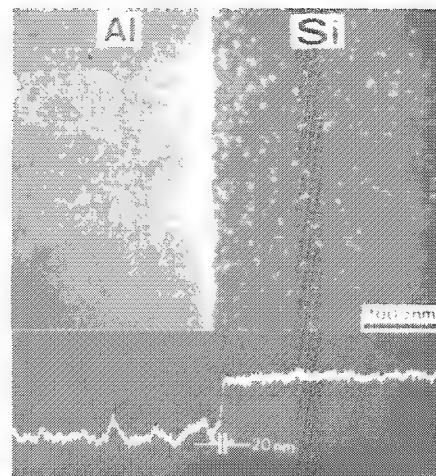


FIG. 3.--Si (LMM) line-scanning profile (bottom) and secondary-electron image (top) of Si-Al boundary.

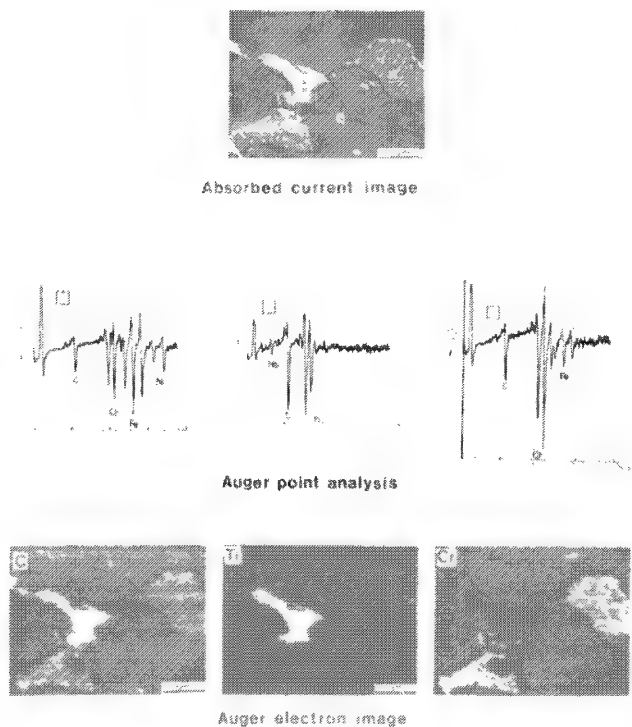


FIG. 4.--Analysis of deposits in high-temperature alloy: absorbed current image (top), Auger spectra (middle), Auger signal maps (bottom); beam voltage 5 kV, probe current  $2.5 \times 10^{-8}$  A, probe diameter 150 nm.

## EXTENDING REPLICATION METHODS TO AUGER SPECTROSCOPY BY USING CONDUCTIVE REPLICAS

P. B. DeGroot and R. H. Scott

Replication of surfaces has been a very useful technique in electron microscopy and microprobe analysis. The method has permitted the study of the surfaces of objects that cannot be easily transported to the laboratory or sectioned to obtain samples of suitable size. X-ray fluorescence analysis of films or particles removed by the replicating medium has been especially useful in corrosion studies.<sup>1,2</sup> In addition to providing a means for analyzing the surfaces of unwieldy objects, replication often enables otherwise inaccessible material in cracks or holes to be removed and exposed for analysis.

It should be helpful to be able to apply the analytical capabilities of the scanning Auger microprobe (SAM) to these replicas as well, particularly for the detection of light elements. Unfortunately, the replicating materials commonly used, such as cellulose acetate, silicone rubber, and various other polymers, are very poor conductors. Auger spectroscopy on these materials is difficult, if not impossible. Therefore, conductive materials were sought that would permit Auger analysis of particles adhering to their surfaces. These materials should also retain the ability to reproduce surface microstructure faithfully.

One successful method of making such a replicating material is to add a conductive filler to cellulose acetate. Lampblack carbon, with particles below 1  $\mu\text{m}$  in diameter, was found to be a very good filler. Other forms of carbon with larger particle sizes produced a rough surface texture in the acetate material that interfered with the accurate reproduction of microscopic surface detail.

The preferred preparation method is to add the carbon black to a small amount of acetone and stir thoroughly to obtain a uniform dispersion of carbon particles. The cellulose acetate is then dissolved in the acetone-carbon black suspension. The proportions of cellulose acetate, carbon, and solvent can be varied over a wide range. However, too much carbon results in a replicating material with poor adhesion properties. Too little carbon produces insufficient electrical conductivity for easy Auger analysis. A formulation with sufficient conductivity and good replicating properties is 1 g cellulose acetate, 0.5 g carbon black, and 10 ml acetone, which yields a moderately viscous black suspension.

Two methods were developed for using this suspension to make C-filled cellulose acetate sheets suitable for replicating. The first is to pour the material into a clean, flat-bottomed glass container and allow the acetone to evaporate. Partially covering the container to slow down the evaporation is necessary to produce a wrinkle-free film. A layer of the suspension about 5 mm deep produces a dried film about 0.2 mm thick. A second, faster, method is to dilute the conductive suspension further with acetone, and apply a thin layer of this solution to the surface of conventional acetate replicating tape. When the conductive film has partially dried to a soft sticky surface, the material is ready for use.

The conductive replicating material is used in the usual manner. The conductive film is moistened with acetone, and the softened surface is pressed firmly onto the surface to be replicated. The film is allowed to dry for about 20 min, then peeled off.

A practical example of the use of such replicas is shown in Figs. 1 and 2. Figure 1 shows the absorbed current image of a replica of a 304 stainless-steel surface that had experienced stress corrosion cracking. The Auger spectrum of this replica surface (Fig. 2) indicates that  $\text{MgCl}_2$  was the corrosion-inducing agent. Note that this spectrum was obtained by means of a relatively high beam current and voltage. Analysis of a similar replica by scanning electron microscopy and energy-dispersive x-ray fluorescence (SEM-EDX)

---

The authors are with Celanese Chemical Company, Inc., at the Corpus Christi, Texas, Technical Center.

failed to detect the Mg, but did detect Cl. Ion-sputtering experiments in the SAM showed the Mg and Cl-containing layer removed by the replica to be only about 0.2  $\mu\text{m}$  thick.

The carbon-filled cellulose acetate still reproduces microstructural surface features accurately, as is demonstrated in Figs. 3 and 4, which are SEM photomicrographs of conventional and C-filled cellulose acetate replicas of a 316 stainless-steel condenser-tube surface that had experienced severe intergranular corrosion. The surface detail shown by the uncoated C-filled replica compares favorably with that of the Pd-Au-coated conventional replica.

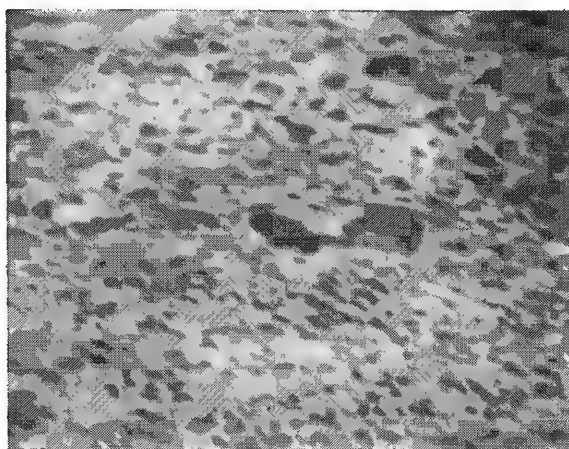


FIG. 1.--Absorbed current SAM photomicrograph of C-filled replica of 304 stainless-steel surface that had experienced stress-corrosion cracking. Dark object in center is hole in replica. Width of image, 330  $\mu\text{m}$ .

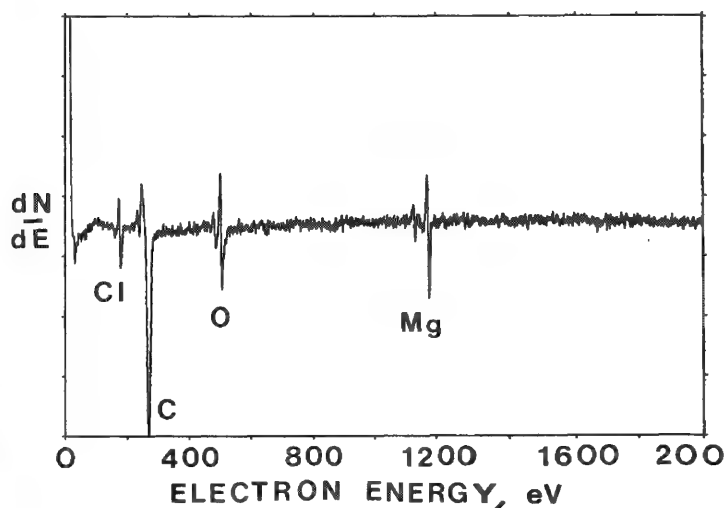


FIG. 2.--Auger spectrum obtained from area of replica shown in Fig. 1. Beam voltage 5 kV, beam current 10  $\mu\text{A}$ , beam incidence 30°.



FIG. 3.--SEM secondary-electron photomicrograph of replica of 316 stainless-steel surface that had intergranular corrosion. Cellulose acetate replica coated with Pd-Au by vacuum evaporation. Image width 95  $\mu\text{m}$ .

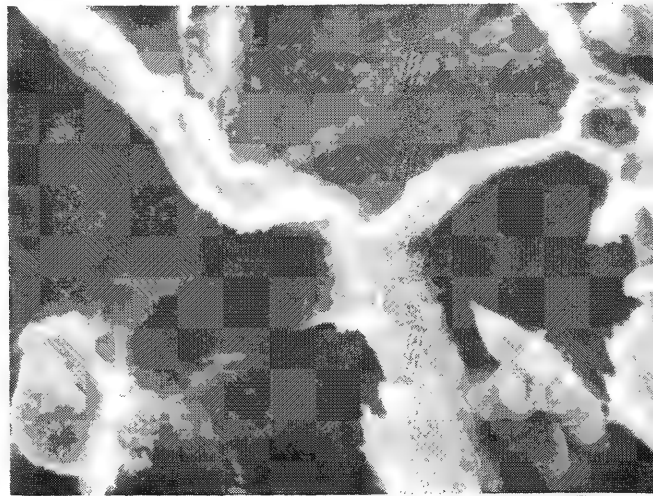


FIG. 4.--SEM secondary-electron photomicrograph of C-filled cellulose acetate replica of same sample as used for Fig. 3. Replica is uncoated. Image width 95  $\mu\text{m}$ .

The carbon-filled replicas do dry more slowly than regular acetate tape. They are also more difficult to pump to a high vacuum. These effects are probably caused by acetone absorption on the high-surface-area carbon filler. To overcome this problem, other

fillers such as silver, or other powdered metals, and other replicating material such as silicone adhesives can be used. These materials have the disadvantage of adding other elements to the Auger spectrum, which may interfere with the analysis of the surface layer removed by the replica.

The use of conductive replicating material brings with it the advantage that SAM methods can be applied to surface layers adhering to the replica. The replicas are not much more difficult to make than conventional ones, and they are still suitable for analysis by other electron microscope and microprobe methods.

#### *References*

1. R. H. Scott, P. B. DeGroot, and John Caron, "Replication-nondestructive analytical and inspection technique," *Materials Evaluation* 35: 45-50, 53, 1977.
2. E. P. Dahlberg, "Techniques for cleaning services failures in preparation for scanning electron microscope and microprobe analysis," *Scanning Electron Microscopy* 1974, 911-918, 1974.



# DETECTION OF MONOLAYER QUANTITIES OF CARBON AND OXYGEN ON SURFACES BY ENERGY-DISPERSIVE X-RAY SPECTROMETRY

R. G. Musket and Y. E. Strausser

The sensitivity of energy-dispersive x-ray spectrometry (EDXS) has been determined for the detection of carbon in thin layers on glass and of oxygen in thin oxides on silicon. In addition 3-sigma minimum detection limits were compared directly to Auger electron spectroscopy (AES) data taken concurrently for the same surface and electron-beam conditions (i.e., 5 keV, 150 nA, 60 sec). Detection limits of about one monolayer for EDXS were within a factor of ten of those for AES, under the conditions employed. A typical EDX spectrum of a thin oxide on SiO<sub>2</sub> is given in Fig. 1. Optimization of the EDXS arrangement by improving the solid angle for x-ray detection and the X-ray take-off angle should lead to even better sensitivity for carbon and oxygen.

Measurements, including *in situ* sputtering, were performed in a standard Auger system with an ultra-thin-windowed Si(Li) x-ray detector attached. The 2000Å-thick ultra-thin window was required to isolate the detector vacuum from the Auger system vacuum during sputtering processes in static argon gas and to preclude light from reaching the Si(Li) crystal. A magnetic electron trap, which was an integral part of the detector probe, was mounted between the window and the sample to prohibit bombardment of the Si(Li) crystal by backscattered electrons.

Implications of these EDXS results with regard to quantifying surface and thin film analysis, with and without sputter-profiling, will be discussed.

```
SI W/19A SiO2          K Z=14 SI
PR=    60S          60SEC          0 INT
U=8192 H=10KEV 4:10   AQ=10KEV 40
```

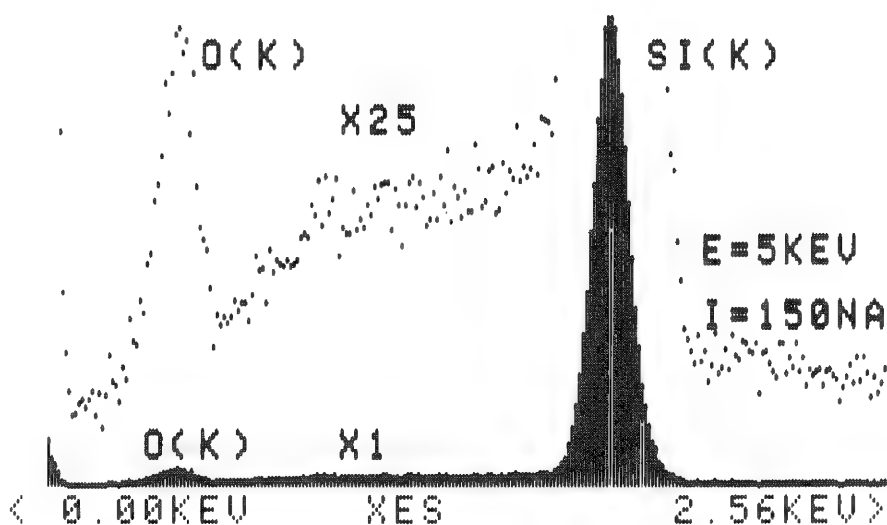


FIG. 1.--Energy-dispersive x-ray spectrum of silicon with 19 Å of SiO<sub>2</sub>.

Author Musket is at Kevex Corp., Foster City, CA 94404; author Strausser, at the Solid State Laboratory, Hewlett-Packard Laboratories, Palo Alto, CA 94304.

## RECONSTRUCTING THE OUTER FEW ÅNGSTROMS OF A SURFACE BY SIMS AND ISS TECHNIQUES

Gene R. Sparrow

The recent advent of several new analytical techniques for surface analysis has shown a definite need for the routine application of these tools in most R&D areas; yet detailed investigations of the surface layers (2-50 Å) have not been reported in the literature despite increasingly numerous publications on surface analysis. Each of the major surface analytical techniques--Auger Electron Spectroscopy (AES), Electron Spectroscopy for Chemical Analysis (ESCA), Ion Scattering Spectroscopy (ISS), and Secondary Ion Mass Spectroscopy (SIMS)--has individual advantages and shortcomings. Scientists involved with active modern analytical laboratories are constantly challenged to maintain a state-of-the-art awareness of new technology as well as an obligation to utilize the right techniques for the right job. It is not sufficient just to provide a solution; it is essential to provide the best solution in the minimum time.

Major considerations for surface analysis are the surface sensitivity and the depth resolution one can ultimately realize from a given technique. Detailed analysis of the top 5-10 Å of a surface is becoming increasingly important, especially for products and procedures requiring critical control of the surface. The outer monolayer of a surface can completely alter the desired chemical and physical properties of a system in adhesion, painting, lubrication, photoconductivity, catalysis, corrosion, etc. Maximum understanding of these particular surfaces is best achieved through techniques that permit study of the outermost atomic layers and subsequent detailed examination of the underlying atomic layers. When the ultimate performance or characteristic of a material is dictated by its surface properties rather than its bulk properties, the usefulness of information depends on the ultimate depth from which the analytical signal originates. In Fig. 1, the solid curve B illustrates a substantial decrease of useful surface information as the average depth from which the spectrum originates increases. Classical techniques, bulk techniques, spark source mass spectrometry, and x-ray techniques generally provide little useful surface information because the signal originates predominantly from the bulk rather than from the surface. The slope of the curve in Fig. 1 certainly depends on the nature of the problem. In some cases, there may be little decrease of useful surface information

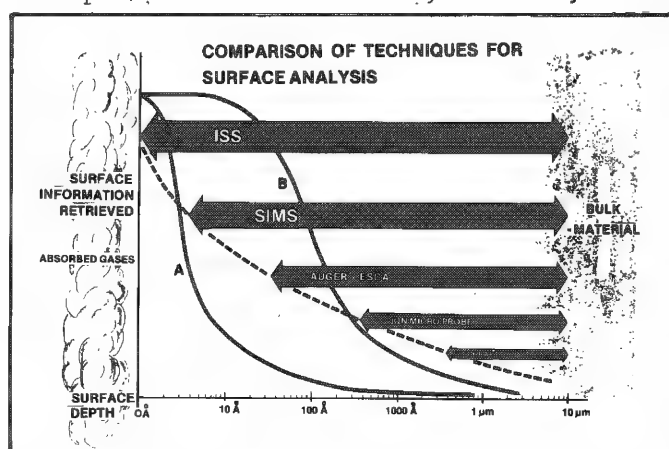


FIG. 1.--Amount of useful surface information retrieved as function of sampling depth from surface. Relative comparison of nominal sampling depths for various techniques.

for several hundred or even thousand Ångstroms, whereas in many systems of the sort depicted in curve A, there may be almost no useful surface information if the analytical signal originates from depths greater than a few Ångstroms. For analysis of thin films the curves shown in Fig. 1 may be repeated symmetrically in each direction from the interfaces between films. As evident from Fig. 1, the usefulness of Auger and ESCA is primarily a result of an analytical signal that originates from the outermost 10-50 Å. But understanding of surface chemistry is improved by other techniques, such as ISS or SIMS, for the study the outermost atomic layers. The most extensive characterization of a material surface would come from use of all four techniques, but that is often too costly and time consuming to be practical. The studies and

The author is with the 3M Company, 3M Center, St. Paul, MN 55101.

applications discussed below illustrate surface-related problems for which routine ISS analysis of the outer few Ångströms furnishes new and essential information not readily obtained by other techniques.

### *Surface Considerations*

A complete characterization of a surface would be nearly impossible, since it would include a detailed coordinated description based on the physical as well as the chemical aspects of the specimen. Larrabee presents a fairly complete discussion of modern techniques available to help characterize surfaces.<sup>1</sup> The techniques for physical characterization of a surface are extensively explained in literature, as is chemical analysis of surfaces from a few to several hundred Ångströms. However, noticeably lacking (aside from specific contrived laboratory experiments involving adsorbed gases) is reliable information showing detailed surface analysis with a depth resolution down to the level of actual molecular bond levels. Early attempts to achieve such "ultrahigh" depth resolution by sector-type ISS were highly successful but generally slow and tedious and limited to laboratory experiments involving single crystals or meticulously prepared surface-adsorbed layers.<sup>2-4</sup> The recent development of a highly sensitive cylindrical mirror analyzer CMA-ISS device by McKinney and Rusch permits routine analysis of surfaces with depth resolution approaching molecular bond distances of 1-2 Å, as discussed below.<sup>5</sup> The factors that affect the analysis of a specimen surface are as follows.

- (1) the physical nature of the surfaces
- (2) the chemical composition and stability of the surface component;
- (3) the surface sensitivity or depth resolution of the analytical technique;
- (4) the elemental detection sensitivity of the analytical procedure;
- (5) the effect of the analytical technique on the specimen;
- (6) the anomalous effect of one matrix component on the measured signal of another component (matrix effect);
- (7) the electrical conductivity of the surface;
- (8) the degree to which the components are homogeneously distributed laterally and in depth;
- (9) the precision of the analytical technique during sputtering and over long periods of time; and
- (10) the chemical reactivity of the surface to vacuum contaminants.

### *Experimental*

*Instrumentation.* The principle and theories regarding ISS are well described in several extensive works<sup>3,4,6-12</sup> and more recently for high performance CMA-ISS.<sup>12</sup> The data shown throughout this work were obtained by means of a commercially available Model 525BX combined ISS/SIMS spectrometer. An ion beam of inert gas  $^3\text{He}^+$ ,  $^4\text{He}^+$ , or  $^{20}\text{Ne}^+$  is formed in an ion gun mounted coaxially within a cylindrical mirror analyzer (CMA) and focuses a low-energy (50-5000eV) monoenergetic beam of ions onto the specimen surface. The energy and intensity of ions scattered from the specimen are recorded. Each element yields a unique scattering energy dependent on its mass. Hence the recorded spectrum identifies only the concentration and mass of the outermost atomic layers.

An automatic device for data acquisition/magnetic data storage was used to obtain all the spectra for these studies. The sensitivity of the CMA-ISS system was in excess of 10 000 cps/nA (for Ag); hence the entire spectrum could be scanned in less than 1 sec. The principle of signal averaging several full lsec scans was used routinely to obtain improved S/N ratio and quantitative results. The spectral derivatives were used when necessary to confirm identifications of trace peaks or unresolved peaks appearing as shoulders on larger peaks.

The instrument used in these studies also yields SIMS measurements (simultaneously or subsequently). The SIMS technique is highly sensitive to outer monolayers, but in general does not uniquely reflect the outer monolayer. Although reliable quantitative results have been obtained from SIMS,<sup>13-20</sup> the spectrum is difficult to interpret for reliable quantitative values for certain elements of major interest, such as C, N, O, F, etc. In addition the sensitivity of SIMS to high-mass elements (especially noble metals) is sufficiently low so as to preclude its use for ultrahigh depth resolution. Thus, SIMS was utilized primarily

to supplement the ISS results. The SIMS technique is a powerful surface analytical technique applicable to numerous other studies and has been well explained previously.<sup>21-27</sup>

### Static Surface Analysis

There are three major considerations one must address when attempting detailed investigations of the outer monoatomic layer of a specimen:

- (1) the depth from which the signal originated within the specimen surface and the precision and anomalies associated with that signal and matrix;
- (2) the rate, extent, and predictability of surface damage as a result of the probe beam energy imparted to the specimen; and
- (3) the sputtering rate of the surface affected by the incoming beam.

The mean free path of electrons has been reported by Tracy<sup>28</sup> and similar experimental results have been obtained.<sup>29</sup> With the exception of a few transition elements these mean free paths, commonly associated with Auger escape depths, are 10-20 Å or greater. Whereas these data can be assumed to represent the true average escape depth of electrons during surface analysis, the energy distribution and thus depth of *all* detected Auger electrons must not be ignored in quantitative calculations. With escape depths of several monolayers one may in principle extract useful information relating to certain specific outer monolayers of a specimen, if some simple calculations are made. However, in most cases it is *routinely* possible to obtain detailed information regarding the outer monolayer by ISS, since only that layer of atoms causes the binary scattering spectral peaks.

The precision and accuracy of results obtained from surface measurements of the outer few monolayers is very critical to proper inference of the surface composition and structure. Much of the previous quantitative surface information reported in literature was obtained by Auger spectroscopy. Factors that affect such results (as reported by Wild<sup>30</sup> are the ionization cross section, Auger transition probability, backscattering factor, and escape depth. It is usually difficult to include such factors in every analysis, and measured sensitivity tables often lead to reliable results.<sup>31</sup> Unfortunately surface roughness<sup>32</sup> can significantly affect Auger quantitative results, as can the composition of the surface matrix.<sup>33</sup> This last work, by Solomon and Meyers,<sup>33</sup> best summarizes the anomalies associated with Auger quantitative analysis.

The need for additional quantitative analysis of these critical outer surface atomic layers is obvious. ISS signal intensities depend almost entirely on the surface density of atoms, so that in principle accurate quantitative results can be obtained for all detected elements. Resonance Charge Exchange (RCE) phenomena indicate that subtle matrix effects exist in a few specific elements, but they are almost insignificant for spectral data obtained at constant primary-beam energy. Tables of relative sensitivities of pure standards reported recently by Erickson and McKinney can be readily used to obtain quantitative results for most ISS studies.<sup>34</sup>

Perhaps as important as the surface depth resolution is the extent of surface damage caused by the primary analyzing beam. The damaging effects of electron-beam probes are well known and often quite extensive.<sup>35</sup> The four basic types of damage are electron-impact desorption of physisorbed species; electron-stimulated redeposition of residual gas molecules at the target area; electron induced-ion migration; and, most important, electron-induced dissociation or decomposition of the surface.<sup>36</sup> The high energy of an analyzing electron beam is sufficient to cause drastic degradation of polymer and organic materials and can also cause chemical reduction of metal oxides<sup>37-40</sup> such as TiO<sub>2</sub>, SiO<sub>2</sub>, etc., to the reduced oxides or even metallic elements. Braun et al.<sup>35</sup> and Mathieu et al.<sup>41</sup> report extensively on detailed experiments regarding both electron-beam and ion-beam effects on surfaces.

The latter work as well as other studies address only ion-beam effects of heavy <sup>40</sup>Ar<sup>+</sup> ion beams, sometimes at energies in excess of 3 keV. The work reported here shows that low-energy, low-mass ion beams such as <sup>3</sup>He<sup>+</sup> at less than 3 keV do not induce significant surface anomalies. Use of such beams not only reduces undesirable damage but also drastically reduces the sputtering rate of material from the specimen surface.

Figure 2 illustrates schematically the major factors that affect the rate at which a surface may be sputter removed or etched. Much work reported in literature was obtained with ion beams of *high mass* (<sup>40</sup>Ar<sup>+</sup>), *high energy* (2-5 keV), frequently *high ion current*

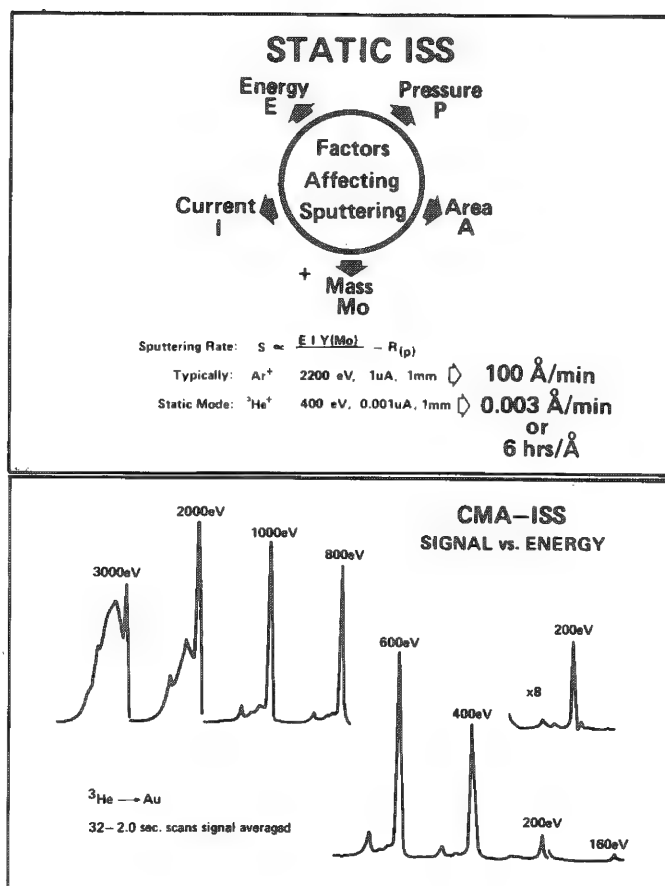
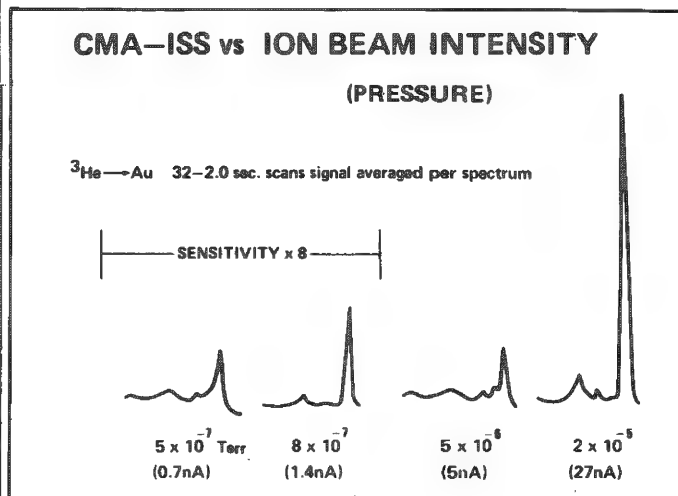


FIG. 2.--Instrumental factors that affect rate at which surface sputtering may occur.

FIG. 3 (bottom left).--ISS signal vs primary ion beam energy at beam currents of about 50 nA.

FIG. 4 (bottom right).--ISS signal vs primary ion beam current and 400eV primary ion energy.



(0.1-1  $\mu A$ ), and often *small areas* (0.1-1  $mm^2$ ). In addition the low sensitivities of some techniques such as "static" SIMS have necessitated long exposure times, as much as 20 min. The ISS technique (Fig. 2) does not create a system in which the ultimate detection sensitivity is directly related to the rate of sample destruction (i.e., sputtering), as in SIMS. Figure 3 illustrates ISS spectra obtained from Au at decreasing primary ion energies. Even at 160 eV almost 8000 cps are obtained at a beam current of about 50 nA. Figure 4 illustrates ISS spectra obtained from Au with  $^3He^+$  at 400 eV and at decreasing ion currents. The ISS spectrum at the right was obtained at about 0.1 nA of primary-beam current in 64 sec on an area of about 4  $mm^2$ . The estimated sputtering rate under these conditions is less than 0.005 Å/min, or 20 hr for a monolayer of atoms!

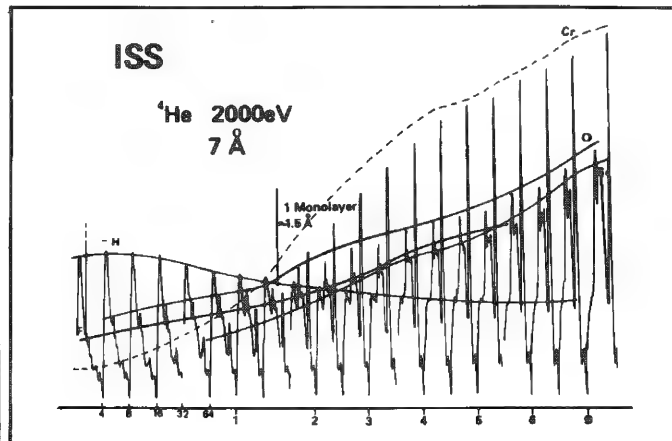
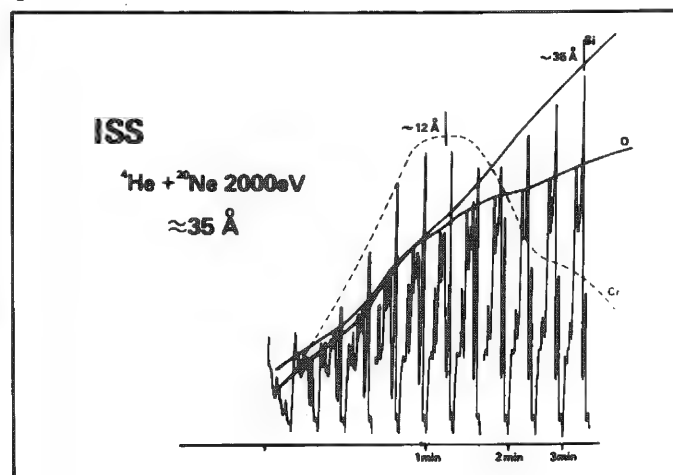
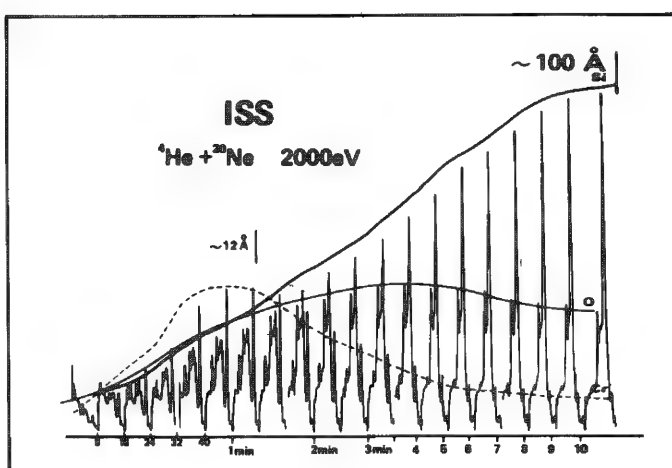
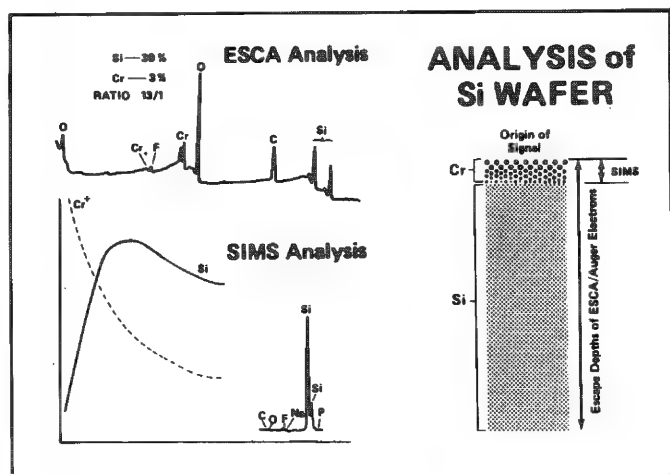
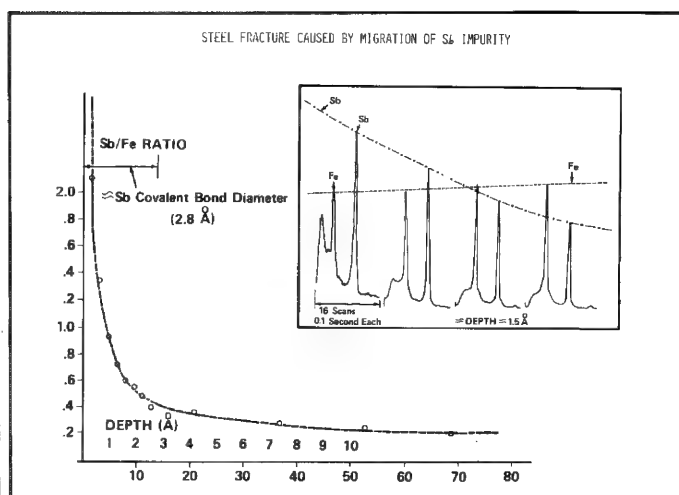
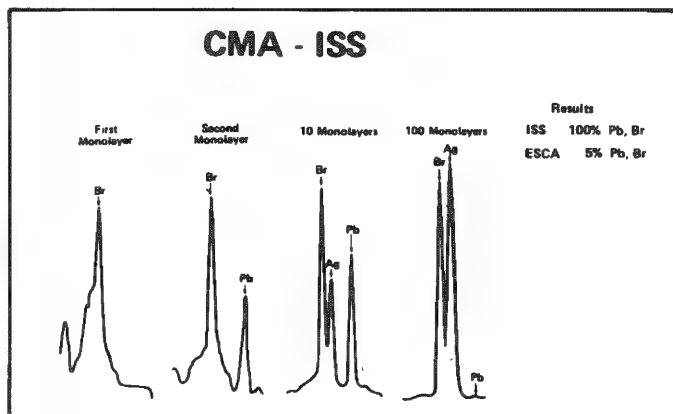
#### Data Acquisition Speed

The normal sensitivity realized by CMA-ISS for most metals is over 10 000 cps/nA of ion beam current at 2000 eV. Data acquisition time is directly related to device sensitivity. Under the above conditions imposed by "static" ISS the signal is sufficient so that a usable spectrum can be acquired in less than 1 min. In these laboratories, a highly sensitive SIMS device is incorporated into the same instrument. Yet the SIMS process is relatively quite inefficient, for the following reasons.

1. The sputtering process (yield) is quite low at these conditions ( $^3He^+$ , 400 eV).
2. Less than 1% of the sputtered material is ionized.
3. Cluster ions are orders of magnitude lower in intensity than elemental ions.
4. Electronegative ions such as C, N, O, and F are very low in intensity.
5. High-mass ions are ejected with a very low energy, which drastically reduces their intensity.
6. Secondary ions may be ejected from below the outer monolayer of atoms.

A "static" mode of operation for ISS is highly favorable for several reasons.

1. Static ISS provides a spectral fingerprint with nearly uniform elemental sensitivities.
2. Static ISS can utilize more ideal "static" ion bombardment conditions (low mass,



energy, and current density.)

3. Static ISS is considerably faster.
4. ISS detects essentially only the outer monolayer of atoms.
5. ISS can detect certain low-mass isotopes for labeling experiments.

### Applications

The extreme surface sensitivity of ISS has been utilized for the following studies.

- (1) surface orientation of adsorbed molecules and crystal lattices;
- (2) shadowing effects of atoms due to adsorption, steric hindrance, or crystal structure;
- (3) stoichiometric changes in outer surface layers (0-10 Å);
- (4) extreme surface segregation;
- (5) monolayer or partial monolayer organic contaminants on clean surfaces; and
- (6) detailed chemistry in the outer 10 Å of prepared surfaces by Ultra High Depth Resolution (UHDR).

Many of these examples are already reported in literature and will not be reviewed here. Perhaps the most dramatic illustration is the work done by Heiland,<sup>42</sup> in which ISS was used not only to determine the geometric orientation of CO adsorbed on W but also whether its position was over W surface atoms or over interstices in the outer lattice. Extreme surface segregation of monolayers has been reported previously<sup>12</sup> (Figs. 5 and 6).

Figure 7 illustrates SIMS and ESCA information from a contaminated Si wafer. The deeper escape depth of ESCA resulted in a *dilution effect* that led to the quantitative results that the "surface" contained 3% Cr. SIMS analysis indicated a very thin surface layer of 100% Cr, probably as an oxide. The raw data from detailed analysis by ISS with UHDR are shown in Fig. 8, 9, and 10. Throughout an estimated sputtered depth of 7 Å, 20 spectra were obtained.

These spectra illustrate the extreme surface sensitivity of ISS. The first few spectra are actually direct observation of a surface monolayer of water being sputtered from the surface. The first spectra indicate no significant elements present, since ISS cannot directly detect hydrogen. In this area of the surface the H atoms are oriented away from the surface and thus prevent detection of the underlying O or other elements until they are sputter removed. The large, broad peak at the beginning of these spectra can be correlated by SIMS data with H. If that is the case, approximate atom concentrations can be calculated from ISS spectral intensities and relative sensitivities. Figure 11 indicates the approximate elemental concentrations of the outer 35 Å of this surface. Assum-

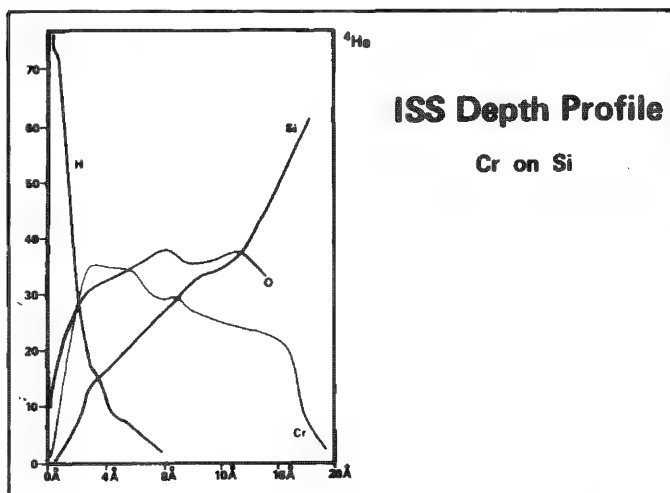


FIG. 11.--Ultra High Depth Resolution depth profile obtained by ISS. Approximately 30 to 40 data points were obtained in this 20 Å surface depth.

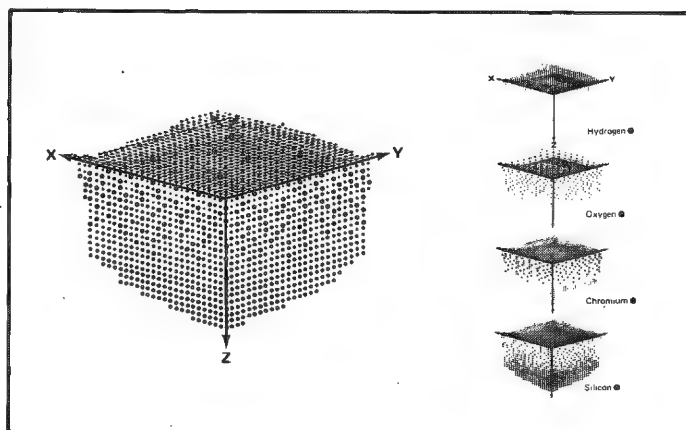


FIG. 12.--Reconstructed surface of Cr-contaminated Si. Actual ISS spectral data were used to calculate concentrations at 2 Å intervals.



ing each monoatomic layer is about 2 Å and ignoring all statistical and physical anomalies of sputtering one can "reconstruct" the elemental structure of a surface as shown in Fig. 12. Each row of atoms represents one atomic layer. When it is done with color codes and appropriate atomic sizes for each element a three-dimensional *reconstructed surface* can be obtained as a quick, easy-to-visualize representation of the specimen.

### Conclusions

The need for very *detailed* chemical analysis of the outer 50 Å of surfaces has been discussed and several representative applications have been presented. New and detailed information not readily obtained by other techniques were obtained with static ISS and Ultra High Depth Resolution (UHDR).

### References

1. G. B. Larrabee, "The characterization of solid surfaces," *Scanning Electron Microscopy* 1: 639, 1977.
2. W. H. Strehlow and D. P. Smith, *Applied Phys. Letters* 13: 34, 1968.
3. H. H. Brongersma and P. H. Mal, *Chem. Phys. Letters* 14: 380, 1972.
4. W. Heiland and E. Taglauer, *J. Vac. Sci. Tech.* 9: 620, 1972.
5. J. T. McKinney and T. W. Rusch, "High performance ISS surface analysis with a cylindrical mirror energy analyzer," 1976 Pittsburgh Conference on Analytical Chemistry and Applied Spectroscopy.
6. D. P. Smith, *J. Appl. Phys.* 38: 340, 1967.
7. H. H. Brongersma and W. J. Schouten, *Acta Electronica* 18: 47, 1975.
8. W. Heiland, *Moderne Verfahren der Oberflächenanalyse*, DECHEMA monograph 78, Weinheim: Chemie Verlag, 1975.
9. E. Taglauer and W. Heiland, *Appl. Phys.* 9: 261, 1976.
10. D. J. Ball, T. M. Buch, D. MacNair, and G. H. Wheatley, *Surface Science* 30: 69, 1932.
11. H. H. Brongersma and W. J. Schouter, *Acta Electronica* 18: 47, 1975.
12. G. R. Sparrow, *Industrial Res.* 18(9): 81, 1976.
13. G. R. Sparrow, Bibliography of quantitative SIMS studies, unpublished, 1978.
14. W. H. Christie, D. H. Smith, R. E. Eby, and J. A. Carter, *Am. Lab.*, March 1978, 19.
15. D. S. Simons, J. F. Baker, and C. A. Evans Jr., *Anal. Chem.* 48: 9, 1976.
16. J. A. McHugh, *Empirical Quantitative Procedures in SIMS*, Schenectady, N.Y.: Knolls Atomic Power Laboratory, Report KAPL-P-4040.
17. A. E. Morgan and H. W. Werner, *Anal. Chem.* 49: 7, 1977.
18. R. J. MacDonald and P. J. Martin, *Surface Sci.* 66: 423, 1977.
19. U. R. Deline, C. A. Evans Jr., and Peter Williams, *Appl. Phys. Letters* 33: 578, 1978.
20. G. R. Sparrow, *Quantitative SIMS Approximations for General Applications in Surface Analysis*, Am. Soc. Mass Spectr., 1977.
21. H. E. Werner, *Mikrochim. Acta*, Suppl. 7: 63-83, 1977.
22. A. Benninghoven, *Surface Sci.* 53: 596, 1975.
23. H. W. Werner, *Vacuum* 24: 493, 1975.
24. A. Benninghoven, *Appl. Phys.* 1: 3, 1973.
25. A. Benninghoven, *Surface Sci.* 35: 427, 1973.
26. H. W. Werner, *Acta Electronica* 18: 51, 1975; *Surface Sci.* 47: 301, 1975.
27. F. G. Rudenauer, *Mikrochim. Acta*, Suppl. 7: 85-94, 1977.
28. C. Tracy, NATO Scanner School Lectures, Ghent, 1972.
29. C. R. Brundle, *J. Vac. Sci. Tech.* 11: 212, 1974.
30. R. K. Wild, *Vacuum* 26: 441, 1977.
31. P. W. Palmberg, G. E. Riach, R. E. Weker, and N. C. MacDonald, *Handbook of Auger Electron Spectroscopy*, Edina, Minn.: Physical Electronics, 1972; C. C. Chang, *Surface Sci.* 48: 9, 1975.
32. P. H. Holloway, *J. Electron Spectr. & Related Phenomena* 7: 215, 1975.
33. J. S. Solomon and V. Meyers, *Am. Lab.*, March 1976, 31.
34. R. E. Erickson and J. T. McKinney, "Quantitative surface analysis by ISS," presented

- at Federation of Analytical Chemistry and Spectroscopy Societies, 1977.
35. P. Braun, W. Färber, G. Betz, and F. P. Viehböck, *Vacuum* 27: 103, 1978.
  36. T. E. Gallon and A. D. Matthew, *Phys. in Technol.* 3: 31, 1972.
  37. S. Thomas, *J. Appl. Phys.* 45: 161, 1974.
  38. C. C. Chang, *J. Vac. Sci. Tech.* 8: 500, 1971.
  39. L. F. Vassamilet and V. E. Caldwell, *J. Appl. Phys.* 40: 1637, 1969.
  40. A. Turos, W. F. Vaader Weg, D. Sigard, and J. W. Mayer, *J. Appl. Phys.* 43: 2777, 1974.
  41. H. J. Mathieu, J. B. Mathieu, D. E. Mclure, and D. Landolt, *J. Vac. Sci. Tech.* 14: 1023, 1977.

## SECONDARY-ION MASS SPECTROMETRY USING SELECTED PRIMARY IONS AND VARIATION OF THE PARTIAL PRESSURE OF SELECTED GASES IN THE SPECIMEN REGION

Felix Guo and D. B. Wittry

In secondary-ion mass spectroscopy (SIMS) it is known that the relative intensities of the various secondary-ion species depend on the partial pressure of oxygen above the surface of the specimen. This dependence can be considered to result from a variation of the work function of the surface due to the balance between oxygen adsorption and sputtering of the surface layers. Recently Morrison and his co-workers<sup>1</sup> proposed a method for improving quantitative SIMS analysis by varying the partial pressure of oxygen above the specimen, so that the intensity ratios of various ion species from the specimen would be the same from the specimen and a standard. From this work, it is apparent that control of the partial pressure of oxygen in the specimen region is essential for obtaining quantitative results with SIMS in empirical procedures.

Bombardment of the specimen with oxygen ions results in higher yields of positive secondary ions and also a reduction in the effect of the partial pressure of ambient oxygen on the intensities of various ion species. This effect can be understood quantitatively if we consider that the increase in the work function of the surface reduces the probability of neutralization of positive ions escaping from the surface.

Fujino and Shiraiwa<sup>2</sup> have reported investigations in which the primary ion beam was changed from  $O^{16}$  to  $N^{14}$  during bombardment. Interpretation of these experiments is difficult because the work function of the surface changes as the primary ion beam changes. In the present work, we use a primary ion beam selected from three possibilities ( $O^{16}$ ,  $O^{18}$ , and  $Kr^{84}$ ) obtained by using a mixture of gases in the plasmatron. Since the natural abundance of  $O^{18}$  is 0.20% we can differentiate between oxygen in the specimen and oxygen implanted in the specimen by the use of  $O^{18}$  for bombardment. In these experiments, we need to eliminate the possibility of an  $O^{16}$  signal from the ambient by blowing  $O^{18}$  on the specimen.

Another advantage of the use of  $O^{18}$  as a primary beam is in identifying oxide peaks when these peaks overlap elemental peaks. By a comparison of the spectra obtained with  $O^{18}$  and  $O^{16}$  primary ions it can be readily determined which peaks represent oxide species. It may also be possible to use the implantation of oxygen ions in the specimen as an internal standard. For example, if the specimen is bombarded with  $O^{18}$  ions, the depth distribution of these ions can be studied with an  $O^{16}$  primary beam. However, we must insure that the mass 18 peak is not due to  $H_2O$ , which may require blowing of  $O^{16}$  on the specimen to reduce the adsorbed  $H_2O$  on the specimen's surface.

Krypton is used as one of the gases in the plasmatron in order to make primary ions of an inert gas available for implantation experiments and experiments in which the effects of adsorbed oxygen and directly implanted oxygen are compared. Krypton was chosen because its ionization potential is less than that of neon and argon, and it is less expensive than xenon.

Figure 1 shows a schematic of the gas system for filling the duoplasmatron and also for blowing  $O^{16}$  or  $O^{18}$  on the specimen. The residual gas analyzer (RGA) we have used is a cycloidal type of high efficiency.<sup>3</sup> The gauge G reads from +30 to -30 psig. In practice the reservoir is filled with equal parts of  $O^{16}$ ,  $O^{18}$ , and Kr to a total pressure of +15 psig and the plasmatron can be operated until the pressure is reduced to about -27 psig. Approximately 100 hr of operation can be obtained from each filling of the 75ml reservoir.

---

The authors are with the Materials Science and Electrical Engineering Departments at the University of Southern California, Los Angeles, CA 90007. The support of this work by NSF Grant CHE-77-10133 and AFOSR Grant 77-3419 is gratefully acknowledged. The U.S. Government is authorized to reproduce and distribute reprints for governmental purposes notwithstanding any copyright notation hereon.

Experimental results on the applications of  $O^{18}$  to the topics described have been obtained.

### References

1. A. D. Ganjei, D. P. Leta, and G. H. Morrison, "Quantitative ion probe measurement using matrix ion species ratios," *Anal. Chem.* 50: 285, 1978.
2. T. Shiraiwa, N. Fujino, et al. *Ion Microprobe Mass Analysis of Steel Using  $O_2^+$  and  $1$  Primary Ion*, U.S.-Japan Joint Seminar on Secondary Ion Mass Spectrometry, 1978, 103.
3. Perkin-Elmer Ultek model No. 607-1500.

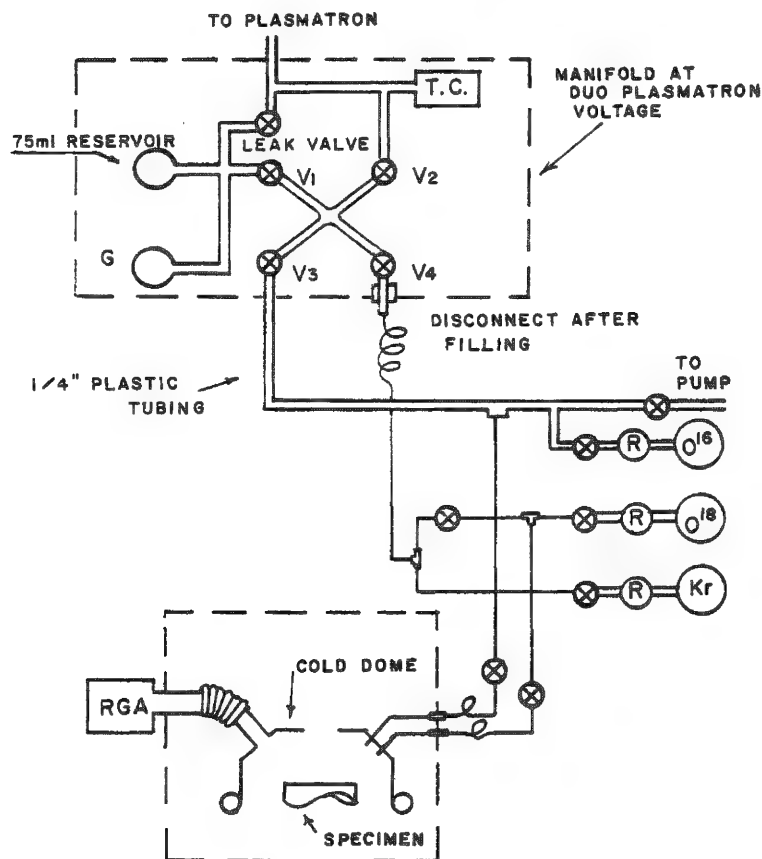


FIG. 1.--Gas system used in the present investigation.

## THE INFLUENCE OF INSTRUMENTAL SENSITIVITY VARIATIONS ON QUANTITATIVE ANALYSIS BY SECONDARY ION MASS SPECTROMETRY

Dale E. Newbury

Several quantitative analysis procedures for secondary ion mass spectrometry (SIMS) have been developed which are based on physical models of secondary ion emission.<sup>1-3</sup> These models attempt to calculate the strong chemical matrix effects that influence the secondary ion signals. In addition to these compositional factors, instrumental factors can also affect the measured secondary ion intensities, such as the spectrometer energy bandpass and the response of the ion detector as a function of mass. Moreover, these factors can vary from instrument to instrument and cause both the absolute sensitivity for a given element and the relative sensitivity for one element compared to another to differ. Generally, the physical models for quantitative analysis either assume that these variations in relative sensitivity are insignificant or that, even if sensitivity variations occur, they are automatically compensated in the model through the use of internal standards or elemental ratioing for normalization.

The recently reported results of the U.S.-Japan Cooperative SIMS Analysis of Metals and Glasses have revealed that strong variations in relative elemental sensitivity do indeed occur among the various SIMS instruments.<sup>4</sup> The relative sensitivity factor  $S_{X/M}$  is defined as:

$$S_{X/M} = (i_X/C_X f_X)/(i_M/C_M f_M)$$

where  $i$  is the measured secondary ion intensity,  $C$  is the atomic concentration,  $f$  is the isotopic abundance, and  $X$  and  $M$  represent any two elements. Values of  $S_{X/M}$  were calculated from secondary-ion spectra measured on two multi-element glasses by twenty-two laboratories representing a broad range of SIMS instrumentation.<sup>5</sup> The ratio of the maximum to the minimum value of the relative sensitivity factors for each element compared to silicon is shown in Table 1. This ratio ranges from 4.5 for Al to 57 for Pb, a substantial variation.

TABLE 1.--Range of relative sensitivity factors reported in U.S.-Japan study.

NBS Glass K-251		NBS Glass K-309	
O/Si	44	O/Si	22
Al/Si	5.5	Al/Si	4.5
Ba/Si	8.2	Ba/Si	9.6
Ta/Si	10.1	Ca/Si	6.2
Pb/Si	57	Fe/Si	8.4
Bi/Si	55		

To test the influence of this observed variation in relative sensitivity on quantitative analysis with a physical model, the secondary ion spectra were analyzed with a local thermal equilibrium (LTE) model.<sup>6,7</sup> Although the details of the LTE model are the subject of considerable debate, the use of a Saha-type equation describing the secondary ion process seems to be one of the most effective procedures at the present time.<sup>8,9</sup> For the present analyses, the known compositional values for two major elements were employed as the required internal standards; no oxide correction was made. Finally, the total of all elements excluding oxygen was normalized to the known sum for those elements (approximately 40 atomic percent). The results are given in Table 2 in terms of an error factor

The author is with the Microanalysis Group, Center for Analytical Chemistry, National Bureau of Standards, Washington, DC 20234.

$$F = C(\text{true})/C(\text{LTE})$$

where C is the atomic concentration. Comparing Tables 1 and 2, we note that the magnitude of the error factors follows the variation in relative sensitivity, with the largest errors observed for the elements with the largest range in relative sensitivity in most cases.

TABLE 2.--Range of error factors observed by LTE analysis.

NBS Glass K-251 (Si, Ba internal standards)		NBS Glass K-309 (Si, Ca internal standards)	
Al	0.27-0.82	Al	0.63-1.7
Ta	2.0-34.3	Fe	0.69-2.95
Pb	1.0-21.9	Ba	0.64-2.02
Bi	1.3-20.8		

As to individual analyses, in instruments with a low relative sensitivity factor, the LTE analysis tended to underestimate the concentration, as shown in Table 3 for glass K-251. A good correlation is found between the sensitivity factor and the accuracy of the LTE analysis: the lower the sensitivity factor, the larger the LTE error factor; i.e., the LTE model underestimates the concentration.

TABLE 3.--Comparison of relative sensitivity factors and LTE error factors in NBS Glass K-251.

Laboratory	$S_{\text{Pb/Si}}$	$F_{\text{Pb}}$
1	0.261	5.9
2	0.095	21.9
3	4.75	1.1
4	0.226	8.0
5	0.305	5.3
6	2.43	1.2
7	0.125	10.2
8	0.294	4.9
9	1.10	1.8
10	0.256	5.4
11	3.17	1.01
12	1.67	1.7
13	1.06	2.4
14	3.08	1.1
15	0.67	2.8
16	0.36	3.8
17	0.083	19.9
18	2.18	1.4
19	0.0862	20.1
20	0.65	3.0
21	0.21	6.4
22	0.86	2.7

The implications of these results for the development of methods of quantitative SIMS analysis are quite profound. The influence of instrumental factors on quantitative analysis is at present as important as the matrix factors. Clearly, instrumental factors cannot be ignored, and at least in LTE analysis, the existing model does not compensate for the effects. In principle, it should be possible to describe the instrumental factors rigorously and to calculate them accurately as part of the analysis--a procedure that would require a detailed study of each SIMS instrument. An alternative approach that avoids a detailed description of the instrumental effects could be constructed from a combination of the relative-sensitivity-factor method and a physical method.<sup>10</sup> A set of relative sensitivity factors  $S_{X/M}$  would be measured on each SIMS instrument operating un-

der a fixed set of conditions from a suite of standards, such as glasses. To apply these sensitivity factors to different matrices, one would then calculate series of matrix correction factors  $M_i$  by an appropriate physical model to yield a modified suite of sensitivity factors suitable for the new matrix:

$$S_{X/M}' = S_{X/M} M_1 M_2 \cdots M_i$$

The value of such an approach is that the original measurement of the sensitivity factor automatically incorporates the instrumental effects, and the matrix correction factors provide the analytical flexibility needed to analyze a broad range of unknowns. Development of the matrix correction factors will be described in a subsequent paper.

### References

1. C. A. Andersen, "Analytical methods and applications of the ion microprobe mass analyzer", in C. A. Andersen, Ed., *Microprobe Analysis*, New York: Wiley, 1973, 531-553.
2. J. M. Schroer, "An outline of secondary ion emission models," in K. F. J. Heinrich and D. E. Newbury, Eds., *Secondary Ion Mass Spectrometry*, Special Publication 427, Washington, D.C.: National Bureau of Standards, 1975, 121-127.
3. A. E. Morgan and H. W. Werner, "Quantitative analysis of low alloy steels by secondary ion mass spectrometry," *Analyt. Chem.* 48: 699-708, 1976.
4. D. E. Newbury, *Report on the United States-Japan Cooperative Analysis of Glasses by Secondary Ion Mass Spectrometry*, 2nd U.S.-Japan Joint Seminar on SIMS, Osaka, Japan, 1978.
5. National Bureau of Standards Research Material 30, "Glasses for Microanalysis," Office of Standard Reference Materials, Washington, D.C.: National Bureau of Standards.
6. C. A. Andersen and J. R. Hinthorne, "Thermodynamic approach to the quantitative interpretation of sputtered ion mass spectra," *Analyt. Chem.* 45: 1421-1438, 1973.
7. CARISMA, a local thermal equilibrium model computer program, Applied Research Laboratories, Sunland, Calif.
8. A. Benninghoven, "Zum Mechanismus der Ionenbildung und Ionenemission bei der Festkörperzerstäubung," *Z. Physik* 220: 159-180, 1969.
9. D. S. Simons, J. E. Baker, and C. A. Evans Jr., "Evaluation of the local thermal equilibrium model for quantitative secondary ion mass spectrometry," *Analyt. Chem.* 48: 1341-1348, 1976.
10. D. E. Newbury, "Quantitative analysis by secondary ion mass spectrometry," in N. S. McIntyre, Ed., *Quantitative Surface Analysis of Materials*, ASTM STP 643, 1978, 127-149.



# ION PROBE ANALYSIS OF NATURAL OLIVINE; SECONDARY-ION INTENSITY VARIATION AND SYSTEMATICS FOR A SIMPLE BINARY SILICATE

Ian Steele and Ian Hutcheon

A major objective of ion-probe analysis is an accurate determination of both major and trace elemental abundances. Several procedures have been described to relate measured secondary-ion (SI) intensities to sample composition. In general these approaches are unsatisfactory for a number of reasons, including: (1) specific to a certain instrument; (2) applicable only for certain samples; (3) valid only for some elements. Although it is unlikely that a single correction scheme can successfully be used for widely differing samples, efforts should continue to investigate possible correction schemes that can be applied to a limited range of samples. Of particular interest in the materials and geological sciences is the analysis of oxides and silicates. For these samples the effect of oxygen partial pressure in the source region on the parameters in a correction procedure is minimized both because of the inherent oxygen in the sample and the common use of oxygen primary beams for analyzing insulators.

The simplest procedure for correcting intensities is to construct a table of relative sensitivity vs element for pure oxides. Readily apparent in such tables are the relationships of SI yield and position in the periodic table to the very large range in sensitivity for different elements. Such tables are useful order-of-magnitude references but ignore matrix effects and are seldom accurate to better than a factor of 10 for correcting SI intensities to elemental concentrations. This approach can be refined by the choice of reference samples close in composition to the unknown, a procedure commonly used in electron-probe analysis to reduce matrix corrections. We present data illustrating systematic variations of SI yield with sample composition in the binary olivine system  $\text{Mg}_2\text{SiO}_4$ - $\text{Fe}_2\text{SiO}_4$  and discuss the use and limitations of this approach for relating SI intensity ratios to elemental composition.

All data were obtained with an AEI IM-20 ion probe attached to an AEI 702 mass spectrometer. The primary beam was mass analyzed  $^{16}\text{O}^-$  at 20 keV and the source pressure was  $< 3 \times 10^{-8}$  torr. SI intensities were determined by pulse counting with an electron multiplier. Samples consisted of seven analyzed, homogeneous, natural olivine samples spanning the binary series from  $\text{Mg}_2\text{SiO}_4$  to  $\text{Fe}_2\text{SiO}_4$ . Total minor elements account for less than 0.5 wt.%. The samples were mounted in epoxy, polished, and carbon coated. This procedure assures that tuning of the SI extraction system is invariant to sample position over an area of about  $1 \text{ cm}^2$ . SI extraction optics were adjusted for maximum transmission for  $^{28}\text{Si}$ . Intensity data for all samples were obtained over a two hour period.

Figure 1 gives sample compositions and SI count rates (arbitrary units) for the major elements. Important features are: (1) smooth curves can represent the SI intensity changes with composition; (2) the  $\text{Si}^+$  intensity shows a distinct minimum although Si is a constant atom fraction in all samples; (3)  $\text{Fe}^+$  SI intensity is near-linear; (4)  $\text{Mg}^+$  SI intensity shows a distinct maximum and then a decrease in intensity with increase in the Mg content of the sample; (5) the  $\text{Mg}^+$  and  $\text{Si}^+$  intensities anticorrelate at high Mg content, which suggests a strong interaction between Mg and Si in the sputtering-ionization process and not between Fe and Mg as claimed in a similar study.<sup>1</sup>

Any correction procedure that normalizes SI intensities to a fixed element (e.g., Si in this system) is immediately constrained by the nonlinear dependence of  $\text{Si}^+$  intensity on bulk composition (Fig. 1). Such normalization is apparently valid only for samples with nearly equal composition. In the olivine system the  $\text{Mg}^+/\text{Si}^+$  ratio is double-valued (Fig. 2) and cannot be used to obtain the major element composition. The  $\text{Fe}^+/\text{Si}^+$  ratio is monotonic (Fig. 2) but the nonlinear change of  $\text{Fe}^+/\text{Si}^+$  with composition limits accuracy unless the shape of the curve is known independently. These problems can be avoided by a plot of  $\text{Mg}^+ / (\text{Mg}^+ + \text{Fe}^+)$  vs the known  $\text{Mg} / (\text{Mg} + \text{Fe})$  in the sample (Fig. 3, curve A). The

---

Both authors are at the University of Chicago, Chicago, IL 60637: Steele in Geophysical Sciences and Hutcheon at the Enrico Fermi Institute. Research supported by NSF 76-02754 (Clayton, Smith), NSF 77-27100 (Smith), NSF 74-19038 (Clayton), NASA 14-001-171 (Smith), NASA 14-001-169 (Clayton).

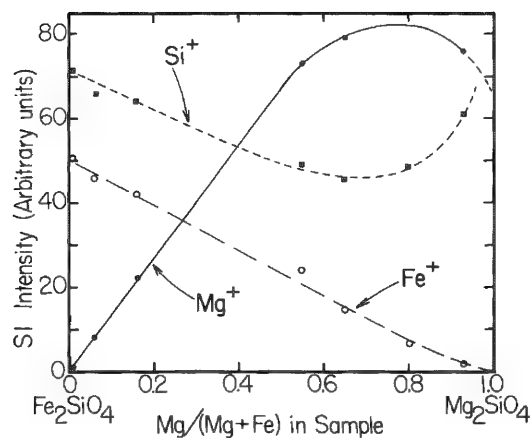


FIG. 1.--Count rate for main isotopes of Si, Mg, and Fe vs sample composition in  $\text{Mg}_2\text{SiO}_4$ - $\text{Fe}_2\text{SiO}_4$  binary system. Curves are approximate fit to points.

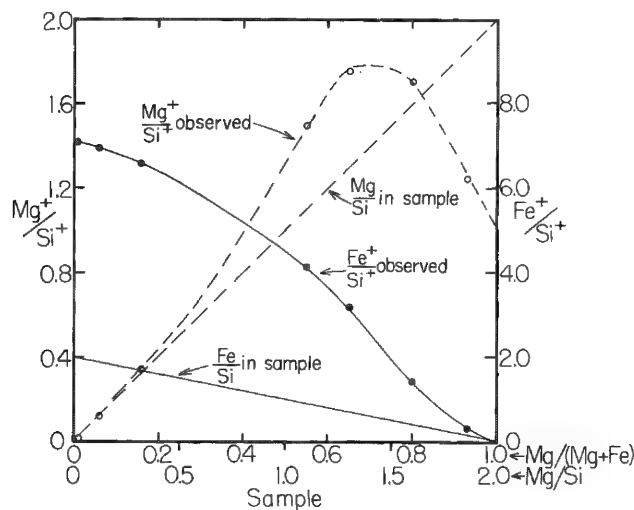


FIG. 2.-- $\text{Mg}^+/\text{Si}^+$  and  $\text{Fe}^+/\text{Si}^+$  vs sample composition in  $\text{Mg}_2\text{SiO}_4$ - $\text{Fe}_2\text{SiO}_4$  binary system. Also shown are the  $\text{Mg}/\text{Si}$  and  $\text{Fe}/\text{Si}$  variations in sample. Note distinct maximum in  $\text{Mg}^+/\text{Si}^+$  curve, which precludes unique compositional determination.

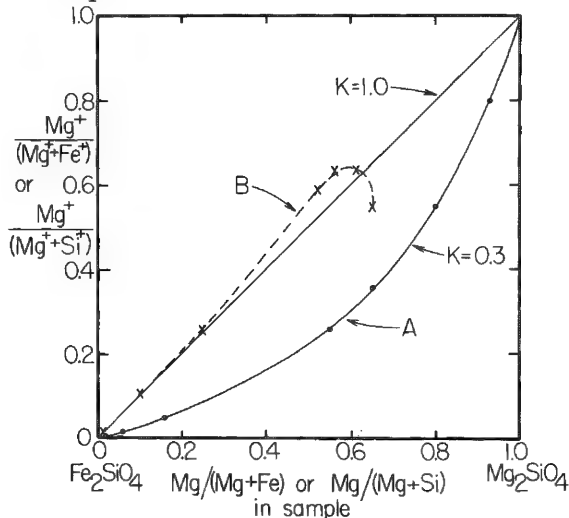


FIG. 3.-- $\text{Mg}/(\text{Mg} + \text{Fe})$  in sample vs  $\text{Mg}^+/(\text{Mg}^+ + \text{Fe}^+)$  in SI spectrum (curve A). Resulting curve allows unique compositional determination; however,  $\text{Mg}^+/(\text{Mg}^+ + \text{Si}^+)$  vs  $\text{Mg}/(\text{Mg} + \text{Si})$  (curve B) is complex.

resulting curve appears symmetric and can be described as;

$$[A(1 - B)]/[(1 - A)B] = K \quad (1)$$

where  $A = \text{Mg}^+ / (\text{Mg}^+ + \text{Fe}^+)$  in SI yield,  $B = \text{Mg} / (\text{Mg} + \text{Fe})$  in target, and  $K = \text{constant}$  ( $= 0.3$  in Fig. 3), dependent on isotopes measured and probably on experimental conditions.

This simple equation relates the observed SI intensity ratio  $\text{Mg}^+ / (\text{Mg}^+ + \text{Fe}^+)$  to the  $\text{Mg} / (\text{Mg} + \text{Fe})$  ratio in the sample. With this procedure unknown major element compositions can be determined irrespective of the composition of the standard for this binary system. Unfortunately, this simple relationship does not hold for  $\text{Mg} / (\text{Mg} + \text{Si})$  vs  $\text{Mg}^+ / (\text{Mg}^+ + \text{Si}^+)$  shown in Fig. 3, curve B, and is apparently not generally applicable to any two elements but only between elements equally affected by changes in bulk composition.

The apparent simple relationship between the measured  $\text{Mg}^+ / \text{Fe}^+$  ratio and the  $\text{Mg} / \text{Fe}$  in the sample over the entire binary system is somewhat surprising and suggests that the processes involved in generating the  $\text{Mg}^+$  and  $\text{Fe}^+$  ions during sputtering, at least in this case, are independent of the physical state of the sample such as preparation, crystal orientation, and composition. The relationship (Eq. 1) is the same as that which describes the distribution of components between two phases which are ideal with respect to these components, such as some coexisting liquid-vapor or solid-solid systems. That in turn suggests the possibility that the sputtering process can be treated in terms of classical equilibrium thermodynamics but without considering exchange equilibria in a plasma,<sup>2</sup> although the latter may also occur.

#### References

1. N. Shimizu, M. P. Semet, and C. J. Allègre, "Geochemical applications of quantitative ion-microprobe analysis," *Geochim. Cosmochim. Acta* 42: 1321, 1978.
2. C. A. Andersen and J. R. Hinthorne, "Thermodynamic approach to the quantitative interpretation of sputtered ion mass spectra," *Anal. Chem.* 45: 1421, 1973.

## ADAPTION OF THE DEITZ DETECTOR TO AN ARL ION MICROPROBE MASS ANALYZER

D. B. Wittry and Felix Guo

The Daly type of detector<sup>1</sup> in our prototype Ion Microprobe Mass Analyzer had a number of disadvantages. The scintillator was not insulated from ground, the light pipe was an early model with poor efficiency, and the background was high. In order to improve the signal-to-background ratio and to provide for efficient detection of negative ions, we have modified our detector based on the type of detector described by Dietz.<sup>2</sup> In this detector several stages of electron multiplication are incorporated before the scintillator. Our detector (Fig. 1) utilizes four stages instead of the six stages in the detector described by Dietz. This modification was necessary to make it possible to utilize the existing housing and a commercially available dual high-voltage feedthrough.

The box and grid dynodes are constructed of Al and have the normal  $\text{Al}_2\text{O}_3$  layer, which provides a high secondary-electron yield. The dynodes are mounted to each other with stainless-steel screw clamps and 1/16in. dia. alumina rod.<sup>3</sup> Several hundred volts per stage are used in order to provide the necessary overall gain so that the signal pulses have an amplitude greater than the pulses due to thermionic emission from the photocathode of the photomultiplier tube.

The voltage per stage in the electron multiplier is determined by an external divider with additional 3.3M $\Omega$  hermetically sealed resistors mounted directly on the dynodes. The arrangement for operating the detector in both the positive and negative secondary ion modes is shown in Fig. 2. The total divider resistance is 240 M $\Omega$ , including a string of 10 resistors of 2 M $\Omega$  for selecting the electron multiplier voltage.

A standard quartz light pipe with a convex end that is coated with scintillator and aluminized was used along with a new detector housing cover plate. The feedthrough for the electron multiplier and for the high voltage to the scintillator utilize existing ports in the detector housing.

Additional construction details and results of performance tests are available.

### References

1. N. R. Daly, "Scintillation type mass spectrometer ion detector," *Rev. Sci. Instr.* 31: 264, 1960.
2. L. A. Dietz, "Electron multiplier-scintillation detector for pulse counting positive or negative ions," *Rev. Sci. Instr.* 49: 1250, 1978.
3. Available from Kimball Physics, Inc., Wilton, NH 03086.

---

The authors are with the Materials Science and Electrical Engineering Departments of the University of Southern California, Los Angeles, CA 90007. The support of this work by NSF Grant CHE-77-10133 and AFOSR Grant 77-3419 is gratefully acknowledged. The U.S. Government is authorized to reproduce and distribute reprints for governmental purposes notwithstanding any copyright notation hereon.

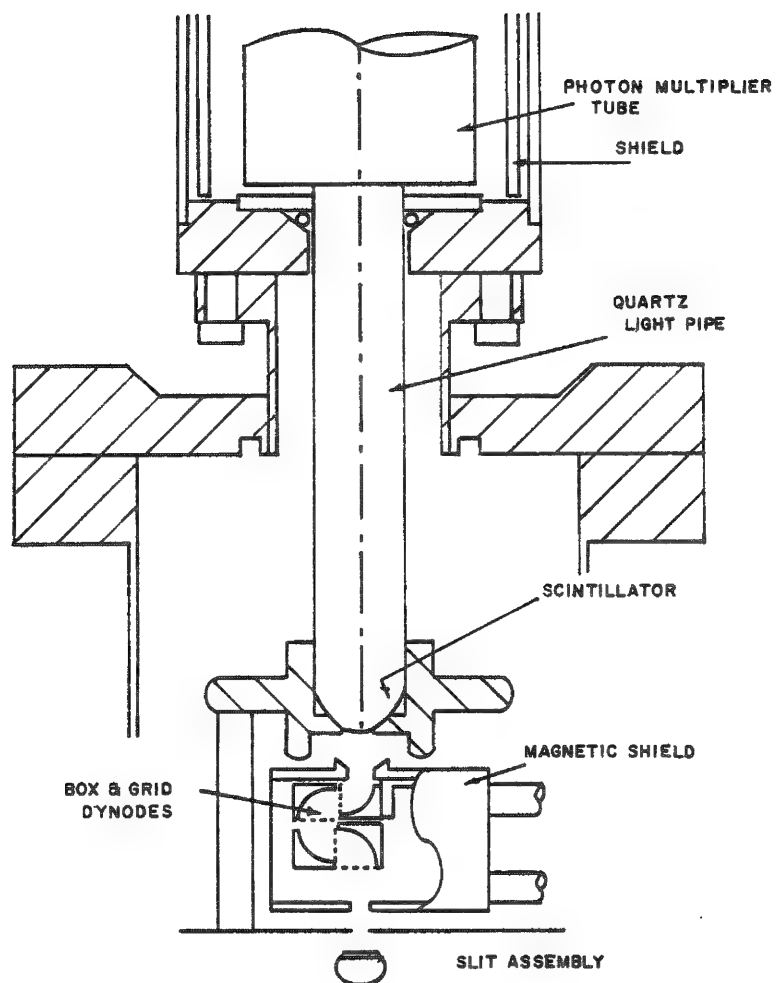


FIG. 1.--Modified Dietz detector.

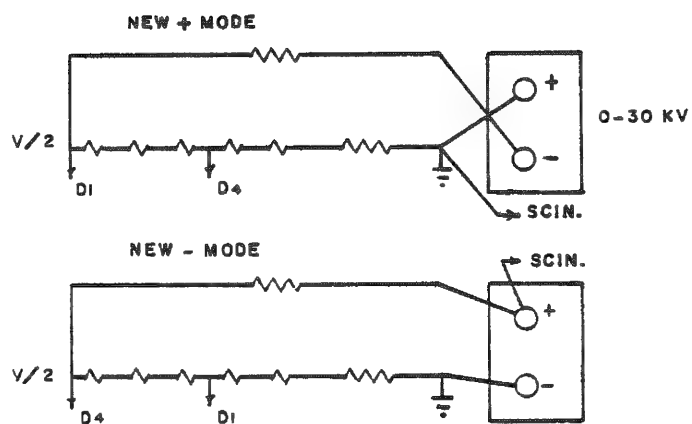


FIG. 2.--Voltage divider and connections used for positive and negative modes; D1 and D4 are first and last dynodes of electron multiplier.

## USE OF THE IMS 3F HIGH MASS RESOLVING POWER

J-M. Gourgout, M. Lepareur, and C. Conty

The IMS 3F was introduced two years ago in August 1977 at the 8th International Conference on X-Ray Optics and Analysis in Boston. The first instrument was delivered in March 1978 and the indications are that the IMS 3F is already very successful on a world-wide basis. This success is due without any doubt to the real needs in research laboratories for a true ion microanalyzer that will perform quantitative as well as qualitative analysis.

In the past, a few authors have insisted that for small-surface analysis the size of the primary beam should be reduced as much as possible without taking the numbers of secondary ions collected sufficiently into account. This approach has inhibited their attainment of the best conditions for secondary ion emission.

Ion microanalysis is the ability to analyze ion species characteristic of the chemical composition of a solid sample *in situ* on small surface areas of the specimen. The principle is that atoms sputtered from the top atomic layers of the specimen surface are ionized after a collision cascade due to energy transfers induced by the penetration of primary ions. This complex process is not yet perfectly mastered, but it is reproducible in the majority of cases.

Previously, two big limitations preventing the full development of these techniques were, first, the analysis of small volumes with high detection sensitivity; and second, the impossibility of separating the atomic ions from the polyatomic ions because of the poor resolving power of existing instruments. The IMS 3F has been developed to solve these two problems by a unique design of transfer optics to combine the traditional high-mass resolution mass spectrometer and ion microscope.

Illustrations of the above are given by the results of analysis on mineralogy and semiconductor samples. An example is in Fig. 1, which shows the separation of  $^{56}\text{Fe}^+$  and  $^{56}(\text{CaO})^+$ . They fully demonstrate the original features of the IMS 3F, whose particular significance is the ability to make secondary-ion images with high mass resolving power. These examples show the importance of the complete knowledge of the contribution of molecular ions with the atomic ions. This is the only way to perform quantitative analysis, especially in mineral samples that can have generally very complex phases.

Isotopic ratio measurements have been obtained, including spectra of flat topped peaks up to a mass resolving power of several thousand.

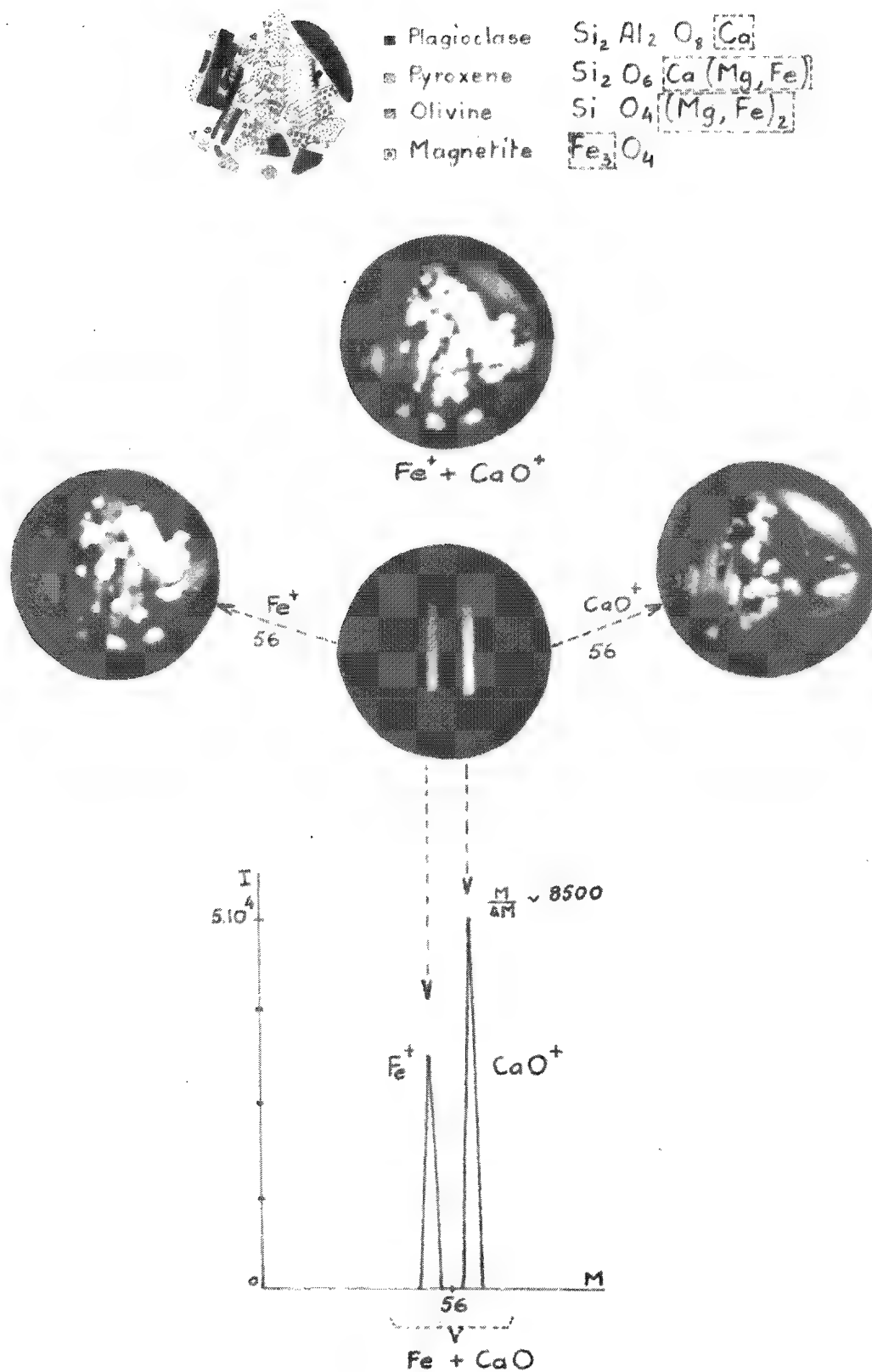


FIG. 1.--Separation of doublet  $^{56}\text{Fe}^+$  and  $^{56}(\text{CaO})^+$  in image mode. Analyzed area was 70  $\mu\text{m}$  in diameter. At mass 56, without high mass resolution, we get molecular ion  $^{56}\text{Fe}^+ + ^{56}\text{CaO}^+$ . Only way to know where (for example) iron and calcium are located is to increase mass resolving power to few thousand and to eliminate either Fe ion or CaO ion.



## ELEMENT DISTRIBUTIONS IN GEOLOGICAL MATERIALS BY IMAGE PROCESSING OF SCANNING ION MICROPROBE DATA

J. H. Schilling

Measuring gradients of element concentrations can further the understanding of the processes involved in the formation of rocks and minerals. Since abrupt changes in concentration occur (at grain boundaries) for such measurements, a resolution of at least a few microns is required. On the other hand, diffusion profiles might extend over a few hundred microns. Imaging element distributions appears to be a good approach to this problem since this technique allows the investigation of larger areas with a high resolution. Furthermore, imaging an area rather than single points minimizes the problem of unintentionally making measurements at peculiar positions on the sample, since such peculiarities are readily identified in an image.

An ARL ion microprobe mass analyzer<sup>1</sup> has been used to obtain scanning images of a geological test sample, an apatite inclusion in a magnetite matrix (Fig. 1). This sample was chosen for its apparent homogeneity in the two different matrices. An incident ion beam of 16.5 keV  $^{16}\text{O}^-$  ions was used on the polished and gold-coated sample. Conventionally taken images from the area indicated in Fig. 1 are presented in Fig. 2 and give an impression of the spatial resolution that can be obtained in such images.

But specific problems are related to this technique. Matrix and topographical effects on the element sensitivity make a quantitative interpretation of such images difficult.<sup>2</sup> Furthermore, sputtered ions from isotopes of different elements, from molecular ions, and from multiply charged ions can interfere and contribute to the same image. Therefore a second set of images of sputtered-ion intensities was collected in a multichannel scaler synchronously with the rastering of the incident ion beam. An area of  $3 \times 3$  divisions (Fig. 2) in the top left part of the lower right quadrant was covered by a total of 3640 points on a raster of 70 lines of 52 points each.

Because of the quantitized presentation of the images, image-processing techniques can be employed to convert these sputtered-ion intensities into element concentrations. The digitized collection of these images was preferred to the quantization of the conventional photographic images since it avoids the difficulties involved in calibrating the photographic recording. It also allows the use of the full dynamic range of this analytical technique (i.e., 5 to 6 orders of magnitude). The image processing involves at first the reconstruction and display of the measured distributions of sputtered ion intensities. Figure 3 gives gray-scale images that contain the same information as in Fig. 2. A logarithmic scale was used for these images to enhance structures occurring at low ion intensities. A three-dimensional display<sup>3</sup> is given in Fig. 4 to give a better impression of the spatial resolution achieved. Line printer images (as in Fig. 5) are suitable for faster display.

As can be seen, the apatite grain does not show a homogeneous distribution of the sputtered  $^{40}\text{Ca}^+$  ions, as would have been expected. Rather, it displays a region of high intensities (top right) and lower ones (bottom left). The application of a first-order quantifying procedure<sup>4</sup> that uses constant sensitivity factors all across the sample resulted in a calcium distribution much more homogeneous in the apatite grain (Fig. 6). To improve this procedure it is necessary to identify areas of different composition in the images. Different sensitivity factors may then be applied to these regions. Owing to the large number of points representing an image it appears impractical to use a supervised algorithm for the detection of areas of equal composition. Rather, image processing can be used. Figure 7 shows a logarithmically scaled histogram of the  $^{54}\text{Fe}^+$  image. Three regions can be identified: points with low, high, and medium intensities. These regions can form the basis for a classifying algorithm. The development of such algorithms is in progress and will be presented.

As can be seen from these preliminary studies, imaging of element distributions of

---

The author is with the National Physical Research Laboratory, Pretoria, South Africa. At present he is an Associate of the National Research Council, Washington, D.C., at NASA's Johnson Space Center in Houston, Tex.

FIG. 1.--Optical micrograph of apatite grain in magnetite matrix showing area where scanning ion images were taken.

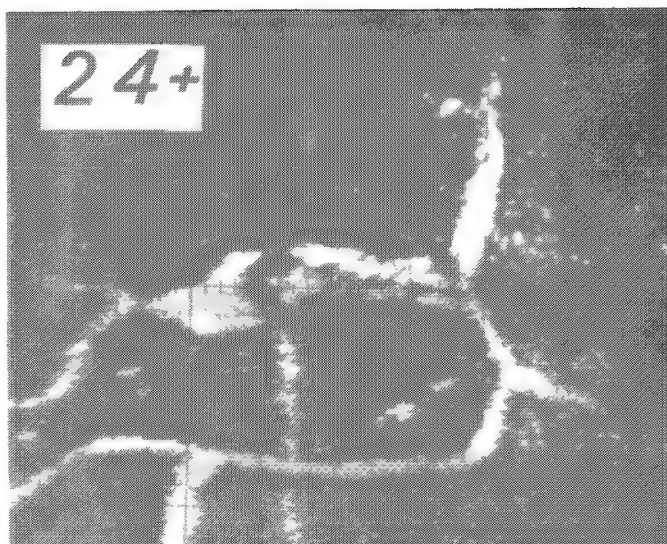
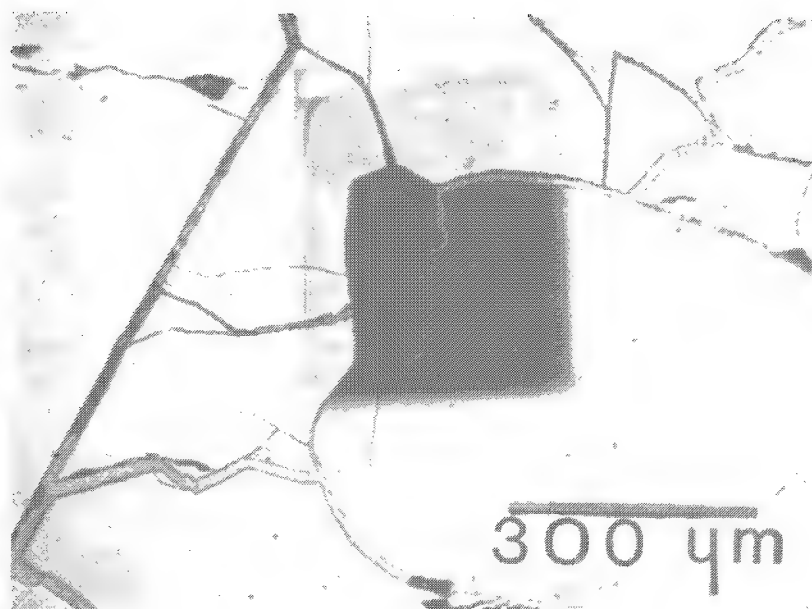
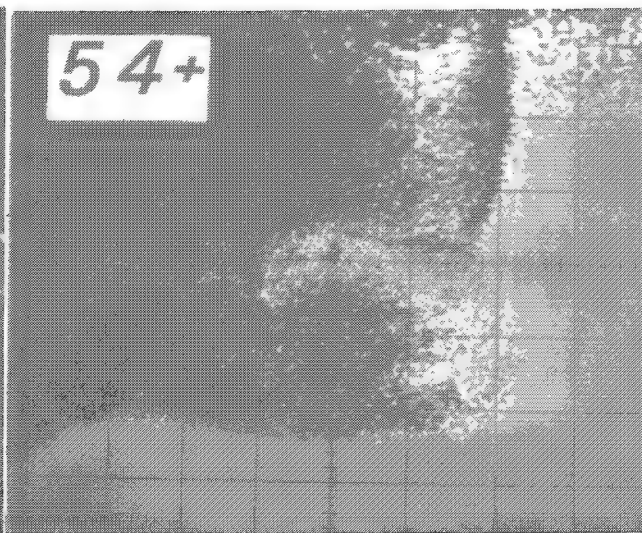
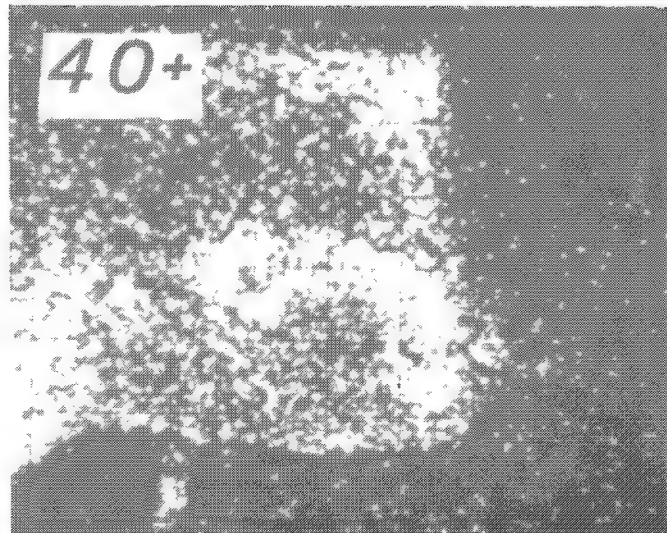


FIG. 2.--Conventionally taken images of sputtered ion intensities from the area visible in Fig. 1 (white for high intensity).



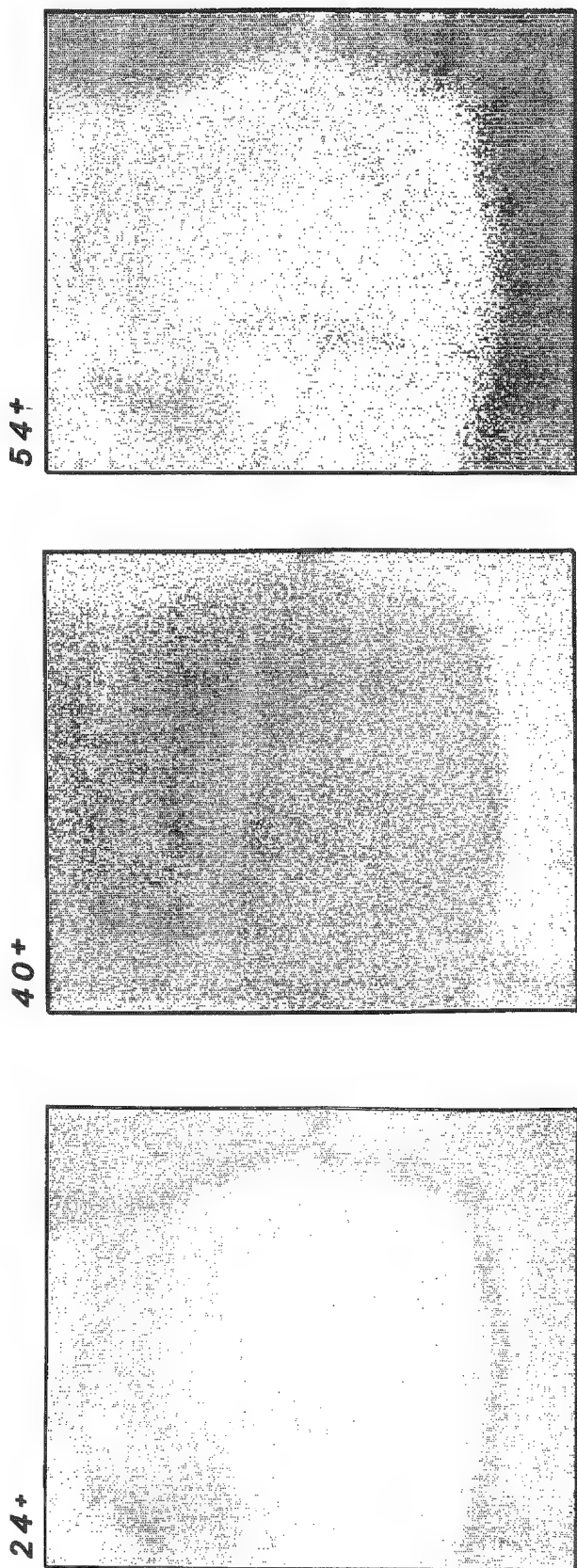


FIG. 3.--Reconstruction of digitized images from top left of bottom right quadrant of Fig. 2 ( $3 \times 3$  divisions). Display in 16 gray levels logarithmically scaled between minimum and maximum intensity (black for high intensity).

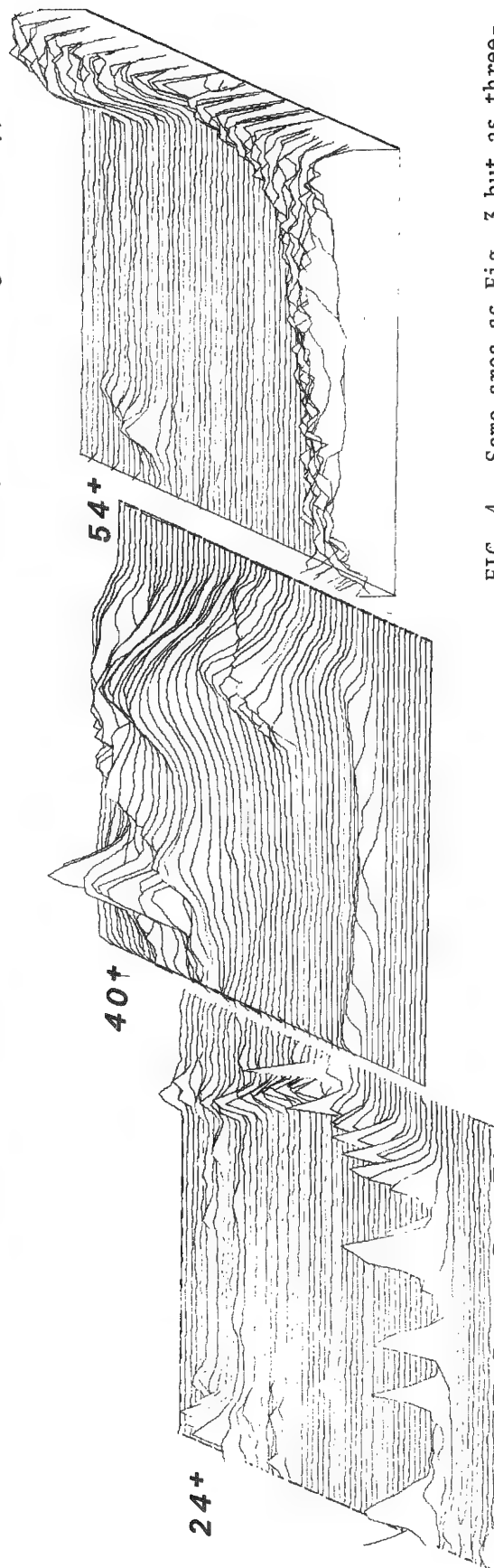
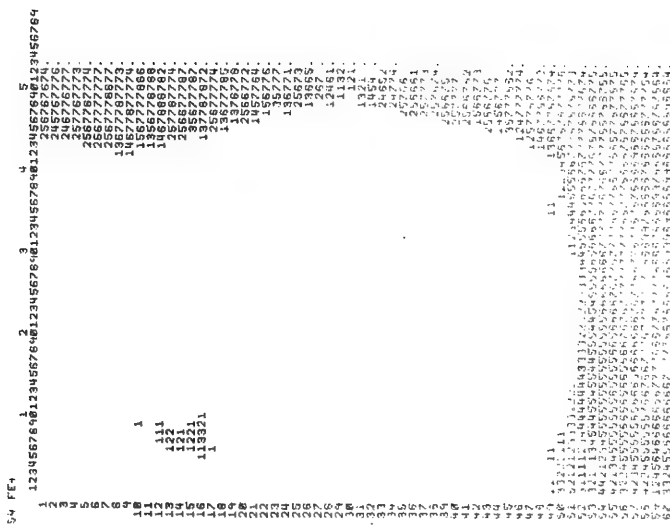


FIG. 4.--Same area as Fig. 3 but as three-dimensional display linearly scaled.



geological material is feasible in a scanning ion microprobe. Image processing should be used to aid the conversion of sputtered ion intensities to element concentrations.



FIG. 7.--Histogram of image of  $^{54}\text{Fe}^+$  intensities logarithmically scaled showing groups of points at different intensities that can be used to identify areas of different composition.

#### References

1. H. Liebl, *The Ion Microprobe: Instrumentation and Techniques*, Special Publication 427, Washington, D.C.: National Bureau of Standards, 1975, 1.
2. D. E. Newbury, R. L. Myklebust, and K. F. J. Heinrich, "Local thermal equilibrium analysis of secondary ion mass spectra from multi-element glasses," *Proc. 11th MAS Conf.*, 1976, 42.
3. S. L. Watkins, "Masked three-dimensional plot program with rotations," *Comm. ACM* 17: 520, 1974.
4. J. H. Schilling and P. A. Buger, "On quantifying images of element distributions obtained with an ion microprobe," *Int. J. Mass Spectr. & Ion Phys.* 27: 283, 1978.

## QUANTITATIVE ION MICROPROBE ANALYSIS OF CHLORINE IN SELENIUM

R. W. LaForce and J. M. Short

Techniques have been developed that permit the quantitative analysis of Chlorine in amorphous selenium films by ion microprobe mass analysis. Selenium is the major element in alloys used in xerographic copying machines. The addition of dopants such as chlorine to selenium is an important means of improving xerographic properties. These properties depend both on the concentration and distribution of the dopant in the thin film used as the photoreceptor. Whereas the electron microprobe can obtain such information above the 0.1% level, trace elements such as chlorine must be analyzed by more sensitive techniques. The ion microprobe was selected as the best and probably the only current technique capable of distributional analysis of a few parts per million of chlorine in a 60  $\mu\text{m}$ -thick selenium film by means of step profiling of a cross section. Details of the refined procedures for sample preparation and instrument operation evolved and tested on Se-based photoreceptors are given below.

### *Sample Preparation*

The paramount objective in sample preparation for Cl analysis is the ability to analyze a specimen that has not been contaminated by foreign materials, especially Cl. To this end, a very rigorous preparation technique has been developed that insures cleanliness of the sample and reproducibility of the technique from sample to sample. Small Se chips are separated from their substrate by thermal shocking and subsequently removed with forceps or a vacuum pick-up device. These chips are then shaped to the proper size ( $2 \times 5 \text{ mm}$ ). To prevent contamination of the sample, all handling materials and tools are given a thorough sonic cleaning in absolute ethyl alcohol. The person preparing the samples must wear Cl-free gloves; the Van-Lab Poly gloves are being used currently, after analysis has shown that they did not contain Cl. At this point the sample, which is typically 60  $\mu\text{m}$  thick, is cast in an epoxy made by Ciba-Geigy and ultramicrotomed at a  $6^\circ$  angle, so that the cross-section thickness is "magnified" by a factor of 8 to 10. The reasons for this beveling process are given in the last section below.

After the sample has been microtomed, it is overcoated with a spectrographic grade of carbon. This material is vacuum deposited on the surface in an indirect manner in order to insure a thin ( $<100\text{\AA}$ ) continuous film. The purpose of the film is to make the surface conductive during analysis. To insure surface conductivity from the section across the epoxy base to the inner sample holder, carbon particles suspended in doubly deionized water (Aquadag) are painted on the epoxy.

The sample is then inserted into a specially designed sample holder, with a spring steel clamp around the outside of the epoxy used as a shim to hold the sample snugly in place. The holder allows x, y, z translation and tilt of the sample, so that the surface to be analyzed (cross section) can be placed both in the same plane and at the same height as the top surface of the sample holder. This surface ultimately determines the height to which the entire structure is elevated when it is placed in the instrument.

### *Instrument Operation*

The following discussion briefly describes some of the parameters investigated in order to arrive at the best reproducible set of operating instructions for the quantitative determination of Cl in Se.

*Duoplasmatron.* When analyzing Se-based photoreceptors, to reduce sample charging effects and to observe the secondary-ion species of interest one must operate the duoplasma-

---

The authors are at the Xerox Corp. in Rochester, NY 14644.



tron and the primary and secondary magnet system in the negative mode, which means that negative primary and secondary ions are used. Oxygen is used for producing a stable, high secondary-ion yield. In our system, ion production begins when the DP pressure reaches 280  $\mu\text{m}$  as a result of the oxygen gas, whereupon the arc-current power supply initiates and maintains a steady-state current of  $50 \times 10^{-3}$  A at 440 V. With the adjustment arm of the Z electrode a  $1 \times 10^{-3}$  A current is drawn from the duoplasmatron. These charged particles, both  $^{16}\text{O}^-$  ions and electrons, are then accelerated to 20 kV by the Spellman high-voltage supply.

*Primary Magnet System.* The initial ion beam current measured directly opposite the DP is always  $\leq 3.0 \times 10^{-6}$  A. After focusing, the resultant current in the primary beam must be high enough to produce good secondary counting statistics, yet low enough to prevent sample degradation due to thermal effects. Normal primary operating conditions yield a beam 12-18  $\mu\text{m}$  in diameter with a sample current of  $1.4\text{-}2.5 \times 10^{-9}$  A. These conditions vary directly as a function of each other and the age of the anode plate in the DP. The beam is constantly rastered, since a static beam would cause thermal degradation in the sample. The average lifetime of the anode plate is 160 hr.

The primary beam is rastered at 2.5 kHz over the sample surface; typically the frame rate is 10 Hz and the line rate is 250 Hz. Changes in raster rates effect secondary yields. The area of sputter is nominally  $80 \times 45 \mu\text{m}$ . A 40% electronic aperture is employed to remove possible edge effects of the smooth-bottom crater produced in the amorphous selenium, i.e., the detected area is 40% of the rastered area.

*Secondary Magnet and Data Acquisition System.* A PDP 11/40 computer with 64K words of core memory is used to control the stepping of the secondary magnet to the desired masses, in this case  $^{35}\text{Cl}^-$  and  $^{80}\text{Se}^-$ . Incremental mass scanning with appropriate delay is essential if peak overshoot is to be minimized. After each 10sec integration period, the computer reads the scalars, applies isotopic abundance corrections, and calculates count rates, the Cl/Se ratio, and the chlorine content by means of an experimentally determined calibration curve. Output of the results are recorded both on a DEC LA180 Printer and a Zeta Research Incremental Plotter. The latter yields on-line digital plots.

*Experimental Results and Discussion.* Quantitative calibration of the Cl/Se intensity ratios was not based on theoretical calculations of the ion yield<sup>1</sup> but rather on the empirical method of deriving working curves from analyzed homogeneous standards.<sup>2</sup>

A linear Cl/Se calibration curve is expected in the case of a dilute solute in a matrix such as in this alloy. Its form is similar to those found in other matrices.<sup>3-5</sup> The calibration curve (Fig. 1) is based on a bulk analysis of chlorine by x-ray fluorescence emission spectroscopy<sup>6</sup> and polarography. The Cl detection limit derived from the peak/background ratio is less than 1 ppm.

The Cl composition profile through the film is obtained from a series of shallow depth profiles in the beveled section taken in a direction perpendicular to the intersection of the sample surface to the top surface of the alloy film. The rastered areas are staggered so that the area detected by the electronic aperture does not quite overlap the previous area. The combination of the data from all analyzed areas yields a Cl profile through the entire thickness of the sample. Figure 2 shows a Cl-profile and its reproducibility in a 60 $\mu\text{m}$ -thick film produced by a single evaporation. X-ray fluorescence analysis was performed on the film surfaces to determine the mean chlorine concentration in the 5  $\mu\text{m}$  region near each surface. The reproducibility is within  $\pm 5\%$ . A second film was prepared by initially evaporating 20  $\mu\text{m}$  of selenium doped with 80 ppm of chlorine, over which was evaporated 40  $\mu\text{m}$  of selenium doped with 20 ppm of chlorine. Figure 3 shows the step profile through the thickness of this particular sample. A drop in the chlorine level over a distance of 5  $\mu\text{m}$  was observed at the interface between the two layers.

Figure 4 shows the chlorine profile obtained by analyzing the ions that were sputtered from the top surface of a film which was prepared by evaporating two layers of chlorine-doped Se. The initial deposition was 60  $\mu\text{m}$  thick; the top layer was 0.3  $\mu\text{m}$  thick. As seen in the figure there is a very steep chlorine profile in the middle of the top layer and another at the beginning of the second layer. The sputtering rate and depth were determined by interferometry measurements of the craters. The depth resolution is about 300 Å on depth profiles.

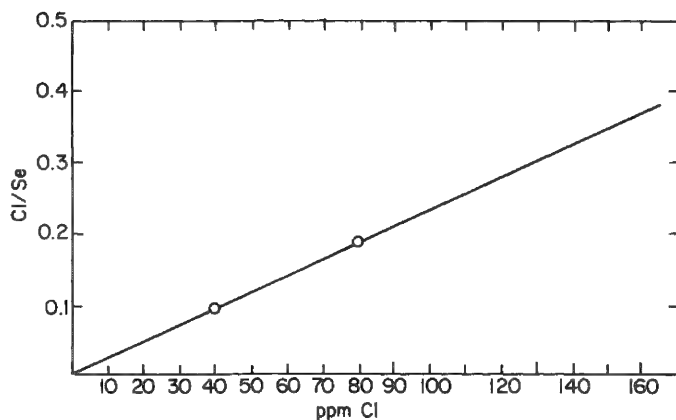


FIG. 1.--Chlorine calibration curve derived from empirical standards that were analyzed by x-ray fluorescence and polarography.

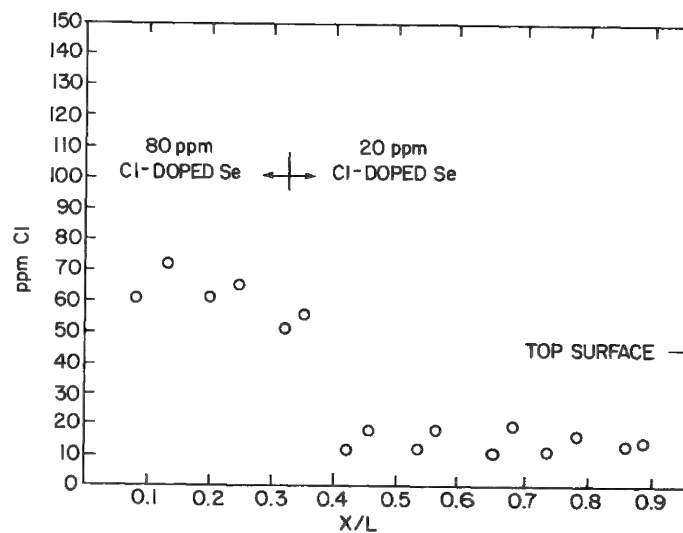


FIG. 3.--Chlorine profile of 60 $\mu$ m-film consisting of initial layer of 20 $\mu$ m-thick Se film doped with 80 ppm Cl and top layer of 40 $\mu$ m-thick Se film doped with 20 ppm Cl.

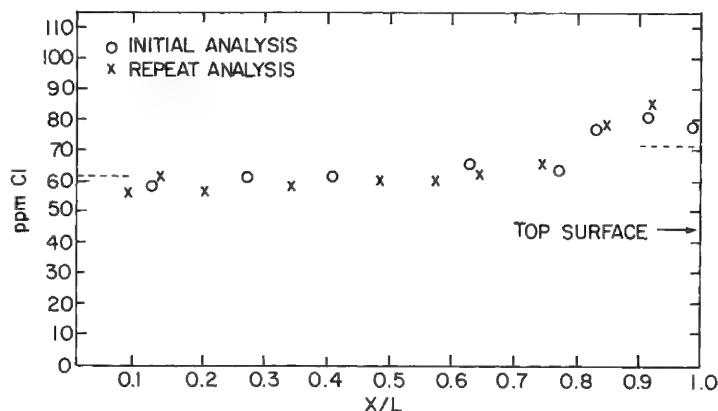


FIG. 2.--Chlorine profile analysis of 60 $\mu$ m-thick Se film doped with 80 ppm Cl. This figure shows 5% reproducibility and agreement with x-ray fluorescence analysis; X/L is fraction of total film thickness. Dashed line indicates values obtained by x-ray fluorescence analysis of top (resp. bottom) surface of film.

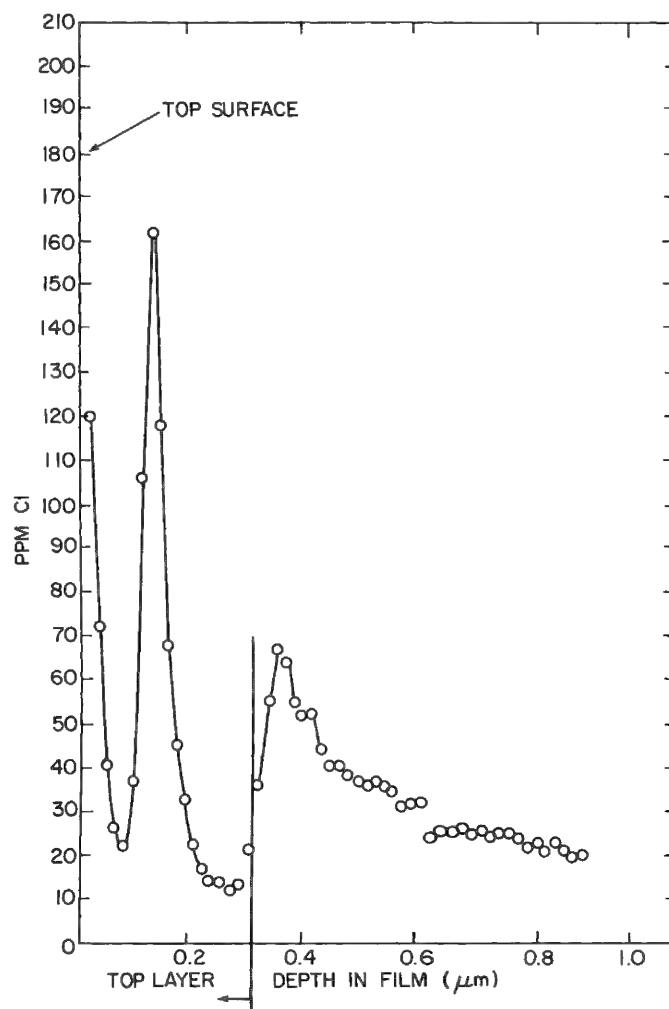


FIG. 4.--Chlorine depth profile obtained by sputtering top surface of film chip that was prepared by evaporating two layers of Cl-doped Se.



The effective depth resolution of the step profiles is limited by the dimensions of the rastered and the apertured areas. Using the shallow-angle beveling technique for sample preparation, one can obtain straight-line step profiles with an effective center-to-center separation of 5  $\mu\text{m}$ ; staggering the analysis areas parallel to the original photoreceptor surface improves it to 2  $\mu\text{m}$ . The use of large static beams and a detector aperture is not possible for selenium films because of sample deterioration owing to local thermal heating effects. This type of sample destruction is not desirable for obvious reasons. The induced charge effects may also become a serious problem if the uncoated area becomes too large.

### *Conclusions*

The agreement of the ion microprobe results with x-ray fluorescence analysis at the surfaces supports the conclusions that no compositional changes due to chlorine mobility under ion bombardment are occurring and that the techniques used permit quantitative microanalysis of chlorine in selenium. Step composition profiles of beveled selenium alloy films can be made with a reproducibility at 60 ppm of  $\pm 3$  ppm, a sensitivity of better than  $\pm 5$  pp, an effective lateral resolution of 2-5  $\mu\text{m}$ , and a Cl-detection limit of about 0.1 ppm. Preliminary work indicates that depth profiles of Cl in selenium alloy films can be made with a depth resolution as good as 150 Å.

### *Acknowledgments*

The authors thank Allen Fowler for his dedicated work in computer programming; K. Johnson, R. Gillmeister, J. Czerniawski, J. Palmer, and F. Sytsma for their contributions in the microtoming of photoreceptor films; and A. Orzechowski for his interferometry measurements.

### *References*

1. J. D. Brown and J. M. Short, *Proc. 12th MAS Conf.* 1977, 138.
2. J. A. McHugh, *Secondary Ion Mass Spectrometry*, K. F. Heinrich and D. Newbury, Eds. NBS Spec. Publ. 427, 1975, 129-134.
3. J. R. Hinthorne and C. A. Anderson, *Am. Mineral* 55: 143-147, 1975.
4. C. A. Andersen, *Int. J. Mass Spectrom. Ion Phys.* 2: 61-74, 1969.
5. J. W. Colby, *Proc. 8th Conf. Electron Probe Analysis Soc.*, 1973, 6A-D.
6. C. V. Bielan and L. R. Bonk, *Siemens Rev.* 43: 14-16, 1976.

## QUANTITATIVE ANALYSIS OF Se ALLOY THIN FILMS BY ION-MICROPROBE MASS ANALYSIS AND TRANSMISSION ELECTRON MICROSCOPY

R. W. LaForce and J. K. Johnson

The xerographic transport properties of vacuum-evaporated thin films of selenium and selenium doped with small quantities of chlorine (0-40 ppm) and arsenic ( $\sim 0.5$  at.%) have been well documented.<sup>1</sup> The successful operation of the doped selenium photoconductors depends heavily on how the dopants are dispersed through the bulk and at or near the surface of the thin film. The detailed characterization of the dopant distribution in these films has been a continuing problem.

The electron microprobe (EMPA) is capable of quantitative analysis above the 0.1% level, but it lacks the depth resolution necessary to define chemical fractionation at or near the thin film surface precisely. A mathematical model was suggested by Brown et al.<sup>2</sup> for analysis of inhomogeneous thin films by EMPA. This approach fails when severe chemical gradients are found near the surface of the film.

LaForce and Short have shown how Se alloy thin films can be quantitatively analyzed for Cl in the low-ppm range.<sup>3</sup> This paper describes two techniques that have been developed to quantify the arsenic distribution in the selenium photoconductor. If the analysis results of an ARL Ion Microprobe Mass Analyzer (IMMA) and an EDAX Energy Dispersive X-Ray Analyzer on a Philips EM200 Transmission Electron Microscope (TEM/EDXA) are combined, the vertical compositional gradients of a film can be determined with a depth resolution better than 500 Å. Effects of the differences between the two instruments in lateral resolution are shown for the analysis of films that exhibit different compositional gradients as a function of depth in the film. In IMMA analysis, quantitative calibration is based on empirical working curves from analyzed homogeneous standards. Quantitative results of TEM/EDXA are obtained by means of the direct element ratio model.<sup>4</sup>

### *Sample preparation and Analytical Results*

*IMMA.* Sample-preparation techniques for ion probe analysis are similar to those used in preparing samples for quantitative Cl analysis.<sup>3</sup> The sample is initially removed from the substrate and embedded in epoxy. After the section is cured, it is ultramicrotomed on a 6° bias in order to "magnify" (by a factor of 8 to 10) the thickness of the cross section (60  $\mu\text{m}$ ). This beveling yields a depth resolution of 2-3  $\mu\text{m}$  when the cross section is analyzed. The section is then inserted into a specially designed sample holder that allows x, y, z translation and tilt of the sample, so that the surface to be analyzed (cross section) can be placed both in the same plane and at the same height as the top surface of the sample holder.

To complete a full cross section analysis, one must also analyze top and bottom surface chips. These chips are mounted on a 2.5cm-dia. slug. They are held in place by a small amount of Aquadag (carbon suspended in deionized water). Both the section and the chips are coated with a 100Å-thick film of amorphous C to insure that the area around the analysis site remains conductive during analysis.

Analytical conditions of the ion-probe instrument were used as defined in Ref. 3. Instrumental parameters used in the quantitative analysis of As in Se are tabulated below.

The high (20%) ionization efficiency of the halogens when negative ions are used allows quantitative analysis in the  $10^{-17}\text{g}$  range for Cl in Se. That is not the case for  $^{75}\text{As}^-$  in Se. Negative primary ( $^{16}\text{O}^-$ ) and secondary ions are required to detect Cl in the As and Se matrix. However, the detection limit for the monoatomic species of As is 0.5 at.% under these conditions. Arsenic, because of its low electron affinity ( $< 1$  eV), has a low

Primary	Secondary	Data Acquisition
Beam $160^-$ Beam diameter 10-15 $\mu\text{m}$ Raster size $80 \times 45 \mu\text{m}$ Raster rate 250 Hz Duoplasmatron pressure 400 $\mu\text{m}$ Sample voltage 1500 V	Negative mode 40% electronic aperture 10s integration time/mass Masses $^{35}\text{Cl}^-$ , $^{80}\text{Se}^-$ , $^{91}\text{AsO}^-$	PDP 11/40 with 64K words of core memory

negative-ion yield. Evans has suggested the use of oxygen as primary ion to force the chemical process of ion production.<sup>5</sup> In this technique oxide species of the matrix elements are formed that may increase sensitivities and detection limits. Figures 1 and 2 show this effect. These data were taken from an amorphous film of compositions  $\text{Se}_{.60}\text{As}_{.40}$ .

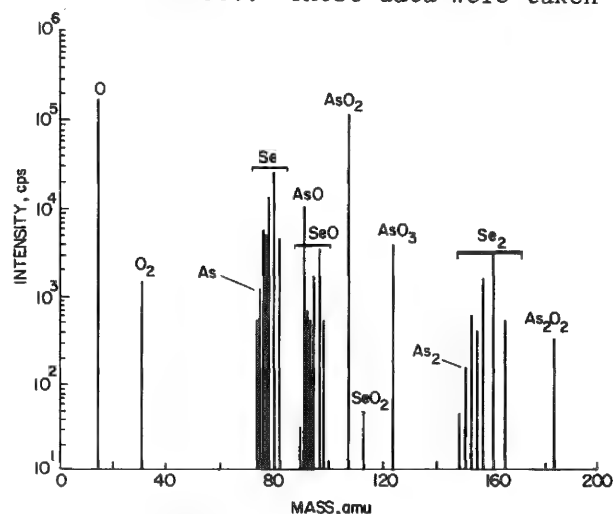


FIG. 1.--Negative secondary-ion spectrum taken from amorphous film of  $\text{Se}_{.6}\text{As}_{.4}$ .

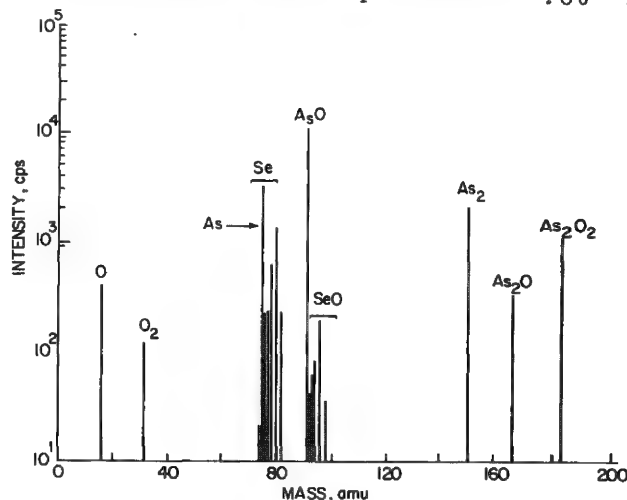


FIG. 2.--Positive secondary-ion spectrum taken from amorphous film of  $\text{Se}_{.6}\text{As}_{.4}$ .

Note that the negative-ion intensity is greater by almost an order of magnitude than the positive-ion intensity. Figure 1 shows that the ion intensities of the polyatomic species of As are orders of magnitude greater than the monomer. It is readily apparent that the oxides of As should be used to increase sensitivity levels during analysis.

Primary-beam-current density must be minimized to about  $1.3 \times 10^{-2} \text{ mA/cm}^2$  in the rastered area to avoid sample degradation owing to thermal effects. This figure, at a raster rate of 250 kHz, gives a sputter rate of about  $100 \text{ \AA s}^{-1} \text{ mA}^{-1} \text{ cm}^{-2}$  in an area  $80 \times 45 \mu\text{m}$ . A 40% electronic aperture is used to avoid crater edge effects.

Two independent analyses of each sample are needed for a complete compositional profile of As through the film thickness. First, an analysis is performed on a photoreceptor chip while the primary beam is impinging perpendicular to the top surface. This analysis allows data to be collected to a depth of 2.5-3  $\mu\text{m}$ . Second, an analysis is performed on the previously mentioned microtomed cross section. Figure 3 shows the "stepping" technique used in order to obtain data with 2-3  $\mu\text{m}$  resolution through the "bulk" of the film. During the analysis of the cross section, data accumulation is terminated at a particular point only when 7-10 consecutive integrations yield the same composition. Then and only then is the sample moved to the next point of analysis.

**TEM/EDXA.** Thin sections of approximately 0.15  $\mu\text{m}$  thickness for TEM examination are normally prepared, by means of an ultramicrotome. The sectioning is done in a plane perpendicular to the photoreceptor surface. By sectioning at a shallow angle to the top surface a magnified area of the photoreceptor top surface may be obtained. A bias angle of  $6^\circ$  yields a magnification of approximately  $10\times$ . The spatial resolution for the Philips EM200, defined by the minimum electron-beam probe size, is 0.5  $\mu\text{m}$ . The depth analysis by this probe size on beveled sections would be 0.05  $\mu\text{m}$ . Use of a computer to control the beam-deflection coils of the TEM permits the direction and incremental stepping of this small electron probe to be accurately controlled across the specimen.

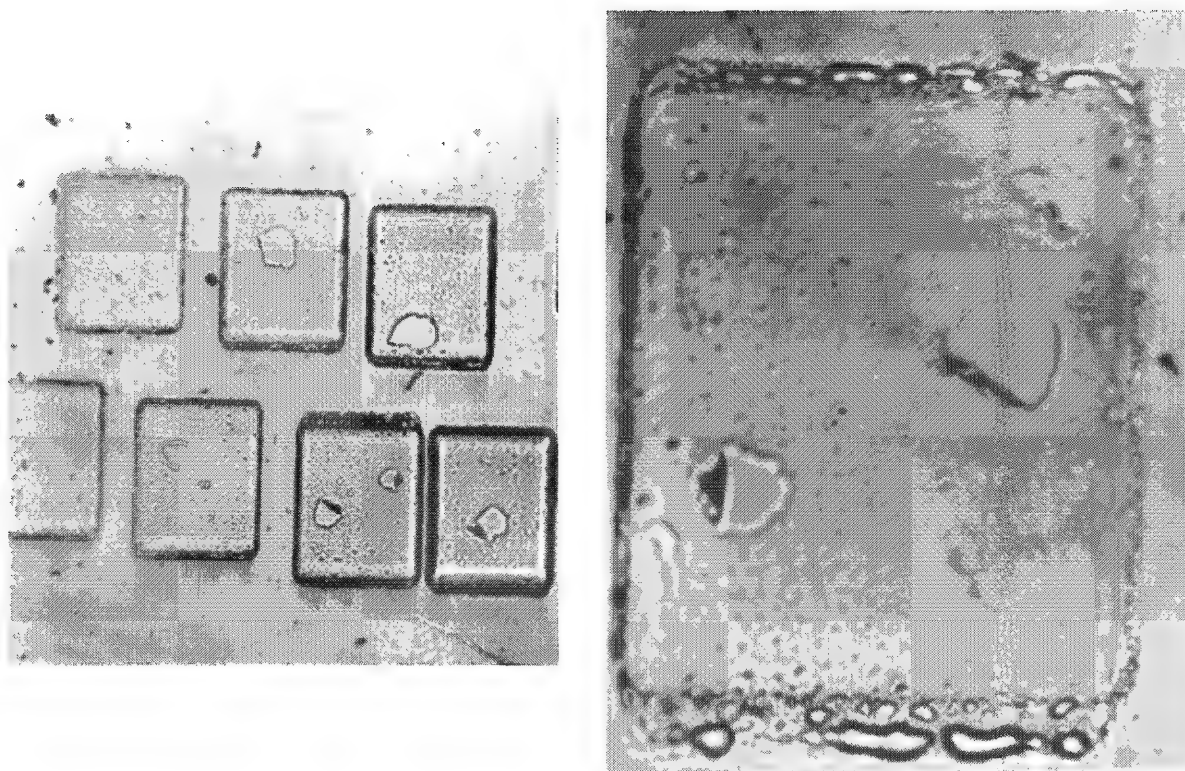


FIG. 3.--Step-profiling technique used in analysis of biased microtomed cross sections.

In the TEM chemical analysis of specimens the analyzed volume depends only on beam diameter, since the finite range of x-ray production is determined mainly by the sample thickness. This relationship immediately yields a great simplification for quantitative analysis. The assumption is made that for very thin specimens all x rays generated by the electron beam can escape without appreciable absorption. Also, electron backscattering and secondary fluorescence of x rays are negligible and can be ignored.

The assumptions are incorporated into a BASIC language program developed by EDAX, called QTHIN.<sup>6</sup> This program was included into software that was written to automate the TEM/EDXA system completely for chemical profiling. Elemental concentrations are determined by use of the Direct Element Ratio Model. Peak intensities are obtained by the simultaneous fitting of all peaks for each element by a least-squares method. The background was calculated over the spectrum segment containing the peaks of interest and subtracted out prior to the intensity calculations.

To evaluate the accuracy of the Direct Element Ratio Model for standardless analysis a series of thin sections of As-Se alloy compositions were analyzed. The thin sections were taken from bulk material that were used as standards for XRF and EMPA analysis, but were treated as unknowns. It was found that agreement was better than  $\pm 5\%$  relative for the 20, 30, 40, and 50% standards. For low arsenic concentrations of 0.5, 2.0, 5.0, and 10.0%, results were accurate to  $\pm 0.3\%$  absolute.

The analyses are typically performed at 80 kV with an electron beam current of 20-50. Each analysis point is run for 400s real time on the EDAX Model 711 Analyzer. An analysis incorporating 20 points over a depth of 1  $\mu\text{m}$  takes approximately 150 min.

#### *Discussion*

Some alloy films are compositionally graded, primarily because of the fractionation of the alloy. Three different films were analyzed by three different techniques in order to determine which technique most precisely described this compositional gradient.

Figure 4 shows a typical As gradient near the top surface of the subject film. The

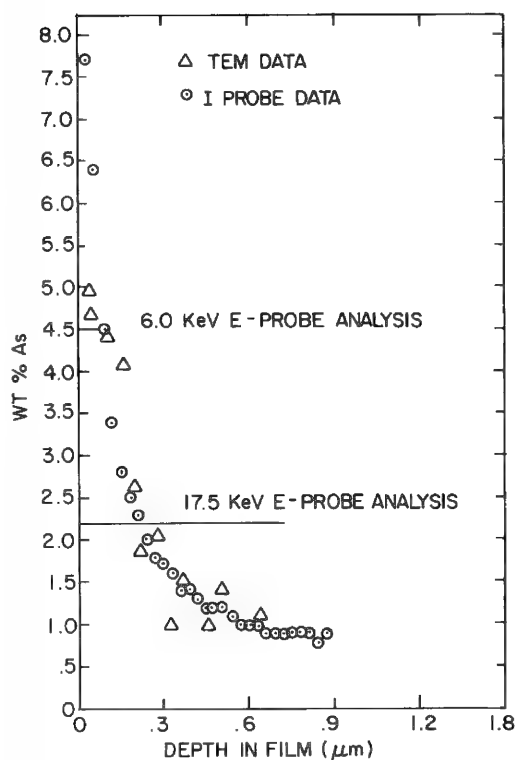


FIG. 4.--Depth profile analysis of AsSe top surface chip.

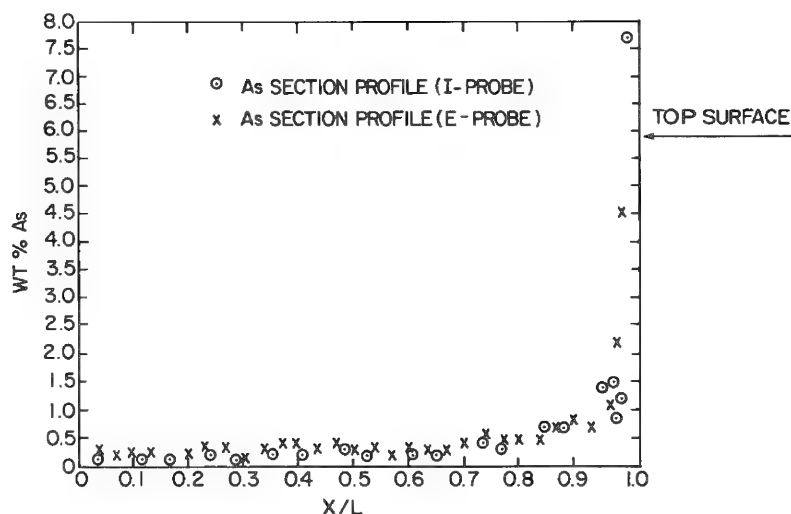


FIG. 5.--Analysis of microtomed AsSe cross section by IMMA and analysis of same sample by EMPA.

initial analysis was performed on the EMPA. Two accelerating potentials were used, 6.0 and 17.0 kV, to define the degree of fractionation. The depths of x-ray production plotted on the graph for EMPA are calculated from the range equation of Anderson,<sup>7</sup>

$$Z_w = \frac{0.064}{\rho} (E_0^{1.68} - E_c^{1.68})$$

where  $Z_w$  is the mean depth of x-ray production,  $\rho$  is the target density,  $E_0$  is the accelerating voltage, and  $E_c$  is the critical excitation potential. The calculated concentrations are an average over these depths. The data from the EMPA analysis show a definite increase in the gradient near the surface. From the EMPA data alone, the peak concentration in the gradient could not be determined.

The second analysis was performed by means of the TEM/EDXA on a ultramicrotomed biased cross section. This sample preparation method results in an effective beam size or depth resolution in a vertical cross section of about 300 Å. The plotted data from the TEM/EDXA analysis show good agreement with the EMPA results. Note that the near surface concentration is higher than that determined by EMPA, which shows that the depth resolution of the TEM/EDXA technique is better than EMPA. The previously mentioned 500 Å resolution of the TEM, although better than EMPA, yields a compositional average owing to the steep nature of this As gradient. Increased depth resolution can be achieved by a reduction in the bias angle at which the cross section is microtomed.

Figure 4 also shows the data obtained with the IMMA. Data acquisition occurred every 100 sec, which corresponds to a depth of 300 Å into a photoreceptor chip. With this added depth resolution, we see that the "surface" concentration is higher than that revealed by EMPA and TEM/EDXA analysis. The IMMA analysis also gives an average over the analyzed depth when such steep gradients are involved. Lower accelerating potential and less beam current density yield better depth resolution. However, lower current density also lowers sensitivity, because of the low negative-ion intensity of As.

Figure 5 shows a comparison between EMPA and IMMA performed on a vertical cross section and a "biased-cut" cross section, respectively. The final three points in the plot of the IMMA data are taken from the plot of the top surface data. The data indicate agreement

between EMPA and IMMA analysis down to concentrations as low as 0.1 wt.% when the matrix is homogeneous.

In some instances IMMA gives poorer depth resolution than TEM/EDXA, and vice versa. The former may occur when fractionation bands are extremely narrow (e.g., 300-600 Å) and the photoconductor surface is rough. This complication arises because 300-450 Å of material are removed from the rastered area as data are accumulated. If the thickness of the fractionation band is near this value it may go undetected. Figure 6 is an example of just such a sample. The TEM photomicrograph taken at 5000× shows a photoreceptor top surface in cross section. Below the top surface are several narrow fractionation bands. The top surface shows a low-frequency undulation in its topography. Figure 7 shows the data obtained from the depth profile of the surface chip by IMMA and the cross-section data obtained by TEM/EDXA analysis. The fractionation pattern does not show up in the IMMA data, doubtless because the undulation in the fractionation band is several times smaller than the size of the rastered area. Since the thickness of the fractionation bands in this particular case happens to be comparable to the depth of the crater formed to obtain one measurement, one crater could cover a fractionation band containing both low and high As, so that the differences would be averaged out. The TEM/EDXA method, on the other hand, samples one point with dimensions equal to or slightly smaller than the width of the bands.

The third film that was analyzed contained a very high frequency surface roughness and much wider fractionation bands (Fig. 8). The data from both analyses are shown in Fig. 9. Note the discrepancy in the surface As value between the two techniques. The low As value obtained by IMMA is a result of the presence of phase-separated trigonal Se crystallization at the top surface masking the higher As concentration in the surrounding amorphous alloy. This small amount of crystallization appears to sputter very rapidly, but in doing so a very narrow fractionation band just under the crystallization goes undetected by IMMA analysis, at a depth of less than 0.15 μm.

As the crater bottom that is being analyzed moves deeper into the film the compatibility of the two analysis techniques becomes very apparent. Again, averaging occurs with either tool: IMMA may have missed very low As concentrations, but TEM/EDXA did not detect the extremely high As peaks.

### Conclusions

The results show the complementary nature of IMMA and TEM/EDXA quantitative analysis for accurately defining vertical compositional gradients of arsenic in selenium photoconductors. Advantages of IMMA techniques are: (1) simple sample preparation, (2) ability to perform simultaneous light-element analysis, and (3) capability for quantitative ppm-level analysis for some elements. Advantages for TEM/EDXA quantitative analysis are: (1) submicron spatial resolution and (2) immediate visual confirmation of any physical anomaly present in the sample.

### Acknowledgments

The authors wish to thank Fred Sytsma, John Czerniawski, JoAnne Palmer, and Roy Takasawa for their diligent efforts in preparation of specimens, and George Chinnici for his photographic support.

### References

1. M. D. Tabak and W. J. Hillegas, "Preparation and transport properties of vacuum-evaporated selenium films," *J. Vacuum Sci. and Tech.* 9(No. 1), 1971.
2. J. D. Brown, J. M. Short, and R. W. LaForce, "Electron probe microanalysis in inhomogeneous thin films," *Proc. 8th Intern. Conf. X-Ray Optics and Microanalysis; Proc. 12th MAS Conf.*, 1977, 150.
3. R. W. LaForce and J. M. Short, "Quantitative ion microprobe analysis of chlorine in selenium," *Proc. 14th MAS Conf.* 1979, 350.
4. J. C. Russ, "The Direct Element Ratio Model for quantitative analysis of thin sections," T. Hall, P. Echlin, and R. Kaufmann, Eds., *Microprobe Analysis as Applied to Cells and Tissues*, New York: Academic Press, 1974, 269-276.
5. C. A. Evans, "Secondary ion mass analysis," *Anal.* 4: 67A-80A, 1972.

6. J. C. Russ, "A BASIC-Lanugage program for dedicated energy-dispersive microanalysis of thin samples in TEM or STEM," *EDAX EDIT*, 8(No. 1): 3-7, 1978.

7. C. A. Anderson, in T. D. McKinely et al., Eds., *The Electron Microprobe*, New York: Wiley, 1966, 58.

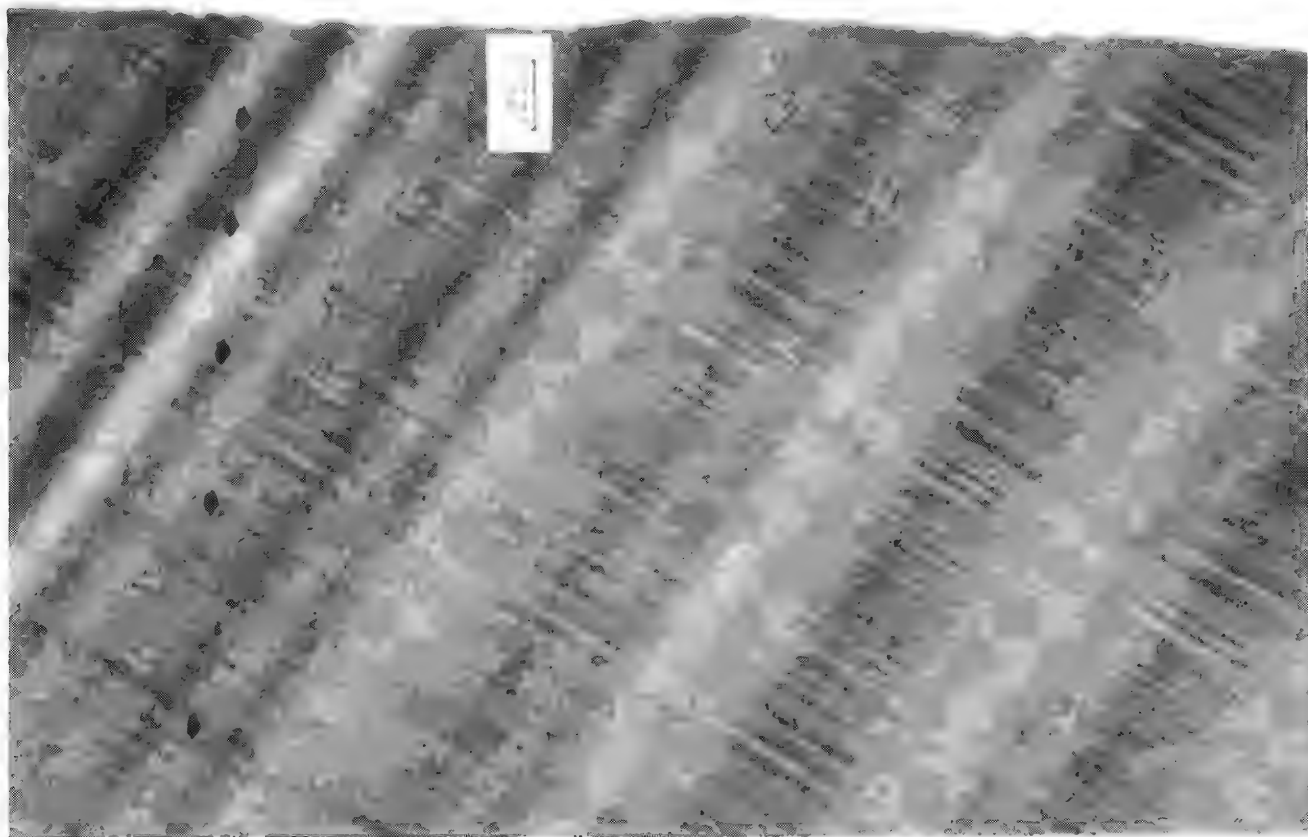


FIG. 6.--TEM photomicrograph (5000 $\times$ ) of near surface region of AsSe microtomed section

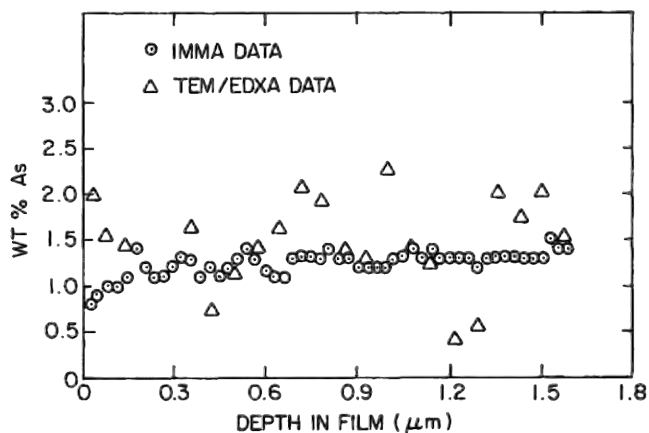


FIG. 7.--Analysis of near surface region (Fig. 6) by TEM/EDXA and IMMA techniques.



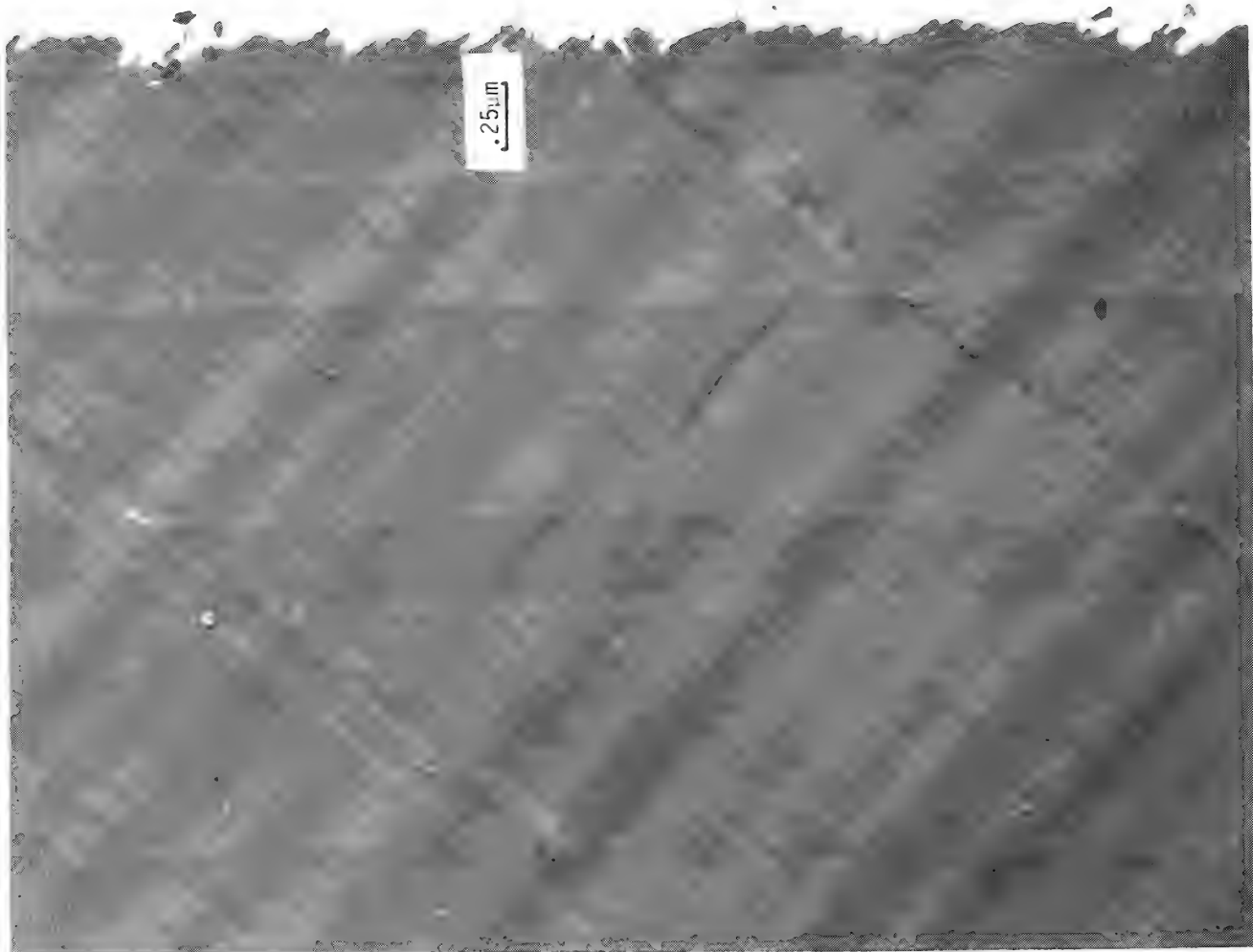


FIG. 8.--TEM photomicrograph (5000×) of near surface region of AsSe microtomed section.

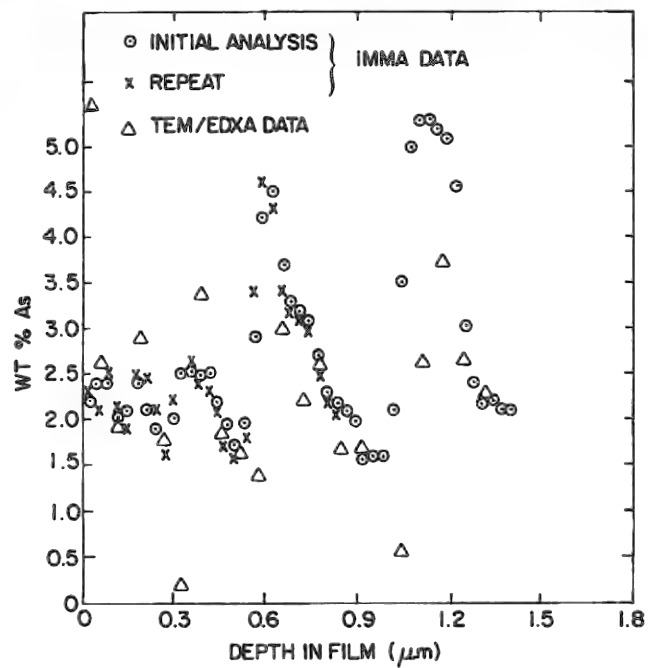


FIG. 9.--Analysis of near surface region (Fig. 8) by TEM/EDXA and IMMA techniques.



## Energy-dispersive Detectors: A Bibliography

C. E. Fiori

This bibliography includes references to publications germane to the application of energy-dispersive detectors to electron-column devices. Applications receiving the major emphasis are the scanning and transmission electron microscopes and the electron beam microprobe. Other applications, such as x-ray fluorescence, are included, but not comprehensively. The cited literature covers such topics as the history, the physics, and the electronics of energy-dispersive detectors; and instrumental applications, artifacts, quantitative analysis applications, characterization and calibration, and applications in fundamental physical measurement. Selected additional topics of use to the reader in understanding or applying the energy-dispersive detector are included.

Detector types considered are the Si(Li), Ge(Li), intrinsic germanium, gas proportional, HgI<sub>2</sub>, and CdTe detectors. A subject index appears below.

The author would appreciate receiving any relevant papers that should be included in future updates of this bibliography.

*Microprobe, SEM Applications:* 15, 17, 22, 50, 71, 77, 84, 89, 92, 99, 101, 176, 182, 183, 184, 188, 209, 210, 227, 236, 237, 250, 251, 252, 255, 256, 259, 260, 263, 270, 274, 275, 276, 277, 288, 294, 302, 303, 304, 305, 306, 313, 314, 319, 330, 339, 348, 351, 352

*XRF, PIXRF Applications:* 33, 34, 40, 41, 47, 51, 68, 69, 96, 97, 100, 110, 120, 126, 129, 130, 154, 155, 163, 164, 165, 166, 171, 180, 209, 213, 216, 218, 242, 271, 282, 288, 295, 296, 328, 333, 347, 348, 358

*Quantitative Applications:* 4, 12, 13, 14, 15, 16, 17, 19, 20, 22, 50, 55, 64, 65, 71, 88, 99, 107, 108, 109, 111, 112, 117, 118, 160, 175, 176, 181, 183, 185, 186, 187, 210, 215, 217, 227, 236, 237, 238, 239, 249, 251, 252, 253, 258, 260, 265, 266, 267, 276, 277, 285, 286, 289, 294, 298, 302, 303, 304, 305, 306, 312, 313, 314, 319, 322, 325, 339, 348, 352

*Electronics:* 42, 63, 72, 73, 75, 79, 80, 81, 82, 83, 89, 92, 102, 104, 122, 127, 131, 170, 173, 174, 178, 193, 219, 230, 231, 232, 233, 234, 287, 312, 315, 324, 344, 348, 357

*Pulse Pile Up:* 52, 89, 92, 102, 104, 241, 279, 320, 344, 348

*Artifacts:* 89, 92, 106, 114, 150, 169, 235, 248, 257, 348

*Escape Peaks:* 89, 92, 217, 235, 318, 348, 350

*Peak Fitting, Determination:* 5, 53, 59, 89, 90, 92, 168, 207, 217, 238, 265, 268, 269, 272, 290, 291, 299, 317, 321, 323, 327

*Physics of Detectors Si(Li):* 1, 2, 26, 66, 74, 98, 119, 123, 137, 139, 142, 149, 162, 177, 194, 197, 199, 200, 201, 204, 226, 331, 359, 360, 362

*Physics of Detectors Ge(Li), Ge:* 61, 66, 113, 134, 135, 136, 137, 138, 139, 140, 143, 144, 145, 146, 147, 157, 158, 159, 195, 200, 201, 204, 222, 223, 224, 225, 228, 342

*Fano Factor, Ionization Energy:* 70, 85, 220, 221, 336, 356

*CdTe:* 57, 95, 161, 204, 292

*HgI<sub>2</sub>:* 56, 58, 292

---

The author is in the Division of Research Services, Biomedical Engineering and Instrumentation Branch, National Institutes of Health, Bethesda, MD 20205.

*Gas Proportional, Ionization:* 27, 32, 35, 42, 49, 54, 66, 86, 167, 196, 198, 203, 210, 243, 246, 300, 301, 310, 329, 334, 343

*Incomplete Charge Collection, Dead Zone:* 2, 6, 59, 78, 89, 92, 98, 132, 153, 161, 195, 204, 205, 212, 228, 332, 348, 355, 359, 360

*Calibration and Characterization:* 36, 37, 38, 39, 43, 44, 45, 46, 87, 110, 141, 172, 196, 200, 206, 212, 217, 244, 245, 285, 326, 335, 340

*Physical Applications:* 76, 152, 189, 190, 191, 307, 308

*TEM Applications:* 8, 9, 11, 14, 16, 21, 23, 106, 114, 115, 117, 118, 150, 248, 259, 261, 262, 273, 276, 297, 311, 353, 354

*Background Fitting:* 5, 11, 89, 91, 92, 190, 217, 254, 268, 269, 284, 291, 297, 306, 307, 316, 317, 325, 333, 338

*Multichannel Analyzers and Accessories:* 28, 52, 62, 148, 202, 239, 345

*Automation:* 4, 99, 109, 181, 280, 298

*Windowless Si(Li) Detectors:* 7, 10, 213, 214, 266, 267, 281, 286

*Si(Li), Ge(Li), Ge Review Papers, Books:* 3, 18, 24, 25, 29, 30, 31, 60, 89, 92, 93, 94, 98, 101, 103, 105, 116, 121, 124, 125, 128, 133, 137, 151, 169, 182, 188, 192, 229, 240, 247, 264, 270, 275, 283, 293, 337, 341, 346, 347, 348, 349, 351, 363

*Additional Topics:* 48, 156, 167

1. Aitken, D., Emerson, D. and Zulliger, H.R., "Response of the Lithium-Drifted Silicon Radiation Detector to High Energy Charged Particles," IEEE Trans. Nucl. Sci. NS-15(1): 456, 1968.
2. Aitken, D., Lakin, W., and Zulliger, H.R., "Energy Loss and Straggling in Silicon by High Energy Electrons, Positive Pions and Protons," Phys. Rev. 179: 393, 1969.
3. Aitken, D.W. and Woo, E., "The Future of Silicon X-ray Detectors," STP 485, American Society for Testing and Materials, 36-56, 1971.
4. Albee, A.L. et al., "Quantitative Analysis of Petrographic Properties and of Mineral Compositions with a Computer-Controlled Energy-Dispersive System," Proc. 8th Intern. Conf. X-Ray Optics and Microanalysis; Proc. 12th MAS Conf., 1977, 181.
5. Armantrout, G.A. and Thompson, H.W., "Spectrum Degradation Effects in Ge(Li) Detectors," IEEE Trans. Nucl. Sci. NS-17(3): 165-175, 1970.
6. Balland, J.C. et al., "Problems Related to Charge Collection Variations in Ge(Li) Detectors with Special Reference to Timing," IEEE Trans. Nucl. Sci. NS-17(3): 405-424, 1970.
7. Barbi, N.C. and Russ, J.C., "Analysis of Oxygen on an SEM Using a Windowless Energy Dispersive X-Ray Spectrometer," SEM/75 (Part I), O.M. Johari, ed. (IITRI) Chicago, IL, 85-91, 1975.
8. Barbi, N.C. and Russ, J.C., "Applications of Energy Dispersive Analysis on the Transmission Electron Microscope in Pathology and Pollution Studies," Proc. of the Electron Microscopy Society of America, 32nd Annual Meeting, 110, 1974.
9. Barbi, N.C. and Skinner, D.P., "Techniques for Electron Microscopic Identification of Small Particles," SEM/76 (Part III), O.M. Johari, ed. (IITRI), Chicago, IL, 393-400, 1976.
10. Barbi, N.C. et al., "Light Element Analysis on the Scanning Electron Microscope Using a Windowless Energy Dispersive X-Ray Spectrometer," SEM/74 (Part I), O.M. Johari, ed. (IITRI), Chicago, IL, 151-158, 1974.
11. Barbi, N.C., and Goldman, L., "Contributions to the Spectral Background in Energy Dispersive X-Ray Microanalysis at Higher Accelerating Voltages," Proc. of a Specialist Workshop in Analytical Electron Microscopy, Cornell University, Ithaca, NY, 121, 1976.
12. Barbi, N.C., Foster, M. and Goldman, L., "Semiquantitative Energy Dispersive Analysis in STEM Using Generated Reference Spectra and Empirical Scale Factors," SEM/78 (Part I), O.M. Johari, ed. (SEM Inc., A.M.F. O'Hare, IL), 307-314, 1977.
13. Barbi, N.C., Foster, M., Skinner, D.P., "A Technique for Rapid Semiquantitative Energy Dispersive Microanalysis," Proc. 8th Intern. Conf. X-Ray Optics and Microanalysis; 12th MAS Conf., 1977, 100.
14. Barbi, N.C., Giles, M.A., and Skinner, D.P., "Estimating Elemental Concentration in Small Particles Using X-Ray Analysis in the Electron Microscope," SEM/78 (Part I); 193-200, 1978.
15. Barbi, N.C., Skinner, D.P. and Blinder, S., "The Calculation of Pure Element X-Ray Intensities from Empirically Derived Expressions and its Application to Quantitative SEM/EDS Analysis," Proc. 11th MAS Conf., 1976, 8.
16. Beaman, D.R. and File, D.M., "Quantitative Determination of Asbestos Fiber Concentrations," Anal. Chem. 48(1): 110, January 1976.
17. Beaman, D.R. and Isasi, J.A., "Electron Beam Microanalysis," ASTM Special Technical Publication 506, Amer. Soc. for Testing and Materials, 1972.

18. Beaman, D.R. and Nagatani, T., "Developments in Instrumentation," in the Electron Microanalyzer and its Applications - Proc. of a meeting sponsored by the National Science Foundation and the Japan Soc. for Promotion of Science, Honolulu, Hawaii, Sept. 1973, p. 5-20.
19. Beaman, D.R. and Solosky, L.F., "Accuracy of Quantitative Electron Probe Microanalysis with Energy Dispersive Spectrometers," Anal. Chem. 44(9): 1598-1610, August, 1972.
20. Beaman, D.R. and Solosky, L.F., "Advances in Quantitative Energy Dispersive Spectrometry," in Proc. 9th Conf. MAS 1974, p. 26.
21. Beaman, D.R., "Analytical Transmission Electron Microscopy and its Application in Environmental Science," in Environmental Pollutants, Y. Taft et al (eds.) 255-295, Plenum, 1978.
22. Beaman, D.R., Solosky, L.F., and Settlemyer, L.A., "X-Ray Analysis with Energy Dispersive Spectrometers," in Tutorial Proc. 8th National Conf. on Electron Microprobe Analysis, New Orleans, Aug., 1973, pp. 73-85.
23. Bender, S.L. and Duff, R.H., "Energy Dispersion X-ray Analysis with the Transmission Electron Microscope," STP 485, American Society for Testing and Materials, 180-196, 1971.
24. Bertolini, G. and Coche, A., Semiconductor Detectors, Netherlands, Wiley 1968.
25. Bertolini, G. et al., "Lithium Drifted Semiconductor Detectors in Nuclear Spectroscopy," EUR 2580-e, 1965.
26. Bertolini, G. Cappelani, F., and Restelli, G., "Construction and Performances of Silicon Lithium Drifted Detectors," Nuc. Inst. and Meth. Vol. 32, 86-92, 1965.
27. Bisi, A., Zappa, L., "Statistical Spread in Pulse Size of the Proportional Counter Spectrometer," Nuovo Cimento 10: 988-94, Italy, 1955.
28. Black, W.W., "A Precision, Computer-Controlled Pulse Generator and its Application," Nuc. Inst. and Meth., Vol. 53, 249-256, 1967.
29. Blum, F. and Brandt, M.P., "The Evaluation of the Use of a Scanning Electron Microscope Combined with an Energy Dispersive X-Ray Analyzer for Quantitative Analysis," X-Ray Spectrometry 2: 121-124, 1973.
30. Bowman, H.R. et al, "Application of High-Resolution Semiconductor Detectors in X-Ray Emission Spectrography," Science, Vol. 151, pp. 562-568, 1966.
31. Brummer, O., "Mikroanalyse mit Elektronen-und Ionensonden," VEB Deutscher Verlag fur Grundstoffindustrie, Leipzig, 73-88, 1978.
32. Campbell, A.J., "Proportional Counter Resolution," Norelco Reporter 14, 103-106, 1967.
33. Campbell, J.L. and Crosse, L.A., "Non-Destructive Analysis of Lead on Apartment Walls," Can. J. Public Health 67: 506-510, 1976.
34. Campbell, J.L. and Crosse, L.A., "Portable Instrumentation for the Determination of Lead in Painted Surfaces," Bull. Env. Sci. Toxicology 16: 469-473, 1976.
35. Campbell, J.L. and Ledingham, K.W.D., "Pulse Height Distributions from Proportional Counters," Brit. J. Appl Phys. 17: 769-774, 1966.
36. Campbell, J.L. and McNelles, L.A., "Americium-241 as a Low-Energy Photon Intensity Standard," Nucl. Instr. Meth. 117: 519-532, 1974.
37. Campbell, J.L. and McNelles, L.A., "An Inter-Comparison of Efficiency Calibration Techniques for Semiconductor X-Ray Detection," Nucl. Inst. Meth. 125: 205-233, 1974.

38. Campbell, J.L. and McNelles, L.A., "Construction of Efficiency Curves for Semiconductor X-Ray Detectors," Nucl. Inst. Meth. 98: 433-444, 1972.
39. Campbell, J.L. et al, "Fabrication of Thin Radioactive Sources Using Biological Staining Techniques," Nucl. Instr. Meth. 93: 173-174, 1971.
40. Campbell, J.L. et al, "Some Biomedical Applications of Proton-Induced X-Ray Fluorescence Analysis," Advs. X-Ray Anal. 17: 457-466, 1976.
41. Campbell, J.L. et al, "Trace Element Analysis of Fluids by Proton-Induced X-Ray Spectrometry," Anal. Chem. 47: 1542, 1975.
42. Campbell, J.L., "Pulse Rise Time Discrimination in X-Ray Proportional Counters," Nucl. Inst. Meth. 65: 333-337, 1968.
43. Campbell, J.L., Goble, R.J. and Smith, H.J., "Efficiency of Planar Ge(Li) Detectors at Very Low Energy," Nucl. Instr. Meth. 82: 183-186, 1970.
44. Campbell, J.L., Jorch, H.H. and Thompson, J.A., "Parametric Representation of X-Ray Detector-Efficiency Curves," Nuc. Inst. and Meth., 140, 167-173, 1977.
45. Campbell, J.L., O'Brien, P., and McNelles, L.A., "On the Efficiency Calibration of Semiconductor X-Ray Detectors," Nucl. Inst. Meth. 92: 269-275, 1971.
46. Campbell, J.L., Smith, H.J., and MacKenzie, I.K., "A Coincidence Technique for Study of Ge(Li) Detector Profiles," Nucl. Inst. Meth. 92: 237-245, 1971.
47. Carlton, D.T. and Russ, J.C., "Trace Level Water Analysis by Energy Dispersive X-Ray Fluorescence," X-Ray Spectrometry, Vol. 5 No. 3, 194-174, July 1976.
48. Catura, R.C. and Smithson, R.C., "Single Photon X-Ray Detection with a CCD Image Sensor," Rev. Sci. Instr. 50(2): 219-220, 1979.
49. Chew, W.M., McGeorge, J.C., and Fink, R.W., "A Multiwire Proportional Counter Technique for Standardization of Low-Energy Photon Sources," Nuc. Inst. Meth. 106: 499-501, 1973.
50. Ciccarelli, M.F., Bolon, R.B., and Lifshin, E., "Quantitative Analysis with an Energy Dispersive Detector," Proc. 10th MAS Conf., 1975, 23.
51. Ciccarelli, M.R. and Goehner, R.P., "A Diffractometer Based Energy Dispersive Elemental Analyzer," Advances in X-Ray Analysis 21, 1978.
52. Cohen, E.J., "Live Time and Pile-Up Correction for Multichannel Analyzer Spectra," Nucl. Instr. Meth. 121: 25-32, 1974.
53. Covell, D.F., "Determination of Gamma-Ray Abundance Directly from the Total Absorption Peak," Anal. Chem. 31: 1785-1790, 1959.
54. Culhane, J.L. et al, "Advances in the Design and Performance of X-Ray Proportional Counters," J. Sci. Inst. 43: 908-912, 1966.
55. Currie, L.A., "Detection and Quantitation in X-Ray Fluorescence Spectroscopy," in X-Ray Fluorescence Analysis of Environmental Samples, T.G. Dzubay, (ed.) Ann Arbor Sci., 289-307, 1977.
56. Dabrowski, A.J. and Huth, G., "Toward the Energy Resolution Limit of Mercuric Iodide in Room Temperature Low Energy X-Ray Spectrometry," IEEE Trans. Nuc. Sci. Vol. NS-25 No. 1, 205-211, Feb. 1978.
57. Dabrowski, A.J. et al, "n-Type Cadmium Telluride Surface Barrier Nuclear Detectors," Revue de Physique Appliquee 12: 297-302, Feb. 1977.
58. Dabrowski, A.J. et al, "Characteristic X-Ray Spectra of Sodium and Magnesium Measured at Room Temperature Using Mercuric Iodide Detectors," Appl. Phys. Lett. 33(2): 211-213, 15 July 1978.

59. Day, R.B., Dearnley, G. and Palms, J.M., "Noise, Trapping and Energy Resolution in Semiconductor Gamma-Ray Spectrometers," IEEE Trans. Nucl. Sci. NS-14, No. 1, 487-491, 1967.
60. Dearnley G. and Northrop, D.C., Semiconductor Counters for Nuclear Radiation, E. and F.N. Son. Ltd., London, 1966.
61. Dearnley, G., Gibbons, P.E. and Ellis, R., "Large Diameter Germanium Crystals for Gamma-Ray Spectroscopy," IEEE Trans. Nucl. Sci. NS-17(3): 282-286, 1970.
62. Deighton, M.O., "Statistical Errors Arising from Use of a Gated Pulse Train for Total Live Time Measurement During Pulse Amplitude Analysis," Nuc. Inst. Meth. 14: 48-52, 1961.
63. Deighton, M.O., "A Time-Domain Method for Calculating Noise of Active Integrator Used in Pulse Amplitude Spectrometry," Nucl. Inst. Meth. 58: 201-212, 1968.
64. Desborough, G.A. and Heidel, R.H., "Characteristics, Performance, and Quantitative Analytical Capability of an Energy-Dispersive Spectrometer on an Electron Microprobe Using Low Operating Voltages," Applied Spectroscopy 27: 456-463, 1973.
65. Desborough, G.A. and Heidel, R.H., "Energy Dispersive Spectrometry for Quantitative Mineralogical Analyses - An Ancillary System on an Electron Microprobe," J. Rsch. U.S. Geol. Sur. 2, No. 4, 441-446, July-Aug 1974.
66. Deslattes, R., Simson, B., LaVilla, R., "Gas Density Stabilizer for Proportional Counters," Rev. Sci. Int. 37 (5), 596-599, May 1966.
67. Drummond, W.E. and Moll, J.L., "Hot Carriers in Si and Ge Radiation Detectors," J. Ap. Phys. vol. 42, No. 13, 5556-5562, Dec. 1971.
68. Dyer, G.R., Gedcke, D.A., and Harris, T.R., "Fluorescence Analysis Using a Si(Li) X-Ray Energy Analysis System with Low-Power X-Ray Tubes and Radioisotopes," Advances in X-Ray Analysis 15: 228, 1972.
69. Dzubay, T.G., Jarrett, B.V., and Jaklevic, J.M., "Background Reduction in X-Ray Fluorescence Spectra Using Polarization," Nuc. Inst. and Meth. 115, 297-299, 1974.
70. Eberhardt, J.E., "Fano Factor in Silicon at 90K," Nucl Inst. and Meth. 80(2): 291-292, 1970.
71. Elad, E. and Gedcke, D.A., "Light Element Analysis with Si(Li) X-Ray Energy Analyzers," Proc. of the Sixth International Conference on X-Ray Optics and Microanalysis, Osaka, Japan, September 5-10, 1971. University of Tokyo Press, 263, 1972.
72. Elad, E. and Nakamura, M., "Germanium FET-A Novel Element for Low Noise Preamplifiers," Nucl. Instr. and Methods 54(2): 308, 1967.
73. Elad, E. and Nakamura, M., "Germanium FET-A Novel Low Noise Active Device," IEEE Trans. Nucl. Sci. NS-15 (1): 283, 1968.
74. Elad, E. and Nakamura, M., "High Resolution X-Ray and Electron Spectrometer," Nucl. Instr. and Methods 41: 161, 1966.
75. Elad, E. and Nakamura, M., "Hypercryogenic Detector-FET Unit--Core of High Resolution Spectrometer," IEEE Trans. Nucl. Sci. NS-15(3): 488, 1968.
76. Elad, E. and Nakamura, M., "Low Energy Spectra Measured with 0.7 KeV Resolution," Nucl. Instr. and Methods 42: 315, 1966.
77. Elad, E. et al., "The Use of a Non-Dispersive X-Ray Spectrometer in Scanning Electron Microscopy," IEEE Trans. Nucl. Sci. NS-17(1): 354, 1969.
78. Elad, E. et al, "Dead Layers in Charged-Particle Detectors," IEEE Trans. of Nucl. Sci NS-20, No. 1, 535-544, 1973.

79. Elad, E., "A Preamplifier with 0.7 KeV Resolution for Semiconductor Radiation Detectors," Nucl. Instr. and Methods 37: 327, 1965.
80. Elad, E., "Drain Feedback - A Novel Feedback Technique for Low-Noise Cryogenic Preamplifiers," IEEE Trans. Nucl. Sci. NS-19, No. 1, 403-411.
81. Elad, E., "FET Preamplifiers for Semiconductor Radiation Detectors," Proc. ISBRA Nuclear Electronics Symposium, Ispra Italy, p. 21, 6-9 May, 1969.
82. Elad, E., "Low-Noise Cryogenic Preamplifiers," STP 485, American Society for Testing and Materials, 57-81, 1971.
83. Elad, E., "Recent Developments in Low Noise Preamplifiers," Proc. of International Symposium on Nuclear Electronics and Radioprotection, Toulouse, Vol. 1, p. 13, (UCLRL Report 18005), 1978.
84. Elette, V. et al, "Energy Dispersion X-Ray Analysis Using a Scanning Electron Microscope," Metallography 5: 557-561, 1972.
85. Fano, U., "Ionization Yield of Radiations II. The Fluctuations of the Number of Ions," Phys. Rev. Vol. 72, No. 1, 26-29, 1947.
86. Fink, R.W., "Proportional-Counter Spectrometer," in Atomic Inner-Shell Processes II, Experimental Approaches and Applications, 169-186, Academic Press, 1975.
87. Fink, R.W., "Radioactive X-Ray Standards," Nucl. Inst. and Meth., 112, p. 243, 1973.
88. Fiori, C.E. et al, "Observations on the Quantitative Electron Probe Microanalysis of Particles," Proc. of the 7th Materials Research Symp., Gaithersburg, MD, Oct. 7-11, 1974, NBS Spec. Publ. 422, 1975.
89. Fiori, C.E., and Newbury, D.E., "Artifacts Observed in Energy-Dispersive X-Ray Microanalysis with the Lithium-Drifted Silicon Detector, (invited tutorial), in SEM/78/1: O. Johari, ed. (A.M.F. O'Hare, IL), 401-422, 1978.
90. Fiori, C.E., Myklebust, R.L., and Heinrich, K.F.J., "A Method for Resolving Overlapping Energy-Dispersive Peaks of an X-ray Spectrum; Application to the Correction Procedure FRAME B," Proc. 11th Conf. MAS, 1976, 12.
91. Fiori, C.E., Myklebust, R.L., and Heinrich, K.F.J., "Prediction of Continuum Intensity in Energy-Dispersive X-ray Microanalysis," Anal. Chem. 48: 1, 172-176, 1976.
92. Fiori, C.E., Myklebust, R.L., and Newbury, D.E., "A Catalog of Artifacts Observed in Energy Dispersive X-Ray Spectrometry and their Influence on Analysis," to appear in Conf. Proc. Book of the NIH Sponsored Workshop on Electron Optical Instrumentation (in press).
93. Fitzgerald, R. and Gantzel, P., "X-ray Energy Spectrometry in the 0.1 to 10Å Range," STP 485, American Society for Testing and Materials, 3-35, 1971.
94. Fitzgerald, R., Keil, K., Heinrich, K.F.J., "Solid-State Energy-Dispersion Spectrometer for Electron-Microprobe X-Ray Analysis," Science, Vol. 159, No. 3814, 528-530, Feb. 1968.
95. For a general review of CdTe detectors see: Proc. 2nd Intern. Symp. on CdTe, Rev. Appliquee, Vol. 12, No. 2, 1977.
96. Frankel, R.S., "Detection of Art Forgeries by X-Ray-Fluorescence Spectroscopy," Isotopes and Radiation Rech, Vol. 8 No. 1, Fall 1970.
97. Frankel, R.S., and Aitken, D.W., "Energy-Dispersive X-Ray Emission Spectroscopy," Applied Spectroscopy, Vol. 24, No. 6, 557-566, 1970.
98. Freund, H.U. et al, "Photon Spectrometry in the Low Energy Region 500 eV to 100 keV" in Radioactivity in Nuclear Spectroscopy 2: 623-649, Hamilton, J.H. and Manthuruthil, J.C. (eds.), Gordon and Breach Sci. Publ., New York, 1972.

99. Friel, J.J., Goldstein, J.I. and McCarthy, J.J., "Combined EDX and WDX Analysis with an Automated Microprobe," 8th Int. Conf. X-Ray Optics and Microanalysis; 12th MAS Conf., 1977, 50.
100. Gedcke, D. and Elad, E., "An Intercomparison of Trace Element Excitation Methods for Energy Dispersive Fluorescence Analyzers," X-Ray Spectrometry, Vol. 6, No. 1, 21, 1977.
101. Gedcke, D.A. and Elad, E., "The Si(Li) X-Ray Energy Analysis Technique: Principles and Applications," Proc. of the Sixth International Conference on X-Ray Optics and Microanalysis, Osaka, Japan, Sept. 5-10, 1971. University of Tokyo Press, 253, 1972.
102. Gedcke, D.A., "The High Counting Rate Limits on Analytical Precision Due to Deadtime Losses," Proc. 10th MAS Conf., 1975, 25.
103. Gedcke, D.A., "The Si(Li) X-Ray Energy Spectrometer for X-Ray Microanalysis," in Quantitative Scanning Electron Microscopy, (Ed. D. Holt, M. Muir, P. Grant), Academic Press, London, 1974.
104. Gedcke, D.A., Elad, E., and Dyer, G.R., "Limitations on the Si(Li) X-Ray Energy Analysis Systems at High Counting Rates," Proc. 6th National Conference on Electron Probe Analysis, 1971, 5.
105. Gedcke, D.A., "The Si(Li) X-Ray Energy Spectrometer for X-Ray Microanalysis," (Review Paper). X-Ray Spectrometry 1: 129, 1972.
106. Geiss, R.H. and Huang, T.C., "Quantitative X-Ray Energy Dispersive Analysis with the Transmission Electron Microscope," X-Ray Spectrometry 4: 196, 1975.
107. Geller, J.D., "A Comparison of MDL Limits Using Energy and Wavelength Dispersive Detectors," SEM/77/Vol 1: O.M. Johari, ed. (SEM Inc., A.M.F. O'Hare, IL.) 281-287, 1977.
108. Geller, J.D., "Energy Dispersive Filtration for Simultaneous Energy and Wavelength Dispersive Analysis," SEM/78/Vol 1: O.M. Johari, ed (SEM Inc. A.M.F. O'Hare, IL.), 201-206, 1978.
109. Geller, J.D., "Minimum Detection Limits in an Automated Microprobe," Proc. 11th MAS, 1976, 73.
110. Giaque, R.D., Garret, R.B. and Goda, L.Y., "Calibration of Energy-Dispersive X-Ray Spectrometers for Analysis of Thin Environmental Samples," in X-Ray Fluorescence Analysis of Environmental Samples, T.G. Dzubay (ed.), Ann Arbor Sci. 153-164.
111. Giaque, R.D., Goulding, F.S., Jaklevic, J.M. and Pehl, R.H., "Trace Element Analysis with Semiconductor Detector X-Ray Spectrometers," Anal. Chem. 45, No. 4, 671-681, April 1973.
112. Giles, M.A. and Barbi, N.C., "Estimating Mass Thickness in Semi-Thin Sections," Proc. 13th MAS Conf. 1978, 57.
113. Glasow, P.A. and Haller, E.E., "The Effect of Dislocation on the Energy Resolution of High-Purity Germanium Detectors," IEEE Trans. on Nucl. Sci. NS-23(1): 92-96, 1976.
114. Goldstein, J.I. and Williams, D.B., "Spurious X-Rays Produced in the Scanning Transmission Electron Microscope," SEM/77/1: O.M. Johari, ed. (A.M.F. O'Hare, IL.) 427-482, SEM Inc. 1978.
115. Goldstein, J.I. and Williams, D.B., "X-Ray Analysis in the TEM/STEM," SEM/77/1: O.M. Johari, ed (A.M.F. O'Hare, IL.), 561-662, 1977.
116. Goldstein, J.I. and Yakowitz, H., Practical Scanning Electron Microscopy, New York: Plenum press, 1975.



117. Goldstein, J.I. et al, "Quantitative X-Ray Analysis in the Electron Microscope," SEM/77/1: O.M. Johari, ed, (A.M.F. O'Hare, IL), 315-324, 1977.
118. Goldstein, J.I., Lorimer, G.W., and Cliff, G., "Quantitative Analysis of Thin Foils--Calibration Standards and Application to Iron Meteorites," Sixth European Congress on Electron Microscopy Proceedings 1: 56-58, 1976.
119. Goulding, F.S. and Hansen, W.L., "Leakage Current in Semiconductor Junction Radiation Detectors and its Influence on Energy-Resolution Characteristics," Nucl. Inst. and Meth. 12: 249-262, 1961.
120. Goulding, F.S. and Jaklevik, J.M., "XRF Analysis - Some Sensitivity Comparisons Between Charged-Particle and Photon Excitation," Nuc. Inst. and Meth. 142: 323-332, 1977.
121. Goulding, F.S. and Landis, D., "Nuclear Spectroscopy and Reactions," Part A, Chap III, in Semiconductor Spectrometer Electronics, ed. J. Cerny, Academic Press, Inc., New York, 1974.
122. Goulding, F.S. and Landis, D.A., "Some Electronic Aspects of Energy Measurements with Solid-State Detectors," IEEE Trans. on Nucl. Sci. Vol NS-25, No. 2, 896-901, 1978.
123. Goulding, F.S. and Lothrop, R.P., "Some Observations of Radiation Damage in Lithium-Drifted Silicon Detectors," Semiconductor Nuclear-Particle Detectors and Circuits, p. 337, National Academy of Sciences Pub. No. 1593, 1969.
124. Goulding, F.S. and Pehl, R.H., "A Survey of Radiation Damage in Semiconductor Detectors," IEEE Trans. on Nuc. Sci., NS 19, No. 1, 91-99, Feb. 1972.
125. Goulding, F.S. and Stone, Yvone, "Semiconductor Radiation Detectors," Science 170: 280-289, 16 October 1970.
126. Goulding, F.S. et al, "Detector Background and Sensitivity of X-Ray Fluorescence Spectrometers," Proc. 20th Ann. Denver X-Ray Conf, Aug 11-13, 1971.
127. Goulding, F.S., "Pulse-Shaping in Low-Noise Nuclear Amplifiers: A Physical Approach to Noise Analysis," Nuc. Inst. and Meth. 100, 493-536, 1972.
128. Goulding, F.S., "Semiconductor Detectors - An Introduction," IEEE Trans. Nucl. Sci. Vol. NS-25, No. 2, 916-920, 1978.
129. Goulding, F.S., Jaklevic, J.M. and Loo, B.W., "Development of Air Particulate Monitoring Systems," UCID-8090 Preprint, EPA Report IAG-D6-0377, Jan. 1978.
130. Goulding, F.S., Jaklevic, J.M. and Thompson, A.C., "Semiconductor Detectors for Fluorescent EXAFS," presented at the Workshop on X-Ray Instrumentation for Synchrotron Radiation Research, SLAC, Stanford, CA, April 3, 1978 (LBL-7542 Preprint).
131. Goulding, F.S., Walton, J. and Malone, D., "An Opto-Electronic Feedback Preamplifier for High-Resolution Nuclear Spectroscopy," Nucl. Inst. and Methods 71: 273-279, 1969.
132. Hall, R.N., "Electron-Hole Recombination," General Electric Research Laboratory, Report 55-RL-1316, Publ. Research Information Services Section, The Knolls, Schenectady, NY, 1955.
133. Haller, E.E. and Goulding, F.S., "Nuclear Radiation Detectors," to be published as a chapter in Handbook on Semi-conductors, eds. E.E. Haller and F.S. Goulding, N. Holland Publishing Co. (LBL-7521 Preprint March 1978).
134. Haller, E.E. and Hansen, W.L., "High Resolution Fourier Transform Spectroscopy of Shallow Acceptors in Ultra-Pure Germanium," Solid State Communications 15: 687-692, 1974.

135. Haller, E.E. et al, "Divacancy-Hydrogen Complexes in Dislocation-Free High Purity Germanium," in Radiation Effects in Semiconductors 1976, ed. N.B. Urli and J.W. Corbett, pp. 309-318, Inst. of Physics, Bristol and London, 1977.
136. Haller, E.E. et al, "Origin and Control of the Dominant Impurities in High-Purity Germanium," IEEE Trans. on Nuc. Sci. NS-23(1): 81-87, 1976.
137. Haller, E.E., "Recent Advances in Common Semiconductor Materials," IEEE Trans. Nucl. Sci. Vol. NS-25, No. 2, 921-926, 1978.
138. Haller, E.E., Hansen, W.L., and Goulding F.S., "Distribution of Donors and Acceptors in High-Purity Germanium Crystals," IEEE Trans. on Nuc. Sci. NS-20(1): 481-487, Feb. 1973.
139. Haller, E.E., Hansen, W.L., and Goulding, F.S., "Photothermal Ionization Spectroscopy," IEEE Trans. Nucl. Sci. NS-22(1): 127, 1975.
140. Haller, E.E., Hubbard, G.S. and Hansen, W.L., "Hydrogen-Multivalent Acceptor Complexes in High Purity Germanium," IEEE Trans. Nuc. Sci. NS-24(1): 48-52, 1977.
141. Hansen, J.S. et al, "Accurate Efficiency Calibration and Properties of Semiconductor Detectors for Low-Energy Protons," Nucl. Inst. Meth. 106: 365-379, 1973.
142. Hansen, W. and Goulding, F.S., "Leakage, Noise, Guard Rings and Resolution in Detectors," Proc. Asheville Conf. NAS-NRC Report No. 32, p. 202, 1961.
143. Hansen, W.L. and Haller, E.E., "Amorphouse Germanium as an Electron or Hole Blocking Contact on High-Purity Germanium Detectors," IEEE Trans. on Nuc. Sci. NS-24(1): 61-63, 1977.
144. Hansen, W.L. and Haller, W.L., "High-Purity Germanium-Observations on the Nature of Acceptors," IEEE Trans. Nucl. Sci. NS-19(1): 260-269, 1972.
145. Hansen, W.L., "High-Purity Germanium Crystal Growing," Nuc. Inst. and Meth. 94: 377-380, 1971.
146. Hansen, W.L., "Selection of Germanium for Lithium-Drifted Radiation Detectors by Observation of Etch-Pit Distributions," Nucl. Inst. and Meth. 80(2): 181-186, 1970.
147. Hansen, W.L., Haller, E.E., "A View of the Present Status and Future Prospects of High Purity Germanium," IEEE Trans. Nucl. Sci. NS-21(1): 279, 1974.
148. Harms, J., "Automatic Dead-time Correction for Multichannel Pulse-Height Analyzers at Variable Counting Rates," Nuc. Inst. Meth. 53: 192-196, 1967.
149. Harvey, N.P. and Pernou, J.P., "The Traverse-Field Silicon Detector," IEEE Trans. Nucl. Sci. NS-17(3): 306-309, 1970.
150. Headley, T.J. and Hren, J.J., "Sources of Background X-Radiation in Analytical Electron Microscopy," 9th Intn. Cong. on Electron Microscopy 1: 504-505, 1978.
151. Heath, R.L., "The Application of High-Resolution Solid State Detectors to X-Ray Spectrometry - A Review," Advan. X-Ray Anal. 15(1): 1-35, 1972.
152. Heinrich, K.F.J., Fiori, C.E., and Myklebust, R.L., "Progress in the Measurement of Relative X-ray Line Intensities," Proc. 11th Conf. MAS 1976, 29.
153. Henck, R. et al, "Trapping Effects in Ge(Li) Detectors and Search for a Correlation with Characteristics Measured on the P-Type Crystals," IEEE Trans. Nucl. Sci. NS-17(3): 149-159, 1970.
154. Herman, A.W., McNelles, L.A., and Campbell, J.L., "Choice of Physical Parameters in Charged Particle Induced X-Ray Fluorescence Analysis," Int. J. App. Rad. Iso. 24: 677-688, 1973.

155. Herman, A.W., McNelles, L.A., and Campbell, J.L., "Target Backings for Charged Particle Induced X-Ray Fluorescence Analysis," Nucl. Instr. Meth. 109: 429-437, 1973.
156. Hewka, P.V., Huth, G.C. and Swinth, K.L., "Biomedical Applications of Avalanche Semiconductor Radiation Detectors," IEEE Trans. Nucl. Sci. NS-17(3): 265-275, 1970.
157. Hubbard, G.S., Haller, E.E. and Hansen, W.L., "Characterization of Polycrystalline Zone-Refined Ingots of High-Purity Germanium," Nucl. Instr. and Meth. 130: 481-485, 1975.
158. Hubbard, G.S., Haller, E.E. and Hansen, W.L., "Ion Implanted N-Type Contact for High-Purity Germanium Detectors," IEEE Trans. on Nuc. Sci. NS-24(1): 161-164, 1977.
159. Hubbard, G.S., Haller, E.E., and Hansen, W.L., "Zone Refining High-Purity Germanium," IEEE Trans. Nucl. Sci. 24: 161-164, 1977.
160. Hurley, R.G. and Goss, R.L., "Quantitative Energy-Dispersive Analysis Using Relative k-Ratios," X-Ray Spectrometry 7: 70-72, 1978.
161. Iwanczyk, J., and Dabrowski, A.J., "The Effect of Charge Trapping on the Spectrometric Performance of n-Type CdTe Surface-Barrier Detectors," Nucl. Instr. and Meth. 134: 505-512, 1976.
162. Jaklevic, J.M. and Goulding, R.S., "Detection of Low Energy X-Rays with Si(Li) Detectors," IEEE Trans. Nucl. Sci. Vol. NS-18, No. 1, 187-191, 1971.
163. Jaklevic, J.M. et al, "Application of X-Ray Fluorescence Techniques to Measure Elemental Composition of Particles in the Atmosphere," 165th Am. Soc. Meeting on Anal. Methods Applied to Air Pollution Measurements, Dallas, April 8-13, 1973.
164. Jaklevic, J.M. et al, "Small X-Ray Tubes for Energy Dispersive Analysis Using Semiconductor Spectrometers," Advances in X-Ray Analysis 15: 266-275, Ed. K.F.J. Heinrich et al, New York: Plenum Press.
165. Jaklevic, J.M. et al, "X-Ray Fluorescence Analysis Applied to Small Samples," Adv. in X-Ray Analysis 21: 171-185, Ed. C.S. Barrett et al, Plenum Press, 1978.
166. Jaklevic, J.M., Loo, B.W., and Goulding, F.S., "Photon-Induced X-Ray Fluorescence Using Energy-Dispersive Detector and Dichotomous Sampler," in X-Ray Fluorescence Analysis of Environmental Samples, ed. T.G. Dzubay, Ann Arbor Science Publ., Ann Arbor, Michigan, 3-17, 1977.
167. Johnson, H. and Deslattes, R., "Production of Alumina Windows," Rev. Sci. Instr. 36: 1381-82, 1965.
168. Jorch, H.H. and Campbell, J.L., "Analytic Fitting of Full Energy Peaks from Ge(Li) and Si(Li) Photon Spectrometers," Nucl. Instr. Meth. 143: 551-559, 1977.
169. Kandiah, K., "Some Limitations of Energy Dispersive X-Ray Spectrometers," Proc. 8th Nat. Conf. on Electron Probe Analysis, New Orleans, 12, ~~1963~~ 1973
170. Karlovac, N. and Gedcke, D.A., "Improvements in High Counting Rate Performance of Si(Li) Energy spectrometers with a Novel Baseline Restoration Technique," Proc. 8th Conf. on Electron Probe Analysis, 1973, 17.
171. Katsanos, A. et al, "An External Beam Technique for Proton-Induced X-Ray Emission Analysis," Nucl. Instr. Meth. 137: 119-124, 1976.
172. Keith, H.D. and Loomis, T.C., "Calibration and Use of a Lithium-Drifted Silicon Detector for Accurate Analysis of X-Ray Spectra," X-Ray Spectrometry 5: 93-103, 1976.

173. Kern, H.E. and McKenzie, J.M., "Methods of Reducing Noise of Junction Field Effect Transistor (JFET) Amplifiers," IEEE Trans. on Nuc. Sci. NS-17(1): 260-268, 1970.
174. Kern, H.E. and McKenzie, J.M., "Noise Studies of Ceramic Encapsulated Junction Field Effect Transistors (JFETs)," IEEE Trans. in Nuc. Sci. NS-17(3): 425-432, 1970.
175. Keyser, R.M., Bartell, D.M. and Moneymaker, R.S., "A Computer Program for Spectrum Analysis," Proc. 10th Conf. MAS, 1975, 22.
176. Kirkendall, T.D., "Comprehensive Qualitative and Quantitative Analysis of Energy Dispersive X-Ray Spectra," Proc. of the 9th Ann. Conf. MAS, 1974, 24.
177. Kraner, H.W., "Si(Li) Coaxial Detectors," IEEE Trans. Nucl. Sci. NS-17(3): 215-220, 1970.
178. Landis, D.A. et al, "Pulsed Feedback Techniques for Semiconductor Detector Radiation Spectrometers," IEEE Trans. Nucl. Sci. NS-18(1): 115-124, 1971.
179. Landis, D.A. et al, "Pulsed Feedback Techniques for Semiconductor Detector Radiation Spectrometers," IEEE Trans. on Nucl. Sci. Vol. NS-18, No. 1, 115-124, 1971.
180. Langhernrich, A.P., Forster, J.W. and Linn Jr., T.A., "Energy Dispersion X-Ray (EDX) Analysis in the Non-Ferrous Mining Industry Analysis Instrumentation," Proc. of the 17th Annual ISA Analysis Inst. Symposium Vol. 9, Houston, Texas, April 19-21, 1971.
181. Leyden, D.E. and Lennox, J.C. Jr., "Data Acquisition and Control of Wavelength and Energy Dispersive X-Ray Spectrometers Using a Single Minicomputer," X-Ray Spect. 5: 137-141, 1976.
182. Lifshin, E. "The Generation and Detection of X-Rays in the Electron Microprobe and Scanning Electron Microscope", Proceedings of the Tutorial Session 7th Conf. on Electron Probe Analysis, 1969, 51.
183. Lifshin, E. and Ciccarelli, M.F., "Present Trends in X-Ray Analysis with the SEM," in SEM 1973, O.M. Johari, ed. (IITRI), Chicago, IL, 1973, vol. 1, 89-96.
184. Lifshin, E., "An Evaluation of a Solid-State X-Ray Detection System for Microprobe Analysis," Proc. 4th Conf. on Electron Microprobe Analysis, 1969, 51.
185. Lifshin, E., "Computer Processing of Solid-State X-Ray Detector Data," Proc. 8th Conf. on Electron Probe Analysis, 1970, 8.
186. Lifshin, E., "Factors Affecting Sensitivity of X-Ray Analysis with Electron Microbeam Instrumentation," To appear in Conf. Proc. Book of the NIH Sponsored Workshop on Electron Optical Instrumentation (in press).
187. Lifshin, E., "Quantitative Microprobe Analysis with Energy Dispersive Detectors-A Status Report," Proc. Denver X-Ray Conf., 1975.
188. Lifshin, E., "X-Ray Generation and Detection in the SEM," Scanning Electron Microscopy, O.C. Wells, New York, McGraw Hill, Chapter 10, 1974.
189. Lifshin, E., Ciccarelli, M.F. and Bolon, R.B., "New Measurements of the Voltage Dependence of Absolute X-Ray Yields," Proc. 12th Ann. Conf. MAS, 1977, 104.
190. Lifshin, E., Ciccarelli, M.F. and Bolon, R.P., "Determinations of the Energy Distribution of the Continuum and the Ratio of Indirect to Direct X-ray Fluorescence," Proc. 8th Nat. Conf. on Electron Probe Analysis, 29, 1973.

191. Lifshin, E., Ciccarelli, M.F., and Bolon, R.B., "Measurement of Characteristic and Continuum X-Ray Production Efficiencies," 7th Int. Conf. on X-Ray Optics and Microanalysis in Moscow-Kiev, July 9-16, 1974.
192. Lifshin, E., Ciccarelli, M.F., Bolon, R.B., "X-ray Spectral Measurement and Interpretation," in Practical Scanning Electron Microscopy, Goldstein, J. (ed.), New York: Plenum, 1975.
193. Llacer, J., "Accurate Measurement of Noise Parameters in Ultra-Low Noise Opto-Feedback Spectrometer Systems," IEEE Trans. Nucl. Sci. NS-22(5): 2033, 1975.
194. Llacer, J., "Geometric Control of Surface Leakage Current and Noise in Lithium Drifted Silicon Radiation Detectors," IEEE Trans. Nucl. Sci. NS-13(1): 103, 1966.
195. Llacer, J., Haller, E.E. and Cordi, R.C., "Entrance Windows in Germanium Low-Energy X-Ray Detectors," IEEE Trans. Nuc. Sci. NS-24(1): 53-60, Feb. 1977.
196. Loomis, T.C. and Keith, H.D., "Accurate Calibration of Efficiencies of X-Ray Detectors: Flow Proportional and Scintillation Counters," App. Spect. 29(4): 316-322, 1975.
197. Lothrop, R.P., "The Effects and Control of Surface States During Lithium Ion Drift in Silicon," UCRL Report No. 19413, 1969.
198. Lukirskii, A.P., Ershov, O.A., and Brytov, I.A., "Operation of Proportional Counters in the Ultra-soft X-Ray Region," Izv. Akad. Nauk, SSSR, Ser. Fiz 27: 798-807, 1963.
199. Madden, N.W. et al, "A High-Resolution Si(Li) Spectrometer with Thermoelectric Cooling," submitted to Nuc. Inst. and Meth. (LRL-7550 Preprint), July 1978.
200. Maor, D. and Rosner, B., "Efficiency of Ge and Si(Li) Detectors at Very Low Energies by an X-Ray Doublet Method," J. Phys. E: Sci. Instrum. 11: 1141-1144, 1978.
201. Martini, M., McMath, T.A. and Fowler, I.L., "The Effects of Operating Temperature on the Behavior of Semiconductor Detectors," IEEE Trans. Nucl. Sci. NS-17(3): 139-148, 1970.
202. Masters, C.F. and East, L.V., "An Investigation Into the Harms Dead Time Correction Procedure for Pulse Height Analyzers Using Monte Carlo Modeling Techniques," IEEE Trans. Nuc. Sci. 17: 383-389, 1970.
203. Mathieson, E. and Sanford, P.W., "Point Anode Proportional Counters," J. Sci. Instr. 40: 446-449, 1963.
204. Mayer, J.W. et al, "Influence of Trapping and Detrapping Effects in Si(Li), Ge(Li) and CdTe Detectors," IEEE Trans. Nucl. Sci. Vol NS-17, No. 3, 221-234, 1970.
205. McMath, T.A. and Martini, M., "The Effect of Charge Trapping on the Spectrometer Performance of p-i-n Semiconductor Detectors," Nucl. Instrum. Meth. 86(2): 245-252, 1970.
206. McNelles, L.A. and Campbell, J.L., "Absolute Efficiency Calibration of Coaxial Ge(Li) Detectors," Nucl. Instr. Meth. 109: 241-251, 1973.
207. McNelles, L.A. and Campbell, J.L., "Analytic Approximation to Peak Shapes Produced by Ge(Li) and Si(Li) Spectrometers," Nuc. Inst. and Methods 127: 73-81, 1975.
208. McNelles, L.A. and Campbell, J.L., "Analytic Approximations to Peak Shapes Produced by Ge(Li) and Si(Li) Spectrometers," Nucl. Instr. Meth. 127: 73-81, 1975.

209. Middleman, L.M. and Geller, J.D., "Trace Element Analysis Using X-Ray Excitation with an Energy Dispersive Spectrometer on a Scanning Electron Microscope," SEM/76/Part I, O.M. Johari, ed. (IITRI), Chicago, IL: 171-178, 1976.
210. Moll, S.H., Baumgarten, N., and Donnelly, W., "Geometrical Considerations for ZAF Corrections in the SEM," Proc. of 8th International Conf. on X-Ray Optics and Microanalysis and 12th Annual Conf. of the MAS, Boston, Mass., 1977.
211. Mulvey, T. and Campbell, A.J., "Proportional Counters in X-Ray Spectro-Chemical Analysis," B. Jour. of Ap. Physics 9: 406-410, 1958.
212. Musket, R.G. and Bauer, W., "Determination of Gold-Layer and Dead-Layer Thicknesses for a Si(Li) Detector," Nuc. Instr. and Methods 109: 593-595, 1973.
213. Musket, R.G. and Bauer, W., "Determinations of Oxide Thickness on Tritided Erbium Films Using Beta-Induced X-Ray Fluorescence," J. of Appl. Physics 47(1): 353-356, 1976.
214. Musket, R.G., "Detection of Proton-Induced Boron X-Rays with a Si(Li) Detector," Nuc. Inst. and Methods 117: 385-389, 1974.
215. Myklebust, R.L. and Heinrich, K.F.J., "Rapid Quantitative Electron Probe Microanalysis with a Nondiffractive Detector System," STP 485, American Society for Testing and Materials, 232-242, 1971.
216. Myklebust, R.L. et al, "Data Reduction Procedure for Monochromatic X-Ray Fluorescence Analysis with a Si(Li) Detector," Proc. 3rd Ann. Conf., Federation of Analytical Chemistry and Spectroscopy Societies, paper 241, 1976.
217. Myklebust, R.L., Fiori, C.E., and Heinrich, K.F.J., "FRAME C: A Compact Procedure for Quantitative Energy-Dispersive Electron Probe X-ray Analysis," Proc. of the 8th Intern. Conf. on X-ray Optics and Microanalysis and the 12th Conf. MAS 1977, 18.
218. Noble, A.C. et al, "Trace Element Analysis of Wine by Proton-Induced X-Ray Fluorescence Spectrometry," J. Agric. Food Chem. 24: 532-535, 1976.
219. Nowlin, C.H. and Blankenship, J.L., "Elimination of Undesirable Undershoot in the Operation and Testing of Nuclear Pulse Amplifiers," Rev. Sci. Inst. 36(12): 1830-1839, 1965.
220. Pehl, R.H. and Goulding, F.S., "Recent Observations on the Fano Factor in Germanium," Nucl. Instr. and Methods 81(2): 329, 1970.
221. Pehl, R.H. et al, "Accurate Determination of the Ionization Energy in Semiconductor Detectors," Nucl. Instr. Met. 59: 45-55, 1968.
222. Pehl, R.H., "Radiation Damage of Germanium Detectors," Proc. of Gamma Ray Spectroscopy in Astrophysics Symposium, Goddard Space Flight Center, Greenbelt, MD, April 28-29, 1978.
223. Pehl, R.H., Cordi, R.C. and Goulding, F.S., "High-Purity Germanium: Detector Fabrication and Performance," IEEE Trans. Nucl. Sci. NS-19(1): 265-269, 1972.
224. Pehl, R.H., Haller, E.E. and Cordi, R.C., "Operational Characteristics of Germanium Detectors at Higher Temperatures," IEEE Trans. Nucl. Sci. NS-20(1): 494-499, 1973.
225. Pehl, R.H., Varnell, L.S. and Metzger, A.E., "High-Energy Proton Radiation Damage of High-Purity Germanium Detectors," IEEE Trans. Nucl. Sci. Vol. NS-25, No. 1, 409-417, 1978.

226. Pell, E.M., "Ion Drift in an n-p Junction," J. of App. Physics 31(2): 291-302, 1960.
227. Plant, A.G. and Lachance, G.R., "Quantitative Electron Microprobe Analysis Using an Energy Dispersive Spectrometer." Proc. 8th Nat. Conf. Electron Probe Analysis, 1972, 13.
228. Poenaru, D.N., Stuck, R. and Siffert, P., "Collection Efficiency and Charge Carrier Losses in Coaxial and Planer Ge(Li) Detectors. Influence on the Time Resolution," IEEE Trans. on Nucl. Sci. NS-17(3): 176-186, 1970.
229. Porter, D.E. and Woldseth, R., "X-Ray Energy Spectrometry," Anal. Chem. 45(7): 604a-614a, June 1973.
230. Radeka, V. and Karlovac, N., "Time-Variant Filters," in Semiconductor Radiation Detectors and Circuits, National Academy of Sciences Pub. No. 1593, p. 553, 1969.
231. Radeka, V., "Charge Amplification Without Charge Leak Resistor," IEEE Trans. Nucl. Sci. Vol. NS-17, No. 3, 433-439, 1970.
232. Radeka, V., "Field Effect Transistor Noise as a Function of Temperature and Frequency," Semiconductor Nuclear Particle Detectors and Circuits, N.A.S. Publ. 1593, Washington, D.C., p. 393, 1969.
233. Radeka, V., "Overload Recovery Circuit for Charge Amplifiers," IEEE Trans. Nucl. Sci. Vol NS-17, No. 1, 269-275, 1970.
234. Radeka, V., "Trapezoidal Filtering of Signals from Large Germanium Detectors at High Rates," IEEE Trans. Nucl. Sci. NS-19(1), 412-428 Feb. 1972.
235. Reed, S.J.B. and Ware, N.G., "Escape Peaks and Internal Fluorescence in X-Ray Spectra Recorded with Lithium Drifted Silicon Detectors," J. Phys. (E). 5: 582-584, 1972.
236. Reed, S.J.B. and Ware, N.G., "Quantitative Electron Microprobe Analysis of Silicates Using Energy-Dispersive X-Ray Spectrometry," J. Petrol. 16: 499-519, 1975.
237. Reed, S.J.B. and Ware, N.G., "Quantitative Electron Microprobe Analysis Using a Lithium Drifted Silicon Detector," X-Ray Spectrom. 2: 69-74, 1973.
238. Reed, S.J.B. and Ware, N.G., "The Measurement of X-ray Peak Intensities with a Lithium Drifted Silicon Detector by Integration Over a Fixed Energy Range," J. Phys. 5(E): 1112-1114, 1972.
239. Reed, S.J.B., "Dead Time Corrections for X-Ray Intensity Measurements with a Si(Li) Detector," J. Phys. 5(E): 994-996, 1972.
240. Reed, S.J.B., Electron Microprobe Analysis, Cambridge University Press, Chapters 9, 10 and 17, 1975.
241. Reed, S.J.B., "Pulse Pile-Up Rejection in Si(Li) X-Ray Detection Systems," J. Phys. 5(E): 997-999, 1972.
242. Rhodes, J.R., "Design and Application of X-ray Emission Analyzers Using Radioisotope X-ray or Gamma Ray Sources," STP 485, American Society for Testing and Materials, 243-285, 1971.
243. Rose, M.E. and Korff, S.A., "An Investigation of the Properties of Proportional Counters I," Phys. Rev. 59: 850-859, 1941.
244. Rosner, B., and Gur, D., "Determination of the Efficiency Curve of a Ge(Li) Detector Near the Germanium K-edge (E=11.04 keV)," Nucl. Inst. Meth 111: 577-580, 1973.

245. Rosner, B., Gur, D. and Shabason, L., "Efficiency of Ge(Li) and Si(Li) Planer Detectors in the 2-5 keV Energy Range," Nucl. Inst. Meth. 131: 81-85, 1975.
246. Rossi, B.B. and Staub, H.H., Ionization Chambers and Counters, McGraw Hill, New York, 1949.
247. Russ, J.C. (ed.), Energy Dispersion X-ray Analysis: X-ray and Electron Probe Analysis, STP 485, American Society for Testing and Materials, Philadelphia, 1970.
248. Russ, J.C. and Barbi, N.C., "Removing Substrate Background in TEM Microanalysis," Proc. of the Electron Microscope Society of America, 32nd Annual Meeting, 568-579, 1974.
249. Russ, J.C. and Barnhart, M.W., "The EDIT System for Computer Reduction of Energy-Dispersive X-Ray Data," 6th International Conf. on X-Ray Optics and Microanalysis, Osaka, Sept., 271-278, 1971.
250. Russ, J.C. and Kabaya, A. "Use of a Non-Dispersive X-ray Spectrometer on the Scanning Electron Microscope," in SEM 1969, O.M. Johari, ed. (IITRI), Chicago, IL, 1969, 57-64.
251. Russ, J.C. et al., "An Integrated System for Elemental X-Ray Analysis of Materials," Advances in X-Ray Analysis, Vol. 16, 1973.
252. Russ, J.C., "A Fast Self-Contained No-Standards Quantitative Program for EDS," Proc 12th Conf., MAS 1978, 46.
253. Russ, J.C., "A Simple Correction for Backscattering from Inclined Samples," Proc 10th Conf. MAS 1975, 7.
254. Russ, J.C., "Background Subtraction for Energy-Dispersive X-Ray Spectra," Proc. 7th National Conference on Electron Probe Analysis, 1972, 76.
255. Russ, J.C., "Energy-Dispersion X-ray Analysis on the Scanning Electron Microscope," STP 485, American Society for Testing and Materials, Philadelphia, 154-179, 1970.
256. Russ, J.C., "Energy-Dispersion X-Ray Detection in the Scanning Electron Microscope" 7th International Congress on Electron Microscopy, Grenoble, 1970, 231-32.
257. Russ, J.C., "Erroneous Si Peaks in Energy Dispersive Spectra," Proc. 24th Annual Denver X-Ray Conference, Denver, Colorado, August 1975, 161-165.
258. Russ, J.C., "Evaluation of the Direct Element Ratio Calculation Method," Jour. De Microscopie vol. 22, No. 2-3, 283-286, 1973.
259. Russ, J.C., "Interactive Displays and Simple Algorithms as an Aid to Qualitative Analysis of Energy Dispersive Spectra," Proc. 13th Conf. MAS 1978, 54.
260. Russ, J.C., "Light Element Analysis Using the Semiconductor X-Ray Energy Spectrometer with Electron Excitation," STP 485, American Society for Testing and Materials, 217-231, June 1970.
261. Russ, J.C., "Microanalysis of Thin Sections in the TEM and STEM Using Energy-Dispersive X-Ray Analysis," Electron Microscopy and Cytochemistry, Proc. 2nd International Symposium, Drienerio, 1973, E.Wisse, W. Th. Daems, I. Molennar, P. van Duijn, eds., 1974, 223-228.
262. Russ, J.C., "Microanalysis of Thin Sections, Coatings and Rough Surfaces," In SEM 1973, O.M. Johari, ed. (IITRI) Chicago, IL, 1973.
263. Russ, J.C., "Obtaining Quantitative Information from an SEM Equipped with an Energy-Dispersive X-Ray Analyzer," Proc. SEM 1973, Conference Series No. 18, Institute of Physics, London and Bristol, 238-241, 1973.



264. Russ, J.C., "Performance Characteristics of the Non-Dispersive X-ray Spectrometer," Proc. 27th Annual Meeting, EMSA, 1969, 92-93.
265. Russ, J.C., "Problems in Using Fixed Energy Windows to Get Intensity Values from Energy Dispersive X-Ray Spectra," Proc. Annual Denver X-Ray Conference, p. 96, 1977.
266. Russ, J.C., "Procedures for Quantitative Ultralight Element Energy Dispersive X-Ray Analysis," in SEM/77/1: O.M. Johari, ed (A.M.F. O'Hare, IL), 289, 1977.
267. Russ, J.C., "Procedures for Quantitative Ultralight Element Energy Dispersive X-Ray Spectra Using Fixed Energy Windows" Proc. 12th Conf. MAS 1977, 97.
268. Russ, J.C., "Processing of Energy Dispersive X-Ray Spectra," Proc. Annual Denver X-Ray Conference, p. 81, 1976.
269. Russ, J.C., "Processing of Energy Dispersive X-Ray Spectra," X-Ray Spectrometry, Vol. 6, No. 1, 37-55, 1977.
270. Russ, J.C., "Progress in the Design and Application of Energy-Dispersion X-Ray Analyzers for the Scanning Electron Microscope," in SEM 1971, O.M. Johari, ed., (IITRI) Chicago, IL, 65-72, 1971.
271. Russ, J.C., "Quantitative Results with X-Ray Fluorescence Spectrometry Using Energy-Dispersive Analysis of X-Rays," X-Ray Spectrometry, Vol. 1, No. 3, 119, July, 1971.
272. Russ, J.C., "Resolving Spectrum Interferences Using Non-Gaussian Peaks," Canadian Spectroscopy, February 1976.
273. Russ, J.C., "TEM and STEM Microanalysis," Proc. 34th Annual EMSA Meeting, p. 562, 1976.
274. Russ, J.C., "Use of Energy-Dispersion X-Ray Analysis on the Electron Microprobe, 6th International Symposium on Microtechniques, Graz, September, 1970, 221-225.
275. Russ, J.C., "X-Ray Methods in the Scanning Electron Microscope," Scanning Electron Microscopy/Methods and Phenomena, W.R. Bottoms, Ed., 1974.
276. Russ, J.C., "X-Ray Microanalysis at High Beam Voltages," in SEM 1976, O.M. Johari ed. (IITRI), Chicago, 1976, Vol. 1, 143-150.
277. Russ, J.C., "X-Ray Microanalysis in the Biological Sciences," J. of Submicroscopic Cytology, Vol. 6, No. 1, A. Bairati, B. Baccetti, R. Laschi, eds., April, 1974.
278. Russ, J.C., "X-Ray Spectroscopy on the Electron Microscope," X-Ray Spectrometry, Vol. 2, No. 1, 1973.
279. Russ, J.C., and Sandborg, A.O., "Evaluation of Pulse Pileup Rejection," Proc. Annual Denver X-Ray Conference, p. 93, 1977.
280. Russ, J.C., and Shen, R.B., "An Efficient Combined ED/WD X-ray Analysis System," Proc. 9th MAS Conf., 1978, 86.
281. Russ, J.C., Baerwaldt, G.C., and McMillan, W.R., "Routine Use of a Second Generation Windowless Detector for energy Dispersive Ultralight Element X-Ray Analysis," X-Ray Spectrometry, Vol. 5 No. 3, 212-222. October 1976.
282. Russ, J.C., Sandborg, A.O., and Barnhart, M.W., "Energy-Dispersive X-Ray Fluorescence Analysis: Use of Multi-Element Detection for Rapid On-Line Classification and Sorting," XVII Colloquium Spectroscopicum International 1973, Florence, September, 1973.

283. Russ, J.C., Shen, R.B. and Jenkins, R., EXAM: Principles & Experiments published by EDAX International, Inc., 1977.
284. Russ, J.C., "Automatic Fitting of Calculated Backgrounds in Energy Dispersive X-Ray Spectra," Proc. 8th MAS Conf. 1977, 102.
285. Russ, J.C., "Measuring Detector Entrance Windows," Proc. 8th MAS Conf. 1977, 105.
286. Sandborg, A.O. and Lichtinger, R.W., "An Energy Dispersive Spectrometer for Elements from 6 to 92," Proc. 8th MAS Conf. 1977, 107.
287. Sandborg, A.O. and Russ, J.C., "Counting Rate Performance of Pulsed-Tube Systems," Proc. Annual Denver X-Ray Conference, p. 65, 1976.
288. Sandborg, A.O., "Energy Dispersion X-ray Analysis with Electron and Isotope Excitation," STP 485, American Society for Testing and Materials, 113-124, 1971.
289. Savitzky, A. and Golay, M.J.E., "Smoothing and Differentiation of Data by Simplified Least Squares Procedures," Anal. Chem. 36: 1627-1639, 1964.
290. Schamber, F.H., "A New Technique for Deconvolution of Complex X-Ray Energy Spectra," Proc. 8th Nat. Conf. on Electron Probe Analysis, 1973, 85.
291. Schamber, R.H., "A Modification of the Linear Least-Squares Fitting Method which Provides Continuum Suppression," STP 485, American Society for Testing and Materials, 241-257, 1971.
292. Schieber, M. (ed.), Proc. Intern. Workshop on HgI<sub>2</sub> and CdTe Nuclear Detectors Jerusalem, June 6-8, 1977.
293. Semiconductor Nuclear Particle Detectors and Circuits, National Academy of Sciences Publication number 1593, Washington, DC 1969.
294. Servant, J.M., Meny, L., and Champigny, M., "Energy Dispersion Quantitative X-Ray Microanalysis on a Scanning Electron Microscope," X-Ray Spectrometry 4: 99-100, 1975.
295. Shen, R.B., "A Simplified Fundamental Parameters Method for Quantitative Energy Dispersive X-Ray Fluorescence Analysis," X-Ray Spectrometry, vol. 6 No. 1, p. 56, 1977.
296. Shen, R.B., Russ, J.C., and Stroeve, A.W., "Modelling Intensity and Concentration in Energy Dispersive X-Ray Fluorescence," Proc. Annual Denver X-Ray Conference, p. 129, 1978.
297. Sherry, W.M. and Vandersande, J.B., "A Background Correction for Energy-Dispersive X-Ray Analysis of Thin Sections," X-Ray Spect. 6(3): 154-160, 1977.
298. Short, J.M., "Time-Shared Computer Treatment of Energy Dispersive X-Ray Data," in SEM 1973, O.M. Johari ed. (IITRI), Chicago, IL, 95-112, 1973.
299. Short, M.A., "Optimum 'Windows' in Quantitative Energy Dispersive Analysis," X-Ray Spect. 5: 169-171, 1976.
300. Sikkema, C.P., "Elimination of End Effects in Proportional Counters," Nuc. Inst. 1: 148-151, North Holland Pub. Co., 1957.
301. Smith, C.F. and Conway, D.C., "Distortion of Proportional Counter Spectra by Counter Poisons," Rev. Sci. Inst. 33(7) 726-729, July 1962.
302. Smith, D.G.W. "An Approach to Fully Quantitative Energy Dispersive Electron Microprobe Analysis," Proc. 10th Conf. MAS, 1975, 21.

303. Smith, D.G.W. "Applications of Quantitative Energy Dispersive Electron Microprobe Analysis in the Study of Mineral Chemistry," Proc. 11th Mtg. Internat. Mineral. Assoc., Novosibirsk, USSR (in press), 1978.
304. Smith, D.G.W. Quantitative Energy Dispersive Microanalysis Short Course Handbook, Vol. 1: Microbeam Techniques (D.G.W. Smith, Ed.), 63-106, Mineralogical Association of Canada, 1976.
305. Smith, D.G.W. and Cavell, P.A. "An Energy Dispersive Technique for the Quantitative Analysis of Clay Minerals by the Electron Microprobe," Proc. 13th Conf. MAS 1978, 45.
306. Smith, D.G.W. and Gold, C.M. "A Scheme for Fully Quantitative Energy Dispersive Microprobe Analysis," Advances in X-ray Analysis 19: 191-201, 1976.
307. Smith, D.G.W., Gold, C.M. and Tomlinson, D.A. "The Atomic Number Dependence of the X-ray Continuum Intensity and the Practical Calculation of Background in Energy Dispersive Electron Microprobe Analysis," X-ray Spectrometry 4: 149-156, 1975.
308. Smith, D.G.W., Reed, S.J.B., and Ware, N.G., "KB/KA Intensity Ratios for Elements of Atomic Number 20 to 30," X-Ray Spectrom. 3: 149-150, 1974.
309. Solosky, L.F. and Beaman, D.R., "A Simple Method for Determining the Acceleration Potential in Electron Probes and Scanning Electron Microscopes," Rev. of Sci. Instr. 43(8): 1100-1102, Aug. 1972.
310. Spielberg, N., "Effect of Anode Material on Intensity Dependent Shifts in Proportional Counter Pulse Height Distributions," Rev. Sci. Instr. 38(2): 291, Feb. 1967.
311. Sprys, J.W., "Specimen Holder for Energy Dispersive X-Ray Analysis in the Transmission Electron Microscope," Rev. Sci. Instr. 46(6): 773, 1975.
312. Statham, P.J. et al, "Quantitative Analysis with an Energy Dispersive Detector Using a Pulsed Electron Probe and Active Signal Filtering," X-Ray Spectrometry 3: 153-158, 1974.
313. Statham, P.J., "A Comparative Study of Techniques for Quantitative Analysis of the X-Ray Spectra Obtained with a Si(Li) Detector," X-Ray Spectrometry 5: 16-28, 1976.
314. Statham, P.J., "A Comparison of Some Quantitative Techniques for Treating Energy Dispersive X-Ray Spectra," Proc. 9th Conf. MAS, 1974, 21.
315. Statham, P.J., "Beam Switching: A Technique to Improve the Performance of Pulse Processing Electronics for E.D.S.," Proc. 11th Conf. MAS, 1976, 11.
316. Statham, P.J., "Corrections for the Bremsstrahlung Background in E.D.S. Microprobe Analysis of Thick Specimens," Proc. 11th Conf. MAS, 1976, 10.
317. Statham, P.J., "Deconvolution and Background Subtraction by Least Squares Fitting with Prefiltering of Spectra," Anal. Chem. 49: 2149, 1977.
318. Statham, P.J., "Escape Peaks and Internal Fluorescence for a Si(Li) Detector and General Geometry," J. Phys. E.: Sci. Instr. 9: 1023, 1976.
319. Statham, P.J., "Measurement and Use of Peak-to-Background Ratios in X-Ray Analysis," Proc. "Neuntes Kolloquium Über Metallkundliche Analyse", Vienna, Austria, Oct. 1978 (to be published in supplementary volume of "Microchemica Acta").
320. Statham, P.J., "Pile-up Rejection: Limitations and Corrections for Residual Errors in Energy Dispersive Spectrometers," X-Ray Spectrometry 6: 94-103, 1977.
321. Statham, P.J., "Pitfalls in Linear and Non-Linear Profile-Fitting Procedures for Resolving Severely Overlapped Peaks," X-Ray Spectrometry 7: 132-137, 1978.

322. Statham, P.J., "Reliability in Data-Analysis Procedures for X-Ray Spectra," Proc. 8th Intn. Conf. on X-Ray Optics and Microanalysis; 12th Conf. MAS, 1977, 95.
323. Statham, P.J., "Resolution Enhancement of X-Ray Spectra," Proc. 8th Intn. Conf. on X-Ray Optics and Microanalysis; 12th Conf. MAS, 1977, 103.
324. Statham, P.J., "The Application of the Harwell Active Pulse Processor to Energy Dispersive X-Ray Analysis in the Electron Microprobe," Proc. 9th Conf. MAS, 1974, 55.
325. Statham, P.J., "The Generation, Absorption and Anisotropy of Thick-Target Bremsstrahlung and Implications for Quantitative Energy Dispersive Analysis," X-Ray Spectrometry 5: 154-168, 1976.
326. Stein, J.D. and White, F.A., "Window Thickness Measurement of Surface Barrier Detectors," IEEE Trans. Nucl. Sci. NS-17(4): 37-39, 1970.
327. Stewart, J.E., "Resolution Enhancement of X-Ray Fluorescent Spectra with a Computerized Multichannel Analyzer," Applied Spectroscopy 29(2): 171-174, 1975.
328. Stewart, J.E., Zulliger, H.R., and Drummond, W.E., "Energy Dispersive X-Ray Fluorescence Spectrometry at High Count Rates with Recovery of Resolution by Computer Processing," Proc. of the 24th Ann. Conf. on Applications of X-Ray Analysis, Denver, Aug. 6-8, 1975.
329. Sutfin, L.V. and Ogalvie, R.E., "Role of the Gas Flow Proportional Counter in Energy Dispersive Analysis," STP 485, American Society for Testing and Materials, 197-216, 1971.
330. Tenny, H., "Rapid Analysis of Particles Using a Non-Dispersive X-Ray Analyzer," Metallography 1: 221-225, 1968.
331. Tove, P.A., Cho, Z.H. and Huth, G.C., "The Importance of the Time Scale in Radiation Detection Exemplified by Comparing Conventional and Avalanche Semiconductor Detectors," Physica Scripta 13: 83-92, 1976.
332. Trammel, R. and Walter, F.J., "The Effects of Carrier Trapping in Semiconductor Gamma-Ray Spectrometers," Nucl. Instrum. Meth. 76: 317-321, 1969.
333. Van Espen, P. and Adams, F., "Evaluation of a Practical Background Calculation Method in X-Ray Energy Analysis," X-Ray Spect. 5: 123-128, 1976.
334. Vogel, R. and Ferguson, L., "Gas Flow Proportional Counter for Electron Probe Light Element Analysis," Rev. Sci. Instr.: 934-938, July 1966.
335. Walter, F.J., "Characterization of Semiconductor X-ray Energy Spectrometers," STP 485, American Society for Testing and Materials, 82-112, 1971.
336. Walter, F.J., "Comments on Measurements of Epsilon and the Fano Factor," in Semiconductor Nuclear-Particle Detectors and Circuits, National Academy of Sciences, Pub. No. 1593, p. 63, 1969.
337. Walter, F.J., "The Impact of Semiconductor Detectors on X-Ray Spectroscopy," IEEE Trans. Nucl. Sci. NS-17(3): 196-214, 1970.
338. Ware, N.G. and Reed, S.J.B., "Background Corrections for Quantitative Electron Microprobe Analysis Using a Lithium Drifted Silicon Detector," J. Phys. (E). 6: 286-288, 1973.
339. Ware, N.G., "Annotated Computer Programs for Electron Probe Microanalysis Using a Lithium Drifted Silicon Detector," Special Report, Research School of Earth Sciences, Australian National University, 1973.
340. Webb, P.P. et al, "Use of Collimated Gamma-Ray Beams in the Study of Ge(Li) Detectors," Nucl. Instr. and Meth. 63: 125-135, 1968.
341. Wendt, M., "Advances in Energy Dispersive X-Ray Microanalysis," Kristall und Technik 13(11): 1259-1275, 1978.

342. Wichner, R., Armantrout, G.A. and Brown, T.G., "Ge Crystal Growth and Evaluation as Ge(Li) Detector Material," IEEE Trans. Nucl. Sci. NS 17(3): 160-164, 1970.
343. Williams, A. and Sara, R.I., "Parameters Affecting the Resolution of a Proportional Counter," Int. Jour. of AP. Rad & Isotopes 13: 229-38, 1962.
344. Williams, C.W., "Reducing Pulse-Height Spectral Distortion by Means of DC Restoration and Pile-Up Rejection," IEEE Trans. Nuc. Sci. NS-15(1): 297-302, 1968.
345. Williams, G., "Role of Multichannel Analyzer in Data Handling," STP 485, American Society for Testing and Materials, 125-139, 1971.
346. Woldseth, R. and Meyer, G.W., "Multi-Element Quality Control," Industrial R/D, June 1978.
347. Woldseth, R., "X-Ray Energy Spectrometry: New Applications in Industry and Medicine," American Laboratory 11: 1975.
348. Woldseth, R., Everything You Always Wanted to Know About XES, Foster City, California, KeveX Corp., 1973.
349. Woldseth, R., Porter, D.E., and Frankel, R.S., "The Analytical X-Ray," Industrial Research, Feb. 1971.
350. Woodhouse, J.B., "Escape Peaks in Si(Li) Detectors," Proc. 7th Nat. Conf. on Electron Probe Analysis, 79, 1972.
351. Yakowitz, H., "Energy-Dispersive X-Ray Spectrometry," J. de Microscopie et de Biologies Cellulaire 22: 1975.
352. Yakowitz, H., "X-Ray Microanalysis in Scanning Electron Microscopy," SEM/1974, (O. Johari, ed.) IITRI, Chicago, Ill, pp. 1029-1042, 1974.
353. Zaluzec, N.J. and Fraser, H.L., "A Modified Specimen Stage for X-Ray Analysis in a TEM" Jour. of Physics E: Scientific Instruments 9: 1051-1052, 1976.
354. Zaluzec, N.J. and Fraser, H.L., "Microchemical Analysis of Thin Metal Foils," 34th Ann. Proc. Electron Microscopy Soc. Amer., Miami Beach, Florida, G.W. Bailey, ed., 1976.
355. Zulliger, H.R. and Aitken, D.W., "Charge Collection Efficiencies for Lithium-Drifted Silicon and Germanium Detectors in the X-Ray Energy Region," IEEE Trans. Nucl. Sci. NS-15(1): 466, 1968.
356. Zulliger, H.R. and Aitken, D., "Fano Factor, Fact and Fallacy," IEEE Trans. Nucl. Sci., NS-17(3): 187, 1970.
357. Zulliger, H.R. and Aitken, D., "The Linearity of the Charge Conversion Function for Cooled Lithium-Drifted Silicon Detectors in Response to X-Ray and Low Energy Gamma Ray Excitation," IEEE Trans. Nucl. Sci. NS-14(1): 563, 1967.
358. Zulliger, H.R. and Stewart, J.E., "X-Ray Fluorescence Analysis with Transmission Target Tubes," Advances in X-Ray Analysis 18: 278, 1975.
359. Zulliger, H.R. et al, "Electric Field Profile and Electron Drift Velocities in Lithium Drifted Silicon," Nucl. Inst. and Meth. 70(2): 125-133, 1969.
360. Zulliger, H.R., "Hole-Electron Production in Semiconductors," J. of Appl. Physics 42(13): 5570, Dec. 1971.
361. Zulliger, H.R., et al, "Electric Field Profile and Electron Drift Velocities in Lithium-Drifted Silicon," Nucl. Instr. and Meth. 70(2): 125, 1969.
362. Zulliger, H.R., Drummond, W.E., and Middleman, L.M., "Properties of Ion-Implanted Silicon Detectors," IEEE Trans. Nucl. Sci. NS-19(3), 1972.
363. Zulliger, H.R., Middleman, L., and Aitken, D., "Linearity and Resolution of Semiconductor Radiation Detectors," IEEE Trans. Nucl. Sci. NS-16(1): 47, 1969.

## Author Index

- Adar, F., 165  
 Aden, G. D., 254  
 Albee, A. L., 227  
 Aratama, M., 30  
 Armigliato, A. 43  
 Bacon, F., 318  
 Barbi, N. C., 285  
 Becker, R. P., 3  
 Benner, R. E., 191  
 Blaha, J. J., 173  
 Bohning, J. E., 114  
 Bolon, R. B., 204, 310  
 Brandis, E. K., 311  
 Brown, J. D., 238, 241  
 Burns, M. S., 61  
 Buseck, P. P., 254  
 Carpenter, R. L., 8  
 Carter, H. W., 1  
 Casciani, F. S., 169  
 Chambers, W. F., 279  
 Chang, R. K., 191  
 Conty, C., 91, 281, 343  
 Cunningham, W. C., 148  
 Cvikevich, S., 39  
 Davidson, D. L., 22  
 DeGroot, P. B., 321  
 DeNee, P. B., 8, 11  
 DeNicola, D. B., 11  
 Desalvo, A., 43  
 Dhamelincourt, P., 155  
 Dornhaus, R., 191  
 Doyle, J. H., 279  
 Dudek, H. J., 211  
 Duraud, J. P., 145  
 Edie, J. W., 81  
 Etz, E. S., 148, 169, 173  
 Farrow, R. C., 141  
 Fiori, C. E., 361  
 Fontaine, J. M., 145  
 Fricke, W. G. Jr., 218  
 Fukuhara, S., 319  
 Gerlach, R. L., 315  
 Gill, M. E., 204  
 Giraud, R., 91  
 Glick, P. L., 81  
 Gold, C. M., 273  
 Goldstein, J. I., 119, 124  
 Gourgot, J. M., 343  
 Gray, G., 218  
 Guo, F., 333, 341  
 Hayashi, S. R., 310  
 Heinen, H. J., 63  
 Heinrich, K. F. J., 201, 221  
 Henoc, J., 91, 281  
 Hinkebein, T. E., 103  
 Hirschfeld, T., 196  
 Hlava, P. F., 103  
 Hovland, C. T., 315  
 Hutcheon, I., 338  
 Ichimura, S., 30  
 Jackson, A. G., 215  
 Johnson, J. K., 354  
 Joy, D. C., 141  
 Kaufmann, R. L., 63  
 Kelly, J. F., 15  
 Koffman, D. M., 47  
 Kotera, M., 35  
 Krisch, T., 241  
 Kriz, J. F., 110  
 LaForce, R. W., 350, 354  
 Landon, D. O., 185  
 Lankford, J., 22  
 Lechene, C., 59, 73  
 Lee, R. J., 15  
 Le Gressus, C., 145  
 Lepareur, M., 343  
 Long, M. B., 191  
 Love, G., 197  
 Lyman, C. E., 135  
 McCarthy, J. J., 305, 307  
 McConnell, M. D., 204  
 McConville, B. E., 80  
 Maenhaut, W., 265  
 Maher, D. M., 141  
 Mamane, Y., 139  
 Marcus, H. L., 317  
 Marinenko, R. B., 221  
 Marntin, B., 85  
 Mehta, S., 119  
 Miller, N. C., 47  
 Mitchell, M. J., 165  
 Montgomery, K. L., 27  
 Morris, W. G., 318  
 Mosley, W. C. Jr., 101  
 Murata, K., 35  
 Musket, R. G., 324  
 Myklebust, R. L., 51, 201, 231, 243  
 Nagami, K., 35  
 Newbury, D. E., iii, 51, 231, 243, 335  
 Nullens, H., 265  
 Okajima, Y., 319  
 Packwood, R. H., 110  
 Pajon, D., 91  
 Pande, S. C., 129  
 Patmore, D. J., 110  
 Pellerin, F., 145  
 Pickrell, J. A., 11  
 Pihl, C., 39  
 Platz, R. M., 77  
 Pueschel, R., 139  
 Quinton, P. M., 73  
 Ramsey, J. N., 165  
 Raymond, R. Jr., 105  
 Rebar, A. H., 11  
 Remond, G., 91  
 Rez, P., 117  
 Rinaldi, R., 43  
 Robinson, W. H., 238  
 Romig, A. D. Jr., 119, 124  
 Rosa, R., 43  
 Rosenstiel, A. P. von, 241  
 Ruegg, F. C., 221  
 Ruffini, G., 43  
 Russ, J. C., 259, 268, 292  
 Sabatini, R. L., 129  
 Sakitani, Y., 319  
 Savoy, R. J., 17  
 Schilling, J. H., 345  
 Schürmann, M. W., 63  
 Scott, R. H., 321  
 Scott, V. D., 197  
 Shaw, H. F., 227  
 Shimizu, R., 30  
 Short, J. M., 350  
 Shuman, H., 54  
 Skinner, D. P., 285  
 Small, J. A., 243  
 Smith, D. G. W., 273  
 Somlyo, A. P., 54  
 Somlyo, A. V., 54  
 Sparrow, G. R., 325  
 Statham, P. J., 247  
 Steele, I., 338  
 Strausser, Y. E., 324  
 Strobe, M. B., 215  
 Todokoro, H., 319  
 Tong, M., 91, 281  
 Tormey, J. McD., 27  
 Van Espen, P., 265  
 Vogel, G., 3  
 Ward, S. M., 27  
 Warner, R. R., 73  
 Wechsung, R. M., 63  
 Wells, O. C., 17  
 Wildman, H. S., 311  
 Willenborg, D. L. 27  
 Williams, D. B., 119  
 Wittry, D. B., 333, 341  
 Zoller, W. H., 148

## *NOTES*

*NOTES*



*NOTES*

## *NOTES*